11th International Biennial Conference on Physics of Estuaries and Coastal Seas

Extended Abstracts

Edited by
Hans Burchard, Beate Gardeike, Iris Grabemann, Jens Kappenberg

CONTENTS

CONTENTS

Revising the Paradigm of Tidal Analysis – the Uses of Non-Stationary Data

DAVID A. JAY

(Department of Environmental Science and Engineering, OGI School of Science and Engineering, Oregon Health & Science University, Portland, OR 97006-8921, djay@ese.ogi.edu)

TOBIAS KUKULKA

(Department of Environmental Science and Engineering, OGI School of Science and Engineering, Oregon Health & Science University, Portland, OR 97006-8921, kukulka@ese.ogi.edu)

1. Introduction

Tidal analyses have focused on the stationary component of time-series of scalar or vector observations. There are probably two reasons for this emphasis. First, only the stationary variance lends itself to easy prediction from astronomical forcing. Second, conventional analysis methods provide little information about the non-stationary variance. These methodological factors have tended to solidify an opinion that tidal time-series (particularly those of surface elevation) are basically stationary, with non-stationary components being regarded as meaningless "noise". Even the most regular surface elevation time-series are mildly chaotic, and tidal currents are often very non-stationary. A number of factors contribute to this non-stationary behavior: internal tides, atmospheric forcing at tidal frequencies, river flow, sea-ice and atmospheric modulation of tidal processes, and time-variable stratification. Not only is such variability present in many tidal records, this alleged "noise" contains useful information regarding both tidal and non-tidal processes. Moreover, tidal analysis of "non-tidal" processes (e.g., biological and sediment transport) is also often a worthwhile exercise. Several examples of the utility of the non-stationary component of tidal time-series are discussed; the results have in each case been derived using continuous wavelet transform tidal analysis methods.

2. River Tides and Climate

Climate studies frequently use river-flow time-series to represent the terrestrial manifestations of climate change and climate cycles. River flow time-series are unfortunately often short, limiting the climate information that can be derived from their analysis. River flow exerts, however, subtle effects on tides, particularly on the overtide structure. Thus, for stations where the tidal data record is longer than the river-flow record, it may be possible to lengthen the historic flow record using hourly surface elevation observations. The tidal record for Astoria (near the mouth of the Columbia River) extends back to 1853. We hope to reconstruct river flow from 1853 to 1929 (the beginning of river flow estimates for the whole Columbia River basin) to make Columbia River flow the longest instrumental climate record for the West Coast of North America. This approach also provides an estimate of river flow closer to the sea than is available from conventional river gauges, which are often located landward of tidal influence. In high precipitation coastal areas, the flow affecting the estuary may be substantially larger than that recorded by the most seaward gauge. In the Columbia, the flow at the mouth can (during winter storms) be 25% greater than the flow at the most seaward river-flow gauge (~85 km from the mouth). Figure 1 shows that useful river flow hindcasts can be achieved from wavelet tidal analyses, with averaging over 7 to 30 d, depending on the desired accuracy. In this case, the quarterdiurnal (D_4) to semidiurnal (D_2) amplitude ratio was employed. Predictions are adequate for flow levels from somewhat below average to maximum (6,000 to 29,000 m^3s^{-1}). Other data analysis schemes may allow predictions for lower flows. In this case, analyses of non-stationary tides provide valuable information regarding the process modulating the tides.

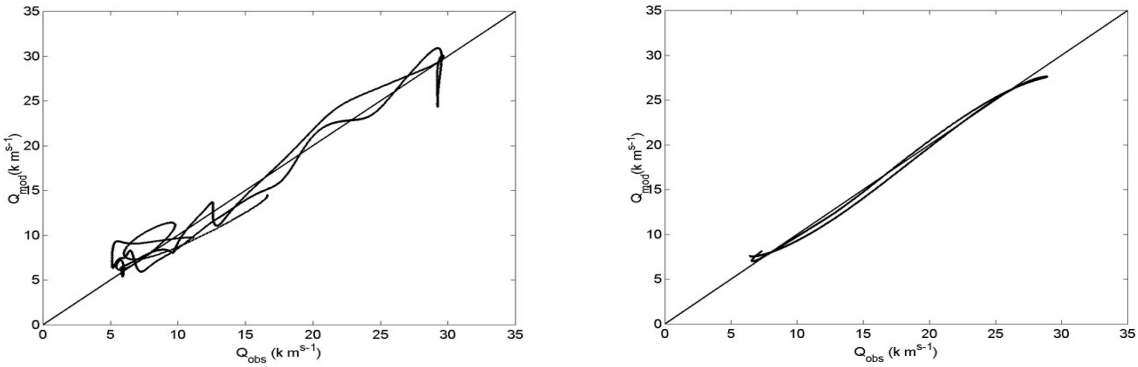

Figure 1: Comparison of routed river flow vs. river flow hindcast from tidal analyses for 1948; left: 7 d average flow; right; 30 d average flow. 1948 had the highest spring flows in the last century.

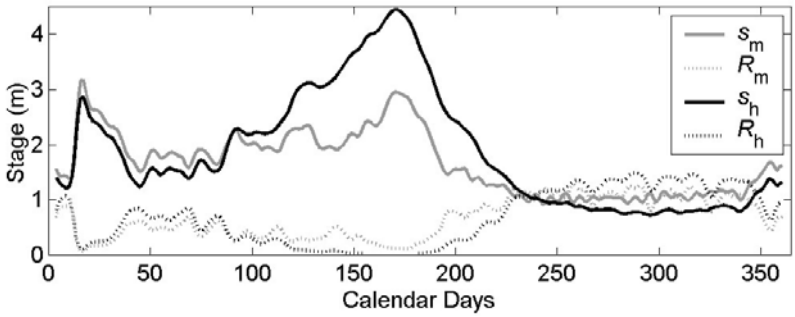

Figure 2: Human alteration of river stage *s* and tidal range *R* in 1974 for a station 85 km from the ocean; *m* indicates modern (observed) conditions, *h* is historic conditions that would have occurred without human alteration of the flow. Modern freshet stage is 1-1.5, m lower and tides are twice historic values.

3. River Tides and Habitat

The interaction of tides and flow in a tidal river has important biological impacts, and human intervention in the flow cycle may have unexpected effects. Flow regulation, irrigation withdrawal and climate change have reduced peak spring flow in the Columbia River to about 55% of its 19th Century value. Winter flows have increased. The spring freshet season was historically an important period of the seaward migration of juvenile salmonids. High spring flows allowed migrating juveniles to access a broad flood plain along the tidal river, as well as providing organic matter, nutrients and micronutrients that enhanced estuarine and coastal productivity during or after the freshet. High turbidity levels may also have reduced predation on juvenile salmonids by visual feeders like seabirds, and encouraged production of alternative prey in the coastal ocean through increased regional production. We have analyzed historic changes in river stage and river tides, and their habitat impacts. A compact method of hindcasting river tides was developed in the process. Prediction is possible to the degree that future river flow is known. Inputs for hindcast or prediction of tides at a fluvial station are coastal tides and river flow.

The method is, because of its compact form, particularly useful for understanding impacts of human management of the system over seasonal to decadal scales. During high-flow years, reduced flows have decreased river stage by 1-3 m in the tidal river. Because of the strong damping of tides by river flow, reducing river flow also increases tidal range. The result is that shallow-water habitats are now at a different elevation and have different tidal properties than was historically the case (Figures 2 to 4). Efforts to restore salmon habitat must take these changes into account. Unless the historic flow cycle were restored, removing dikes would result in winter (not-spring) inundation of former flood-plain habitats. Conversely, restoring historic flow patterns without removing dikes would greatly decrease the area of shallow-water habitat during spring in high flow years like 1880 and 1974, because the limited amount of habitat outside of dikes would be deeply submerged.

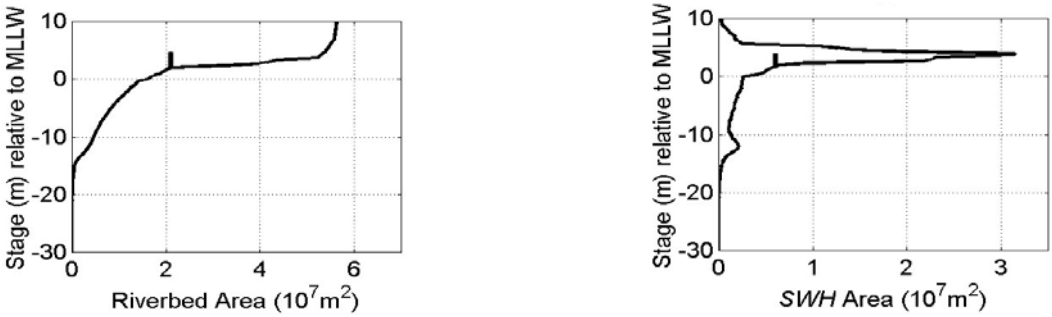

Figure 3: Left: the hypsometric curve km-60 to 90; right: shallow water habitat *SWH* area as a function of stage *s*; the vertical segment shows the position of dikes. Modern stage rarely overtops the dikes to access the floodplain. Historic freshet flows would now lap up against the dikes, eliminating most *SWH* area.

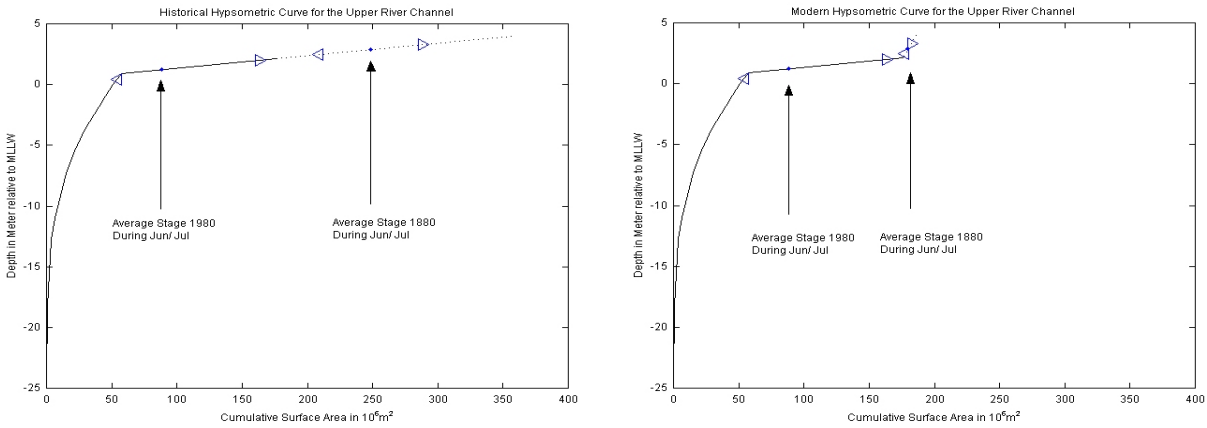

Figure 4: Comparison of extent of total lower-river shallow water habitat area during the 1880 and 1980 spring freshets; left: without dikes, right with dikes that prevent inundation of the flood plain.

4. Evaluating Environmental Impacts

Non-stationary tidal properties can also serve as indicators of human impacts in situations of regulatory interest. In Morro Bay, CA, analyses of tidal currents show that river flow modifies the tidal regime of the interior of the bay where shoaling has occurred in recent decades (Figure 4). Increased river flow causes weaker alongchannel tidal currents through frictional damping of the tides, with an enhanced D_4 wave. In contrast, variations in intake flow at the power plant at the mouth of the bay do not appreciably influence tidal processes in the interior of the bay. Impacts of the power plant on circulation in the interior of the bay are minimal because the power plant is located at the mouth of the bay where channels are relatively deep, whereas river flow enters the shallow interior of the bay. Because river flow is usually small (1-10 $m^3 s^{-1}$) and less than the maximum intake flow volume (~30 $m^3 s^{-1}$), the sensitivity of the test is clear. Again, analyses of non-stationary tides inform us regarding non-tidal process.

5. Analyses of Sediment Transport

Estuarine sediment transport is an example of a process primarily controlled by the tides (mean flow speeds would rarely suffice to move sediment without tidal flow), yet with sufficient additional factors and non-linear influences that the resulting signal is rarely stationary even during periods of relatively stable river flow. Figure 6 shows estuarine turbidity maximum (ETM) tidal and non-tidal suspended partiulate matter (SPM) transport from May to November 1997. The May-June 1997 freshet was the strongest since 1974, causing strong SPM export (negative values in Figure 6). By d. 210, flows had returned to stable, seasonal levels, yet the sediment transport thereafter responds to non-tidal

influences (e.g., wind waves re-suspension in peripheral areas) such that the resulting mean and tidal transports are episodic. They could not be predicted or accurately described using conventional tidal analysis tools.

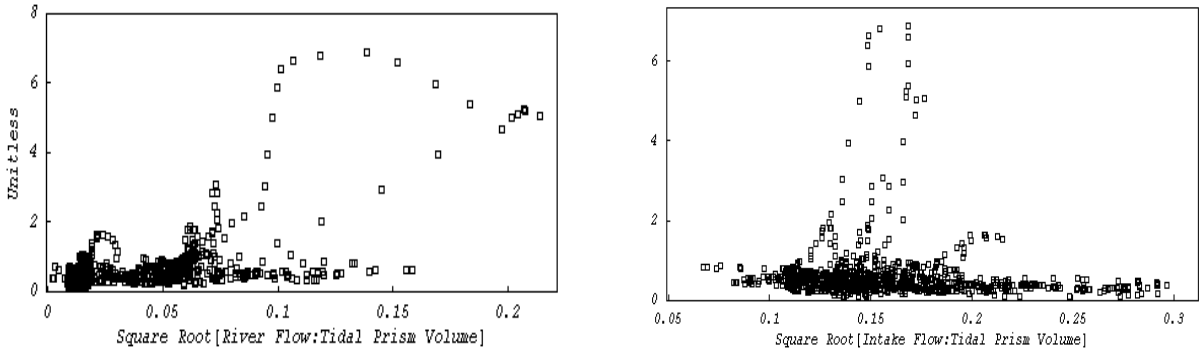

Figure 5: D_4 alongchannel current impedance amplitude vs. (left) the square root of river flow to tidal prism ratio and (right) the square root of power plant intake flow to tidal prism ratio. Anomalous high values at right correspond to high-flow periods.

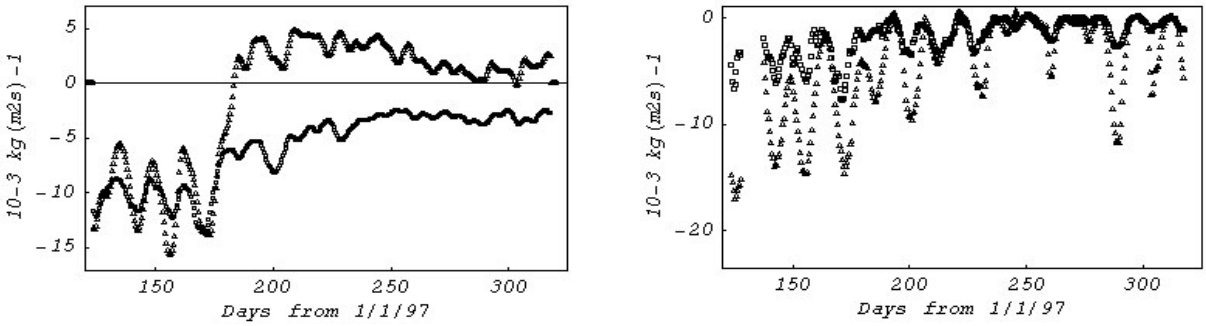

Figure 6: Subtidal (left) and tidal (right) SPM transport in the Columbia ETM at surface (□) and bed (▽)

6. Perspective on the Uses of Non-Stationary Tides

Consideration of these examples of non-stationary tidal processes suggests two lessons. The first is that the non-stationary part of tidal signals contains valuable information regarding the tidal response to non-tidal influences and the non-tidal processes as well. The second point is that the assumption of stationarity is actually a handicap when the signal is manifestly non-stationary. It was, for example, possible to achieve a compact and accurate method to predict river tides because the assumption of stationarity was abandoned, and the apparatus of tidal constituents with it. When one recognizes a signal as non-stationary on times scales of days to weeks, then tidal constituents become useless. Tidal constituents are useful as a means to represent the variability of tidal species only when tides are stationary over a long enough period (15 –30 d) to allow separation of the major constituents within the diurnal (D_1) and D_2 species. The species themselves are more robust. They remain useful up to the point where the modulation of tidal processes by external forcing is so rapid that D_1 and D_2 can no longer be separated. This occurs when the spectrum of the non-tidal forcing extends from the subtidal up into the tidal band. Prediction of stationary tides is much the most successful form of geophysical prediction ever devised. Precisely because tidal prediction has been so successful it is useful, possible, and necessary to move on to non-stationary tidal processes for new insights.

Acknowledgments: Development of wavelet tidal analysis tools and sediment transport analyses were supported by the National Science Foundation. Applications were supported by the National Marine Fisheries Service, the US Army Engineers, and Duke Energy North America.

Observations of the spring-neap modulation of the estuarine circulation in a partially mixed estuary

Cesar H. A. Ribeiro, Joanna J. Waniek and Jonathan Sharples, (*School of Ocean and Earth Science, Southampton Oceanography Centre, Southampton, SO14 3ZH, United Kingdom*, char1@soc.soton.ac.uk)

1 Introduction

Long-term mean circulation within an estuary is often considered as being driven by the gravitational circulation, with fresher water flowing seaward on the top of the near-bed denser seawater, which flows into the estuary. This process competes with tidal, wind and internal mixing in controlling stratification. Modulation of tidal mixing on the spring-neap cycle has been shown to lead to similar modulation of stratification [*Simpson et al.*, 1990]. Wind-induced mixing also affects vertical stability and may extinguish the gravitational flow [*Goodrich et al.*, 1987].

Theoretical work [*Nunes Vaz et al.*, 1989] and laboratory experiments [*Linden and Simpson*, 1988] suggest that the development of stratification during periods of low mixing occur alongside acceleration of the gravitional circulation. Just recently this behaviour has been observed during a semi-diurnal cycle, where pulses of estuarine circulation followed the combined changes in the turbulent mixing and the longitudinal density gradient [*Stacey et al.*, 2001]. Hence modulation of the estuarine circulation might be expected following the variability of the vertical mixing on other time scales.

Here we present a 71-day time-series of tidally-averaged flow, calculated from an ADCP dataset, and illustrate its relationship both with *in situ* stratification and with the strength of the mixing. It is shown that the estuarine circulation in Southampton Water is modulated by the spring-neap tidal cycle and is also affected by wind-induced mixing and by abrupt non-tidal changes in the water level in the adjacent coastal water.

2 Data sampling and analysis

Southampton Water is a partially mixed estuary in southern England. It has a monthly cycle alternating stronger and weaker springs and neaps, due to the relatively high amplitude of the N_2 harmonic combined with a weak M_2 constituent. The estuary is straight, approximately 10 km long and 1 km wide, following a NW-SE orientation, and its main channel is dredged to 14 m depth at lowest tide. The tidal range varies from 4.5 to 1.5 m, and maximum depth-averaged currents within a semi-diurnal cycle range from 1.0 ms^{-1} at strong spring ebb to 0.2 ms^{-1} at weak neap ebb.

A mooring was deployed for 71 days, halfway along of the estuary beside the main shipping channel at a depth of 8 m at spring low water. The mooring consisted of a 1200 kHz ADCP on the estuary bed and two Brancker XL-210 conductivity-temperature probes, one placed at 1.0 m below the surface (attached to a navigation buoy) and one at 0.5 m above the estuary bed (on the ADCP frame). The ADCP recorded data in 25-cm bins every 4 min and the C-T sensors sampled every 10 min. Water level time-series were

obtained from two tide gauges, one at each end of the estuary sampling every 12 min. The astronomical tide was eliminated in the tide gauge time-series and the water level slope between the head and the mouth of the estuary was calculated from the non-tidal water level variability. Meteorological data were acquired at a station 4 km up estuary from the mooring site.

Least-squares tidal harmonic analysis was applied to normalised depth velocities, interpolated onto a fixed vertical axis ($\eta = z/H$, with H the total depth) in order to remove the short-term variability of water depth. This analysis was carried out by running a 12.5 hour window through the time-series and sliding it forward by an one-hour time step. This semi-diurnal harmonic analysis included the semi-diurnal frequency (M_2) and several shallow water components. The aim of this running-window harmonic analysis was to calculate profiles of u_o, the mean current over a tidal cycle, for each η by using

$$u_{(\eta)} = u_{o(\eta)} + \sum_{i=1,N} A_{i(\eta)} \cos(\omega_i t + \phi_{i(\eta)}) \qquad [\mathrm{ms}^{-1}] \tag{1}$$

where A_i, ω_i and ϕ_i are respectively the amplitude, frequency and phase of the i harmonic constituent.

3 Results

The calculated mean surface and near-bed velocities for the period of 71 days show the behaviour of the non-tidal flow over five consecutive spring-neap cycles (Fig.1). A consistent, bi-directional signal of the estuarine circulation was observed only during two weak and one strong neap tides in the series (days 77, 92 and 106). No clear signal of the estuarine circulation was present during the first and the fifth neap tides (days 63 and 121), both strong neaps characterised by a maximum velocity within a semi-diurnal tidal cycle higher than 0.4 ms^{-1}.

A weak bi-directional non-tidal flow was present at the early second neap tide for 1.5 days (days 76 to 78), but it collapsed with a sudden rise of the non-tidal water level in the whole estuary (25 cm in 3 hours). This surge also caused a rapid reduction in the stratification, and reversed the non-tidal barotropic gradient in the estuary, from a mouth-to-head to a head-to-mouth surface slope. No asssociated wind event was observed.

On the third neap tide a strong pulse of estuarine circulation occurred for 24 hours (day 94). During this period the tidal current amplitude was less than 0.4 ms^{-1} and the wind had weakened after a strong event when winds from the south peaked up to 30 ms^{-1} for 24 h. Stratification also increased during this short period, decreasing later following the collapsing of the estuarine circulation when strong winds resumed.

Prolonged calm weather conditions were present during the onset and persistence of the estuarine circulation for six days (days 104 to 110) at the forth neap tide. The end of this mean circulation feature occurred simultaneously with the increase of the near-bed velocity ($u_b > 0.4$ ms^{-1}) and it seems to have been caused by greater tidal mixing towards the next spring tide. At the same time the continuous decrease in the bottom-surface density difference also suggests this vertical mixing.

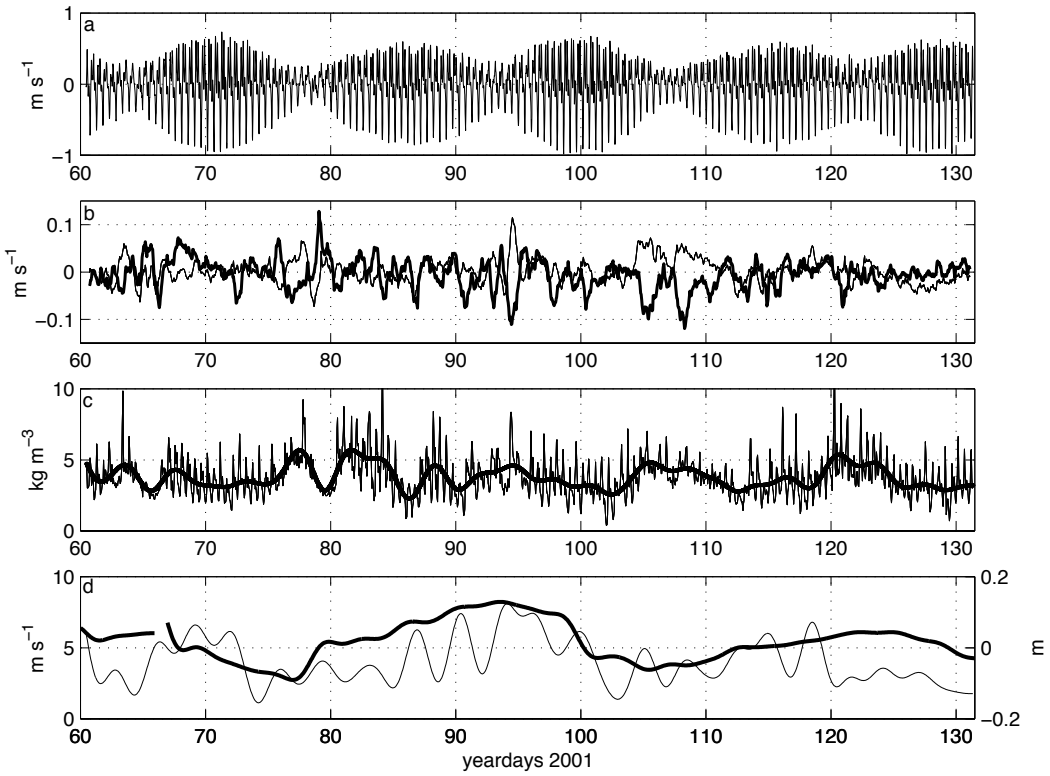

Figure 1: Time-series of the depth mean along estuary velocity (a), the surface (bold line) and bottom (thin line) tidally averaged velocities (b), the 1-hour mean and 72-h filtered bottom-surface density difference (c) and the 72-h filtered wind speed (thin line) and non-tidal water level difference between the head and the mouth of the estuary (bold line) (d). Seaward velocities are represented by negative values. Positive slope indicates higher water level at the head of the estuary.

4 Conclusions

The results show the variability of estuarine circulation related to the reduction of the turbulent mixing driven by both tide and wind. The observation of the onset, persistence and destruction of the estuarine circulation, particularly at the forth neap-to-spring cycle (days 104 to 111), clearly illustrated the relation between the turbulent mixing and the gravitational mean flow. The effects of the vertical mixing effects on eliminating the estuarine circulation were successfully observed, as shown by Linden and Simpson [1988] in laboratory experiments. Our results suggested a monthly modulation of the estuarine circulation in Southampton Water, with pulses of net transport following the two-layer circulation on the weaker currents ($u_b < \pm$ 0.3 ms^{-1}) at neap tides. However the occurrence and duration of these net fluxes are conditioned by the vertical mixing induced by wind and by the non-tidal variability of the water level in the coastal region adjacent to the estuary.

Acknowledgments: The authors would like to thank the crew of *R.V. Bill Conway* and to the ABP for the tide gauges dataset. This work was supported by NERC and C. H. A. Ribeiro had a personal grant from CNPq.

References:

Goodrich, D. M.; W. C. Boicourt; P. Hamilton and D. W. Pritchard, Wind-induced destratification in Chesapeake Bay, *Journal of Geophysical Research*, *17*, 2232-2240, 1987.

Linden, P., and J. E. Simpson, Gravity-driven flows in a turbulent fluid, *Journal of Fluid Mechanics*, *172*, 481-497, 1986.

Nunes Vaz, R. A., G. W. Lennon and J. R. de Silva Samarasinghe, The negative role of turbulence in estuarine mass transport, *Estuarine, Coastal and Shelf Science*, *28*, 361-377, 1989.

Sharples, J. and J. H. Simpson, Semi-diurnal and longer period stability cycles in the Liverpool Bay region of freshwater influence, *Continental Shelf Research*, *15*, 295-313, 1995.

Simpson, J. H.; J. Brown; J. Matthews and G. Aleen, Tidal straining, density currents, and stirring in the control of estuarine stratification, *Estuaries*, *13*, 125-132, 1990.

Stacey, M. T.; J. Burau and S. G. Monismith, Creation of residual flows in a partially stratified estuary, *Journal of Geophysical Research*, *106*, 17013-17037, 2001.

The role of the tide on the salt wedge displacement and mixing in the Itajaí estuary, southern Brazil

CARLOS A.F. SCHETTINI

(Center of Earth and Marine Sciences, University of Vale do Itajaí, C.P.360, 88302.202, Itajaí, SC, Brazil, guto@cttmar.univali.br)

KLAUS RICKLEFS

(Research and Technology Centre Westcoast, University of Kiel, Hafentoern, 25761, Buesum, Germany, ricklefs@ftz-west.uni-kiel.de)

RODRIGO ZALESKI

(Center of Earth and Marine Sciences, University of Vale do Itajaí, C.P.360, 88302.202, Itajaí, SC, Brazil, a.r.z@bol.com.br)

STEFAN BRANDT

(Research and Technology Centre Westcoast, University of Kiel, Hafentoern, 25761, Buesum, Germany)

1. Introduction

The Itajaí estuary is a microtidal salt-wedge type, river dominated where the main transport mechanism is the fluvial advection. The regime of the fluvial discharge is irregular along the time, with random distribution of flood peaks as response of the sub-tropical weather instabilities. On general basis, the estuarine hydrodynamics can be distinguished in two main modes. There is a intermediate to high discharge periods mode, which usually lasts for hours to few days and are highly dominated by the river freshet, and the low discharge mode observed between the flood peaks, which can lasts for several months (Schettini, 2002).

The river discharge is the main driven determinant of estuarine hydrodynamics in general terms. The salt intrusion follows an inverse and non-linear relationship with the river discharge. During prolonged low discharge periods the salt intrusion can reach more than 30 km upstream. During mean discharge periods the salt intrusion is about 15-20 km upstream. When the discharge exceed 1000-1200 $m^3.s^{-1}$ all salt water is flushed out of estuarine basin (Schettini & Truccolo, 1999). The position of salt intrusion is not a simple function of the river discharge, but also is a function of the time elapsed since the last flash flood.

During periods of low river discharge the tide gain weight on hydrodynamics control. The role of the tide was previously assessed through some 25-hour experiments, given a site-specific interpretation. The objective of this paper is to assess the influence of the tide through the observation the salinity distribution along the all estuary in high and low tidal phases and along a complete spring-neap cycle.

2. Field data & data reduction

To evaluate the role of the tide it was performed daily during 15 days surveys twice a day, at low and high tide. Salinity vertical profiles were acquired every 1-1.5 km from the mouth to upstream of the salt intrusion using a real-time CTD probe ME-Grisard (www.me-grisard.de). Every survey was carried out in less than 1.5 hour, giving us a quasi-synoptic view of estuarine structure at a given tidal phase.

Daily river discharge data were obtained with the National Electric Energy Agency (ANEEL) for the Indaial lymnimetric station, situated at 90 km upstream of estuarine mouth.

The raw data acquired with the CTD probe were reduced for 0.25-m vertical resolution using Matlab routines (Mathworks, Inc.). The longitudinal salinity distributions were made using Surfer software (Golden Softwares, Inc.). The maximum salt intrusion of 2 and 30 ‰ isolines were extract then from these maps.

The mixing was evaluated by the total content of mixed water along the estuary. The mixed water was defined as the water with salt concentration between 2 and 30 ‰. Fresh and salt waters were those with salinity lesser than 2 and higher than 30 ‰, respectively. The proportion of water masses was achieved by measuring the area distribution of each other on the salinity distribution maps. The narrowness of the estuary, as well as the no existence of intertidal areas justifies this procedure.

3. Results

The Figure 1 presents a synthesis of the results. During the 15-day experiment the tidal height between consecutive surveys varied from 0.7 at the beginning and at the end of the period, to 0.2 at the middle, clearly indicating the spring-neap cycle (Figure 1A). The river discharge was low during the first 7 days, with a flash flood discharge peak at 8th day, disturbing the experiments. Even thus, we continue the experiment as we saw the opportunity to evaluate the estuarine response to the flash flood and the salt intrusion after that (Figure 1B).

During the first eight days of experiment, before the flash flood, the salt intrusion ranged from 17 to 21 km, considering the 2 ‰ isoline, and 4 to 12 km, considering the 30 ‰ isoline. Along this period the isolines of low and high water converges as the tidal height decrease, reaching the smallest difference about of 2 km at January 14th. After the flash flood peak, the isolines were pushed downstream up to 4 km from the inlet. The low water isolines stayed nearly stationary, mainly the 30 ‰, meanwhile the high water isolines just start move upstream after the flash flood cease and decrease to about 500 $m^3.s^{-1}$ (Figure 1C).

The content of mixed water in the estuary varied according the variation of the tidal height and the river discharge as well (Figure 1D). During the period before the flash flood, the content of mixed water increased from high water to low water. A steady behavior was observed during the first five-day period, with about 50 % of mixed water at high water, and about 80 % at low water. During these days the tidal height were higher than 0.5 m. At the 6th day, the tidal height decreased bellow 0.4, and since then the content of mixed water was practically the same for both high and low water, and slightly lesser than in previous days. After the flash flood peak the content of mixed water during the low water became smaller than the high water, staying like this until the end of the experiment when they reverse again although staying close each other.

The relationship between tidal height of consecutive surveys and the displacement of the salt intrusion is presented in the Figure 2, regarding to both limits of 2 and 30 ‰. There is a significant difference between them, where the 30 ‰ reference appears to be more efficiently controlled by tide than the 2 ‰. The explanation coefficient for the former was $r^2 = 0,76$, meanwhile for the latter it was $r^2 = 0,14$. The curve slopes also demonstrate the higher tide dependence of the 30 ‰ horizontal displacement than the 2 ‰.

The results support partially the hypothesis that tide do not play a role in the estuarine hydrodynamics. This is thru when the tidal height is less than 0.4 m, when the salt intrusion can be close of a salt wedge at a rest. On the other hand, when the tidal heigh is higher than 0.5 m, it appears that the estuary experiment periods of intense mixing during the ebb phase (e.g., Dyer, 1997), when the content of mixed water increase.

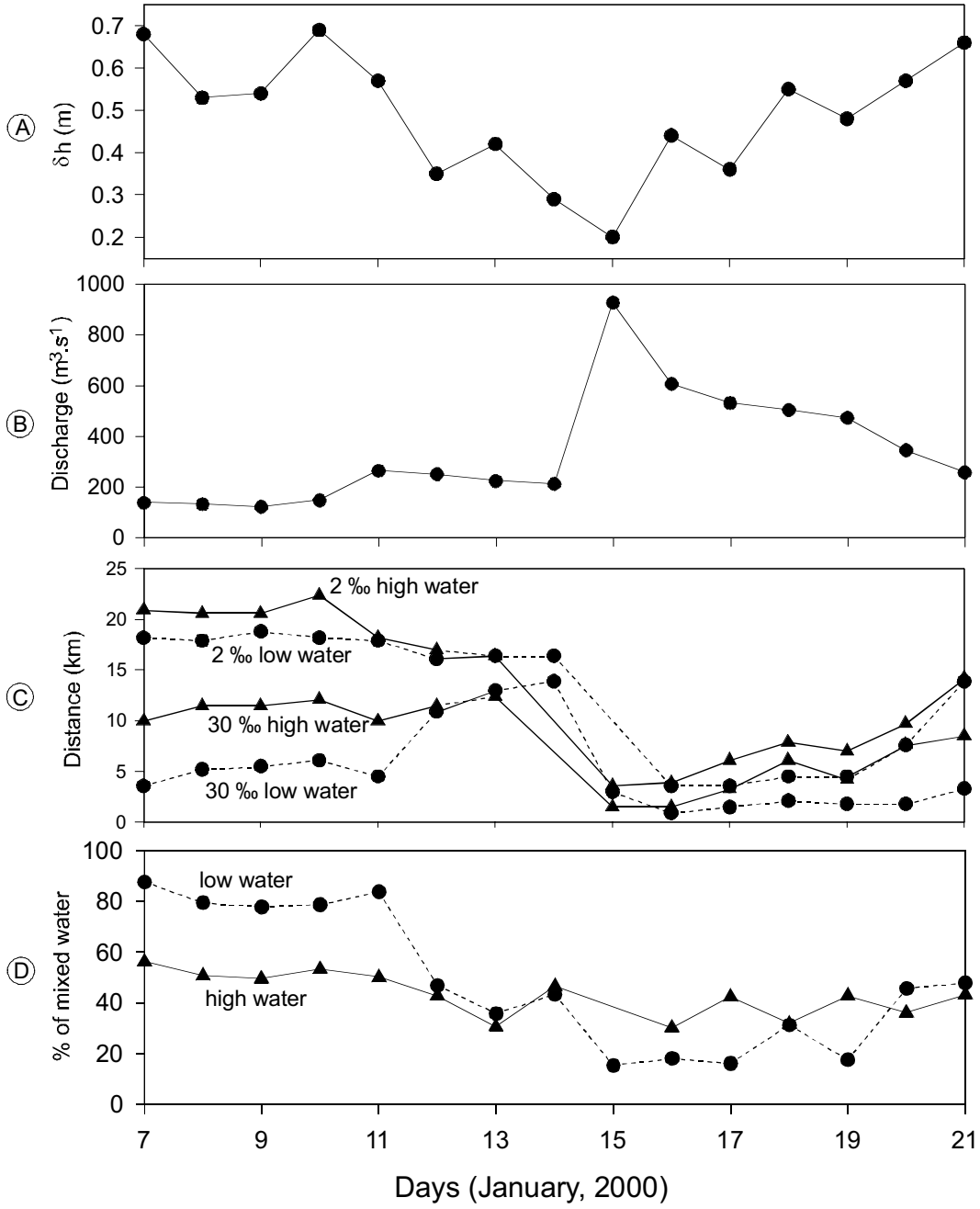

Figure 1:(A) daily tidal heigh, (B) river discharge, (C) 2 and 30 ‰ haloclines horizontal position and (D) mixed water content in the estuary along the fortnight monitored period.

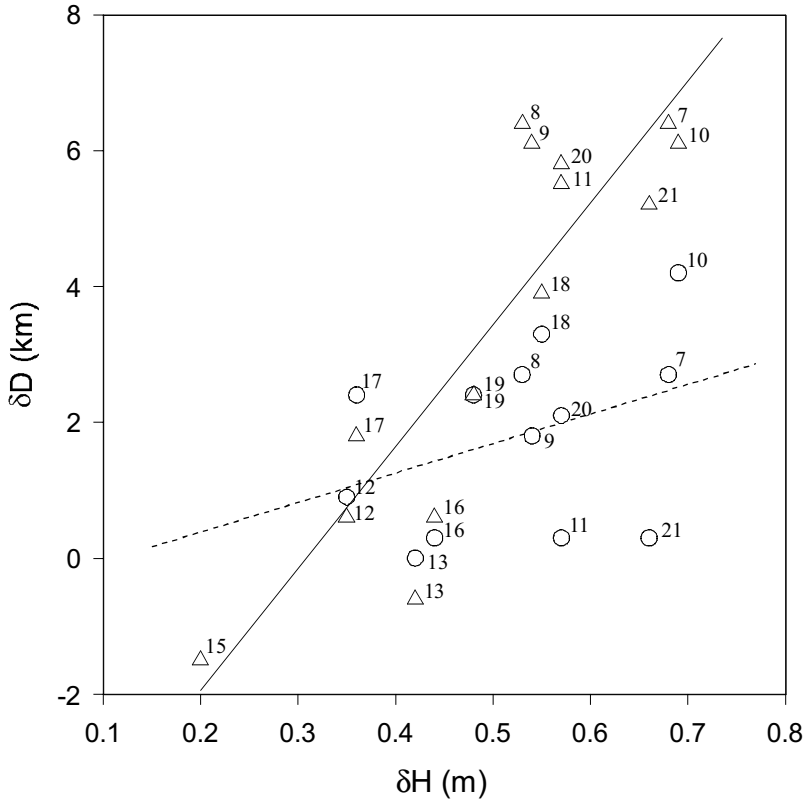

Figure 2: Relationship between the tidal height and 2 (circles) and 30 ‰ (triangles) isolines horizontal displacement. The numbers mean the month days.

Acknowledgments: The results presented here are part of the joint cooperation project "transport and transformation processes in the Itajaí estuary - Transit", between University of Kiel and University of Vale do Itajaí, funded by DLR/Germany and ProPPEx/Univali./Brazil.

References:

Dyer, K.R., *Estuaries, a physical introduction*, New York, John Wiley & Sons, 195p, 1997.

Schettini, C.A.F., Caracterização física do estuário do Rio Itajaí, *Revista Brasileira de Recursos Hídricos*, 7, 123-142, 2002.

Schettini, C.A.F. & Truccolo, E.C. Dinâmica da intrusão salina no estuário do Rio Itajaí-açu. In: Congresso Latino Americano de Ciências do Mar, 8, Trujillo, Perú, Resumenes ampliados…Tomo II, UNT/ALICMAR, p639-640, 1999.

Spatial Structure of Secondary Flow in a Curving Channel

SUSAN A. ELSTON

(School of Earth & Atmospheric Sciences, Georgia Institute of Technology, Atlanta, Georgia, and Skidaway Institute of Oceanography, Savannah, Georgia, United States, susan@skio.peachnet.edu)

JACKSON O. BLANTON

(Skidaway Institute of Oceanography, Savannah, Georgia, United States, jack@skio.peachnet.edu)

HARVEY E. SEIM

(Department of Marine Sciences, University of North Carolina – Chapel Hill, Chapel Hill, North Carolina, United States, hseim@email.unc.edu)

1. Introduction

Secondary circulation (or secondary flow) in an estuary affects the dispersion and distribution of various properties along the channel axis. Among such properties, understanding the relationship between secondary circulation and its impact on the transfer and the distribution of momentum is fundamental. We examine the differences in the strength and distribution of secondary circulation in two adjacent channel bends of opposite curvature in order to diagnose how secondary circulation contributes to an increase in longitudinal momentum downstream.

Secondary circulation encompasses several mechanisms whose result is to vertically overturn the water column along the secondary (transverse) axis of a channel. A secondary circulation may be composed of one or more cells that could potentially act to reduce or enhance local gradients. A physical manifestation of secondary flow is often observed in the field as one or more foam lines down the longitudinal axis of an estuary.

Several mechanisms can generate a secondary flow. Most commonly, secondary flow can be attributed to channel curvature, planetary rotation (the Coriolis effect), frictional effects of irregular channel bathymetry or geometry, and/or the differential advection of density associated with the tides. Secondary flow resulting from channel curvature is driven by a local imbalance between the vertically varying outwardly directed centripetal acceleration and the cross-channel pressure gradient (Bathurst, Thorne, and Hey 1977). While the direction of cross-channel flow is invariant during flood and ebb, its strength differs depending on the orientation of the along-axis flow (cyclonic vs. anticyclonic) in the channel bend (Dyer 1997). A secondary circulation due to the frictional interaction with lateral and/or bottom boundaries is complex and often difficult to separate. Most often, frictional effects are parameterized and modeled with an eddy viscosity.

2. Study Area and Methods

This research was conducted in the Satilla River, a naturally sinuous coastal plain estuary that is one of the Georgia Land Margin Ecosystem Research sites (GA LMER) along the southeastern coast of the United States. In this study, we examined two differently curved domains (A and B) under neap and spring conditions. Domain A is a concave reach (bend to the north) located between 12 and 16 km from the mouth of the Satilla River in St. Andrews Sound and has a radius of curvature of approximately 1500 m. Domain B is a convex reach (bend to the south) adjacent to Domain A and is located between 16 and 20 km upriver from the ocean with a radius of curvature of approximately 800 m. In an effort to further discern features of the flow field, Domain A and B were subdivided into a series of lateral cross-sections, each approximately 1 to 2 km apart. We used a towed RD Instruments 600 kHz Acoustic Doppler Current Profiler (ADCP) to measure three-dimensional currents, a profiling

Falmouth Scientific Instrument Conductivity-Temperature-Depth (CTD) sensor, and a flow-thru Thermosalinograph (TS) system to capture synoptic variations in temperature, salinity, and bathymetry.

In order to describe the how the longitudinal momentum is transported laterally by secondary circulation, we systematically defined the along and cross-channel components of the flow field by rotating the towed ADCP data in each domain along the principal axis as defined by the mean cross-sectional depth averaged transport. The advantage to forming the principal axis in this manner is to properly weight the flow field for changes in bathymetry. The rotated component velocities were then multiplied by a constant density to form the quantities of axial (ρu) and transverse momentum (ρu) per unit volume. The lateral flux of along channel momentum per unit volume was formed by the product of the constant density and the along channel and cross-channel velocities (ρuv). This quantity is referred to as the flux of total momentum through a cross-section.

3. Results and Discussion

Secondary flow observed during this experiment varied between 25 cm s^{-1} and 75 cm s^{-1} on the fortnightly time scale. The highest transverse velocities were observed during spring tide in cross-sections where the ratio of the effective channel width to radius of curvature was near unity. For simplification, we consider four adjacent cross-sections (two in Domain A and two in Domain B) during maximum ebb at spring tide when the signal of secondary circulation in the Satilla is maximized.

In each cross-section, we found a persistent transverse circulation pattern that was consistent with secondary flow driven by channel curvature. In concave Domain A, near surface transverse velocities were directed toward the north while flow at depth was directed toward the south. Similarly, in convex Domain B, near surface transverse velocities were directed toward the south while flow at depth was directed toward the north.

Cores of maximum axial and transverse momentum were observed in each cross-section and increased in strength downstream. The core of maximum axial momentum was most often located in or near the shallows while the core of maximum transverse momentum was found shifted to the side of the axial momentum core, toward the outside of the channel bend. The observed cross-channel flux of total momentum is consistent with flow directed along the thalweg (i.e., the lateral flux of axial momentum is directed toward the deep channel) and when plotted as a vector diagram, this data resemble the transverse velocity flow pattern.

Observations of axial and transverse velocities are used to determine the reasonableness of the spatial and temporal characteristics of the secondary flow in the cross-sections. In a similar manner, the spatial and temporal attributes of changes in the location of core momentum between cross-sections are used to determine if a change in its location is consistent with flow due to secondary circulation. The continuity equation is used to calculate the vertical velocity and to provide a time estimate for the vertical transport of momentum by the transverse circulation. Assuming typical axial and transverse velocities for the Satilla River during this experiment (U = 1 m s^{-1}, V = 0.4 m s^{-1}), we determine that the vertical velocity (W) is 0.6 cm s^{-1}. Given this vertical velocity, the time for a water parcel in the secondary circulation to reach the bottom of the water column is 2500 s (~ 42 minutes), and it must travel an axial distance of 2.5 km to reach a position similar to its starting point in the transverse circuit. These results suggest that a secondary circulation can be best described as a three-dimensional helix in the axial direction, in contrast to a closed circulation cell at one location in space.

Next, using the observed axial velocity, the measured distance between adjacent cross-sections, and the measured lateral distance that the momentum core shifted at each cross-section, we calculated the lateral velocity. The calculated lateral velocities were consistent with the observed lateral velocities in each cross-section, including those significantly different due to changes in channel width and radius

of curvature. Based on our observations, we found that the time for a water parcel located in the core of momentum to reach the bottom of the water column was around 2100 s (35 minutes) and it traveled a distance of 2.2 km downstream before returning to a similar position in the transverse circulation. These results are consistent with the observed changes in the location of the core momentum between adjacent cross-sections. This suggests that secondary circulation is responsible for the observed lateral shifts in core momentum between the cross-sections in two opposing bends in a predictable, helical pattern. We illustrate the nature of the helical flow pattern in Figure 1, which is based on a realization of the observed momentum field at spring tide in Domain A during maximum ebb. Note that the lengths of the arrows in Figure 1 are different. They schematically represent the three-dimensional helical structure of the secondary circulation and demonstrate that there is an imbalance in the lateral flux of along channel momentum in the downstream direction (i.e., momentum increases downstream because of secondary flow).

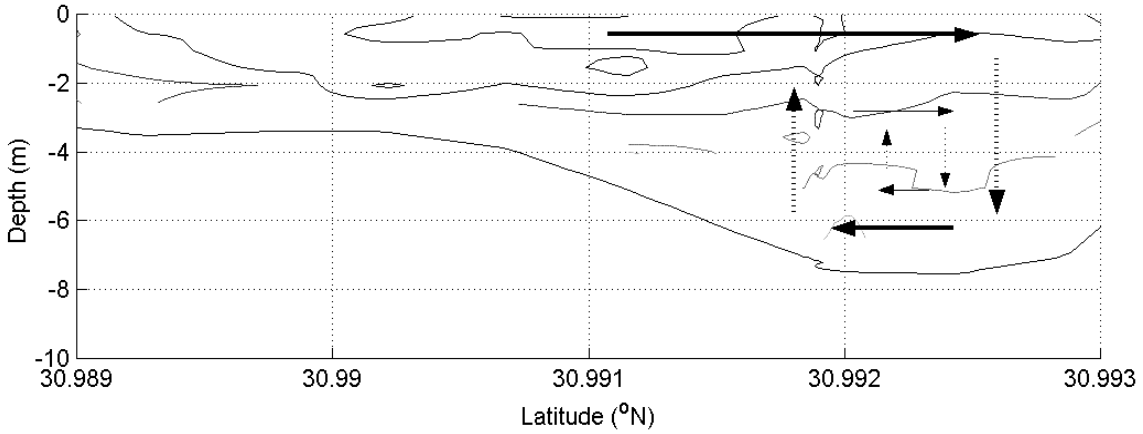

Figure 1: Schematic of momentum transfer in a lateral cross-section of the Satilla River by secondary circulation. The contours are of transverse velocity in m s^{-1}. The different length arrows are used to represent the three-dimensional helical nature of the secondary circulation and show that there is an imbalance in the lateral flux of along channel momentum in the downstream direction.

These results are consistent with our previous studies, which show that the primary mechanism for driving secondary flow in the Satilla is channel curvature. The observed secondary circulation pattern was as expected and as predicted by theory, in which transverse flow is to the outside of the channel bend at the surface and toward the inside of the channel bend at depth. Observed secondary flow in this estuary is considerably higher than simple scaling arguments would suggest and often varies on average between 30 cm s^{-1} and 50 cm s^{-1} on the fortnightly time scale. Observed secondary flow also varies within and between cross-sections due to varying effective channel width and local radius of curvature.

Our calculations for the transit time and the distance to complete a secondary circulation are smaller than but on the same order as those of Seim et al. (in press). They estimate that a water parcel starting near the centerline of the channel will take approximately 100 minutes to complete a circulation and will travel approximately 3 km downstream before it returns to its starting location in the transverse circulation. The differences between our results and those of Seim et al. (in press) are due primarily to differences in the timing, location, and nature of the two experiments. Observations by Seim et al. (in press) were based on a moored ADCP that sampled the flow field once every 15 minutes. Their observations were made in the deep channel for a 10-day period that ended shortly before the maximum spring tide. The design of their experiment focused on processes in the along channel direction and consequently did not capture any lateral information. The disparity in the observed axial velocities and resultant calculations between these two studies is due directly to the availability of this lateral data. Despite these differences, our results support the conclusions of Seim et al. (in press) that

the shape of the secondary circulation is helical and that when secondary flow is super-imposed on the axial flow field it leads to an increase in the flux of momentum in the downstream direction.

4. Conclusions and Implications

Our research supports previous studies and extends the understanding and description of the lateral variability in the 'spatial structure' of secondary flow. We demonstrate that secondary flow (secondary circulation) is best described as a helix down the axis of the estuary and that it has a non-negligible contribution to the momentum flux in the downstream direction. The implication is that the strength and presence of a secondary circulation significantly modifies the momentum balance and cannot be neglected. Knowledge of the role secondary circulation plays in changing the distribution of momentum will better enable us to predict important parameters such as the length of the salt intrusion and to determine the dispersion and distribution of various waterborne properties (e.g., larvae, sediment, and pollutants) in the estuarine environment.

Acknowledgements: The authors acknowledge the financial support of the Land Margin Ecosystem Research Program of the National Science Foundation (Grant No. DEB 9412089) to the University of Georgia and the State of Georgia through its Coastal Zone Management Program, and a Presidential Fellowship to the lead author from the Georgia Institute of Technology.

References:

Bathurst, J. C., C. R. Thorne, and R. D. Hey, Direct measurements of secondary currents in river bends, *Nature, 269,* 504-506, 1977.

Dyer, K. R., *Estuaries: A Physical Introduction, Second Edition*. Chichester, England: John Wiley & Sons, Ltd, 1997.

Seim, H. E., J. O. Blanton, and T. F. Gross, Direct stress measurements in a shallow, sinuous estuary, *Continental Shelf Research*, in press.

Oceanographic characteristics of Baia de Todos os Santos, Brazil: circulation, seasonal variations and interactions with the coastal zone

Mauro Cirano, (*Instituto de Geociências, Universidade Federal da Bahia, 40170-280, Salvador, Brazil*, mauro@cpgg.ufba.br)

Guilherme C. Lessa (glessa@cpgg.ufba.br)

1 Introduction

Baía de Todos os Santos (BTS) is a large coastal bay, situated at 12°50'S and 38°38' W, that borders part of the third major city in Brazil, Salvador (population of 3 million inhabitants), and the largest petrochemical complex in the southern hemisphere. The bay has an area of 1270 km^2 and an approximate maximum width (west-east axis) and length (north-south axis) of 32 and 50 km, respectively. The 30-year mean annual precipitation in Salvador is 2075 mm, but 44% of this amount falls between March and July. Average annual river discharge is 111 m^3 s^{-1}.

Despite its socio-economic relevance, only three papers (*Wolgemuth* [1981], *Montenegro* [1999] and *Lessa* [2001]), have been published on the oceanography of the bay. These papers dealt with the analysis of sparsely distributed (both in space and time) data and numerical modeling of the tidal circulation in the bay. Given the lack of good quality data, a comprehensive overview of the oceanographic characteristics of the BTS and its interaction with the coastal zone, is yet to be published in the scientific literature.

In the year of 1998 the State Government launched a large-scale water quality project in the bay that i) moored 30 instruments in 20 stations (Figure 1) to sample the velocity field, temperature, salinity and pressure for more than 15 continuous days during summer (dry) and winter (wet) seasons; ii) performed synoptic hydrographic cruises to evaluate the distribution of properties throughout the water column during a complete tidal cycle at spring and neap tides and iii) installed three meteorological stations around the bay. The velocity field was measured with (i) 16 Aanderaa RCM-7 and RCM-8 current meters, (ii) 10 InterOcean S4 current meters and (iii) 2 RDI ADCP profilers of 300 kHz. The pressure field, converted to elevation, was sampled with 3 SeaBird SBE-26 tide gauges and 5 high-resolution pressure sensors (0.4 cm) installed in some of the InterOcean S4 current meters. For the hydrographic cruises, water properties were sampled with 4 SeaBird SBE-19 CTDs.

The main goal of this article is to present the results of a comprehensive analysis of this data set, which will help us to determine the leading driving forces that regulate the water circulation inside the bay and around the adjacent coastal region.

2 Oceanographic Characteristics

2.1 Water Properties

During summer, the maximum difference in the mean temperature is up to 3°C between the warmest surface waters at station 1 (T = 29.9°C) and the relatively colder surface

waters at oceanic stations 9-12. In the water column, the vertical difference in the mean temperature is of the order of 0.1-0.4°C, and differences of more than 1°C are only observed at oceanic stations. Except for the region close to Paraguaçu Channel (station 4), and perhaps close to small rivers, the bay is dominated by oceanic water, with average salinities higher than 36.4. At the shelf region, the average salinity is always above 37. Worth mentioning is the above-average temperature and salinity at station 3, which suggests that i) evaporation rates were higher than precipitation rates in the preceding days and ii) residence times are high in that section of the bay.

Water properties during winter were quite distinct from those in summer, which is ascribed to the increasing local precipitation. Horizontal mean salinity differences at the surface were up to 4.2 between the northernmost station and the adjacent ocean. The vertical differences in the mean salinity are also more pronounced, with differences of more than 1 in various stations inside the bay. Compared to summer, the temperature distribution were more homogeneously distributed throughout the region.

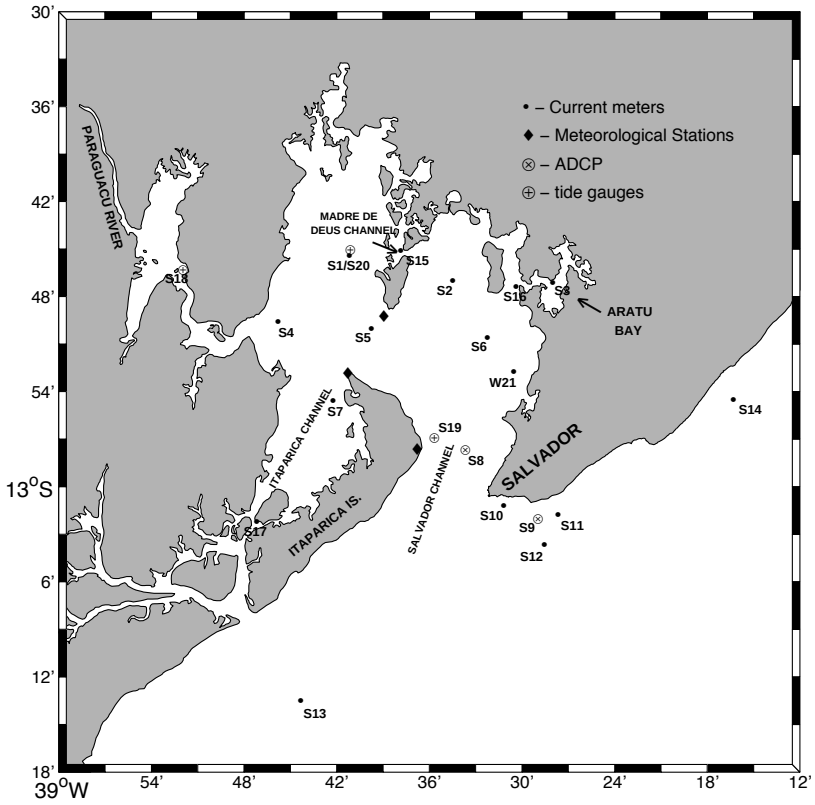

Figure 1: Map of Baia de Todos os Santos, showing the location of the current meter moorings, the ADCPs, the meteorological stations and the tide gauges for summer season. The measurements during wintertime were performed at similar locations, but for winter an additional site (W21) was added.

2.2 Winds

Winds inside the bay during summer had a maximum speeds of 10.3 m s^{-1}, and followed a well established daily pattern of strong sea breezes during the day and calm land breezes at night. Strong afternoon winds attained maximum speeds at around 14:30 h and tended to arrive from around 100°. Mean wind speed was 3.2 m/s, with a unimodal distribution centered at 2.3 m s^{-1}. No well defined pattern is observed during winter,

when the average wind speed was higher (4 m s^{-1}) and with bimodal distribution (2.1 and 5.0 m s^{-1}). The strongest winds tended to arrive from 160°, although with a more scattered distribution (between 120° and 200°).

2.3 Tides

The tides are semi-diurnal, with the diurnal components accounting for 7% to 11% of the total tidal amplitude, with slightly larger values during summer. The amplitude of the M_2 constituent varies between 0.66 m and 0.68 m in the ocean, but increases significantly up the bay, where it reaches 1.06 m at station 18. Along with the tidal range, tidal asymmetry also becomes more important landwards, as it is indicated by the M_4/M_2 ratio rising gradually along the stations from 0.015 in the ocean to 0.09 at station 18.

The M_2 phase angle gradually increases from 90° in the ocean to 109° at station 18, implying a time lag of 40 minutes between the tides in the ocean and in the most inland station. In reality, measured high-tide time lags between stations 13 and 18 varied between 45 minutes and 1.5 hours, with larger lags during the summer spring tides, when tidal asymmetries were more pronounced.

The astronomical tides explained between 98% and 99% of the observed tidal variation during the two monitoring periods, as meteorological tides of just 0.19 m were recorded. These anomalies were in phase in all stations during winter, but curiously up to 180° out of phase inside and outside the bay during summer.

2.4 Currents

The currents inside the BTS (stations 1-8 and 15-21) are clearly tidally driven. The correlation coefficients and the percentage of variance explanation between the predicted and the observed time series show values above 0.90 and 85% respectively. Outside the bay the correlation coefficients and the levels of variance explanation decrease with the increasing distance from the bay mouth, until the tidal signature is completely obscured at stations 13 and 14.

The maximum velocities occurs at the two entrances of the bay, the Salvador Channel (station 8) and Itaparica Channel (station 17), where the M_2 component has magnitudes of 65 cm s^{-1} and 50 cm s^{-1} respectively. The S_2 component has about half of the M_2 strength. Other regions of relatively more intense flow are the central part of the bay (station 5), with 35 cm s^{-1} for M_2 and the Madre de Deus Channel (station 15), where the near surface flow for M_2 is 45 cm s^{-1}. In the remaining stations, the M_2 component of the flow ranged from 16 to 28 cm s^{-1}. Outside the bay, tidal currents are important only at stations 9 and 10. In the latter, a constriction imposed by an ebb-tidal delta causes the M_2 component to reach values of more than 60 cm s^{-1}.

Tidal ellipses are generally oriented along the main channels of the region and eccentricity is small. For the locations where the water column were sampled in two depths, it was also observed that the orientation of the ellipses did not vary more than few degrees throughout the water column.

2.5 Residual Currents

The residual circulation was calculated for the 15 days long time series. Inside the bay,

the results from summer and winter are very similar, with velocities not exceeding 5 cm s^{-1} (equals 65 km of traveling in 15 days).

At the central part of the bay (station 5), surface currents flow to the southeast whereas the bottom currents flow to the northwest. Considering that the same pattern occurs in both seasons and that residual velocities are of the order of 5 cm s^{-1}, it is suggested that this is a permanent feature and may be related to a gravitation circulation. At the lower western part of the bay, the residual circulation at stations 7 and 17 suggests that there is a preferential southwest flow that directs part of the outflow of the central bay through Itaparica Channel.

Apart from station 10, located close to a tidal channel, the inner-shelf residual circulation is clearly seasonal. During summer, the predominant easterlies appear to drive south-westward currents of up to 15 cm s^{-1} near the surface, also generating a significant velocity shear in the water column. During winter, the predominant winds are from southeast, and the associated currents flow to the northeast with magnitudes comparable to those in summer.

3 Conclusions

According to the oceanographic characteristics, the study region is defined by two different scenarios, both in terms of water properties and circulation. Inside the bay, the circulation is primarily driven by tides and the patterns, as expected, do not differ from summer to winter. Outside the bay the influence of tidal circulation is diminished and shelf dynamics, probably driven by winds and meteorological tides, plays an important role. If water circulation inside the bay is not altered by the seasons, the same cannot be said about the water properties, which show increased dilution of sea water during the winter season and a distinct temperature distribution between seasons.

Acknowledgments: The authors were funded by CNPq (Brazilian Research Council) Grants 301249/00-8 and 574555/97-8. We are thankful to the Environmental Department of the State Government of Bahia (*Centro de Recursos Ambientais*) for providing all the data sets related to *Projeto Bahia Azul*.

References:

Lessa, G. C, J. M. L. Domingues, A. C. S. P. Bittencourt, and A. Brichta, The Tides and Tidal Circulation of Todos os Santos Bay, Northeast Brazil: a general characterization, *An. Acad. Bras. Ci., 72(2)*, 245-261, 2001.

Montenegro, A. M., C. A. Fonseca, and E. J. D. Campos, Implentação do modelo oceânico da Universidade de Princeton para o estudo da circulação e dispersão de materiais na Baia de Todos os Santos, *PUC, Ci. Biol. e do Meio Amb., 2(2)*, 10-18, 1999.

Wolgemuth, K. M., W. C. Burnett, and P L Moura, Oceanography and suspended material in Todos os Santos Bay, *Rev. Bras. Geoc., 11(3)*, 172-178, 1981.

Sill dynamics and energy propagation in a jet-type fjord

MARK INALL, FINLO COTTIER, COLIN GRIFFITHS

(Scottish Association for Marine Science, Dunstaffnage Marine Laboratory, Oban. PA34 4AD, Scotland. Email: mei@dml.ac.uk)

TOM RIPPETH

(School of Ocean Science, University of Wales Bangor, Menai Bridge, Anglesey LL59 5EY, Wales.)

1. Introduction

Fjords may be classified into two broad categories: wave-type and jet-type. The division is dependent on the properties of the barotropic tide as it passes over the sill and the degree of stratification in the fjord basin. If flow is greater than the speed of the mode 1 internal wave (internal Froude number, Fr_1, greater than 1), a tidal jet forms on the lee side of the sill. Physical pathways whereby the barotropic energy is transformed at the sill and propagated through the fjord have implications for the efficacy of vertical mixing in such jet-type systems. Furthermore, climatic and strategic considerations have motivated much research in recent years of stratified flow over sill and through straits (e.g. Farmer and Armi, 2001). The upper basin of Loch Etive on the west coast of Scotland is a fine example of a jet-type fjord (Figure 1).

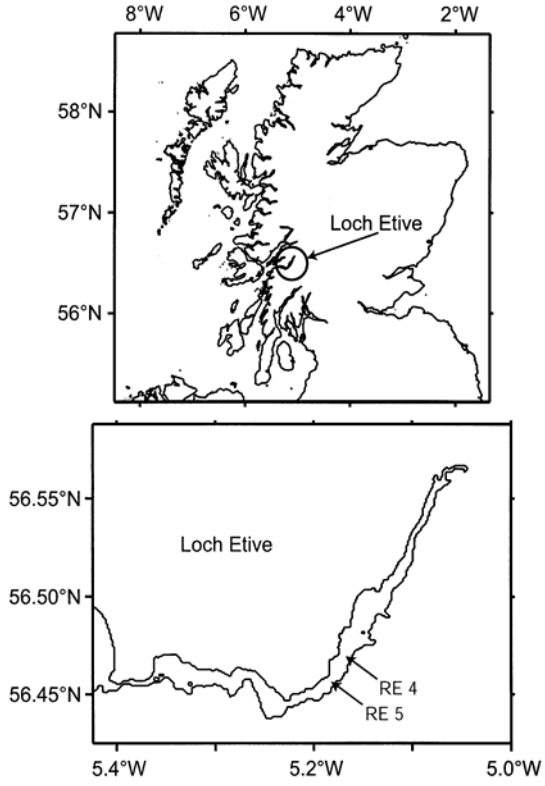

Figure 1 Location map of Loch Etive (upper panel), coastal outline of Loch Etive system with standard CTD stations RE4 and RE5 shown (lower panel).

2. Observations

A basin-wide survey of Loch Etive was undertaken in June 2001 in an attempt to follow the pathways by which the barotropic energy disperses into, and dissipates within the loch. Moorings were deployed along the axis of the basin, and instrumented with acoustic doppler current meters (ADCPs), and temperature and salinity sensors. Bottom pressure recorders were levelled-in either side of the sill. Simultaneous tidal cycle surveys were undertaken over the sill using a vessel mounted ADCP and a hand-held CTD, and along the axis of the basin using a towed undulating CTD. Standard CTD profiles where made at the reference stations RE1 to RE7 (Figure 2).

Bottom pressure recorders have revealed both a frictional mean sea level set-up of 0.11 m in the upper basin, and marked asymmetry in the barotropic forcing of the upper basin, both presumably a result of tidal constrictions seaward of the sill. A simple hydrodynamic tidal model has been used to investigate the frictional values necessary reproduce the free surface elevation measurements. The asymmetry is reflected in the tidal flows over the sill, with a fast flood tide and a slower, prolonged ebb (Figure 4).

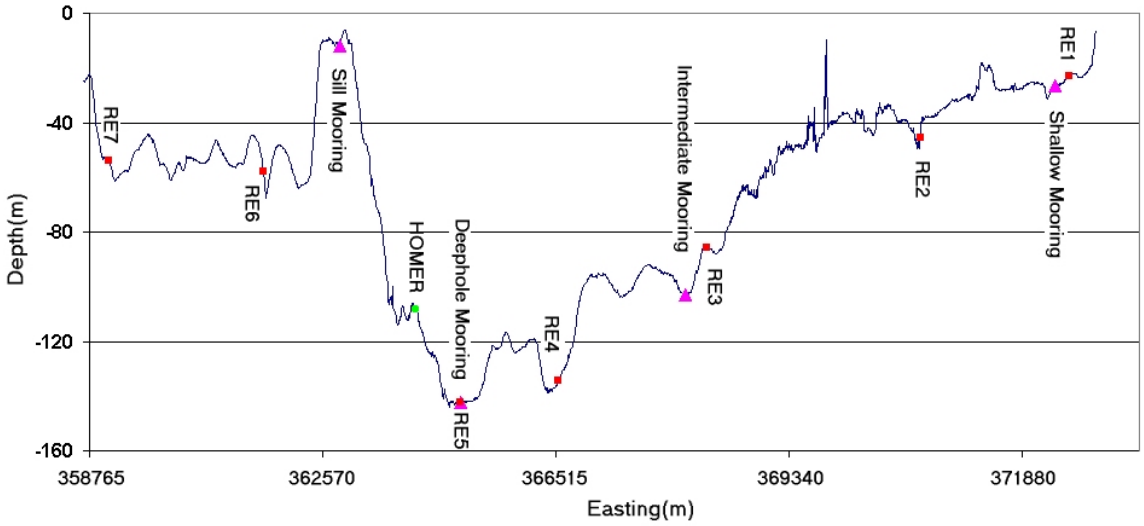

Figure 2 Bathymetric cross-section along the axis of the upper basin of Loch Etive: CTD stations RE1 to RE7 (circles), current meter and T/S moorings (triangles), and experimental yo-yo CTD mooring (HOMER)

3. Jet forcing at the Sill

A detailed ADCP survey across the sill has allowed us to examine some of the sill processes, particularly those occurring on the lee side as the jet separates from the bed creating high vorticity and strong vertical recirculation at that point (Figure 3).

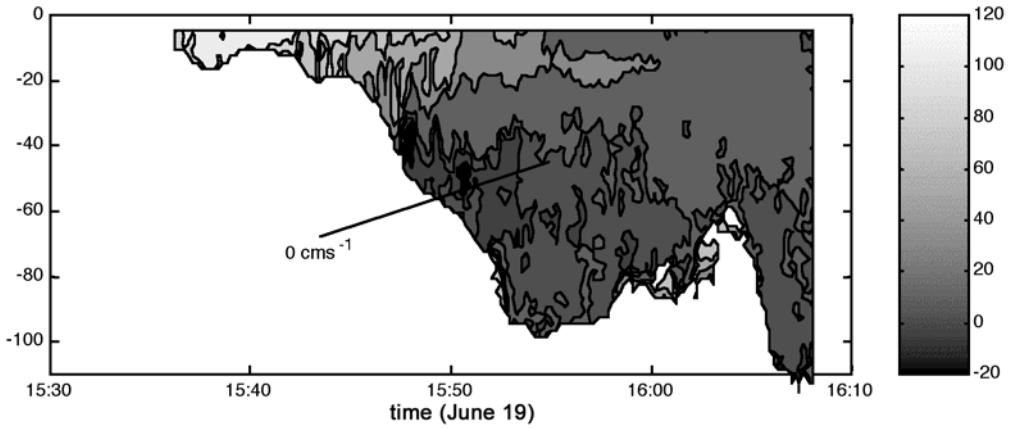

Figure 3 Cross-sill flow at maximum flood tide from the sill (left), towards RE5 (right) from the vessel mounted ADCP. The horizontal scale for the figure is 1500m.

Throughout the spring/neap cycle the inflow always becomes supercritical (Fr_1>1) at some point during the flood tide (Figure 4b). Flow separation occurs throughout the spring flood tide of June 19, and is identified as a 'post-wave' regime, where separation occurs in the lee of the sill (Baines, 1995). Flow over the sill is intense enough to promote aspiration from twice the sill depth, and at high values of the non-dimensional parameter NH/U, where N is the buoyancy frequency, H is sill height, and U the flow over the sill (Figure 4c), separation is due to upstream blocking of denser fluid below the aspiration depth (approximatelty 35m). However at lower values of NH/U flow against the adverse pressure gradient below the internal lee wave crest may also contribute to flow separation.

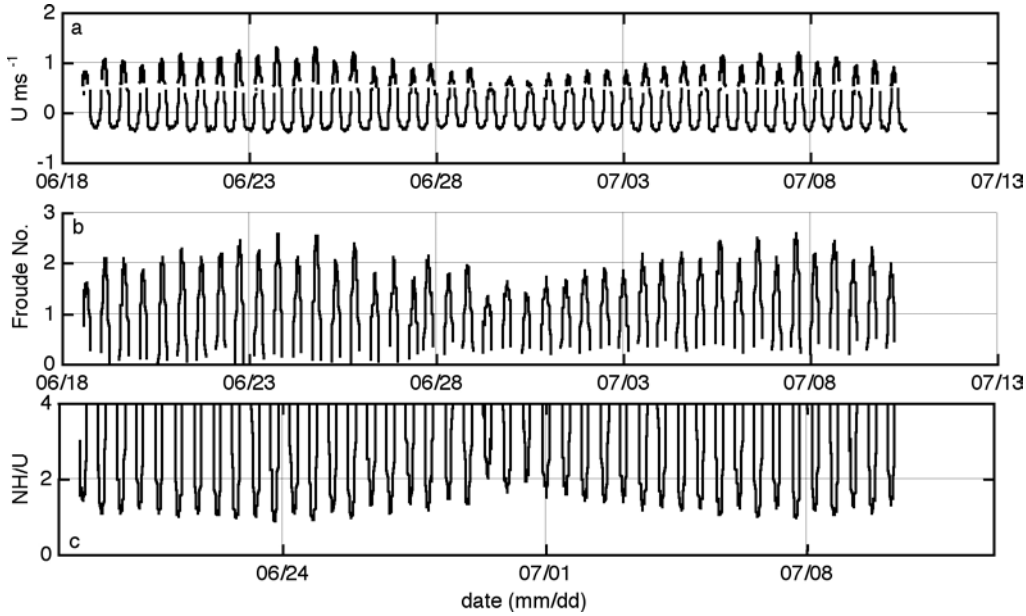

Figure 4 Depth avarage cross-sill flow from the sill-moored ADCP (a), bold line indicates supercritical flow. Baroclinic mode 1 Froude number (b). Non-dimensional parameter NH/U, values greater than 4 not shown (c).

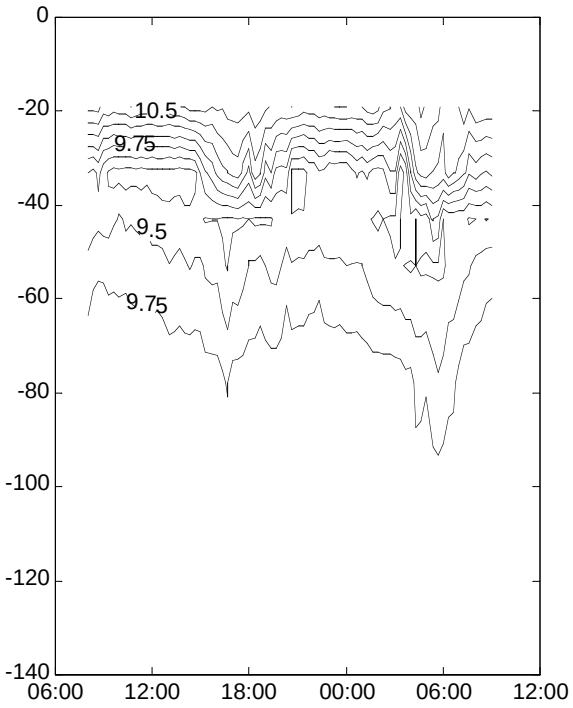

Figure 5 Temperature contours at RE5. No data are available below 100 m and above 20 m)

4. Basin Response

Despite the periodically high Froude numbers, moored instruments along the axis of the loch basin have revealed large oscillations of the pycnocline (10 m amplitude) below sill depth, and pulse-like depressions in the pyconcline above the aspiration depth (Figure 5) .

CTD data reveal gently sloping isopycnals along the basin axis, and linear theory predicts a decrease in the phase speed of the M2 baroclinic mode 1 internal oscillation (C_1) from 0.71ms^{-1} at RE5, to 0.31 ms^{-1} at RE1. However, it appears from moored thermistor, and towed, undulating CTD records that the oscillations do not represent a linear internal wave train, and the pulse-like depression propagates from RE5 to RE1 with a constant speed of 0.2ms^{-1}. There is a propagation of baroclinic energy away from the sill into the basin interior and we can estimate the energy transfer and investigate the generation and dissipation.mechanisms.

The development of the pulse can be seen in the undulating CTD records (Figure 6). As the flood tide weakens, and the flow becomes sub-critical, a depression of the 21.6 sigma-theta surface develops (Figure 6a to 6c). As the flow then ceases, the pulse propagates away from the sill at 0.2 ms^{-1} (Figure 6c).

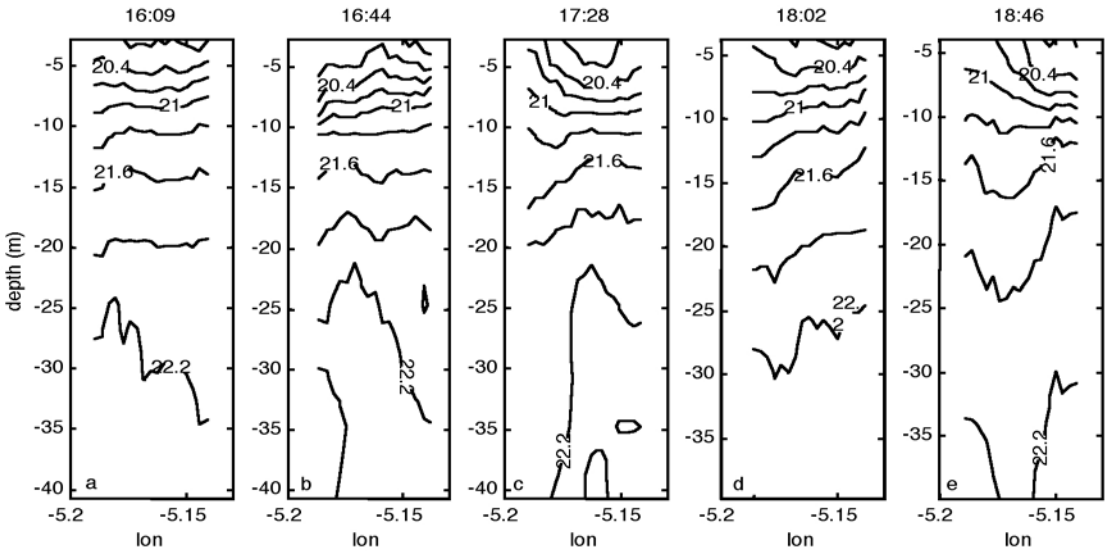

Figure 6 Contours of σ_θ from the towed undulating CTD on June 19. The center time for each section is shown, the horizontal scale for each panel is 3800m, running from RE5 to RE3 (from left to right in each panel).

5. Energetics

From this detailed observational study of the forcing and response of a jet-type fjordic system, we shall go on to quantify the pathways of tidal energy, from the loss of barotropic tidal energy to the forcing and energy loss of a tidal jet, through to the transfer to the baroclinic field and ultimately to mixing. An attempt to do this in a wave-type fjord was partially thwarted by the sparsity of observations and complexity of the chosen fjord (Inall and Rippeth, 2002), however we anticipate producing a more tightly constrained energy budget from this study.

References:

Baines, P.G., *Topographic Effects in Stratified Flows,* Cambridge University Press, Cambridge, 1995.

Farmer, D.M and L. Armi, Stratified flow over topography models versus observations, *Proceedings of the Royal Society of London A,* 457, 2827-2830, 2001

Inall, M.E. and T.P. Rippeth, Dissipation of Tidal Energy and Associated Mixing in a Wide Fjord, *Environmental Fluid Mechanic,* in press, 2002.

The long side-heated cavity as a model for density-driven flows in estuaries

Bertram Boehrer, *UFZ-Umweltforschungszentrum Leipzig-Halle GmbH, Sektion Gewässerforschung, Brückstr. 3a, D-39114 Magdeburg, Germany*, boehrer@gm.ufz.de

1 Introduction

Laboratory and numerical experiments of flows in a simple configuration can be used to verify and enhance our understanding of flows in the environment. We consider the steady-state flow in the long side-heated cavity. This simple model allows the variation of the control parameters Rayleigh number Ra (exact definition below), aspect ratio A and Prandtl number Pr, to critically investigate theoretically derived scales.

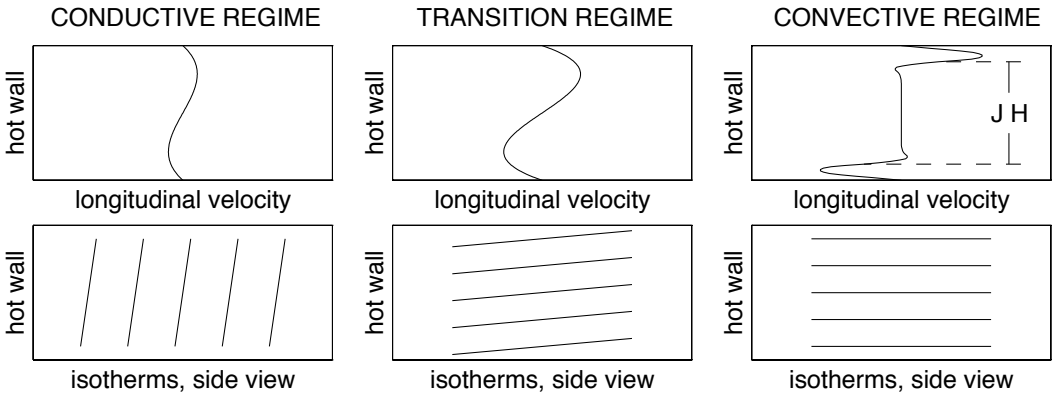

Figure 1: Sketches of longitudinal velocity (upper row) and several isotherms (lower row) in a side view of a long tank for the three flow regimes. In the convective regime, we find a stagnant core of height JH, which separates sharply from the flowing layers along the lid and the bottom of the cavity (from Boehrer 1997).

The long side-heated cavity has served as a model for environmental flows in a number of cases. Since Hart (1972) it is known that a long enough cavity forced from its end regions will establish a flow that is close to an exact solution of the Navier-Stokes-Fourier equations. These conditions refer to the conductive regime of Fig. 1, where we find cavity-filling counter currents in good thermal contact with each other. A number of mathematical, numerical and experimental studies have been undertaken to correlate the features found inside the cavity to the control parameters:

$$Ra = \frac{g\alpha\Delta T H^3}{\nu\kappa} \tag{1}$$

$$Pr = \frac{\nu}{\kappa} \tag{2}$$

$$A = \frac{H}{L} \tag{3}$$

where α, ν and κ denote fluid properties of thermal expansion, viscosity and thermal conductivity. H and L are the cavity dimensions height and length, while ΔT represents the temperature difference between the end walls and g the gravity.

In this short contribution, we only consider the case of thin layers flowing along the boundaries of the cavity (convective regime in Fig. 1). From scaling arguments we conclude the thickness of the flowing layers. Finally the experimental evidence is critically compared, which proves that all experiments comply with the scaling.

2 Scaling analysis

The basic statement is that the thickness of an intrusion layer increases with the conductivity of its stratifying species. Heat spreads with its thermal conductivity κ in water. If above assumption is right, the flowing layer thickness after a time period t shall correspond to

$$\delta \sim (\kappa t)^{1/2} \tag{4}$$

In the case of the long cavity, the time for vertical growth should scale with the time required for the intrusion to flow through the tank of length L at a certain speed u.

$$t \sim L/u \tag{5}$$

For $Pr > 1$ the momentum diffuses faster than heat. Thus a buoyancy-driven layer assumed to grow by heat conduction must be assumed to flow in a viscous balance, which is derived in the usual way:

$$0 = -\frac{1}{\rho} \cdot \frac{\partial p}{\partial x} - \nu \frac{\partial^2 u}{\partial z^2}\,, \tag{6}$$

$$0 = -\frac{1}{\rho} \cdot \frac{\partial p}{\partial z} - g\alpha T\,. \tag{7}$$

x and u refer to distance und speed along the horizontal coordinate, z is anti-parallel to gravity g, ρ is the fluid density and p refers to the pressure. By cross-differentiation, we eliminate the pressure term. Using the scales δ for z, L for x, ΔT for T, and U for u, we find a velocity scale

$$U \sim \frac{g\alpha\Delta T\delta^3}{\nu L}. \tag{8}$$

Combining equations 4, 5 and 8, Boehrer (1997) found:

$$\delta/H \sim (RaA^2)^{-1/5} \tag{9}$$

This scale can be visible only for cases when the conductive thickness overcomes the dynamic thickness, which is given by the inflow Q divided by the flow speed of the intrusion u. In the case of the side heated cavity, this was calculated by Patterson and Imberger (1980), and thus equation 9 is valid for:

$$(RaA^2)^{-1/5} > Ra^{-3/16}A^{-1/4} \Longrightarrow Ra < A^{-12} \tag{10}$$

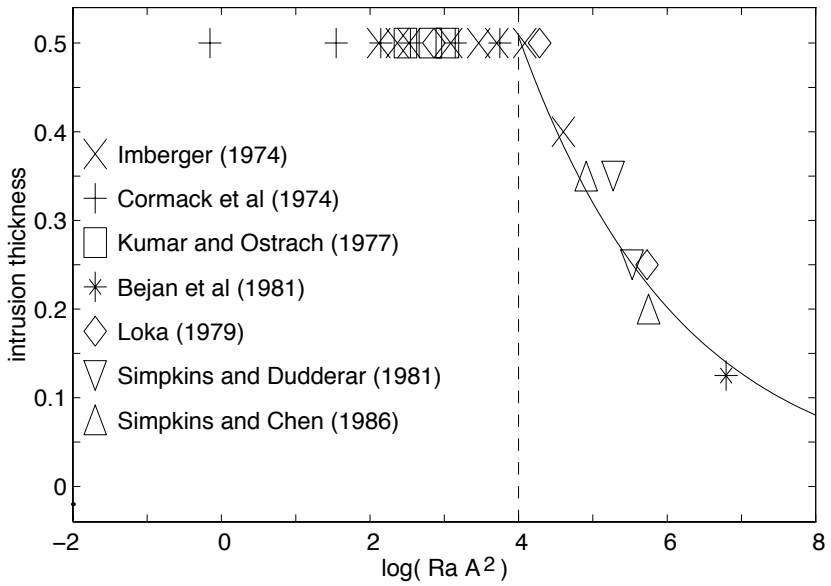

Figure 2: Intrusion thickness δ/H versus RaA^2. The experimental values decrease monotonically from a point $RaA^2 \approx 1 \times 10^4$ (broken line). The solid line is based on the above scaling and shows the function $\delta/H = 3.2 \cdot (RaA^2)^{-1/5}$ (from Boehrer 1997).

3 Experimental Data

We use all experimental evidence available in the scientific literature and include the data in one plot of intrusion thickness versus RaA^2 (Fig. 2). The experiments of the various groups cover a wide domain for control parameters of Ra, Pr and A:

- $70 \leq Ra \leq 1.59 \cdot 10^9$
- $7 \leq Pr \leq 1380$ and
- $0.01 \leq A \leq 0.25$.

All of the data have been produced by laboratory experiments except for Cormack et al (1974), which have been done numerically and where the very low Rayleigh number data originates from. Despite the immense range covered, and the origin of the data from many independent groups, all experimental evidence aligns very well with each other and the curve $\delta/H = 3.2(RaA^2)^{1/5}$ for values $RaA^2 > 10^4$ indicating that the intrusion thickness is a consequence of the conductive spreading of the intrusion in the vertical. Below $RaA^2 = 10^4$, the layer thickness of the intrusion is limited to 0.5, as the lower half is occupied by the cold counter current then. As a consequence, the opposite intrusions come into direct thermal contact with each other.

4 Further work

By varying the configuration of the forcing, similar consideration have been developed for the case of throughflows through channels or straits (Hogg et al. 2001; Karakaş and Boehrer 2002). Other work considered the onset of lateral structure by Coriolis effects (Boehrer 2001).

References:

Bejan A., Al-Homoud A. and Imberger J., Experimental study of high-Rayleigh-number convection in a horizontal cavity with different end temperatures, *J. Fluid Mech. Vol 109*, 283-299, 1981.

Boehrer B, Convection in a long cavity with differentially heated end walls, *Int. J. Heat Mass Transfer*, 40, 17, 4105-4114, 1997.

Boehrer B, Steady-state convection in a rotating long cavity, *Geophys. Astrophys. Fluid Dynamics*, 95, 105-126, 2001.

Cormack D.E, L.G. Leal and J.H. Seinfeld, Natural Convection in a shallow cavity with differentially heated end walls, Part 2 Numerical results, *J. Fluid Mech., 65*, 230-246, 1974.

Hart J.E., Stability of thin non-rotating Hadley circulations, *J. Atmos. Sci. 9*, 687-697, 1972.

Hogg A.M., Ivey G.N. and Winters K.B., Hydraulics and mixing in controlled exchange flows *J. Geophys. Res. 106, C1*, 959-972, 2001.

Imberger J., Natural Convection in a shallow cavity with differentially heated end walls. Part 3. Experimental results, *J. Fluid Mech. 65*, 247–260, 1974.

Karakaş G. and B. Boehrer, Estimation of effective vertical viscosity and diffusivity in turbulent exchange flows by numerical experiments. *Let's face chaos through non-linear dynamics*, Univ. of Maribor, Maribor, Slovenia, 2002.

Kumar A. and S. Ostrach, Case Western Reserve Univ., Dept Mech Aerospace Engng Rep. FTAS/TR-77-132 (from Bejan et al 1981) 1977.

R.R. Loka, M.S.thesis, Dept Mech and Aerospace Engng, Case Western Reserve Univ. (from Ostrach et al. 1980) 1979.

S. Ostrach, R.R. Loka, and A. Kumar, Natural convection in low aspect ratio rectangular enclosures, *19 th Nat. Heat Transfer Conf.*, Orlando, Florida 1980.

J.C. Patterson, and J. Imberger, Unsteady natural convection in a rectangular cavity, *J. Fluid Mech. 100:1*, 65-86 1980.

P.G. Simpkins and T.D. Dudderar, Convection in rectangular cavities with differentially heated end walls, *J. Fluid Mech., 110*, 433-456 1981.

P.G. Simpkins and K.S. Chen, Convection in horizontal cavities, *J. Fluid Mech., 166*, 21-39, 1986.

Estimation of the Vertical Eddy Diffusivity: Observation in Swan River Estuary

AMIR ETEMAD-SHAHIDI

(Department of Civil Engineering, Iran University of Science & Technology, Tehran, Iran, P.O. Box 16675-163, etemad@iust.ac.ir)

1. Introduction

A clear understanding of the vertical mass transport is of importance in both geophysical and environmental studies of stratified natural water bodies. The rate of vertical transport is commonly parameterized by using the concept of vertical eddy diffusivity, $k\rho$, which relates the vertical transport of the mass to the gradient of density profile. The magnitude of $k\rho$ is not constant may vary by several orders of magnitude depending on the turbulence properties and background stratification. Therefore, it is necessary to quantify $k\rho$ for different situations. The common method for estimationg $k\rho$ is microstructure measurements in the field. Since direct mesurement of $k\rho$ is not an easy task in the field [Etemad-Shahidi and Imberger 2001], indirect methods have been developed and invoked in the field studies. These indirect methods have been used both in the lakes and ocean [e.g. Wuest et. al 1996, Toole et. al 1994]. However, the statistics of the obtained values of $k\rho$ have been rarely calculated. The purpose of this study is to address this issue in the pycnocline of an estuary.

2. Method

2.1 Osborn method

for a steady and laterally homogenous shear flow, using energy partitioning arguments, Osborn [1980] estimated the vertical eddy diffusivity as:

$$k_{OS} = \frac{b}{N^2} = 0.2\frac{\varepsilon}{N^2} \tag{1}$$

where, b is the buoyancy flux, ε is the rate of dissipation and N is the buoyancy frequency. The main disadvantage of this method is the uncertainty in the magnitude of b. This method, however, is still used commonly in field experiments.

2.2 Osborn- Cox method

The method of Osborn-Cox [1972] is based on the balance between the production of temperature variance and destruction of it by molecular diffusion. For a steady and laterally homogeneous turbulent flow, the vertical eddy diffusivity is estimated as:

$$k_{OC} = 3KC_3N^2 \tag{2}$$

where, $C_3 = (\partial T'/\partial x_3)^2 \,/\, (\partial T/\partial x_3)^2$ is the vertical Cox number, and K is the molecular diffusivity of heat and T' is the temperature fluctuation.

2.3 Method of Ivey-Imberger

Ivey and Imberger [1991] using scaling argument and a range of data sources from laboratory and numerical experiments found that the mixing efficiency ,$R_f = b / (b+\varepsilon)$, was a function of the turbulent nondimensional numbers which show the relative importance of viscosity, inertia and buoyancy forces. These nondimensional numbers are defined below:

$$Fr_t = (\frac{\varepsilon}{N^3 L_T})^{1/3}, R_t = (\varepsilon^{1/3} {L_T}^{4/3} / \nu)^{4/3} \text{ and } Fr_\gamma = (\varepsilon / \nu N^2)^{1/2} \quad (3)$$

where, L_T is the Thorpe scale characterising the size of the turbulent events and ν is the molecular viscosity. Ivey *et. al* [1998] improved this finding by performing further direct numerical simulations. The maximum mixing efficiencty was found to be about 0.3 where Fr_t becomes unity and $Re_t > 75$.

In order to evaluate the performance of these methods, a field experiment was conducted during 5-8th of March, 1996 in Swan River estuary. The turbulence properties was documented by a microstructure probe called PFP. During the experiment the collected 189 microstructure profiles were divided into stationary segments and a total of 165 stationary turbulent patches within the pycnocline were selected.

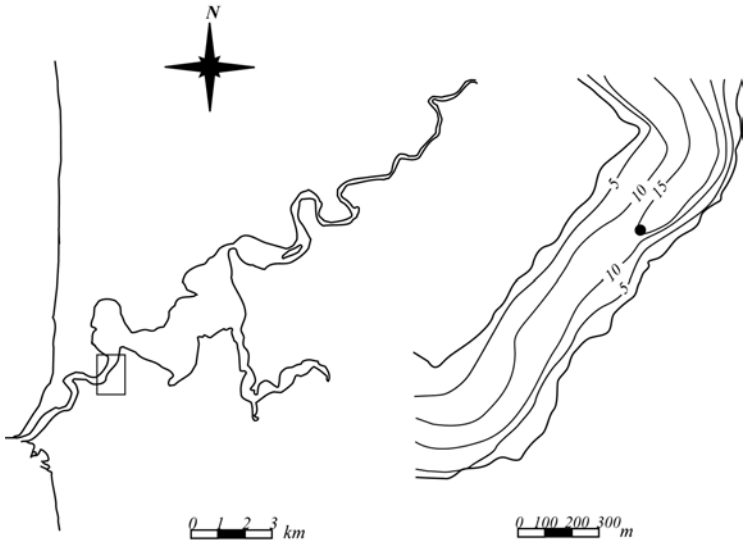

Figure 1: The map of the Swan River estuary and the Bathymetry of Blackwall Reach. The station is marked by a full circle.

3. Results and discussion

Figure 2 shows a more or less log normal distribution for k_{OS}, where the median, mode and the mean are 2.8×10^{-4} m^2s^{-3} and 2.3×10^{-5} m^2s^{-3} respectively. Compared to the other methods, these estimates are higher that could be accounted for by considering that this method is derived for steady shear driven turbulence with a mixing efficiency of about 0.2 which is not valid for all flows [Etemad-Shahidi and Imberger 2002].

Figure 3 displays the histogram of log k_{OC}, .The distribution is relatively skewed towards smaller values and the variation of estimates is about four orders of magnitude. The mean and median values of k_{OC} are 3.4×10^{-4} m^2s^{-3} and 4.9×10^{-6} m^2s^{-3} respectively. Noting the temporal and spatial intermittency of turbulence in the pycnocline, the latter value basically shows that the diffusion is in not important in this flow. This conclusion is in line with the direct measurements of. Etemad-Shahidi and Imberger

[2002] which showed that the down gradient flux in the turbulent patches is compensated with the consequent up gradient flux within the turbulent events.

Finally figure 4 displays the histogram of log k_{II}. The distribution is similar to the previous one. The mean and median values of k_{II} are 9×10^{-5} m^2s^{-3} and 6.6×10^{-6} m^2s^{-3}, respectively which are both close to those of k_{OC}. This could be explained by considering that both of these methods are obtained for steady and laterally homogenous flows. In Brief it could be conferred that the method of Osborn is not appropriate for this flow and other indirect methods of Osborn-Cox or Ivey-Imberger gives a better estimate of the rate of vertical eddy diffusivity.

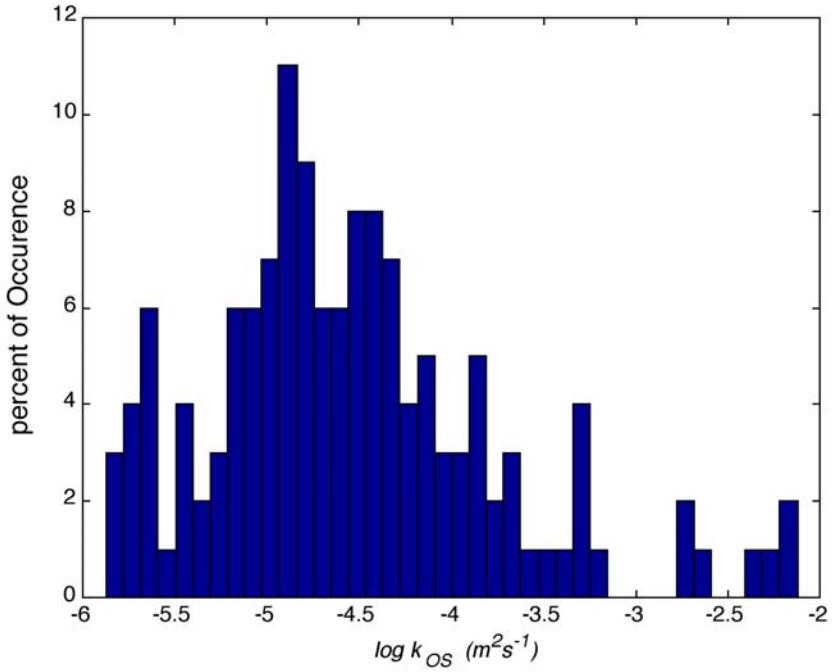

Figure 2: Histogram of log k_{OS}. The mean and median values of k_{OS} are 2.8×10^{-4} m^2s^{-3} and 2.3×10^{-5} m^2s^{-3} respectively.

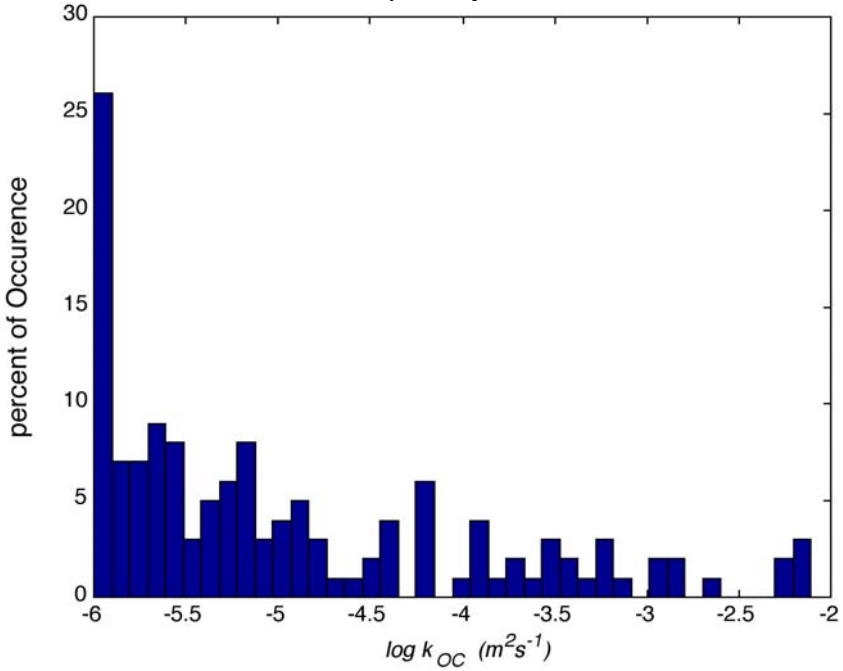

Figure 3: Histogram of log k_{OC}. The mean and median values of k_{OC} are 3.4×10^{-4} m^2s^{-3} and 4.9×10^{-6} m^2s^{-3} respectively. Note that a minimum value of 10^{-6} m^2s^{-3} is assumed.

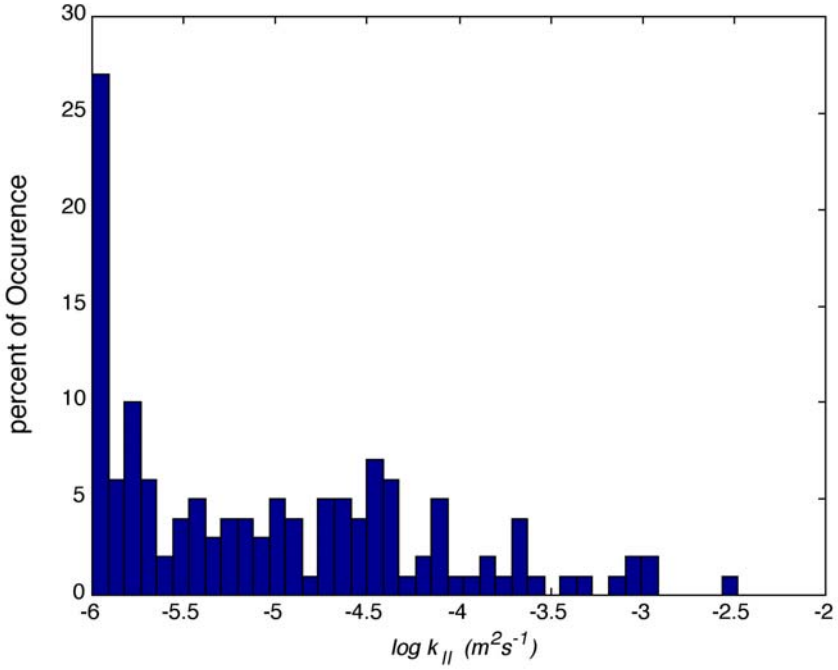

Figure 4: Histogram of log k_{II}. The mean and median values of k_{II} are 9.0×10^{-5} m^2s^{-3} and 6.6×10^{-6} m^2s^{-3} respectively. Note that a minimum value of 10^{-6} m^2s^{-3} is assumed.

Acknowledgments: The author is grateful to Pecs2002 organizing committee for the awarded travel grant.

References:

Etemad-Shahidi A. and J. Imberger, Anatomy of turbulence in a narrow and strongly stratified estuary, *J. of Geophysical Research-Oceans*, under press, 2002.

Ivey, G. N. and J. Imberger, On the nature of turbulence in a stratified fluid. part 1 the energetics of mixing, *J. Physical Oceanography, 21*:650-658, 1991.

Ivey, G. N., J. Imberger, and J. R. Koseff. Buoyancy fluxes in a stratified fluid, in *Physical processes in lakes and oceans*, Coastal and estuarine studies, 54, edited by J. Imberger, pp. 311-318. AGU, 1998.
Osborn, T. R., Estimation of the local rate of the vertical diffusion from dissipation measurements, *J. Physical. Oceanogr*aphy, 10(1), pp. 83-89, 1980.

Osborn, T. R. and C.S. Cox, Oceanic fine structure. *Goephysical Fluid Dynamics*, *3*, pp.321-345, 1972.

Toole, J.M., K. Polzin and R. Schmidt, Estimates of diapycnal mixing in the abyssal ocean, *Science,* 264, pp. 1120-1123,1994

Wuest, A., D.C. Van Senden and J. Imberger, Comparison of diapycnal diffusivity measured by tracer and microstructute techniques, *Dynamic of Atmosphere and Ocean* 24, pp. 27-39, 1996

Trapped internal waves over undular topography and mixing in a partially mixed estuary

JULIE PIETRZAK

(Fluid Mechanics Section, CiTG, Delft University of Technology, Stevinweg 1, 2628 CN Delft, The Netherlands, J.Pietrzak@citg.tudelft.nl)

ROBERT JAN LABEUR

(Fluid Mechanics Section, CiTG, Delft University of Technology, Stevinweg 1, 2628 CN Delft, The Netherlands, R.J.Labeur@citg.tudelft.nl)

1. Abstract

The flow of a stratified fluid over small scale topographic features in an estuary may generate significant internal wave activity. Lee waves and upstream influence generated at isolated topographic features, have received considerable attention during the last few decades. Field surveys of a partially mixed estuary, the Rotterdam Waterway, in 1987 also showed a plethora of internal wave activity generated by isolated topography, banks and groynes. Additionally it revealed a spectacular series of resonant internal waves trapped above low amplitude bed waves. The internal waves reached amplitudes of 3 - 4 m in an estuary with a mean depth of 16 m. The waves were observed during the decreasing flood tide and are thought to make a significant contribution to turbulence production and mixing. However, while stationary linear and finite amplitude theories can be used to explain the presence of these waves it is important to further investigate the time dependent and non-linear behaviour of these waves. With the development of advanced non-hydrostatic models it now becomes possible to further investigate these waves through numerical experimentation. This is the focus of the work presented here.

The non-hydrostatic finite element numerical model of Labeur was used in the experiments presented here. The model has been shown to work well in a number of stratified flow investigations. Here we first show that the model reproduces the field data and for idealised stationary flow scenarios that the results are in agreement with the resonant response predicted by linear theory. Then we explore the effects of non-linearity and time dependence and consider the importance of resonant internal waves for turbulence production in stratified coastal environments.

2. Introduction

Understanding the mechanisms for mass and momentum transfer in estuaries is a topic of widespread interest. Internal waves are known to play an important role in the transfer of mass and momentum. Observations in estuaries, laboratory studies and theoretical studies all suggest that internal waves may play an important role in the production of turbulent kinetic energy and mixing in estuaries. Internal waves may be generated by various mechanisms, notably by sub-critical tidal flow over topography. Indeed since small scale topography is an ubiquitous feature of most estuaries and coastal seas, so too are internal waves. The literature on stratified flow over topography is extensive, the study of the subject began with the pioneering work of *Long* (1953) and more recently has been summarised in the review by *Baines* (1995). *Kranenburg and Pietrzak* (1989) demonstrated through laboratory and analytical studies that internal waves could increase the local production of turbulence by 40 % and suggested that this could have significant effects for turbulence modelling in estuaries. Internal waves can lead to mixing upon breaking. *Pietrzak et. al.* (1991) summarised the results from five field surveys which were carried out in the Rotterdam. The surveys showed internal wave generation by small scale topography, freely propagating waves over a flat section of the estuary and internal wave generation and rotor formation by large scale features at the banks. Their study concluded that internal

waves contributed significantly to mixing and turbulence production in a partially mixed estuary. Here we further investigate internal wave activity with the aid of a numerical model.

3. Observations

The Rotterdam Waterway is a man made tidal channel, with a predominantly semi-diurnal tide. The freshwater discharge at the head of the estuary is regulated so that the discharge tends to have a constant value of about 2000 m^3s^{-1}. Dredging maintains the estuary at a constant depth, except for the banks, so that generally only small scale topography persists. Two measuring boats were used in each survey, one vessel was anchored and took profiles of velocity and density at 2 m depth intervals, while the other vessel recorded acoustic echo-sounding transects using a 210 khz transducer. The surveys revealed the plethora of internal wave activity in the Rotterdam Waterway. The first two surveys dealt with topographic wave generation over a pronounced series of bottom topographic features, with typical bed wavelengths of 30-50 m and amplitudes of 0.5 - 1.0 m. It is the second survey that forms the focus of the numerical simulations presented here.

Fig. 1 shows an example of resonant trapped internal waves over undular bed topography. Notably the wave height of the largest internal wave was approximately equal to half the water depth and the amplitude of the internal waves was 4-8 times the height of the topography.

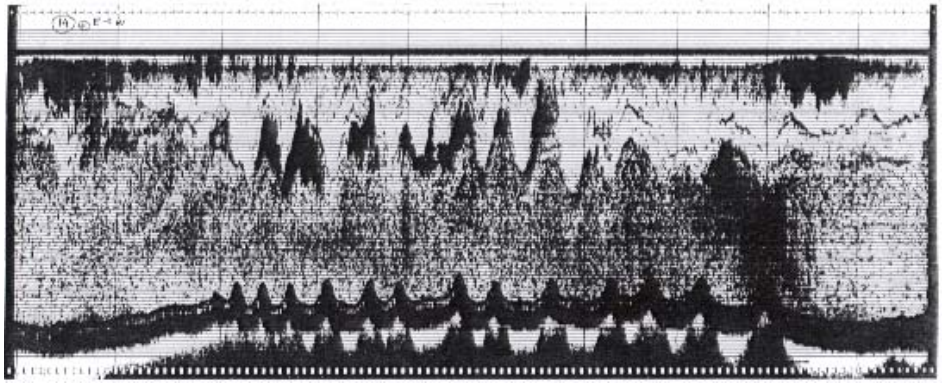

Figure. 1 A 1 km echo-sounding showing internal wave activity along the axis of the Rotterdam waterway. Track 4 was taken between 15.46-15.52 h, 21 Oct. 1987. The tick marks are at 100 m intervals, *Pietrzak et. al.* (1990) and *Kranenburg et. al*. (1991).

During the ebbing tide a series of resonant trapped waves were observed. Initially the long wave components in the topography were excited. The shorter wavelength components became apparent as the tidal flow decelerated. For example, the wavelength seen in the images decreased from 80 m to 50 m to 40 m to 30 m during Tracks 1 to 4, with amplitudes of 1 m, 2 m, 4 m and 4 m respectively. Finally Track 5 had a 3 m amplitude response with a wavelength of about 30 m. During the time of the observations the Froude number decreased from 0.9 to 0.6. Tidal variations in the flow influence the internal wave response. If the time variation is slow enough in comparison to the time scale of the tide, then quasi-steady theory can be used to interpret the data. In the previous analysis of the data Pietrzak et. al. (1990) and Kranenburg et. al. (1991) linear and finite amplitude analyses were carried out. These analyses help to identify the physical mechanisms causing the large amplitude response seen in the acoustic images.

The conditions for resonance are satisfied if the free internal wavelength that coincides with the unforced internal wave equation has the same wavelength as the topographic forcing. If the topography had been monochromatic only one wavelength would have been resonant and the amplitude of the response over the topography would be expected to diminish. However, since the topography has contributions from other wavelengths it was possible for contributions from other

wavenumbers to become resonant as the tidal flow decelerated. In order to investigate this further a non-hydrostatic numerical model is employed.

4. Model

FINEL 3D, is the numerical model employed in these simulations. It has been developed by R.J. Labeur, while working at Svasek hydraulics, Royal Haskoning. It is based on the full Navier Stokes equations, with equations for temperature and salinity and an equation of state is used to calculate density. FINEL 3D is a fully 3-dimensional flow model. As no assumptions have been made with respect to the vertical pressure distribution the model is suitable for non-hydrostatic flow simulations. The Navier-Stokes equations are discretised horizontally in space using a finite element grid, using triangular elements. An arbitrary number of vertical grid points can be used. The resulting coupled set of algebraic equations are solved with a fully implicit algorithm using BiCGSTAB as an iterative solver. The transport equations for temperature and salinity are solved parallel to the flow equations. Subsequently, in each time step, the body forces resulting from the computed density distribution are calculated and added to the equations of motion.

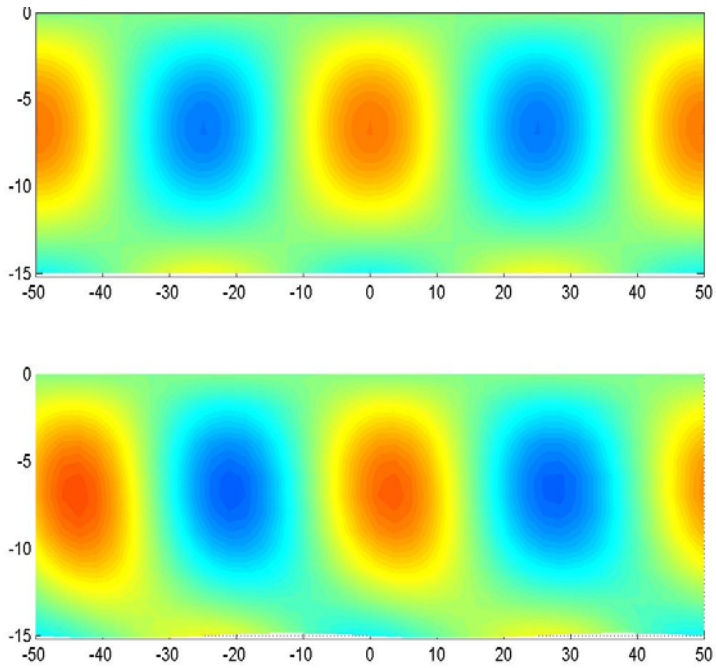

Fig. 2 Vertical velocities calculated from the analytical solution (above) and from the numerical model.

In this study the numerical model has been validated against linear small amplitude wave theory. The basic numerical set up consists of stationary flow over a series of sinusoidal bed waves. The horizontal extent of the model domain extends from $-50 \leq x \leq 50$ m. The vertical extent is 15 m. The bed waves have a wavelength of 50 m and an amplitude of 0.25 m. This configuration compares with the flow situation observed in the estuary. Fig. 2 shows the vertical velocities calculated from the analytical solution and from the numerical model. Good agreement is seen between the two. The phase errors are thought to be due to reflections from the open boundaries. A sponge layer was implemented at the open boundaries in order to minimise boundary reflections, the simple sponge layer was found to be quite effective in reducing boundary reflections and minimising phase errors. A large amplitude internal wave response is also observed in the numerical experiments. The results from the numerical

simulations are in good agreement with those from linear wave theory, supporting the theory that the waves are resonant trapped internal waves.

Further test cases are being carried out to explore the effects of internal waves on stratification in a partially mixed estuary. The estuary of particular interest to us is the Rotterdam Waterway, a partially mixed estuary. Here data collected in 1987 have been reanalysed with the help of the non-hydrostatic finite element numerical model FINEL3D. The model has been validated against linear wave theory. The model can reproduce the field data and for idealised stationary flow scenarios the results are in agreement with the resonant response predicted by linear theory. The non-linear model is an important tool for scenario testing and furthering our understanding the effects of non-linearity and time dependence. Neither effect could be studied in detail with the simple analytical models employed so far.

References:

Baines, P.G. *Topographic effects in stratified flows*. Cambridge University Press, pp 482, 1995.

Kranenburg, C. and Pietrzak, J.D. Internal lee waves in turbulent two-layer flow. *J.Hydr. Engrg*, ASCE, Vol.115 No. 10, 1352-1370, 1989.

Kranenburg, C., Pietrzak, J.D. and Abraham,G. Internal waves over undular bottom topography. *J. Fluid Mech*. 226, 205-217, 1991.

Long, R. R. Some aspects of the flow of stratified fluids. I. A theoretical investigation. *Tellus*, 5, 42, 1953.

Pietrzak, J.D., Kranenburg,C. and Abraham,G. Resonant internal waves in fluid flow. *Nature*, 344, 844, 1990.

Pietrzak, J.D., Kranenburg, C., Abraham, G., Kranenburg, B. and van der Wekken, A. Internal wave activity in the Rotterdam Waterway. *J.Hydr. Engrg*, ASCE, Vol.117 No. 6, 738-757, 1991.

Quantifying turbulent mixing in a Mediterranean-type, microtidal estuary.

JONATHAN SHARPLES

(Southampton Oceanography Centre, Southampton University, School of Ocean and Earth Science, Empress Dock, Southampton, SO14 3ZH, UK, j.sharples@soc.soton.ac.uk)

MICHAEL COATES

(School of Ecology and Environment, Deakin University, PO Box 423, Warrnambool, Victoria, 3280, Australia, mcoates@deakin.edu.au)

JOHN SHERWOOD

(School of Ecology and Environment, Deakin University, PO Box 423, Warrnambool, Victoria, 3280, Australia, jsher@deakin.edu.au)

1. Introduction

The highly-stratified salt-wedge estuaries of southern Australia combine very small tidal influences with a Mediterranean climate in which river flows have a strong seasonal cycle. As a result of negligible freshwater inputs in summer and autumn, a sandbar usually builds up across the mouth, isolating the estuary from the open ocean. As rainfall increases in late autumn and winter, water levels in the estuary gradually build up, until the mouth is forced open. River input can then flush the entire estuary with freshwater. Periods of lower river input result in upstream propagation of a salt wedge. River flow stops in early summer, and so the coastal alongshore transport of sand builds up at the mouth to again block the estuary. During the blocked phase high salinity water becomes isolated in the bottom of deep basins along the estuary, with the strong halocline leading to the development of anoxia and high sulphide concentrations.

The chemical, biological, and ecological environments are closely coupled to the timing of blocking and opening events, and thus to the patterns of seasonal rainfall. Throughout the year, but particularly during the blocked phase, the estuarine environment is controlled strongly by weak vertical mixing across what is often a very strong halocline. As a first attempt to quantify the seasonal characteristics of one of these estuaries, two experiments were carried out on the Hopkins River Estuary, Victoria, Australia, in April and in October 2000. The main objective was to observe the vertical turbulent mixing during the low current blocked phase (April), and during the high surface flow open phase (October). At the same time samples were also collected for nutrient and dissolved oxygen analysis, with the aim and quantifying the significance of the deep anoxic basins in the estuary for the productivity of the surface waters that has been observed. The results illustrate the remarkably sharp partitioning between the surface and bottom waters, with very weak turbulent transfer between them. Nevertheless, despite the observed weak mixing, the presence of sharp nutriclines and oxyclines suggested that the transfer rates of nutrients (ammonia and dissolved reactive phosphorus) from the bottom water into the surface layer, and of dissolved oxygen from the surface to the bottom water were quite high and capable of supporting significant surface productivity. This sharp transition in environments between the layers was associated with sharply defined regions of primary phytoplankton and bacterial production. A thin, concentrated particulate layer, possibly of bacteria, just below the halocline during the blocked phase appeared to have a marked effect on the vertical temperature structure of the estuary, apparently generating a localised region of convective overturning.

2. Method

At the start of each experiment an along-estuary survey of salinity, temperature, and dissolved oxygen was conducted, using a YSI 600XL multi-parameter probe. Following the initial along-estuary surveys, a number of fixed stations were sampled for turbulence and current characteristics, and nutrient and oxygen profiles. Vertical profiles of salinity, temperature, and turbulent dissipation (ε, m^2 s^{-3}) were measured using a Self Contained Autonomous Microstructure Probe (Ivey & Imberger, 1990). SCAMP free-falls through the water at a nominal speed of 10 cm s^{-1}, sampling at a rate of 100 Hz. Salinity and temperature profiles were constructed with a 1 cm resolution from an accurate conductivity-temperature sensor. Turbulent dissipation was calculated by fitting the temperature gradient wavenumber spectrum, as sampled by a differentiation circuit connected to each of two FP07 thermistors, to the Batchelor spectrum (Ruddick *et al*., 2000). Vertical profiles of the vertical diffusivity of density (K_ρ (m s^{-2})) was estimated as a function of turbulent dissipation rate and the local buoyancy frequency (e.g. Osborn, 1980).

Currents were measured with a 1200 kHz RD Instruments ADCP, with a 25 cm vertical bin size and an averaging period of 30 seconds (current s.d.=1.1 cm s^{-1}). Water samples were collected using a onboard peristaltic pump connected to a nylon pipe and a close-interval sampling intake (Jorgensen *et al*., 1979). Samples for nutrient (ammonia, DRP, nitrate), dissolved oxygen, and sulphides were collected with a vertical resolution of 50 cm (April) and 20 cm (October).

3. Results

The along-estuary survey of salinity in April 2000 showed the blocked phase of the estuary having a typical surface layer salinity of 10 to 12 ppt, with isolated deep pools in the upper estuary containing high salinity (25 – 30 ppt) bottom water (Fig. 1a). In contrast in October,

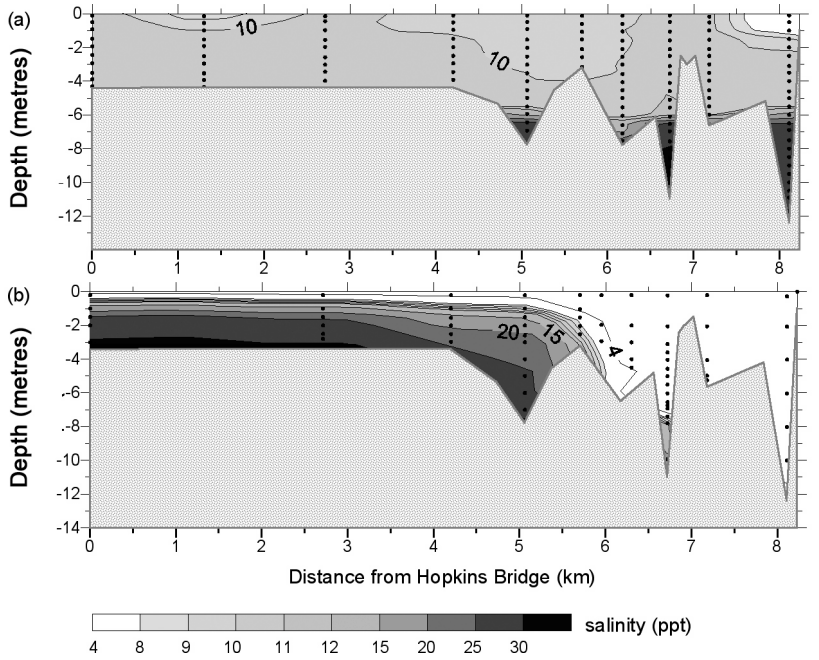

Figure 1. (a) Salinity section along the estuary, April 2000; (b) salinity survey, October 2000. The distances are measured from the Hopkins Bridge, about 700 metres upstream from the estuary mouth. Data could not be obtained below the bridge due to the lack of boat access.

much of the upper estuary, including some of the deep water, had a salinity of < 1.0 ppt, and a narrow surface layer of approximately 1 metre thickness throughout the middle and lower reaches. There was

clear evidence of a well-defined wedge of saline water intruding up estuary a distance of 6 km (Fig. 1b). Surface water in April had very high dissolved oxygen concentrations, typically 8 mg L^{-1} corresponding to 120% saturation, presumably reflecting high near-surface primary production rates. High salinity water in the deep pools, left over from the previous seasonal intrusion of the salt wedge, contained no dissolved oxygen and had very high concentrations of sulphide, reaching concentrations of 500 mg L^{-1}. The survey in October appears to have taken place after a freshwater input event had previously flushed much of the estuary. The first deep pool (8.1 km) contained water predominantly of salinity < 1 ppt, with only the bottom sample having a higher salinity (5 ppt). The second deep pool (6.7 km) contained a deep layer of high salinity water and zero dissolved oxygen. Water of the same salinity at the nose of the salt wedge had a dissolved oxygen concentration of 1 – 2 mg L^{-1}, implying that the deep water at 6.7 km was old seawater left over from the previous blocked period.

Current measurements in April 2000 rarely exceeded 5 cm s^{-1} at the surface, 1 – 3 cm s^{-1} in the interior of the deep basins, though sometimes showing near-bed increases to 3 – 5 cm s^{-1} at the bottom of the basins. In October, surface flows ranged from 10 – 20 cm s^{-1} out of the estuary, usually over a bottom layer weakly flowing upstream (1 – 2 cm s^{-1}).

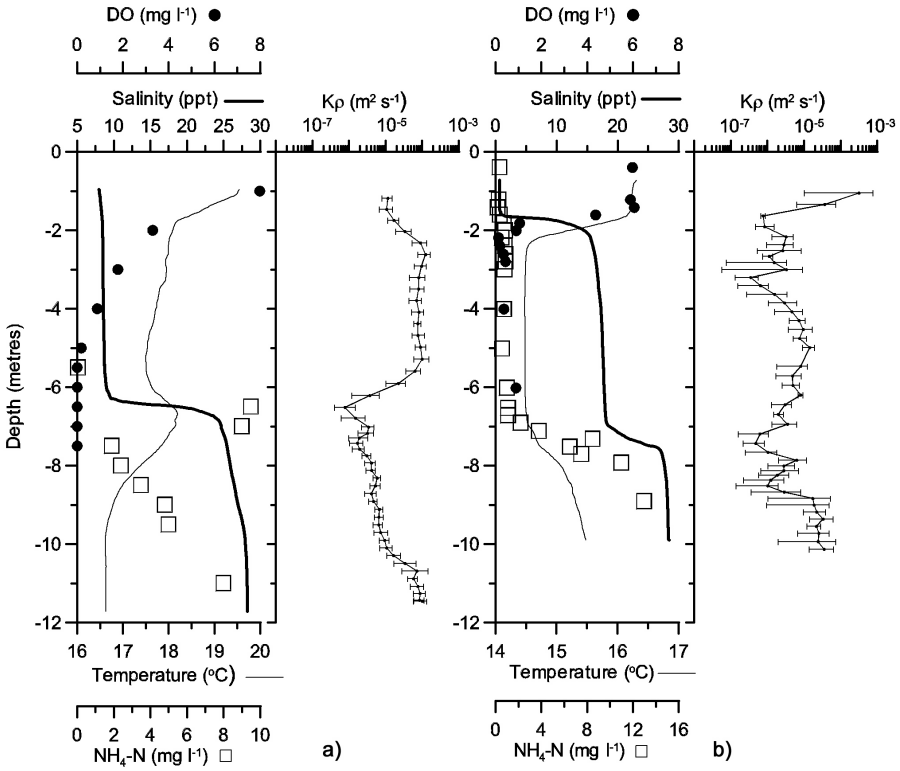

Figure 2. Vertical profiles of salinity, temperature, dissolved oxygen, NH_4-N, and vertical turbulent diffusivity in (a) April 2000 and (b) October 2000. Error bars on the diffusivity profiles represent 95% confidence intervals, estimated using a bootstrap technique.

Examples of vertical profiles in the deep basin at 6.7 km from the bridge (Fig. 2) illustrate markedly different environments during the 2 surveys. In April 2000 (Fig. 2a) the water was strongly stratified in two layers, with a low salinity (8 – 10 ppt) surface layer separated from a higher salinity (25 – 30 ppt) bottom layer by a very sharp halocline (thickness ≈30 cm). A localised increase in temperature was also evident just below the halocline, associated with a layer of photosynthetic, sulphur bacteria. Turbulent diffusion was very low at the halocline (10^{-6} m^2 s^{-1}), with higher values at the surface and bottom boundaries (10^{-5} m^2 s^{-1} and 10^{-4} m^2 s^{-1} respectively). Nutrients were very low in the surface layer, increasing linearly below the halocline to the bed. The peak in NH_4-N just below the halocline is for the filterable (i.e. dissolved) form of this nutrient. (A 0.45 μm filter was used.) Dissolved oxygen

decreased exponentially away from the surface, dropping to 0 mg L^{-1} almost 1 metre above the halocline. In October 2000 (Fig. 2b) the new seawater had apparently made further progress upstream since the time of the salinity survey in Fig. 1b, with a 3 layer structure showing old seawater below a depth of 7 metres, an intermediate layer of relatively new seawater input by the salt wedge, and a narrow surface layer of salinity < 1 ppt. Mixing across both haloclines was very low (10^{-6} m^2 s^{-1}), increasing at the surface (5×10^{-4} m^2 s^{-1}) and bottom (5×10^{-5} m^2 s^{-1}) boundaries. The recently-supplied moderate salinity water in the middle layer was already almost devoid of dissolved oxygen, and significant NH_4-N was only available in the bottom layer.

4. Conclusions

The two survey periods have illustrated two possible states of this intermittently closed estuary. When the estuary mouth is blocked the deep pools in the estuary become anoxic and highly sulphurous, supporting a dense and layered community of phytoplankton and bacteria associated with a very strong halocline. The oxygen demand by processes at and below the halocline can be estimated from the dissolved oxygen gradient and turbulent diffusivity to be approximately 8 g m^{-2} day^{-1}. A major source of nutrients to the water column appears to be in the estuary sediments, with the flux of NH_4-N up through the bottom layer estimated to be about 50 mmol m^{-2} day^{-1}. However, the observed nutrient spike at about 7 metres depth in April is believed to be sustained by re-mineralization of the organic matter falling from the surface zones by bacterial communities just below the pycnocline. The large gradient that results is estimated to produce a flux of bacterially-produced NH_4-N up through the halocline of about 120 mmol m^{-2} day^{-1}**.** This value shows the potental of bacterially-mediated remineralization to supply nutrients into the overlying surface waters. In October 2000 a salt wedge appeared to be returning seawater into the bottom of the estuary following earlier flushing by freshwater. However, by a distance of 7 km into the estuary much of the dissolved oxygen in this water had been removed. Assuming a mean inflow speed of 2 cm s^{-1}, and a typical wedge thickness of about 3 metres, it is estimated that the oxygen demand by the sediments amounted to a removal rate of 5 g m^{-2} day^{-1}. Diffusive flux of oxygen from the surface layer into the salt wedge was estimated to be only 1 g m^{-2} day^{-1}, insufficient to maintain oxic conditions in this highly productive estuary.

Our results show that there are two quite different estuarine environments under the two flow regimes. In April, the estuary has become, effectively, a meromictic lake containing a highly productive layer just below the pycnocline. That layer is believed to supply, though diffusion, all the nutrients required by the overlying surface waters. In October, however, that layer is absent and the nutrients are supplied by a combination of sources, such as by diffusion from the sediments, from river runoff and from the incoming salt wedge.

Acknowledgments: This research was supported by an Australian Research Council Small Grant. The authors wish to thank Colin Magilton and Alan Mainwaring for their assistance during the field programme.

References:

Ivey, G. N., and J. Imberger, On the nature of turbulence in a stratified fluid. Part I: the energetics of mixing. *J. Phys. Oceanogr., 21*, 650-658, 1990.

Jorgensen, B.B., J. G. Kuenen and Y. Cohen, Microbial transformations of sulphur compounds in a stratified lake (Solar Lake, Sinai). *Limnol. Oceanogr. 24*, 799-822, 1979.

Osborn, T. R., Estimates of the local rate of vertical diffusion from dissipation measurements. *J. Phys. Oceanogr., 10*, 83-89, 1980.

Ruddick, B. R., A. Anis, and K. Thompson, Maximum likelihood spectral fitting: the Batchelor spectrum. *J. Atmos. Ocean. Tech*., *17*, 1541-1555, 2000.

A finite difference method for non-hydrostatic free-surface flows that is more accurate than Boussinesq approximations but equally efficient.

G.S. STELLING[A,*,1] AND M. ZIJLEMA[A,B]

[a]*Fluid Mechanics Section, Faculty of Civil Engineering and Geosciences, Delft University of Technology, Stevinweg 1, 2628 CN Delft, The Netherlands*

[b]*National Institute for Coastal and Marine Management/RIKZ, P.O. Box 20907, 2500 EX The Hague, The Netherlands*

Abstract

A numerical technique is presented for the approximation of vertical gradient of the non-hydrostatic pressure arising in the Reynolds-averaged Navier-Stokes equations for simulating non-hydrostatic free-surface flows. It is based on the Keller-box method that take into account the effect of non-hydrostatic pressure with a very small number of vertical grid points. As a result, the proposed technique is capable of simulating relatively short wave propagation, where both frequency dispersion and nonlinear effects play an important role, in an accurate and efficient manner. Numerical examples are provided to illustrate this; accurate wave characteristics are already achieved with only two layers.

KEY WORDS: free-surface flow; non-hydrostatic pressure; Keller-box scheme; wave propagation

1. Introduction

The design of efficient and accurate numerical algorithms is an essential prerequisite for the simulation of wave propagation from deep water through the surf zone, particularly for coastal engineering-type applications. Boussinesq-type wave equations with improved dispersion characteristics formulated by, e.g., Madsen and Sørensen [1] and Nwogu [2] are well suited to model different wave phenomena, especially in shallow water regions, such as nonlinearity, dispersion and shoaling. Also, these models include implicitly refraction and diffraction. Since, the Boussinesq-type wave models are based on an efficient depth-integrated formulation, they also have become very popular for real-life applications involving wave dynamics in coastal regions and harbours. However, a well-known drawback of the Boussinesq-type modelling is the assumption of an irrotational and inviscid flow. As a consequence, neither the interaction of waves with rotational currents nor the effects of viscosity on the wave motion can be simulated.

An alternative route is a numerical solution for incompressible turbulent fluid flows involving gravity waves based on the time-dependent three-dimensional Reynolds-averaged Navier-Stokes equations. This approach is not only suitable to model wave-dominated flows over the entire range of water depths but also for simulating wave disturbance in real fluid with rotation and shear. A number of studies have been reported in which the features of this approach in the context of wave dynamics have been investigated.

In the papers of Casulli and Stelling [3], Casulli [4] and Stelling and Busnelli [5], a fractional step method is proposed that describes the inclusion of non-hydrostatic pressure by solving a Poisson equation in the hydrostatic free-surface flow model of Casulli and Cheng [6]. This hydrostatic model solves the 3D shallow water equations in Cartesian co-ordinates whereby the vertical accelerations are neglected and the vertical velocity is obtained from the (local) continuity equation. Such a model is sufficiently accurate for large-scale flow phenomena like tidal and wind-driven flows in coastal seas,

* Correspondence to: Guus Stelling. Tel.: +31 15 2785426; fax: +31 15 2784842
[1] E-mail: g.stelling@ct.tudelft.nl

lakes, estuaries and rivers, but prohibits a correct calculation of short surface waves. The underlying motivation for the proposed fractional step approach is that the existing shallow water solver need not to be adapted, since the correction to the hydrostatic pressure is done after the shallow water equations have been solved. As a consequence, this reduced the effort of software maintenance to a minimum. Moreover, Mahadevan *et al*. [7] have shown that this technique also leads to a more stable and efficient non-hydrostatic calculations than in a case without splitting the pressure into hydrostatic and non-hydrostatic parts. An example of the latter procedure can be found in Mayer *et al*. [8], where 2D Euler equations including total pressure is solved and the surface elevation is determined by means of a kinematic boundary condition along the free surface.

The method of decomposing the pressure into hydrostatic and non-hydrostatic components has also been employed by Stansby and Zhou [9] and Zhou and Stansby [10]. However, their method is formulated in the sigma co-ordinate system, except for the horizontal non-hydrostatic pressure gradient which is retained in Cartesian co-ordinates since, sigma transformation of the horizontal gradients may introduce large truncation errors near a steep bed resulting from the summation of large terms of opposite sign [11]. These truncation errors can cause spurious flows. Like Casulli and Stelling [3], a conjugate gradient method is employed for the solution of Poisson pressure equation. In the former paper, they also demonstrated the use of their model for simulating waves and currents over trenches and hills. Another procedure of similar purport is discussed by Li and Fleming [12]. However, they discretized the momentum equations with the MacCormack's explicit scheme and thus suffering from the CFL stability restriction related to the gravity wave speed. Furthermore, the Poisson equation for the non-hydrostatic pressure is solved by means of a multigrid technique.

It is recognized that sufficiently large number of vertical grid points is required in a 3D free-surface Navier-Stokes computation for describing wave dispersion characteristics up to an acceptable level of accuracy. In practice, this number is about 10 to 20; see, for instance, [4], [10], [12] and [13]. Combined with the solution of the elliptic equation for the non-hydrostatic pressure, this greatly increases the computational effort that may hamper three-dimensional applications with a sufficiently fine grid.

In this paper, we present an accurate approximation of vertical gradient of the non-hydrostatic pressure based on the Keller-box or Preissmann scheme; see, e.g., [14]. This scheme belongs to the class of implicit finite difference schemes which are of a higher order of accuracy compared to the explicit schemes involving the same number of grid points. The scheme is also referred to as the Hermitian spline method, see, e.g., [15]. In fact, it is a discrete analogue of the Boussinesq-type of wave models; the vertical dependency of the non-hydrostatic pressure can be considered to be resolved by a finite series of spline functions. The splines are described by the pressure itself and its vertical derivative. In this manner, the implicit scheme calculates the vertical gradients of the non-hydrostatic pressure at different vertical grid points simultaneously. The results presented in this paper show that this procedure allows a very small number of layers (in the order of 1 to 3) for the accurate simulation of relatively short waves. Even in the case of one layer, i.e. the depth-averaged mode, it predicts the frequency dispersion for fairly short waves in shallow water with an accuracy similar to that of the Boussinesq-type wave model of Peregrine [16].

References

1. Madsen PA, Sørensen OR. A new form of the Boussinesq equations with improved linear dispersion characteristics. Part 2. A slowly-varying bathymetry. *Coastal Engng.* 1992; **18**: 183-204.

2. Nwogu O. Alternative form of Boussinesq equations for nearshore wave propagation. *J. of Waterway, Port, Coastal and Ocean Engng.* 1993; **119**: 618-638.

3. Casulli V, Stelling GS. Numerical simulation of 3D quasi-hydrostatic, free-surface flows. *J. Hydr. Engng. ASCE* 1998; **124**: 678-686.

4. Casulli, V. A semi-implicit finite difference method for non-hydrostatic, free-surface flows. *Int. J. Numer. Meth. Fluids* 1999; **30**: 425-440.

5. Stelling GS, Busnelli MM. Numerical simulation of the vertical structure of discontinuous flows. *Int. J. Numer. Meth. Fluids* 2001; **37**: 23-43.

6. Casulli V, Cheng RT. Semi-implicit finite difference methods for three-dimensional shallow water flow. *Int. J. Numer. Meth. Fluids* 1992; **15**: 629-648.

7. Mahadevan A, Oliger J, Street R. A nonhydrostatic mesoscale ocean model. Part II: numerical implementation. *J. Phys. Oceanogr.* 1996; **26**: 1881-1900.

8. Mayer S, Garapon A, Sørensen LS. A fractional step method for unsteady free-surface flow with applications to non-linear wave dynamics. *Int. J. Numer. Meth. Fluids* 1998; **28**: 293-315.

9. Stansby PK, Zhou JG. Shallow-water flow solver with non-hydrostatic pressure: 2D vertical plane problems. *Int. J. Numer. Meth. Fluids* 1998; **28**: 541-563.

10. Zhou JG, Stansby PK. An arbitrary Lagrangian-Eulerian σ (ALES) model with non-hydrostatic pressure for shallow water flows. *Comput. Meth. Appl. Mech. Engng.* 1999; **178**: 199-214.

11. Stelling GS., Van Kester JAThM. On the approximation of horizontal gradients in sigma co-ordinates for bathymetry with steep slopes. *Int. J. Numer. Meth. Fluids* 1994; **18**: 915-935.

12. Li B, Fleming CA. Three-dimensional model of Navier-Stokes equations for water waves. *J. of Waterway, Port, Coastal and Ocean Engng.* 2001; **127**: 16-25.

13. Lin P, Li CW. A σ-coordinate three-dimensional numerical model for surface wave propagation. *Int. J. Numer. Meth. Fluids* 2002; **38**: 1045-1068.

14. Lam DCL, Simpson RB. Centered differencing and the box scheme for diffusion convection problems. *J. Comput. Phys.* 1976; **22**: 486-500.

15. Rubin SG, Khosla PK. Polynomial interpolation methods for viscous flow calculations. *J. Comput. Phys.* 1977; **24**: 217-244.

16. Peregrine DH. Long waves on a beach. *J. Fluid Mech.* 1967; **27**: 815-827.

17. Dingemans MW. *Water wave propagation over uneven bottoms*. World Scientific: Singapore, 1997.

18. Van der Vorst HA. Bi-CGSTAB: a fast and smoothly converging variant of Bi-CG for the solution of nonsymmetric linear systems. *SIAM J. Sci. Stat. Comput.* 1992; **13**: 631-644.

19. Van der Vorst HA. Iterative solution methods for certain sparse linear systems with a non-symmetric matrix arising from pde-problems. *J. Comput. Phys.* 1981; **44**: 1-19.

20. Chen, X. Three-dimensional hydrostatic and non-hydrostatic modeling of seiching in a rectangular basin. In *Proc. of 6th International Conference Estuarine and Coastal Modelling*, 2000; 148-161.

21. Weilbeer H, Jankowski JA. A three-dimensional non-hydrostatic model for free surface flows - development, verification and limitations. In *Proc. of 6th International Conference Estuarine and Coastal Modelling*, 2000; 162-177.

22. Namin MM, Lin B, Falconer RA. An implicit numerical algorithm for solving non-hydrostatic free-surface flow problems. *Int. J. Numer. Meth. Fluids* 2001; **35**: 341-356.

23. Beji S, Battjes JA. Experimental investigation of wave propagation over a bar. *Coastal Engng.* 1993; **19**: 151-162.

24. Luth HR, Klopman G, Kitou N. Project 13G: Kinematics of waves breaking partially on an offshore bar; LDV measurements for waves with and without a net onshore current. Delft Hydraulics, Technical report H1573, 1994.

25. Dingemans MW. Comparison of computations with Boussinesq-like models and laboratory measurements. Delft Hydraulics, Technical report H1684.12, 1994.

26. Berkhoff JCW, Booy N, Radder AC. Verification of numerical wave propagation models for simple harmonic linear water waves. *Coastal Engng.* 1982; **6**: 255-279.

27. Wei G, Kirby JT, Sinha A. Generation of waves in Boussinesq models using a source function method. *Coastal Engng.* 1999; **36**: 271-299.

Modelling of estuaries using Finite Element Methods

OLE SVENSTRUP PETERSEN

(DHI Water & Environment – Agern Alle 11, DK-2970 Hørsholm, Denmark , osp@dhi.dk)

LARS STEEN SØRENSEN

(DHI Water & Environment)

OLE RENE SØRENSEN

(DHI Water & Environment)

1. Introduction

The environment in tidal estuaries is generally the result of a dynamic balance between tides and surges, riverine runoff and the sea salinity, local meteorological conditions, the topography and sediment fluxes and deposits. It is further characteristic, that salt and freshwater meets within the estuary, commonly creating a relatively complex stratified situation. On longer timescale, the topography itself may adjust to the prevailing regime of waves, currents and sediment fluxes, thus contributing to the delicate balance that establishes the estuary. Quantitative understanding and modeling of such a dynamic environment can therefore be a challenging but often necessary task. We have therefore initiated development of a modelsystem, aimed at describing these processesThe model is applied to Mariager Fjord, a Danish tidal estuary with a 20 km long narrow inlet, where an extensive set of observations for 1998 exists.

2. Mariager Fjord

Mariager Fjord, shown in Figure 1, is located on the East Coast of Jutland and may be considered as a representative of a micro tidal estuary. However, due to its origin in a drowned glacial tunnel valley, it has some special characteristics. The fjord is 40 km long with a 20 km long shallow inlet with up to 5 km wide tidal flats and a narrow (50-100 m) tidal channel approximately 7 m deep. The inner part is relatively deep, up to 30 m. There is a small freshwater inflow to the inner part, 3 m^3/s on yearly average, thus the inner part is permanently stratified, with salinities up to 25 PSU in the bottom waters, corresponding to the salinity in Kattegat.

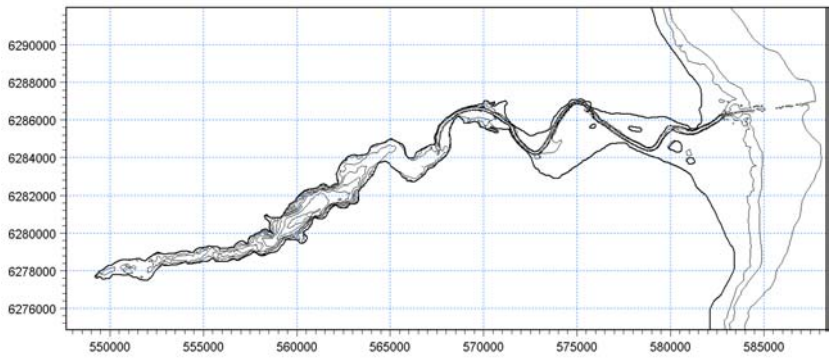

Figure 1: Mariager Fjord before the reclamation with observation stations indicated.

The exchange of water with Kattegat is due partly to the daily tidally induced flows, partly due to "events", taking place 1-3 times per year, where the water levels in Kattegat raises during longer periods, causing relatively large inflows of saline water. Due to the differences in salinity, the

inflowing water enters the inner parts of the fjord in the deepest layers, from where it gradually is mixed vertically, mainly by the action of the winds.

After a massive oxygen depletion during August 1998, discussion was raised whether a reclamation covering parts of the mouth of the inlet could have reduced the exchange of water to the estuary and thereby accelerated the deoxygenation. The effect of the reclamation is mainly to reduce the cross sectional area of the inlet, mostly during high water levels, as the reclamation rests only on the shallow parts of the inlet, thereby affecting the larger inflow events. Further, the smaller width of the mouth may reduce the mixing efficiency between outflowing brackish water and the Kattegat water, thereby changing the properties of the inflowing waters.

An important issue is the separation in timescale: the effects of a reduced inlet cross section is to change the actual flow through the tidal inlet, while the effects on the stratification and renewal of water in the inner parts of the estuary only can be seen on timescales comparable with the residence time.

3. The study

To quantify the effects of the reduced inlet cross section a study was designed comprising *i)* a detailed 2D depth averaged model, resolution of the order 20 m, describing the tidal flow during selected weekly periods and *ii)* a coarse 3D model with a 0.5 m vertical resolution, describing the stratification and vertical mixing in the inner parts during a 1 year period. A designated measurement programme for model calibration, including 1 year continuous observations of water levels and properties, bathymetric surveys of shallow parts of the inlet and longitudinal CTD transects was also part of the programme.

The 2D depth averaged model is based on an unstructured mesh, capable of resolving the very narrow inlet and the tidal channel through the outer parts of the estuary, while at the same time economically provide a fair resolution of the Kattegat and inner parts of the estuary, as shown in Figure 2. Briefly, the model is part of the MIKE 21 FM system and here we solve the shallow water equations using a Petrov-Galerkin method and an explicite time marching. The flooding and drying of tidal flats is described using a so-called slot-method. The model is forced by observed wind, river runoff and water levels in Kattegat.

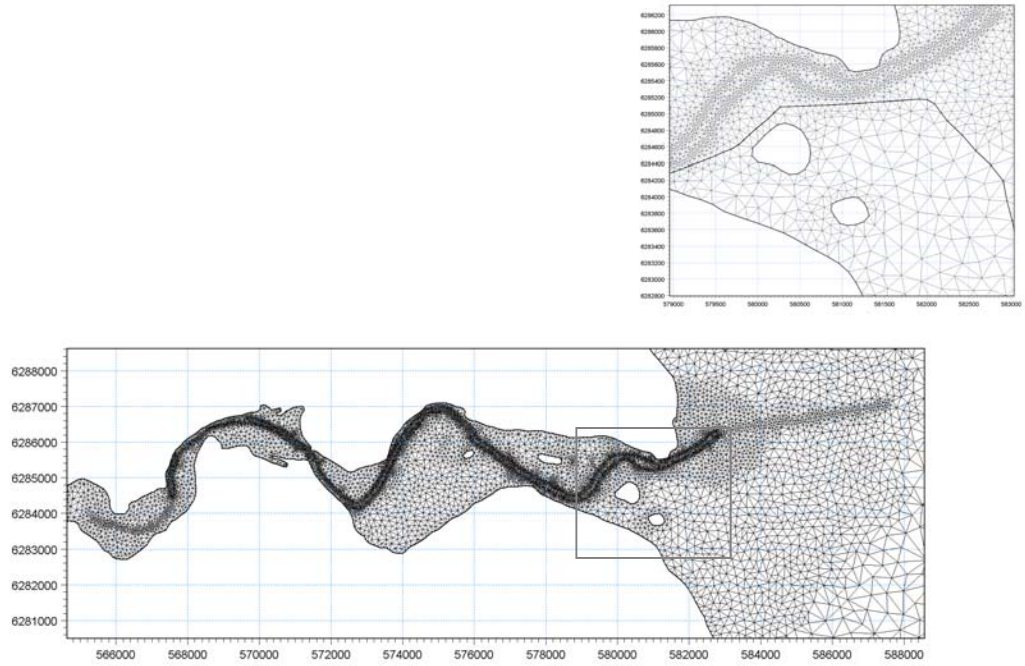

Figure 2: Computational mesh for the Mariager Fjord model. The mesh actually covers a larger part of the Kattegat

The 3D model is based on a standard 3D Cartesian finite difference model, with z-level vertical discretization. The background for this choice is that focus is on the vertical stratification, thus to accomplish 1 y simulation a very coarse horizontal mesh is necessary, making it necessary to do some idealization of the narrow channel. In the present setup the outer part has been replaced by a straight channel, designed to retain the hypsometric characteristics of the outer part, i.e. same width of flats, depth of channel and cross-section area. The model is forced using wind, runoff, meterology and water levels in the Kattegat. The model is calibrated using time series of discharges from the 2D model.

In Figure 3 are shown examples of modeled water levels using the 2D model. The simulations generally indicated a minor effect of the reclamation on the tidal discharges. Figure 4 displays vertical transects of the salinity in situations with and without a distinct saline wedge. As an integral result is shown the effective residence times for salt in three parts of the estuary, estimated from simulate fluxes.

In conclusion the study has indicated the feasibility of using 2D and 3D models to describe transports to a tidal estuary.

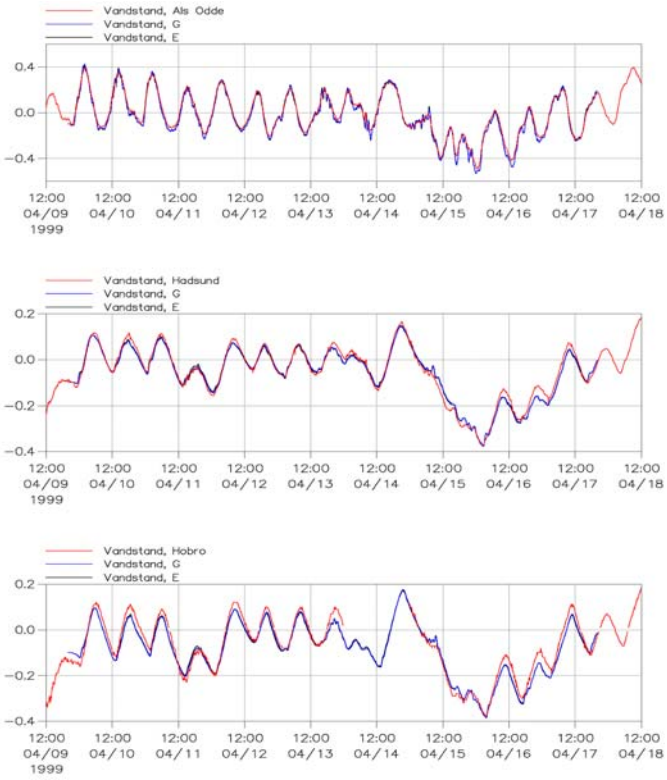

Figure 3: Observed and modelled water levels in stations 1 (upper) ,2 and 3 in Mariager Fjord

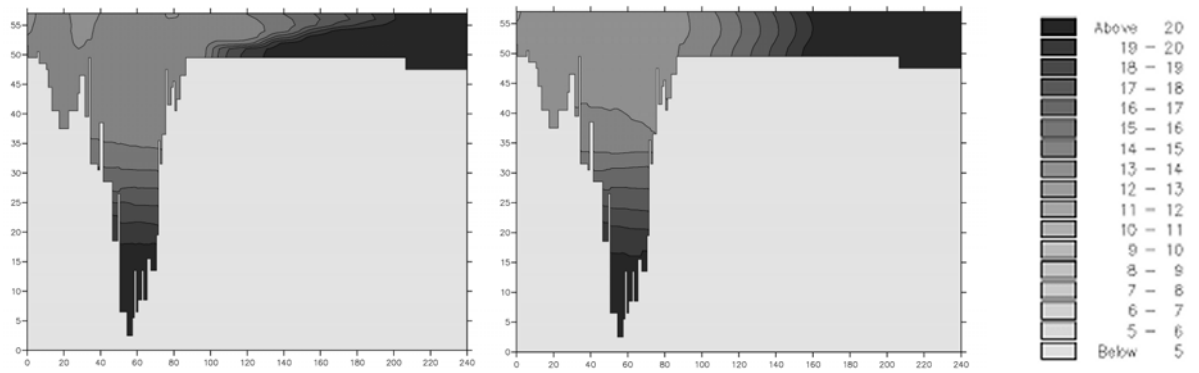

Figure 4: Examples of modelled distribution of salinity in Mariager Fjord

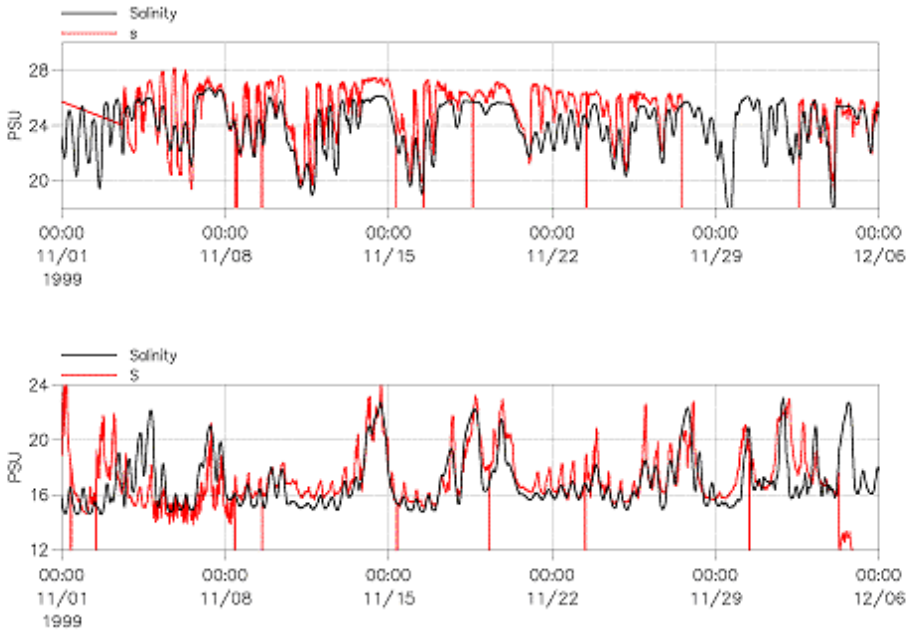

Figure 5: Computed and observed salinity in stations 1 and 2

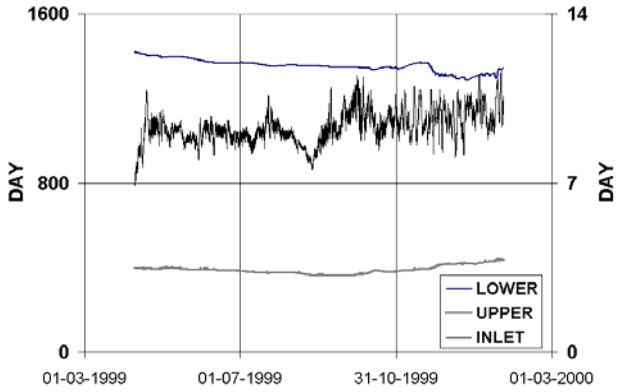

Figure 6: Calculated residence times for salt in different parts of Mariager Fjord

A methodology to estimate the residence time of estuaries

FRANK BRAUNSCHWEIG

(Instituto Superior Técnico, Sala 363, Nucleo Central, Taguspark, P-2780-920, Oeiras, Portugal, frank.maretec@taguspark.pt)

PAULO CHAMBEL

(Instituto Superior Técnico, Sala 363, Nucleo Central, Taguspark, P-2780-920, Oeiras, Portugal, paulo.chambel.maretec@taguspark.pt)

FLÁVIO MARTINS

(Escola Superior de Tecnologia - University of Algarve, Campus da Penha, P-8000-117Faro, Portugal, fmartins@ualg.pt)

RAMIRO NEVES

(Instituto Superior Técnico, Sala 361, Nucleo Central, Taguspark, P-2780-920, Oeiras, Portugal, ramiro.neves.maretec@taguspark.pt)

1. Introduction

The residence time has long been used as a classification parameter for estuaries and other semi-enclosed water bodies. It aims to quantify the time water remains inside the estuary, being used as an indicator both for pollution assessment and for ecological processes. Estuaries with a short residence time will export nutrients from upstream sources more rapidly then estuaries with longer residence time. On the other hand, the residence time determines if micro-algae can stay long enough to generate a bloom. As a consequence, estuaries with very short residence times are expected to have much less algae blooms then estuaries with longer residence time. In addition, estuaries with residence times shorter than the doubling time of algae cells will inhibit the formation of algae blooms (EPA, 2001). The residence time is also an important issue for processes taking place in the sediment. The fluxes of particulate matter and associated adsorbed species from the water column to the sediment depend on the particle's vertical velocity, water depth and residence time. This is particularly important for the fine fractions with lower sinking velocities. The question is how to compute the residence time and how does it depend on the computation method adopted.

A large number of different methods have been proposed, ranging from simple integral estuary-wide formulas to more complex methodologies (Dyer, 1973), (Zimmerman, 1976), (Geyer, 1997), (Hagy *et al.*, 2000). All of those approaches attempt to account for advection and mixing inside the estuary, but, because they are based on integral methods, they lack to describe accurately the dynamics of the water masses. Using high-resolution hydrodynamic models it is possible to overcome that problem simulating explicitly the transport processes. In this paper, a methodology to quantify residence time in estuaries is proposed. The methodology is based upon the MOHID primitive equation hydrodynamic model, coupled to its lagrangian transport module. Besides the estimation of overall estuary residence time, the subdivision of the estuary into monitoring boxes enables the quantification of residence times inside each box and the water exchange among the boxes.

2. Methodology

A way to estimate the residence of water inside estuaries and, at the same time, the dynamics of the water masses was implemented in the MOHID model. The MOHID model is a modular 3D water modelling system (Miranda, *et al*. 2000). The currents are calculated in the hydrodynamic module, which is a full 3D hydrodynamic model, assuming the hydrostatic and Bousinesq approaches. The hydrodynamic model uses the turbulence formulation of the general ocean turbulence model – GOTM

(Buchard *et al.*, 1999). Two transport models are coupled to this hydrodynamic module using eulerian and lagrangian formulations respectively. In this paper only the lagrangian transport model was used.

The estuaries were divided into boxes. These boxes have two functions: on one hand, they are used to release lagrangian tracers at the beginning of the simulation and, on the other hand, they are used to monitor the tracers passing through them during the simulation. With this approach two basic questions, related to the physical dynamics of the estuaries can be answered:

- In which boxes are located the water masses initially released in box *i*? The answer to this question can show how a specific area can influence other areas of the estuary. In this way, the user looks from the origin of the water masses (one box) to their destination (all boxes).
- From which boxes came the water masses that occupy box *i* at a certain instant? The answer to this question can show the influence over a given area from other areas in the estuary. In this way, the user looks to the destination of water masses (one box), from given origins (all boxes).

The conventional residence time indexes quantify the estuary as a whole. With the method described here, it is possible to quantify the "residence time" of each region of the estuary. This is useful, for example, to identify vulnerable zones regarding eutrophication. This is especially important in estuaries with low overall residence times but exhibiting vulnerable regions with high residence times. This methodology is applied in three Portuguese estuaries: the Tagus estuary, the Mondego estuary and the Sado estuary. In each estuary the MOHID modelling system has been used to calculate the estuary residence time and the water exchange between the monitoring boxes.

3. Results

The model uses a 3D structured grid with generic vertical geometry (Martins *et al.*, 2001). In this set of simulations only one layer was used in the vertical direction. 2D depth integrated results are thus obtained. The method is illustrated here using the results for the Tagus Estuary. The Tagus Estuary domain covers an area of 90km by 76km (195 by 166 grid points). The grid cells have a space step between 300m and 3500m. The boxes where placed in a way to include the whole estuary, limited at the estuary mouth by the limits established in a previous work.

The hydrodynamic model was forced imposing the tide elevation at the open boundary and using the mean river discharges of the most important rivers. The influence of wind over the residence time was also studied. Initially the estuaries where filled with lagrangian tracers, in a way that the total volume associated to the tracers match the total volume of the estuary. The simulations were carried out at least until 80% of the tracers had moved to the shelf.

The evolution of the tracer's fraction inside each box (volume of all tracers inside the box divided by the total volume of water in the box) was calculated.

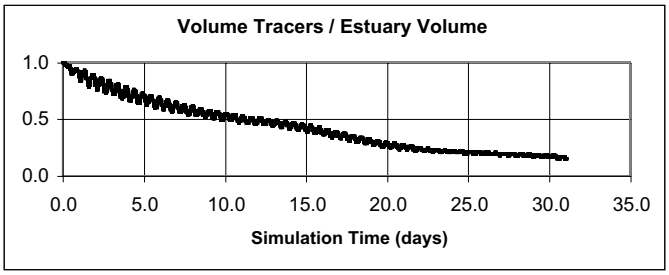

Figure 1: Evolution of the ratio between the volume of lagrangian tracers inside the estuary and the total estuary volume as a function of time (Tagus estuary).

Figure 1 shows the fraction of tracers inside Tagus Estuary over a 30 day simulation period. One can see that after 25 days only 20% of the initial water mass remains in the estuary.

This definition of residence time only accounts for the time required to expel a fraction of estuarine water, but does not account for the history of the renewal process. A way to account for that history of the water renewal process is to integrate, in time, for each box *i*, the volume of particles from origin *j* present inside the box.

$$\tau_{i,j}(T) = \int_0^T \frac{V_{i,j}(t)}{V_i(t)} dt$$

If the water inside the estuary were not renewed at all, a graphical representation of this function (τ vs. *t*) would be a straight line with unitary slope.

As the water is renewed in the estuary, the contribution of the initial water for the actual water inside the estuary tends to zero and the integral tends to a constant value. The function τ(T) gives the relative contribution of the initial water mass over the total volume that passed inside the estuary.

This method can be applied for the estuary as a whole or for each region inside of it. Figure 2 represents the evolution of the relative contribution of the initial water mass for the whole estuary as a function of the simulated time. For each instant, Figure 2 represents the relative contribution of the initial water mass (expressed as time). As the initial tracers leave the estuary, the integral tends to a constant value. In case of the Tagus estuary 12 days is reached after 32 days of simulation. This value means that the initial water inside the estuary has influenced it as a whole on a fraction of 12/32 (which represents _(T) / T), while the new water has influenced it on a fraction of 20/32.

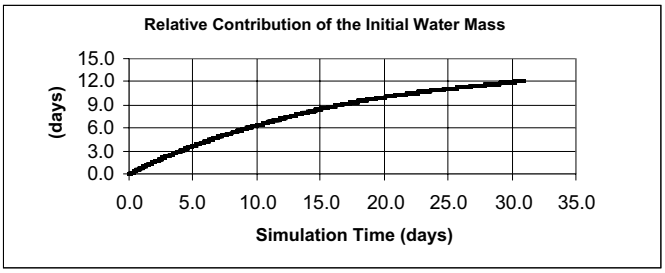

Figure 2: Relative contribution of the initial water mass as function of the simulated time.

The boxes approach used in this study allows defining, for each box, a graph like the one shown in Figure 2. These graphs would not only have into account the influence of the water initially located in the box, but also the water that initially belonged to different boxes. Using this approach, the relative contribution, as fraction of _(T) / T, of each box over all boxes can be defined. For the Tagus Estuary this result is shown Figure 3.

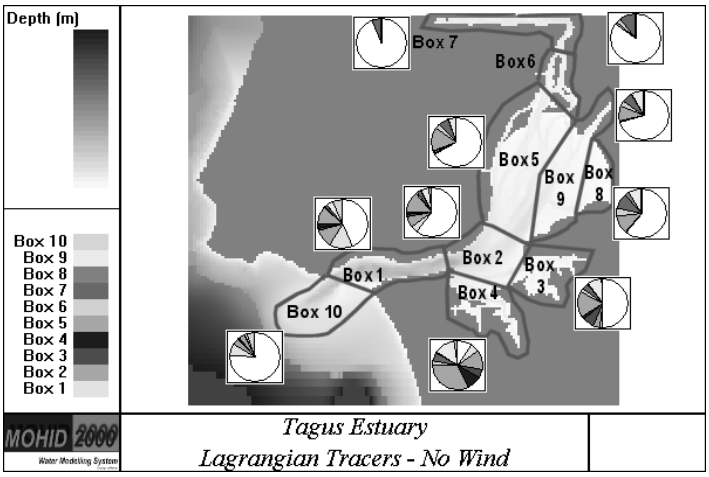

Figure 3: Relative contribution in each box after 30 days of simulation. The white part represents the new water (either river or seawater).

This kind of information helps to understand the residence time, the mixing and the water patterns of each estuary region.

4. Conclusions

The two parameters described in this paper (tracer's fraction and relative contribution) are extensions of the traditional methods to determine the residence time in estuaries. They have the disadvantage of requiring detailed simulations of the system but have the advantage of giving more information about the physical dynamic of the estuary.

Acknowledgments: This work was carried within the FESTA II research project funded by the FCT (Fundação para a Ciência e Tecnologia) by the contract nº POCTI-MGS/34457/99.

References:

Buchard, H., K. Bolding and M. R. Villarreal, GOTM, a General Ocean Turbulence Model, Theory, implmentation and test cases. *Report EUR18745 EN, European Comission, 103 pp.*, 1999.

Dyer, K., Estuaries: A physical introduction, Wiley-Interscience, New York, 1973.

EPA, Nutrient Criteria Estuarine and Coastal Water, *Environment Protection Agency, Appendix C*, 2001.

Geyer, W. R., Influence of wind on dynamics and flushing of shallow estuaries. *Estuarine Coastal Shelf Sci 44: pp 713-722*, 1997

Hagy, J. D., L. P. Sanford and W. R. Boynton, Estimation of net physical transport and hydraulic residence times for a coastal plain estuary using box models, *Estuaries 23(3) pp 328-340*, 2000.

Martins, F., R. Neves, P. Leitão and A. Silva, 3D modelling in the Sado estuary using a new generic coordinate approach, *Oceanologica Acta*, 24:S51-S62, 2001.

Miranda, R., F. Braunschweig, P. Leitão, R. Neves, F. Martins and A. Santos, Mohid 2000 A costal integrated object oriented model, *Hydraulic Engineering Software VIII, pp 391-401*, WIT Press, 2000.

Zimmerman, J.T.F., Mixing and flushing of tidal embayments in the western Dutch Wadden Sea, Part I: Distribution of salinity and calculation of mixing time scales, *Netherlands J Sea Res 10(2) pp 149-191*, 1976.

Flow regimes in estuaries and channels with standing tidal waves and significant cross channel depth variations

CHUNYAN LI

(Skidaway Institute of Oceanography, 10 Ocean Science Circle, Savannah, Georgia,31411, USA, chunyan@skio.peachnet.edu)

1. Introduction

Coastal estuaries and waterways are usually shallow, or the tidal amplitude (a) is on the order of 10% or more of the mean water depth (h), implying strong nonlinear effects. The nonlinear effects can generate non-zero mean circulations in both vertical water column [e.g. Johns, 1970; Jay and Smith, 1990a,b] and horizontal dimensions [Zimmerman, 1981] particularly at where there is a significant cross-channel depth variation. In a modeling study, Li and O'Donnell [1997] (LO) have calculated the tidally driven residual circulation in shallow estuaries and tidal channels with lateral depth variation. A two-dimensional, depth-averaged model is used. The solution is presented for v-shaped channels. Exchange flow is found to be correlated with the topography. Generally, a net landward flow occurs over the shoals and is balanced by a return flow in the channel. This flow pattern is the opposite of the density driven flow [Hamrick, 1979].

The LO work is however only applicable to progressive or partially progressive waves in long tidal channels. For a standing wave, the net inward/outward transport of water approaches to zero in the LO theory, contrasting some observations in short channels. This is apparently caused by an approximation made in the LO model - the lateral (cross-channel) variation of the first order tide is neglected. The effect of this approximation needs to be evaluated especially for short estuaries in which the usually small advection (as in long tidal channels) becomes more important because of the vanishing nonlinear continuity effects in a standing wave condition. Since short channels are quite common along the east coast of the U.S. between barrier islands, it is of great interest to examine the tidally driven flows in standing wave conditions and in channels with significant lateral depth variations. Our question here is then, for short channels (estuaries) with standing wave conditions, will the dynamic balance stay the same as in the LO theory? To properly address this question, we use a more accurate analytic model and a numerical model to focus on the nonlinearly induced subtidal flows in short channels.

2. Models and Solutions

The LO model solution for tidally induced residual circulation in an estuary with lateral depth variation is obtained by assuming that the first order tide is the same as that in a flat bottom channel, i.e. lateral variations in the first order tide are neglected. This approximation has significantly simplified the solution. However, the possibility that lateral variations in the first order tide can impact the residual flow can not be assessed. To include the effect of the lateral variation of the first order tide due to lateral depth variation, we use the solution of Li and Valle [1999] (LV) as the first order tide which is applicable to narrow tidal channels with arbitrary lateral depth variations. The second order tidally-induced flow can be readily obtained using the LO method. For brevity, the first order equations are

$$\frac{\partial \mathbf{u}_1}{\partial t} = -g\nabla\zeta_1 - \beta\frac{\mathbf{u}_1}{h}, \quad \frac{\partial \zeta_1}{\partial t} + \nabla\cdot(h\mathbf{u}_1) = 0 \tag{1}$$

in which $\mathbf{u}_1=(u_1, v_1)$, $\_1$, $h(y)$, t, g, and $\_=8C_DU/3\pi$, are the first order velocity, the first order elevation, mean depth, time, gravitational acceleration, and the friction coefficient, respectively. The operator $\nabla = (\partial/\partial x, \partial/\partial y)$, where x and y are the coordinates. The depth function is arbitrary subject

to some conditions described in LV. The friction coefficient is calculated based on the drag coefficient C_D and the velocity scale U. The second order equations are

$$\overline{(\mathbf{u}_1 \cdot \nabla)\mathbf{u}_1} = -g\nabla\overline{\zeta_2} - \beta\frac{\overline{\mathbf{u}_2}}{h} + \beta\frac{\overline{\mathbf{u}_1\zeta_1}}{h^2}, \quad \nabla\cdot(\overline{\zeta_1\mathbf{u}_1}) = 0 \tag{2}$$

in which $\mathbf{u}_2$ and ζ_2 are the second order velocity and elevation, respectively. The overbar represents a temporal average over one tidal cycle. As in LO, we define the transport velocity to be the mass flux divided by the mean water depth, or

$$\mathbf{u}_T = \overline{\mathbf{u}_2} + \frac{\overline{\zeta_1\mathbf{u}_1}}{h} \tag{3}$$

The solution based on LO and LV is

$$u_T = 2\frac{\overline{\zeta_1 u_1}}{h} - \frac{h}{\beta}\left(\overline{u_1\frac{\partial u_1}{\partial x}} + \overline{v_1\frac{\partial u_1}{\partial y}} + g\frac{\partial\overline{\zeta_2}}{\partial x}\right), \quad v_T = -\frac{1}{h}\frac{\partial}{\partial x}\left(\int_0^D h u_T dy\right) \tag{4}$$

where

$$\frac{\partial\overline{\zeta_2}}{\partial x} = \frac{\beta}{g\int_0^D h^2 dy}\int_0^D\left[2\overline{\zeta_1 u_1} - \frac{h^2}{\beta}\left(\overline{u_1\frac{\partial u_1}{\partial x}} + \overline{v_1\frac{\partial u_1}{\partial y}}\right)\right]dy \tag{5}$$

and D is the width of the tidal channel/estuary.

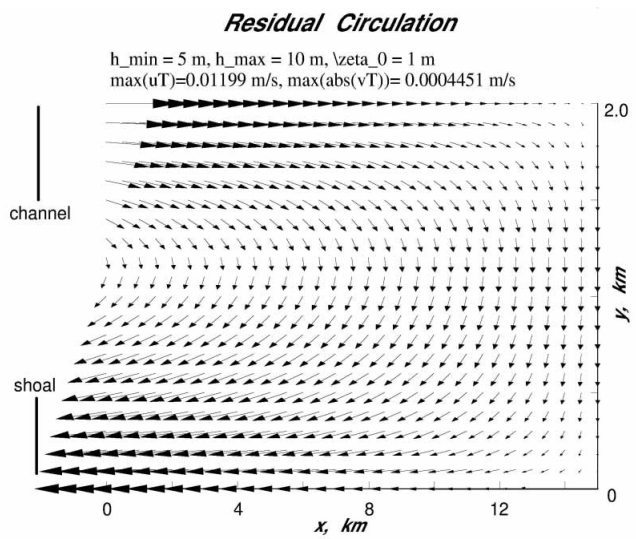

Figure 1. Residual Circulation in half of the analytic model.

In addition to the analytic model, a numerical model is also used to calculate the tidally induced residual flows in short channels with standing waves. The Alternative Directional Implicit (ADI) finite difference method is applied to the 2-D depth –averaged nonlinear shallow water equations with quadratic bottom friction. A finite difference numerical scheme for the equations is adopted. The time interval _*t* is considered over two successive operations. The first operation calculates the elevation and longitudinal velocity implicitly. The lateral velocity is then calculated explicitly. The second operation calculates the elevation and lateral velocity implicitly from known values of both the velocity and the elevation of the first operation. The longitudinal velocity of the second step is then calculated explicitly. This scheme combines the advantages of implicit methods which are unconditionally stable for linear equations and the computational advantages of explicit methods.

3. Results

The solutions are calculated for depth functions identical to those of LO, i.e., an exponential function of water depth with a minimum on the either side and a maximum in the middle of the model, forming a symmetric v-shaped profile of bottom in a cross-section. The verifications of the models are made by

checking the momentum and mass balances. The relative error of these balances is on the order of 10^{-4} to 10^{-2} for all conceivable parameters. The results of the analytic and numerical models are consistent with each other. Note that the present models are valid for both long and short channels. For long tidal channels, in which the tidal waves are progressive or partially progressive, the results are similar to the LO model. The only difference between the present models and the *ad hoc* LO model for long channels is that the latter has slightly larger residual velocities. The flow patterns, that the net inward flow occurs over the shoal and the net outward flow occurs in the channel, are the same. The present models for short tidal channels however, show that the pattern of the tidally induced mass flux is just the opposite of the LO model (which is only applicable to long channels). In other words, the net inward flow is through the deep water balanced by a return (outward) flow over the shoals (Figure 1). Here "short channels" are those shorter than 1/8 of the dynamic wave length. And here the "dynamic wave length", defined by $2\pi\sqrt{gh}/\sigma$ (σ is the angular frequency of the tide), is usually different from the geometric length (LO). For these short channels, the phase difference between elevation and velocity is around 90 degree, indicating a standing wave condition. Figure 2 shows the results obtained by calculating the analytic solution with channels of different lengths. Obviously, there is a shift in flow pattern as the channel length (normalized by a quarter of the dynamic wave length) increases. Since the exchange flow is a shear flow, the vorticity is an appropriate quantity for the analysis of the mechanisms that drive the residual flows. A similar experiment is done using the numerical model which shows the same pattern (omitted here). An analysis of the analytic solution shows that similar to the LO results, there are three major contributions to the total transport vorticity defined by $\nabla \times \mathbf{u}_T$: those of continuity, advection, and pressure gradient origins, respectively. Figure 3 shows the relative importance of each of these contributions. Note that the first term, the "continuity" component (same as the "Stokes" component in LO) is the smallest of the three and the advection is the main component. This is in direct contrast to the LO model for long channels in which the advective effect is the smallest while the continuity effect is the largest. Apparently, for standing waves, the velocity and elevation have a close to 90 degree phase difference which makes the continuity effect close to zero. As a result, the advective transport of vorticity becomes the leading contributor in the vorticity equation. Therefore, the shift of flow regimes between short and long channels is caused by the change of role the advection plays in the vorticity balance. Conceptually, during flood, the velocity in the channel is larger than that in the shoal, a result of bottom friction (LV), generating vorticity. During ebb, the vorticity has an opposite sense. But because of friction, the ebb should possess less kinetic energy as during flood which results in a decrease in channel velocity, and a decrease in shoal velocity with a less extend, which results in a less intensive shear (compared to flood) between channel and shoal. Thus the ebb generated vorticity does not fully balance the flood generated vorticity. And the net vorticity will have the same pattern as the flood condition – the net flow is thus inward in the channel and outward over the shoal.

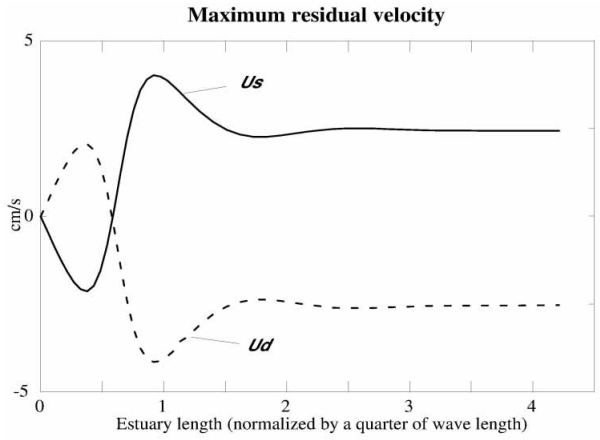

Figure 2. Shift of flow regimes from short to long channels. Us and Ud are the depth averaged residual velocities in shallow shoal and deep channels, respectively.

4. Summary

Numerical and analytic models are used to investigate the change of subtidal flow regimes, when the tidal characteristics change, in channels of variable water depth. Particularly, our focus here is the subtidal flows in channels much shorter than the dynamic tidal wave length, determined by the depth distribution of the channel, and the major tidal frequency. These "short" channels, which are characteristically different from major estuaries and tidal rivers by their short lengths, are quite common along the east coast of the U.S.

between barrier islands. The model results show a switch of flow regimes between "long" and "short" channels. In the "long" channels with progressive tidal waves, the nonlinear effect of the continuity due to the surface fluctuation and the mean seaward pressure gradient are the major contributors to the mean flows. In the "short" channels with standing tidal waves (phase difference between elevation and velocity is around 90 degree), the nonlinear effect of the continuity due to the surface fluctuation is minimized such that the main contribution of the mean flow is from the advection and nonlinear bottom friction. As a result, the vorticity balance requires an inward mean flow through the deep channel and an outward flow through the shallower waters in the same cross section of the channel.

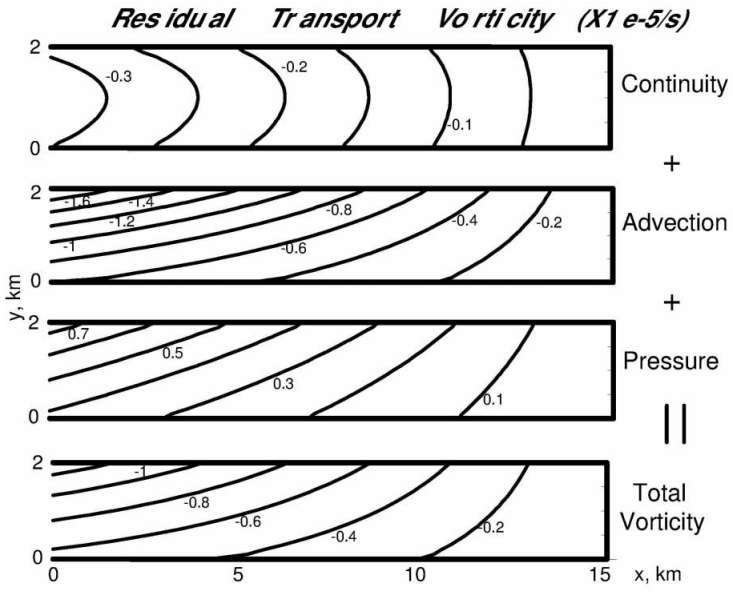

Figure 3. Residual transport vorticity and different contributions.

References:

Hamrick, J.M., Salinity intrusion and gravitational circulation in partially stratified estuaries, PhD Dissertation, U. of California, Berkeley, pp451, 1979.

Jay, D.A. and J.D. Smith, Residual circulation in shallow estuaries, 1. Highly stratified, narrow estuaries, *J. Geophys. Res., 95*, 711-731, 1990a.

Jay, D.A. and J.D. Smith, Residual circulation in shallow estuaries, 2. Weakly stratified and partially mixed, narrow estuaries, *J. Geophys. Res., 95*, 733-748, 1990b.

Johns, B., On the determination of the tidal structure and residual current system in a narrow channel, *Geophys. J. Roy. Astron. Soc, 20,* 159-175, 1970.

Li, C., and O'Donnell, Tidally driven residual circulation in shallow estuaries with lateral depth variation, *J. Geophys. Res., 102*, 27,915-27,929, 1997.

Li, C., and A. Valle-Levinson, A two-dimensional analytic tidal model for a narrow estuary of arbitrary lateral depth variation: the intratidal motion, *J. Geophys. Res., 104*, 23,525-23,543, 1999.

Zimmerman, J.T.F., Dynamics, diffusion and geomorphological significance of tidal residual eddies, *Nature*, 290, 549-555, 1981.

The influence of different parameterisations of meteorological forcing and turbulence schemes on modelling of eutrophication processes in a 3D model of estuary

VLADIMIR MADERICH

(INSTITUTE OF MATHEMATICAL MACHINE AND SYSTEM PROBLEMS, KIEV, UKRAINE, VLAD@IMMSP.KIEV.UA)

OLEKSANDR NESTEROV

(TARAS SCHEVCHENKO UNIVERSITY OF KIEV, UKRAINE, NESTER@IRPEN.KIEV.UA)

SERGEY ZILITINKEVICH

(DEPARTMENT OF EARTH SCIENCES, METEOROLOGY, UPPSALA UNIVERSITY, SWEDEN, SERGEJ@MET.UU.SE)

1. Introduction

In numerical modelling of water ecosystems, the role of the weather is accounted for through the atmospheric fluxes of energy and gases at the water surface. They provide the upper boundary conditions for the hydrodynamic module in a water ecosystem model. This obviously requires the highest possible accuracy in specification of the air-water turbulent fluxes turbulence description in the water body. In this paper a three-dimensional coupled hydrodynamic-water quality model has been applied to the Dnieper-Boog estuary in the Black Sea. The influence of different parameterisations of meteorological forcing and turbulence closures on the hydrodynamics and water quality characteristics has been studied

2. Model

The hydrodynamics is simulated using the time-dependent, free surface, primitive equation model (*Margvelashvili et al.* [1997]). The based on WASP5 eutrophication kinetics (*Ambrose et al.* [1994]) the submodel of water quality simulates the transport and transformation reactions of four interacting systems: phytoplankton kinetics, the phosphorus cycle, the nitrogen cycle, and the dissolved oxygen balance.

Following Stanev and Beckers [1999] the studied domain has been divided into upper and bottom layers, each was with own sigma-coordinate system to describe effect of deep and narrow ship channel in the Dnieper-Boog Estuary (see Figure 1). Both parts were coupled on assumption of continuity of all parameters and fluxes through interface. .

The model was run with two different parameterisations of vertical turbulent mixing of momentum, heat, suspended and diluted matter. The algebraic closure of *Blumberg and Mellor* [1987] and two-equation $\kappa - \varepsilon$ model with stability functions from *Burchard and Petersen* [1999] were compared.

Surface boundary conditions for hydrodynamic model are flux conditions for the momentum, temperature, and dissipation rate (for $\kappa - \varepsilon$ closure), which depend on surface flux parameterisation schemes. The atmospheric fluxes were calculated from standard data on the wind speed and the air temperature/humidity/cloudiness using flux-calculation schemes of *Blackadar* [1979]. The refined formulations of the near surface flux parameterisation also was given according to *Zilitinkevich et al.* [2001]. The proposed technique accounts for generally essential difference between the roughness lengths for momentum and scalars and includes a newly discovered effect of the static stability in the free atmosphere on the surface layer scaling. Recommended by *Zilitinkevich et al.* [2001] correction

functions depend, besides bulk Richardson number, on one more stability parameter, involving the Brunt-Väisälä frequency in the free atmosphere, and on the roughness lengths .

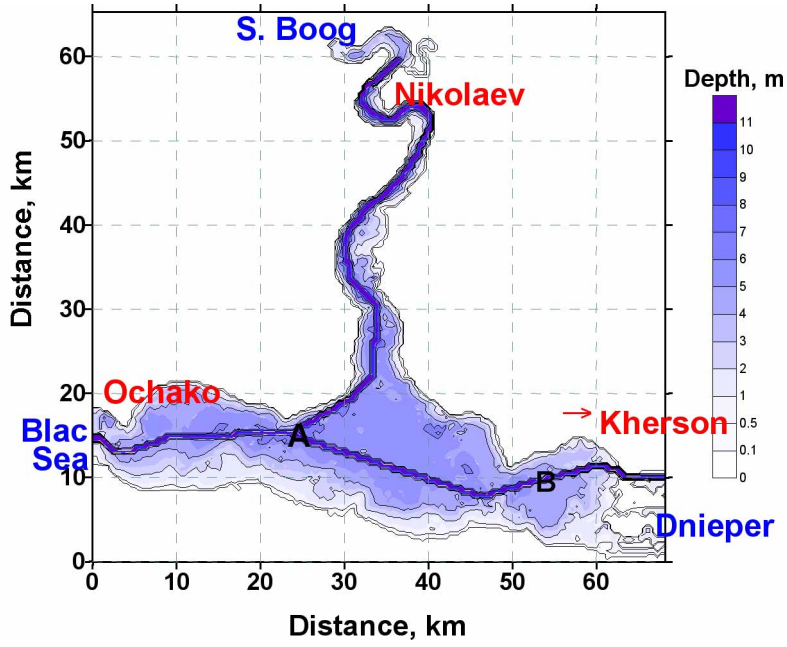

Figure 1: Dnieper-Boog Estuary.

3. Results and discussion

The model was applied to predict circulation and eutrophycation processes in period March-August 1998 for which data in the Dnieper-Boog Estuary were collected in frame of US-Ukraine joint programme. The Dnieper-Boog Estuary (see Figure 1) is the largest of all the Black Sea estuaries. Its limits are defined by the Dnieper delta on the East, the Kinburn strait in the West, the confluence of rivers Ingul and Southern Boog on the North. The average depth is of order 4-5m, but the estuary has narrow 12 m depth ship channel tha connects two ports of Nikolaev and Kherson with the Black Sea.

A set of runs were carried to study the influence of different parameterisations of meteorological forcing and turbulence closure schemes on modelling of eutrophication processes in the estuary. First run was carried out with $\kappa - \varepsilon$ model and flux-calculation scheme of *Blackadar* [1979] (Scheme B). In Figure 2 the model results of computations of salinity and dissolved oxygen are compared with the survey data. As seen from figure the model reproduces observed distributions quite well. The figure show important role of man-made channel in the salt and other scalar fields transport. Second run was carried out with $\kappa - \varepsilon$ model and flux-calculation scheme of *Blackadar* [1979] with refined formulations of *Zilitinkevich et al.* [2001] (Scheme ZB). The correlation for the April-August period between results of use of two fluxes schemes (ZB and B) for bottom salinity and NO3 in the point A (see Figure 1) is given in Figure 4. This figure shows sensitivity of salinity and water quality parameters to the flux of energy parameterization, especially for periods of weak wind and static stability in atmosphere surface layer. It can be explained by 3D nature of density and wind circulation and mixing processes in the estuaries. Third run was carried out with algebraic scheme used by Blumberg and Mellor [1987] and flux-calculation scheme of *Blackadar* [1979]. The comparison of temperature and salinity profiles calculated by these turbulence schemes in point B (see Figure 1) is given in Figure 5. Again the salinity and other variables in the coupled model demonstrated dependence on the turbulence closure (see also Chen and Annan [2000]).

The sensitivity of the eutrophication model to the details of physical environment arising from different parameterisations of atmosphere-water body interaction and turbulence models shows that precision of eutrophication modelling of depends on the quality of such parameterization.

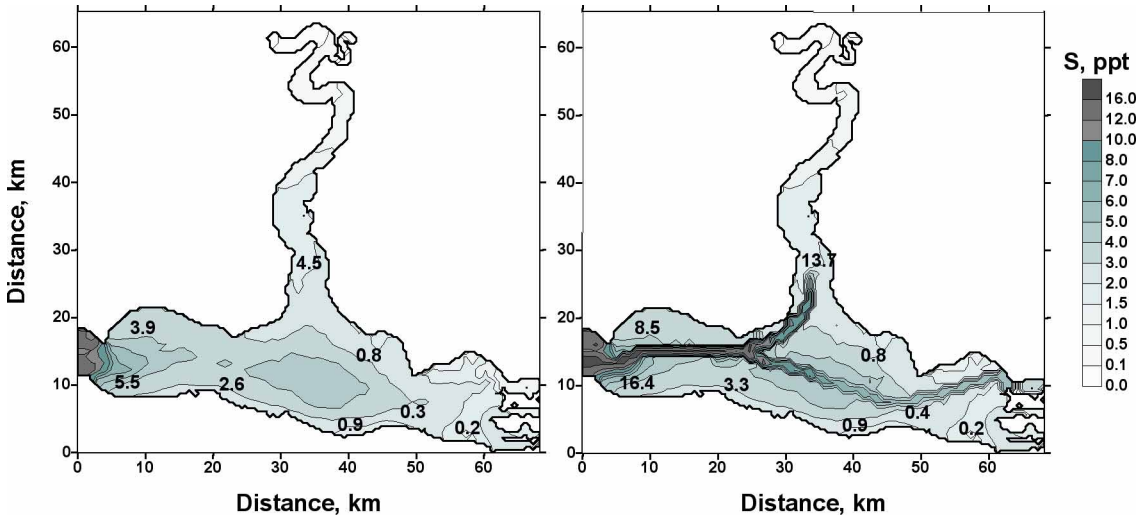

Figure 2: Comparison of measured 12-15 August 1998 and computed surface and bottom salinity, ppt.

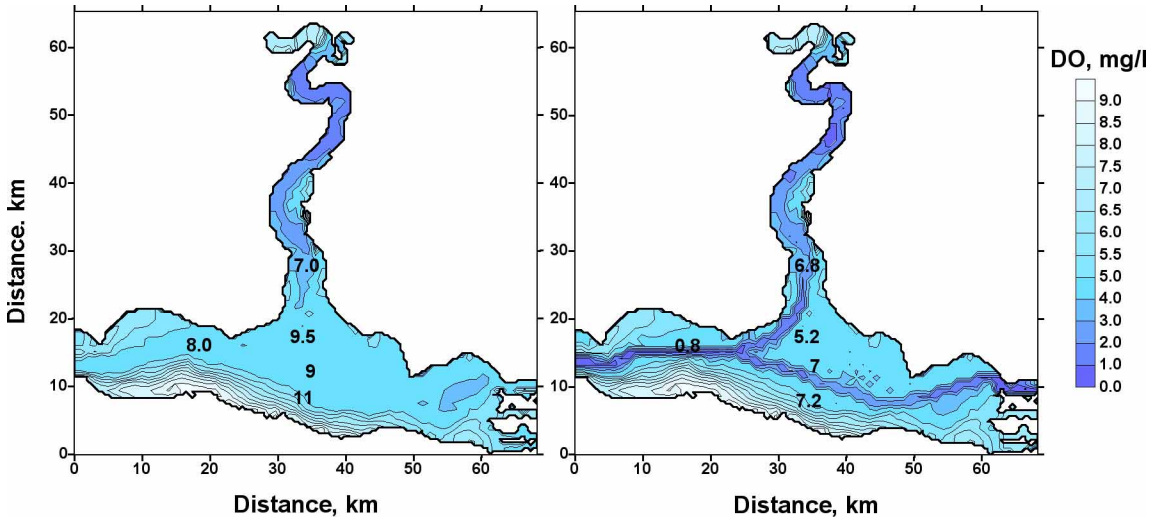

Figure 3: Comparison of measured 12-15 August 1998 and computed surface and bottom DO, mg/l.

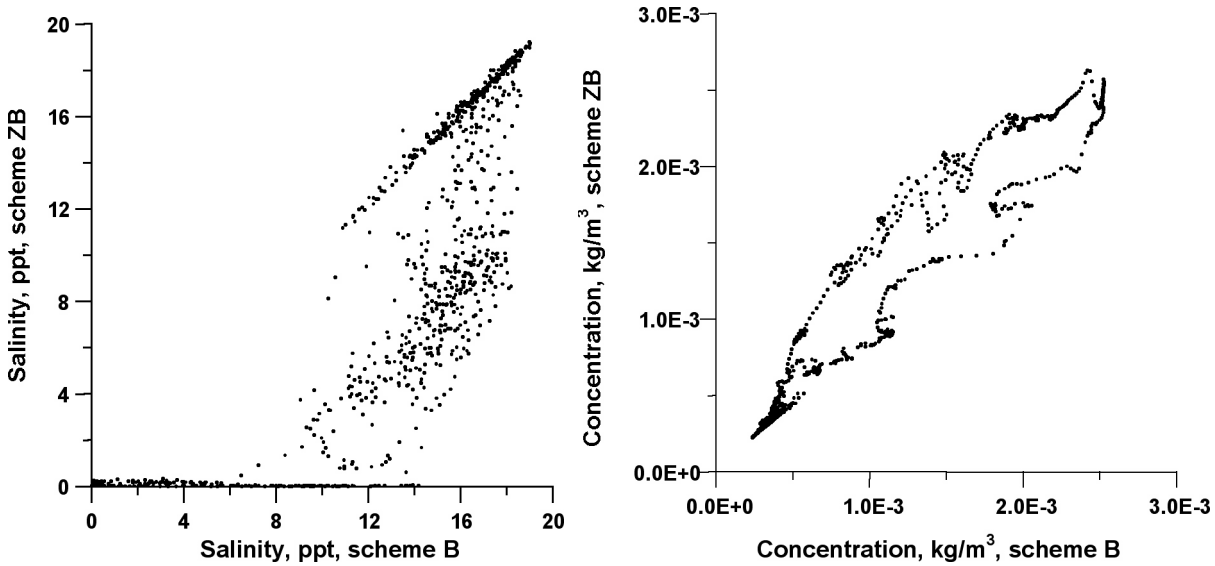

Figure 4: Bottom salinity and NO3 correlation for the two surface fluxes schemes: (ZB) and (B) in the point A (see Figure1) for the time period April-August.

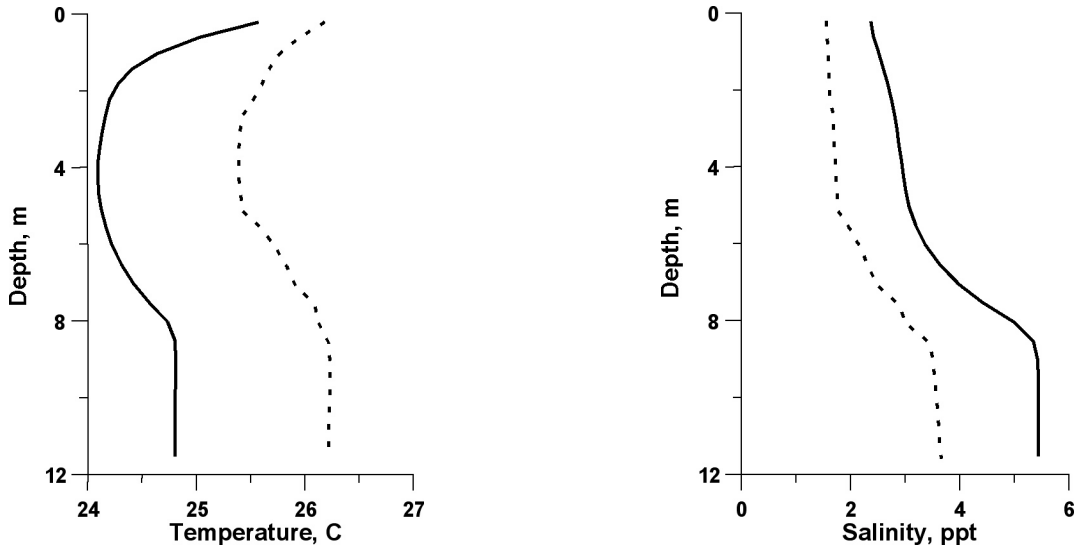

Figure 6: Temperature and salinity profiles for $\kappa - \varepsilon$ turbulence closure (solid) and algebraic closure at the point B (see Figure 1) 13 August 1998. The Blackadar surface fluxes scheme is used.

Acknowledgments: This work was partially supported by the grant of the Royal Swedish Academy of Sciences "Weather effects on water ecosystems".

References:

Ambrose, R. B., Wool T. A. , and Martin J. L., The water quality analysis simulation program, WASP5. U. S. Environmental Protection Agency, Environmental Research Laboratory, Athens, GA, 1994. 210 pp, 1993.

Blackadar, A., High resolution models of the planetary boundary layer. *Advances in Environmental Science and Engineering, 1, No 1*. Pfafflin and Ziegler, Eds. Gordon and Briech, NY, 50-85, 1979.

Blumberg, A.F. and Mellor, G.L. A description of a three-dimensional coastal ocean circulation model, *Three-Dimensional Coastal Ocean Models, N. Heaps (ed), Am. Geoph. Union,* 208p, 1987.

Burchard,H., Petersen, O., Models of turbulence in the marine environment – a comparative study of two-equation turbulence models, *Journal of Marine Systems 21*, 29-53, 1999.

Chen, F., Annan, J.D., The influence of different turbulence schemes on modelling primary production in a 1D coupled physical-biological model. *Journal of Marine Systems, 26*, 259-288, 2000.

Margvelashvili, N., Maderich, V., Zheleznyak M., THREETOX - computer code to simulate three-dimensional dispersion of radionuclides in homogeneous and stratified water bodies. *Radiation Protection Dosimetry*, *73*, 177-180, 1997.

Stanev, E. V., Beckers, J.-M., Numerical simulations of seasonal and interannual variability of the Black Sea thermohaline circulation, *Journal of Marine Systems, 22*, 241-267, 1999.

Zilitinkevich, S. S., Perov, V. L., and King, J. C., Near-surface turbulent fluxes in stable stratification: calculation techniques for use in general circulation models. Submitted to *Quart, J. Roy. Met. Soc*., 2001.

Characteristics of an Unsteady Wake in the Firth of Forth

SIMON NEILL

(Centre for Applied Oceanography, Marine Science Laboratories, Menai Bridge, Wales, UK, s.p.neill@bangor.ac.uk)

ALAN ELLIOTT

(Centre for Applied Oceanography, Marine Science Laboratories, Menai Bridge, Wales, UK, a.j.elliott@bangor.ac.uk)

1. Introduction

The Firth of Forth flows 100 km from its tidal limit at Stirling to the North Sea (Figure 1). Approximately 57 % of the region is intertidal (Buck, 1993), the narrow meandering channel in the upper part of the estuary opening into a sheltered area of bays and extensive tidal flats, especially to the seaward side of the road and rail bridge. Tides in the Firth of Forth are semi-diurnal with a spring range of 5 m and neap range of 2.5 m (Webb and Metcalfe, 1987). The flood tide typically lasts 7-9 hours with a maximum current speed of 0.8 m s^{-1}. In contrast, the ebb is correspondingly shorter and has a peak current of about 1.1 m s^{-1} on a mean tide. Shallow water tidal constituents in the Firth of Forth are responsible for periods of relatively steady currents, known locally as the lackie tide, which can be most pronounced around the times of slack water. The unusual tidal flow, combined with the relatively high tidal range and deep channels (maximum depth of 76 m), make the Firth of Forth a challenging estuary to model.

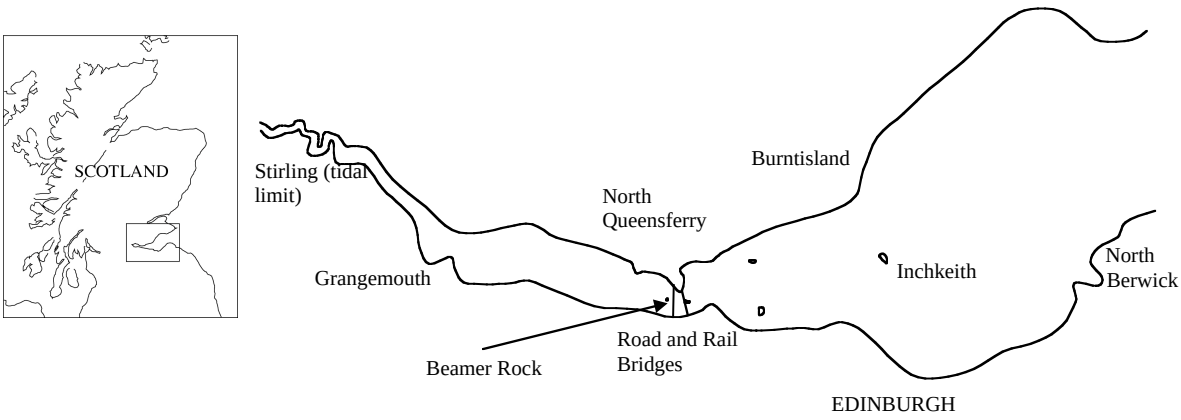

Figure 1: The Firth of Forth.

Numerous islands in the Firth of Forth lead to the formation of complex systems of wakes and eddies. The length scales of the islands vary from 50-1,000 m, and the approach velocity is typically 0.5-1.0 m s^{-1} at mid-flood/ebb. By using the island wake parameter P (Wolanski *et al.*, 1984) where

$$P = UD^2 / \nu_T L$$

U = free stream velocity, D = water depth, L = cross-stream island length and ν_T = vertical eddy viscosity, it is possible to predict the occurrence of either a steady ($P << 1$) or unsteady ($P >> 1$) wake. P has been applied with varying success to a wide range of islands of length scales 100-7,400 m by Pattiaratchi *et al.* (1986) and Ingram and Chu (1987). The main difficulty with the Island Wake

Parameter is obtaining an accurate value for the eddy viscosity. In the present work, a value of ν_T = 0.3 $m^2 s^{-1}$ was used as this was consistent with the values produced by a depth-averaged numerical model of the region.

Beamer Rock, a 50 m wide island (at mean sea level) is located close to the Forth Bridge and produces a very distinct wake which is generally stronger on the ebb due to both tidal asymmetry and the deeper water (and hence less bottom frictional influence) in the ebbing lee side of the island (~ 30 m) compared to the flooding lee (~ 15 m depth). Through video footage and ADCP data, the unsteady nature of the wake has been recorded. This paper explores the Island Wake Parameter and other dimensionless numbers that can be used to describe island wake phenomena. ADCP data and numerical modelling are central to the discussion.

2. In-Situ Data

ADCP data was collected through the wake during a full neap tidal cycle. Typical near-surface vectors averaged between depths of 3.3-8.3 m are shown in Figure 2. The approaching velocity was ~ 0.8 m s^{-1} which led to a recirculation in the lee of the island, with strong evidence of an unsteady flow due to the alternating direction of the near-surface vectors in sequential transects through the wake. Also shown in Figure 2 is the surface temperature, collected concurrently with the ADCP data. Generally, the surface temperature was 12.4°C outside the wake influence zone, and 11.8° within the wake. Examination of the vertical velocities suggested the presence of increased vertical mixing in the wake. Approaching the island, vertical velocities were ± 0.05 m s^{-1}, while in the lee of the island vertical velocities increased to ± 0.15 m s^{-1} in the first transect through the wake (100 m from the island), then reduced to ± 0.08 m s^{-1} in the second transect (200 m downstream of the island). A typical temperature profile taken away from the island wake (Figure 3) indicates how increased vertical mixing in the wake could lead to a decrease in the surface temperature.

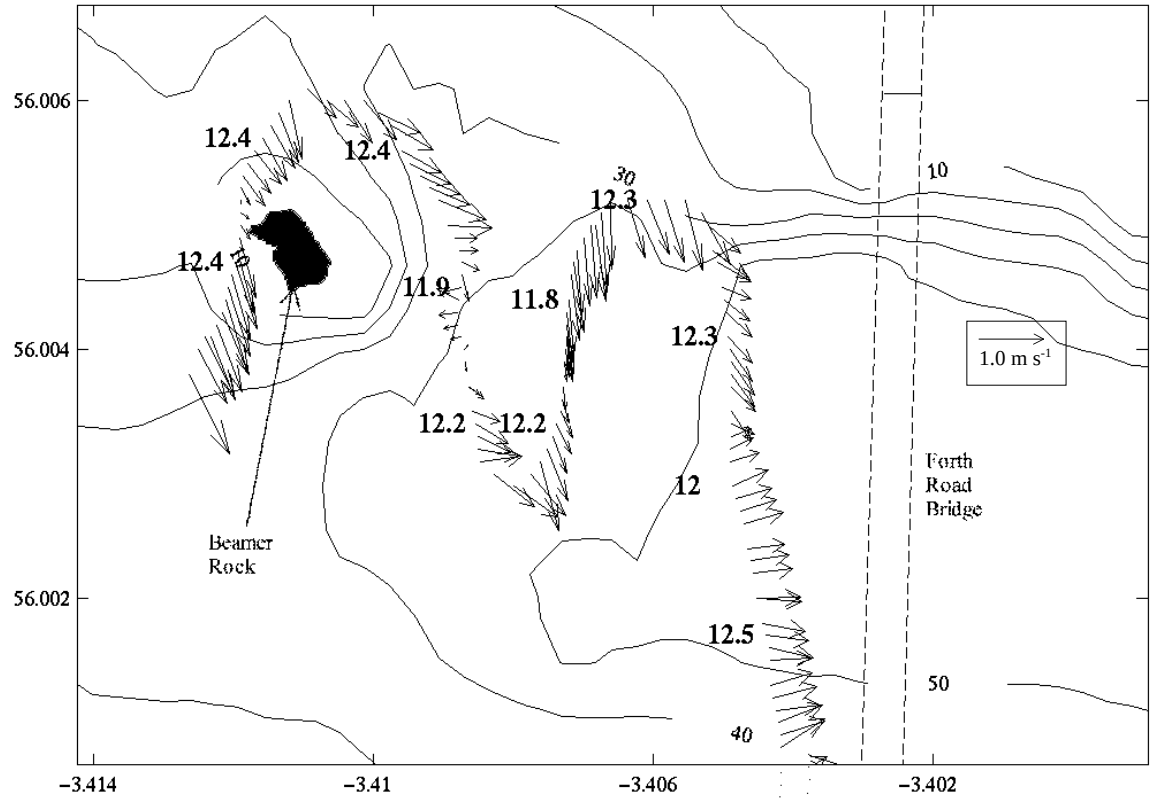

Figure 2: ADCP data through island wake (surface temperature in °C, depth contours in m)

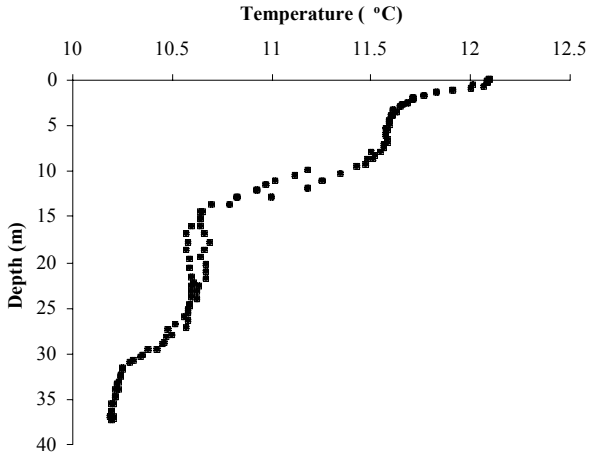

Figure 3: Typical temperature profile away from island wake

3. Numerical Modelling

An explicit 2D depth-averaged model has been applied to cases of simplified bathymetry representative of Beamer Rock and the surrounding water at a resolution of 12.5 m. Using an approach velocity characteristic of that observed (0.8 m s^{-1}) the model produced a von Kármán vortex street, shown in Figure 4 by the continuous injection of two particle tracks. Von Kármán's theory states that the pattern of vortices in a vortex street follows the relationship

$$h/l = (1/\pi)\sinh^{-1}(l) = 0.281$$

where h = distance between rows of vortices and l = distance between vortices shed from one side of the island. Taking values from Figure 4 of h = 98 m and l = 345 m, h/l = 0.285 which is in good agreement with the theory.

4. Discussion

The Island Wake Parameter for Beamer Rock during a neap ebb has been estimated using in-situ and modelled values. From the ADCP data, U = 0.8 m s^{-1} and from the numerical model, ν_T = 0.3 m^2 s^{-1}. Using characteristic length scales for the island width L = 50 m and water depth D = 40 m, P can be calculated as 85 >> 1. Wolanski *et al.* (1984) state that for these flow conditions friction is negligible, hence eddy shedding will occur.

For length scales of order 50 m and velocities of order 1 m s^{-1}, the spin-up time for the development of recirculation in an island wake is very short (of order L/U = 1 minute). Therefore, since bottom friction is not a limiting factor to the near-field wake development (P >> 1), wake oscillation and eddy shedding can occur at time scales much less than a tidal cycle. This is important in the case of Beamer Rock in the Firth of Forth for two reasons. Firstly, the influence of the lackie tide is pronounced in the Beamer Rock area, creating a prolonged period of steady flow around the time of slack water, hence reducing the time period over which wake instabilities could potentially occur. Secondly, Beamer Rock has a steep bathymetry and stands only 0.5 m above mean sea level. Combined with the moderate tidal range (5 m at springs), this further minimises the time window over which conditions are ideal for the formation of an unsteady wake that would be visible as a surface feature. Applying the experimental and numerical modelling work of Lloyd and Stansby (1997), in water depth of 40 m (and given a suitable approach velocity) an unsteady wake is likely to occur from the time when the island pierces the water surface until the island is submerged by approximately 5 m. Therefore,

despite having little surface expression when the island is submerged, the unsteady nature of the wake should still be visible in ADCP and density data.

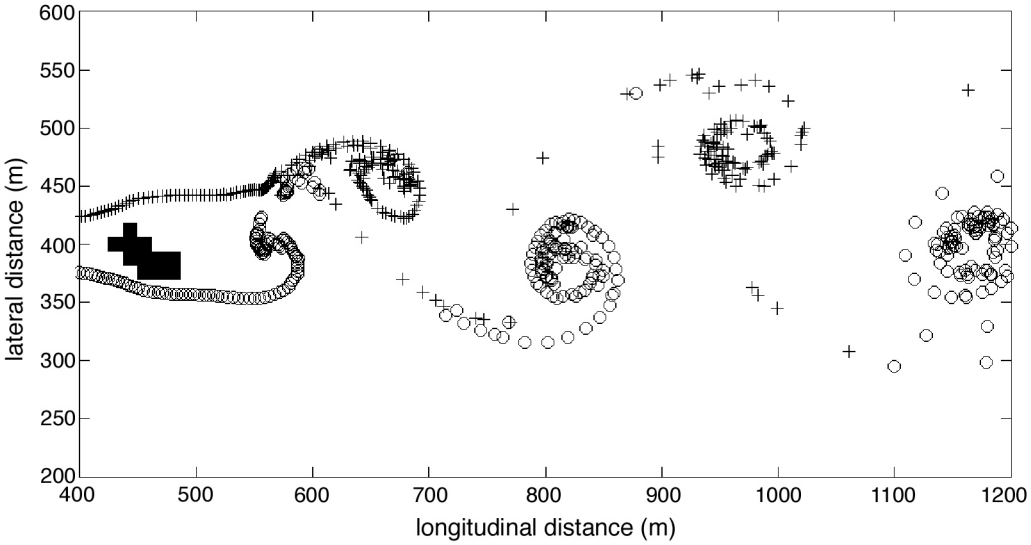

Figure 4: Model output of flow past Beamer Rock, visualised by continuous particle injection.

The numerical modelling and in-situ data analysis of this work is on-going and will be reported on at the conference.

Acknowledgments: This work is supported by the Engineering and Physical Sciences Research Council (EPSRC) in the UK as part of project GR/M88020. Thanks to Gwynne Parry Jones and Ben Powell who assisted with the collection of the in-situ data. Thanks also to Scott Couch at Oregon State University for providing the depth-averaged numerical model.

References:

Buck, A.L., *An Inventory of UK Estuaries: Volume 4. North and East Scotland*, Joint Nature Conservation Committee, Peterborough 1993.

Ingram, R.G. and Chu, V.H., Flow around islands in Rupert Bay: an investigation of the bottom friction effect. *Journal of Geophysical Research*, 92 (C13), 14521-14533, 1987.

Lloyd, P.M. & Stansby, P.K., Shallow-water flow around model conical islands of small side slope. 2: submerged. *Journal of Hydraulic Engineering*, 123 (12), 1068-1077, 1997.

Pattriaratchi, C., James, A. and Collins, M., Island Wakes and headland eddies: a comparison between remotely sensed data and laboratory experiments. *Journal of Geophysical Research*, 92 (C1), 783-794, 1986.

Webb, A.J. and Metcalfe, A.P. Physical aspects, water movements and modelling studies of the Forth estuary, Scotland. *Proceedings of the Royal Society of Edinburgh*, 93B, 259-272, 1987.

Wolanski, E., Imberger, J. and Heron, M.L., Island wakes in shallow coastal waters. *Journal of Geophysical Research*, 89 (C6), 10553-10569, 1984.

The influence of low-frequency sea level changes on the hydrodynamics and salinity distribution in a micro-tidal estuary

Joanne O'Callaghan, Charitha Pattiaratchi and David Hamilton

Centre for Water Research, University of Western Australia, Nedlands, WA, 6009, Perth, Australia. email: ocallagh@cwr.uwa.edu.au

Introduction

The main driving forces of circulation, which in turn determine the distribution of water properties such as salinity, temperature and nutrients within positive estuaries, are river flow from the landward end and changes in water level at the seaward end of the estuary. In macro-tidal estuaries, sea level changes are dominated by astronomical tides whilst in micro-tidal estuaries, non-tidal low-frequency changes in water level have a significant effect on sea-level, with resultant impacts on current velocities, salinity and water temperature. This investigation was undertaken to determine the influence of low frequency changes in water level on the distribution of currents and salinity in the Swan River Estuary, Western Australia (Fig. 1), using field measurements from December 2001.

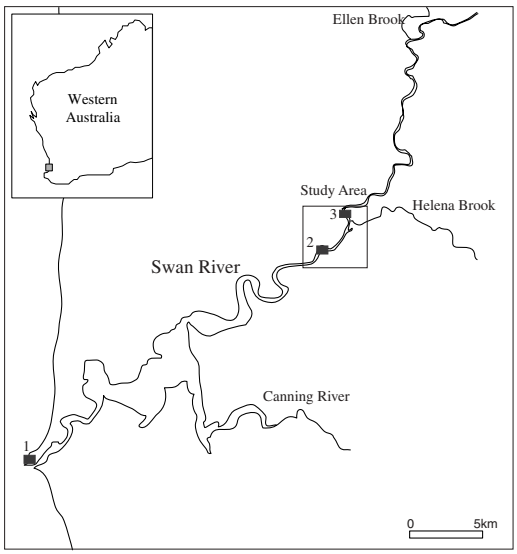

Figure 1: Location Map of Swan River Estuary, Western Australia showing the study site. Water elevation data are from Fremantle (1), Longitudinal CTD transects were completed, starting at Ron Courtney Island (2) and current profiles were collected from Success Hill (3).

Study Area

The Swan River Estuary is in south-west Western Australia and is surrounded by the city of Perth. It is a partially mixed diurnal estuary, with a maximum tidal range < 0.8 m. Tidal oscillations vary over the spring-neap cycle, with a single high- and low-water observed during spring tides and a double high-water observed during neap tides. Low frequency oscillations of water level along this coastline are characterised by periods of 5-10 days with amplitudes up to 0.5m. These may be associated with coastally trapped waves, such as continental shelf waves, or may be directly forced by weather systems. Hence, the estuary circulation responds at a range of frequencies, with tides providing semi-diurnal/diurnal changes and the spring-neap cycle which is superimposed on low frequency forcing with periods of 5-10 days.

The estuary can be divided into two zones; the lower estuary, which is a deep basin with average depth 12m, and width 3km and the shallow upper estuary, with average depth $<$ 5m and width 250m. Previous investigations of the estuary (e.g. Stephens and Imberger, 1996) have focused on the lower estuary, and have identified two major physical forcing mechanisms: (1) freshwater surface flow downstream and (2) baroclinic propagation of the salt wedge upstream. There are few field studies of the upper estuary circulation, despite the fact this is a region where algal blooms appear to be initiated (Chan and Hamilton, 2001). A study by Hamilton et. al.(2001) was done concurrently with a river remediation strategy involving de-stratification. This study indicated spatial changes of physical parameters, including turbidity, over the diurnal tidal cycle.

Methods

Field data were collected in the upper estuary during Dec-Jan 2001/2, approximately 45 km from the mouth of the estuary. A NORTEK Aquadopp current profiler was deployed at Success Hill (Fig. 1 from Dec. 5, 2001 (day 339) to Jan. 3, 2002 (day 003). One-minute velocity averages were collected every five minutes. Vertical CTD and turbidity profiles were completed from day 346 to 353 over a longitudinal transect with a length of 6km. Vertical profiles were collected using an F-Probe from the Centre for Water Research with a distance between each profile of approximately 600m. Water elevation data for Fremantle Port were obtained from the Coastal Data Centre, Department of Transport, Western Australia (Fig. 1).

Results

Current and pressure data from the Aquadopp current profiler covered two neap and one spring tide (Fig. 2). Trends of the spring-neap cycle were captured, with a double high water occurring for the neap (342 to 344) and the diurnal cycle throughout the spring tide (348-353). A 72-hour low pass filter was performed on the pressure data and overlies the daily fluctuations (Fig. 2). An increase in water elevation of 30cm, independent of tidal forcing, was also observed from day 344 to 347. This is an example of low frequency sea-level changes, which in turn effects physical parameters in the estuary (Fig. 3).

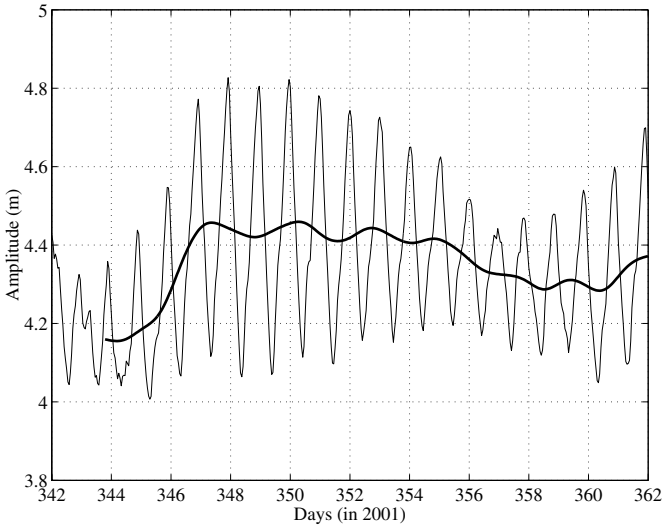

Figure 2: Pressure data from Aquadopp from day 342-362 at 5 minute intervals (oscillating line) and using a 72-hour low pass filter on the 5 minute data (smoothed line).

Salinity transects from the upper estuary for days 348 and 353 are shown in Fig. 3. Profiles are represented by vertical lines, with the first profile 39 km from the mouth of the estuary and the last profile at 45 km (Success Hill: refer Fig. 1). The daily movement due to tides may be up to 2-3 km (Hamilton et. al, 2001), but the net distance of upward propagation is less than 200m. Longitudinal transects of day 346, 347 and 348 showed only small changes in the location of the 12 isohaline. However, there were differences in the position of this isohaline from day 348 to 352. On day 348, (Fig. 3a) the 12 isohaline crossed the bed 3000m upstream of the origin. By day 352 (Fig. 3b) the 12 isohaline crossed the bed around 6000m upstream. The net distance covered by the bottom waters was approximately 3 km. Thus, the change in water level that occurs from day 344 to 348 (Fig. 2), was reflected in large changes in the location of the salt wedge, taken as the 12 isohaline, with a lag of 1-2 days.

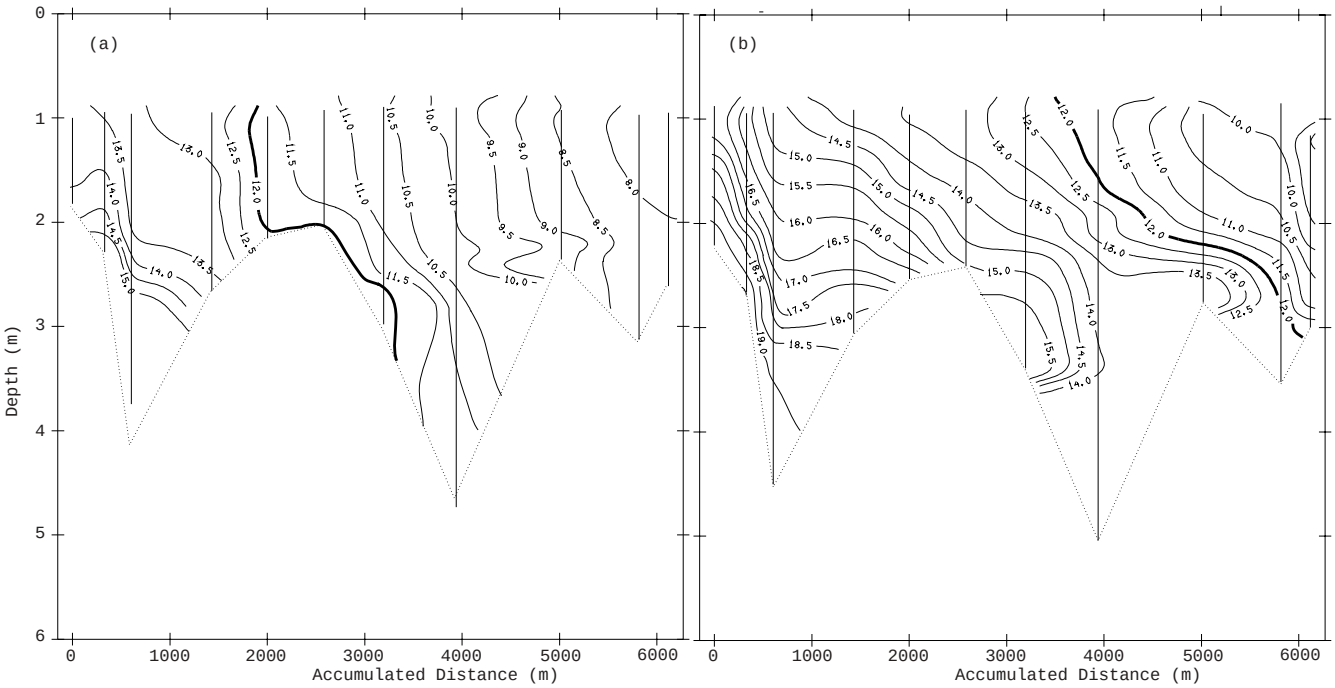

Figure 3: Salinity Transects for (a) day 348 (b) and 352. Accumulated distance refers to the distance upstream of the start of the longitudinal transects (Ron Courtney Island: see Fig. 1). The highlighted isohaline (12) shows that the distance covered by the salt wedge due to low frequency forcing was approximately 3 km.

Power spectral density plots for water elevation data for 2001 (Fig. 4a) shows two peaks; the diurnal tide and the low frequency sea level changes. These occur at periods between 6 and 14 days, corresponding to variations in weather system patterns for winter and summer, respectively. Power spectral density plots of alongshore currents for surface (3.6 m from bed) and bottom (0.6 m from bed) data (Fig. 4b) show peaks at 24 hours and 11 days. Spectral peaks in surface and bottom currents show that the surface currents tend to have more energy, with the 24 h period having the largest peak. However, for near-bed currents the low frequency period has a larger spectral peak than at the 24h frequency. Thus, the salt wedge propagation in the lower layer was driven by the energy from low frequency sea-level changes.

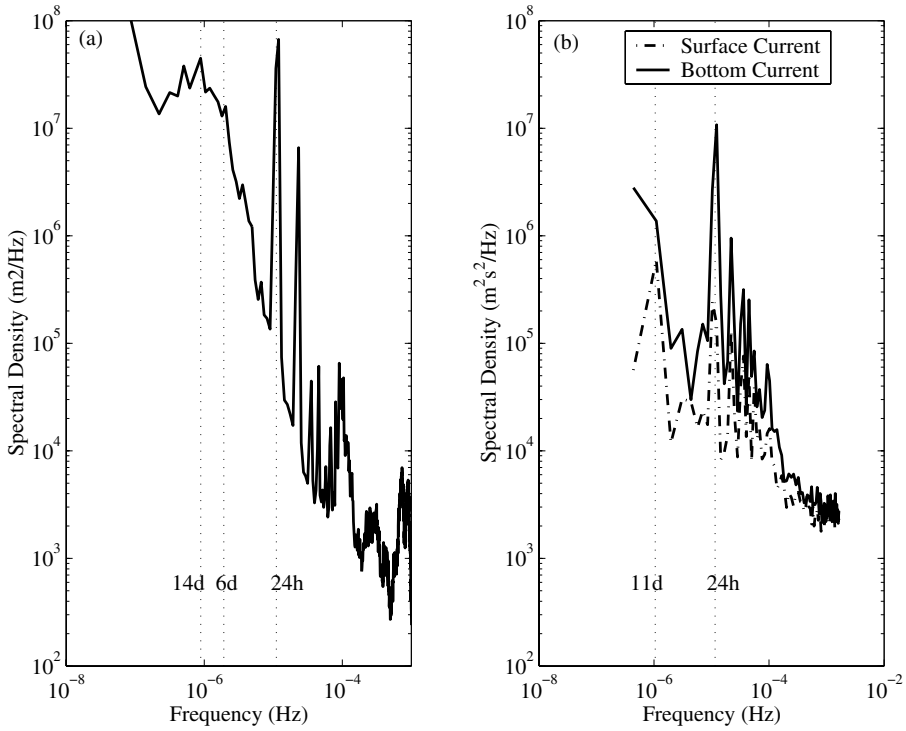

Figure 4: Power spectral density plots of (a) water elevation data from Fremantle for 2001 and (b) surface and bottom currents in the alongshore direction for the duration of the deployment.

References

Chan, T. and Hamilton, D.P. (2001) The effect of freshwater flow on the succession and biomass of phytoplankton in a seasonal estuary. *Marine and Freshwater Research* 52, 869-884.

Hamilton, D., Chan, T., Robb, M., Pattiaratchi, C. and Herzfeld, M. (2001) The hydrology of the upper Swan River with focus on an artificial de-stratification trial, *Hydrological Processes*, 15(13), 2465-2480.

Stephens, R. and Imberger, J. (1996) Dynamics of the Swan River Estuary: the seasonal variability. *Marine and Freshwater Research*, 47, 517-529.

Salinity Effects of Riverine Diversions to Barataria Basin, a Bar-Built Estuary

DONGHO PARK, MASAMICHI INOUE, AND WM. J. WISEMAN, JR.

Coastal Studies Institute and Department of Oceanography and Coastal Sciences, School of the Coast and Environment, Louisiana State University, Baton Rouge, LA, 70803, USA

Barataria Basin is located immediately west of the birdfoot delta of the Mississippi River. It includes a large bar-built estuary, marshes, and upland swamps. Land loss due to subsidence and exacerbated by human activity is a chronic and important problem in coastal Louisiana. One potential solution to this problem is diversion of river water and its associated nutrients and sediments from the Mississippi River into the adjacent marshes. This promotes the maintenance of the marsh. The added freshwater, though, alters the region in which commercially important living marine resources, e.g. oysters, can prosper. In order to assess the affect of river diversions, a circulation model was developed.

The waters of Barataria Basin range from 1 to 3 meters in depth. The dominant diurnal tides at the mouth of the estuary have a range of approximately 60 cm during tropic tidal conditions. The shear associated with the tidal currents effectively mixes the shallow water column. Additional mixing is due to wave-bottom interactions and Langmuir circulations. Thus, a vertically integrated model was assumed, as a first approximation to the estuarine dynamics. The model included baroclinic pressure gradients. It was forced at the sea surface with observed wind and precipitation and with computed evaporation. Precipitation over the marsh was converted to runoff using a hydrologic model developed for this study. Open boundary conditions in the coastal ocean, water level and salinity, were derived from observed conditions at the mouth of the estuary. The model grid size was 100 m. A high-resolution advection scheme was coded to replace the traditional centered difference scheme. When compared to results from a previous version of the model, with a larger grid size of 463 m, the present model performs significantly better in terms of its ability to model the observed tidal propagation up the complicated channels of the estuary (Figure 1).

The model was run once without diversion structures and once with the inclusion of two existing diversion structures that were forced to run at their maximum design discharge rates as well as freshwater inflow from the Gulf Intracoastal Waterway, a navigation canal that traverses the upper reaches of the Basin. Differencing the solutions from the two runs permitted the effect of the freshwater diversions to be assessed in terms of water levels, salinity distributions, and transports. The ecologically important variable, salinity, was measurably altered by the active diversions. Within the convoluted tidal creeks and marshes near the diversion outfalls, salinities decreased by as much as 5. In the middle reaches of the estuary, salinities decreased by 2. The lower reaches of the estuary were relatively unaffected due to both dilution and effective flushing driven by the wind and tides (Figure 2). Salinities could not, of course, be significantly lowered in the nearly fresh regions of the upper estuary.

Issues remain to be resolved with the open boundary conditions and regarding possible three-dimensional effects in the deeper regions of the estuary. When compared to observed salinities, the model output did not adequately track strong salinity intrusions. The salinities at the open boundary were inferred from salinities observed at the mouth of the Basin and, thus, known to be in error. Furthermore, while the waters of the Basin are generally shallow, the deep passes connecting the estuary to the coastal ocean and the coastal ocean proper are known to be strongly stratified. The model does not allow saline intrusions along the bottom near the mouth of the estuary. The estuary includes a boat channel that extends from the deepest pass northwards to the Intracoastal Waterway. This channel is also capable of supporting stratified shear flows. Nevertheless, over most of the Basin, where the assumptions of the model are believed to be valid, the dispersion of salinity is thought to be qualitatively reproduced.

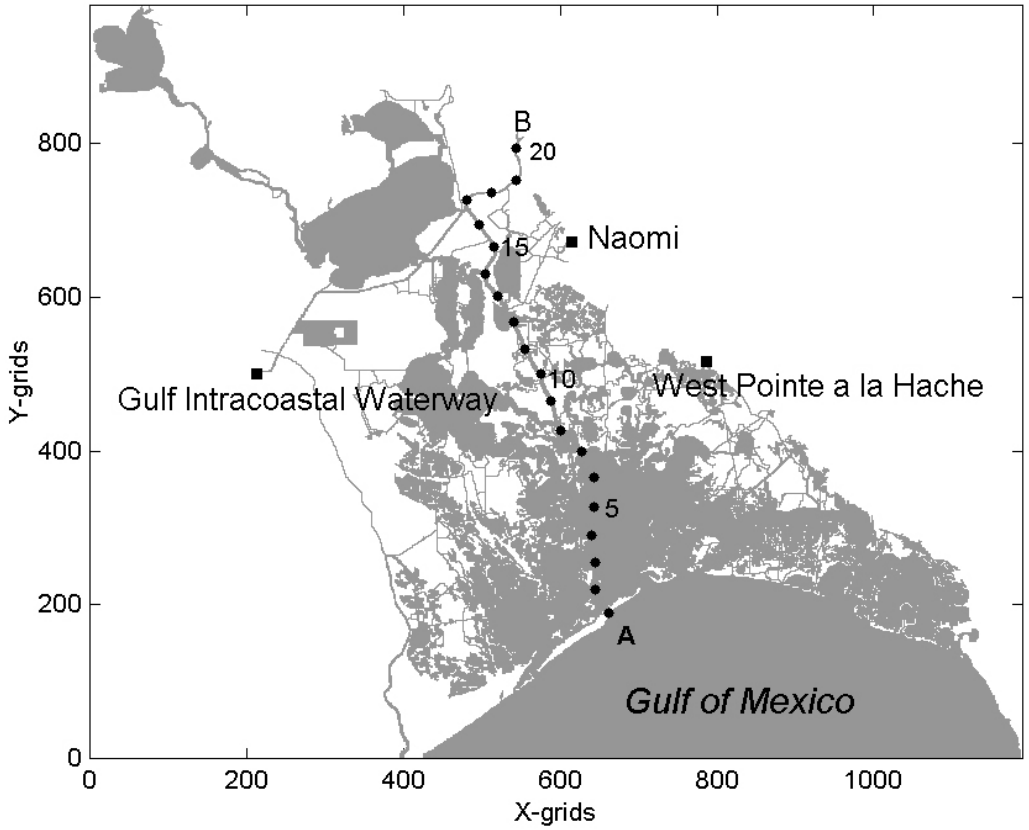

Figure 1. Model grid. Each dot represents a model grid point. The sources of controllable freshwater input are indicated by black squares. The stations indicated by black circles run along the Barataria Waterway, a dredged ship channel, and are sampled to produce figure 2.

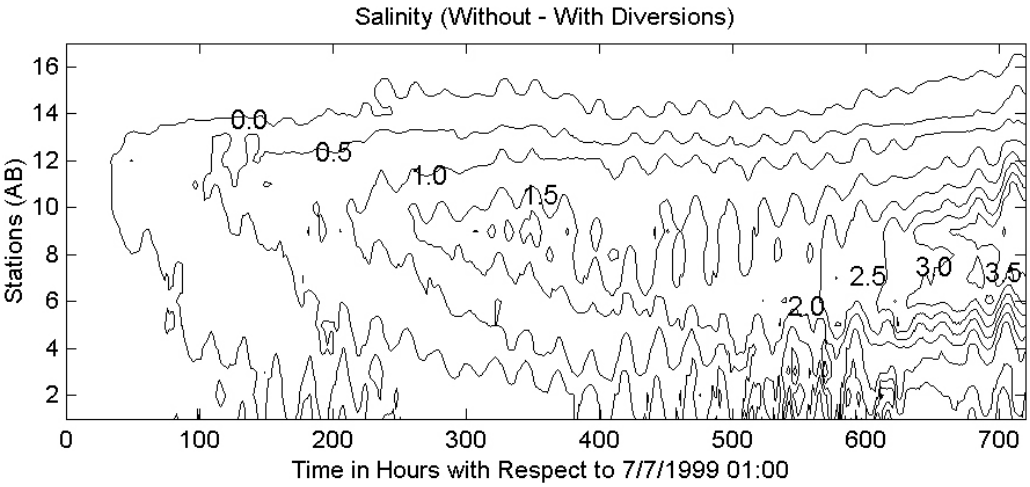

Figure 2. Time-distance plot of the salinity difference between model runs with and without controllable freshwater discharges. Contour interval is 0.5.

Observations of Bathymetric and Curvature Effects on the Transverse Variability of the Flow in a Coastal Plain Estuary

ROSARIO SANAY AND ARNOLDO VALLE-LEVINSON

(Center for Coastal Physical Oceanography, Old Dominion University, Norfolk, VA 23508, USA)

1. Introduction

Hydrographic and horizontal velocity measurements were used to describe the tidal and subtidal flow around a headland over laterally varying bathymetry in the lower James River, Virginia. Three shipboard surveys were conducted throughout semidiurnal cycles along two parallel cross-estuary transects in the vicinity of the headland. In general, the tidal forcing, the river discharge and the wind conditions were different for each cruise. Both tidal and subtidal signals of the along-channel velocity component showed lateral variability related to the bathymetry and curvature. The subtidal flow was up-estuary over the shoals and closest to the headland two-layer estuarine circulation developed in the channel. In every cruise, the subtidal velocity data depicted an anticyclonic gyre over the transect closest to the headland, likely in response to friction and curvature effects. The lateral flow showed patterns that differed from the secondary circulation expected from curvature effects only in one of the three cruises. This might be explained by the counteracting effects of the lateral density gradients and wind forcing observed.

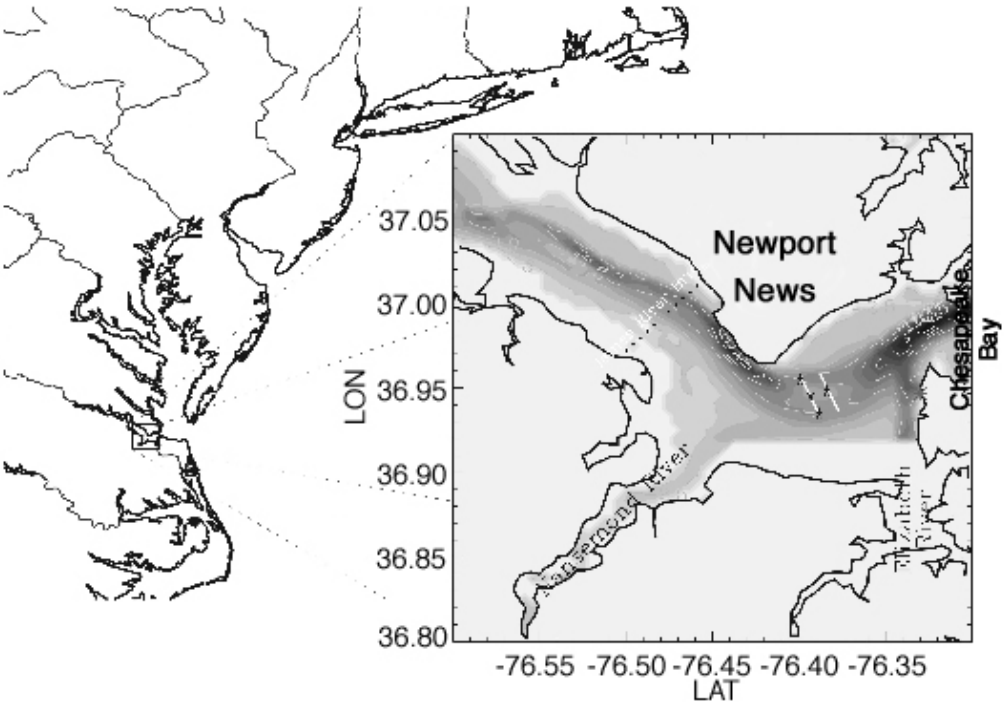

Fig 1. Map of the study area and the cruise track (white lines) of the ship borne ADCP surveys. The bathymetry is denoted by tones of gray (dark means deeper). The CTD-stations are indicated by asteriks

2. Study area

The James River Estuary is the southern most tributary to the Chesapeake Bay. The transition area between these two systems is characterized by abrupt lateral bathymetry changes associated with navigational channels and shoals and by a strong coastline bend associated with a prominent headland,

Newport News, located in the north. The across-channel depth ranges from 3 m (Hampton Flats) to17 m (navigation channel). The radius of curvature of the bathymetry in the area is 10 km. This system is a typical example of a partially stratified coastal plain estuary forced mainly by river discharge and tidal forcing. Mean annual river discharge recorded at Richmond, Virginia ranges from 500 m^3 s^{-1} in March to 80 m^3 s^{-1} in August (Wood and Hargis, 1971). Both, tidal elevation and tidal current are mostly semidiurnal, where M_2, N_2 and S_2 are the more energetic (M_2 represents 80 % of the total tidal energy). The interaction among them generates fortnightly and monthly variability in the tidal current (Valle-Levinson et al., 2001). Wind forcing and remote forces (e. g. wind-driven mean sea level fluctuations in the Chesapeake Bay) may also play an important role in the dynamics. The wind forcing is primarily from the northeast, northwest and southwest.

3. Data collection

Three shipboard surveys were conducted along a rectangular track seaward of the Newport News headland (Fig. 1). The surveys took place throughout two secondary spring (Feb 2001, May 1998) and one secondary neap (March 2001) semidiurnal cycles. Each survey sampling consisted of continuous velocity measurements and density profiles.

The current velocity profiles were obtained with an acoustic Doppler current profiler (ADCP) in conjunction with a Trimble differential global positioning system (DGPS). The ADCP was mounted pointing downward on a catamaran and towed from the starboard side of the ship along the track. The ship steamed at 2.5 m s^{-1}, allowing the track (8 km) to be repeated 11 times through out the total period of sampling on each cruise. Density profiles were sampled with a SEA-BIRD CTD at stations indicated in Figure 1.

The tidal and subtidal signals were separated from the current velocity observations by using sinusoidal least squares fitting techniques to semi-diurnal and quarti-diurnal harmonics. The velocity fields were rotated such that the along-channel component was aligned to the maximum inflow/outflow. The subtidal signal of the data includes the effects of tidal rectification, wind, baroclinic gradients and curvature effects. The density data were subject to the same fit analysis as the current velocity profiles.

Hourly wind velocity data were obtained from NOAA at stations CBBT , Kiptopeke and Sewells Point. Daily streamflow data were obtained from USGC at station Richmond.

4. Results

Along Channel Flow

Despite the fact that the three cruises took place under different wind, river discharge and tidal forcing conditions, the general structure of the along channel mean flow was quite similar for all the cruises. It exhibited a transverse variability related to the bathymetry (Fig. 2). It featured two-layer circulation over the channels (main and secondary channels) in both transects. This feature was consistent with Kasai et al. (2000), in the sense that 2-layer estuarine circulation was developed at the deepest part of the estuary. Over the shoal, the mean-flow was up-estuary for the transect closer to the headland and weak down-estuary mean flow at the eastern transect. These results might be attributed to the non-linearities of the dynamics of tidal flow as indicated by the theoretical results of Li and O'Donnell (1997). They found that the vertically integrated exchange flow was correlated with topography, as a net inflow occurred over the shoals and net outflow in the channels.

The strongest mean outflow in all the cruises was found at the upper layer of the main channel as expected from reduced friction effects there.

The semidiurnal tidal amplitude of the along-estuary velocity exhibited transverse variability related to the bathymetry. Maximum velocity amplitudes were located on the upper layer of the main channel, decreased over the shoals, and then increased slightly on the upper layer of the secondary channel. Bottom friction effects were evident in decreasing the amplitudes of the currents near the bottom and over the shallow areas. The semidiurnal phase of the along-channel velocity also showed a lateral and vertical variability, with the shoals and bottom part of the channels leading the rest of the cross-section area by about 20 degrees or 40 minutes. The phase lag may be due by the combined effects of friction and inertia. The tidal features at the shoals (amplitudes and phase) generated lateral gradients of the along-channel flow that induced convergence processes. These features were consistent with other studies (Valle-Levinson et al., 2000, Li and Valle-Levinson, 1999).

Nonlinear effects also were explored by the M_4/M_2 tidal amplitude ratio. This ratio features maximum values at the shallowest part of each transects, which was more evident on the western transect.

Lateral Channel Flow

The lateral mean flow for all the cruises featured convergence and divergence areas associated with the shoals and shoulders of the main channel.

In general, the lateral flow at the eastern transect showed mean flow outward the bend on the upper layer and mean flow inward the bend on the lower layer. At the western transect the lateral circulation was mostly outward the bend at southern part. One of the cruises showed some differences with this general lateral flow. This might be due to counteracting effects of the lateral density gradients and wind forcing observed.

The theoretical strength of the secondary circulation due to the channel curvature and Coriolis effects were obtained by using scaling analysis provided in Geyer (1993) and Seim and Greeg (1997). This analysis suggested that curvature effects (0.03 m s^{-1}) dominated over Coriolis effects (0.002 m s^{-1}). This result was consistent with the evaluation of the Rossby number, which was bigger than one in the complete domain. The across-channel baroclinic force also was at least one order of magnitude less then the centrifugal force during the periods of sampling.

The radius of curvature during ebb was smaller than during flood, consequently the centrifugal force during ebb drove stronger lateral flow than during flood. This feature explains some of the diferences of the mean lateral circulation between eastern and western transect.

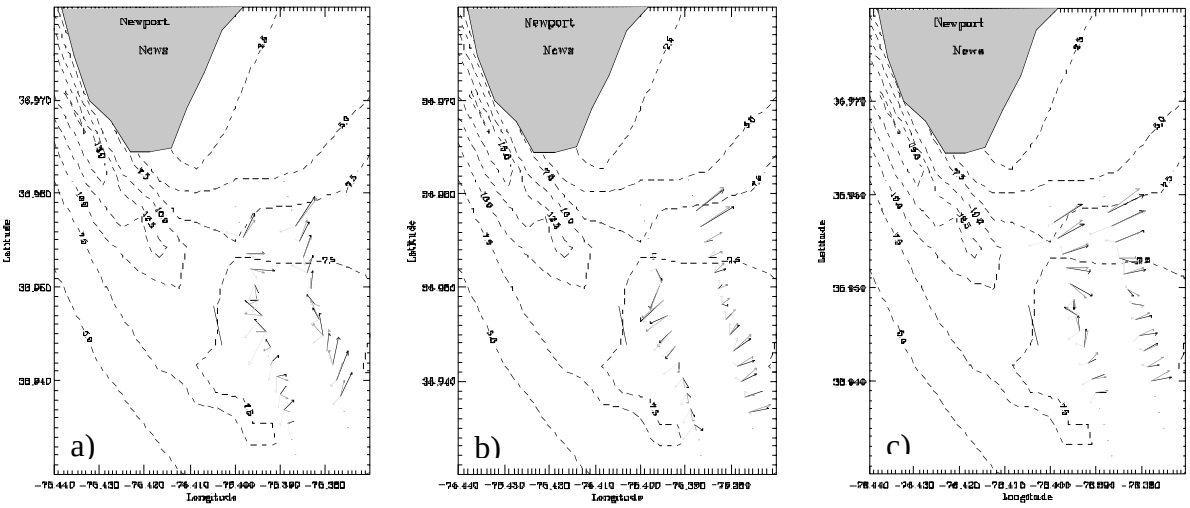

Fig 2. Subtidal current for the three surveys at three different water levels, surface (black arrows), below the surface (dark gray arrows) and near bottom (light gray arrows). a) May 98 survey, b) February 2001 survey and c) March 2001 survey. Maximum mean flow was ~ 20 cm s^{-1}.

5. Summary

The along channel tidal and subtidal flow exhibited transverse variability related to the bathymetry. The the flow over the shoals featured minimum tidal amplitudes, and net mean inflow. The flow over the channels showed maximum amplitudes of the tidal amplitudes and the mean flow showed estuarine circulation. The tidal phase difference between the shoals and channels and transverse shears of the along channel flow caused convergence and divergence processes. These results were consistent with observational studies reported in the literature.

The lateral circulation was dominated by curvature effects. Coriolis effects and baroclinic pressure gradients were one order of magnitude less than the curvature term. The centrifugal force during ebb drove stronger lateral flow than during flood. In every cruise, the subtidal velocity data depicted an anticyclonic gyre over the transect closest to the headland, likely in response to friction and curvature effects.

References

Geyer , W. R., Three-dimensional tidal flow around headlands. J. Geophys. Res., 98: C1, 955-966, 1993.

Kasai A., A. E. Hill, T. Fujiwara, and John H. Simpson, Effects of the earth's rotation on the circulation in regions of frshwater influence, J. Geophys. Res., 105: C7, 16961-16969, 2000.

Li and O'Donnell, Tidally driven residual circulation in shallow estuaries with lateral depth variation. J. Geophys. Res., 102: C13, 27915-27929, 1997.

Li, C. and A. Valle-Levinson, A two dimensional analytical model for a narrow estuary of arbitrary lateral depth variation: The intratidat motion. J. Geophys. Res., 104: C10, 23525-23543, 1999.

Seim, H. E., and M. C. Greeg,The importance of aspiration and channel curvature in producing strong vertical mixing over a sill, J. Geophys. Res., 102: C2, 3451-72, 1997.

Valle-Levinson, A., C. Li, T.C. Royer and L. P. Atkinson, Flow patterns at the Chesapeake Bay entrance, Coast. Shelf Res., 18, 1157-1177, 2001.

Valle-Levinson et, A., C. Y. Li, K. C. Wong, and K. M. M. Lwisa, Convergence of lateral flow along a coastal plain estuary, J. Geophys. Res., 105: C7, 17045-17061, 2000.

Unsteady horizontal mixing in estuaries and channels

Luciano Soldini, Alessandra Piattella, Alessandro Mancinelli, Roberto Bernetti, (*Istituto di Idraulica, Università di Ancona, Via delle Brecce Bianche, 60131 Ancona, Italy*, lsoldini@idra.unian.it)

Maurizio Brocchini, (*DIAM, Università di Genova, Via Montallegro 1, 16145 Genova*, brocchin@diam.unige.it)

1 Introduction

We investigate possible applications to typical estuarine and channel flow conditions of a recently developed shock-capturing model for the solution of the Nonlinear Shallow Water Equations (NSWE) described in *Brocchini et al.* [2001]. The WAF method (e.g. *Toro* [2000]), used to solve the equations in object, provides a powerful and flexible technique for modelling shallow flows which admit discontinuous (shock) solutions. The proposition is to show that an accurate enough description of the flow can be achieved through numerically cheap solutions of the NSWE. In particular we focus on potentialities and deficiencies of the model in reproducing important features like the large-scale eddies with vertical axis (macrovortices hereinafter) which are responsible for much of the horizontal mixing occurring at the boundaries between the main channel and the flood planes (see figure 1).

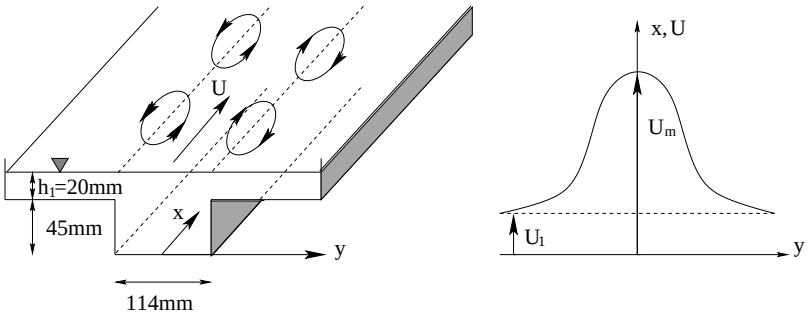

Figure 1: Left: sketch of the flow configuration. Right: sketch of the transversal profile of the mean longitudinal velocity.

The model under analysis solves the NSWE which can be seen as the limit for vanishing eddy viscosity ($\nu_T \to 0$) of the set of equations

$$\begin{aligned} d_t + (ud)_x + (vd)_y &= 0 \\ u_t + uu_x + vu_y + gd_x &= gh_x - \frac{c_f|\mathbf{u}|u}{d} + \nu_T \nabla^2 u \\ v_t + uv_x + vv_y + gd_y &= gh_y - \frac{c_f|\mathbf{u}|v}{d} + \nu_T \nabla^2 v \end{aligned} \qquad (1)$$

in which $d = h + \eta$ is the total water depth, $\mathbf{u} = (u, v)$ is the vector of the depth-averaged velocity and c_f the Chezy bed resistance coefficient.

2 Generation mechanisms of vorticity

The importance of macrovortices for the horizontal mixing of channel flows is well documented (e.g. *Tamai et al.* [1986]) and a number of studies have been devoted to the effects

of the bed-friction on the evolution of macrovortices (e.g. *Chu et al.* [1991]). The role of macrovortices in coastal hydrodynamics is also being recognized. They are investigated, for example, as originating from instabilities of the mean longshore current or as possible causes for the unsteady behaviour of patterns like rip-currents previously considered as steady phenomena.

Different generation mechanisms of vorticity characterize the flow under analysis.

2.1 Vorticity generation by a propagating bore

During the first stages of evolution a bore, which can either represent a flood wave moving downslope in a river or a tidal wave running upstream in an estuary, propagates along the channel with a curved front. In these conditions vorticity (ω) can be generated even within the inviscid NSWE scheme ($c_f = 0$ and $\nu_T = 0$) in virtue of the transverse gradient of the energy dissipated (E_D) at the bore front (*Pratt* [1983]). The jump in potential vorticity ω/d across the front of a bore propagating in the $x-$direction and located between points of coordinates x_1 (downstream) and x_2 (upstream) is:

$$\left[\frac{\omega}{d}\right]_{x_1}^{x_2} = \sqrt{\frac{2}{gd(x_1)d(x_2)[d(x_1)+d(x_2)]}}(E_D)_y, \quad E_D = \frac{g[d(x_2)-d(x_1)]^3}{4d(x_1)d(x_2)}, \quad \omega = v_x - u_y. \quad (2)$$

2.2 Vorticity generation in almost-steady mean conditions

Once the bore has left the domain under investigation an almost-steady mean condition is slowly achieved characterized by nearly flat free surface and a non-uniform profile of the longitudinal velocity component u (see right panel of figure 1). This solution is, however, unstable and perturbation techniques can be used to assess the initiation of instabilities which are thought to increase in amplitude and manifest in the form of macrovortices (e.g. *Chu et al.* [1991]).

Such studies provide useful benchmarks for assessing the performances of numerical solutions in which macrovortices arise mainly due to a generation mechanism similar to that described in section 2.1. Although the free surface is almost flat a jump in water depth is present due to the jump in bathymetry $[h]_{y_1}^{y_2}$. Once the flow becomes unstable a spatially non-uniform velocity component is generated in the transverse direction. Hence, conditions similar to that occurring at a curved bore front are achieved and potential vorticity is generated proportional to $\partial\,[d]_{y_1}^{y_2}\,/\partial x$ in analogy to what described by (2).

3 Numerical experiments

Since in the model $\nu_T = 0$ no lateral mixing could characterize a perfectly-accurate numerical solution apart from that due to seabed friction (which we keep constant and such that $c_f = 0.007$). However, real numerical solutions are affected by numerical errors among which truncation errors play a predominant role. In particular the WAF method, which is second-order accurate in time and space, reduces to a first-order scheme close to features with steep gradients. In those regions a limiter is used which, reducing the order of accuracy of the scheme, allows for non-oscillatory solutions. Then the leading-order truncation

error is of the form:

$$\nu_N \nabla^2 u \quad \text{in which} \quad \nu_N = \frac{1}{2}(1 - C)\lambda \Delta x \tag{3}$$

hence a diffusive-type contribution, similar to that appearing at the right hand side of (1) influences the solution. Moreover the classical generation mechanism of vorticity through a no-slip condition is reintroduced. The size of the numerical diffusion is proportional to the mesh size Δx, the celerity λ of the propagating signal and the Courant number C.

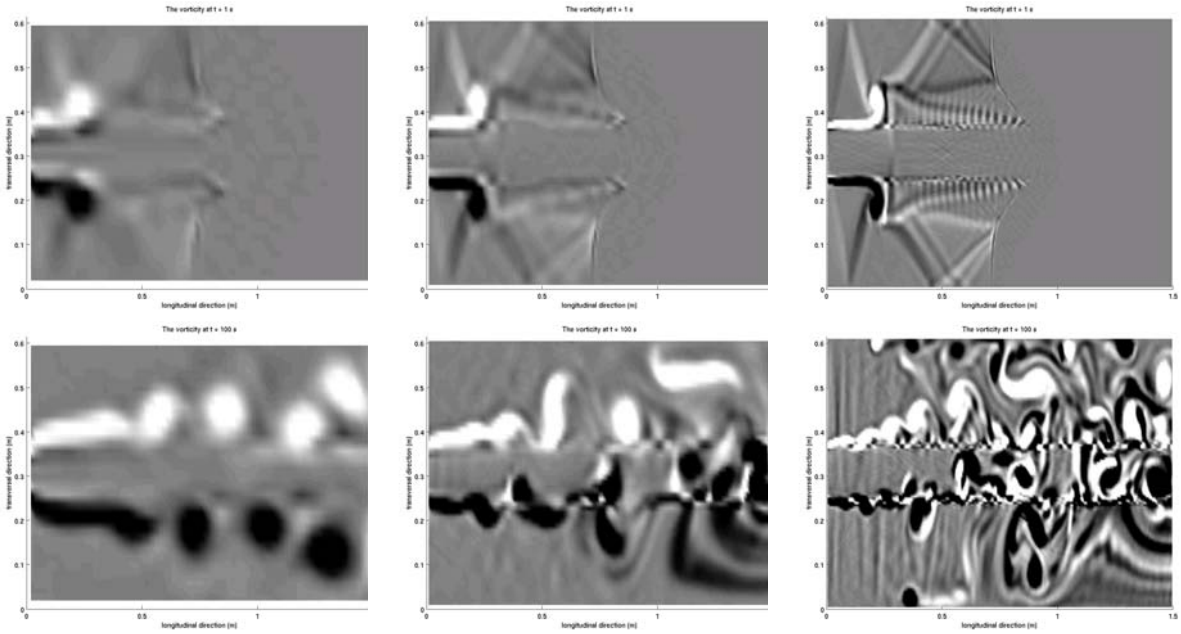

Figure 2: Top row: vorticity patterns at $t = 1$s for $\Delta x/h_1 = 1.00$ (left), $\Delta x/h_1 = 0.50$ (middle) and $\Delta x/h_1 = 0.25$ (right). Bottom row: vorticity patterns at $t = 100$s for the same values of $\Delta x/h_1$. Contour values increase from negative (black) to positive (white) in the range $-2.5s^{-1} \leq \omega \leq 2.5s^{-1}$.

In order to obtain accurate solutions we try to reduce the effects of the numerical viscosity which, being proportional to Δx, can be minimized by refining the mesh. Note that, at times, a different persective is taken and a numerical viscosity is used either to stabilize the solution or to model the physical viscosity by means of the numerical one.

To verify the influence of the numerical resolution on the results we run a number of numerical experiments with the configuration sketched in figure 1 and tested the dependence of the flow patterns on the size of the grid (here $\Delta x = \Delta y$). Sample results of the vorticity patterns are reported in figure 2. It is clear that vorticity is generated during both early ($t \leq 5$s) and late stages of flow evolution ($t > 5$s) in qualitative agreement with the mechanisms of sections 2.1 and 2.2 (i.e. positive in the top half of the channel and negative in the lower half). The effect of decreasing the grid size is mainly to produce a more and more complicated pair of arrays of vortices which becomes ustable (see the vortex meandering) at earlier and earlier times. Moreover, refining the mesh allows for resolution of vorticity patterns at smaller and smaller scales. However, quantification of the influence of the grid size still requires additional work.

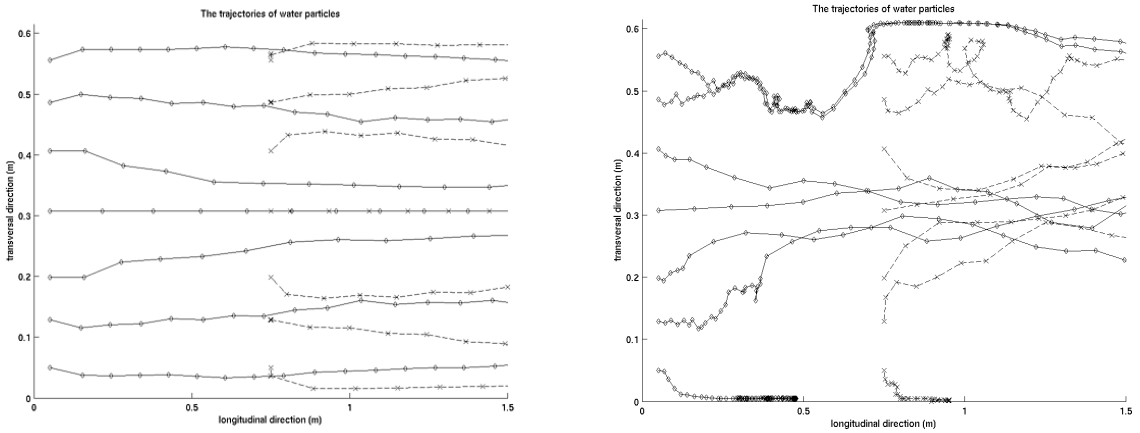

Figure 3: Particle trajectories for the case $\Delta x/h_1 = 0.5$ and propagating for 40s starting from $t = 1$s (left) and $t = 80$s (right). Diamonds and crosses represent the position of particles released at sections $x = 0$ and $x = 0.75$ respectively.

In order to analyze the motion of passive tracers like sediment or nutrients we can refers to either Eulerian-type (like the divergence of the mass flux) or Lagrangian-type (like the trajectories of particles) indicators. In figure 3 an example is given of the trajectories of water particles, i.e. $\mathrm{d}\mathbf{x}/\mathrm{d}t = \mathbf{u}$, during the two stages of evolution described in sections 2.1 and 2.2. From the left panel of the figure it is evident that particles are advected by the transient bore along almost rectilinear patterns. Later, after the bore has left the domain, the flow is dominated by the meandering of macrovortices which induces the very complicated patterns of the right panel of figure 3. These patterns are currently being investigated in dependence both of the grid influence on the solution and of physical effects presently neglected (like inertia, drag, lift, diffusion, etc.).

References:

Brocchini, M., Bernetti, R., Mancinelli, A. and Albertini, G., An efficient and robust flow solver for nearshore flows based on the WAF method, *Coast. Eng.*, *43*, 105-129, 2001.

Chu, V. H., Wu, J. H. and Khayat, R. E., Stability of transverse shear flows in shallow open channels, *J. Hydr. Eng. - ASCE*, *117*, 1370-1381, 1991.

Pratt, L. J., On inertial flow over topography. Part 1. Semigeostrophic adjustment to an obstacle, *J. Fluid Mech.*, *131*, 195-218, 1983.

Tamai, N., Asaeda, T. and Ikeda, H., Study on the generation of periodical large surface eddies in a composite channel flow, *Water Resour. Res.*, *22*, 1129-1138, 1986.

Toro, E. F., *Shock-capturing methods for free-surface shallow flows*, J. Wiley and Sons, New York, Chichester, Brisbane, 2000.

Modeling the salt wedge dynamics of the Itajaí Estuary

H. JACOB VESTED

(DHI Water & Environment – Agern Alle 11, DK-2970 Hørsholm, Denmark , hjv@dhi.dk)

CARLOS SCHETTINI

((Center of Earth and Marine Sciences - CTTMar, University of Vale do Itajái - UNIVALI, R. Urugai 458, C. P. 360, Itajai - SC - Brasil 88302 -202, guto@cttmar.univali.br)

OLE SVENSTRUP PETERSEN

(DHI Water & Environment,, osp@dhi.dk)

1. Introduction

The Itajaí Estuary is located in Southern Brazil in the state of St. Catarina. It can be characterised as a micro-tidal estuary, where the average tide at the mouth is about 0.8 m. The average river discharge is about 250 $m^3.s^{-1}$ and more than 1000 $m^3.s^{-1}$ during high flow. The estuary is highly stratified and a salt-water wedge is observed most of time. During average river discharge conditions the salt intrusion reaches about 18-20 km upstream, and the maximum observed salt wedge intrusion ever was 32 km. At a flow rate of 500-800 $m^3.s^{-1}$ a freshwater plume is well developed off the river mouth and at 1000-1200 $m^3.s^{-1}$ all salt is washed out of the estuary. The river plume extends several kilometres offshore during high flow, inducing complex patterns in the near shore coastal circulation.

Modelling the salt-water wedge and fresh water plume dynamics of Itajaí estuary poses several difficulties. It requires a high accuracy three-dimensional hydrodynamic model coupled with a salinity transport model. Further the model must be able resolve in details the river part, the estuary itself as well as the open sea where strong gradients occur both horizontally as well as vertical. This is demanding both from a numerical accuracy point of view as well as from limiting the computational time of simulations. The application of a hydrodynamic model with a variable and unstructured grid is applied in order to reproduce the extensive observation of the salt-water wedge under different flow conditions while at the same time analyse the applicability of the model for this type of estuary.

2. The numerical model

The model solves the three-dimensional shallow water equations, using a hydrostatic approximation, coupled to transports of salinity and heat through an equation of state. The free surface is described using vertical sigma co-ordinates and solution of a generalised wave equation (Lynch and Werner, 1991). The model further includes a full 3D k-epsilon model. The numerical solution is based on standard Galerkin linear finite elements using an unstructured mesh with linear triangles horizontally and a surface and bottom adaptive layered discretisation vertically (Burchard and Petersen, 1997). Time stepping is made using a semi-implicit method, where the gravity wave terms in the wave equation and the vertical terms in the momentum and transport equation are solve implicitly.

3. Model results

The model set-up is shown in Figure 1, and covers the coastal area in the vicinity of the estuary mouth, the estuary and the river up to 35 km from the mouth. The resolution varies from 500 m in t coastal area to 100 m in the river section. The vertical resolution follows the bathymetry and is discretised using 10 layers, with finest resolution near the surface. Boundary conditions are observed water levels at the ocean and the river discharge at the inland boundary. The simulations cover a 2 week period. The coastal area is included in order to accomodate the partial mixing of estauarine water in the vicinity of the mouth, and thereby establish a more accurate inflow salinity.

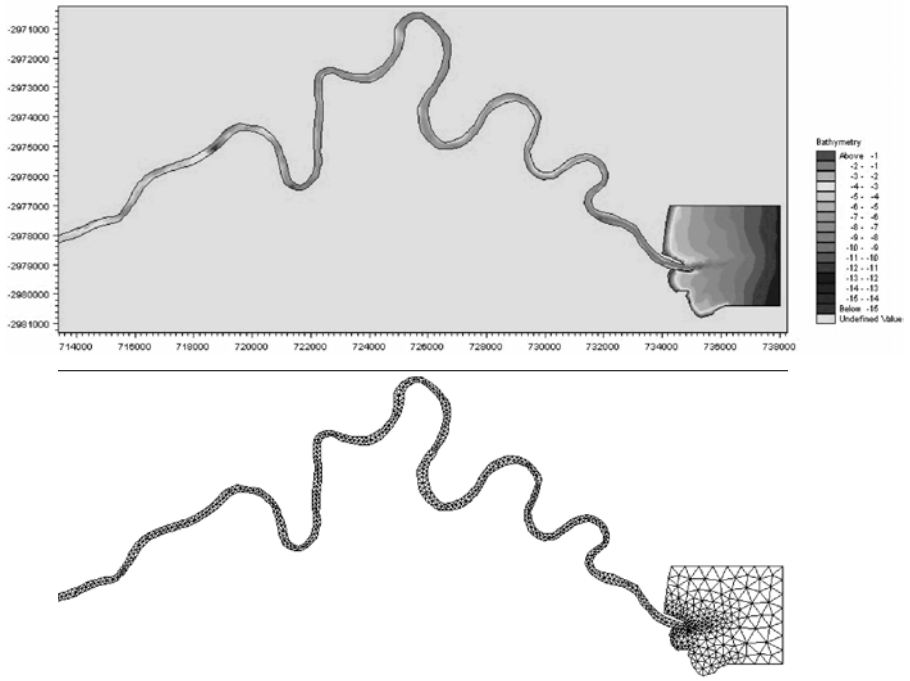

Figure 1: Bathymetry and unstructured mesh of the Itajai Estuary

The simulated results are compared with water level gauges in 3 stations and salinity transects of the salt-water wedge for different levels of the river run-off.

In Figure 2 is shown time series of computed and observed elevations at an upstream station for a typical spring and a neap period. The tides in the estuary have a significant quarterjournal component. Further, it is characteristic that the tidal wave proceeds nearly undistorted up through the estuary.

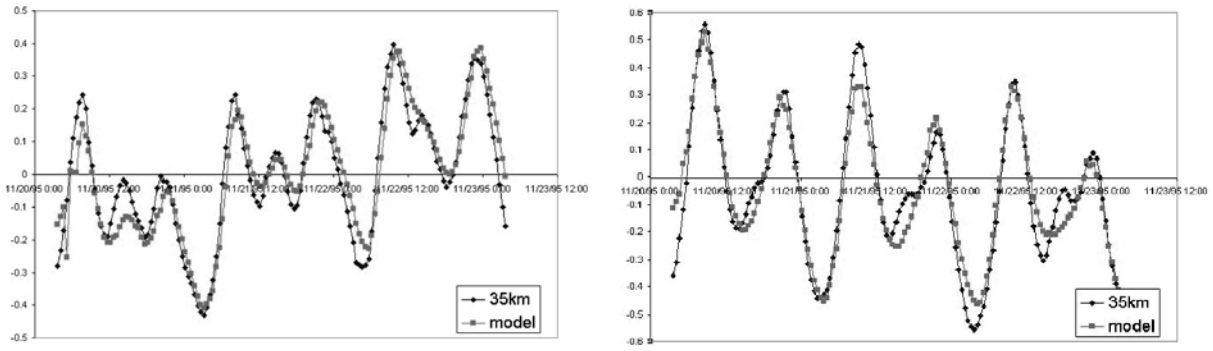

Figure 2: Modelled and observed water levels 35 km from the estuary mouth.

In Figure 3 and 4 are shown transects of the salinity up through the estuary at low and high tide. The uppermost tip of the intrusion is relatively stationary at 20 km, while the 30 PSU contour travels between 5 and 10 km during the tide. It is further evident that the height of the wedge increases during raising tide. The length of the saline wedge represents a relatively delicate balance between the baroclinic pressuregradients and the friction and vertical mixing along the interface.

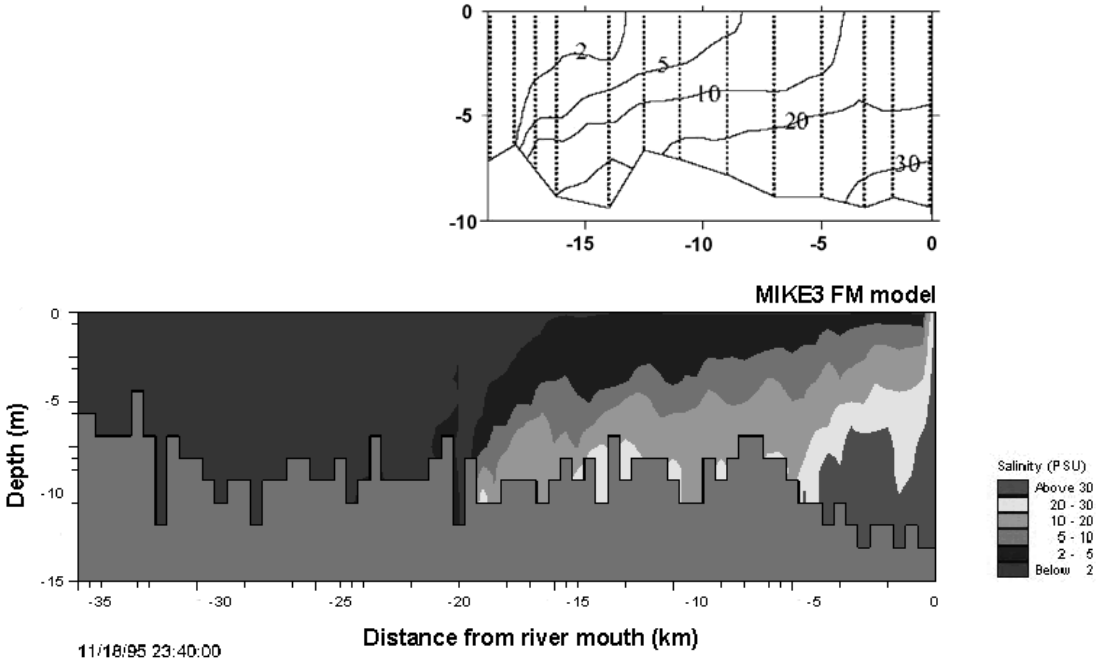

Figure 3: Observed an modelled salinity distribution at low tide

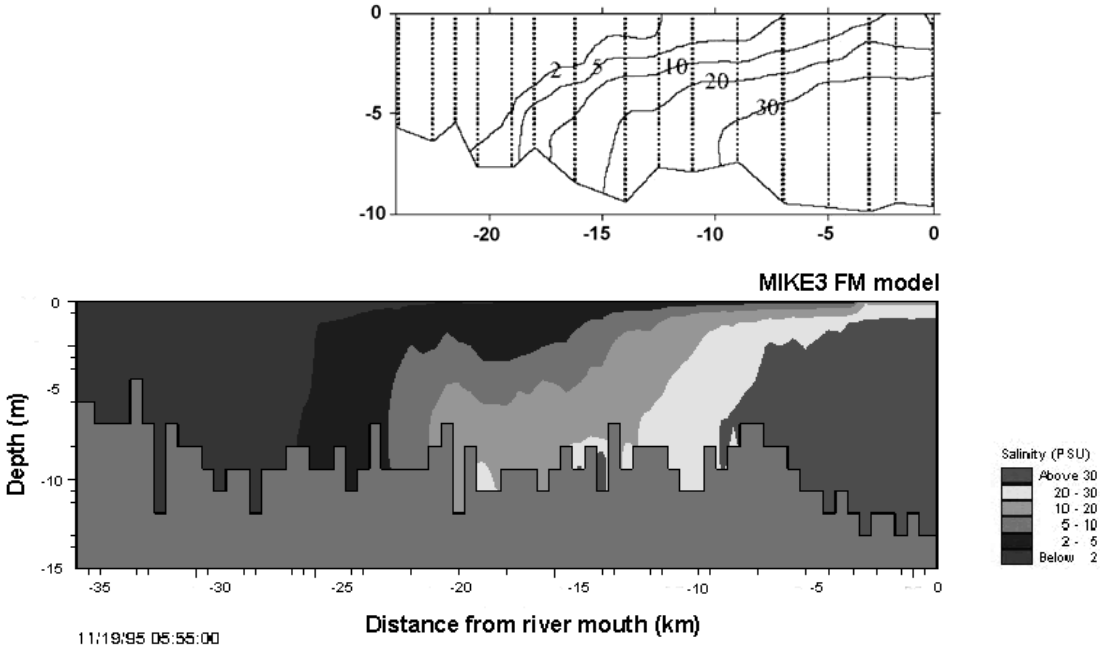

Figure 4: Observed and modelled salinity distribution at high tide

4. Summary

The study has shown the usefulness of the model to in applications to estuarine flows. As a first step is here discussed the effects of tides, river runoff and salinity intrusions. It is however planned, to include sediment and water quality related parameters at a later stage.

References

Lynch, D. R. and Werner , F. E. Three-dimensional hydrodynamics on finite elements. Part II: Non-linear timestepping model. *International Journal for Numerical Methods in Fluids,*12,507-533 (1991).

Burchard, H. and Petersen, O. Hybridization between σ- and z-coordinates for improving the internal pressure gradient calculation in marine models with steep slopes. *International Journal for Numerical Methods in Fluids*, 25, 1003-1023, (1997).

Observations of Reynolds stress profiles in a partially mixed estuary

Joanna J. Waniek, Cesar H.A. Ribeiro and Jonathan Sharples, (*Southampton Oceanography Centre, School of Ocean and Earth Science (SOES), European Way, Southampton SO14 3ZH, United Kingdom*, jowa@soc.soton.ac.uk)

1 Introduction

Turbulence in the presence of stratification and shear plays an important role in the dynamics of shallow tidal flows like those found in estuaries. For example, it is now well established that in many estuaries modulation of tidal mixing by the spring–neap cycle can drive fortnightly cycles in the strength of vertical stratification (see e.g. for laboratory studies Linden and Simpson [1988]; for observations Sharples et al. [1994], Ribeiro et al. [this issue]). The interaction between turbulence, stratification and shear has been the focus of numerous laboratory, numerical and observational studies in the open ocean (for review see Gregg [1991] and references therein). Except for the recent work of Peters [1997] and Stacey et al. [1999], there is little known about e.g. the vertical structure and the time development of turbulence in the energetic flows found in partially mixed estuaries.

Because of the primary role they play in flow evolution, the turbulent quantities of particular interest in estuarine flow are the along– and across–channel Reynolds stresses, which represent the vertical transport of horizontal momentum by turbulence. In this paper ADCP observations of turbulence in stratified water column, principally profiles of the turbulent shear stress throughout a tidal cycle, will be presented.

2 Methods

Location: The study site is Southampton Water, a partially mixed estuary, which is characterised by an unusual tidal regime, with strong shallow water tidal constituents promoting an extended double high water up to three hours long (Pugh [1987]). This extended period of slack high water is followed by an short, intense ebb, with high velocities and elevated turbulence. A "young flood stand" briefly reduces the tidal flood current strength, and so may reduce the vertical turbulent mixing in the middle of the flood period. The study site, Cadland navigation buoy, is located nearly in the middle of the length of Southampton Water, where the main channel has a width of ca. 1 km. The water depth at the study site reaches 9 m during neap high water and 6 m at neap low water.

Experimental setup: In order to observe the interaction of turbulence, shear and stratification in a water column over a whole tidal cycle, a 25 h survey at neap tide was performed. A four beam 1200 kHz Acoustical Doppler Current Profiler (ADCP) of the sentinel type was deployed on the seabed. The ADCP recorded single–ping data at 1 s time resolution in 25 cm bins upward looking. During the survey a microstructure probe, the Self Containing Autonomous Microstructure Profiler (SCAMP) was deployed in free fall configuration from a boat anchored at Cadland Buoy. Using SCAMP profiles of temperature and conductivity (salinity) were acquired approximately every 6 minutes. Two

additional temperature–conductivity loggers were deployed, one at ca. 1 m below the surface, and the second one at the sea floor. All salinity measurements were calibrated using discrete measurements of water sample salinities carried out on a Guildline salinometer.

Analysis techniques and significance proof: The ADCP data were processed to obtain 10 minute average profiles of mean velocity and Reynolds stress. The turbulence quantities were calculated using the variance technique described in detail by Lohrmann et al. [1990]. The shear stress is obtained from differences in along–beam velocities following the method published by Stacey et al. [1999] in which

$$\overline{v\prime w\prime} = \frac{\overline{u_1\prime^2} - \overline{u_2\prime^2}}{4 \sin\theta \cos\theta}, \tag{1}$$

where u_1 and u_2 are the velocities along the first and second beam, which lie in the longitudinal–vertical plane and θ is the angle between each beam and the vertical. x, y and z are defined to be the lateral (cross–estuary), longitudinal (along–estuary) and vertical dimensions. The velocities u, v, and w indicate the lateral, longitudinal and vertical velocity component, respectively.

To proof if the estimated Reynolds stresses are significantly different from zero the Reynolds stress time series was decomposed into two statistically uncorrelated series, with the same power density function (PDF) spectra, by lagging and leading one member of the original pair of the time series by an amount $\tau \geq \tau_0$, in wich τ_0 is the autodecorrelation time. The lagged covariance function was than calculated using:

$$R_{v'w'}(\tau) = \overline{v'(\tau)w'(t+\tau)}, \tag{2}$$

and $R_{v'w'}(\tau)$ at lag τ=0 was compared against its value for all lags and leads greater than τ_0. The estimated covariances are significant, if $R_{v'w'}(0)$ stands out from $R_{v'w'}(\tau)$ for $\mid \tau \mid \geq \tau_0$ (Lueck and Wolk, [1999]).

3 Results

Velocity data collected between 8 a.m. on 14.08.01 and 8 a.m. on 15.08.01 (day 226.3–227.3) show the typical strong semi–diurnal asymmetry in tidal motions in Southampton Water. The first flood period in the along–channel component is characterised by relatively low velocities up to 15 cm s^{-1}. The velocities during the second flood are higher with a magnitude of about 20 cm s^{-1} and a maximum at middepths. The short ebb periods show higher velocities with amplitudes up to 50 cm s^{-1}. In contrast to the flood the more intense currents during the ebb periods are evident through the whole water column (Fig.1a).

During the survey the strongest stratification, indicated by a maximum difference in density between surface and bottom of 1.6 kg m^{-3}, was reached during the ebb tide at day 226.35–226.45, shortly before low water, and is due to tidal straining. The gradients weakened as a consequence of the combined effect of tidal mixing, straining and advection during the following flood (day 226.6–226.75) but even at high water at day 226.8 the water column remains slightly stratified with density difference of 0.5 kg m^{-3} (Fig.1b).

The relative strength of the stratification and shear expressed by the gradient Richardson number Ri_g followed the structure of the buoyancy field (not shown). Elevated difference in Ri_g were observed for the high water periods at e.g. day 226.8 and day 227.35,

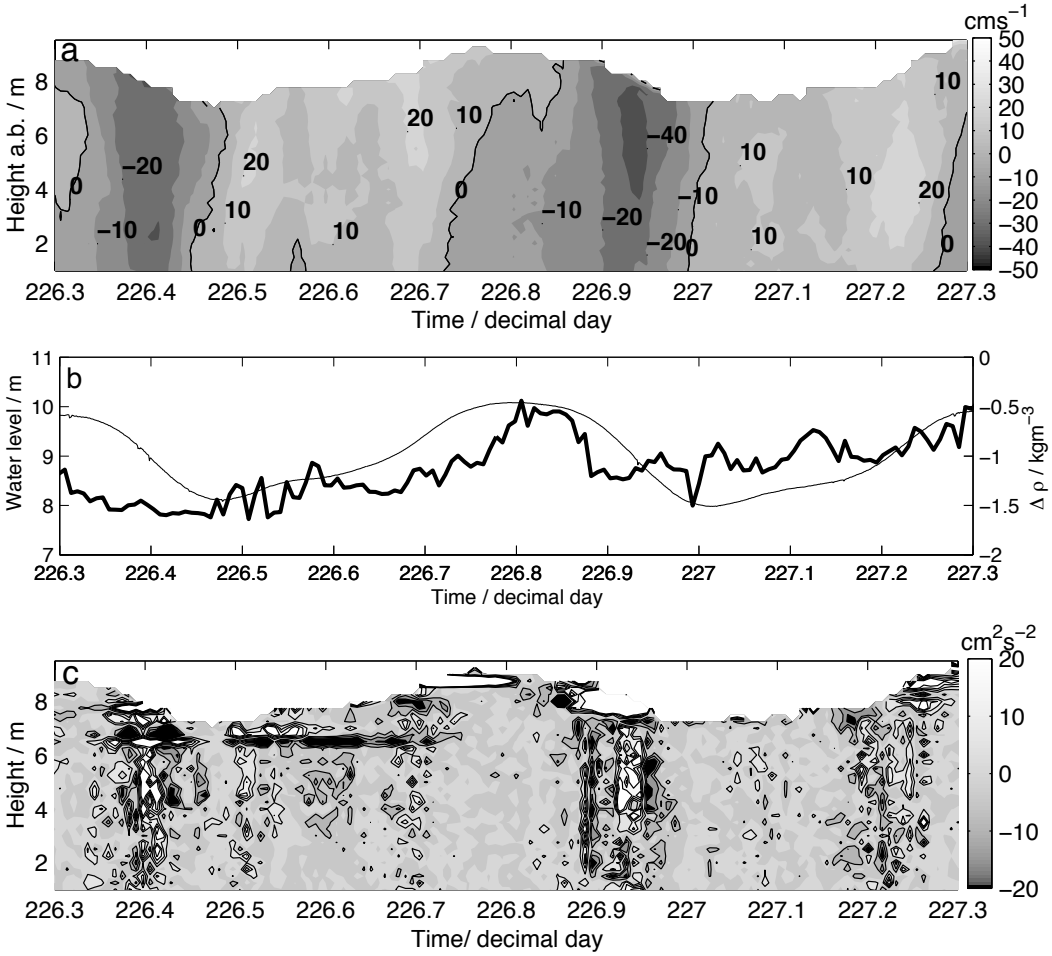

Figure 1: Physical conditions during the 25 h experiment at Cadland Buoy on 14–15. August 2001: The along channel current component (flood – positive, ebb – negative) in cms^{-1} (a), the density difference between surface and bottom layer in kgm^{-3} (bold line) together with the tidal height in metres (b) and (c) the along–channel Reynolds stress $\overline{v'w'}$ in $\mathrm{cm}^2\,\mathrm{s}^{-2}$. Each profile is a 10–min average of the ADCP data.

where the gradient Richardson number was very small near the bottom, compared to the interior of water column during the ebb and flood tide. The ebb and flood tides, were generally characterised by Ri_g smaller than the critical value of 0.25. However, during both flood periods (day 226.5–226.8 and day 227–227.3) Ri_g was occasionally higher than the critical value. Because the tidal energy was weak during these periods, the shear associated with these periods was not sufficient to offset the stratifying effects of advection.

The along–channel Reynolds stresses show similar asymmetric behaviour over the tidal cycle (Fig.1c). First of all the variation from ebb to flood is seen through most of the water column, with positive values occuring during the ebb tides, negative on floods and without significant stresses during the slack water (Stacey et al. [1999]). On ebb tides the along channel Reynolds stress values reached 20 $\mathrm{cm}^2\mathrm{s}^{-2}$ and were distributed over much of the

water column. In contrast the flood tide showed Reynolds stress values of 5-10 cm^2s^{-2} and the elevated Reynolds stresses were observed from 4 m above the sea bed (e.g. day 226.5–226.7). Comparing the Reynolds stress at τ=0 against the PDF of $R_{vw}(\tau)$ for all τ showed that the along channel stress was significantly different from zero during the ebb and flood tides. During the deceleration phase of each tide e.g. at day 226.8 and day 227 no turbulence activity producing Reynolds stress was observed.

Extrapolation of a linear fit to the Reynolds stress profiles results in time series of friction velocity u^{*2}, which show significantly higher values of u^{*2} during the ebb tide (12–20 cm^2s^{-2}) compared to the flood tide (8–10 cm^2s^{-2}). This asymmetry in bed stress provides a potential mechanism for moving sediment: higher values of shear stress during ebb than on floods create more suspended sediment, as is evident in the suspended particular matter measurements, resulting in upstream flux of the suspended material during the following flood.

Acknowledgments: This study was supported by NERC and by a personal grant for C. Ribeiro from CNPq. The author wishes to thank captain and crew of RV. Bill Conway, all volunteers participating in the 25 hours survey and all of those who assisted in the data collection effort.

References:

Gregg M. C., The study of mixing in the ocean: a brief history, *Oceanography*, *4*, 39–45, 1991.

Linden P. F. and J. E. Simpson, Modulated mixing and frontogenesis in shallow seas and estuaries, *Cont. Shelf Res.*, *8*, 1107–1127, 1988.

Lohrmann A., B. Hackett and L. D. Roed, High-resolution measurements of turbulence, velocity, and stress using a pulse–to–pulse coherent sonar, *J. Atmos. Oceanic. Technol.*, *7*, 19–37, 1990.

Lueck R. G. and F. Wolk, An efficient method for determining the significance of covariance estimates, *J. Atmos. Oceanic. Technol.*, *16*, 773–775, 1999

Peters H., Observations of stratified turbulent mixing in an estuary: Neap-to-spring variations during high river flow, *Estuarine Coastal and Shelf Science*, *45*, 69–88, 1997.

Pugh D. T., *Tides, surges and mean sea level: a handbook for engineers and scientist*, John Willey and Sons, Chichester, 1987.

Sharples J., J. H. Simpson and J. M. Brubaker, Observations and modelling of periodic stratification in the upper york river estuary, Virginia, *Estuarine, Coastal and Shelf Science*, *38*, 301–312, 1994.

Stacey M. T., S. Monismith and J. R. Burau, Observations of Turbulence in a Partially Stratified Estuary, *J. Phys. Oceanogr.*, *29*, 1950–70, 1999.

"Stress calculations from PIV measurements in the bottom boundary layer"

THOMAS OSBORN

(The Johns Hopkins University, 3400 N Charles Street, Baltimore, MD 21218, USA, osborn@jhu.edu)

W.A.M. NIMMO SMITH, W. ZHU, L. LUZNIK, AND J. KATZ

(The Johns Hopkins University, 3400 N Charles Street, Baltimore, MD 21218, USA)

1. Introduction

Turbulence measurements with a Particle Image Velocimetry (PIV) system were made in the bottom boundary layer of the coastal ocean. The submersible PIV system was deployed in water 12m deep about 5km off the New Jersey coast. The system consisted of two 12-bits-per-pixel, 2K x 2K digital cameras, operated simultaneously. Each camera imaged a 40cm x 40cm vertical plane aligned with the current which was illuminated by a light sheet. A pair of flash-lamp pumped, dye lasers at the surface generated double pulses, which were transmitted through optical fibers to submerged probes that produced the light sheets. Computers recorded the double exposure images from each frame, but a hardware-based 'image shifter' displaced the exposures relative to each other. Naturally occurring particles - sediment, plankton or other material - were used as tracers.

Calculations of the turbulent stress, in the presence of waves, are possible by using second order structure functions. This approach is an extension of the approach of John Trowbridge (Trowbridge,1998; Shaw and Trowbridge, 2001).

2. Measurements

Details of the measurement system are outlined in Bertuccioli et. al. (1998), Doron et. al. (2001) and Nimmo Smith et. al. (2002). Further information about the system along with some animations of the data are available on our web site http://cloudbase.me.jhu.edu/.

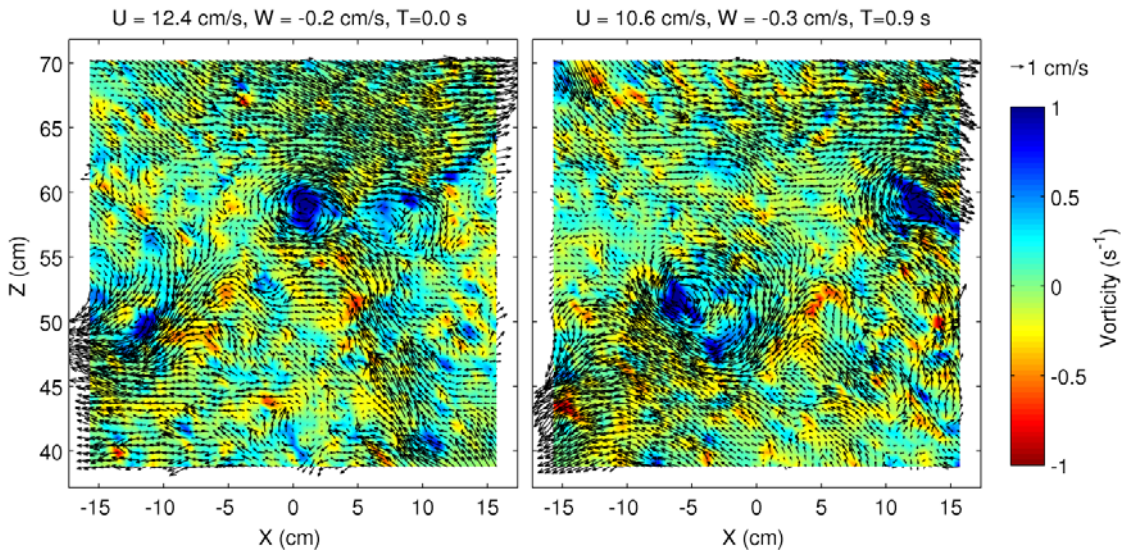

Figure 1. Two PIV images taken with the same camera 0.9 secs apart. The in plane velocities are shown as vectors while the vorticity is color coded with the scale along the side. Note especially the two vortices which are propagating to the right with the mean flow.

3. Stress Calculation

The Reynolds' stresses arise from the decomposition of the velocity field into mean and fluctuating parts. It is convenient to separate the fluctuations into two types, turbulence which causes mixing and dissipation and waves which generally cause neither. Writing the horizontal velocity component, u,as a sum of the mean, $\overline{u}$, the wave motion, $\tilde{u}$, and the turbulent fluctuations, u'.

$$u = \overline{u} + \tilde{u} + u'.$$

The same notation for the vertical component yields:

$$w = \overline{w} + \tilde{w} + w'.$$

The Reynolds stress is the product of the fluctuations:

$$(u - \overline{u})(w - \overline{w}) = (\tilde{u} + u') \cdot (\tilde{w} + + w').$$

$$(\tilde{u} + u') \cdot (\tilde{w} + w') = \tilde{u}\tilde{w} + u'w' + \tilde{u}w' + u'\tilde{w}$$

$$(u - \overline{u})(w - \overline{w}) = \tilde{u}\tilde{w} + u'w' + \tilde{u}w' + u'\tilde{w}$$

The wave turbulence cross terms $\tilde{u}w'$and $u'\tilde{w}$ are usually assumed to average to naught but as pointed out by Alex Hay (per. com.), the presence of a solid boundary can convert horizontal wave motion into vertical motion with spatial scales associated with the topographic features. We will return to this point later but for now will adopt the usual approach and assume these terms do not contribute to the correlation giving the desired result;

$$< (u - \overline{u})(w - \overline{w}) >=< u'w' >$$

Now, if the measurement axes are inclined (as they almost certainly will be) then the measured velocity components are a combination of both the horizontal and vertical components.

$$U = u \cdot \cos\theta + w \cdot \sin\theta$$

$$W = -u \cdot \sin\theta + w \cdot \cos\theta$$

$$(U - \overline{U}) \cdot (W - \overline{W}) = (\tilde{u} + u') \cdot (\tilde{w} + w')(\cos^2\theta - \sin^2\theta) + \left((\tilde{w} + w')^2 - (\tilde{u} + u')^2\right)\cos\theta \cdot \sin\theta$$

for small θ, $\cos\theta \to 1$ and $\sin\theta \to \theta$ and thus:

$$(U - \overline{U}) \cdot (W - \overline{W}) \cong (\tilde{u} + u') \cdot (\tilde{w} + w') + \left((\tilde{w} + w')^2 - (\tilde{u} + u')^2\right)\theta$$

near the ocean floor, the horizontal orbital velocity component is larger than the vertical and much larger than the turbulent fluctuations

$$(U - \overline{U}) \cdot (W - \overline{W}) \cong u'w' + \tilde{u}^2\theta$$

and the latter term overrides the desired measurement.

Trowbridge (1998) introduces, and Shaw and Trowbridge (2001) further develop, a technique for overcoming the wave contamination problem by using measurements from two sensors spaced apart by an amount that is large compared to the stress containing eddies but small compared to the wavelength of the surface waves. The application of this technique is slightly different for PIV data because of some of the innate characteristics of the data i.e., the strong alignment of the velocity components measured at different locations.

The second order structure function is the covariance of the velocity differences.

$$D_{mn}(\vec{x},\vec{r},t) =< (u_m(\vec{x},t) - u_m(\vec{x}+\vec{r},t))(u_n(\vec{x},t) - u_n(\vec{x}+\vec{r},t)) >$$

where the brackets <> denote some appropriate average.

$$D_{mn}(\vec{x},\vec{r},t) =< (u_m(\vec{x},t)\cdot u_n(\vec{x},t) - u_m(\vec{x}+\vec{r},t)\cdot u_n(\vec{x}+\vec{r},t) + u_m(\vec{x},t)\cdot u_n(\vec{x}+\vec{r},t) + u_m(\vec{x}+\vec{r},t)\cdot u_n(\vec{x},t)) >$$

If the velocity field is steady, homogeneous and reflexive symmetric

$$D_{mn}(\vec{x},\vec{r}) = 2 < u_m(\vec{x})\cdot u_n(\vec{x}) > -2 < (u_m(\vec{x})\cdot u_n(\vec{x}+\vec{r}) >$$

$$D_{mn}(\vec{x},\vec{r}) = 2 < u_m(\vec{x})\cdot u_n(\vec{x}) > \cdot(1 - R_{mn}(\vec{x},\vec{r}))$$

Thus, the value of $D_{mn}(\vec{x},\vec{r})$ increases from 0 at $\vec{r} = 0$, to $2 < u_m(\vec{x})\cdot u_n(\vec{x}) >$ when $\vec{r}$ exceeds the scale of the stress containing eddies.

As long as $\vec{r}$ is less than the scale of the surface waves, the wave contamination problem is avoided. The best way to see this point is to expand the second order structure function for U and W to see how the wave orbital motion and the inclination of the measurement frame enter into the result. For convenience we modify the notation as follows: $\vec{x}$ is denoted by x_i since we are considering locations along a horizontal axis. For our data we are interested in values of $\vec{r}$ that are parallel to the horizontal (*x* axis) so $\vec{r}$ is denoted by r_j. U and the various u's denote horizontal velocity components while W and the w's denote vertical components, subscript *i* denotes the location x_i and subscript *j* denotes the location $x_i + r_j$

$$d_{ij}(t) = D_{13}(\vec{x}_i,\vec{r}_j,t) =< (U(x_i,t) - U(x_i + r_j,t))(W(x_i,t) - W(x_i + r_j,t)) >$$

$$d_{ij} =< (U_i, -U_j)(W_i - W_j) >$$

$$(U_i,-U_j)(W_i,-W_j) = \begin{Bmatrix} (\tilde{u}_i + u_i')\cdot\cos\theta_i + (\tilde{w}_i + w_i')\cdot\sin\theta_i \\ -(\tilde{u}_j + u_j')\cdot\cos\theta_j - (\tilde{w}_j + w_j')\cdot\sin\theta_j \end{Bmatrix} \bullet \begin{Bmatrix} -(\tilde{u}_i + u_i')\cdot\sin\theta_i + (\tilde{w}_i + w_i')\cdot\cos\theta_i \\ +(\tilde{u}_j + u_j')\cdot\sin\theta_j - (\tilde{w}_j + w_j')\cdot\cos\theta_j \end{Bmatrix}$$

The turbulent terms give similar results to what we found before:

$$\begin{aligned} &(u_i'\cdot w_i')\cdot(\cos^2\theta_i - \sin^2\theta_i) + (u_j'\cdot w_j')\cdot(\cos^2\theta_j - \sin^2\theta_j) \\ &-u_i'^2\cdot\cos\theta_i\cdot\sin\theta_i + u_i'\cdot u_j'\cdot\cos\theta_i\cdot\sin\theta_j - u_i'\cdot w_j'\cdot\cos\theta_i\cdot\cos\theta_j \\ &+w_i'^2\cdot\cos\theta_i\cdot\sin\theta_i + u_j'\cdot w_i'\cdot\sin\theta_i\cdot\sin\theta_j - w_i'\cdot w_j')\cdot\cos\theta_j\cdot\sin\theta_i \\ &+u_j'\cdot u_i'\cdot\cos\theta_j\cdot\sin\theta_i - u_j'\cdot w_i'\cdot\cos\theta_i\cdot\cos\theta_j - u_j'^2\cdot\cos\theta_j\cdot\sin\theta_j \\ &+u_i'\cdot w_j'\cdot\sin\theta_i\cdot\sin\theta_j - w_i'\cdot w_j'\cdot\cos\theta_i\cdot\sin\theta_j + w_j'^2\cdot\cos\theta_j\cdot\sin\theta_j \end{aligned}$$

With the PIV system θ has the same value at both locations. The digital cameras are leveled and aligned, relative to each other across both sheets, to within 1 pixel (1 pixel is 1/2048 of the vertical window dimension, nominally 0.5 m) in the nominal 1.5 m maximum separation. Hence, the difference in angle between two points (on separate light sheets) is 1/6144 radians or 0.01 degrees. Combining that with the small angle expansion of the trigonometric functions the turbulent terms (to order θ and written as correlations) are:

$$\begin{aligned} &(u_i'\cdot w_i')\cdot(1 - R_{13}(x_i,r_j)) + (u_j'\cdot w_j')\,(1 - R_{13}(x_i + r_j,-r_j)) \\ &-u_i'^2\cdot\theta\cdot(1 - R_{11}(x_i,r_j)) - u_j'^2\cdot\theta\cdot(1 - R_{11}(x_i + r_j,-r_j)) \\ &+w_i'^2\cdot\theta\cdot(1 - R_{33}(x_i,r_j)) + w_j'^2\cdot\theta\cdot(1 - R_{33}(x_i + r_j,-r_j)) \end{aligned}$$

The wave terms are:

$$\left\{\tilde{u}_i\cdot\cos\theta_i - \tilde{u}_j\cdot\cos\theta_j + \tilde{w}_i\cdot\sin\theta_i - \tilde{w}_j\cdot\sin\theta_j\right\} \bullet \left\{-\tilde{u}_i\cdot\sin\theta_i + \tilde{w}_i\cdot\cos\theta_i + \tilde{u}_j\cdot\sin\theta_j - \tilde{w}_j\cdot\cos\theta_j\right\}$$

Since the alignment of the two cameras means the orientation of the velocity measurements is the same at all measurement points, terms like $\tilde{w}_i\cos\theta_i - \tilde{w}_j\cos\theta_j$ have values on the order of

$(\tilde{w}_i - \tilde{w}_j)\cos\theta = \frac{\partial \tilde{w}}{\partial x} r_j = k\tilde{w} r_j$ (where k is the wave number of the surface wave in the x direction) rather than $\tilde{w}(\cos\theta_1 - \cos\theta_2) = \tilde{w}(\frac{\theta_2^2 - \theta_1^2}{2})$. (The latter value is appropriately used in Trowbridges's analysis because his two sensors are not necessarily collinear.) Similarly, $(\tilde{u}_i \cdot \sin\theta_i - \tilde{u}_j \cdot \sin\theta_j) = \frac{\partial \tilde{u}}{\partial x} r_j \cdot \theta = k\tilde{u} r_j \theta$. For such terms we will use the shorthand notation of the form $\Delta\tilde{u}_{ij} = \tilde{u}_i - \tilde{u}_j$.

The wave terms can now be rewritten:

$$\left\{(\tilde{u}_i - \tilde{u}_j) + (\tilde{w}_i - \tilde{w}_j)\cdot\theta\right\} \bullet \left\{-(\tilde{u}_i - \tilde{u}_j)\cdot\theta + (\tilde{w}_i - \tilde{w}_j)\right\} = (\Delta\tilde{u}_{ij})^2 \cdot \theta + (\Delta\tilde{w}_{ij})^2 \cdot \theta + \Delta\tilde{u}_{ij} \cdot \Delta\tilde{w}_{ij} + O\left[\theta^2\right]$$

Thus, the wave contamination of the stress estimate, which used to be a term on the order of $\tilde{u}^2 \cdot \theta$, is now of the order $(\Delta\tilde{u}_{ij})^2 \cdot \theta$. The effect is smaller by a factor of $(kr)^2$, which is on the order of 10^{-3} for a wave of 6 seconds period and a separation of 1.5 m.

Now following the normal assumption that the wave and turbulent fluctuations don't correlate, we can write

$$d_{ij} = <(U_i, -U_j)(W_i - W_j)> = \begin{bmatrix} (u_i' \cdot w_i') \cdot (1 - R_{13}(x_i, r_j)) + (u_j' \cdot w_j')\,(1 - R_{13}(x_i + r_j, -r_j)) \\ -u_i'^2 \cdot \theta \cdot (1 - R_{11}(x_i, r_j)) - u_j'^2 \cdot \theta \cdot (1 - R_{11}(x_i + r_j, -r_j)) \\ +w_i'^2 \cdot \theta \cdot (1 - R_{33}(x_i, r_j)) + w_j'^2 \cdot \theta \cdot (1 - R_{33}(x_i + r_j, -r_j)) + \\ (\Delta\tilde{u}_{ij})^2 \cdot \theta + (\Delta\tilde{w}_{ij})^2 \cdot \theta + \Delta\tilde{u}_{ij} \cdot \Delta\tilde{w}_{ij} + O(\theta^2) \end{bmatrix} +$$

The structure function begins at zero with no separation and rises to (minus) twice the stress as the separation exceeds the scale of the stress containing eddies, as long as the waves are of much larger scale than the turbulent eddies. Otherwise, if the spatial scale becomes too large, then $\Delta u_{ij} = (\tilde{u}_i - \tilde{u}_j) = \frac{\partial \tilde{u}}{\partial x} r_j = k\tilde{u} r_j$ is no longer small compared to u' and the whole wave contamination problem resurfaces.

Acknowledgments: This work has been supported by the Office of Naval Research and the National Science Foundation.

References:

Bertuccioli, L., G.I. Roth, T.R. Osborn and J. Katz, Turbulence measurements in the bottom boundary layer using particle image velocimetry. *Journal of Atmospheric and Oceanic Technology* 16, 1635-1646, 1998.

Doron, P., L. Bertuccioli, J. Katz, T.R. Osborn, Turbulence characteristic and dissipation estimates in the coastal ocean bottom boundary layer from PIV data. *J. Phys. Oceanogr.* 31 2108-2134, 2001.

Nimmo Smith, W.A.M., Atsavapranee, P., Katz, J. and Osborn, T.R., PIV measurements in the bottom boundary layer of the coastal ocean. *in press in Experiments in Fluids,* (2002).

Shaw, W. J. and J. H. Trowbridge The direct estimation of near-bottom turbulent fluxes in the presence of energetic wave motions *Journal of Atmospheric and Oceanic Technology*, Vol. 18, No. 9, pp. 1540–1557, 2001.

Trowbridge, J. H., On a technique for measurement of turbulent shear stress in the presence of surface waves. *Journal of Atmospheric and Oceanic Technology.* 15, 290-298, 1998.

Turbulent production and dissipation in a region of tidal straining

EIRWEN WILLIAMS, JOHN SIMPSON, TOM RIPPETH AND NEIL FISHER

University of Wales, School of Ocean Sciences, Menai Bridge, Anglesey, LL59 5EY

eirwen.williams@bangor.ac.uk

1. Introduction

In regions of strong horizontal gradients of density, water column mixing interacts with tidal straining to induce periodic stratification at the M_2 frequency (*Simpson et al*. [1990], *Rippeth et al*. [2001]). In the Liverpool Bay region of freshwater influence (ROFI), maximum stratification occurs around low water after the ebb, when fresher water in the upper layers has moved seawards over the denser layers near the bed. During the flood the tidal straining mechanism acts to reduce the stability of the water column, with complete vertical mixing occuring near high water.

We will report on the first measurements of the rate of turbulent kinetic energy (TKE) production and TKE intensity in the Liverpool Bay ROFI using the variance method applied to along-beam velocity measurements from a high frequency acoustic Doppler current profiler (ADCP) moored on the sea bed. Simultaneous measurements were made of the rate of dissipation of TKE using a free-falling microstructure profiler. The two sets of measurements exhibit similar patterns, with the high production (P) and dissipation (ε) levels extending throughout the water column on the flood, but confined to the lower part of the water column on the ebb. Towards the end of the flood, the action of the tidal straining mechanism on an already mixed water column creates instabilities in the water column which provide energy for convective mixing. The vertical velocity measurements from the ADCP will be examined for further evidence of convective motions during the flood.

The relative magnitude of the stirring and straining terms governs the periodic stratification of the water column; stratification only occurs on the ebb if the straining mechanism out-competes the tidal stirring. The power available for stirring will be compared with the input from straining to obtain an estimate for the efficiency of mixing.

We will also present the results of recent observations in the York River estuary, Virginia, in which the ADCP variance method was used to obtain a 14-day time series of Reynolds stresses and rate of production of TKE. This is a more strongly stratified regime than the Liverpool Bay ROFI; comparisons will be made of the observations of turbulent parameters in the two regimes.

The York River ADCP observations were made using RDI's mode 12, which allows a much faster sampling rate than can be used with mode 1 which was used in Liverpool Bay. The uncertainty in the estimation of the Reynolds stresses and the rate of production of TKE from the ADCP data is analysed and the noise level resulting from the use of mode 1 will be compared with that resulting from the use of mode 12. The information obtained from this analysis will enable us to devise an optimum sampling strategy for future observations in terms of depth cell size, sampling rate and averaging strategies.

2. Observational Methods and Analysis

Observations were made in September 2001 in the Liverpool Bay ROFI which experiences periodic stratification. A 600kHz ADCP was moored on the sea bed for 5 days and measured along-beam velocities in 1m bins at a frequency of 2Hz using profiling mode 1; ensemble averages were recorded by the instrument every 2 seconds.

For a 48-hour period during this deployment, measurements were also made using the FLY free-falling microstructure profiler (*Dewey et al.* [1987]). The profiler was operated from the RV Prince Madog II close to the mooring site of the ADCP. A series of 6-8 profiles was made every hour; each profile taking 20-30 minutes to complete. Each series of profiles was used to make one dissipation estimate every hour. A CTD cast was also made every hour close to the mooring position.

In the York River, a 14-day time series was obtained using two moored ADCPs: one 1.2MHz and one 600kHz. Both recorded along-beam velocities with a depth cell size of 50cm. Profiling mode 12 was used, with the average of 10 pings recorded at approximately 1Hz.

For both the Liverpool Bay and York River data, the Reynolds stresses and rate of production of TKE were calculated from the ADCP data over a 10-minute averaging period using the variance method (*Stacey et al*. [1999]). The uncertainty in the estimates of these parameters were calculated both theoretically and empirically for both sets of data.

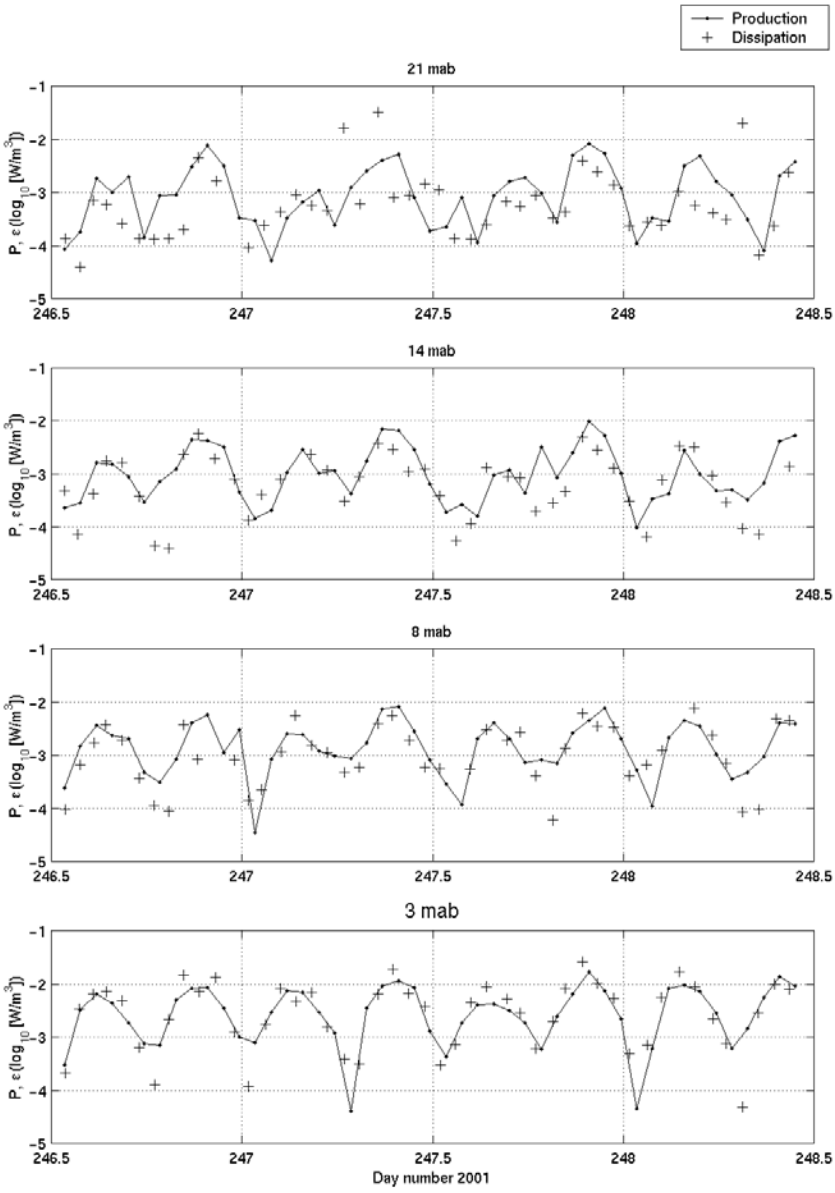

Figure 1: Time series of rates of dissipation and production of turbulent kinetic energy

3. Results

Some results from the Liverpool Bay observations are shown in figure 1. The results show close tracking of dissipation and production estimates, particularly near the bed. For both P and ε, the data were averaged temporally over 1 hour and spatially over 1m. Both P and ε show high values (O 10^{-2} W/m^3) extending throughout the water column at times of peak flow on the flood phase of the tidal cycle (day numbers 246.9, 247.4, 247.9). On the ebb the peak values of P and ε are lower; in the upper part of the water column the noise in the production estimates is much more evident.

Further results on the cycle of production from the York River will be used to compare strong and marginally stratified conditions and to demonstrate the lower noise level resulting from the increased ping rate.

4. Initial Conclusions

Production and dissipation are closely consistent at 1 hour averages. With the lower noise levels obtained using mode 12, there arises the possibility of an improved comparison of P and ε which may reveal the differences between them due to the other terms in the TKE equation.

References:

Dewey, R.K., W.R. Crawford, A.E. Gargett and N.S. Oakey (1987) A microstructure instrument for profiling oceanic turbulence in coastal bottom boundary layers. *J. Atmos. Oceanic. Technol.*, 4, 288-297

Rippeth, T.P., N. Fisher and J.H. Simpson (2001) The cycle of turbulent dissipation in the presence of tidal straining. *J. Phys. Oceanogr.*, 31, 2458-2471

Simpson, J.H., J. Brown, J. P. Matthews and G. Allen (1990) Tidal straining, density currents and stirring in the control of estuarine stratification. *Estuaries*, 13(2), 125-132

Stacey, M.T., S.G. Monismith and J.R. Burau (1999) Measurements of Reynolds stress profiles in unstratified tidal flow. *J. Geophys. Res.*, 104, 10933-10949

An estimate of water exchanges between the East Frisian Wadden Sea and the southern North Sea

EMIL STANEV, (*Institute for Chemistry and Biology of the Sea, University of Oldenburg, Postfach 2503, D-26111 Oldenburg, Germany*, e.stanev@icbm.de)

GÖTZ FLÖSER, (*Institute for Coastal Research, GKSS Research Centre, Max-Planck-Strasse, 21502, Geesthacht, Germany*, goetz.floeser@gkss.de)

JÖRG-OLAF WOLFF, (*Institute for Chemistry and Biology of the Sea, University of Oldenburg, Postfach 2503, D-26111 Oldenburg, Germany*, wolff@icbm.de)

1 Introduction

In estuarine physics the flushing time T is normally defined as the time required to replace the volume of existing fresh water V_f in the estuary at the rate of the river discharge (R). This time scale is also known as residence time $T = V_f/R$. There are various other time scales that serve the purpose of defining a certain aspect of the exchange of waters in a given volume, e. g. the "turn-over time" measuring the time needed for the total mass of material originally within a box to be reduced by a factor of e^{-1} (Prandle, 1984). The prism method to calculate the flushing of estuaries influenced mainly by tides suggests that $T = T_t(V + P)/P$, where T_t is the tidal period, $V + P$ the water volume at high tide and P is the tidal prism, i. e. the difference in volume between high and low tide. Both definitions assume that "old water" leaving a defined volume is completely replaced by "new water" (be it river water or open ocean water).

In the individual basins of the East Frisian Wadden Sea the tidal prism is comparable to the water volume residing in the back barrier area, giving for the exchange (flushing) time values $\sim$ 1-2 T_t. However, numerous earlier estimates in similar coastal systems give numbers, which are 10-20 times larger. According to Postma (1954), the flushing time of fresh water discharged near Den Oever is 13 tidal periods. Van Bennekom et al. (1974) found flushing times of $\sim$ 14 and 26 tidal periods for the western and eastern parts of the Dutch Wadden Sea, respectively (see e. g. Zimmerman, 1976).

At present, the flushing times of inter tidal basins in the East Frisian Wadden Sea are not well known. Unlike the Dutch Wadden Sea, the German Wadden Sea is usually well mixed and water mass analysis based on salinity data alone cannot give accurate estimates. It is also known that the amount of exchanged water is controlled by local topography and forcing. In addition, the efficiency of water exchange is modulated by turbulent mixing and Lagrangian steering. Provided that the water entering the inter tidal basins during flood is essentially the same water, which has left the basins during ebb, the net exchange is rather small.

The current uncertainties in quantitative estimates of the water exchange regime are based on an insufficient observational data base as well as on an incomplete physical understanding of the system. We propose in this paper to objectively estimate the exchange of water between the intertidal flats of the East Frisian Wadden Sea and the southern

North Sea due to advection and diffusion using observations and high-resolution numerical simulations.

2 Observations

In the years 2000 to 2002, various hydrographic parameters in the German Wadden Sea were measured by GKSS using pile stations and ship campaigns. The pile stations were positioned in the tidal basin between the islands Langeoog and Baltrum. Among others the following oceanic parameters were measured: current speed and direction, turbidity, gauge level, wave height, conductivity and temperature. In addition important meteorological data have been recorded, e.g. air pressure and temperature, precipitation, wind speed and direction, and solar irradiation. All data are averaged over a 10 minute time interval and then transmitted via a telephone line to GKSS every hour.

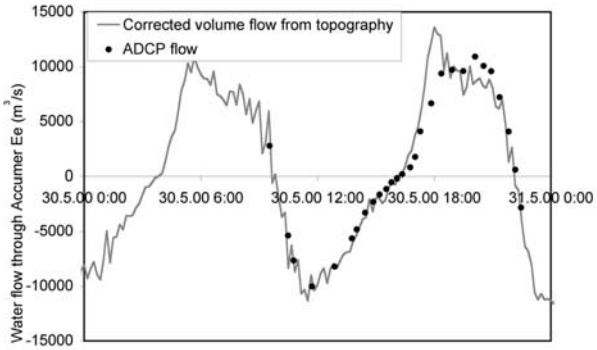

Figure 1: Observed and reconstructed water transport through the Accumer Ee on August 25^{th}, 2000

.

In 2000, the water exchange between the East Frisian Wadden Sea and the southern North Sea was also measured with an ADCP along transects between the islands Langeoog and Baltrum comprising four ship experiments on May 26th and 30th and on August 25th and 30th. We have measured vertical profiles of current velocities and calculated the volume flow during a full tidal cycle on these days.

The gauge level time series exemplify the general characteristics of the region: The spring tidal amplitude is 3.4 m, at neap tide it is about 1.8 m. The tidal signal arrives at the pile station near the tidal inlet Accumer Ee at 53 42.657 N 7 28.273 E one hour earlier than the two land stations at Dornumersiel and Bensersiel where it arrives almost simultaneously.

Interesting is the asymmetry of the tidal signal: the water flow through the tidal inlet as measured during the four ship campaigns shows that the rate of change is much higher during high tide than during low tide. Another kind of asymmetry is observed during the ship campaigns: the vertical shear of the horizontal velocities is stronger during flood than during ebb flow.

Both measured flow characteristics contradict the view presented by Postma (1982)

where temporal and / or vertical asymmetries are postulated as being a cause for the net near-bottom inward transport of suspended particle matter. Our measurements indicate quite different current characteristics than those given by Postma. Thus, it remains unclear how, in the observed region, suspended matter is transported into the Wadden Sea.

3 The numerical model

The numerical simulations are based on a the General Estuarine Transport Model (GETM), which is a 3-D primitive equation numerical model (Burchard and Bolding, 2002). The first application of this model to the area of our study is described in detail in the paper by Stanev et al. (2002).

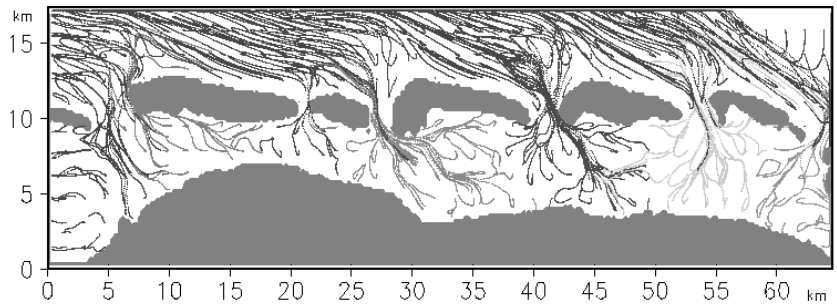

Figure 2: Lagrangian trajectories.

We would like to point out some important model features. The model has a horizontal resolution of 200 m and terrain following coordinates in the vertical. It is forced at its open boundaries with sea level data from the operational model of German Hydrographic Office for the German Bight. Sub-grid parameterizations use the k-ϵ turbulent closure scheme. The lateral boundaries of the model are time dependent thus representing the most important characteristic of inter-tidal basins, i. e. the continuous process of flooding and drying.

The comparison of our numerical simulations with observational data is addressed in Stanev et al. (2002). The transport patterns are illustrated below with the trajectories of Lagrangian particles released in every 64-th grid cell.

By calculating the displacements of particles from their initial position we can calculate the flushing time T_a, which is due to advection only. For the basins of Wangerooge, Spiekeroog, Langeoog and Baltrum T_a is 4.8, 3.7, 4.8 and 1.5 $\times$ T_t, respectively.

4 Discussion and conclusions

The comparison of water exchanges between the East Frisian tidal flats and the southern North Sea using different methods, i. e. simple hydrological arguments, direct velocity measurements and high-resolution hydrodynamic modeling results is very promising. Because all methods have certain inaccuracies it might allow us to find out and concentrate on more accurate physics for the processes that are of importance.

This is an important issue since calculating water transports from ADCP data is not very accurate. In the paper we present the results from two numerical experiments: one is driven by observed tidal oscillations during a spring tide period. The other one is actually an imitation of a model run, in which the dynamics are switched off. In the latter case the sea level is horizontal and is equal to the sea level corresponding to the mean forcing signal at the open boundary. In Fig. 3a the volumes of the intertidal basins of the Islands Spiekeroog and Langeoog are shown. Fig. 3b gives the volume changes, which approximately equal the water flux between intertidal basins and ocean (Stanev et al., 2002). Fig. 3c displays the difference between the volume changes in the two runs, which actually gives a measure for the error in the transport estimated without physics.

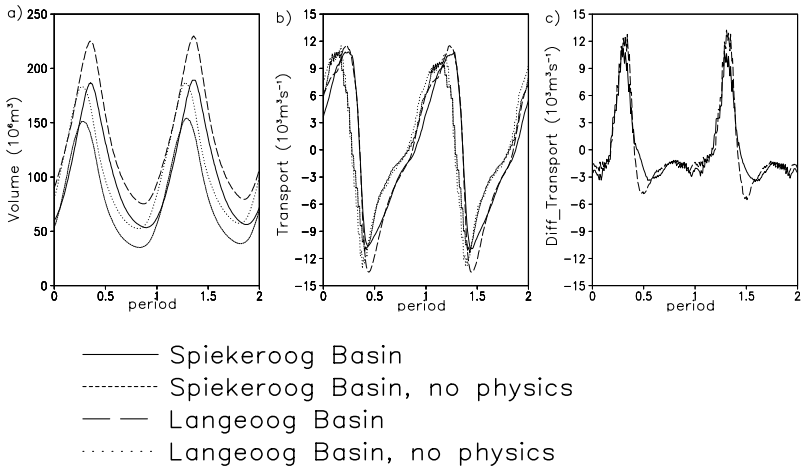

Figure 3: Temporal variability of water volume (a), its time rate of change (b) and the contribution of physical processes (c).

Acknowledgment: We would like to thank Hans Burchard and Karsten Bolding for providing the GETM model and Rolf Riethmüller for discussions with regard to the pile data.

References:

Bennekom, A. J. van, W. W. C. Gieskes and S. B. Tijssen, Eutrofication of Dutch coastal waters. *Proc. Roy. Soc.* **B 189**, 359-374, 1974.

Burchard, H. and K. Bolding, GETM, A general estuarine transport model. Scientific documentation. Tech. Rep. EUR 20253 EN, European Commission, 157 pp., 2002.

Postma, H., Hydrography of the Dutch Wadden Sea. *Tijdschr. K. ned. aardijksk.*, **67**: 4-33, 1954.

Prandle, D., A modelling study of the mixing of 137Cs in the seas of the European continental shelf. *Phil. Trans. R. Soc.*, London, **A310**: 407-436, 1984.

Stanev, E. V. J.-O. Wolff, H. Burchard, K. Bolding, and G. Flöser, On the Circulation in the East Frisian Wadden Sea: Numerical modeling and data analysis. submitted to *Ocean Dynamics* 2002.

Zimmerman, J. T. F. Mixing and flushing of tidal embayments in the western Dutch Wadden Sea. Part I: Distribution of salinity and calculation of mixing time scales. *Ned. J. Sea Res.* **10**, 149-191, 1976.

Waves in inlets

PAULO SALLES

(Engineering Institute, National Autonomous University of Mexico, Apdo. Postal 70-472, Coyoacán 04510, México D.F., México, psaa@pumas.iingen.unam.mx)

RODOLFO SILVA

(Engineering Institute, National Autonomous University of México, Apdo. Postal 70-472, Coyoacán 04510, México D.F., México, rodo@litoral.iingen.unam.mx)

JUAN CARLOS ESPINAL

(Engineering Institute, National Autonomous University of México, Apdo. Postal 70-472, Coyoacán 04510, México D.F., México, juancarlos@litoral.iingen.unam.mx)

1. Introduction

Inlet hydrodynamics are complex. They result from the interaction between the fluid motion and the bottom floor, which often has a complicated spatial distribution (channels, bars, deltas, platforms…). The fluid motion is in turn generated both by currents (tidal-induced, wind-driven, wave-generated, river flow...) and by waves, which propagated at frequencies ranging from a few seconds to several hours or more.

In spite of that, inlet hydrodynamics, and in general inlet stability, are commonly studied with emphasis on the currents (e.g., Bruun, 1978; Salles, 2000). This is reasonable when the inlet is tide dominated, which is the case when the tidal amplitude is large compared with the wave energy at the inlet gorge. In addition, even if considerable wave energy exists in the vicinity of the inlet, many inlets have a well-developed ebb-delta that causes the waves to break before reaching it. However, in cases were no ebb-delta is present and the tidal amplitude is small, waves can play a major role in sediment transport, and in general in inlet morphodynamics.

In order to analyze the effects of waves on inlet dynamics, a series of projects have started, including field measurements, mathematical and numerical modeling. This study is the first effort in that sense, and consists of numerical simulations of the hydrodynamics in Laguna de Términos, Mexico, a large coastal lagoon system, and in particular in Puerto Real, a flood-dominated inlet, to compare the sediment transport capacity with and without waves.

2. Study area

The Laguna de Términos coastal system is located in the coastal plains of the State of Campeche. It communicates with the Gulf of Mexico through two natural inlets, Carmen and Puerto Real inlets, east and west of the Carmen barrier island, respectively, and Sabancuy Inlet, a small artificial inlet, 43 km northeast from Puerto Real Inlet. The system is composed by a main water body with 3.5 m average depth and a surface area of approximately 1,700 km^2, and a series of adjacent lagoons, some of which are the deltas of rivers entering the main lagoon (see

Figure 1), with a total surface area of 800 km^2. The flood area, up to the +1.0 m relative to the mean sea level, is of 4,000 km^2.

The climate is tropical humid and is characterized by three stations, regulated by the rain intensity: little precipitation (March to May), heavy rains (June to October), and intermediate precipitations with strong northerly winds or *Nortes* (November to February). The average yearly precipitation is 1,805 mm (David *et al.*, 1998), and the yearly evaporation has been estimated to be 1,512 mm, which give an average effective input, considered uniformly distributed over the entire system, of 23 $m^3.s^{-1}$. The aquatic vegetation is represented by sea grass (*Thalassia testudinum, Halodelue wrightii* y

Syringodium filiforme), and the lagoons are surrounded by mangrove (*Rhizophora mangle, Avicennia germinans, Laguncularia racemosa, y Conocarpus erectus*). The predominant winds are moderate with north-northeast and east-southeast wind speeds lower than 5 $m.s^{-1}$, except during the *Nortes* season, in which frontal passages can have average sustained north-northwest wind speed in excess of 12.5 $m.s^{-1}$ (Mancilla *et al.*, 1980).

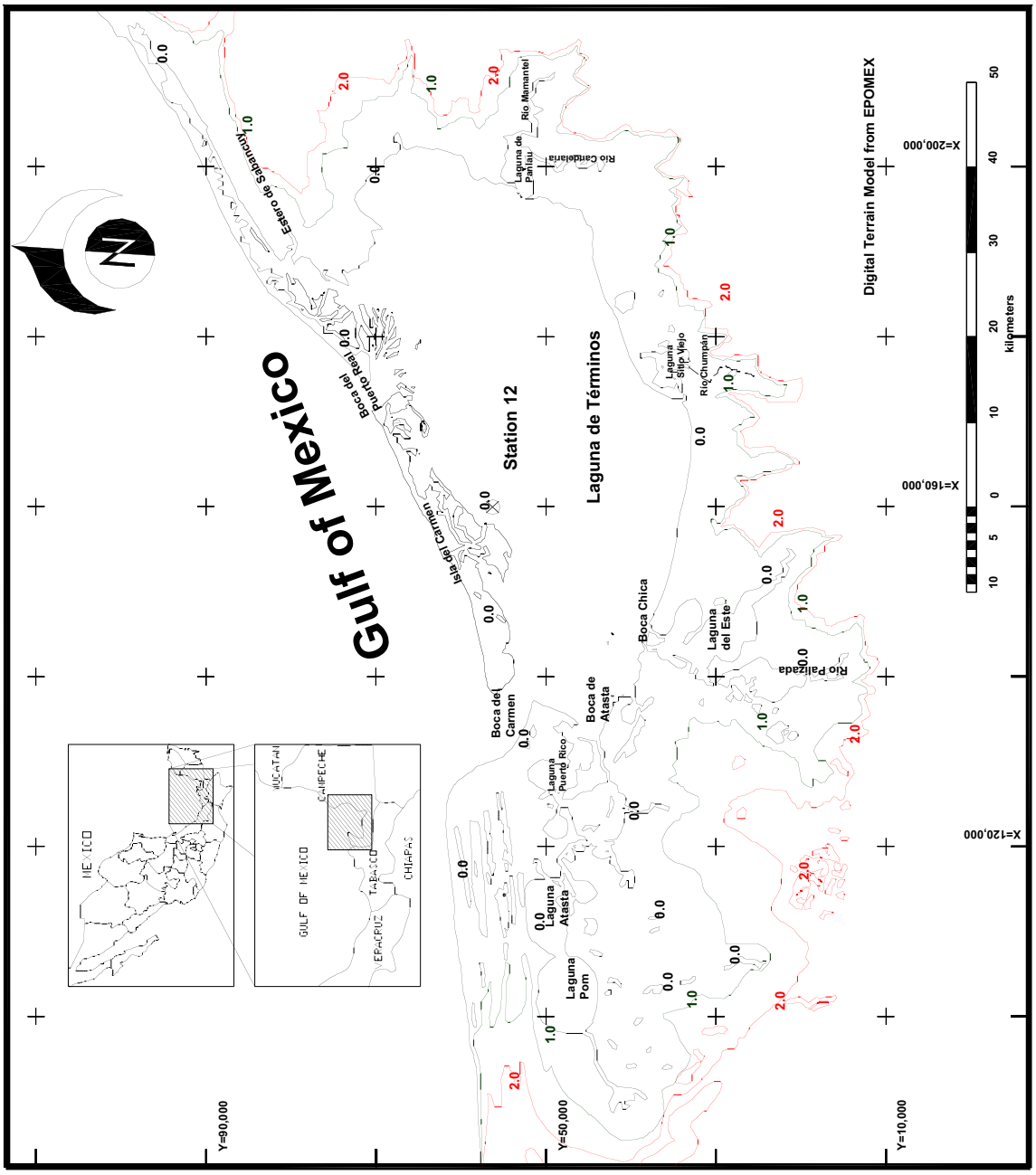

Figure 1. Map of Laguna de Términos, with lines corresponding to +0.0, +1.0 and +2.0 m.

Most of the fresh-water input to the system comes from three rivers (see Figure 1): Palizada river with monthly-averaged discharges ranging from 115 to 510 $m^3.s^{-1}$ (288 $m^3.s^{-1}$ yearly average), Candelaria and Mamantel rivers, whose discharges occur in the Panlau lagoon, and range monthly from 23 to 197 $m^3.s^{-1}$ (72 $m^3.s^{-1}$ yearly average), and Chumpán river with discharges ranging from 0.3 to 50 $m^3.s^{-1}$ (18 $m^3.s^{-1}$ yearly average).

The tide in the area is mixed-diurnal (Marina, 2001), with the diurnal components being the largest, as shown in Table 1. The average amplitude is 0.424 m, the high high water is 0.923 m and the low low water is –0.662 m, with respect to the mean water level (0.000 m). According to measurements of the water level fluctuations at the inlets and an intermediate point between the inlets (St. 12 in Figure 1), the phase lag of the tide as it propagates inside the lagoon is important, as shown in Table 2. For instance, the high O_1 tide occurs 1.7 hours later at Carmen Inlet and 5.01 hours later at Station 12. It can be seen that the propagation of the tide is from northeast to southwest in that zone of the Gulf of Mexico. Furthermore, the propagation experiences selective dampening inside the lagoon, as a result of higher friction and energy transfer from one component to another.

Table 1. Main harmonic components

Component	M_2	S_2	N_2	K_1	O_1	P_1
H (m)	0.076	0.019	0.021	0.111	0.120	0.036
Phase (º)	78.58	73.63	67.35	315.17	318.93	321.44

Table 2. Phases of the main harmonic components (in degrees and hours:minutes), relative to Puerto Real.

Component	M_2	S_2	N_2	K_1	O_1	P_1
Puerto Real	0	0	0	0	0	0
Carmen	-33 / 1:08	-8 / 0:16	-39 / 1:22	-36 / 2:24	-24 / 1:43	-27 / 2:01
St. 12	-134 / 4:38	-254 / 8:28	---	-67 / 4:27	-70 / 5:01	-41 / 3:04

The density stratification due to vertical gradients of salinity and/or temperature has been found to be important only locally in some areas of the system and during the rainy season, in particular in the river mouths (Herrera-Silveira *et al.*, 2002), and never at the ocean inlets. Therefore, this stratification as not been taken into account in this study, which focuses on the inlet hydrodynamics.

3. Numerical model

Numerical simulations of the tidal dynamics in the system, using RMA-2V (Donnell *et al.*, 1997), a vertically integrated finite-element model that solves the non-linear momentum and continuity equations, complemented with COPLA-2DH (COPLA-RD, 1998), a wave parabolic model for the wave propagation under the presence of currents, were performed in order to estimate the flow characteristics at the inlet. Finally, the bedload and suspended load sediment transport at different locations was computed by means of a combined wave-current bottom boundary layer flow model (e.g., USACE, 2001). The environmental parameter considered for this studies were: waves, wind, tides, river discharge, Coriolis effects, bathymetry, and grain size (d_{50}= 0.2 mm), for two different scenarios: (1) spring tide and 1 m waves, and (2) storm surge and 3 m waves.

4. Preliminary Results and Discussion

Preliminary results of sediment transport (considering maximum river discharges, and no direct wind effects) with and without waves have been computed as an example for six points distributed across the Puerto Real Inlet gorge (Figure 2), as show in Figure 3.. It can be seen that the ratio of the wave-current total sediment transport to the pure current value is significantly large: 77 (on average) for the storm surge case (with 3 m waves) and 29 for the spring tide case (with 1 m waves).

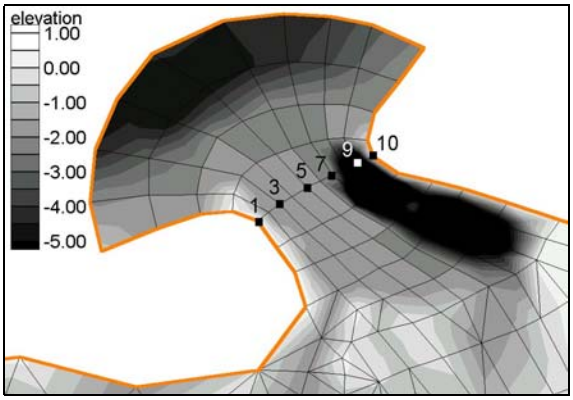

Figure 2. Points for sediment transport computations

Although a similar analysis of the effects of waves on sediment transport can be done analytically, this example shows the importance of considering waves when studying the morphological evolution of coastal features as inlets. In Laguna de Términos, especially in the flood dominant Puerto Real Inlet, the wave effects on sediment transport are considerable. The large sediment transport capacity obtained when considering waves in this inlet is consistent with the observed morphologic evolution.

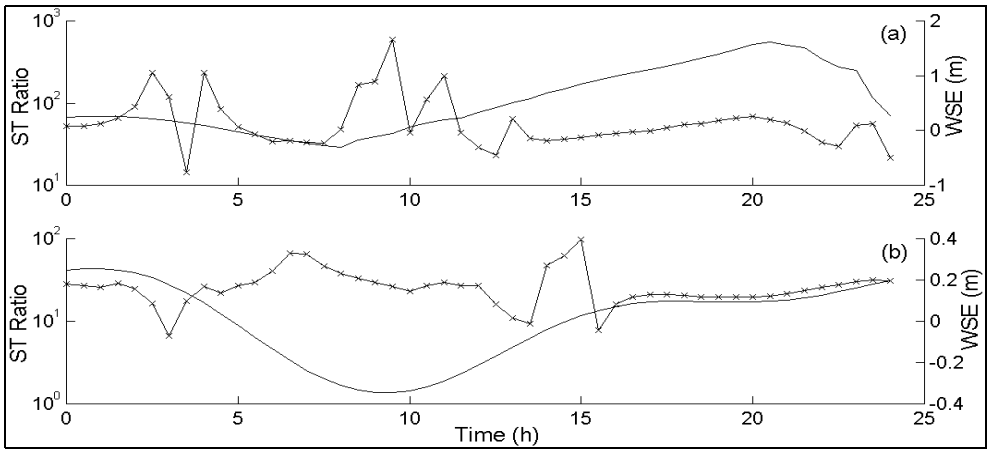

Figure 3. Cross-sectional averaged ratio of total sediment transport with and without waves (crosses) with forcing: (a) 1 m storm surge superimposed to spring tide and 3 m waves, and (b) spring tide with 1 m waves

Acknowledgments: This work was partially supported by the UNAM-PAPIIT project number IN106101.

References:

Bruun, P. (1978). Stability of Tidal Inlets, Theory and Engineering, Elsevier.

COPLA-RD (1998). Modelo integral de propagación de oleaje y corrientes en playa., Manual de Usuario, versión 1.0. Universidad de Cantabria.

David, L. T. and B. Kjerfve (1998). "Tides and Currents in a Two-Inlet Coastal Lagoon: Laguna de Términos, México." Continental Shelf Research 18(10): 1057-1079.

Donnell, B. P., J. I. Finnie, J. V. Letter, W. H. McAnally, L. C. Roig and W. A. Thomas (1997). User's Guide to RMA2 WES Version 4.3. US Army Corps of Engineers - Waterways Experiment Station Hydraulics Laboratory. pp.

Herrera-Silveira, J. A., R. Silva Casarín, P. Salles Afonso de Almeida, G. J. Villalobos Zapata, I. Medina Gómez, J. C. Espinal González, A. Zaldivar Jiménez, J. Trejo Peña, M. González Jáuregui, A. Cú Escamilla and J. Ramírez Ramírez (2002). Análisis de la Calidad Ambiental Usando ndicadores Hidrobiológicos y Modelo Hidrodinámico Actualizado de Laguna de Términos. CINVESTAV-IPN, Mérida, EPOMEX, Instituto de Ingeniería-UNAM. 187 pp.

Mancilla, M. and M. Vargas (1980). “Los primeros estudios sobre la circulación y el flujo neto de agua a través de la laguna de Términos, Campeche, México.” An. Instituto de Ciencias del Mar y Limología, UNAM 7(2): 1-12.

Marina, S. d. (2001). Tablas de Mareas, Golfo de México y Mar Caribe. Dirección general de Oceanografía Naval.

Salles, P. (2000). Hydrodynamic Controls on Multiple Tidal Inlet Persistence. MIT/WHOI Joint Program in Applied Ocean Sciences and Engineering, Massachusetts Institute of Technology / Woods Hole Oceanographic Institution: 272 pp.

USACE (2001). Coastal Engineering Manual. Washington D.C.

Seasonal variability in the near-surface salinity field of the northern and eastern Gulf of Mexico

WILLIAM W. SCHROEDER

(Marine Science Program, The University of Alabama, Dauphin Island Sea Lab, 101 Bienville Blvd., Dauphin Is., AL, USA, 36528, wschroeder@disl.org)

STEVEN L. MOREY

(Center for Ocean – Atmospheric Prediction Studies, The Florida State University, Tallahassee, FL, USA, 32306-2840, morey@coaps.fsu.edu)

JAMES J. O'BRIEN

(Center for Ocean – Atmospheric Prediction Studies, The Florida State University, Tallahassee, FL, USA, 32306-2840, obrien@coaps.fsu.edu)

1. Introduction

Historic hydrographic data show a seasonal pattern in the near-surface salinity field of the northern and eastern Gulf of Mexico (GoM). Numerical simulations of the GoM using the Navy Coastal Ocean Model (NCOM) predict a similar signal. In this study, the roles of mesoscale eddy activity and the annual cycle of both river discharge and wind forcing are examined in connection with the seasonal pattern of the salinity field. It is demonstrated that the annual cycle of the wind-driven transport of buoyant, low salinity water near the Mississippi River Delta greatly influences the interseasonal spatial pattern of the near-surface salinity field in the northern and eastern GoM. Model results show that low salinity waters produced by the Mississippi River plume are directed westward onto the broad Louisiana -Texas shelf in the fall and winter and remain insulated from deeper Gulf waters as they are trapped along the coast. On the other hand, the river plume spreads over deeper slope waters east of the delta in the spring and summer forming a low salinity surface layer that can then interact with the offshore circulation. Mesoscale eddies associated with the Loop Current often entrain these lower salinity waters and transport them great distances. This mechanism for redistributing the freshwater discharged by large rivers in the northern GoM is described from the model results and compared with observational data sets.

2. The Gulf of Mexico Environment

The circulation in the GoM is dominated by the energetic Loop Current and its associated eddies. The Loop Current (LC) enters the basin through the Yucatan Channel and exits through the Florida Straits to the east, forming an anticyclonically flowing current. The LC penetrates northward and intermittently pinches off large anticyclones with irregular periods from 3 and 17 months (see *Sturges and Leben* [2000]). These anticyclones drift westward where they decay against the western continental margin. Associated with the LC and the large anticyclones are a wealth of smaller cyclonic and anticyclonic eddies interacting in a seemingly chaotic manner. All of these features have vertical scales from several hundred to 1000 m and thus remain offshore of the continental shelf break.

Wind patterns over the northern GoM are typified by light southeasterly winds during the summer, with frequent cold fronts shifting the mean winds to northeasterly and northerly during the fall and winter. The influence of the seasonality of the winds on the GoM circulation is small compared to the energetic LC-induced circulation, but can be important near the coast.

Coastal regions of the GoM exhibit large variability in salinity, which in turn has a large influence on the coastal ocean stratification. Filaments and lenses of low salinity water have been observed throughout the Gulf. The source of this low salinity water is freshwater discharged by large rivers to the Gulf, primarily the Mississippi River. The Mississippi River has an annual mean discharge of over

13,000 m^3/s (as measured by the U. S. Geological Survey gauging station 7374000) with the neighboring Atchafalaya River discharging at about one-half the rate. The monthly climatology of the Mississippi River discharge has a maximum in April of over 22,000 m^3/s and a minimum in September of just over 6,300 m^3/s. A unique feature of the Mississippi River is that the discharge locations are located at the end of a delta extending to very near the edge of the continental shelf. Thus, if the river plume is directed toward the east, it will extend over deep water, whereas it will flow over the wide Louisiana-Texas (LATEX) shelf should it be directed westward.

Occasional plumes of low salinity water have been observed along the eastern edge of the mean position of the LC, just offshore of the West Florida Shelf (see *Gilbes, et al.* [1996]), and have been shown to be likely linked to discharge from the Mississippi River. Monthly climatology of near surface (10 m) salinity from the 1998 World Ocean Atlas (WOA98) (see *Conkright, et al.* [1998]) shows a seasonal signal along this path, which would be consistent with more frequent occurrences of these plumes during the summer months. The purpose of this work is to investigate, using a numerical model of the GoM together with observational data, this seasonal variability of upper ocean salinity in the northern and eastern GoM in connection with these low salinity plumes. The roles of seasonal variability of river discharge and seasonally varying wind stress over the northern GoM on the fate of the freshwater discharged by the Mississippi River are examined in connection with the LC-induced offshore circulation.

3. The Model

The NCOM is a three-dimensional primitive equation hydrostatic ocean model developed at the Navy Research Laboratory (see *Martin* [2000]). The model's hybrid sigma (terrain following) and z (geopotential) level vertical coordinate is useful for simulating upper ocean processes in domains encompassing both deep ocean basins and very shallow shelves. The NCOM is set up to simulate the entire GoM and Caribbean north of Honduras (15° 30' N) to 80° 36' W with 1/20° between like variables on the C-grid, 20 sigma levels above 100 m and 20 z-levels below 100 m to a maximum depth of 4000 m. The model is forced by discharge from 30 rivers, transport through the open boundary (with monthly climatology temperature and salinity) yielding a mean transport through the Yucatan Strait of approximately 30 Sv, and monthly climatology surface heat and momentum flux. A surface salinity flux has the effect of uniformly evaporating an amount of water at a rate equal to the sum of the annual average discharge rates of the 30 rivers.

4. Results and Discussion

Monthly climatology salinity averaged over 1°x1° boxes at 10 m from both the WOA98 and NCOM simulations with steady river discharge and monthly varying river discharge show similar seasonal signals along the eastern edge of the mean position of the LC (Figure 1). The salinity minimum occurs in the summer during which the model salinity field has a tongue-like spatial pattern with lower values to the north near the Mississippi River. The amplitude of the seasonal signal decreases with distance from the freshwater source. The similar results from the two model experiments suggest that seasonal variability of river discharge does not play an important role in determining the variability of the surface layer salinity far from the river mouth.

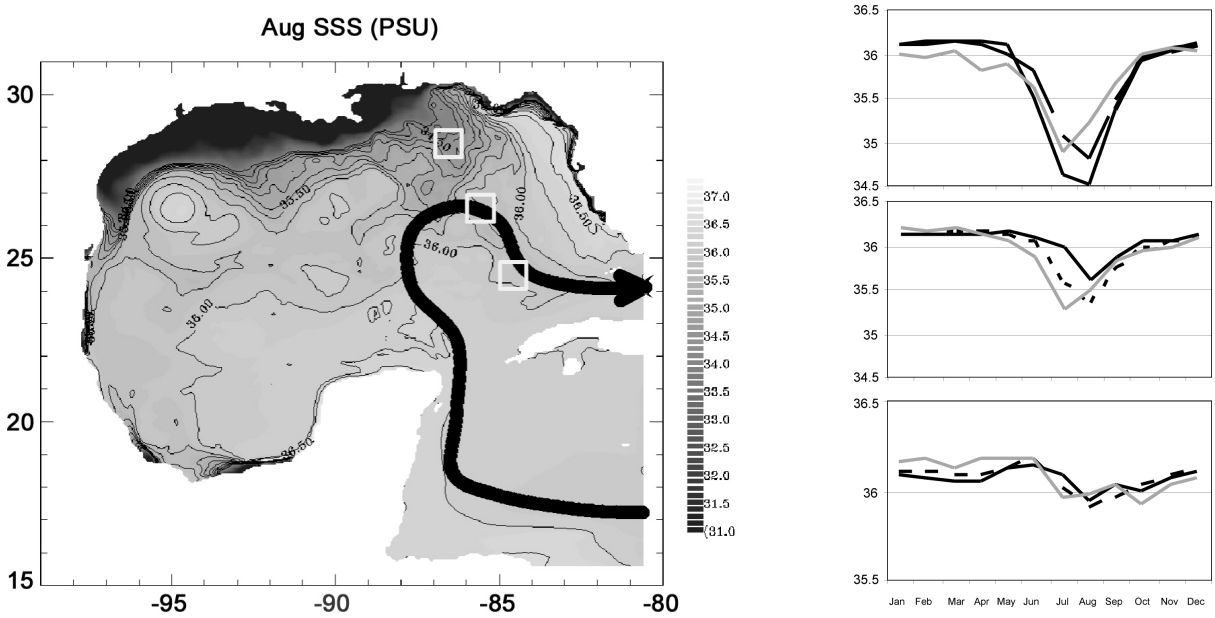

Figure 1: Left: NCOM mean August surface salinity shown with the mean position of the LC. Right: Monthly climatology surface salinity from 1°x1° boxes (shown north to south) from WOA98 (10 m) (gray), NCOM with steady river discharge (dashed), and NCOM with monthly river discharge (black).

Continuous underway observations of surface salinity made during the Northeastern Gulf of Mexico Physical Oceanography Program: Chemical Oceanography and Hydrography Study (NEGOM) cruises (Minerals Management Service sponsored Texas A & M University Study) are consistent with the salinity fields predicted by the NCOM simulations. Spreading of low salinity water from the Mississippi River eastward is evident over the deep DeSoto Canyon during the summer, with no such eastward spreading evident during the winter (Figure 2).

Ekman transport of the buoyant low salinity water near the mouth of the Mississippi River is responsible for the seasonal eastward and westward spreading of the plume. During the winter, when the wind is from the north, the plume turns westward and is coastally trapped, insulated from the deep ocean by the wide LATEX shelf. In the summer months, the light southerly winds direct the plume eastward over the deep DeSoto Canyon. Jets formed by interacting eddy pairs found throughout the GoM can entrain buoyant low salinity water which has spread offshore over the deep water in which these eddies exist. That is, water discharged by the Mississippi River can interact with the eddies near the DeSoto Canyon when the plume spreads in this direction primarily in the summer. These jets often form a pathway to the LC, which transports this low salinity water far from its origin in the northern GoM (See Schroeder, et al. [1987]).

The mechanism responsible for the seasonal signal of upper ocean salinity found along the eastern edge of the LC has two ingredients. The first is the spreading of the Mississippi river plume over the deep DeSoto Canyon to the east in the summer and the wide LATEX shelf to the west in the winter, directed by the seasonally varying wind stress. Entrainment of water by jets between interacting deep water eddies forms the second ingredient, to which there is no seasonal component.

Acknowledgments: The authors thank Drs. Paul Martin, Alan Wallcraft, and others at the Navy Research Laboratory for their development of and assistance with the Navy Coastal Ocean Model. The Texas A&M Oceanography Department provided the plots for Figure 2. Simulations were performed on the IBM SPs at Florida State University and the Naval Oceanographic Office. Computer time was provided by the DoD High Performance Computing Modernization Office. This project was sponsored by funding provided by the DoD Distributed Marine Environment Forecast System, by the Office of Naval Research Secretary of the Navy grant awarded to Dr. James J. O'Brien, and by a NASA Office of Earth Science grant to the COAPS authors.

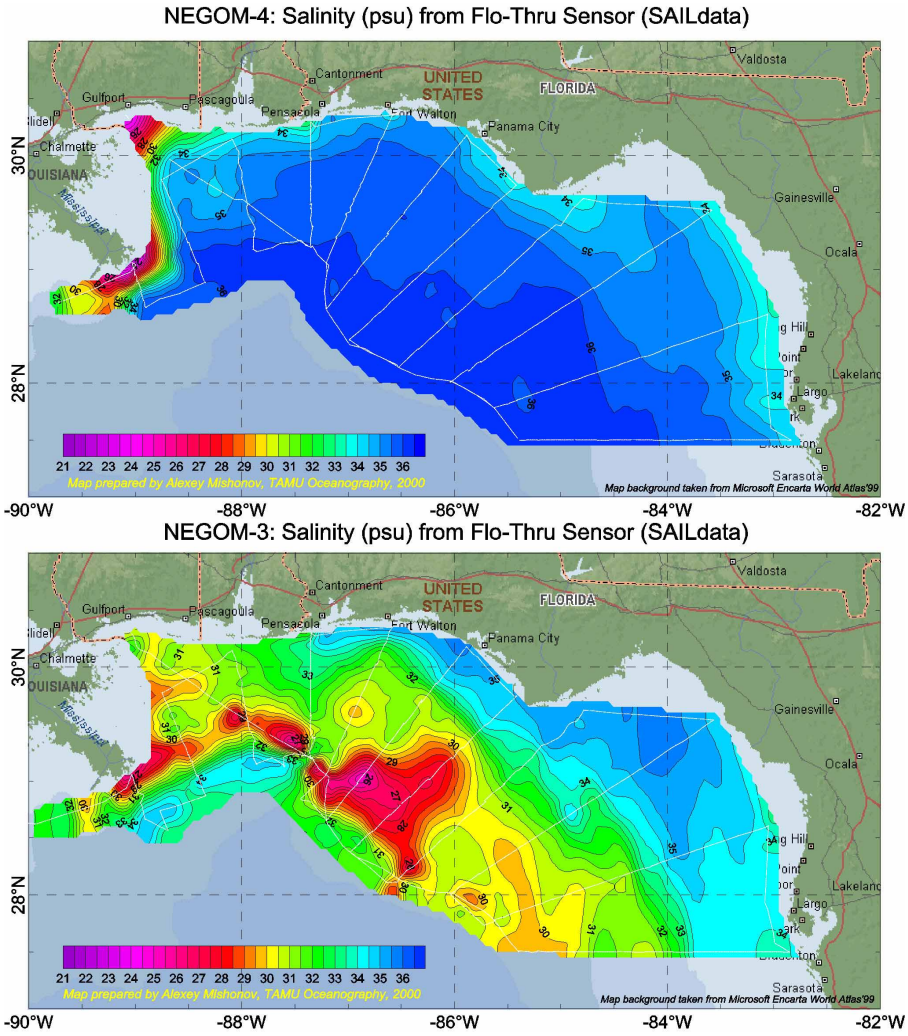

Figure 2: Surface salinity from continuous underway measurements from the NEGOM cruises Nov. 13-24, 1998 (top), and July 25 – Aug. 6, 1998 (right). (Provided by the Department of Oceanography, Texas A & M University)

References:

Conkright, M., S. Levitus, T. O'Brien, T. Boyer, J. Antonov, and C. Stephens, World Ocean Atlas 1998 CD-ROM Data Set Documentation.. Tech. Rep. 15, NODC Internal Report, Silver Spring, MD, 16 pp., 1998.

Gilbes, F., C. Tomas, J. J. Walsh, and F. E. Muller-Karger, An episodic chlorophyll plume on the West Florida Shelf, *Continental Shelf Research, 16*, 1201-1224, 1996.

Martin, P., A description of the Navy Coastal Ocean Model Version 1.0. NRL Report NRL/FR/7322-009962, Naval Research Laboratory, Stennis Space Center, MS, 39 pp., 2000.

Schroeder, W. W., S. P. Dinnel, W. J. Wiseman., Jr., and W. J. Merrell, Jr., Circulation patterns inferred from the movement of detached buoys in the eastern Gulf of Mexico, *Continental Shelf Research, 7*, 883-894, 1987.

Sturges, W., and R. Leben, Frequency of ring separations from the Loop Current in the Gulf of Mexico: A revised estimate, *Journal of Physical Oceanography, 30*, 1814-1819, 2000.

Subtidal variability of flow around a cape

ARNOLDO VALLE-LEVINSON AND CATHY BROWN

(Center for Coastal Physical Oceanography, OEAS Department, Old Dominion University, Norfolk, Virginia, USA, arnoldo@ccpo.odu.edu, cathy@ccpo.odu.edu)

1. Introduction

Studies of flows around capes have documented the generation of secondary circulations resulting from curvature effects [e.g. Geyer, 1993]. These circulations develop at intratidal time scales and consist of surface flow away from the cape and bottom flow toward the cape. On average, tidal flows interacting with capes or headlands tend to produce a pair of counter-rotating eddies that have been portrayed in the horizontal plane [e.g. Signell and Harris, 2000]. Little is known about the vertical structure of the mean flow around a cape and on its subtidal variability. Our objective is then to illustrate the subtidal variability of the vertical structure of the flow at a site off a cape and to document the dynamics associated with the flow. This objective is addressed with current velocity profiles obtained for almost five months. The velocity profiles were combined with time series of near-surface and near bottom salinity, near surface and near-bottom temperature, sea level, and wind velocity .

2. Observations

Data were collected off Cape Henry (36° 55.768'N, 75° 59.955'W), the southern cape at the entrance to Chesapeake Bay (Fig.1), from January 20 to June 9, 2000 over a depth of 6 m. The velocity profiles were measured with a 614.4 kHz RD Instruments Acoustic Doppler Current Profiler (ADCP) equipped with pressure sensor. A total of 45 pings were averaged over 15 minutes at vertical bins of 0.5 m and with the first bin at ~0.8 m from the bottom. Salinity and temperature values were measured with SeaBird's SBE-37 recorders. Hourly wind velocity and sea level data were obtained from NOAA stations at Chesapeake Bay Bridge Tunnel (#8638863), Kiptopeke (#8632200) and Solomons Island (#8577330)(E, K, S respectively on Fig. 1).

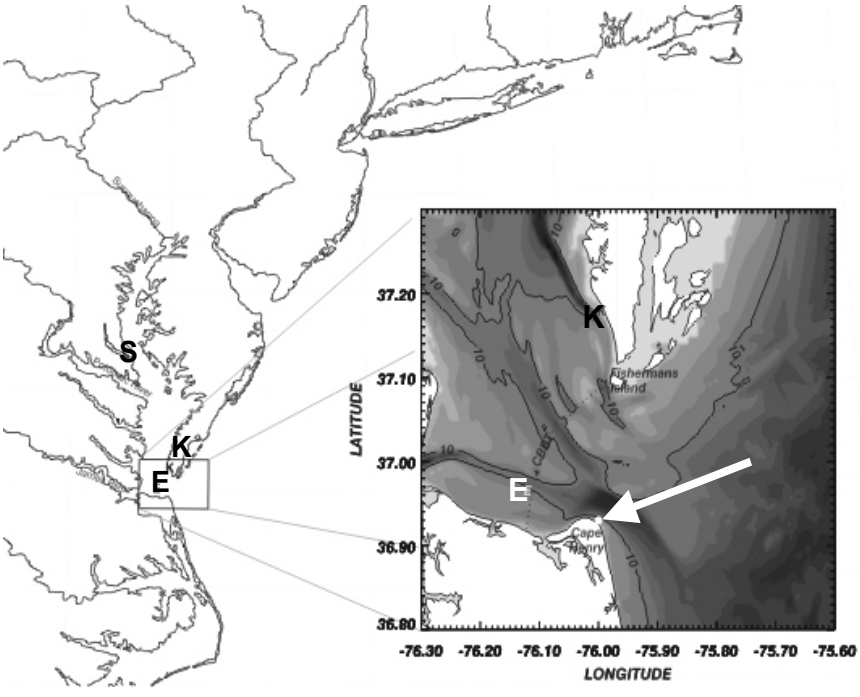

Figure 1. Map of the study area showing the lower Chesapeake Bay in the context of the eastern United States. The mooring location is indicated by the arrow pointing at a small white circle at the entrance to the bay. The dark dotted line indicates the Chesapeake Bay Bridge Tunnel (CBBT). The symbol E denotes the location of the wind station at CBBT.

3. Data Processing

Flow measurements were purged from values for which the "error velocity" exceeded 5 cm/s or the "percent good" fell below 80%. The purged velocity values were rotated 37° counterclockwise to maximize the inflow/outflow direction. Positive values represented flows out of the estuary for the principal-axis component, and toward Fishermans Island for the transverse component. All time series were filtered with a Lanczos low-passed filter of 34-hr half-power. Therefore, this study concentrates on the subtidal variability of flow profiles. The ADCP record was also decomposed into Empirical Orthogonal Functions (EOFs) to explore the different modes of variability and to support the findings on the site dynamics.

4. Results

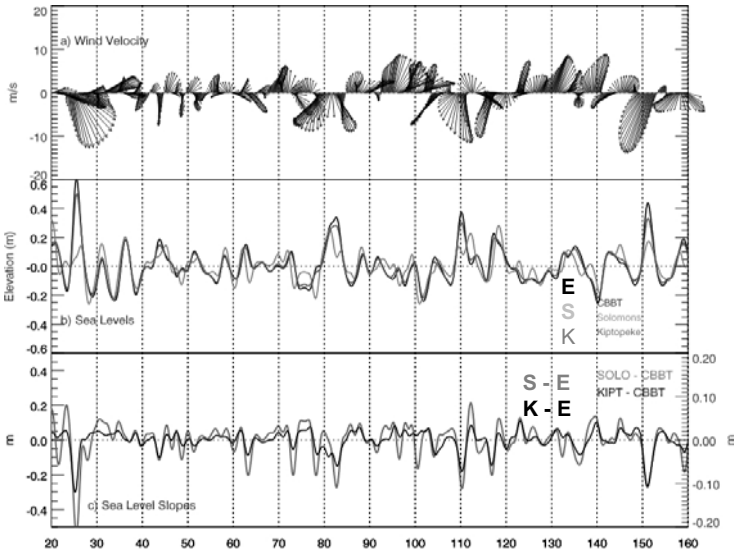

Figure 2. Wind forcing and sea level response during observation period.

Three predominant directions characterized wind forcing: northwesterly, northeasterly and southwesterly (Fig. 2a). The strongest wind pulses had a northerly component and produced increases in non-tidal sea-level (Fig. 2b) and set-up in the lower bay as indicated by negative slopes (Fig. 2c). Also, southwesterly winds caused decreases in non-tidal sea level (Fig. 2b) and sea level set-downs (positive slopes, Fig. 2c). Salinity records (not shown) illustrated weakly stratified conditions that suggested limited influence of baroclinic pressure gradients to the dynamics of the study area.

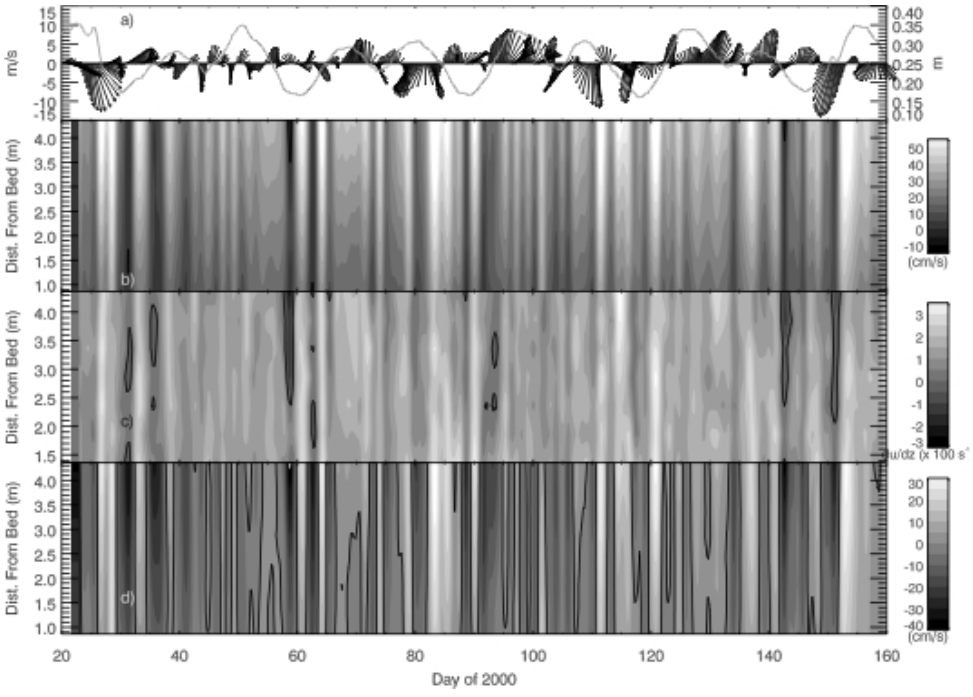

Figure 3. Low-passed variability of a) wind and amplitude of tidal current; b) principal axis of flow (positive is outflow); c) vertical shear of the flow principal axis (H 100 s^{-1}; dark contour delineates regions of negative shears); and d) anomalies from the mean for the subtidal flow.

Non-tidal currents flowed out of the estuary practically during the entire period of observation (Fig. 3b). Most of the subtidal variability of the flow was produced by the wind. Net outflow was strongest when winds were from the northwest and southwest because of the orientation of the estuary. There were only a few instances when the subtidal flow was directed into the estuary associated with northeasterly winds. However, not every northeasterly wind caused net inflow. The vertical shears associated with the non-tidal flows were mostly positive (Fig. 3c). Strongest positive shears developed with southwesterly and northwesterly winds. Negative shears (subsurface outflow stronger than surface outflow) appeared preferentially with northeasterly winds. Anomalies of the non-tidal flow, relative to the overall mean at each depth, were strongly positive with northwesterly winds and strongly negative with northeasterly winds (Fig. 3d). This response indicated that the non-tidal flows at the study site were most sensitive to northerly winds.

A fortnightly modulation of tidal forcing, as depicted in Figure 3a, appeared associated with stronger subtidal flows during spring tides than during neap tides (Fig. 4a). These subtidal flows, again, were in the same direction throughout the water column. The unidirectional flows contrast with the typical density-induced exchange flows that strengthen during neap tides in several estuaries and that have been extensively documented. In the transverse direction, the non-tidal flows were very weak and were independent of tidal forcing (Fig. 4b). Centrifugal accelerations should have been stronger at spring tides and would have produced surface flow away from the cape and bottom flow toward the cape. This was not the case in our observations (Fig. 4b), which indicated that non-linear advection was relatively weak. On the other hand, the enhancement of unidirectional principal-axis outflows during spring tides at our study site (Fig. 4a) is consistent with tidal rectification mechanisms that most likely arise from bottom friction. Therefore, bottom friction should play a role in the dynamics of the subtidal variability, in contrast to advective accelerations and baroclinicity, as explored next.

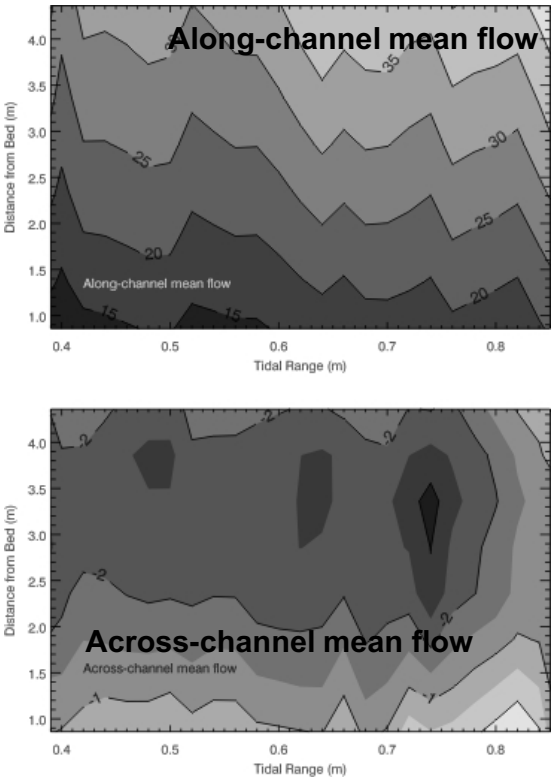

Figure 4. Mean flow as a function of tidal range.

The relationship among wind forcing, sea level slopes and bottom friction that is implied by the observations in Figures 3 and 4 is investigated through the principal-axis component of the subtidal, depth-averaged momentum balance in which advective acelerations are neglected:

$$\frac{\partial \langle u \rangle}{\partial t} - f\langle v \rangle = -g\frac{\partial \eta}{\partial x} + \frac{\tau_{sx} - \tau_{bx}}{\rho H} \qquad (1)$$

where the x axis is positive seaward; <v> and <u> are the transverse and principal axis components of the subtidal flow, respectively; f is the Coriolis parameter ($8.\_10^{-5}$ s^{-1} for 37° N); and g, H, _, _, $\__{sx}$, and $\__{bx}$ are the acceleration due to gravity (9.8 m/s^2), water column depth (6 m), density of the water (1020 kg/m^3), sea surface elevation, surface stress and bottom stress, respectively. The surface stresses are calculated as in Large and Pond (1981) with a rotated wind velocity (37° counterclockwise). Bottom stresses are estimated as $\__{bx} = \_C_b\ u_b\ |u_b|$ using a non-dimensional bottom drag coefficient C_b of 0.0025 and the near-bottom (bin closest to the bottom) flow u_b.

Every term in the momentum balance (1) is calculated and presented in Figure 5. The shaded region of Figure 5 represents the barotropic pressure gradient associated with the sea level slope between middle and lower bay. Negative (onshore) winds cause negative sea level slopes, i.e., water piling up

in the onshore direction. These negative sea level slopes are well explained by the wind stress (negative _sx). In fact, sea level slopes and wind are strongly coherent at every subtidal frequency. The momentum balance improves when bottom stresses are added, most notably for positive slopes. The inclusion of local accelerations produces marginal improvements to the balance. Overall then, the subtidal variability of the flow off Cape Henry is well represented by depth-integrated, frictional dynamics. This is verified by the first EOF that is very strongly coherent with the depth-averaged flow (Fig. 6a). The first mode explains 95% of the subtidal variability and changes little with depth. The second EOF explains 3% of the subtidal variability and is strongly coherent with the vertical difference between surface and bottom flows (Fig. 6b). This second mode changes sign with depth and depicts a weak depth-dependent response to wind-forcing and sea level slopes. In summary, the subtidal variability of the flow over the shallow area off Cape Henry is dominated by wind forcing. Its structure is practically uniform throughout the water column and seems to be indifferent to the presence of the cape.

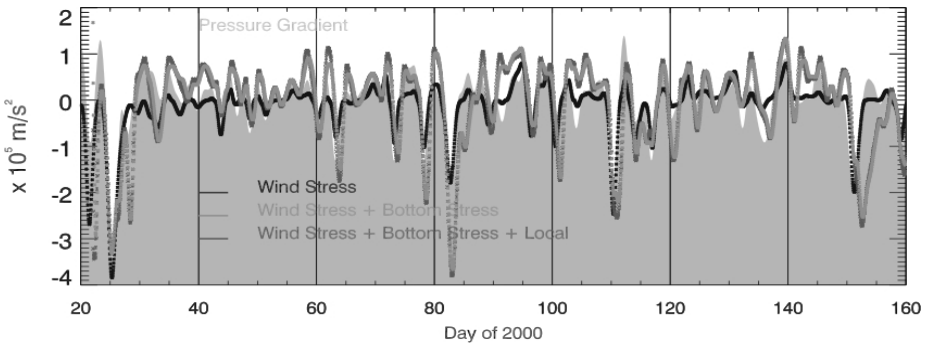

Figure 5. Terms in the momentum balance. The shaded region represents the barotropic pressure gradient, which is nearly balnced by wind stress.

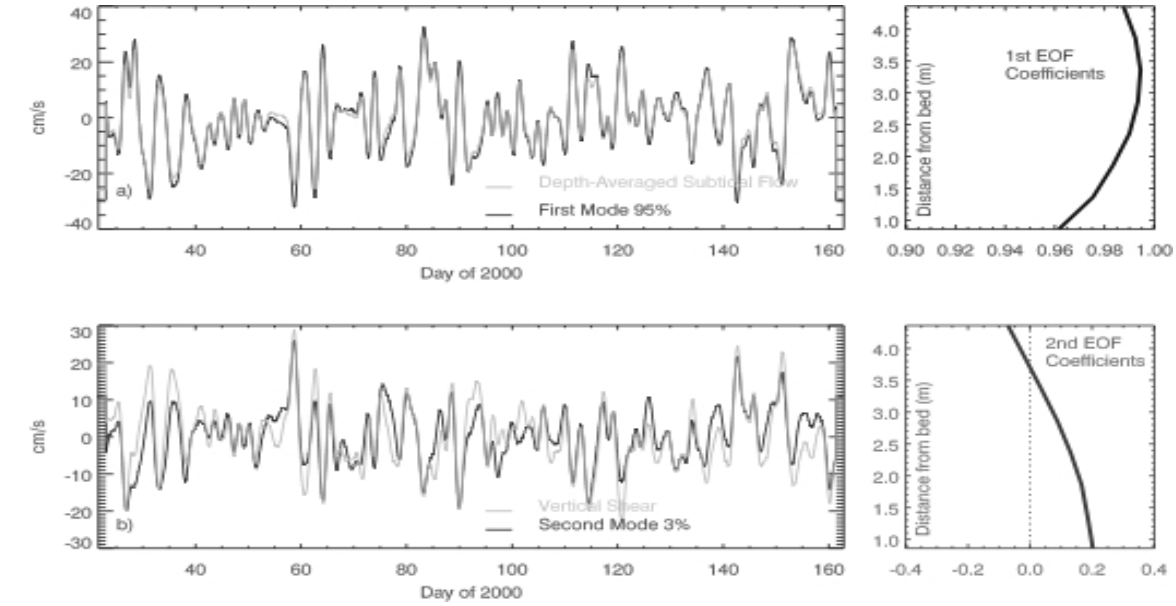

Figure 6. First two EOFs compared to vertically averaged flow and vertical shears, respectively.

References:

Signell, R.P., and Harris, C.K. Modeling sandbank formation around tidal headlands. Estuarine and Coastal Modeling, Proceedings of the 6th International Conference, Edited by Malcolm Spaulding, H. Lee Butler, ASCE Press, pp. 209-222, 2000.

Geyer, W.R., Three-dimensional tidal flow around headlands, J. Geophys. Res., 98(C1), 955-966, 1993.

Mapping the mixing hot spots in a stagnant fjord basin

LARS ARNEBORG

(Department of Oceanography, Göteborg University, Box 460, SE-405 30 Göteborg, Sweden, laar@oce.gu.se)

CAROL JANZEN

(Scool of Ocean Sciences, University of Wales, Bangor, Menai Brige, Anglesey, LL59 5EY, UK, oss805@bangor.ac.uk)

BENGT LILJEBLADH

(Department of Oceanography, Göteborg University, Box 460, SE-405 30 Göteborg, Sweden, beli@oce.gu.se)

TOM P. RIPPETH

(Scool of Ocean Sciences, University of Wales, Bangor, Menai Brige, Anglesey, LL59 5EY, UK, t.p.rippeth@bangor.ac.uk)

JOHN H. SIMPSON

(Scool of Ocean Sciences, University of Wales, Bangor, Menai Brige, Anglesey, LL59 5EY, UK, j.h.simpson@bangor.ac.uk)

1. Introduction

The aims with the present study are to i) map the spatial distribution of vertical diffusion in the deep basin of Gullmar Fjord, and to ii) compare the basin average vertical diffusion obtained from microstructure shear probes with that obtained from moored conductivity/temperature (CT) loggers.

Vertical diffusion of heat and salt in the stagnant waters of deep fjord basins is important for oxygen conditions in the basins. The main effect of the vertical diffusion is that it reduces the density, which enables dense and oxygen rich waters outside the fjord to penetrate to the bottom of the fjord, and replace the old and oxygen depleted waters (e.g. *Aure and Stigebrandt* [1990]). Much is known about the bulk effects of tides on the vertical diffusion in fjord basins (e.g. *Stigebrandt* [2002]), but very little is still known about the processes that lead to the turbulence and diffusion. There are turbulence models, e.g. the k-ε model, that can describe the diffusion in wind-driven surface- and tidal bottom-boundary layers. These fail, however, in deep basins, where the wind-driven shear is absent, and where the tidal velocities are so small that the tidal boundary layer mixing becomes insignificant. Recent experiments in the Brazil basin (*Ledwell et al*. [2000]) show that i) vertical diffusion is much enhanced above rough topography relative to above smooth topography, and that ii) the enhanced diffusion is probably caused by breaking internal waves that are generated by tidal currents flowing over the rough topography. Experiments in lakes (*Goudsmit et al.* [1997]) indicate that the vertical diffusion is mainly related to internal seiches, and is concentrated to thin boundary layers at the sloping bottoms. Experiments in fjords with tracers (*Stigebrandt* [1979]) and microstructure shear probes (*Inall and Rippeth* [2002]) show that the vertical diffusion in the interior of fjord basins is generally not large enough to explain the basin averaged vertical diffusion. No experiments have, however, shown exactly where the dissipation takes place. Is it concentrated to the waters above rough topography, as in the abyssal ocean, or is it restricted to thin bottom boundary layers, as in lakes? These questions motivated an intensive study in Gullmar Fjord, some results of which are presented here.

Gullmar Fjord located on the Swedish west coast (Fig. 1) is a 28 km long, and 1-2 km wide sill fjord, with sill depth about 43 m and maximum depth about 120 m. Gullmar Fjord is characterised by weak tides (<0.2 m amplitude), weak fresh-water runoff (≈25 m^3s^{-1}), short residence times above sill level (1 - 2 weeks), and yearly renewals of the otherwise stagnant basin water below 50–60 m depth. *Arneborg*

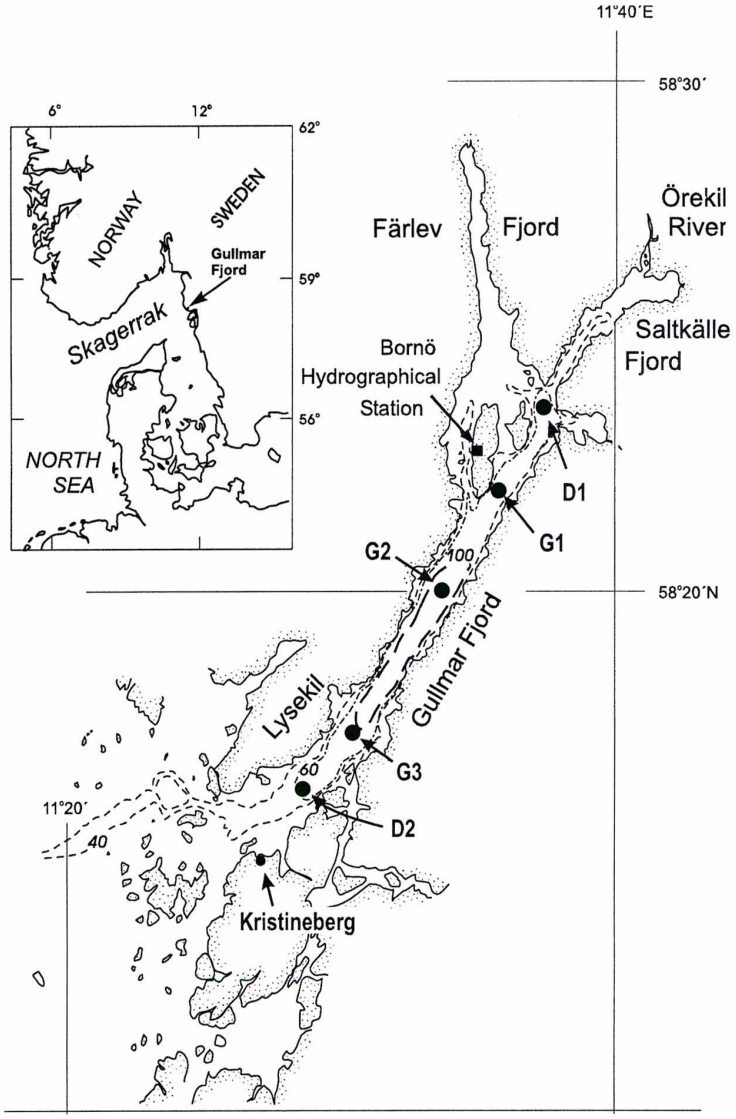

Figure 1: Sketch of Gullmar fjord, showing the location of the 5 stations D1, G1, G2, G3, and D2, where dissipation measurements were performed. Moorings with ADCPs (and CTs) were deployed at stations (G1), G2, and (G3).

and Liljebladh [2001] investigated the basin average vertical diffusion and related it to the dynamics in the fjord based on time series from moored ADCPs and CT loggers. They found that the magnitude and time-variation of the work against buoyancy forces by vertical diffusion in the deep basin can be explained by three equally important energy sources. These are i) internal waves of tidal frequency, generated by interaction of the barotropic tides with the sill, ii) internal waves generated by an external seiche, and iii) the internal seiches in the fjord. They did, however, not perform turbulence measurements in the fjord, and could therefore only speculate about the spatial distribution of the diffusion, and the detailed processes leading from the barotropic tides, the barotropic seiche, and internal seiches down to turbulence and mixing.

2. The Experiment

During three days in the beginning of August 2001, two microstructure profilers onboard two research vessels were used in an intensive effort to map the spatial and temporal variations of vertical mixing in the deep stagnant basin of Gullmar Fjord. One profiler, the MSS profiler (*Prandke et al.* [2000]) was

used to obtain a continuous time series of turbulent kinetic energy dissipation at station G2 (see Fig. 1) near the deepest part of the fjord. The measurements were performed as bursts of 4 profiles. The interval between bursts was 1-2 hours. During the same period the FLY profiler (*Dewey et al.* [1987]) was used to obtain 6 sections through the fjord, with stations at D1, G1, G2, G3, and D2, see Fig. 1. Bursts of 6 profiles were performed at each station visit. The profiles were taken while steaming with approximately 1 knot, and one burst took approximately 20 min, which means that one burst was distributed over the distance of 0.5 to 1 km. During one month, including the 3-day period, moorings with ADCPs and CT loggers were deployed at station G1, G2, and G3. In addition one ADCP mooring was deployed in the main entrance and one CT mooring was deployed outside the fjord.

3. Results

The intensive 3-day period was characterised by very variable wind conditions, which forced seiching motions in the deep basin with period close to 1 day. The superposition of the internal seiche and internal semi-diurnal tides caused vertical oscillations at station G3 with amplitudes larger than 10 m, and horizontal current speeds with amplitudes of about 0.1 ms^{-1} in the deep waters. Based on the density decrease rates obtained from the mooring data the horizontally averaged vertical diffusion coefficient is found to be in the order of 10^{-4} m^2s^{-1} in the deepest parts of the fjord, decreasing to 10^{-5} at 50 m depth. Assuming a constant flux Richardson number, one can determine the dissipation, corresponding to these diffusion coefficients. With a flux Richardson number in the range 0.1-0.2, one gets horizontal average dissipation rates in the order $1\text{-}2\cdot10^{-8}$ W/kg below 60 m depth. Figure 2 shows

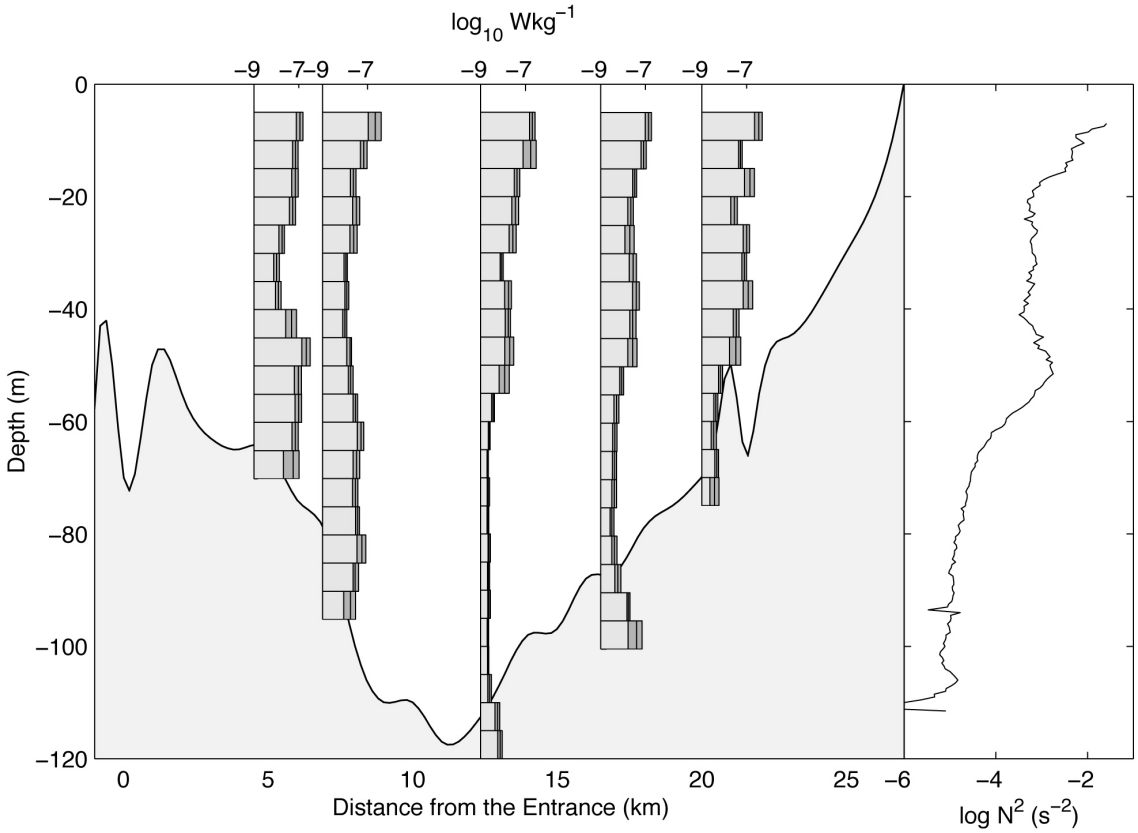

Figure 2: Left panel: Bin averages of dissipation rates in 5 m bins, based on all FLY microstructure profiles at each station. The darkest shaded boxes show the 95% confidence intervals for the average values, estimated with a bootstrapping method. Also shown is the depth of the fjord as function of distance from the entrance. Right panel: Buoyancy frequency squared based on an average of all density profiles obtained with the MSS probe at station G2.

the distribution of dissipation in the fjord, as obtained from averages of all FLY profiles at each station. At the inner stations the dissipation levels below 60 m range from $2 \cdot 10^{-9}$ Wkg^{-1} at station G1 to $4 \cdot 10^{-9}$ Wkg^{-1} at station D1, with some enhancement closest to the bottom caused by boundary layer turbulence. This shows that the dissipation levels in the inner parts of the fjord are up to a factor of 10 too small to explain the basin average vertical diffusion. At the outer stations, G3 and D2, however, the dissipation levels below 60 m increase to $3\text{-}5 \cdot 10^{-8}$ Wkg^{-1} at station G3, and 10^{-7} Wkg^{-1} at D2. A weighted average of the dissipation levels gives a horizontally averaged dissipation in the order of $1\text{-}2 \cdot 10^{-8}$ Wkg^{-1}, i.e. enough to explain the horizontally averaged vertical diffusion obtained from the mooring data. About 90 % of the vertical diffusion through the 60 m level takes place in the1/3 of the basin area closest to the sill. The enhanced dissipation rates at station G3 are not limited to a boundary layer closest to the bottom, but are distributed relatively uniformly over the water column below 50 m. What then causes the enhanced dissipation levels close to the sill? The ADCP at station G3 shows clearly enhanced shear below 60 m relative to the stations G2 and G1. The shears at G3 that are calculated from 4-hour averaged velocities, low-pass filtered in the vertical direction, passing vertical wave lengths larger than 10 m, are not large enough to cause Richardson numbers below 1. It is, however, clear that a superposition of the high-frequency and high-wavenumber internal wave field upon the filtered field, will result in a higher probability for critical Richardson numbers and turbulence at G3 than at the inner stations with less background shear.

Acknowledgments: The present work was supported by EU through the OAERRE project EVK3-CT99-00002.

References:

Arneborg, L, and B. Liljebladh. The internal seiches in Gullmar Fjord. Part II: Contribution to basin water mixing. *J. Phys. Oceanogr*., 31, 2567 - 2574. 2001

Aure, J. and A. Stigebrandt. Quantitative estimates of eutrophication effects on fjords of fish farming. *Aquaculture*, *90*, 135-156. 1990.

Dewey, R.K., W.E. Crawford, A.E. Gargett, and N.S. Oakey. A microstructure instrument for profiling oceanic turbulence in coastal bottom boundary layers. *J. Atmosph. Ocean. Tech*., 4, 288-297. 1987.

Goudsmit, G.H., F. Peeters, M. Gloor, and A. Wüest. Boundary versus internal diapycnal mixing in stratified waters. *J. Geophys. Res. 102,* 27903-27914.

Inall, M.E., and T.P. Rippeth. Dissipation of tidal energy and associated mixing in a wide fjord. Submitted to *J. Env. Fluid Mech*. 2002.

Ledwell, J.R., E.T. Montgomery, K.L. Polzin, L.C. St. Laurent, R.W. Schmitt & J.M. Toole. Evidence for enhanced mixing over rough topography in the abyssal ocean. *Nature, 403*, 179-182. 2000.

Prandke, H., K. Holtsch, and A. Stips, MITEC technology development: The microstructure/turbulence measuring system MSS, *Tech. Rep. EUR 19733 EN*, European Commission, Joint Research Centre, Ispra, Italy, 2000.

Stigebrandt, A. Observational evidence for vertical diffusion driven by internal waves of tidal origin in the Oslofjord. *J. Phys. Oceanogr. 9*, 435-441.

Stigebrandt, A. Vertical mixing and circulation in fjord basins. Submitted *to Surveys in Geophysics*. 2002.

Three-dimensional flow structure in the vicinity of headlands

ALEXIS BERTHOT

(PhD student, Centre for Water Research, University of Western Australia,35 Stirling Highway Crawley WA 6009, berthot@cwr.uwa.edu.au)

CHARITHA PATTIARATCHI

(Centre for Water Research , University of Western Australia,35 Stirling Highway Crawley WA 6009, pattiara@cwr.uwa.edu.au)

1. Introduction

The interaction between currents and surface and sub-surface topographic features such as reef systems, islands and headlands generate complex three-dimensional circulation patterns which significantly influence the distribution of pollutants, sediments and biological material in vicinity of the topographic feature. In addition to being an interesting geophysical phenomenon, the formation of sandbanks; generation of scour holes; enhanced biological productivity; distribution of coral larvae have all being attributed to wake effects around islands and reefs systems. Over the past decade, the formation and structure of these flows in two dimensions have been investigated using theoretical, field, numerical and remote sensing techniques. In contrast, the three-dimensional effects of island wakes have received very little attention.

The residual circulation pattern in a topographically generated eddy has been approximated to that in a tea cup with downwelling in the eddy core and upwelling near the centre. This results in the convergence of flow towards the centre of the eddy near the seabed and divergence at the surface with downwelling at the eddy. Secondary circulation patterns are also formed through the curvature of the flow past the structure similar to that observed in the vicinity of river bends. Although limited field measurements and numerical models have provided some evidence for such secondary circulation, no detailed field and numerical studies have been undertaken to document the three-dimensional structure of headland wakes.

2. Numerical Model

The three-dimensional primitive equation model, HAMburg Shelf Ocean Model (HAMSOM), which is based upon a semi-implicit numerical scheme, is used in this study. The model is described by Backhaus (1985) and Stronach et al. (1993). The model provide the three-dimensional velocity field and is forced at the model boundaries using the M2 tidal component. An idealised gaussian shape headland (6 km long) is used to investigate the importance of different processes: vertical structure (i.e. presence of secondary flow), effects of Earth's' rotation…

3. Results: Idealised gaussian headland

During the mid-flood or mid-ebb stages of the tide, when the currents are strongest (max transport rates) no eddy is formed (Figure 1). It is apparent that an eddy is observed only when the tidal currents reverse from the flood to ebb stage of the tide or vice-versa similar to those observed elsewhere (Pattiaratchi et al., 1986). During this slack water period, the tidal currents are generally weak (Figure 2). Over a tidal cycle, the residual flow forms two eddies a clockwise eddy on the east side and an anticlockwise eddy on the west side (figure 3).

Secondary Circulation

The secondary circulation and the vertical currents for a tidal flow past of the gaussian headland are shown on Figures 1&2. In this case the bathymetry is represented by a flat bottom in order to observe the effect due only to the headland.The secondary flow is calculated by determining the transverse component of the current in each layer compared to the depth average current (by definition the depth averaged transverse velocity is zero; Chant and Wilson 1997, Kalkwijk and Booij 1986).

These results are for a headland in the Northern Hemisphere (Coriolis positive).Two profiles normal to the main flow are considered: one on the West side of the headland and the other on the East side.The vertical velocities are mainly the result of the tidal wave travelling through the domain, but important variations due to the headland are still visible.

At maximum currents Flood, we observe downwelling and recirculation on the west profile (the east shows a weaker vertical circulation, Figure 1). At slack water, as the East profile is intersecting the center of the transient eddie, we can observe that the secondary flows are diverging at the surface and slightly converging at the bottom (figure 2). The results for the maximum current and slack water during the ebb are not shown here but we would observe the same type of secondary circulation

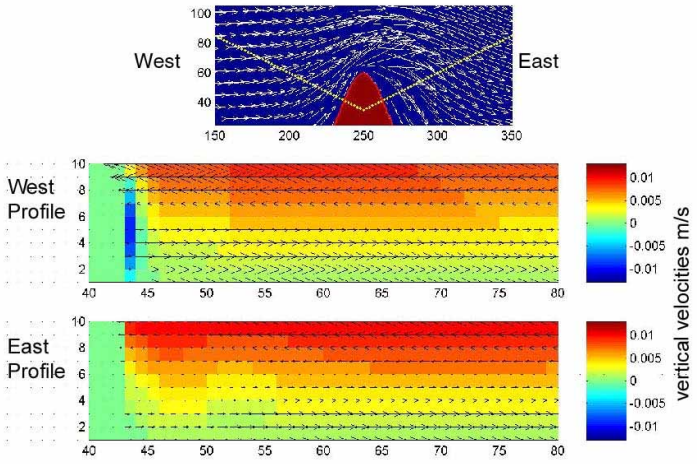

Figure 1: Flow past the gaussian headland under maximum currents (Flood) West and East profiles show the secondary currents (represented with black arrows)

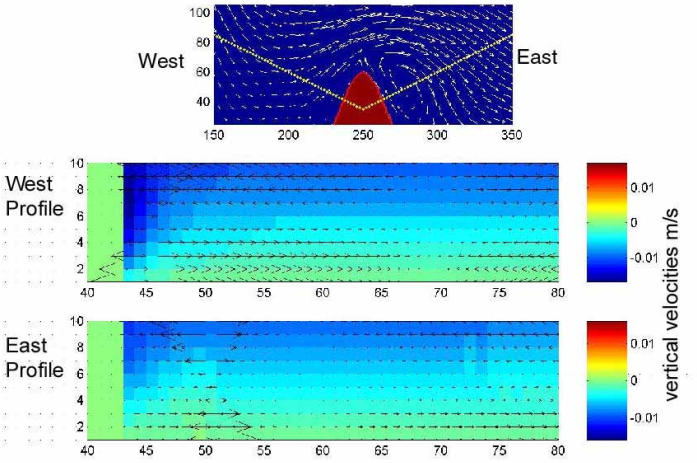

Figure 2:Flow past the gaussian headland at slack water (Flood). West and East profiles show the secondary currents (represented with black arrows)

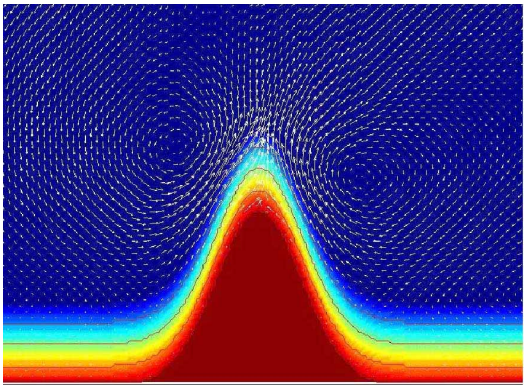

Figure 3. Residual currents in the vicinity of the gaussian headland.(Figure showing two eddies on either side of the headland) .

Effect of the Earth's rotation

Considering the residual currents over one tidal cycle, we observe the formation of two eddies (Figure 3): one clockwise on the east side and one anticlockwise on the east side. To investigate the role of the Coriolis force we run the hydrodynamic model for a headland situated in the Northern Hemisphere (Coriolis positive) and for a headland situated in the Southern Hemisphere (Coriolis negative).

The residual secondary flows in the bottom layer are converging toward the center of the eddy on both clockwise and anticlockwise eddies (Figures 4 & 5). Nevertheless by observing the strengh of the secondary flow, it appears that the secondary currents are stronger on the anticlockwise eddy for the Northern hemisphere and in the clockwise eddy for the Southern Hemisphere.

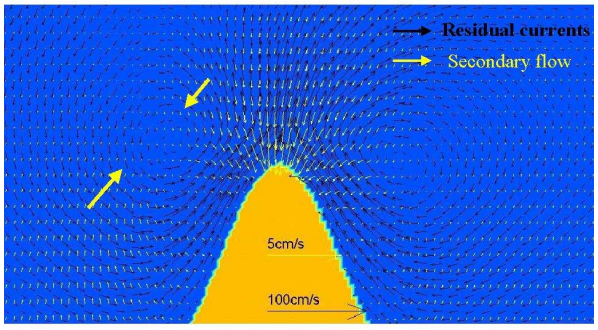

Figure 4. NORTHERN HEMISPHERE Residual bottom currents in the vicinity of the gaussian headland.[residual currents are represented with black arrows and the secondary circulation with yellow arrows]

Figure showing the convergence of the secondary circulation toward the tip of the headland and toward the center of the eddies. The secondary currents are stronger on the west eddy.

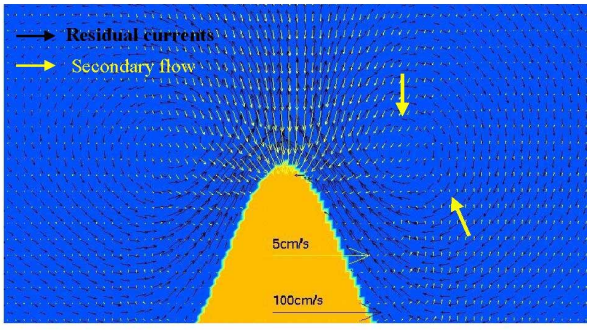

Figure 5. SOUTHERN HEMISPHERE Residual bottom currents in the vicinity of the gaussian headland.[residual currents are represented with black arrows and the secondary circulation with yellow arrows]

Figure showing the convergence of the secondary circulation toward the tip of the headland and toward the center of the eddies. The secondary currents are stronger on the east eddy.

4. Discussion

Results of the present model enable us to gain further understanding and detailed structure of the 3 dimensional hydrodynamic flow around headland.The secondary flows calculations (for the instantaneous currents and for the residual over a tidal cycle) also enabled us to identify the validity of the different theories proposed for the formation of the headland associated linear sandbanks (Pingree 1978, Heathershaw and Hammond 1980). Those results will be later compared with the results of numerical study and field measurement (using an ADCP and moored instruments) at Cape Levillain,a headland with an attached sandbar.

Acknowledgements: US Office of Naval Research

References:

Backhaus J. O. 1985. A three dimensional model for the simulation of shelf sea dynamics. Deutsche Hydrographische Zeitschrift, 38: 165-187.

Chant, R. J. and R. E. Wilson. 1997 Secondary circulation in a highly stratified estuary. Journal of Geophysical Research, vol 102, No. C10, p 23,207-23,215

Heathershaw A.D. and Hammond F.D.C. 1980. Secondary circulation near sand banks in coastal embayments. Dt Hydrogr. Z., 33, 135-151.

Kalkwijk, J. P. T. and R. Booij 1986. Adaptation of secondary flow in nearly horizontal flow. Journal of Hydraulic Research 24., (1): 19-37.

Pattiaratchi C. B., Hammond T. M. and Collins M. B. 1986. Mapping of tidal currents in the vicinity of an offshore sandbank from remotely-sensed data. Int. J. of Remote Sensing, 7: 1015-1029.

Pingree R. D. 1978. The formation of the Shambles and other banks by tidal stirring of the seas. Journal of the Marine Biological Association, UK, 58, 211-226.

Stronach J. A., Backhaus J. O. and Murty T. S. 1993. An Update on the Numerical Simulation of Oceanographic Processes in the Waters between Vancouver Island and the Mainland: The GF8 Model. Ocean. Mar. Biol. Annual Review, 31: 1-86.

Inner shelf dynamics in coastal Virginia

Hector H. Sepulveda and Arnoldo Valle–Levinson, (*Center for Coastal Physical Oceanography, OEAS Department, Old Dominion University, Norfolk, Virginia, USA* andres@ccpo.odu.edu, arnoldo@ccpo.odu.edu)

1 Introduction

The area that connects the Delaware Bay, U.S.A., at the north and the Chesapeake Bay at the south it is called the Delmarva Peninsula. The tidal characteristics of this area have not been properly described yet (*Lentz et al*, [2001]). Both bays are estuarine system that have an important forcing on the inner continental shelf of the Mid-Atlantic Bight. The southern inner shelf off the Delmarva Peninsula, the Virginia part of this peninsula, and the Chesapeake Bay entrance are the motive of this study.

In general, the dynamical balance in a shallow shelf is usually dominated by barotropic tides. Wind stress, horizontal density gradient and bottom friction are more important players of the residual circulation. Nonlinear dynamics play a role in the mixing of buoyant currents.

The currents from the Delmarva Peninsula act as an ambient flow that interacts with the dynamics at the mouth the Chesapeake Bay, enhancing the southward flow (*Valle-Levinson and Lwiza* [1998])

The main objective of this presentation is to describe the dynamics and spatial structure of the flow off the southern Delmarva Peninsula and its interaction with the Chesapeake Bay mouth.

2 Observations

The inner shelf of coastal Virginia was studied during five different cruises done between the Chesapeake Bay mouth and the Maryland-Virginia border (Figure 1) during May 8-12, 2000 (Del1), September 17-18, 2000 (CH1900), November 9-11, 2000 (CH2400),February 20-23, 2001 (Del3) and February 15, 2002 (Del5). These cruises included surveys of the area (Del1, CH190, Del3) and 12 or 25 hour repetitions of particular tracks (Del1, CH2400, Del5). Hydrographic measurements included conductivity, temperature and depth (CTD Sea Bird Instruments) casts, surface temperature and conductivity (CT) measurements and a tow of an undulating CTD (SeaSciences Acrobat, during CH1900 only). Velocity measurements were done with RD Instruments Acoustic Doppler Current Profilers (ADCP).

3 Data Processing

The ADCP data was averaged into five minute ensembles and 1 m vertical bins. Ship speed was 5 kn during most of the cruises to ensure and adequate spatial resolution. The ship velocity was removed using the bottom track from the ADCP. The quality control criteria for these measurement included error velocities less than 10 cm/s, "percentage

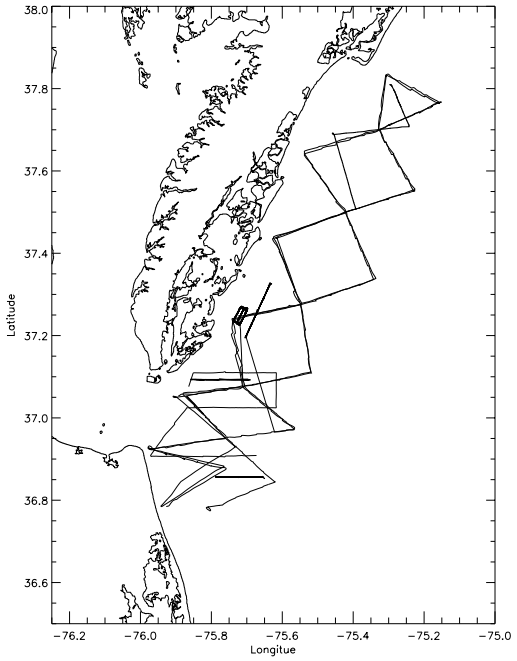

Figure 1: Map of the study area with all the tracks overlaped

good" greater than 85% and ship velocity greater that 2 kn to remove the data collected while on a CTD station. CT and CTD data were filtered for spikes.

The velocity signal vertically averaged and later separated into a tidal and a subtidal field using two different methods. For those records that where a repeated survey of an area (Del1, CH2400, Del5), a least-squares fit to a sinusoidal function described in *Lwiza et al* [1991] was used. The one-time surveys (Del1, CH1900, Del3) were studied using as a base the method described by *Candela et al* [1992] with both a Biharmonic and a Gaussian function. There was no significant difference in the calculated RMS error with the use of Biharmonic or a Gaussian function. During our first explorations, the final RMS error was not strongly dependent on the number and location of nodes as elsewhere (e.g. *Valle-Levinson and Lwiza*, [1998]).

4 Results

During Del1, CH1900 and Del5 cruises five transects were done back and forth at the study area (Figure 2). The U (E-W) and V (N-S) components of the vertically averaged components (dotted line) are compared in Figure 2 with the reconstructed field after fitting the velocities to a semidiurnal (12.42) signal using the Candela et al [1992]. The average RMS error was approximately 10 cm/s for Del3 and CH1900 (U and V components), and 15 cm/s for both U and V during Del1. This fit improves by half for Del1 and Del3 if only

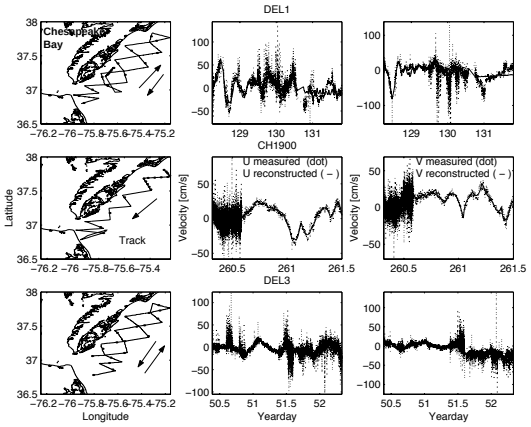

Figure 2: Vertically averaged velocities (dotted line) and the reconstructed velocities from the Candela et al method (solid line). The arrows indicate the direction the survey was conducted. The dots on the track indicate the location of the nodes used in the detiding.

one of the directions is selected. For the lower half of the CH1900 track the fit improves even more, to 3.0 cm/s of RMS error in both components. We speculate that for Del1 and Del3 these differences are due to changes in the experimental conditions, as the tow body that carries the ADCP is protected or not by the ship from heavy wind and wave conditions. The existence of an aliasing in the measured signal has to be considered as the survey were conducted either against or with the direction of propagation of tidal phase (North to South). During Del1, a 15 km along shore transect was repeated during 25 hours. The method described in *Lwiza et al,* [1991], was used to fit a diurnal and a semidiurnal signal to these velocity records. The transect was located in front of one of the several inlets present along the coast of the Delmarva Peninsula. The mean residual velocity values obtained were 10 cm/s for the E-W component and 17 cm/s for the N-S component. There was no evidence of a two layer circulation during this period. The flow was directed in the S, S-W direction, entering the inlet. The semidiurnal component explained 80% of the variance in both E-W and N-S directions. The mean amplitude of the semidiurnal current was 15 cm/s for U and V, with an RMS error of 7 cm/s. The amplitudes of the diurnal tidal signal had mean values of 9 cm/s and 15 cm/s for the U and V components, respectively. These observations are particularly relevant as they suggest the inlets along the Delmarva coast play a role in the transport of nutrients or larvae. Two other transects, located north and south of the Chesapeake Bay mouth, were repeated for 13 hours during the CH2400 cruise. The north and the south transect had mean U and V residual velocities of the order of 4 cm/s. Mean semidiurnal amplitudes were 25 cm/s for the E-W component and 5 cm/s for the N-S component. The semidiurnal signal represented a 95% of the variance in the E-W direction, but only a 40% in the N-S. For the south transect, the mean semidiurnal amplitudes were 13 cm/s and 5 cm/s for the E-W and N-S components, respectively. The variance represented by the semidiurnal

signal had a median of 77% in the E-W component and 40% in the N-S component.

An undulating CTD was towed from north to south for 24 hours during the CH1900 survey. This provided with a high resolution dataset of the hydrographic conditions. The analysis from this hydrographic data shows a weak stratification in the area, this conditions were also observed at the CTD profiles from the other cruises. This suggest a weak baroclinic forcing.

The sampling surveys were designed with the idea of separating the tidal and subtidal field using the techniques described by Candela et al [1992]. However, the RMS errors obtained show a poor adjustment to the field velocity and difficult a significant interpretation of the subtidal field. Other traditional approaches consist in using a numerical model to describe the tidal field in this area. This new step adds the complication of choosing initial and boundary conditions for this area. A limited area model based of the linear shallow-water equations will be implemented using the techniques described in Dowd and Thompson (1996) in order to further analyze the dynamical balance in the area. Tidal forcing as boundary conditions will be obtained as a result of the data assimilation. The three dimensional structure of the field will be also studied with a three dimensional with the extension of the Candela method described my Münchow (2000).

References:

Candela, J., and R.C. Beardsley, and R. Limeburner, Separation of tidal and subtidal currents in ship-mounted acoustic Doppler current profiler observations, *Journal of Geophysical Research, 97(C1)*, 769-788, 1992.

Dowd, M., and K.R. Thompson, Extraction of tidal streams from a ship-borne acoustic Doppler current profiles using a statistical-dynamic model, *Journal of Geophysical Research, 101(C4)*, 8943-8956, 1996.

Lentz, S., and M. Carr, and T.H.C. Herbers, Barotropic tides on the North Carolina Shelf, *Journal of Physical Oceanography, 31*, 1842-1859, 2001.

Lwiza, K.M.M., and D.G. Bowers and J.H. Simpson, Residual and tidal flow at a tidal mixing front in the North Sea, *Continental Shelf Research*, 11(11), 1379-1395, 1991.

Mnchow, A., Detiding three-dimensional velocity survey data in coastal waters. *J. ATMOS. OCEAN. TECH., 17*, 736-748, 2000.

Valle-Levinson, A., and K.M.M. Lwiza, On the influence of downwelling winds of the Chesapeake Bay outflow, in *Physics of Estuaries and Coastal Seas*, Dronkers and Sheffers (eds.), Balkema, Rotterdam, 247-256, 1998.

Large scour holes induced by coastal currents

MAJID JANDAGHII ALAEE

(Ports and Shipping Organization,751 Enghelab Ave. Tehran 15994, IRAN. jandaghi@ir-pso.com)

CHARITHA PATTIARATCHI

(Centre for Water Research, University of Western Australia, Nedlands 6009, Australia. pattiara@cwr.uwa.edu.au)

ALI DASTGHEIB

(Ports and Shipping Organization,751 Enghelab Ave. Tehran 15994, IRAN. a_dastgheib@ir-pso.com)

1. Introduction

Investigations on generation of scour holes around breakwaters, causing minor or sever damages to these expensive marine structures, such as the review by *Oumerac*i (1994 a and b) have shown that more basic knowledge on scouring around breakwaters is required. In a 2-dimensional case, scour in front of an upright breakwater is mainly due to the action of standing waves which causes a steady streaming pattern in a vertical plane resulting in a alternating scour and deposition patterns in front of breakwaters.

In a three-dimensional case, laboratory tests by *Sumer and Fredsoe* (1997) proposed that the major mechanism behind the scour around the heads of rubble mound breakwaters is the formation of lee-wakes vortices in each half period of waves. According to this mechanism, sediment swept into these vortices is carried out by these flow structures and eventually deposited away from the head of breakwater. Therefore a net scour over a period of waves results in a scour hole in front of a breakwater and adjacent to it.

In addition to the aforementioned mechanism, *Fredsoe and Sumer* (1997) suggested that the plunging breakers occurring at the breakwater head may cause scouring. The resulting scour hole is located at the lee side of the break water head with a size in a similar order of size of the jet induced by plunging.

Bathymetric surveys around breakwaters of Rajaee Port, Bandar Abbas-Iran, reveal that a large hole is present in the vicinity of the breakwaters heads. The surveys show that the diameter of the hole is of several hundred meters and its depth varies up to –20 m, while the natural depth in the neighbouring areas is about –12 m. The size and location of the hole changes slightly due to the changes in the dominant hydrodynamic conditions in the region.

Figure 1: Khuran (Clarence) Strait and the location of Rajaee Port

Rajaee Port, the second biggest port in Iran, is located in the Khuran (Clarence) Strait possessing berths of 5000 m long and two arms of breakwaters of about 5100m. The port is well protected against the waves with Hs=0.8m while a tidal range of 4.2 m causes a strong tidal current of 1.2 m/s around the breakwaters. Previous studies by the authors reveal that a noticeable secondary circulation induced by the tidal flow curvature is generated in the vicinity of the breakwaters heads (*Alaee and Dastgheib* 2001; *Alaee and Pattiaratchi*, 1999). The influence of this secondary circulation on the main flow results in a flow pattern which is capable to generate a scouring mechanism.

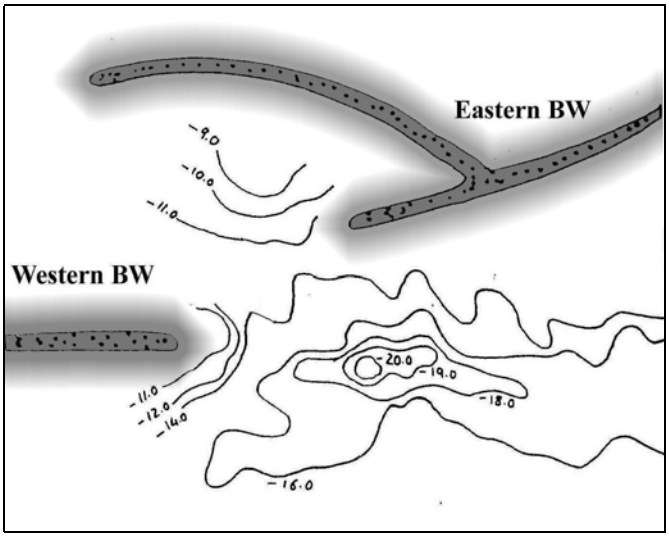

Figure 2: Location of the scour hole between the breakwater heads

In present study, the flow pattern in the Clarence Strait and particularly, in the vicinity of Rajaee Port has been successfully simulated. A set of runs using a 3-D numerical model (HAMSOM) confirms the presence of a strong secondary circulation induced by the flow curvature. These results are in very good agreement with the results of predicting method suggested by *Alaee et al* (1998). Moreover, according to the most interesting part of results, the model predicts the location and size of the scour hole which are in very good agreement with the field surveys. On this basis, it is recommended that the interaction between strong coastal currents and large obstacles, such as breakwaters must be considered as a likely cause of scouring.

2. Numerical simulations

In order to investigate the mechanisms responsible for the generation of the scour hole in front of Rajaee breakwaters, a three-dimensional numerical model (HAMSOM) was employed.

Figure 3: Numerical model domains

Due to the relatively high tides in the strait (maximum tidal range of 4.2m) the numerical model was set up for simulating the velocity structure induced by the tidal flow. For this purpose two model domains were selected, as shown in Figure 3.

The numerical results reveals the presence of relatively powerful secondary circulation in front of Rajaee port breakwaters. This secondary circulation which is mainly due to the curvature of the streamlines is shown in Figure 4: velocity vectors on the surface and the contours of main flow velocity for a typical hour.

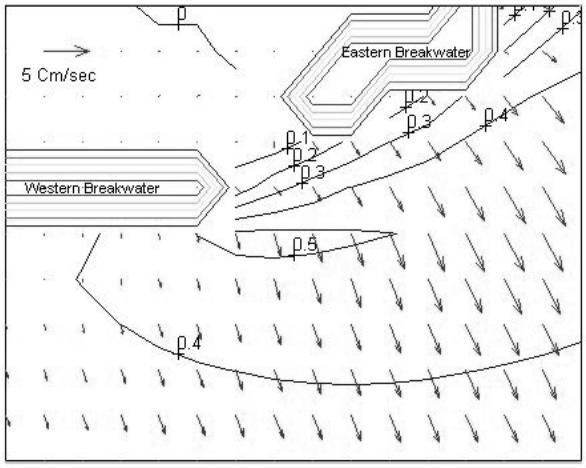

Figure 4: Secondary circulation induced by the tidal flow curvature around Rajaee Breakwaters

The results show that the maximum predicted secondary circulation is about 0.16 m/sec while the maximum main flow is about 1.0 m/sec. These results indicate that the strength of the secondary circulation is about 15% of the main flow which is in good agreement with the *Alaee*'s formula for estimate of the strength of secondary circulation induced by the flow curvatures (*Alaee et al.* 1998). For prediction of the position of scour hole near Rajaee Port a critical mean velocity was chosen due to median size of bed grains (d_{50}). Using time averaged mean velocity, contours of main flow and the location of maximum secondary circulation the position of scour hole can be estimated as Figure 5.

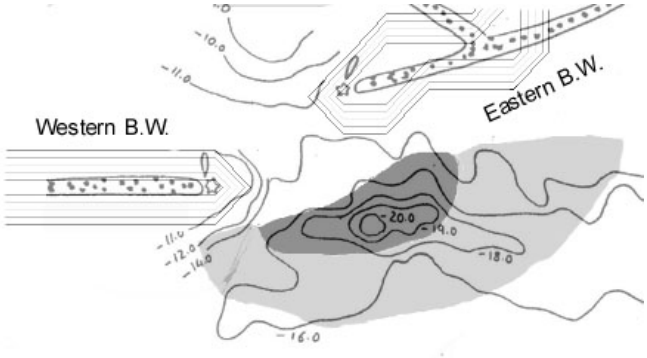

Figure 5: Observed and numerically predicted scour hole in Rajaee Port

3. Conclusions

Recent studies by the authors indicate that curving coastal currents result in a flow curvature-induced secondary circulation. The combination of the main and secondary flow may result in scouring. In the case of Rajaee Port, this study reveals that the existing scour hole in front of the rubble mound

breakwaters is most likely a product of the new flow structure due the generation of secondary circulation.

References:

Alaee, M.J. and C. Pattiaratchi (1999). A case study of scouring due to the 3-D structure of flow around breakwaters. *Proc. of the fifth international conference on coastal and port engineering in developing countries*,Vol 1,pp266-276.

Alaee, M.J., C. Pattiaratchi, and G.Ivey (1998) Dynamincs of Isalnd Wakes, PhD *Thesis,Centre for Water Research, University of Western Australia*.

Fredsoe, J. and B. M. Sumer (1997). Scour at the round head of a rubble-mound breakwater. *Coastal Engineering*, 29: 231—262.

Oumeraci, H. (1994a). Review and analysis of vertical breakwater failures — lessons learned. *Coastal Engineering, Special Issue on Vertical Breakwaters*, 22: 3—29.

Oumeraci, H. (1994b). Scour in front of vertical breakwaters — Review of problems. *Proc. Int. Workshop on Wave Bamers in Deep Water*, Port and Harbour Research Institute, Yokosuka, Japan, Jan. 10—14 1994: 281—307.

Sumer, B. M. and J. Fredsoe (1997b). Scour at the head of a vertical-wall breakwater. *Coastal Engineering*. Vol. 29, 201—230.

Seasonal changes in the vertical structure of a Scottish sea loch

FINLO COTTIER, MARK INALL, COLIN GRIFFITHS

(Scottish Association for Marine Science, Dunstaffnage Marine Laboratory, Oban, Argyll, PA34 4AD, Scotland, fcott@dml.ac.uk)

1. Introduction

Fjordic and estuarine sites typically undergo seasonal changes in the vertical structure of the water column. In essence, these changes influence the stability of the water column through the variation in horizontal fluxes, thermal exchange at the surface and the efficacy of mixing processes. At the surface, buoyancy is added in the form of freshwater run-off and solar heating on scales ranging from diurnal to seasonal. In contrast, the properties of the deep water vary slowly by diffusional processes that may be modified by enhanced vertical mixing. In some instances a rapid change in the deep water may occur under suitable conditions causing dense water inflow or complete convective overturn.

The basic system describing the changes in water column stability in a fjordic environment is well documented. In this study we look specifically at aspects of enhanced vertical mixing and the seasonal variation in the strength of an internal wave field. Again, internal waves in fjordic systems are well described (Stigebrant and Aure, 1989) so we have revisited this phenomenon by analysing salinity, temperature and current data from a near-continuous 13-month mooring deployment.

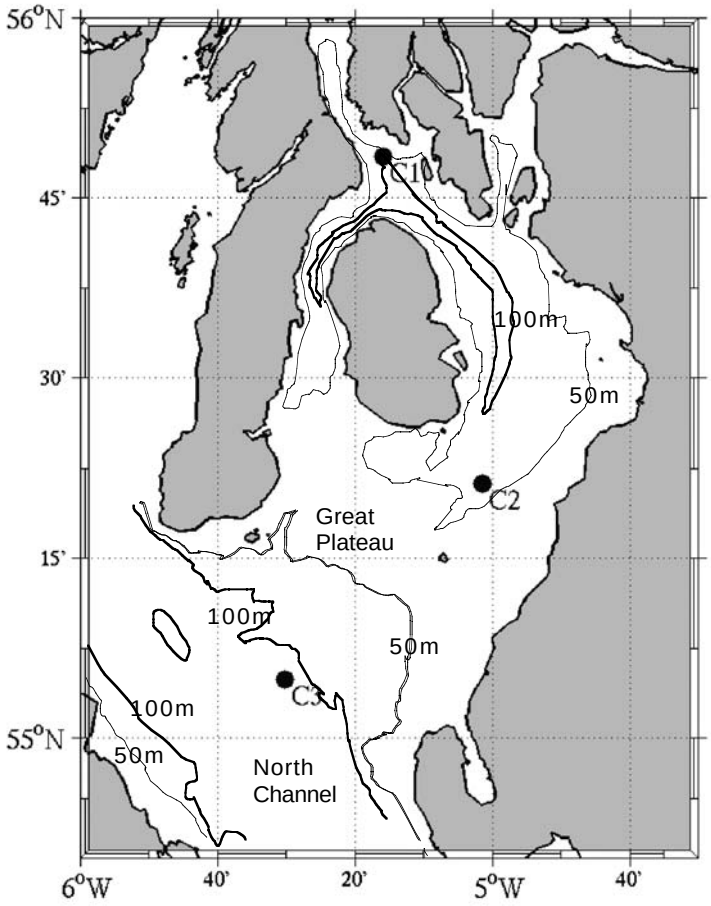

Figure 1: Location map showing the position of the 15-month ADCP deployment, C1, and the stations occupied by Inall and Rippeth (2002), C2 and C3.

2. Location and Data Collection

Our area of study is the topographically complex Clyde Sea on the Scottish west coast. The main basin reaches depths of around 200 m and is separated from the strongly tidal and well-mixed North Channel by a broad, shallow sill having a maximum water depth of 40 m. The main basin links to Inchmarnock Water, which in turn is fed by Lower Loch Fyne. Further, there is an extensive system of estuaries connected to the Clyde Sea basin accounting for a substantial annual discharge of freshwater (Edwards et al, 1986).

There is semi-diurnal advection of the dense North Channel water across the sill though its entrainment into the deep waters of the Clyde Sea is periodic. The combination of a strong density gradient in the basin and strong barotropic tidal forcing presents suitable conditions for the generation of internal waves at the sill that propagate in the basin.

It has been hypothesised, and to some extent demonstrated, that these internal waves are present and contribute to the enhancement of vertical mixing in an otherwise stable environment (Inall and Rippeth, 2002). However, it is clear that the presence and magnitude of this baroclinic signal is closely linked to the presence and magnitude of the density gradient. Our hypothesis is that contribution to vertical mixing by an internal wave varies seasonally because of the seasonal changes in stratification. Our source of primary data from which to test this hypothesis is a 300kHz RDI ADCP moored at a depth of 110m in 150m of water. Additional data obtained from the mooring include the temperature field as recorded by an array of 10 miniloggers. Salinity and temperature profiles of the water column were recorded approximately every three months during a period of 13 months.

3. Analysis

Interaction of a barotropic oscillation with changes in topography will tend to generate linear internal oscillations in the density field when the relevant internal Froude number is not small, but less than unity. The Clyde Sea is a good example of this, experiencing the interaction of a semi-diurnal barotropic tide with a broad, relatively shallow sill, and a maximum mode-one internal Froude number of 0.4. We use both the temperature record and the current data to present observational evidence for the existence and of the internal wave field in the Clyde Sea and to describe its properties.

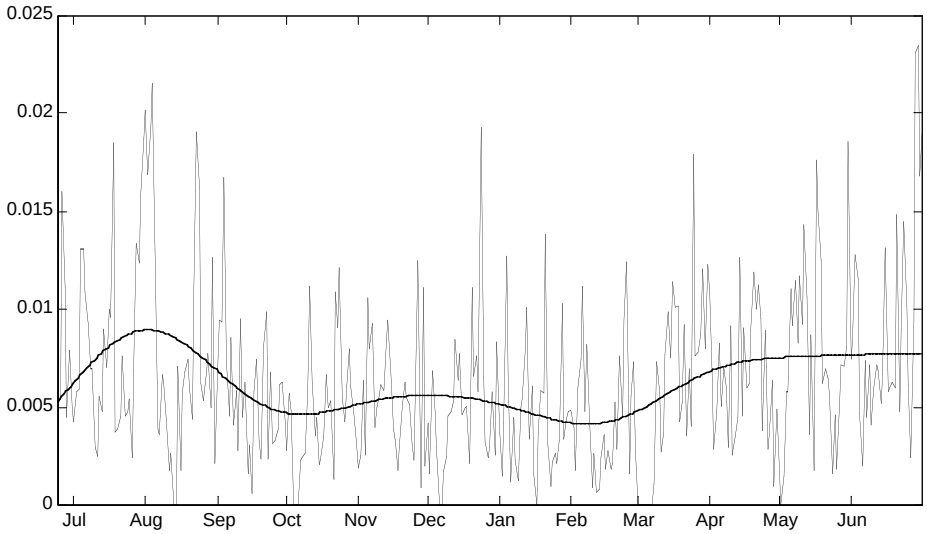

Figure 2: In addition to spring/neap variations in the daily baroclinic power signal at M2 frequencies (fine line), the signal in a depth bin between 12 to 20 m from the surface passed through a 90 day low-pass filter shows a qualitative decrease through the autumn and winter (bold line). Power at this frequency is restored through the spring and summer.

Spectral techniques are then used on the ADCP data to analyse the baroclinic part of the signal. By focusing on the principal M2 component we show that the energy contained in the baroclinic tide varies with depth and varies seasonally.

From the changes in the density field we can link the variation in the baroclinic signal to changes in the degree of vertical stratification. Using this result an estimate of the seasonal contribution to vertical mixing may be made. Further, by comparing the spectral response of the barotropic and the baroclinic parts of the spectrum we show explicitly that the point of generation for the baroclinic tide is the sill.

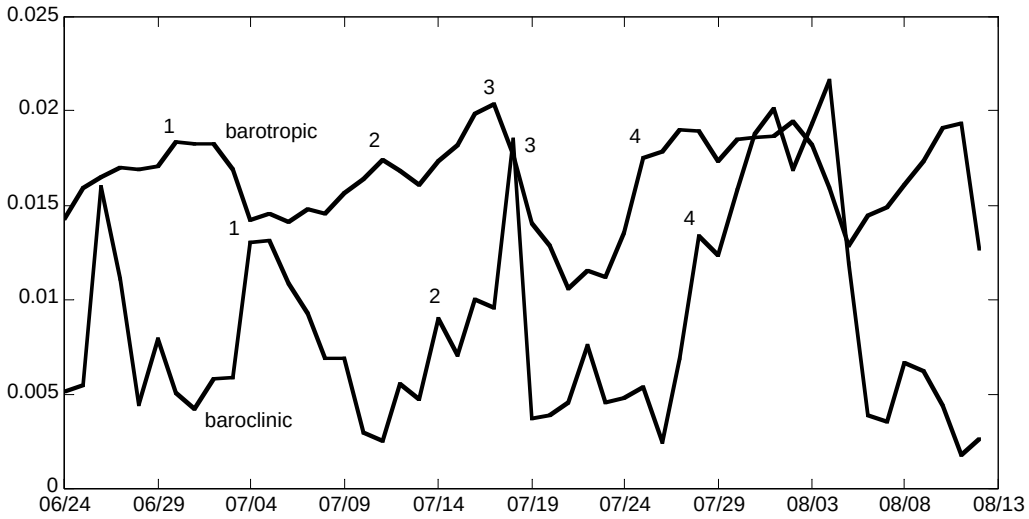

Figure 3: Power of the M2 frequency in the barotropic (solid line) and baroclinic (broken line) components of the current velocity measure at C1. The baroclinic response lags the barotropic by approximately 3 days, corresponding to the difference in propagation speeds between the sill and the mooring site.

As a coda to this study, additional ADCP analysis is directed towards looking at the instrument response to a complete convective overturn event, which occurred in late November. We analyse the ADCP record for characteristic signatures of the convective event.

References

Edwards, A., M.S. Baxter, D.J. Ellett, J.H.A. Martin, D.T. Meldrum and C.R. Griffths, Clyde Sea Hydrography. *Proceedings of the Royal Society of Edinburgh*, 90B, 67-83, 1986.

Inall, M.E. and T.P. Rippeth, Dissipation of Tidal Energy and Associated Mixing in a Wide Fjord, *Environmental Fluid Mechanic*, in press, 2002.

Stigebrandt, A and J. Aure, Vertical mixing in basin waters of fjords. *Journal of Physical Oceanography*, 19, 917-926, 1989.

Wind Fields Retrieved from Nautical Radar-Image Sequences

Heiko Dankert, Jochen Horstmann, Wolfgang Koch
and Wolfgang Rosenthal
GKSS Research Center, Institute for Coastal Research, Department of Coupled Modelling Systems, D-21502 Geesthacht, Germany, dankert@gkss.de

1 Introduction

An algorithm is presented for retrieving wind vectors from nautical radar-image sequences and its application. Thereby data sets from different locations in the North Sea and Baltic Sea have been analyzed. The image sequences were recorded by the wave monitoring system (WaMoS), which has been developed at GKSS Research Center [1], [2].

The frictional force of the local wind field generates the small-scale roughness of the sea surface. This small-scale roughness raises the radar backscatter and therewith the variance of the mean radar cross section (RCS). The small scattering elements are oriented in the wind direction. Therefore, the RCS of the sea surface first of all depends on the wind speed and on the azimuthal angle between the antenna viewing direction and the wind direction. Due to this dependency the wind vector can be deduced from radar images of the sea surface.

The algorithm consists of two parts, one for wind direction and another for wind speed retrieval. Wind directions are locally extracted from wind induced streaks, which are approximately in line with the mean wind direction. The algorithm assumes wind direction as normal to the gradient of the amplitude image, which is approximated by finite differences over an appropriate length. The resulting wind direction is taken as normal to the retrieved local gradients. Wind speeds are derived from the RCS, by parameterization of its dependency on the wind vector using a Neural Network. The algorithm was tested and validated using data from a radar mounted in the North Sea. The applicability of nautical radars for wind retrieval is shown for both tower based and ship borne (moving) instruments.

2 Investigated data

All analyzed data sets discussed here were taken by WaMoS, a system that allows to digitize time series of sea clutter images. It utilizes a nautical radar operating at 9.5 GHz (X-band) with horizontal polarization near grazing incidence. An area within a radius of about 2 km is covered with a resolution of ≈10 m in range and ≈12 m in azimuth at a distance of about 750 m from the antenna. The instrument is operated on several towers in the North Sea, e.g. on the Norwegian Oil Platform "Ekofisk" and in the shallow water area at the island of Helgoland. Further experimental sites were located in the Norwegian Sea in fall 1995, the Odra Lagoon in summer 1997 and the German Bight in spring 1998.

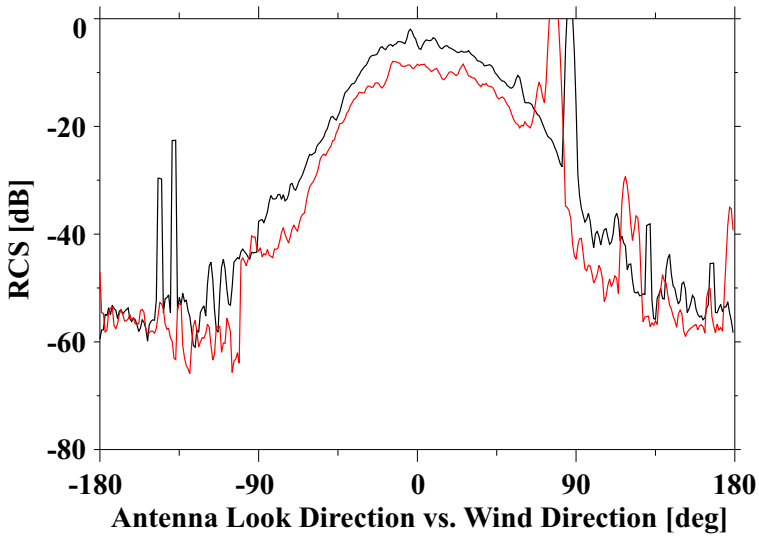

Figure 1: Radar look direction versus range-integrated RCS for different wind speeds c_w. For the black curve $c_w \approx 5.5$ ms^{-1} and the red curve $c_w \approx 3.8$ ms^{-1}.

3 Wind direction retrieval

There are two methods for wind-direction retrieval from radar image sequences. One is based on the well known dependency of RCS on radar look direction [3] and the second on the direction of wind induced streaks visible in radar images [4] (this issue). In Fig. 1 the radar-look direction versus RCS is plotted for different wind speeds. In contrast to VV polarized radars and radars operating at moderate incidence angles there is only one peak at up wind [3]. Therefore the wind direction dependency of the RCS can be used to find the wind direction. However, it is not always possible to retrieve the entire azimuth, which is the case for radars based at the coast.

The second method is based on wind-induced streaks, which are visible in radar images (see Fig. 2) and are aligned in wind direction. These streaks have a typical spacing of 200 to 500 m and may be caused by features such as local turbulences, streaks from foam or surfractants that are aligned with the surface wind. Wind induced streaks were also visible in synthetic aperture radar imagery at similar and larger scales and are used to retrieve the wind direction [4], [5] (this issue). In this paper the wind-induced streaks are assumed to be approximately in line with the mean wind direction

The wind-induced streaks have periods much longer then surface waves. By integrating a radar-image sequence over time (typically 32 images representing 1 min of data), signatures with higher variability in time (like surface waves) are averaged out. Only static patterns like the breakwaters and quasi-static signatures, with frequencies much lower then the integration time, remain visible. The wind-induced streaks are defined to be oriented normal to the local gradients derived from smoothed amplitude images. The average image is therefore further iteratively smoothed and subsampled to obtain a so-called Gaussian pyramid. From level to level the resolution decreases by a factor of two; the image size decreases correspondingly to a pixel size of 100 m, 200 m and 400 m, representing scales between 200 and 800 m. From these pixels the local directions are

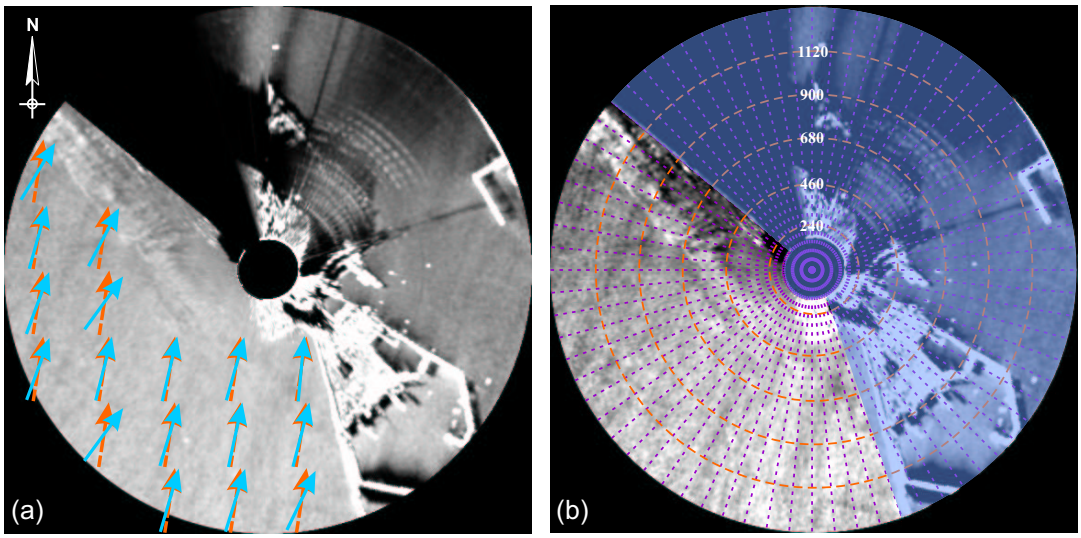

Figure 2: Mean RCS of a radar-image sequence of 64 images taken on the island of Helgoland on November, 26th 1999. The wind speed was 18 ms^{-1} and the measured wind direction 188°. The retrieved local wind direction at the ocean surface are given in (a) by the superimposed blue arrows and the orange dashed lines give the global in situ wind direction at a height of about 90m. For wind-speed retrieval the blue mark covers areas in (b) are not considered for wind-speed retrieval. The polar image is divided into subareas in range and azimuth. The numbers give the distance from the radar antenna [m].

computed with a 180° ambiguity. The 180° ambiguity can be removed using the results of the first method. In Fig. 2a the resulting mean directions are plotted for one sample scale. It can be seen that they agree well to the wind direction measured at the radar platform.

4 Wind speed retrieval

It is well known that the backscatter of the ocean surface is primarily caused by the small-scale surface roughness, which is strongly influenced by the local wind field and therefore allows the backscatter to be empirically related to wind. Investigation of 2 months of radar-image sequences, representing 444 acquisition times show a strong wind speed dependency of the RCS for wind speeds between 5 and 15 ms^{-1}. For wind speeds above 15 ms^{-1} there is a large scatter, which cannot be explained so far.

To retrieve the wind speed a NN is used as a multiple nonlinear regression technique to parameterize the relationship between the ocean surface wind speed and RCS [6] (this issue). As a first step, an NN was trained to retrieve the wind speed from the radar-image sequences. Therefore each sequence is integrated over time to get the mean intensity, which is correlated with the wind. The mean image as seen in Fig. 2 is divided into subareas of three 200 m-range intervals starting at 680 m and azimuth intervals of 5°. The mean intensity of each range-azimuth cell together with corresponding antenna-look direction and the in-situ data (wind speed and direction) are the input parameters to the NN. Areas with shadows due to buildings or static patterns (blue area) were not considered for the training of the NN.

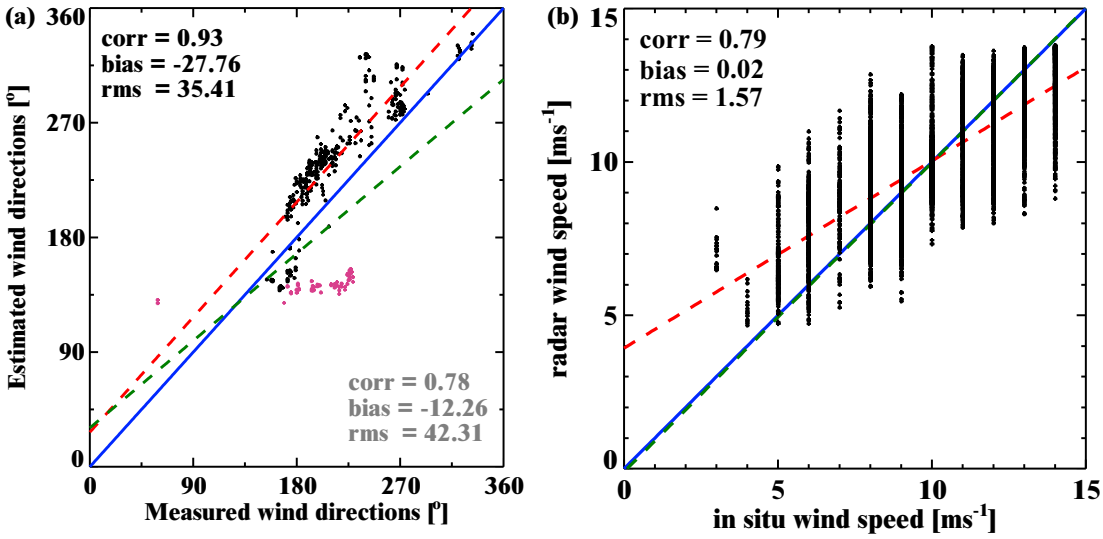

Figure 3: Scatterplots of in-situ wind directions versus radar-derived wind directions (a) and in-situ wind speeds versus wind speeds retrieved using the NN (b). For the wind directions, the purple points give exceptional image sequences, recorded during low-tide. The statistical values in grey are for all considered data sets and in black only for image sequences without the exceptions.

5 Comparison to in-situ data

The wind vector has exemplary been determined for a data set of 444 image sequences, which were acquired at the island of Helgoland. In Fig. 3a in-situ measurements of wind directions are plotted versus radar retrieved directions. There is a clear dependency between them. The correlation coefficient is 0.78 considering all image sequences. Some exceptions are visible (purple), where the estimated wind direction is about the same and seems to been independent from the measured direction. All of these outliers were retrieved at low tide and do not represent the directions causes by the wind. They result from the bathymetry, which is imaged by the radar due to the strong tidal currents and the breaking waves. Omitting these low-tide images the correlation becomes 0.93. The effects due to bathymetry can be solved by eliminating the static bathymetry pattern, by averaging of series of low-tide images and subtracting the mean image from each low-tide image. This high-pass filter lets only the variable wind signatures pass. Fig 3(b) gives a scatterplot of the in-situ wind speeds versus radar retrieved wind speeds. The radar-wind speeds were retrieved using a NN with input of RCS and wind directions. A correlation of 0.79 and a rms error of 1.57 ms^{-1} could be achieved.

6 Conclusions and outlook

An algorithm for ocean-wind field retrieval utilizing nautical radar-image sequences has been developed and tested on data sets from different locations. The wind directions are extracted from wind induced streaks. In most cases the wind direction could be retrieved except for a few sequences except recorded during low-tide, where bathymetry becomes the significant imaged pattern in the radar images. Comparison resulted in a correlation

of 0.93. In this paper the wind direction was estimated for local areas to get a field of wind directions. The wind speed is retrieved from the RCS and wind direction information using a NN. Comparison of RCS derived wind speeds to in-situ measurements resulted in a correlation of 0.79 and a rms error of $\approx$ 1.57 ms^{-1}. As can be seen in Fig. 2 more then 50 % of the area covered by the radar couldn't be considered, because of the harbor constructions of the island, shadows due to buildings and the island itself. Further image sequences recorded during low tide couldn't be considered as well for wind retrieval. And furthermore the coarse-sampled in-situ wind speed data could not give better results here. Overall the results show that it is possible to use the nautical-radar data for the retrieval of wind fields.

Acknowledgments

The authors were supported by the European Commission in the framework of the European project MaxWave (project no.: evk: 3-2000-00544). All radar image sequences were kindly made available by the company Oceanwaves.

References

[1] F. Ziemer, "An instrument for the survey of the directionality of the ocean wave field," in *Proc. of the WMO/IOC Workshop on Oper. Ocean Mon. Using Surface Based Radars*, Geneva, 1995, vol. 32, pp. 81–87.

[2] K. Hessner J.C. Nieto Borge and K. Reichert, "Estimation of the significant wave height with x-band nautical radars," in *Proceedings of the 18th International Conference on Offshore Mechanics and Arctic Engineering (OMAE)*, St. John's, Newfoundland, Canada, 1999, number OMAE99/OSU-3063.

[3] H. Hatten, J. Seemann, J. Horstmann, and F. Ziemer, "Azimuthal dependence of the radar cross section and the spectral background noise of a nautical radar at grazing incidence," in *Proc. Int. Geosci. Remote Sens. Symp. 1998,*, Seattle, USA, 1998.

[4] J. Horstmann, W. Koch, and S. Lehner, "High resolution wind fields retrieved from SAR in comparison to numerical models," in *Proc. Int. Geosci. Remote Sens. Symp.*, Toronto, Canada, 2002.

[5] J. Horstmann, W. Koch, S. Lehner, and R. Tonboe, "Ocean winds from RADARSAT-1 ScanSAR," *Can. J. Remote Sens.*, in press.

[6] J. Horstmann and S. Lehner, "Global ocean wind fields from SAR data using scatterometer models and Neural Networks," in *Proc. Int. Geosci. Remote Sens. Symp.*, Toronto, Canada, 2002.

Tidal and subtidal attenuation in the Patos Lagoon access channel

ELISA HELENA L. FERNANDES

(Fundação Universidade Federal do Rio Grande (FURG), Depto. de Física, CP 474, Rio Grande-RS, CEP 96201-900, Brazil. E.Fernandes@furg.br)

ISMAEL MARIÑO-TAPIA

(University of Plymouth, Institute of Marine Studies, Drake Circus, Plymouth, PL4 8AA, United Kingdom, imarino-tapia@plymouth.ac.uk)

KEITH RICHARD DYER

(University of Plymouth, Institute of Marine Studies, Drake Circus, Plymouth, PL4 8AA, United Kingdom, kdyer@plymouth.ac.uk)

OSMAR OLINTO MÖLLER

(Fundação Universidade Federal do Rio Grande (FURG), Depto. de Física, CP 474, Rio Grande-RS, CEP 96201-900, Brazil, osmar@calvin.ocfis.furg.br)

1. INTRODUCTION

Processes affecting the hydrodynamics of coastal lagoons, including exchanges between the lagoon and the adjacent inner continental shelf, are controlled by tidal and subtidal oscillations. Tidal exchanges are continuous and are predictable as they are periodic. Subtidal processes arise in response to meteorological forcing over time scales on the order of days. The subtidal forcing can be separated into 1) non-local forcing, which includes coastal sea-level changes due to changes in barometric pressure and non-local wind (driven by the Ekman transport acting 90^{o} to the left of the wind); and 2) local forcing, which includes local wind stress (acting on the surface of the water) and freshwater inflows. Modelling experiments were carried out to assess the attenuation of the tidal and subtidal oscillations in the Patos Lagoon access channel (Figure 1).

2. METHODOLOGY

The energy spectrum of a month long time series of water elevation from January 1992 was calculated in order to identify the frequency separating the tidal and subtidal oscillations (Figure 2). The diurnal (D), semi-diurnal (SD) and quarter-diurnal (QD) energy peaks can be observed in the spectrum, characterizing the Patos Lagoon mixed tide with diurnal predominance. The diurnal tidal oscillations are approximately one order of magnitude greater than the semi- and quarter-diurnal peaks, and although the energy spectrum suggests subtidal oscillations, spectral peaks cannot be identified.

A high-pass/low-pass filter (Fast Fourier Transformation technique – FFT) was then applied to the time series of water elevation in order to separate the high frequency time series, representing the tidal oscillations, and the low frequency time series, representing the long period (subtidal) oscillations. The high and low frequency water elevation time series were then used as the ocean boundary condition to force the TELEMAC model in two independent simulations in order to individually study the behavior of the tidal and subtidal oscillations in the access channel. The surface boundary condition was a stress calculated from the components of the wind velocity (prescribed as 7 ms^{-1} from the NE), and a flow rate of 3000 m^3 s^{-1} was prescribed at the top of the lagoon. Simulations were carried out based on finite element mesh of 2631 triangles. Fernandes *et al.* (2001) and Fernandes *et al.* (*in press*) present the calibration and validation of the TELEMAC model for the Patos Lagoon

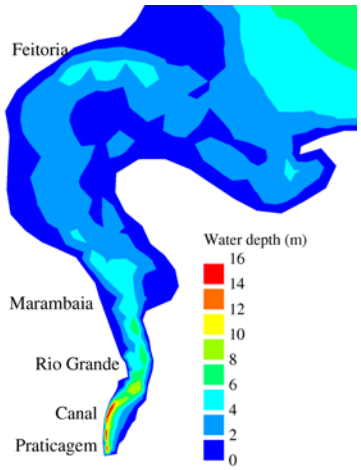

Figure 1 – The Patos Lagoon estuary.

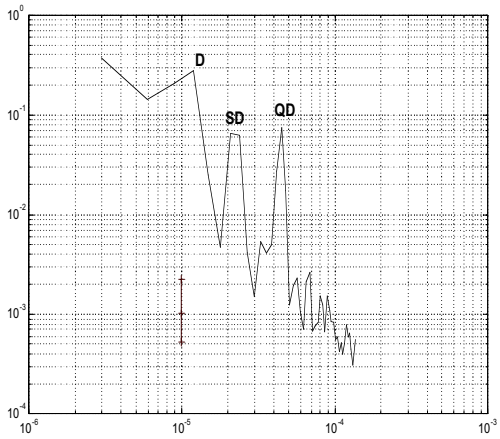

Figure 2 – Energy spectrum of the time series of water elevation – January 1992.

3. RESULTS

Kjerfve & Knoppers (1991) comment that the single, long and narrow channel that usually connects choked coastal lagoons to the ocean naturally serves as a hydraulic low-pass filter in reducing or eliminating tidal effects inside the lagoon. Modelling results indicate that the Patos Lagoon is no exception. The entrance channel not only filters the astronomical tides but also attenuates the long period oscillations generated offshore, and the tidal and subtidal influence is rapidly reduced as it progresses landwards. Some oscillations can still be observed 20 km inland, but they disappear at the top of the estuary (60 km from the mouth). Moller *et al.* (1996) also point out the attenuation of these oscillations throughout the channel, although a coefficient describing the tidal and subtidal attenuation was not calculated.

Ippen & Harleman (1961) developed a method that relates the relative times of high water along the estuary, the tidal amplitudes, and the phase change to a damping coefficient that specifies the change in amplitude with distance along the estuary caused by friction. Such a method would be appropriate for estimating the tidal attenuation in the Patos Lagoon estuary if a more comprehensive data set was available. We propose another method to estimate the tidal and subtidal attenuation by shifting from the time domain into the frequency domain, and applying a cross-spectral analysis (8 Hanning windows to a time series of 745 points) carried out in pairs between the original time series prescribed at the ocean boundary and the predicted time series of water elevation calculated at selected points throughout the estuary. The cross-spectral analyses result in a co-spectrum (spectral density function), a coherence spectrum and a phase spectrum. The resulting spectral density function provides the attenuation coefficient of the tidal and subtidal signals at different frequencies.

A cross-power spectrum defines the relationship between two variables. If these variables are completely independent the co-spectrum is zero, and if they are identical it becomes the ordinary power spectrum. The derived coherence between the two times series is a measure of how well correlated the two sequences are as a function of frequency, being equal to 1 if one signal is a constant times the other (Butt, 1999). The coherence spectrum has a confidence limit, which is the limit below what the coherence values can occur by chance. Therefore, for frequencies at which the coherence is below this limit, any co-spectral estimate would be unreliable.

Figure 3 shows the co-spectrum, coherence and phase spectra at different locations along the estuary (Figure 1) when the model is forced with the tidal signal. The prescribed time series and the predictions at Praticagem (Figure 3A) match very well and reach a coherence level of almost 1, which is well above the 95% significance level of 0.22, keeping in phase all the time. The co-spectrum at Canal (Figure 3B) indicates a strong reduction of the tidal energy, and although the time series are still in phase in the frequencies of interest (0.000011 – 0.000045 Hz), the average coherence between them

is reduced to 0.75. Results for Rio Grande (Figure 3C), Marambaia (Figure 3D), and Feitoria (Figure 3E) show a co-spectrum equal to zero, indicating that the prescribed water elevation at the mouth is completely independent from the predicted water elevation at these points and no tidal signal reaches these areas.

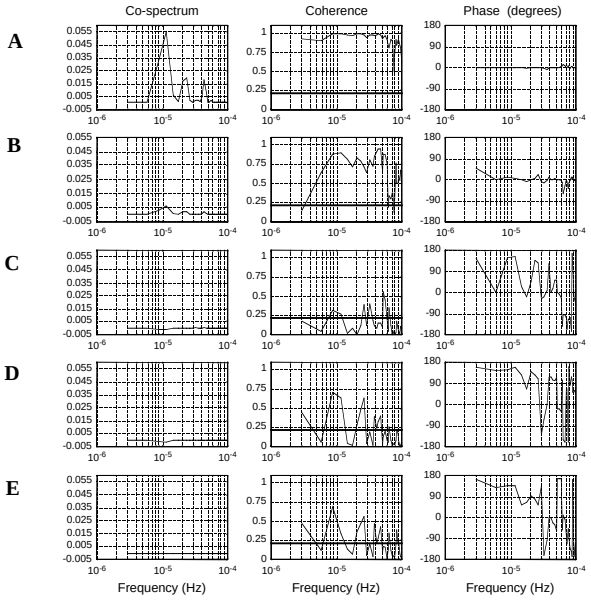

Figure 3 – Cross-spectrum results when applying the tidal forcing. Co-spectrum, coherence and phase spectrums at (A) Praticagem, (B) Canal, (C) Rio Grande, (D) Marambaia and (E) Feitoria.

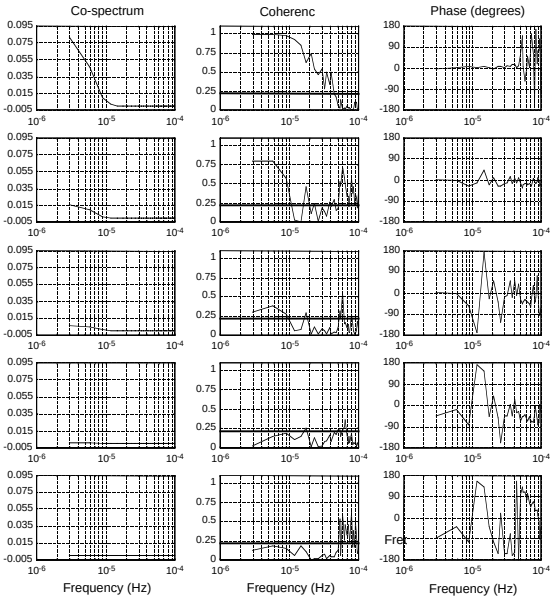

Figure 4 – Cross-spectrum results when applying the subtidal forcing. Co-spectrum, coherence and phase spectrums at (A) Praticagem, (B) Canal, (C) Rio Grande, (D) Marambaia and (E) Feitoria.

The spectral density function at diurnal frequencies is attenuated from the prescribed 0.22 at the ocean boundary to 0.006 at Canal, which represents an attenuation of 97.3% of the signal. Similar attenuation was observed at the semi-diurnal frequencies. The spectral density function at quarter-diurnal frequencies indicates an attenuation of 96.2% of the tidal signal at Canal. Such values show that the diurnal and semi-diurnal tidal signals are similarly attenuated whereas the quarter-diurnal signal is less attenuated along the Patos Lagoon estuary. The opposite case is presented by Smith (1977) for Corpus Christi Bay, which is connected to the Gulf waters through a channel approximately 19 km in length that also acts like an exponential filter. The diurnal tidal amplitudes are reduced to approximately one-third of their values at the Aransas Pass, while semi-diurnal period constituents are reduced to less than 15% of their values at the coast.

The cross-spectral analysis of the long period (subtidal) oscillations throughout out the estuary is presented in Figure 4. Results indicate that the data used to force the model and the predicted time series at Praticagem (Figure 4A) are highly coherent and in phase. However, the subtidal energy peak is strongly reduced as the signal progresses towards Canal (Figure 4B), and although a small subtidal peak can still be observed at Rio Grande (Figure 4C), it completely disappears after this point. Results for Marambaia (Figure 4D), and Feitoria (Figure 4E) show a co-spectrum equal to zero, indicating that the prescribed water elevation at the mouth is completely independent of the predicted water elevation at these points and no subtidal energy reaches these areas. The coherence between the two time series is below the confidence level for most of the time, indicating that any co-spectral estimates would be unreliable. The spectral density function decreases from 0.325 at the ocean boundary to 0.015 at Canal, with an attenuation of 95.4% of the subtidal energy.

Moller *et al.* (2001) comment that the subtidal dynamics of the Patos Lagoon can be divided in two distinct periods. During most of the year the circulation is wind driven due to low to moderate river discharge, while during the annual flood peak in late winter, the riverine input plays the main role. Thus, the time series of water elevation from January 1992 is only representative of the summer

months, when the freshwater discharge is low to moderate and the weather fronts over the region are not so intense. For such conditions, results presented here indicate that although the subtidal energy propagates further, the tidal and subtidal oscillation have similar magnitudes during the studied period. This picture is expected to change during the winter months, when the area is marked by the passage of much stronger weather fronts and the subtidal oscillations combined with the riverine input from the north of the lagoon are expected to overcome the tidal effect.

On the other hand, these experiments are based on simplified conditions and consider a constant wind and freshwater discharge at the top of the lagoon. Thus, the long-period oscillations considered here are limited to the non-local effect, represented by the water elevation at the ocean boundary. The observed predominance of subtidal energy will possibly be enhanced when time series of wind velocity and freshwater discharge are available to be included in the calculations.

Further simulations based on improved initial and boundary conditions are currently being carried out in order to investigate the tidal and subtidal attenuation throughout out the seasons in 1992. For now, the presented numerical predictions of the water elevation at different points throughout the estuary proved to be an alternative method to estimate the attenuation of the tidal and subtidal oscillations in the channel. Moreover, the calculated attenuation coefficients indicate that the tidal and subtidal amplitude is quite reduced as soon as it leaves the entrance channel. These results agree with the conclusions of Kjerfve and Magill (1989) e Moller et al. (1996).

Acknowledgments: This research was sponsored by the *Conselho Nacional de Desenvolvimento Científico e Tecnológico (CNPq)*, Brazil, contracts 200012/97-5 and 540467/01-4. The authors wish to gratefully acknowledge Mr. John Baugh (HR Wallingford) for giving support to the use of TELEMAC-2D.

References

Butt, T. 1999. Sediment transport in the swash-zone of natural beaches. PhD Thesis, Institute of Marine Studies, University of Plymouth, UK.

Fernandes, E.H.L., Dyer, K.R., and Niencheski, L.F.H. (2001). TELEMAC-2D calibration and application to the hydrodynamics of the Patos Lagoon (Brazil), *Journal of Coastal Research* 34, 470:488.

Fernandes, E.H.L., Dyer, K.R., Moller, O. O., and Niencheski, L.F.H. (2001). The Patos Lagoon hydrodynamics during an El Niño event (1998), *Continental Shelf Research,* in press.

Ippen, A. T. & Harleman, D. R. F. 1961. One-dimensional analysis of salinity intrusion in estuaries. Technical Bulletin No. 5, pp 1-52. Committee on Tidal Hydraulics, CORPS of Engineers, US Army.
Kjerfve, B. & Knoppers, B. A. 1991. Tidal chocking in a coastal lagoon. In: *Tidal Hydrodynamics*. Ed. B. B. Parker. pp. 169-181.

Kjerfve, B. and Magill, K.E. (1989). Geographic and hydrodynamic characteristics of shallow coastal lagoons. *Marine Geology* 88, 187-199.

Moller, O. O., Lorenzzetti, J. A., Stech, J. L. & Mata, M. M. 1996. The Patos Lagoon summertime circulation and dynamics. *Continental Shelf Research* 16, 335-351.

Moller, O. O., Castaing, P., Salomon, J. C. & Lazure, P. 2001. The influence of local and non-local forcing effects on the subtidal circulation of Patos Lagoon. *Estuaries* 24 , 275-289.

Smith, N. P. 1977. Meteorological and tidal exchanges between Corpus Christi Bay and the northwestern Gulf of Mexico. *Estuarine and Coastal Marine Science* 5, 511-520.

The effect of variable depths and currents on wave development

HEINZ GÜNTHER, GERHARD GAYER AND WOLFGANG ROSENTHAL

(Institute for Coastal Research, GKSS Research Center Geesthacht, Max-Planck-Str., D-21502 Geesthacht, Germany, guenther@gkss.de, gayer@gkss.de, rosenthal@gkss.de)

1. Introduction

In coastal areas detailed knowledge of the surface wave field is very important for the understanding of hydrodynamic and transport processes. The interaction of waves with the bottom and current is one of the keys to understand and predict developments in coastal seas.

Substantial progress has been made in the recent years in predicting ocean surface gravity waves. The third generation WAM model (*Komen et al*. [1994]) has demonstrated its excellent performance on global and regional scales, which are the deep-water ocean and the shallow shelf sea areas. However, difficulties have been found in the coastal zone. The space and time scales in these areas are normally too small to allow the non-linear interactions to control the energy balance. The growth and decay of waves is dominated by the input energy from the atmosphere and by enhanced dissipation of wave energy in the water column and at the sea floor. In particular the dissipation in the water column by turbulent diffusion (*Rosenthal* [1989]), which is not included in most coastal wave models, has been identified as a key process to explain the self-similar spectral shape (*Günther and Rosenthal* [1995]).

In this paper a brief description of the K-model is presented followed by examples of model applications in the tidal area of the Waddensea and around Helgoland to demonstrate the impact of changing currents and water depth on the wave development. In these situations the propagation effects (shoaling and refraction) are balanced by the source functions and especially by the wave dissipation of wave energy.

2. Wave Model

The K-model is a discreet spectral wave model solving the action density balance equation in wave number space (see *Schneggenburger, Ch., H. Günther, W. Rosenthal* [2000] and *Schneggenburger, Ch., H. Günther, W. Rosenthal* [1998]). It was developed for small-scale (typical grid resolution from 50 m up to a few 100 m) applications with non-stationary currents and water depths. Restricted to the essential physical processes in such environments, the model includes in the source functions the energy input (modified Snyder source term and Phillips source term), energy dissipation (turbulent diffusion) and energy dissipation by bottom friction. The source and sink terms are balanced by the propagation terms, which include refraction and shoaling.

The model is forced by wind fields (at 10 m height, typically every hour) and current and water level fields (typically every 20 minutes). At land boundaries of the model area free outflow of energy is assumed. At the open sea boundaries wave spectra have to be used. For the following examples these spectra are taken out of a North Sea model runs with a coarse resolution of 30 km with an input frequency of 1 hour.

3. Applications

In the following two applications of the model are discussed. In 3.1 the impact of sea floor changes on waves and currents in a Waddensea area to the southwest of the Elbe river estuary is investigated. In 3.2 a study of the Helgoland area to quantify the impact of variable water depth and/or currents on the wave development and propagation is presented.

3.1 Waddensea

To estimate the impact of topographical changes on the wave and current climate in a Waddensea area in the southern North Sea, we examined the results of the spectral wave model and a hydro-dynamical model for different storms and for a 20 days period of moderate weather conditions. Two bathymetries were used, one representing the actual condition and a worst case scenario of dredging sand in an area of approximately 6 km^2 increasing the water depth by 2 m from 10 m to 12 m at once.

The model results are compared to find the area of changes and the places where major changes occur. During a north-westerly storm in January 1994 the biggest differences (after dredging – before dredging) are found to be approximately 20 cm in significant wave height (see figure 1, white areas are land or dry flats. White lines show the 0 and 10 m water depth contours giving an indication of the bathymetry with tidal channels and adjacent flats). The waves at the boundary of the model area had a height of about 6 m during the peak of the storm.

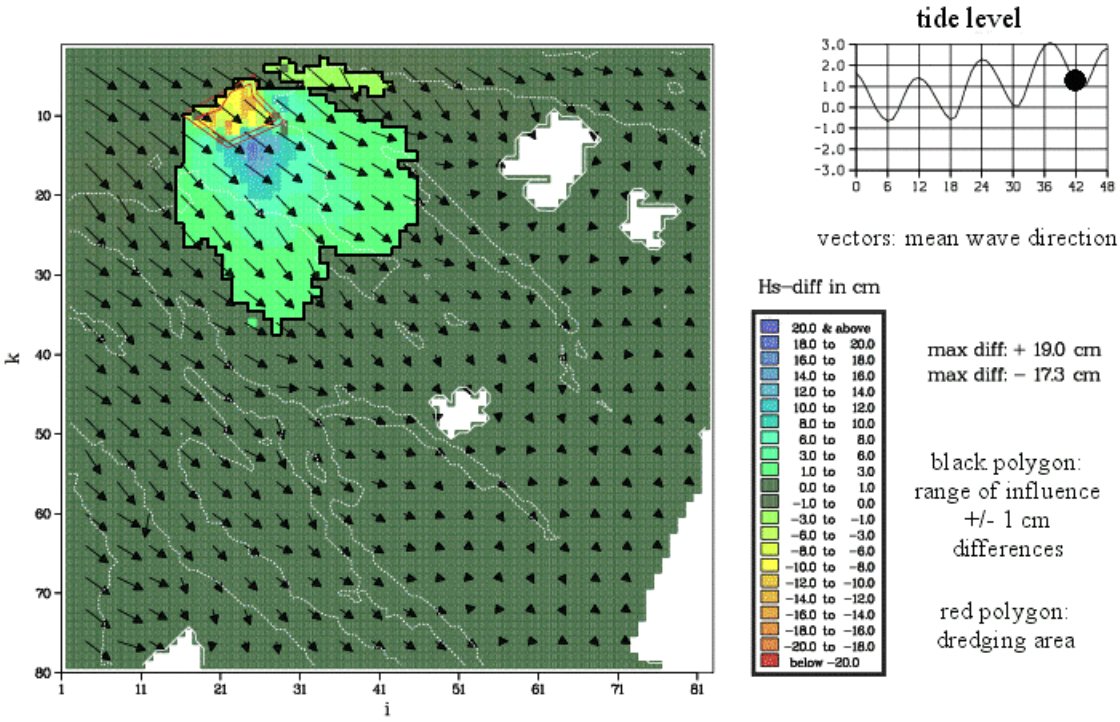

Figure 1: Differences of significant wave height (after dredging – before dredging) 1994 01 28 18:00.

Only in a spatially limited area at and in the vicinity of the dredging site the wave climate is changed noticeably due to differences in shoaling and energy dissipation. Currents are altered only slightly after dredging.

3.2 Helgoland

We investigated the influence of variable current and water level fields on the results of the spectral wave model near the North Sea island Helgoland. This area is characterized by strong water depth gradients (from 50 m – 0 m over a distance of 5 km) especially to the southwest from the island. Two model runs were performed, one with unchanged initial bathymetry, another one taking spatial and temporal water level and current variations into account.

During a storm in October 1998 with wind speeds up to 24 m/s – the wave model calculated a significant wave height of 5.5 m on a coarse North Sea grid at the nearest grid point to the fine grid area of interest (50 m resolution) – the waves approached the island from a direction of 290 degrees.

Above the slope the wave heights increased to a maximum of 6.5 m due to refraction and shoaling effects.

Performing the second model run with time series of current and water level variations the shoaling and refraction of waves changed significantly. At high tide shortly after the storm peak a difference plot of significant wave heights shows especially off the western coast 2 stripes of high differences (see figure 2). In front of the coast positive differences of up to 1.5 m can be observed which can be explained with greater water depths and reduced energy dissipation. Further to the west negative differences of up to 1.5 m show that due to greater water depths the shoaling of waves locally is reduced. The shoaling now takes place in front of the coast, adding there to the high positive differences.

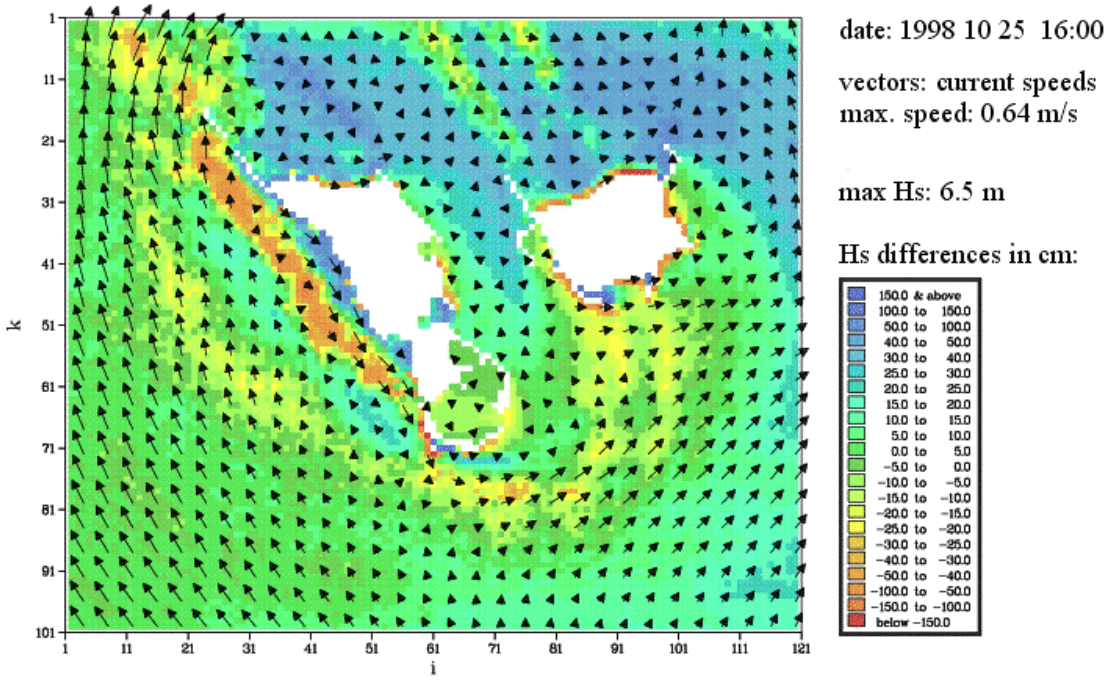

Figure 2: Differences of significant wave height (variable depth/currents – constant fields).

4. Conclusions

In small-scale coastal applications the influence of water level and current variations cannot be neglected. The example of the coastal area of the island of Helgoland showed that locally the balance effects with shoaling in case of sloping bottom and in the presence of in-stationary water depth and current fields led to high differences in significant wave height fields compared to the scenario with constant bathymetry. In case of the Waddensea area example changing the bathymetry locally led to much smaller differences due to a reduced bottom slope compared to the Helgoland area.

Acknowledgements: Those studies were done in close co-operation with the BAW (Bundesanstalt für Wasserbau), Hamburg.

References:

Komen, G. J., L. Cavaleri, M. Donelan, K. Hasselmann, S. Hasselmann, P. A. E. M. Janssen, *Dynamics and Modelling of Ocean Waves,* Cambridge University Press, Cambridge, UK, ISBN 0 521 43291, 560 pages, 1994

Rosenthal, W., *Deviation of Phillips a-Parameter from Turbulent Diffusion as a Damping Mechanism*, In: Radar Scattering from Modulated Wind Waves, Komen, G. J. and W. A. Oast (eds.), Kluwer Academic Publishers, 1989

Günther, H. and W. Rosenthal, *A Wave Model with a Non-linear Dissipation Source Function*, in Proceedings of the 4th International Workshop on Wave Hindcasting and Forecasting, October 16-20, 1995, Banff, Alberta, Canada, pp. 138-148; und GKSS 96/E/62 ISBN 0344-9629.

Schneggenburger, Ch., H. Günther, W. Rosenthal, *Spectral wave modelling with non-linear dissipation: validation and applications in a coastal tidal environment*, Elsevier Coastal Engineering, 41, pp 201 – 235, 2000.

Schneggenburger, Ch., H. Günther, W. Rosenthal, *Shallow water wave modeling with nonlinear dissipation: application to small scale tidal systems*, GKSS 98/E/7, 1998.

Sort-period fluctuations of surface circulations in Sagami Bay induced by the Kuroshio warm water intrusion

HIROFUMI HINATA

(National Institute for Land and Infrastructure Management, 3-1-1 Nagase, Yokosuka 2390826,Japan, hinata-h92y2@ysk.nilim.go.jp)

TETSUO YANAGI

(Research Institute of Applied Mechanics, Kyusyu University, 6-1 Kasuga-Koen, Kasuga 8168580, Japan, tyanagi@riam.kyushu-u.ac.jp)

MASASHI MIYANO

(Ecoh Company Limited, 2-6-4 Kitaueno, Taito-ku, Tokyo 1100014, Japan, miyano@echo.co.jp)

TAKASHI ISHIMARU

(Tokyo University of Fisheries, 4-5-7 Konan, Minatoku, Tokyo 1100014, Japan, isi@tokyo-u-fish.ac.jp)

HIROSHI KAWAMURA

(Center for Atmospheric and Oceanic Studies, Tohoku University, Aramaki, Aobaku, Sendai 9808578, Japan, kamu@ocean.caos.tohoku.ac.jp)

1. Introduction

Sagami Bay is located at the southeastern part of Honsyu, Japan and is connected to the Pacific Ocean through Oshima West Channel and Oshima East Channel (Fig.1). The Kuroshio flows eastward off

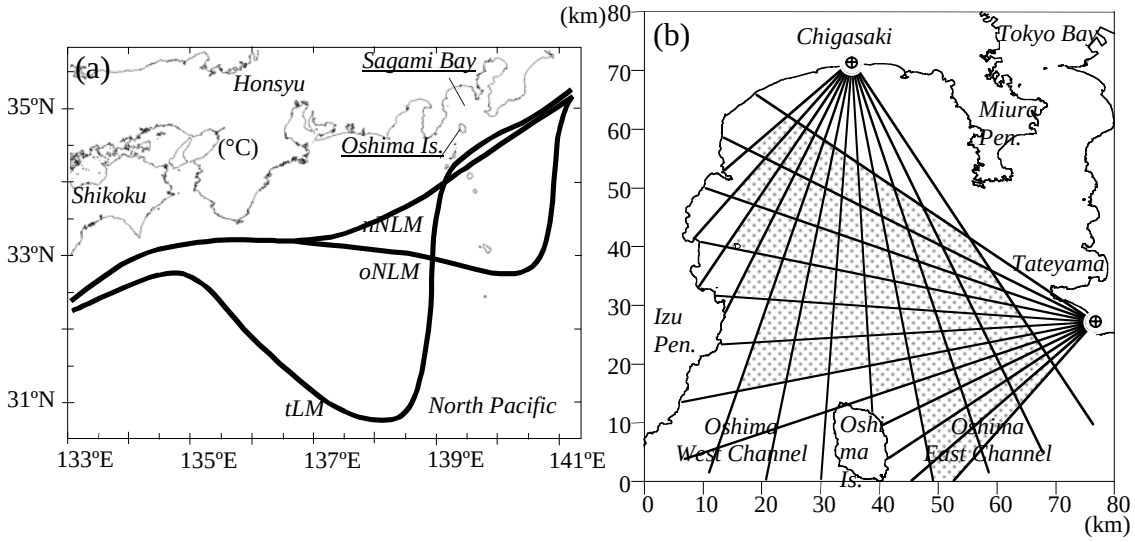

Fig. 1. (a) Schematic diagram of three typical paths of the Kuroshio. (b) Observational region.

Sagami Bay with three quasi-steady paths – the nearshore non-large-meander path (nNLM), the offshore non-large-meander path (oNLM) and the typical large-meander path (tLM) (Kawabe, 1985). It is well known that when the Kuroshio takes the path of tLM, the Kuroshio Warm Water (KWW)

intrudes into the bay through Oshima west cahnnel and cyclonic and anti- cyclonic circulations are veloped in the central part of the bay and the lee of Oshima Island, respectively (Taira and Teramoto, 1986, Kawabe and Yoneno, 1987, Iwata and Matsuyama, 1989). However, characteristics of short-period fluctuations with a period of several days and precise structures of the circulations remain unknown. In this study, the characteristics of short-period fluctuations and precise flow structures of surface circulations in Sagami Bay have been investigated by field observation based on High Frequency Oceanic Surface Radars (HFOSRs).

2. Observation

The observation site is shown in Fig.1. Two HFOSRs of Frequency Modulated Interrupted Continuous Wave type (FMICW) were set up at Tateyama and Chigasaki during the period from December 7, 2001 to March 6, 2002. Radio waves of the radars have a center frequency of 24.515 MHz with a sweep bandwidth of 100 KHz, which results in a range resolution of 1.5 km. Regression analysis shows that the HFOSRs radial current velocity is about 0.93 times that from bottom mounted upward looking Acoustic Doppler Current Profiler (ADCP). And the standard deviation of residual is 6.5 cms^{-1}. Details are described in Yanagi et al. (2002). 25 hr running averaged HFOSRs current velocities were analyzed by Empirical Orthogonal Function (EOF) analysis.

3. Results

KWW had been intruded into the bay through Oshima West Channel during the period from December 15, 2000 to January 16, 2001 (Period 1). And during the Period 1, cyclonic and anti-cyclonic circulations were generated in the central part of the bay and lee of Oshima Island, respectively (Fig.2 (a)).

EOF analysis shows that the first two EOF modes (Fig.3) are dominant and together account for 55% of the variance in the dataset. Time dependent amplitude of the first mode fluctuates with a period of about 8-10 days and is highly correlated with variations of sea level in and around Sagami Bay. Increase of sea level drives a positive mode1 response and decrease of sea level a negative response. Fig.2 (b)-(d) shows temporal variations of surface current field reconstructed by EOF mode 1-2 plus the temporal mean field. Velocities and sizes of the circulations change corresponding to the sea level variations with a period of about 8-10 days. The sea level changes in Period 1 in and around Sagami Bay are mainly due to the short period fluctuations of the Kuroshio Front (Hinata et al., 2002).

Based on mooring observations and satellite infrared images, Kimura and Sugimoto (1993) pointed out that periodic fluctuations of 5-8 days and 10-12 days in the Kuroshio region are caused by the small-scale meander of the Kuroshio front with wavelength of about 100km and 200 km, respectively. Sea surface temperature in the Kuroshio region off Sagami Bay on December 15, 2000 is shown in Fig.4. Warm water filaments can be seen in the Kuroshio frontal region and they have about 100-150 km wavelength. These results suggest that the fluctuations of two circulations in Sagami Bay are caused by the small-scale meander (warm water filament) of the Kuroshio front with wavelength of 100-150 km.

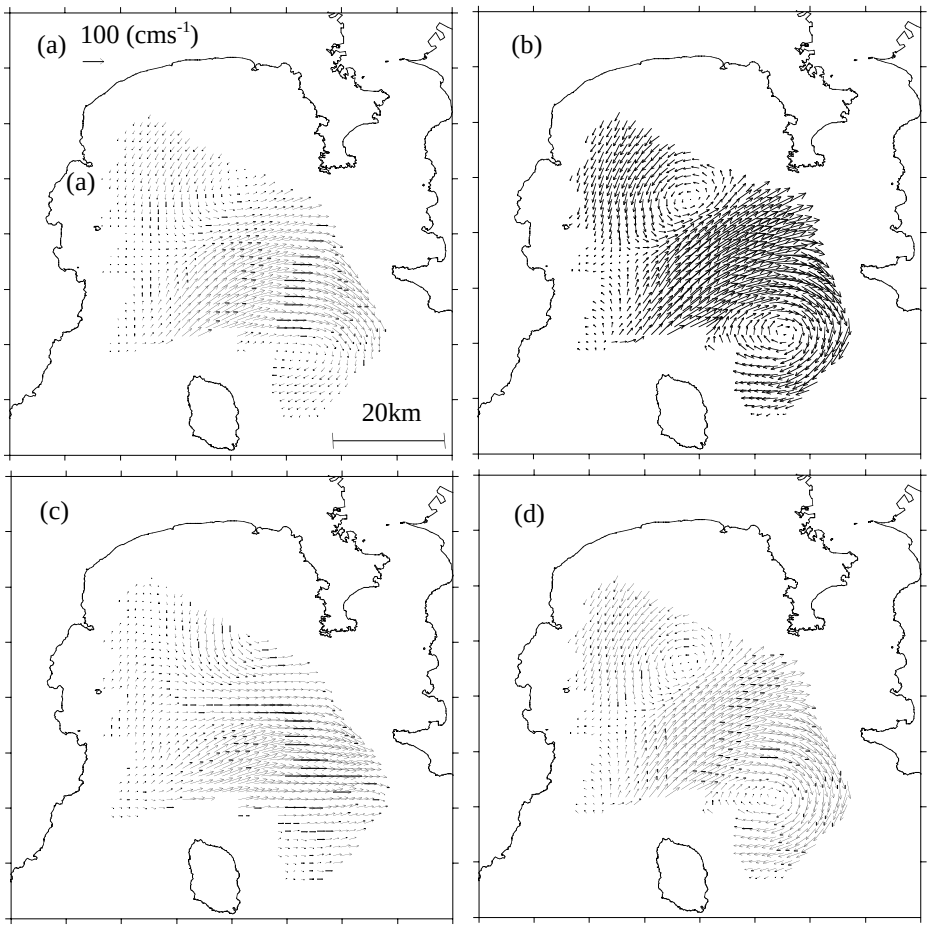

Fig. 2. Surface current maps. (a) Temporal mean flow field , (b) 12:00, Dec. 31, 2000, (c) 12:00, Jan. 03, 2001 and (d) 00:00, Jan. 07, 2001. (b) ,(c) and (d) use EOF mode 1-2 plus the mean field.

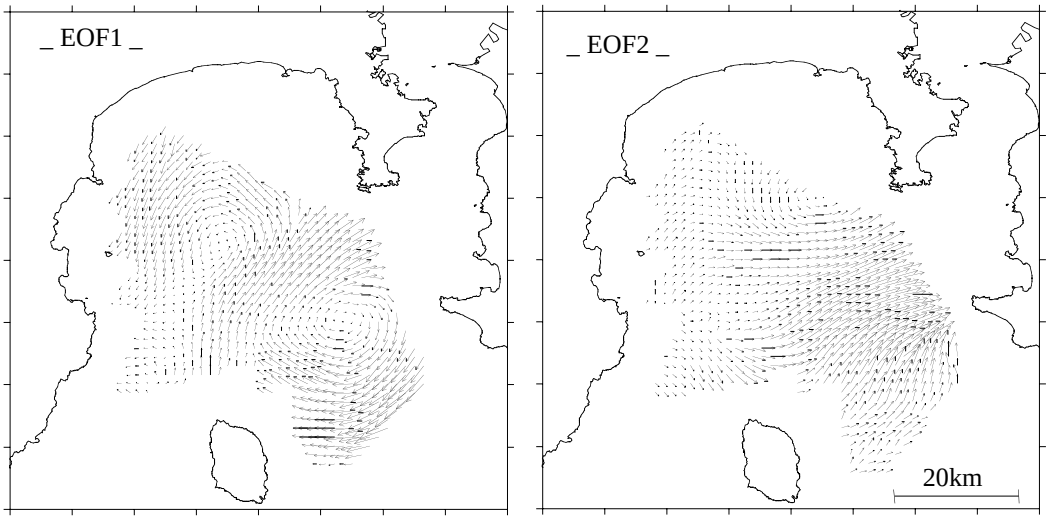

Fig. 3. Eigenvector plots of EOF1 and EOF2.

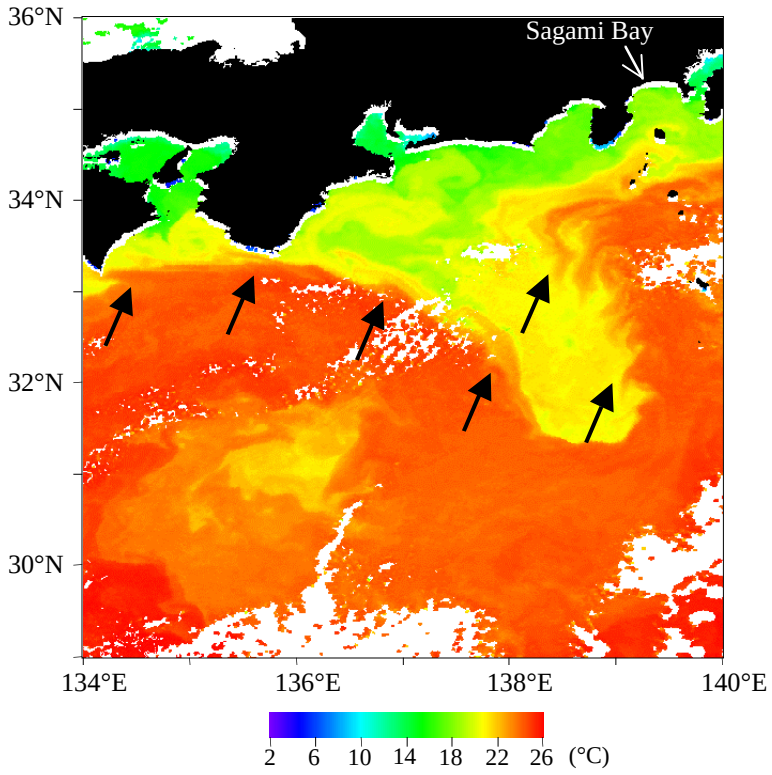

Fig. 4. AVHRR sea surface temperature image in the Kuroshio region off Sagami Bay at 19:52 on December 15, 2000 (JST). Arrows indicate warm water filament in the Kuroshio frontal

References:

Kawabe, M. : Sea level variations at the Izu Islands and typical stable paths of the Kuroshio. *J. Oceanogr. Soc. Japan*, 41, 283-294, 1985.

Kawabe, M. and M. Yoneno : Water and flow variations in Sagami Bay under the influence of the Kuroshio Path. *J. Oceanogr. Soc. Japan*, 43, 283-294, 1987.

Kimura, S. and T. Sugimoto: Short-Period fluctuations in meander of the Kuroshio's path off cape Shiono Misaki. *J. Geophys. Res.*, 98, 2407-2418, 1993.

Hinata, H., H. Miyano, T. Yanagi, T. Ishimaru, T. Kasuya, and H. Kawamura: Short-period fluctuations of surface circulation in Sagami Bay induced by the Kuroshio warm water intrusion through Oshima west channel - Relation to small-scale meander of the Kuroshio front -. *Oceanography in Japan* (in press).

Iwata, S. and M. Matsuyama : Surface circulation in Sagami Bay: the response to variations of the Kuroshio axis. *J. Oceanogr. Soc. Japan*, 45, 310-320, 1989.

Taira, K. and T. Teramoto: Path and volume transport of the Kuroshio current in Sagami Bay and their relationship to cold water masses near Izu Peninsula *: J. Oceanogr. Soc. Japan*, 42, 212-223, 1986.

Yanagi, T., M. Shimizu, M. Nomura, and K. Furukawa : Spring-Neap tidal variations of residual flow in Tokyo Bay, Japan. *Proceedings of 10th Physics of Estuaries and Coastal Seas*, edited by A. Levinson, 2001.

A non-hydrostatic numerical model for calculating of free-surface stratified flows in the coastal sea

YULIYA KANARSKA, VLADIMIR MADERICH

(Institute of Mathematical Machine and System Problems, Glushkova av. 42, 03187 Kiev, Ukraine, kanarska@ukrpost.net)

1. Introduction

The non-hydrostatic effects are important in a wide spectrum of stratified flows in the coastal seas. The examples are the buoyant plumes from submerged outfalls, internal waves of large amplitude generated by the tidally driven flows over a steep topography and exchange flows over the sills in the sea straits. In this paper a three-dimensional numerical model for simulation of the free-surface stratified flows in the coastal sea is presented. The model is a non-hydrostatic extension of free-surface primitive equation POM model with vertical sigma-coordinate (*Blumberg and Mellor* [1987]). The pressure field was decomposed on hydrostatic and non-hydrostatic components. The model equations were integrated with mode splitting technique and four-stage procedure, where the level was determined at first. The hydrostatic, non-hydrostatic components of pressure, velocity and scalar fields were calculated at subsequent stages. Unlike the most of non-hydrostatic models 2D depth-integrated momentum and continuity equations were integrated explicitly at first stage, whereas 3D equations were solved implicitly at rest stages. This approach is particularly advantageous for the shallow stratified flows and is fully compatible with the POM model.

The model was tested against laboratory experiments check its ability to reproduce local scale non-hydrostatic phenomena in coastal sea. The surface solitary wave interaction with the vertical wall, the formations of solitary «bulges» in thin pycnocline as the result of the collapse of mixed region and water exchange through strait are considered.

2. Model Descriptions

The model is based on the 3D Reynolds-averaged Navies-Stokes equations for Boussinesq fluid. The concept of eddy viscosity and diffusivity is used with two-equation model of turbulence model to define turbulent stresses and scalar fluxes. The sigma-coordinate system for the vertical direction is used. The pressure and velocity fields are decomposed on hydrostatic and non-hydrostatic components. The mode splitting technique (*Blumberg and Mellor* [1987]) for external and internal modes was applied. The finite-difference solutions of governing equations were derived using four-stage procedure:

1 stage: Free surface level.

The calculation of free surface elevation is performed by explicit method from depth-integrated shallow water equations like the POM model. The initial 2D velocity fields on each external stage is determined by direct integrating of general non-hydrostatic 3D velocity fields from previous internal step.

2 stage: Hydrostatic components of velocity and pressure.

The 3D hydrodynamic equations without non-hydrostatic pressure are solved with internal time step semi-implicitly (*Casulli and Stelling* [1998]) to determine provisional values of velocity. The advection, horizontal viscosity and diffusion were discretized explicitly. The obtained three-diagonal system is solved by a direct method.

3 stage: Non-hydrostatic components of velocity and pressure.

The non-hydrostatic components of velocity are computed by correcting the provisional velocity field with the gradient of non-hydrostatic pressure to satisfy continuity equation for sum of hydrostatic and

non-hydrostatic velocity. The obtained discretized Poisson equation for the non-hydrostatic pressure reduced to the non-symmetric 15 diagonal linear system, part of which arise from the sigma-transformation components. The preconditioned biconjugate gradient method is used for solving this system. Once the non-hydrostatic pressure is determined the corresponding components of velocity fields are calculated.

4 stage: Scalar fields.

The scalar fields (temperature and salinity, turbulent quantities) are computed by using semi-implicit numerical scheme in vertical direction. The obtained three-diagonal system is solved by a direct method.

3. Numerical Application and discussion

Impact of solitary surface wave on vertical wall. Here, results of a computation are compared with the laboratory experiments on solitary surface wave interaction with a vertical wall in the wave flume with depth H. As seen in Fig. 1, the model predicted well maximum of elevation η at the wall. The time dependence of wave pressure on undisturbed surface p is shown in Fig. 2. Non-hydrostatic model reproduced quite well observed in experiments characteristic two-peak profile of pressure with depression near to the moment of maximum runup that was caused by the vertical acceleration of fluid at the wall.

Propagation of intrusive "bulge" in the pycnocline. The second example concerned with the formation and evolution of large amplitude intrusive "bulge" that was generated by collapse of mixed region in the thin pycnocline. The results of simulation are compared in Fig. 4 with experiment 302 of *Maderich et al.* [2001] that was conducted in the tank 6.7x0.4x0.19 m. The tank was filled with two homogeneous layer of different salinity. The circular mixed region with diameter 0.19 m collapsed in the centre of tank. The resulted solitary bulges (compare Fig. 4 and 5) moved with almost constant speed that exceeded values, predicted by theory of weakly nonlinear long internal waves.

Exchange flows through long straits with sill. Here, the exchange flow through shallow and narrow strait connected two deep and wide basins filled by water of different density is considered. The laboratory experiment 701 (*Maderich* [2000]) was simulated. The strait is rectangular with length L=60.5 cm, maximal depth H=8 cm and constant width A=0.9 cm. The sill with h/H =0,5 is placed in the centre. The buoyancy difference is $g\Delta\rho/\rho$=1.48 cm/c^2. This difference was maintained by heating of left basin and cooling of right one. The exchange in the strait is maximal. The sill together with right end of strait hydraulically control the exchange, whereas only flow in the lower layer is critical at left end of the strait. The flow is laminar, however, measurements showed broadening of thermocline at the left side of sill (see. Fig.6). The computations by non-hydrostatic model were carried out with laminar viscosity and conductivity and resolution 250x8x100. The internal and external time step were 0.015 s and 0.001 s. The simulated density distribution also showed difference between thickness of interface on both sides of sill (see Fig.7). The detailed investigation of velocity field in Fig.8 shows presences of complicated flow structure at left side of the sill. The supercritical flow slows down in the point of internal hydraulic jump that causes countercurrent. It lifts dense water along the left side of sill and turns finally to left, forming broad interface layer. The broadening of pycnocline downstream of sill or contraction was frequently observed in the sea straits, however, it was attributed to the turbulent mixing only. The comparison of non-hydrostatic and hydrostatic calculations was carried out with the same resolution. Fig.9 indicates essential contribution of nonhydrostatic components at the slope and foot of the sill with the difference in velocities about 20%. Non-hydrostatic calculations is stable for high resolution, whereas hydrostatic calculations was unstable for the same internal step and requires to reduce internal step by one half.

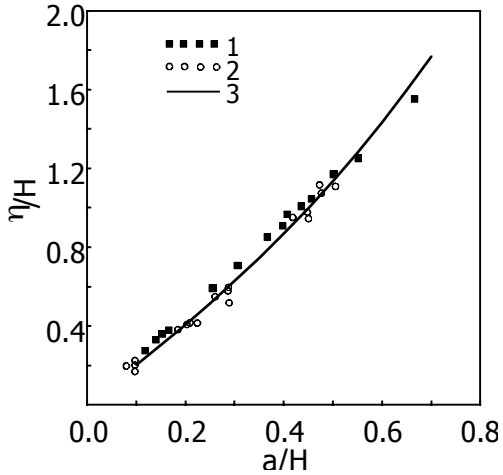

Figure 1: Runup on the vertical wall as a function of soliton height as measured by *Maxworthy* [1979] (1), *Zagriadskaya and Ivanova* [1978] (2) and calculated (3).

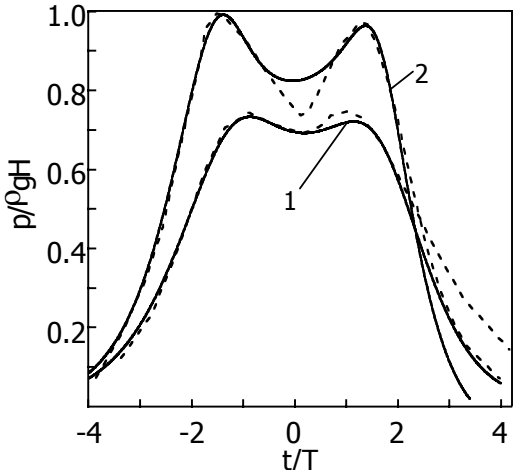

Figure 2: Time dependence of wave pressure for dimensionless soliton height *a/H* =0,5 (1) and 0.7 (2). Solid line is simulation and dash line is experiment (*Zagriadskaya and Ivanova* [1978]).

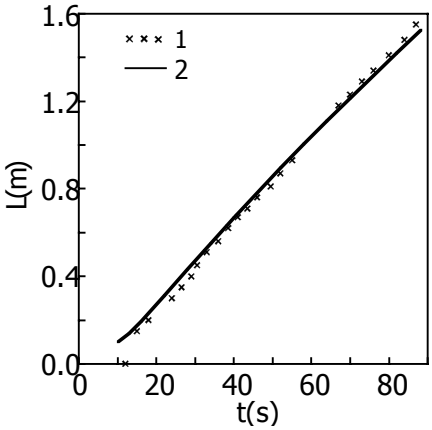

Figure 3: Intrusion length as a function of time in experiment 302 (*Maderich et al.* [2001]) (1) and calculated (2).

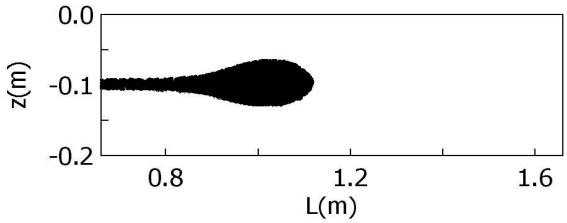

Figure 4: Computed intrusion visualized with markers.

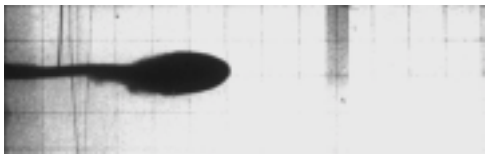

Figure 5: Dye-visualized intrusion in experiment 302.

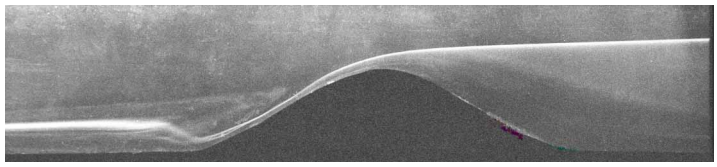

Figure 6: Photo of experiment 701 (*Maderich* [2000])

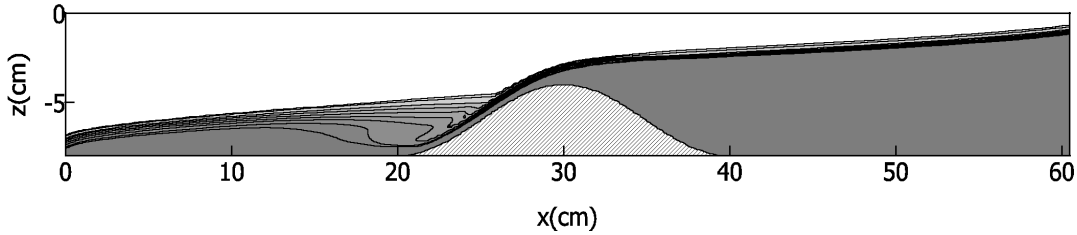

Figure 7: Computed density distribution for experiment 701.

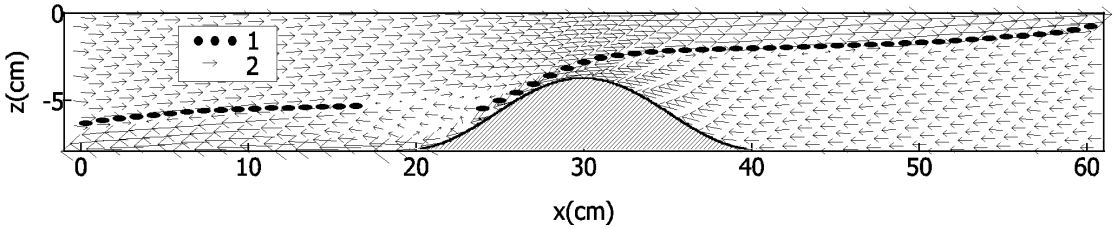

Figure 8: Interface position in experiment 701 (1) and non-hydrostatic velocity field (2).

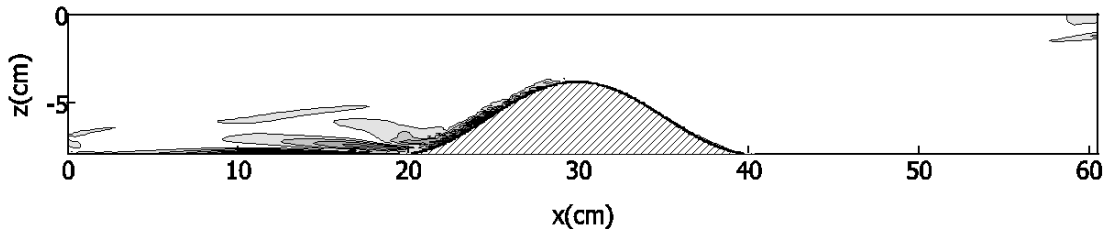

Figure 9: Module of difference between hydrostatic and non-hydrostatic velocity fields

4. Conclusions

The non-hydrostatic model for simulating of free-surface stratified flows in the coastal sea has been developed. The numerical algorithm is a non-hydrostatic extension of POM model and fully compatible with it. Several oceanographically motivated examples of non-hydrostatic currents were considered. They demonstrate the effectiveness of this tool for wide spectrum of coastal sea problems.

Acknowledgments: This study was partially supported by CRDF project "Improved methodology for assessing the impacts of the Aegean-Black Sea exchange".

References:

Blumberg, A.F. and Mellor, G.L. A description of a three-dimensional coastal ocean circulation model, in N.S. Heaps (ed.), *Three-Dimensional Coastal Ocean Circulation Models*, *Coastal and Estuarine Sciences*, vol. 4, AGU, Washington, DC, 1987, pp. 1–16.

Casulli V., Stelling G. S., Numerical simulation of 3D quasi-hydrostatic, free-surface flows. *J. Hydr. Eng., 124,* 678-686, 1998.

Maderich V. S., Two-layer exchange flows through long straits with sill. *Oceanic Fronts and Related Phenomena. Konstantin Fedorov Int. Memorial Symp., IOC Workshop Rep. Series*, N 159*,* UNESCO'2000, 326-331, 2000.

Maderich, V., van Heijst, G.J., Brandt, A. Laboratory experiments on intrusive flows and internal waves in a pycnocline. *J. Fluid Mech., 432*, 285-311, 2001.

Maxworthy T., Experiments on collisions between solitary waves. *J. Fluid. Mech., 76, 177—185*, 1976.

Zagriadskaya N. N., Ivanova S. V. Action of long waves on the vertical obstacle. *Izv. VNIIG, 138,* 94-101, 1988.

Fortnight shifts of circulation in Ise Bay and its effect on the hypoxia

AKIHIDE KASAI, SATOMI AKAMINE, TATEKI FUJIWARA

(Graduate school of Agriculture, Kyoto University. Kyoto, 606-8502, Japan, kasai@kais.kyoto-u.ac.jp, satomia@kais.kyoto-u.ac.jp, fujiwara@kais.kyoto-u.ac.jp)

TAKUMA KIMURA

(4th Regional Coast Guard Headquarters. 2-3-12 Irifune, Minato, Nagoya, 455-8528, Japan)

HIROKATSU YAMADA

(Fisheries Research Division, Mie Prefectural Science and Technology Promotion Centre. 1-6227-4 Shiroko, Suzuka, 510-0243, Japan)

1. Introduction

Ise Bay is one of the major ROFIs (regions of freshwater influence) on the Pacific coast of Japan (Fig. 1). Three large rivers flow into the bay head in the north and the water inside the bay is stratified through the year. In the south the bay opens to the Pacific Ocean via narrow Irago Strait, in which strong tidal currents mix the water. Water exchange between Ise Bay and the Pacific Ocean takes place through Irago Strait.

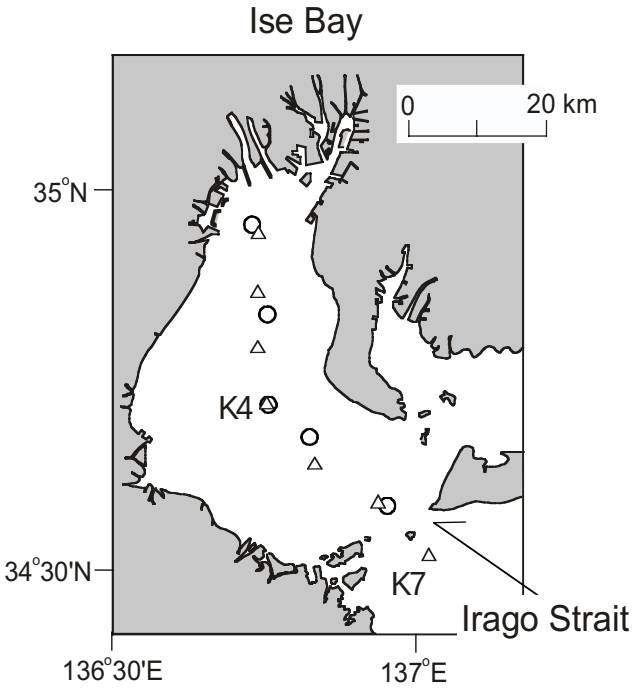

Figure 1: Map of study area. Triangles and circles indicate observation points by Kyoto University and Mie Prefectural Science and Technology Promotion Centre, respectively.

Recent surveys on Ise Bay have shown that the flow pattern is different from the classical estuarine circulation; the strait water does not intrude into the lower layer, but intrudes into the middle layer along the eastern coast of the bay in summer, because the density of the strait water is equivalent to that in the intermediate layer inside the bay (*Takahashi et al.*, [2000]; *Kasai et al.*, [2002]). This middle layer intrusion leads the hypoxia of the bottom bay water, which is excluded from the exchange circulation (*Fujiwara et al.*, [2002]). However, there are some observations that show the bottom layer intrusion of the strait water, following the classical estuarine circulation theory. These studies indicate the intrusion depth could change temporally, but its transition process and the mechanism are still unknown. In this study, therefore, we try to clarify 1) time change in the mixing condition at Irago Strait, 2) time change in the intrusion depth of the strait water, and 3) effects of the intrusion depth on the distribution of the hypoxia.

2. Observations

Observations of temperature, salinity, and dissolved oxygen (DO) concentration were conducted along the longitudinal section of Ise Bay. Observational stations are shown in Fig. 1. To elucidate the transition process of the intrusion depth and succeeding change in the circulation pattern and the DO

distribution, the observations were carried out repeatedly three times a month from June 2000 to August 2001.

3. Results and discussion

Figure 2 shows examples of the vertical profile of density at Irago Strait (Stn. K7). In the spring tide (thick lines), the water below 20 m was mixed well and nearly homogeneous. On the other hand, it was weakly stratified in the neap tide (thin lines). It is obvious that mixing condition at Irago Strait was strongly affected by the tidal strength. There is a negative correlation ($r^2 = 0.61$) between the tidal range and the density difference between 10 m and 55 m depth at the strait (Fig. 3). The stronger the tidal currents are, the more water is mixed.

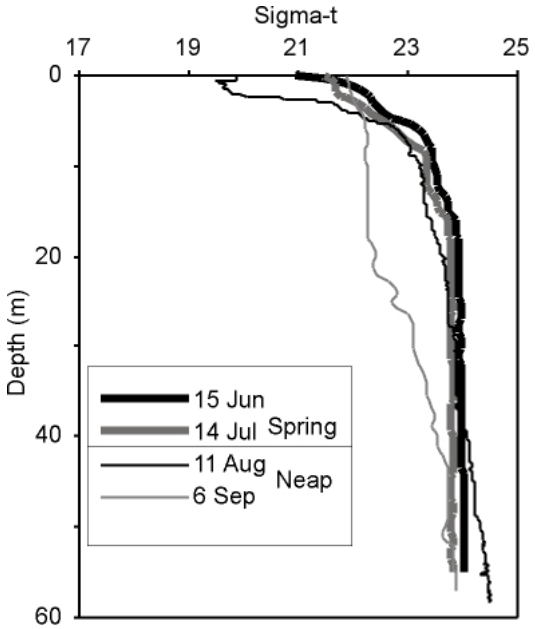

Figure 2: Vertical profiles of density at Irago Strait in the spring tide (15 June and 14 July) and the neap tide (11 August and 6 September).

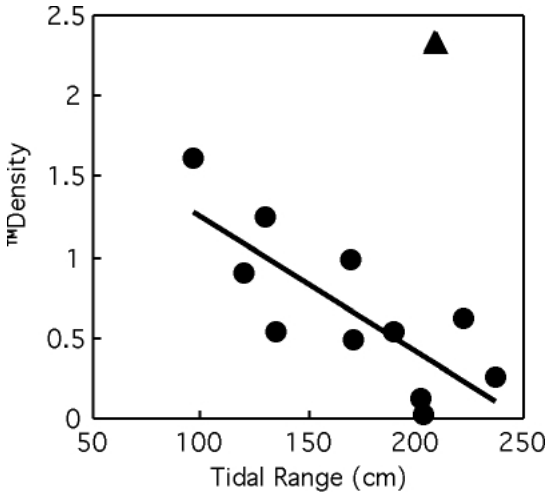

Figure 3: Relationship between tidal range and density difference (55m-10m depth) at Irago Strait (St. 7). The data shown by a trianlge is the exception because of the unsusual heavy rain.

Vertical distributions of density along the longitudinal section are shown in Fig. 4. In the spring tides, the density deeper than 15 m at Irago Strait was equivalent to that of the middle layer inside the bay. A prominent bottom front was created at the bay mouth (25-30 km from the bay head). This bottom front separated the Irago water from the dense bottom water inside the bay. On the contrary, at the neap tide, the densities deeper than 15 m at Irago Strait and inside the bay were similar to each other. It appears that the Irago water intruded through the bottom layer during the neap tide. The weaker tidal current insufficiently mixes the strait water as shown in Fig.2, and thus the bottom water inside the bay becomes lighter than that at the bay mouth where the water tends to stratify. This difference in density at the bay mouth leads the shift of the intrusion depth. The hydrographic condition changed in a short time period, according to the tidal strength.

In order to know the time change in the intrusion depth, we define the intrusion depth, assuming the strait water intrudes through the layer that has the same density as that of the strait water. First, the densities at three depths were selected in Irago Strait (Stn. K7): beneath the pycnocline, at the bottom, and their average as the representative densities of the intrusion water. Secondly the top, bottom, and

the centre of the intrusion depth inside the bay (Stn. K4) were defined as the depth that was the same density as those beneath the pycnocline, at the bottom and their average in Irago

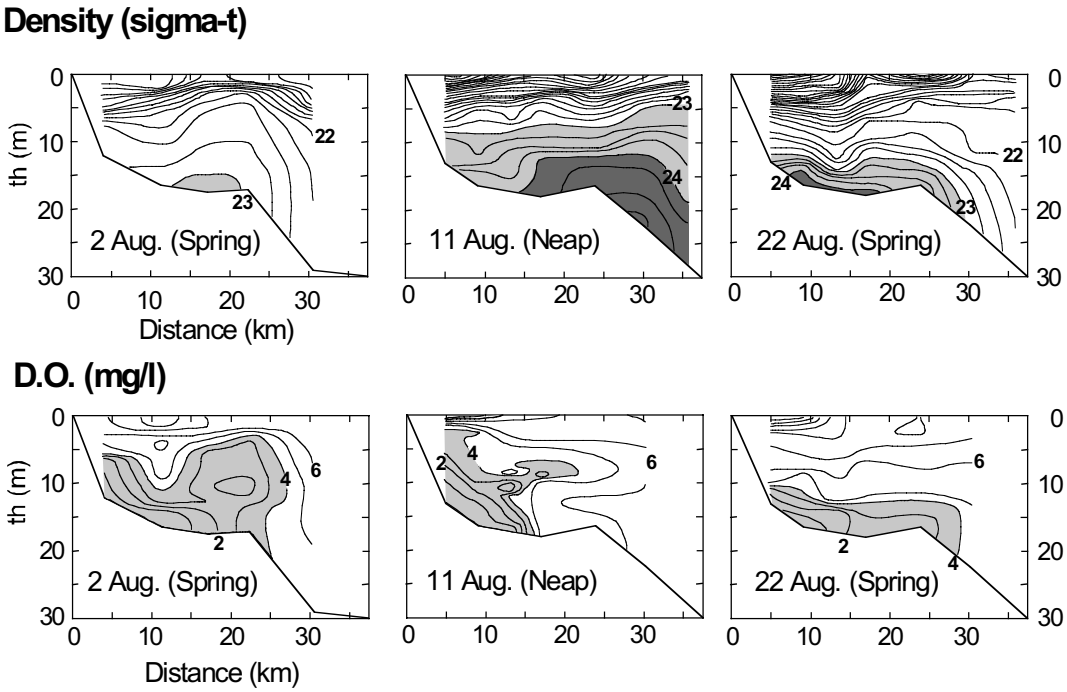

Figure 4: Vertical distributions of density and dissolved oxygen along the longitudinal section. Darker areas indicate dense water (> 23) in the upper pannels and hypoxic water (< 4 mg l^{-1}) in the lower pannels.

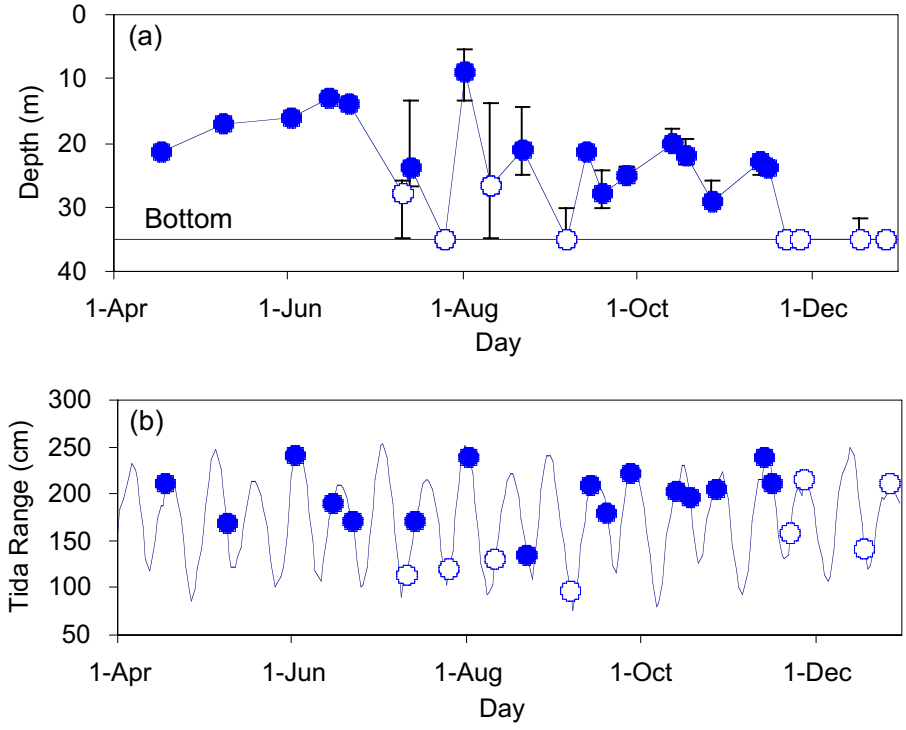

Figure 5: Time change in (a) the intrusion depth and (b) the tidal range. Open and closed circles indicate middle layer and bottom intrusion, respectively. Error bars in the upper pannel indicate the top and bottom depth of the intrusion layer.

Strait, respectively. The time change in the intrusion depth is shown in Fig.5. The strait water always intruded through the bottom layer in winter. In summer, on the other hand, the intrusion depth shifts frequently according to the tidal range; the strait water intrudes into the shallow layer during the spring tide than the neap. A significant correlation ($r^2 = 0.77$) was found between the intrusion depth and the tidal range (Fig. 6).

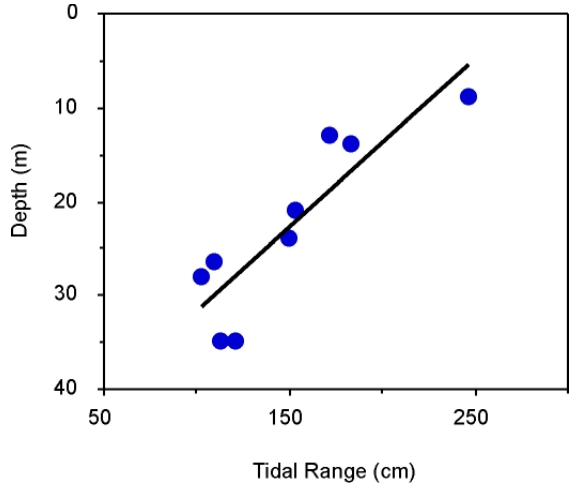

Figure 6: Relationship between tidal range and the intrusion depth.

The distribution of hypoxic water frequently changed due to the shits of the intrusion depth (Fig. 4). During the spring tides, the hypoxia distributed widely above the bottom. On the other hand, the hypoxic water was pushed to the bay head and/or uplifted to the middle layer by the oxygen-rich strait water during the neap. The patterns of the distribution of DO were similar to those of temperature (not shown here), indicating the hypoxia is affected by the flow pattern. Cold relict water becomes hypoxia at the bottom (*Kasai et al.*, [2002]), but its shape and/or distribution changes frequently. When the strait water intrudes through the middle layer (spring tide) the hypoxia develops in the lower layer, while it reduces by the bottom intrusion (neap tide).

References:

Fujiwara, T., T. Takahashi, A. Kasai, Y. Sugiyama, and M. Kuno, The role of circulation in the development of hypoxia in Ise Bay, Japan. *Estuarine, Coastal and Shelf Science, 54*, 19-31, 2002.

Kasai, A., T. Fujiwara, J. H. Simpson, and S. Kakehi, Circulation and cold dome in a gulf-type ROFI. *Continental Shelf Research*. in press.

Takahashi, T., T., Fujiwara, M. Kuno, and Y. Sugiyama, Seasonal variation in intrusion depth of oceanic water and the hypoxia in Ise Bay. *Umi no Kenkyu*, *9*, 265-271, 2000.

Numerical Simulation of Wave Transmission at Submerged Breakwaters compared to Physical Modeling

STEPHAN MAI

(Franzius-Institut for Hydraulic, Waterways and Coastal Engineering, Nienburger Str. 4, D-30167 Hannover, Germany, smai@fi.uni-hannover.de)

NINO OHLE

(Franzius-Institut for Hydraulic, Waterways and Coastal Engineering, Nienburger Str. 4, D-30167 Hannover, Germany, Nino.Ohle@fi.uni-hannover.de)

KARL-FRIEDRICH DAEMRICH

(Franzius-Institut for Hydraulic, Waterways and Coastal Engineering, Nienburger Str. 4, D-30167 Hannover, Germany, daekf@fi.uni-hannover.de)

CLAUS ZIMMERMANN

(Franzius-Institut for Hydraulic, Waterways and Coastal Engineering, Nienburger Str. 4, D-30167 Hannover, Germany, zi@fi.uni-hannover.de)

1. Introduction

The design of sea dikes requires knowledge about the wave parameter right in front. Especially the wave propagation along the foreland with structures like summer dikes or submerged breakwaters, determines the wave characteristics at the toe of the dike. Shoaling, refraction, wave breaking, bottom friction and wave transmission are the predominant processes within this area.

Standard numerical models, like SWAN (see *Ris. et al.* [1994]), are good tools for the simulation of these processes. Nevertheless physical model tests are still needed to calibrate the parameter and validate the numerical models.

This paper deals with the wave transmission at summer dikes respectively submerged breakwaters using the numerical model SWAN as well as laboratory tests in the *Large Wave Channel (GWK)* of the *Coastal Research Center (FZK)* and in the *Wave Basin Marienwerder (WBM)* of the *Franzius-Institute*, both located in Hannover, Germany. The focus is put on the analysis of wave spectra influenced by wave transmission.

2. Physical and Numerical Model Test

The model tests in the wave flume GWK with dimensions of 324 m x 5 m x 7 m were carried out at prototype scale. Figure 1 (left) shows the experimental set-up with a summer dike build on a foreland (top) and the wave breaking induced by the summer dike (bottom). The height of the foreland is 1.4 m. The summer dike had a crest height of 1.6 m above the foreland, a crest width of 3 m and a slope of 1:7. The parameters of the incoming wave field were varied from 0.6 m to 1.2 m for the significant wave height and from 3.5 s to 8.0 s for the peak wave period at water levels from 3 m to 4.5 m. The wave propagation was measured at 26 locations along the flume. A detailed description of the experiments in the GWK is given by *Mai et al.* (1999a).

The model tests in the wave basin WBM with dimensions of 40 m x 24 m x 1.1 m were carried out in a side channel with a width of 1.7 m. Figure 1 (right) shows the experimental set-up with a submerged rubble mound breakwater with a height of 0.5 m, a crest width of 0.2 m and a slope of 1:2 (top) and the wave breaking at the breakwater (bottom). The parameters of the incoming wave field were varied from 2.5 cm to 17.5 cm for the significant wave height and from 1 to 1.75 s for the peak wave period

at water levels of 0.45 m to 0.7 m. Further information on the experiments in the WBM is given by *Daemrich et al.* (2002).

The data, i.e. time series of water level elevation, collected in both experiments was analyzed in time domain and also in frequency domain. An example of this analysis is given in figure 2 and figure 3.

In addition to the physical model tests numerical model tests were carried out using the phase –averaged model SWAN *(*see *Ris,* 1997) applying the same boundary conditions (bathymetry, water level and wave spectrum). A description of the calibrated model parameter is given by *Mai* (1999b). An example of the results of the numerical analysis is given in figure 2 and 3.

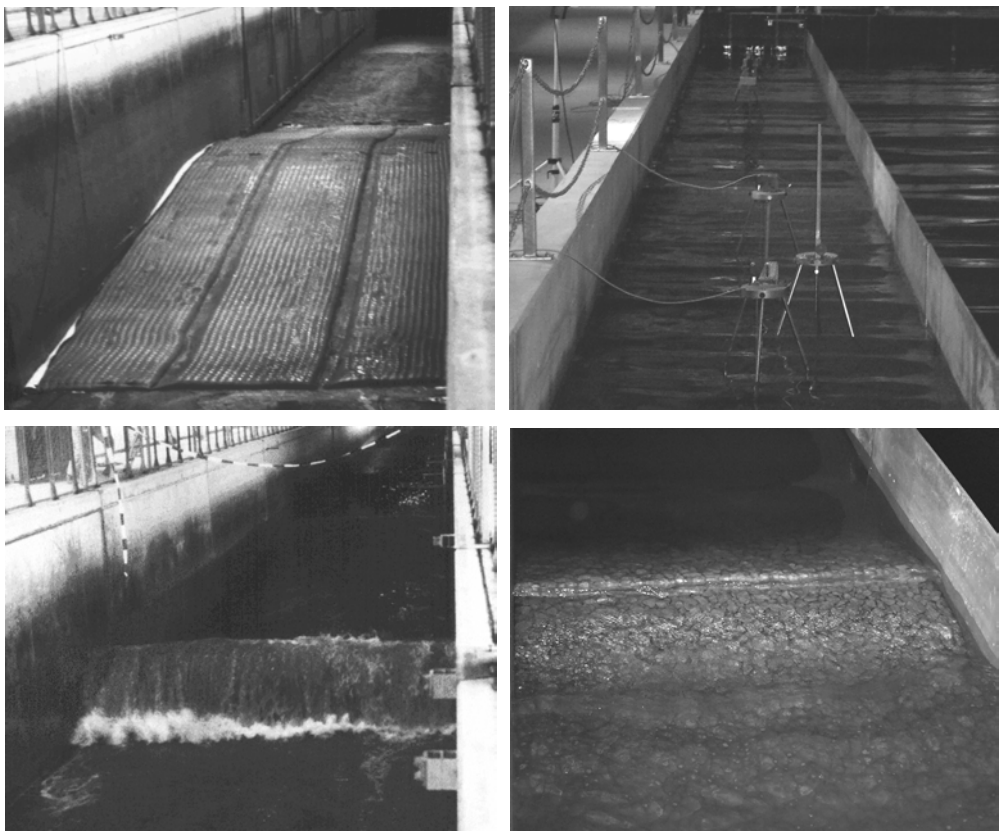

Figure 1: Experimental set-up in scale in the *Large Wave Channel* and the *Wave Basin Marienwerder* at the University of Hannover

3. Results

As shown in previous studies (see *Mai et al.* [1999b]) the characteristic wave parameters (significant wave height and peak wave period) were reproduced correctly by the numerical model. Figure 2 exemplifies this for the significant wave height measured in the GWK at a water level of 4 m and incoming waves with a significant wave height of 1 m and a peak period of 8 s. Besides that, the analysis of the wave spectra at two positions (see figure 2) in the flume also reveals a quite good agreement for the spectral properties as shown in figure 3. On the left hand side of figure 3 the non influenced wave spectrum in front of the submerged breakwater is shown. The right hand side of figure 3 gives a comparable chart for the influenced wave spectrum behind the breakwater.

Due to the transmission at the breakwater the wave spectrum is changed not only with respect to the total energy but also with respect to the spectral shape. The loss of total energy results in the decrease of significant wave height (see figure 2) while the change in the spectral shape results in lower mean

wave periods. The change in the wave spectrum is caused by non-linear wave transformation over the submerged breakwater resulting in a transfer of energy from the spectral peak to the higher harmonics (see *Isobe et al.* [1996]). However the spectral peak remains nearly constant (see *van der Meer et al.* [2000]).

A measure for the energy transfer is the change in the ratio of the energy of the second harmonic (2H) and the energy of the spectral peak (1H). Figure 4 (left) shows the increase of this ratio E_{2H}/E_{1H} directly at the summer dike for a water level of 4 m and incoming waves with a significant height of 1 m and a peak period of 8 s. The energy of the spectral peak with a frequency f_p was calculated by integration of the power spectral density from 0.5 f_p to 1.5 f_p. The energy of the second harmonic was set to the integral of the spectral density from 1.5 f_p to 2.5 f_p.

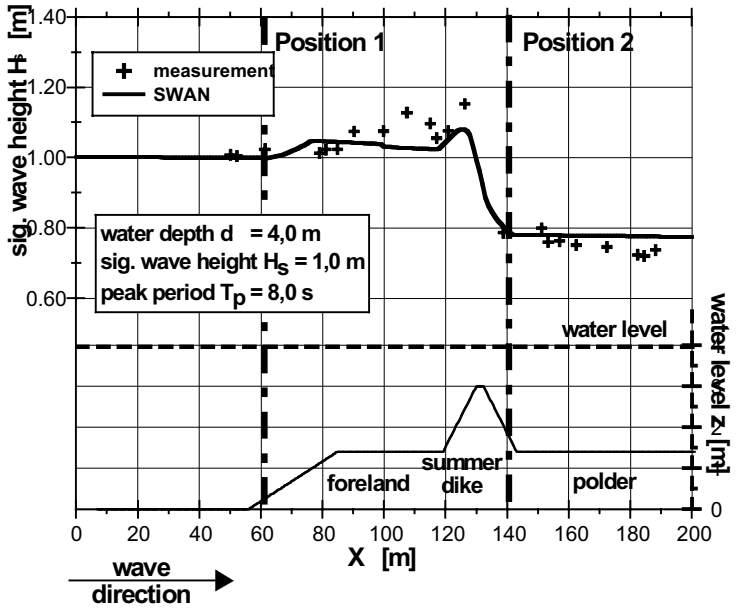

Figure 2: Change of the significant height of waves propagating over a foreland with summer dike - comparison of physical modelling (GWK) and numerical modelling (SWAN) (see *Mai et al.* [1999b]).

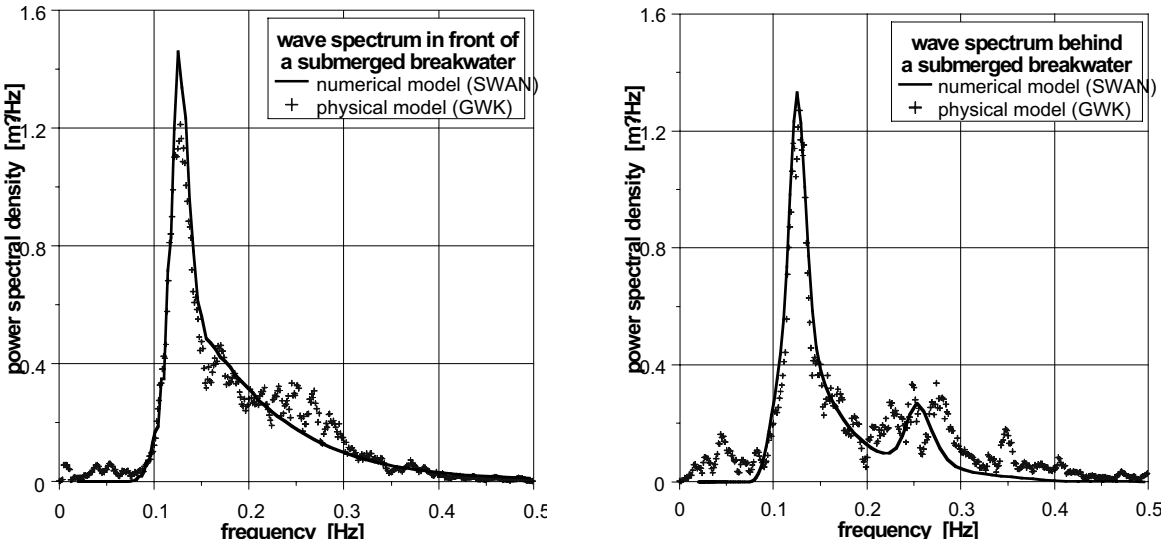

Figure 3: Spectrum of the incoming (left) and the transmitted (right) wave spectrum - comparison of physical modelling (GWK) and numerical modelling (SWAN).

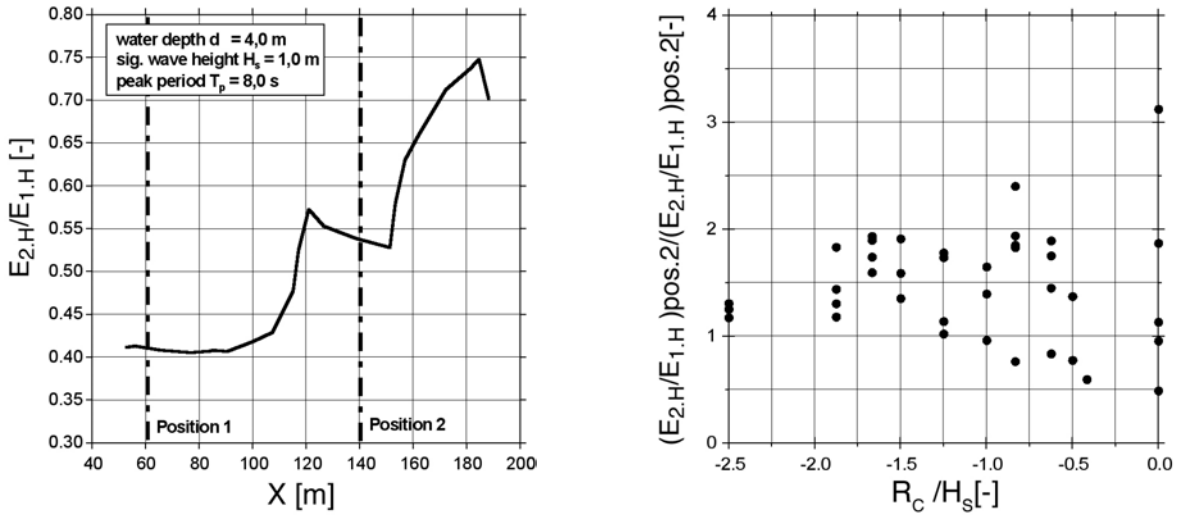

Figure 4: Ratio of the energy content of the first and second spectral peak (left) and normalised relative ratio of the energy content as a function of relative freeboard (right)

The change in the ratio E_{2H}/E_{1H} due to wave transmission is given in figure 4 (right) as a function of the relative freeboard, i.e. the ratio of negative water depth over the crest of the breakwater and the significant wave height. Except for small relative freeboards, i.e. very small transmission coefficients, the ratio E_{2H}/E_{1H} always exceeds unity. Similar results were also given by *van der Meer et al.* [2000]. The influence of wave transmission on the spectral shape diminishes for high relative freeboards.

References:

Daemrich, K.-F., Mai, S. and N. Ohle, Wave Transmission at Rubble Mound Structures, *Proceedings of the 1st German-Chinese Joint Symposium on Coastal Engineering*, Rostock, Germany, 2002 (in print)

Isobe, M., Watanabe, A. and S. Yamamoto, Nonlinear Wave Transformation due to a submerged Breakwater, *Proceedings of the 24th ICCE*, Orlando, Florida, pp. 767-780, 1996

Mai, S., Ohle, N. and K.-F. Daemrich, Numerical Simulations of Wave Propagation compared to Physical Modeling, *Proceedings of HYDRALAB-Workshop*, Hannover, Germany, pp. 217 - 226, 1999a

Mai, S., Ohle, N. and C. Zimmermann, Applicability of Wave Models in Shallow Coastal Waters, *Proceedings of the 5th International Conference on Coastal and Port Engineering in Developing Countries* (COPEDEC), Cape Town, South Africa, pp. 170-179, 1999b

Ris, R.C., Holthuijsen, L.H. and N. Booij, A Spectral Model for Waves in the Near Shore Zone, *Proceedings of the 24th ICCE*, Kobe, Japan, pp. 60-70, 1994

Ris, R.C., Spectral Modelling of Wind Waves in Coastal Areas, Communications on Hydraulic and Geotechnical Engineering, *Report No. 97-4*, TU Delft, 1997.

Van der Meer, J.W., Regeling, E. and J.P. de Waal, Wave Transmission: Spectral Changes and its effects on run-up and overtopping, *Proceedings of the 27th ICCE*, Sydney, Australia, pp. 2156-2168, 2000

Coastal cell circulation driven by tidal and longshore wave-generated currents detected by Landsat-7

MAURICIO ALMEIDA NOERNBERG

(Center for Marine Studies - UFPR, P.O. Box 50.002, 83255-000, Pontal do Paraná, Brazil, mauricio@cem.ufpr.br)

EDUARDO MARONE

(Center for Marine Studies - UFPR, P.O. Box 50.002, 83255-000, Pontal do Paraná, Brazil, edmarone@ufpr.br)

1. Introduction

Mid size circulation cells, as mega rip currents, are not a common features in sandy exposed beaches with a rectilinear shape. In a very fortunate occasion, it was possible to identify this kind of feature, of around 9 km size, using a single Lansat-7 image. It occurred in the South Brazilian Bight area, at the Paraná coastal region, in the southern part of the Paranaguá bay mouth, where a post-frontal high wave energy situation, in combination with the particular configuration of the beach and bathymetry, as well as spring tide conditions, allowed the formation of the coastal cell. Apart of showing a potential explanation for the fate of the observed mega rip formation, this work shows that the use of Landsat imagery is a powerful tool to study these phenomena.

2. Area Characteristics

The studied sandy beach area is located on the central region of Paraná State, South Brazil (25^{o} 40' S; 48^{o} 25' W) and has an extension of 32 km. The Northern part belongs to the mouth area of the Paranaguá Bay, where alternate coastline accretion and erosion processes, of around hundreds of meters in few years, has occurred (*Noernberg*, 2001). The tide on the inlet is semidiurnal with a mean range of 1.7 m, and maximum ebb currents reach 130 cm/s. Waves studies has shown maximum wave heights in the range between 2.3 and 3.9 meters, coming from SE and ESSE and periods in the range 11.9 to 16.8 sec. The beaches' characteristics vary from dissipative on North to intermediate on South. The sediment is composed mainly by well-selected very fine sand to fine sand in central area (*Borzone et al*., 1996). In the Southern part, intense erosive processes have occurred, which are located in urban-resort areas. The dominant processes that act in the region are linked with the atmospheric inputs, mainly related with frontal passages, as wind waves, and the tidal dynamic imposed by the Paranaguá bay outlet.

3. Environmental Conditions and the Landsat Image

After the action of a frontal system, with winds from SW acting for 7 days and force up to 13.7 m/s in 09/23/99, a Landsat-7 ETM+ image taken in 09/26/99 was acquired, corresponding to a spring tide period at the beginning of the flood. The image analysis showed that the incident waves had a period of 9.1 s and a wavelength of 130 m, reaching the isobath of 20 m from 115 degrees.

The use of a mask to improve the variance response of the water, eliminating the land signal, was applied over the image. The band 3 (660 nm) of Landsat was used because it shows better correlation with suspended sediment, particularly when high values occur (between 10 and 50 mgl^{-1}) (*Choubey and Subramanian*, 1990). The use of the observed changes in the suspended sediment concentration allowed for the identification of return/rip currents, which may vary in dimension, spacing and intensity along the beach area. The increase on size, intensity and spacing of these currents is caused by the increase of the incident waves energy.

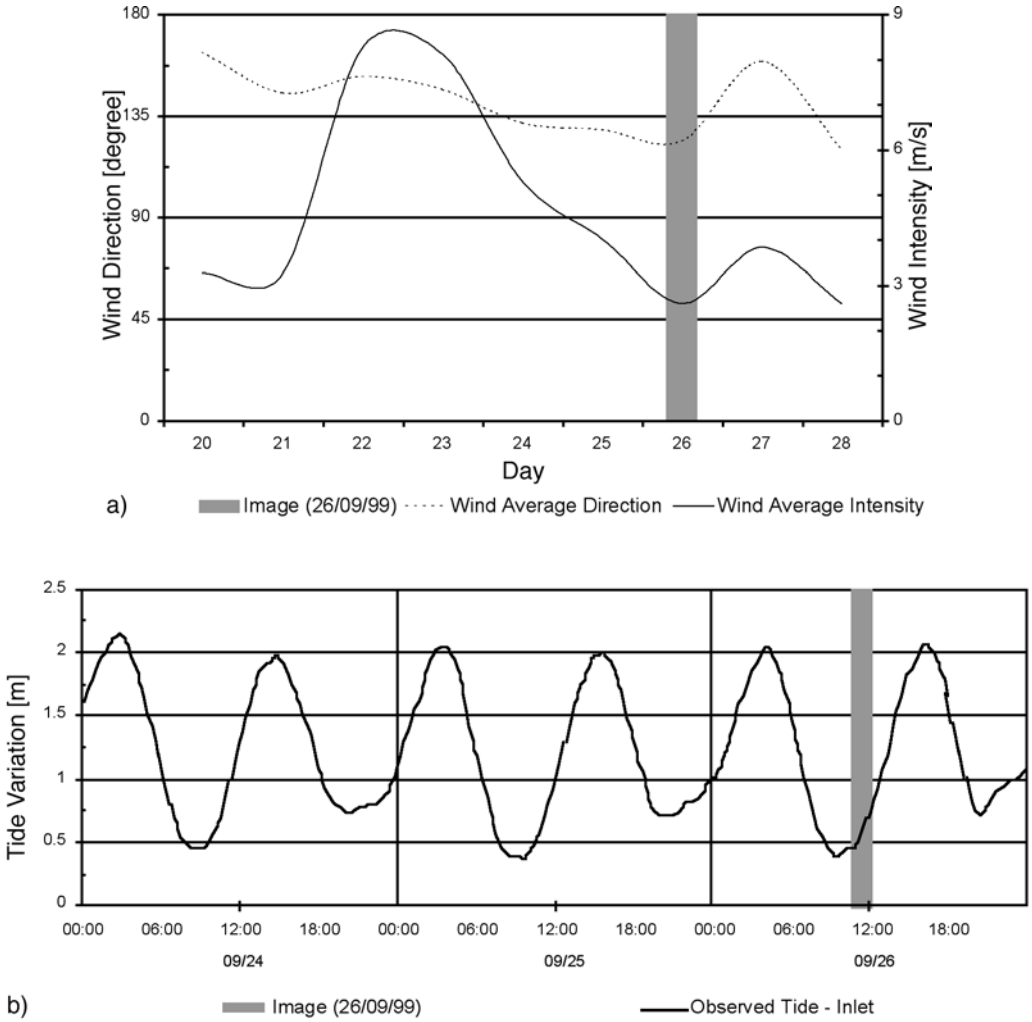

Figure 1 Environmental conditions during the image acquisition: a) wind direction and intensity, b) tide variation.

4. The Cell Circulation

Considering the whole beach extension, the Paranaguá Bay delta influence and the waves and tides action, it is possible to better understand the circulation cell of larger scale observed at the central part of the studied area. This feature is formed at the convergence of both coastal currents moving one southward and other northward. Near the mouth of the bay, the surf zone is larger, not showing rip currents. Southward, on the other hand, the extension of the surf zone diminishes. Ten kilometres south of the outlet, rip currents appears, 150 away one of the next and with a extension of about 170 m seaward. The spacing and length of the return currents increases progressively to South, up to 18 km from the bay mouth, reaching values of around 350 m and 550 m, respectively, indicating higher wave energy and that they arrive more parallel to the coast. Accordingly to this size, they can be classified as erosive mega rip currents (*Short*, 1985). South of the central part of the beach, the size and spacing diminishes, but they remain all along the southern part of the beach.

In the central part a strong convergence zone was identified as the main reason for the appearance of the mega rip. The southern coastal current is related with the ebb current coming from the Paranaguá bay inlet, moving to South due to bathymetric constrictions (islands and bars). The wave refraction at the delta as well as the not perpendicular propagation with respect to the beach also contributes for the southward flow. On the other hand, the longshore currents moving to North are mainly generated by the oblique incidence of the surface waves. Both currents converge on the middle part and, then, flows

seawards. This convergence happens in the same area where the stronger return currents were observed. The flow seaward surpasses the 10 m isobath, reaching up to 9 km off the coast as a mega-rip current.

However, this is a process with intense time-space variability and depends of the energy supply of the frontal system, acting with a week time scale, at the moment of the image acquisition, which must be considered. Sets of several as clear images for different conditions and periods need to be studied to allow more general conclusions.

This circulation cell is caused by the combination of the large energy waves interacting with the coastline and bathymetry, as well as the spring tidal currents and represents an important process that contributes in the exchange of material and energy between the surf zone and the shallow platform. A better understanding of this type of processes could allow for a better explanation of sediment transport related problems.

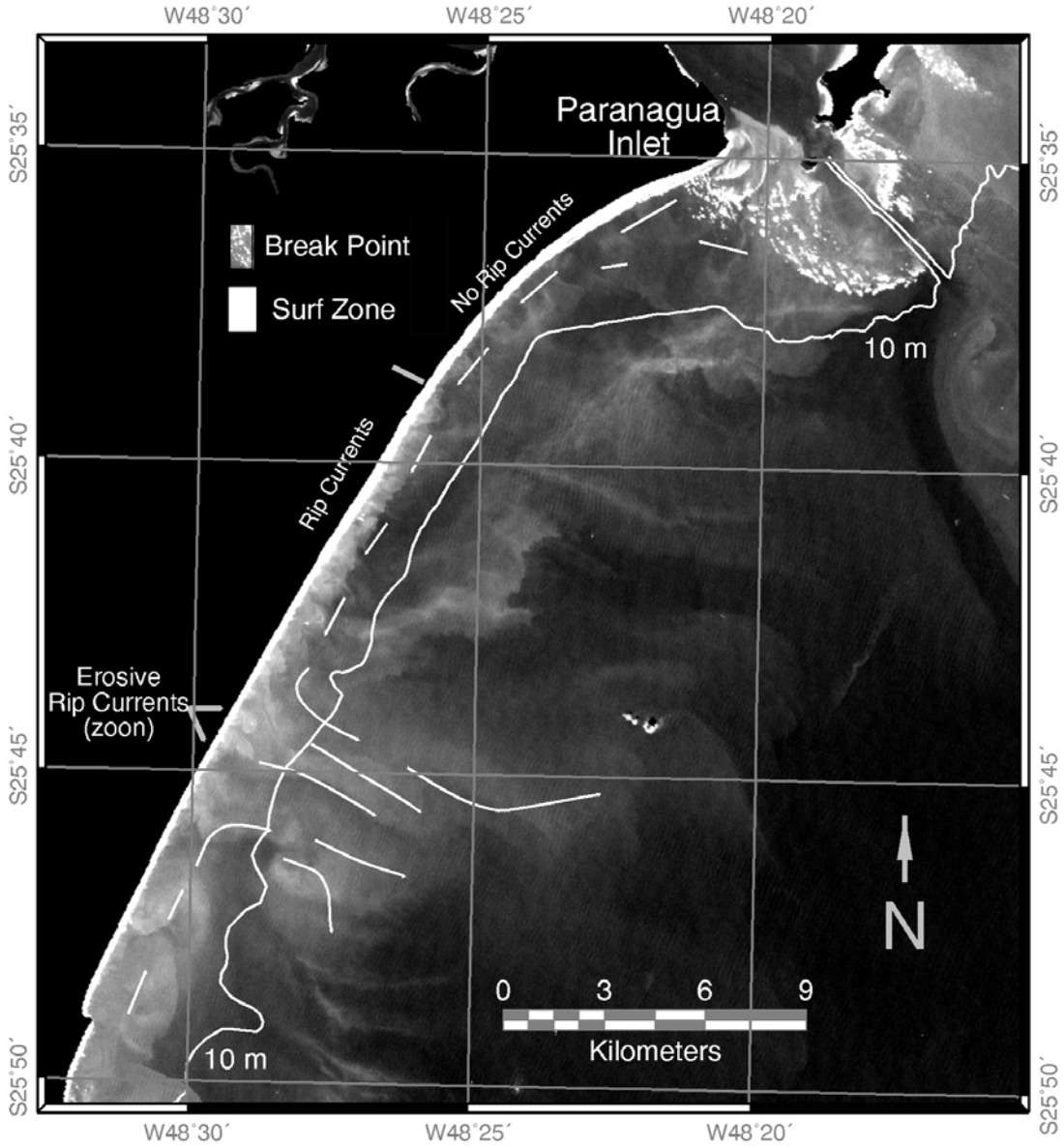

Figure 2 Mega-rip current detected by Landsat-7 ETM+ (lighter areas mean greater suspended sediments concentration)

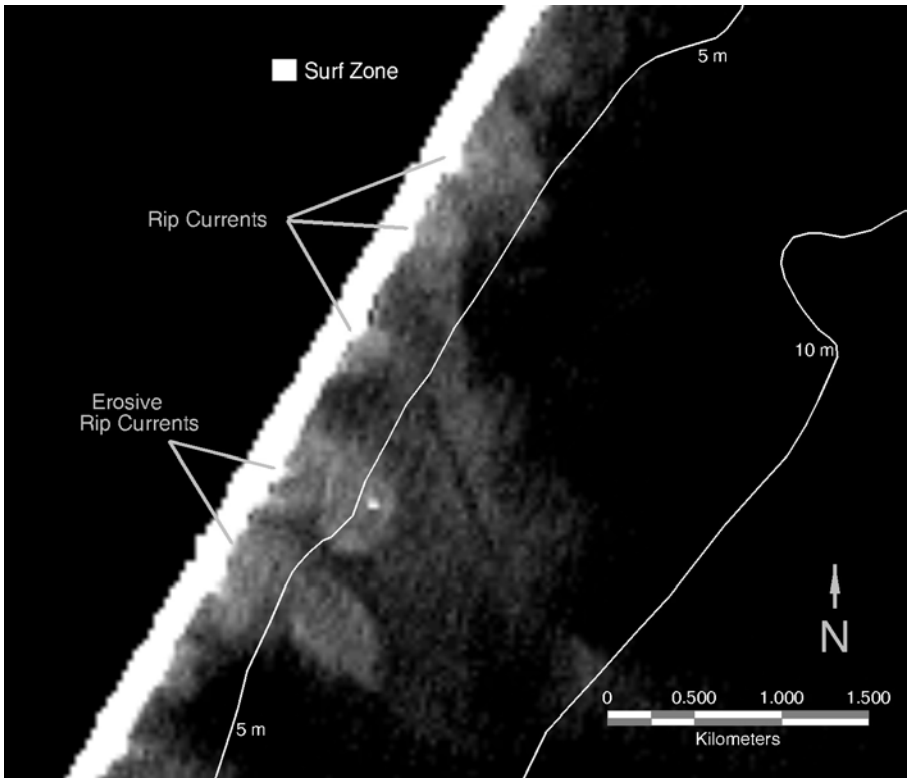

Figure 3 Zoon showing erosive rip currents.

Acknowledgments: The authors are grateful to the cooperation APPA-CEM (Administração dos Portos de Paranaguá e Antonina – Centro de Estudos do Mar) for the concession of a grant and support.

References:

Borzone, C.A, Souza, J.R.B., Soares, A.C., Morphodynamic influence on the structure of inter and subtidal macrofaunal communities of subtropical sandy beaches, *Revista Chilena de História Natural*, 69, 565-577, 1996.

Choubey, V.K. and Subramanian, D.W., Nature of suspended solids and IRSIA-LISSI data: a case study of Tawa Reservoir (Narmada Basin), *Remote Sensing of Environment*, 34, 207-215, 1990.

Noernberg, M.A., *Processos morfodinâmicos no complexo estuarino de Paranaguá – Paraná – Brasil: um estudo a partir de dados in situ e Landsat-TM*, Ph.D. Thesis, Universidade Federal do Paraná, Curitiba, Brazil, 2001.

Short A.D., Rip-currents type, spacing and persistence, Narrabeen beach, Australia, *Marine Geology*, 65, 47-71, 1985.

HYDRODYNAMICS OF COLEROON INLET AND ITS INFLUENCE ON PICHAVARAM MANGROVE ECOSYSTEM, EAST COAST OF INDIA

P.KASINATHA PANDIAN[1], M.V.RAMANAMURTHY[2], S.RAMESH[1] AND S.RAMACHANDRAN[1]

[1] *Institute for Ocean Management, Anna University, Chennai-600 025, INDIA*

E-mail : kasinath_iom@yahoo.com

[2] *Integrated Coastal and Marine Area Management – Project Directorate (ICMAM-PD), Department of Ocean Development, NIOT Campus, Pallikaranai, Chennai-601 302, INDIA. E-mail:* mvr@icmam.tn.nic.in

ABSTRACT

Tidal inlets serve as an extremely important conduits for the exchange of water and sediments between bays, lagoons or estuaries and the continental shelf. Ecosystem that depends on these inlets, often influenced by morphological changes at inlets due to natural and man-made activities. Pichavaram mangrove swamp lies between Coleroon and Uppanar estuaries, located in the east coast of India. These mangrove swamps receives seawater through Coleroon located at a distance of 15 km. Recent studies conducted at the Pichavaram swamps revealed that the degradation of mangroves is taking place, which has been attributed to lack of tidal prism and siltation in mangrove system.

In this study, an attempt has been made to study the hydrodynamic characteristics of the inlet and interconnection of creek system of Coleroon inlet. Physical measurements have been carried out to study the dynamic and sediment characters. The influx of creek system vary with the season and high influx rates are observed immediately after the monsoon period. The flushing of sediments at the inlet is due to freshwater runoff during monsoon period.

Numerical modelling study has been undertaken using one dimensional flow model (DYNLET1) to estimate the flow pattern in the creek system. It is observed from the study that making artificial channels at locations identified through modelling could improve the flushing characteristics of mangrove ecosystem. This will save the mangroves from degradation and it will enhances the flushing rate.

Key Words: Tidal inlet, Coleroon, Pichavaram, magroves, numerical modelling

1. Introduction

In the Cauvery delta, the mangrove vegetation is spread irregularly and grows close to Pichavaram. The mangrove of Pichavaram is located on the Coromandal coast, 250 kms south of Chennai city, at the northern extremity of the Cauvery delta in Tamil Nadu state of south India. Geographically it is located at 11º 25' N and 79º 47' E. It is a highly populated region, but the mangrove is relatively well preserved because it enjoys the status of Reserved Forest since 1880 (Meher Homji, 1991). As the forest covers an area of 1400 ha, this represents a human pressure of atleast 18 persons per ha of forest (Kerrest, 1981).

The mangrove is located between the Vellar river in the north, the Coleroon river in the south and the Uppanar river in the west. It communicates with the sea by a shallow opening, which is the only mouth in the sandy littoral strand. The Coleroon river, an important branch of Cauvery river, receives most of its contribution (about 75%) from the so called northeast monsoon, during October to December due to depressions and cyclones formed in the Bay of Bengal. The Pichavaram mangrove is

linked to a system of irrigation, receives enough water from January to March but experiencing extreme phase of dryness during summer from April to June. This situation improves towards the middle of July, based on southwest monsoon. Avicennia marina and Rhizophora are the two major species of mangroves seen on the Pichavaram(Meher Homji, 1991).

2. Materials and Methods

The Pichavaram mangrove is linked with the sea by number of channels and the rivers Coleroon, Vellar and Uppanar. The channels are shallow in depth, approximately 1 m, and width varies from 5 to 200 m. In the southern part channels becomes narrow with mud flats emerging at the lowest tides. Therefore, in order to study the hydrodynamics of the southern part, that is on the Coleroon inlet system, physical measurements have been carried out during 1999 and 2000 in four different phases such as southwest monsoon, northeast monsoon, fair weather period and presouthwest monsoon. The physical measurements were made on tides, currents, channel cross-section and sediment characteristics to analyze the influence of flow conditions on sedimentation at mangrove swamp. Self recording RCM 7 currentmeters have been used for current measurements and self recording tide recorder WTR 9 of Aanderaa Instruments, Norway, have been utilized for the tide measurements at 6 locations (Stations C1 to C6) starting from Pichavaram inlet mouth (C1) in the north to Coleroon estuary (C6) in the south. Sediment samples have also been collected and analysed for their mean sizes. All these data has been utilized for the modeling study using DYNLET1 (Amein and Cialone, 1993) one dimensional flow model.

3. Results and Discussion

Tides

Tides were measured at 6 locations at 30 minute interval. Tide is semi-diurnal in nature with slight inequality. The spring tidal range at off Pichavaram mangrove swamp is 0.9 m and neap tidal range of 0.3 m. The time lag of occurrence of high and low tides at difference stations with reference to open sea tides off Pichavaram during four phases of observations and the ratio of tidal range at the location to open sea have been measured. As the tide propagates from the Coleroon river (stn C5) to Pichavaram mangrove swamp, which is located between C4 and C1. The tidal range dampens by 30 % when it reaches to inlet point of mangrove swamp and about 40 % at the extreme end of the mangrove swamp. Since most of the time in a year, the circulation is governed by tides, the understanding of tide induced currents will help in planning management solutions for regeneration of mangroves.

Currents

Current speed and direction were measured at 6 locations where tides were measured. These currents are mainly tide induced and the direction is parallel to longitudinal axis of the channels. The magnitude of the currents and direction at different locations have been recorded. The Pichavaram mangrove swamp has two inlets viz 1) Coleroon (stn C5) and 2) Chinnavaikkal (stn C1). The current observations indicate that the flow is governed by the Coleroon inlet though it is located at distance of 11 km from the mangrove swamp. The reason for the same can be attributed to existence of equilibrium at tidal inlet between tidal prism and long shore sediment transport. The bed slope variation between inlet mouth and extreme point in the mangrove swamp is 50 cm, which is mild slope that favours the tidal flux entry.

Longshore Sediment Transport

Longshore sediment transport on this Pichavaram coast is high in August for about 72 x 10^3 m^3/month and it was low from January to March at a rate of < 7 x 10^3 m^3/month. The transport was towards north from March to October amounting to 326 x 10^3 m^3/year and towards south from November to

February about 88 x 10^3 m^3/year. The annual gross transport was 414 x 10^3 m^3/year and net transport was 238 x 10^3 m^3/year towards north. The sediment transport rate along the shorefront of Pichavaram is relatively low as compared to the rest of the east coast indicating that the movement of littoral drift is relatively less in this part (INDOMER, 2000).

Modeling Study

Pichavaram mangrove wetlands receive freshwater from Uppanar river during northeast monsoon and tidal water (seawater) from Coleroon river inlet and Chinnavaikkal for all seasons. Due to sparse rainfall, the freshwater supply is reduced resulting in closing of inlets. The Chinnavaikkal inlet is almost closed due to sedimentation at inlet which is a usual phenomenon due to wave induced littoral drift. Normally the inlets that are closed due to littoral drift are opened in monsoon by high river flow. If sufficient inflow from river is not there, they remain closed for all the seasons. The Coleroon inlet is open because of sufficient volume of tidal water exchange and river water flow. Therefore, the only source of water, available for mangrove areas is Coleroon inlet for all seasons.

The Pichavaram mangrove system receives the seawater from Coleroon through creek system for nutrient cycling. In order to sustain or regenerate the mangrove areas, understanding of flow field in the creek system is necessary. Hence, the application of one dimensional flow model DYNLET1 (Amein and Cialone, 1993) has become essential to study the flow field and to arrive suitable measures to increase the flow in mangrove system. Data collected during physical measurements have been used as input for the model. The other relevant data have been suitably assumed for setting up the model.

From the application of model, it has been observed that creation of artificial channels will improve the flushing characteristics. Therefore, several locations have been identified for the artificial channels by running one dimensional model DYNLET1 based on the slope characteristics of the locations.

4. Conclusions

Based on the data collected from field measurements, a numerical study was conducted using one dimensional flow model DYNLET1 for the computation flow field in the creek system. The water levels observed at C6 and C1 are considered as open boundary condition and constant water level is improved at C2. Then the model was run for 6 tidal cycles and the predicted results are in agreement with the observed tides and currents. In order to improve the flow in the mangrove swamp, artificial channels were suggested at several locations considering that it will produce fruitful results in saving the mangroves.

References

Amein, M. and Cialone, M.A. (1993) “DYNLET1 : Dynamic Implicit Numerical Model of One Dimensional Tidal Flow Through Inlets”, Instruction Report CERC-93-3, U.S.Army Engineer Waterways Experiment Station, Coastal Engineering

INDOMER (2000) “Abstract Report on Hydrodynamics Study at Pichavaram Tidal Inlet”, Indomer Coastal Hydraulics (P) Ltd., Goa, Report submitted to M.S.Swaminathan Research Foundation, chennai, 45 p.

Meher Homji, V.M. (1991) “Mangroves of the Kaveri Delta”, In: Coastal Zone Management, (ed) R.Natarajan, S.N.Dwivedi and S.Ramachandran, Ocean Data Centre, Anna University, pp 236 – 248.

Kerrest, R. (1981) “Contribution to the Ecological Study of the Pichavaram Mangrove”, (in French), Doctoral Thesis, University of Toulouse, France.

MARITEC (1997) “Bathymetric Survey of Pichavaram Mangrove Swamp”, Maritec Corporation (India) Ltd., Chennai, Report submitted to M.S.Swaminathan Research Foundation, chennai, 88 p.

Tissot, C. (1987) “Recent Evolution of Mangrove Vegetation in the Cauvery Delta : A Palynological Study”, J. Mar. Biol. Assn. India, 29 : 16 – 22.

Month-long ADCP-ased turbulence measurements in a tidal inlet

Harvey Seim, (*Department of Marine Sciences, University of North Carolina at Chapel Hill, NC*, hseim@email.unc.edu)

Jim Hench and Rick Luettich, (*Institute of Marine Sciences, University of North Carolina at Chapel Hill, NC*, hench@email.unc.edu, luettich@email.unc.edu)

1 Introduction

Tidal inlets are likely sites of enhanced turbulent mixing owing to the high flow speeds and strong shears that often characterize them. These same qualities make the collection of turbulence measurements difficult. There are relatively few turbulence measurements in sea straits, and almost all have been collected with free-falling microstructure profilers (Wesson and Gregg, 1994; Gregg et al., 1999; Peters, 1999) though moored techniques have been used recently (e.g. DiIorio and Yuce, 1999). These measurements are typically intense in space but rather limited in time. We here present observations of the vertical components of the Reynolds stress collected with an acoustic doppler current profiler (ADCP) in an inlet connecting a small inland sea and the ocean. A different perspective on turbulence variability and its controls is gained from the time-intensive, vertically-resolved but spatially-limited measurements.

The technique of using an ADCP to measure the Reynolds stress has been recently popularized (Lu and Lueck, 1999; Stacey et al., 1999a; Stacey et al., 1999b). Lu and Lueck (1999) provide a brief review of the various techniuqes employed. The "variance" technique used herein relies on the geometry of the system and for a four beam configuration requires a nearly exact upright orientation. Significant tilt leads to smearing of the vertical components of the Reynolds stress tensor into other components of the tensor in the instrument frame of reference.

The Reynolds stress measurements were collected as part of a program studying inlet circulation. Three moorings, each consisting of an upward-looking ADCP and a pair of SeaBird microcats, were deployed for approximately 7 weeks around Beaufort Inlet, NC in August and September, 2001. In addition to the mooring array deployment, 3 anchor stations of 13 or 25 hour duration were occupied, during which time continuous ADCP measurements and CTD profiles at 10 minute intervals were collected. This note focuses on the ADCP observations collected in the inlet throat.

An upward-looking, 4 beam 1200 kHz RDI workhorse sentinel collected the velocity estimates used to form the Reynolds stress. The ADCP was housed in a bottom frame that was anchored by stakes jetted into the bottom by divers. The frame was leveled to within 1-2 degrees of horizontal. The beams were inclined at 20 degrees to the vertical and data were stored in beam coordinates. The instrument pinged once a second and collected 600 samples over 10 minutes every half hour. Mode 1 (RDI, 1998) was used with 30 centimeter bins, resulting in an approximate single ping standard deviation of 10.9 cm/s according to RDI software. Observations from the first 17-day deployment are used below. Means and variances of the along-beam velocities and unbiased estimators of two

components of the Reynolds stress tensor (Stacey et al., 1999a) were formed for each 10 minute average of data at each bin location.

2 Results

Beaufort Inlet connects Bogue Sound to the Atlantic Ocean. The bathymetry in the region is generally shallow ($< 10\ m$) but complicated by the presence of dredged channels that create relatively deep pathways through the inlet. Tides in the Atlantic are dominated by the 0.5 m M_2 component, but within the sounds tides are difficult to identify, hence the inlets are small enough to choke the tide. Currents are tidally dominated and this is reflected in the Reynolds stress variability. Currents typically exceed 1 m/s on ebb but peak at values closer to 0.5 m/s on flood. The figure shows two time periods, one near times of spring tide and one near neap tide. Peak currents on spring ebb are nearly 2 m/s, and exceed 1 m/s 2.5 meters above the bottom (mab) on most tides. Currents on flood exceed 1 m/s only on spring tides and typically reach on 0.5 m/s.

Reynolds stresses exceed 50 cm^2/s^2 on spring ebb tides and typically reach 20 cm^2/s^2 on most ebb tides, but seldom reach 10 cm^2/s^2 during flood tide. Reynolds stress decreases roughly linearly with height above the bottom but during strong southerly winds, and especially during ebb, very large stress is seen in the upper 2-4 m measured by the ADCP.

The remarkable difference between ebb and flood bottom stress persists over the spring-neap cycle. Ebb stress is typically 3-5 times as large as that on flood and reflects the much larger currents on ebb than on flood. This is likely related to the strong mean export in this part of the inlet; mean currents over the measurement period are directed seaward at 0.1-0.2 m/s. Net riverine inflow to the system is small, and unless other inlets to the sounds are importing seawater, there must be net inflow over some part of the inlet.

As in Stacey et al. (1999b) the stress measurements are somewhat noisy so composite tidal cycles have been formed by averaging 4 tidal cycles near maximum and minimum tidal range, similar to Peters (1999). These composites are then used to examine vertical structure of the Reynolds stress, turbulent production and the mixing length.

Vertical shear of the horizontal current is maximum near the bed and decreases to less than 0.02 s^{-1} within 5 mab. Above this height the shear on ebb extends to the surface during low wind conditions and is essentially zero on flood, but can be of either sign in the upper water column when the winds exceed 5 m/s. Southerly winds reinforce flood tide shear and can decrease or reverse shear in the upper water column on ebb. This can be seen in contours of the neap tide composite data (Figure 1) where the shear changes sign in the upper water column.

The strength of the turbulent production can be estimated as $P = - < u'w' > (\partial \overline{u}/\partial z)$; estimates from the composite data are presented in Figure 1. Peak values exceed $10^{-4}\ m^2/s^3$ near the bed. The bottom-generated turbulence can extend to nearly the surface on ebb but is typically trapped within a 4-6 m of the bottom on flood even during spring tides. The exception to this occurs during periods of reasonably strong winds, and presumably breaking waves, and causes production to increase near the ocean surface.

Assuming a local turbulent balance, stimates of the vertical eddy viscosity A_v can be formed as $- < u'w' > /(\partial \overline{u}/\partial z)$. Obviously the formulation can not work where mean shear is near zero, and can not be expected to work in the near surface when wave breaking,

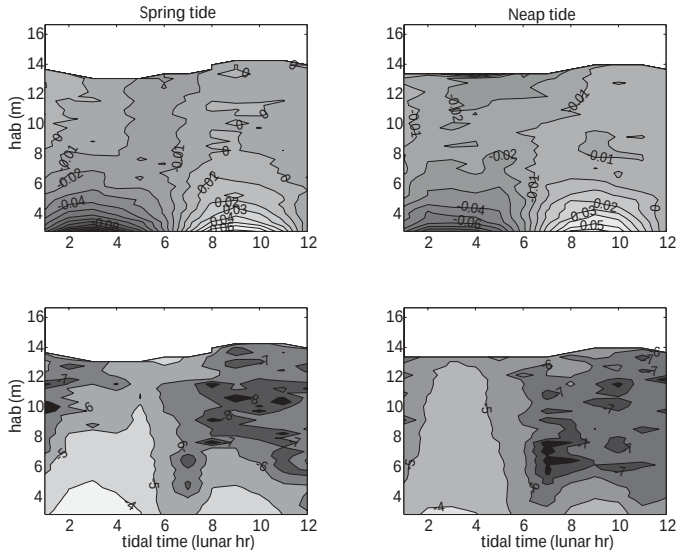

Figure 1: Contour plots of shear of the along-channel current (in s^{-1}, top) and logarithm of the turbulent production (m^2/s^3, bottom) during spring tide (left) and neap tide (right) conditions from the composite data.

rather than mean shear, is the source of energy. Nevertheless, reasonably consistent estimates results at times of non-zero mean shear and give values $10^{-3} - 10^{-1}$ m^2/s. A simple scaling of the eddy viscosity is $A_v = u_* l_o$ where $u_* = sign(- < u'w' >)|- < u'w' > |_{z=0}^{1/2}$ is the friction velocity and l_o is the mixing length. A parobolic mixing length profile $\kappa(z/H)H(1 - z/H)$, where κ is von Karman constant of 0.4 and H is the water depth, is shown for comparison. Only during spring ebb tide does the observed mixing length rise to the theoretical prediction; in all other cases the observed scales are smaller. The difference is greatest during flood tides, and neap tides in particular.

The near bottom Reynold's stress and the depth-averaged tidal currents are highly correlated. Estimates of the drag coefficient $C_d = - < u'w' > /\overline{u}^2$ based on the 10 minute averaged data vary systematically between 0.0021 on ebb and 0.0013 during flood.

3 Discussion and Conclusions

The variance technique for measuring Reynolds stress profiles from a bottom mounted deployment would appear to be well-suited to studies of turbulence in estuaries. Continuous estimates of near bottom turbulent production in these energetic flows would nicely complement other measurement techniques. Whereas shear probes are designed to sense the smallest levels of turbulence in the ocean and do not resolve intense turbulence well, the Reynolds stress estimated from the ADCP is noise-limited at low turbulence levels and better suited to measuring very energetic flows.

In the case of Beaufort Inlet bottom-generated turbulence dominates the 15 m deep water column on ebb flows, but its influence is trapped in the lowest 5 m on flood. Preliminary examination of observations of the density field reveal a dense inflow that begins

as the tide changes for ebb to flood. The near-bottom stratification it causes may act to suppress overturning as the tidal current changes direction and limit overturning scales throughout the flood. As can be seens from the estimates of C_d the difference in stress between ebb and flood flows is persistent. Quantifying this relationship is being actively pursued.

The near-surface maxima in Reynolds stress associated with southerly winds raises the intriguing possibility of measuring the momentum flux associated with wave breaking. Though Reynolds stress estimates from point measurements of turbulent velocities can be contaminated by surface gravity waves (Trowbridge, 1997), the author is unaware of studies of the susceptibility of the ADCP measurements to contaimination from surface gravity waves. It should be noted that the near surface stress was high only during strong southerly winds and peaked during ebb flow, when currents would oppose wave propagation, consistent with times of enhance wave breaking. Obviously simultaneous high quality wave measurements will be required to resolve this issue.

Acknowledgments: Mark Stacey was kind enough to share his insights on using ADCPs in this mode and some of his processing scripts. The work was supported by a grant from the Office of the President of the University of North Carolina.

References:

Di Iorio, D. and H. Yuce, 1999. Observations of Mediterranean flow into the Black Sea, *J. Geophys. Res.*, 104, 3091-3108.

Gregg, M. C., E. Ozsoy and M. A. Latif, 1999. Quasi-steady exchange flow in the Bosphorus, *Geophys. Res. Lett.*, 26, 83-86.

Lu, Y and R. G. Lueck, 1999. Using a broadband ADCP in a tidal channel. Part II: turbulence, *J. Atmos. Ocean Tech.*, 16, 1568-1579.

Peters, H., 1999. Spatial and temporal variability of turbulent mixing in an estuary, *J. Mar. Res.*, 57, 805-845.

RD Instruments, 1998. Workhorse technical manual, RD Instruments, San Diego, CA.

Stacey, M. T., S G. Monismith and J. R. Burau, 1999. Observation of turbulence in a partially stratified estuary, *J. Phys. Ocean.*, 29, 1950-1970.

Stacey, M. T., S G. Monismith and J. R. Burau, 1999. Measurements of reynolds stress profiles in unstratified tidal flow, *J. Geophys. Res.*, 104, 10,933-10,9490.

Trowbridge, J. H., 1997. On a technique for measurement of turbulent shear stress in the presence of surface waves, *J. Atmos. Ocean Tech.*, 15, 290-298.

Wesson, J. and M. C. Gregg, 1994. Mixing at Camarinal Sill in the Strait of Gibraltar, *J. Geophys. Res.*, 99, 9847-9878.

Calibration of coupled flow-wave models and generation of boundary conditions for the central Dithmarschen Bight, Germany

JORT WILKENS AND ROBERTO MAYERLE

(Coastal Research Laboratory, Institute of Geosciences, University of Kiel, Otto-Hahn-Platz 3, D-24118 Kiel, Germany, jwilkens@corelab.uni-kiel.de)

1. Introduction

To increase the knowledge of the distribution of wave energy over the tidal flat area of the Dithmarschen Bight (see Figure 1), a process-based, coupled flow-wave model has been set up. The wave model incorporates either the HISWA model (HIndcast Shalow WAter waves, see *Holthuijsen* ET AL [1989]) or the SWAN model (Simulating WAves Nearshore, see *Booij* ET AL [1999]). Both have been applied within the Delft3D modelling system (see *Roelvink* ET AL [1994]), coupled to the FLOW module to take current effects on the waves into account.

Short-term (five periods of one day) calibration of the coupled model has been carried on the basis of a one-month measurement campaign (September 1996) with five Wave Rider buoys (data from *Niemeyer* [1995] – for their location, see Figure 2). The two outer (western) buoys have been used for defining the (swell) boundary conditions, while the inner buoys were used for evaluation of the model results. A comparison has been made between the results of the applied wave models.

To generate (swell) boundary conditions for medium-scale modelling, a larger coupled flow-wave model that covers the entire German Bight has been developed and applied. This model has been forced by wind only (data available from *Luthardt* [1987]) and has been calibrated with the measurements of the two outer (western) wave buoys of the previously mentioned campaign.

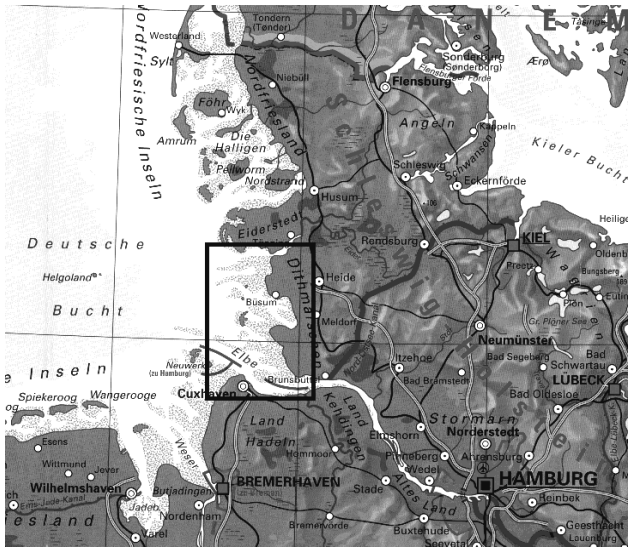

Figure 1: Location of the Dithmarschen Bight – south-eastern North Sea

2. The Dithmarschen Bight – domain and processes

The Dithmarschen Bight, on the North Sea coast of Germany, is a tidal flat area in the north-eastern part of the German Wadden Sea. The hydrodynamics in the area are mainly controlled by the tide with a tidal range of about 3.5m. Waves up to 3.5m have been observed in the western part of the domain. Figure 2 shows the model bathymetry and location of the Wave Rider measurements.

A large portion of the domain falls dry during low tide and wave breaking takes place at the edge of the tidal flats. Depending on the hydrodynamic conditions, swell energy is able to penetrate further into the area through the main tidal channels. Due to the complex bathymetry, with tidal flats and channel depths of about 10-15m, the resulting current and wave fields are rather complex.

The local wave energy originates from swell waves entering from the western model domain boundary and the locally generated wind waves.

3. Model set-up

The model domain measures approximately 35km from West to East and 50km from South to North. The bathymetry is mainly based on 1996 measurements, where some gaps have been filled with data from 1995 and 1997. The open sea boundaries are located in relatively deep water (10 to 15m).

The flow model is based on a finite difference, curvilinear grid with grid spacing between 80 and 200m in the centre and up to 800m in the outer areas. The boundary conditions for this model have been generated by a nesting sequence (see Figure 3), which includes the Continental Shelf Model (see *Verboom ET AL* [1992]), wherein the boundary conditions are astronomical, and the German Bight Model (see *Hartsuiker* [1997]). Wind forcing using Luthardt [1987] data is considered. A previous study, concerning the calibration of the nesting sequence and flow model (see *Palacio ET AL* [2001]), ensured proper open sea boundary conditions.

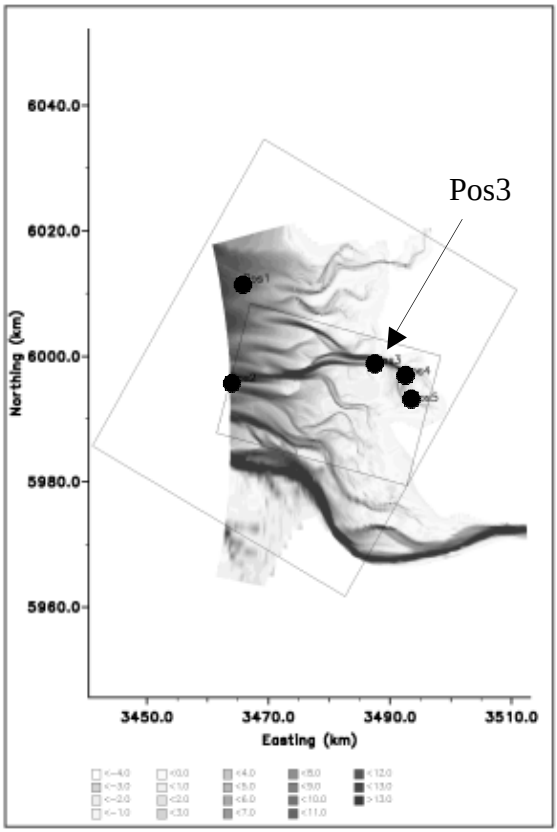

Figure 2: Bathymetry of the domain and location of the wave measurements

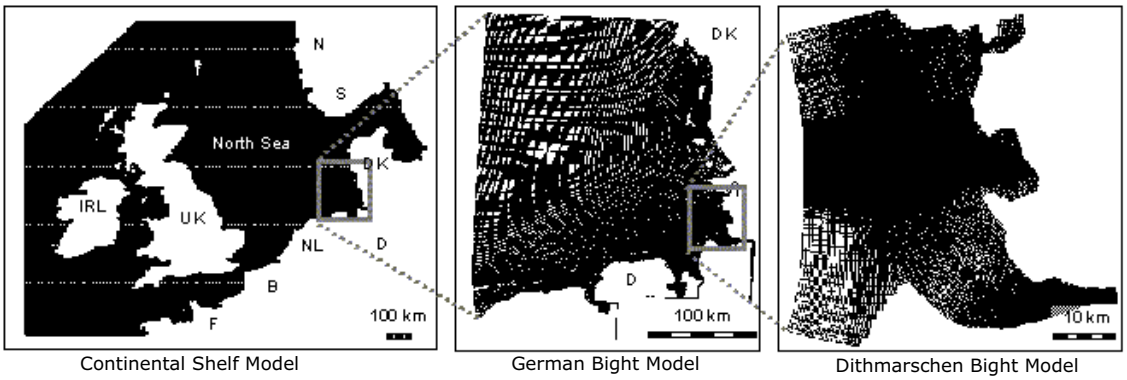

Figure 3: Nesting sequence for the flow model

The wave model (either HISWA or SWAN) has been coupled to the flow model. This leads to the inclusion of computed water levels and flow velocities in the wave model. For HISWA, two separate grids (an overall, coarse grid and a detailed, high-resolution grid) have been created, since this wave model accepts only rectangular grids. The SWAN model is based on the curvilinear flow grid, therefore avoiding interpolations between the grids.

4. Wave Model forcing – wind and boundary conditions

The applied models (the flow models in the nesting sequence as well as the wave models) include forcing by wind based on the *Luthardt* [1987] interpolation model. This model interpolates

measurements from stations along the coast and on oil platforms in a 'smart' way, to produce reliable wind data.

The boundary conditions have been determined with two different approaches. In the first, the conditions have been based on the measurements at the two western buoys, which are located relatively close to the up-wave boundaries.

The second approach is based on nesting the Dithmarschen Bight Model into the larger German Bight Model (see Figure 4). The latter model is forced only by wind (again from *Luthardt* [1987]). The results of the simulated wave parameters at the two western buoys have been compared to the measurements. This method enables the generation of boundary conditions for longer periods without measurements and yields good results.

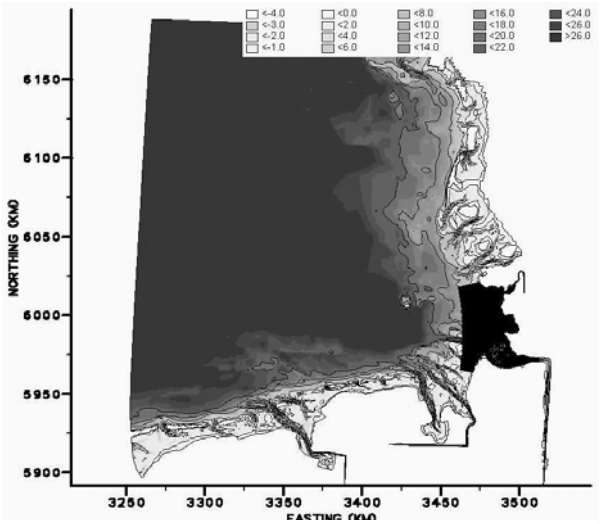

Figure 4: Bathymetry of the German Bight Model with the location of the Dithmarschen Bight Model

5. Model results

The wave heights near the coastline are relatively low, due to the sheltering effect of the tidal flats. This, combined with the complex current patterns and bathymetry, complicates the accurate prediction of the wave characteristics. However, after a detailed calibration both wave models are able to capture main trends and yield acceptable results in a quantitative comparison. As an example, the measured and predicted (with SWAN) significant wave heights are shown for Pos3 (see Figure 2 for its location) in Figure 4. The HISWA model produces similar results. Evaluation of the wave directions and periods lead to equivalent conclusions. The largest discrepancies can be found for the very low waves (up to 0.15m). Furthermore, the SWAN model seems to over-predict the higher waves (more than 0.5m)

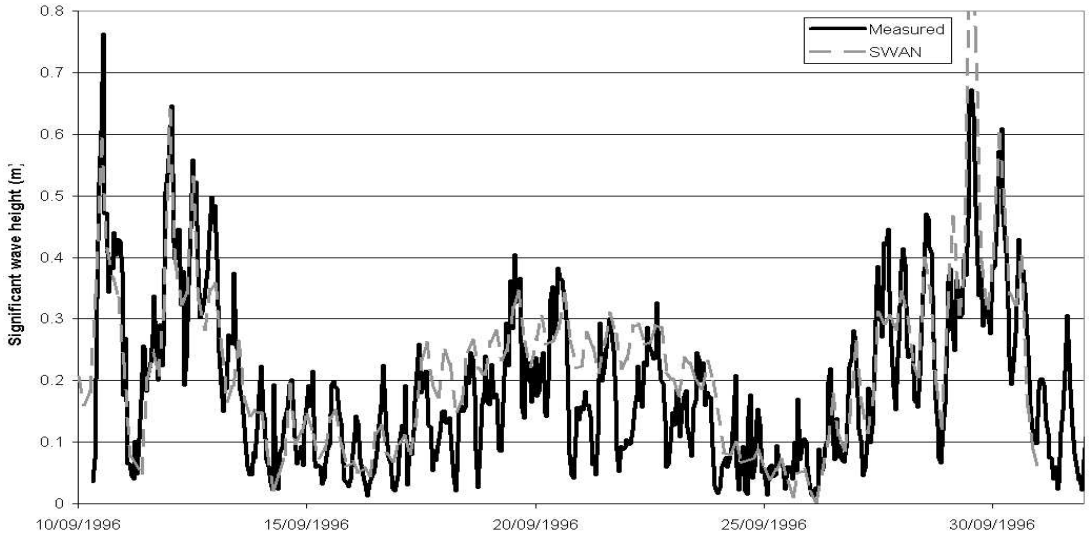

Figure 4: Hsig measured and modelled (with SWAN) at Pos3

The application of the SWAN model in the German Bight, with wind forcing only, resulted in rather

good results in terms of significant wave heights and wave directions. However, for some periods, the model was not able to produce results in good agreement to the measured data.

6. Discussion

The prediction of swell waves and locally generated waves with either of the applied wave models for the Dithmarschen Bight produced good results, especially when the complex conditions are considered. The occurring discrepancies are mainly under very calm conditions, where the significant wave heights did not exceed 0.2m. This may be outside the range of successful application. The overall results showed that the predicted wave breaking took place in the areas where wave breaking is observed. Unfortunately, the extent of available measurement data to evaluate this is rather limited. The HISWA model sometimes underestimated peaks in the wave heights, where SWAN overestimated these. It could not be concluded that one model is better than the other.

The generation of boundary conditions, based on the two western wave buoys proved to be acceptable. However, since most wave energy entering the domain dissipates on the western edges of the tidal flats, this could not be evaluated extensively with the available measurements.

The generation of boundary conditions with the larger German Bight Model, where only wind forcing was applied, showed good results for 80% of the measurement period (discrepancies below 15-20% of the measured wave height and 5-10° in the wave direction). During the other 20%, the directional discrepancy was about 30° and the wave height discrepancy up to 40% of the measured value. Further calibration with recent measurements is expected to improve these results.

Acknowledgments: The results presented here are part of the investigations carried out within the research project "Predictions of Medium Scale Morphodynamics – Promorph", which is funded by the German Ministry of Education and Research from 2000 to 2002. The authors would like to thank the Coastal Research Station of the Lower Saxon Central State Board for Ecology (Norderney, Germany) for providing the wave data used in the model calibration.

References:

Booij, N., R.C. Ris and L.H. Holthuijsen. A third-generation wave model for coastal regions, Part I, Model description and validation. Journal of Geophysical Research, Vol. 104, No. C4, pp. 7649-7666, 1999.

Hartsuiker, G. Deutsche Bucht and Dithmarschen Bucht, Set-up and calibration of tidal flow models. Delft Hydraulics, report no. H1821, 1997.

Holthuijsen, L.H., N. Booij and T.H.C. Herbers. A prediction model for stationary, short-crested waves in shallow water with ambient currents. Coastal Engineering, No. 13, pp. 23-54, 1989.

Luthardt, H. Analyse der wassernahen Druck- und Windfelder über der Nordsee aus Routine-Beobachtungen. Hamburger Geophysikalische Enzelschriften, Reihe A83. Fachbereich Geowissenschaften, University of Hamburg, Germany, 109 pp. In German. 1987.

Niemeyer, H.D., R. Goldenbogen, E. Schroeder and H. Kunz. Untersuchungen zur Morphodynamik des Wattenmeeres im Forschungsvorhaben WADE. Die Kueste, H.57, Heide. In German. 1995.

Palacio, C., C. Winter and R. Mayerle. Set-up of a hydrodynamic model for the Meldorf Bight. EWRI/ASCE World Water and Environmental Resources Congress Proceedings, 2001.

Roelvink, J.A. and G.K.F.M. van Banning. Design and development of Delft3D and application to coastal morphodynamics. Hydroinformatics , Verwey, Minns, Babovic & Maksimovic (eds.), Balkema, Rotterdam, pp. 451-455, 1994.

Verboom, G.K., J.G. de Ronde and R.P. van Dijk. A fine grid tidal flow and storm surge model of the North Sea. Continental Shelf Research, Vol. 12, No. 2/3, pp. 213-233, 1992.

Siltation by sediment-induced density currents

HAN WINTERWERP (*WL|delft hydraulics, PO Box 177, 2600 MH Delft, The Netherlands, also: Delft University of Technology,* han.winterwerp @wldelft.nl)

THIJS VAN KESSEL (*WL|delft hydraulics, PO Box 177, 2600 MH Delft, The Netherlands,* thijs.vankessel@wldelft.nl)

1 Introduction

Many ports throughout the world are located in turbid environments. As a result, siltation rates in channels and harbour basins are large, and frequent maintenance dredging is required to safeguard navigation. The costs of maintenance are often high, and may increase further as a result of more strict legislation and regulations. Today, tools to predict these siltation rates are available in the form of three-dimensional (3D) numerical models. The present paper discusses further developments of such 3D-models.

The dynamics of concentrated benthic mud suspensions (CBS) are governed by sediment-fluid interactions. An extreme example of these interactions is shown in Fig. 1, showing the collapse of the concentration profile when the flow becomes supersaturated Winterwerp, 2001). The upper panel shows the evolution towards a Rousean profile for a hypothetical open-channel flow of 16 m depth, a flow velocity of 0.2 m/s and an initial mean concentration of 23 mg/l. When the initial concentration is increased to 24 mg/l, shown in the lower panel, the suspension becomes supersaturated and the concentration profile (and turbulence field) collapses.

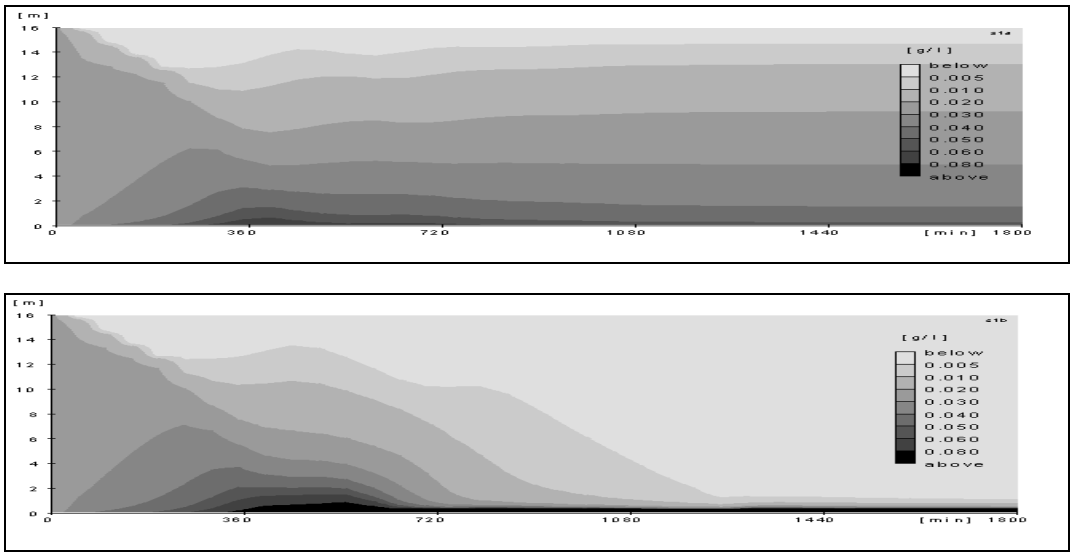

Fig. 1: Collapse of vertical concentration profile, computed with 1DV model.

The effect of these sediment-fluid interactions on the siltation in harbour basins is studied with the DELFT3D model suite for an idealised coastal area, and for a real-world situation, viz. Rotterdam harbour area. In particular, the following effects were studied:

- the modelling of CBS though the coupling of the turbulent water movement and suspended sediment;
- the development and behaviour of CBS induced by a trench in the seabed and in the mouth of a harbour basin c.q. estuary, and;

- the effect of CBS on sediment fluxes and siltation rates in harbour basins

2 Modelling buoyancy effects for cohesive sediment suspensions

The present study was carried out with a research version of the DELFT3D model suite. In this version, the feedback between suspended sediment and the turbulent flow field is implemented as described in the next sections. This interaction is referred to as the "coupled" mode in the remainder of this abstract. For detailed information, the reader is referred to Lesser et al., 2003.

The sediment-fluid interaction is modelled though the inclusion of the following processes:

- hindered settling, which augments vertical concentration gradients,
- buoyancy destruction in the k-ε turbulence model to account for the damping of mixing,
- sediment-induced barocline pressure gradients in momentum equations to model the sediment-induced density current.

3 An idealised case: coastal area with access channel

To assess the behaviour of the coupled model, and of the impact of sediment-induced density currents on the sediment dynamics, a schematised model was set up. This model represents a coastal area with a navigational channel, a river and a harbour basin. The length of the model is about 77 km, its width about 30 km, excluding the river and harbour. The water depth is 16 m everywhere, except for the harbour and access channel, which have a depth of 24 m. At the southern model boundary, a sinusoidal velocity with 0.7 m/s amplitude is prescribed, whereas at the northern model boundary a sinusiodal water level is prescribed with 1.5 m amplitude. Computations were performed with 0.1 and 0.5 g/l suspended sediment concentration at the model boundaries. The settling velocity was set at 0.5 mm/s, and water-bed exchange processes were not modelled, i.e. all sediment remains in the "water column".

The following impact of the fluid-sediment coupling was observed:

- the near-bed concentration increases by about 50 to 100 %,
- the sediment flux into the harbour basins increases slightly,
- the sediment flux out of the harbour basin decreases with 50 %,
- the net sediment import into the harbour increases with a factor 2 to 3.

4 A real-word case: Rotterdam harbour area

Next, the model is applied to a real-world case, i.e. the so-called RIJMAMO-model which includes the Rotterdam harbour area. This model includes a Rhine discharge through the Rotterdam Waterway of 1,260 m^3/s and a discharge of 750 m^3/s through the Haringvliet Sluices. Contrary to the idealised case, sedimentation and erosion are modelled with the descriptions by Krone and Partheniades with $\tau_{crit,\ sed} = \tau_{crit,\ ero} = 0.11$ Pa and $M = 0.005$ kg/m^2/s. The settling velocity is 0.6 mm/s, and the sediment concentration at the model boundaries 0.1 g/l.

Four different simulations were carried out; in this abstract only the results with a model boundary concentration of 0.1 g/l are presented in Table 1 and Fig. 2 and 3.

Table 1 shows that sediment-induced density currents cause the calculated sediment fluxes into the channels and basins of Rotterdam Port to increase by a factor of about 3 for a 0.1 g/l boundary condition. The gross sediment import is more than doubled, whereas the gross sediment export increases with less than 50%.

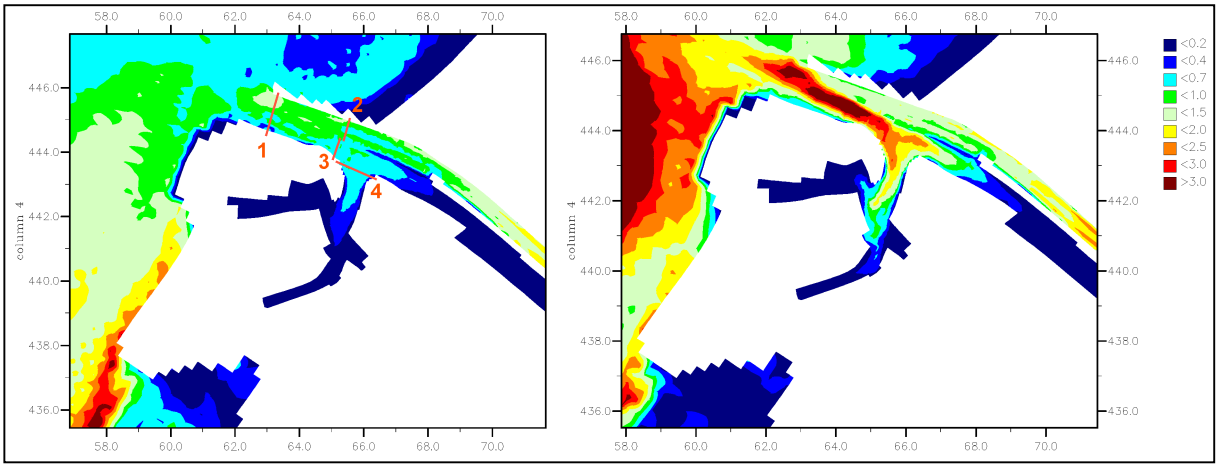

Fig. 2: Computed tide-averaged suspended sediment concentration in the lower layer. Left panel: simulation g14 (uncoupled); right panel: simulation g13 (coupled).

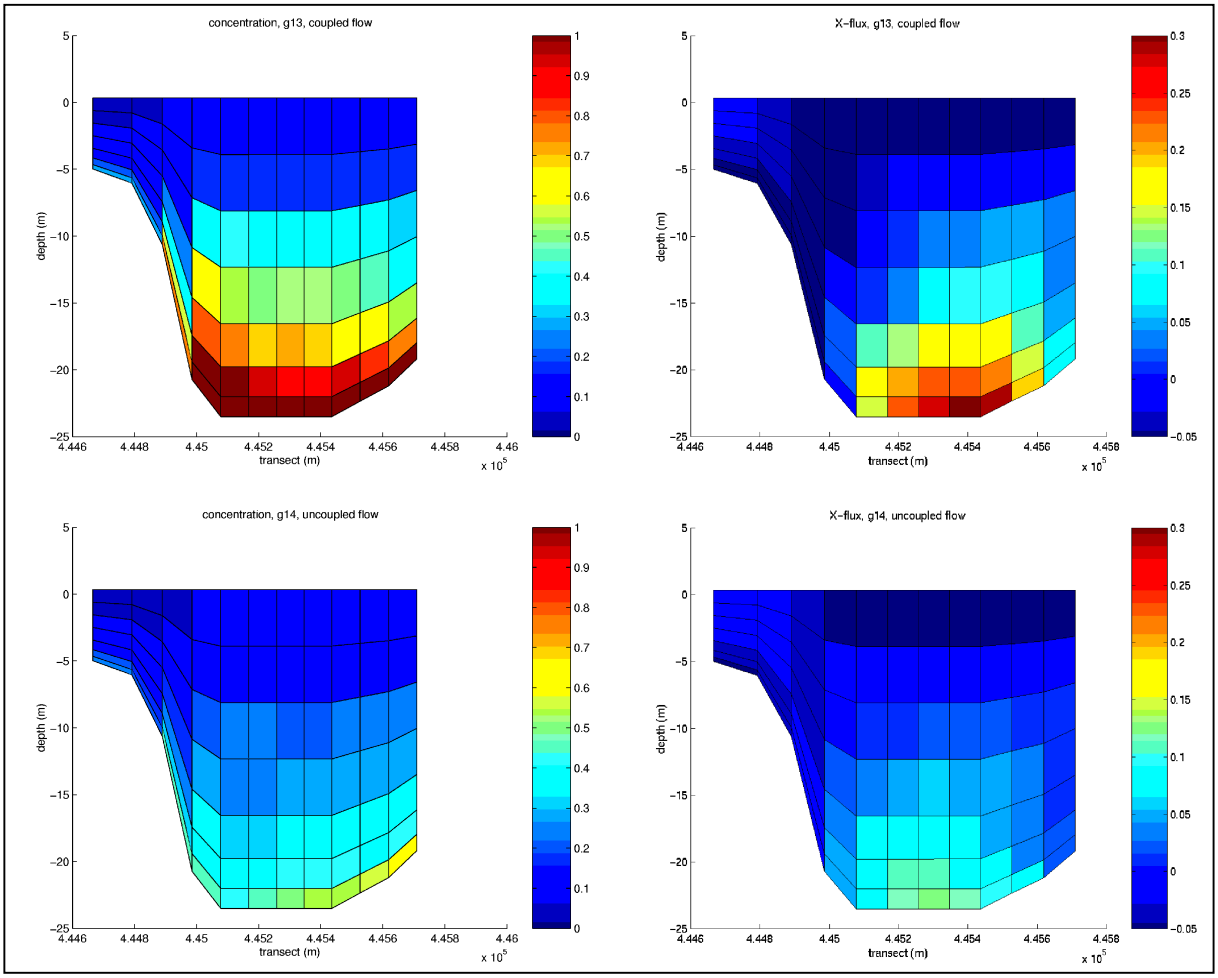

Fig. 3: Vertical tide-averaged suspended sediment concentration in kg/m^3 (left) and sediment flux in kg/m^2/s (right) in Maasmond transect for the simulations g13 (top panel) and g14 (bottom panel).

run ID	coupl	cross section	sediment flux [kg/s] mean	gross import	gross export	water flux [m^3/s] mean	max. ebb	max. flood
sim g13	yes	1.Maasmond	884	1503	-620	-1,264	-12,929	10,575
sim g13	yes	2. R'dam Waterway	76	466	-390	-1,304	-9,067	5,490
sim g14	no	1. Maasmond	325	719	-395	-1,263	-12,886	10,298
sim g14	no	2. R'dam Waterway	50	365	-315	-1,292	-8,959	5,476

Table 1: Water and sediment fluxes for idealised schematisation.

5 Discussion and conclusions

The present study describes the results of numerical experiments to establish the role of sediment-induced density currents on the sediment transport fluxes and subsequent siltation rates in navigational channels and harbour basins. The study is carried out with a three-dimensional numerical model in which water movement and suspended sediment transport are coupled through the equation of state. It is concluded that sediment-induced density currents augment the sediment transport fluxes by a factor of 3 to 5. This large effect is the result of:

1. an increase in vertical concentration gradients by the effects of hindered settling and damping of vertical mixing through sediment-induced buoyancy, and
2. density currents induced by horizontal gradients in suspended sediment concentration.

Acknowledgements: This work was financed through corporate research funds of Delft Hydraulics. We like to thank Mr. Rinze Bruinsma for his help with the computations and post-processing and dr. Johan de Kok and Mr. Teus Blokland for their valuable comments.

References:

Lesser, G. R., Kester, J.A.T.M., Roelvink, J.A. and Stelling, G.S., Development and validation of a three-dimensional morphological model, submitted to *Coastal Engineering*, special issue on morphodynamics, 2003.

Kessel, T. van, 3D fine sediment calculations with RIJMAMO model, Delft Hydraulics Report no. Z3282, The Netherlands, 2002.

Winterwerp, J.C., Stratification effects by cohesive and non-cohesive sediment, *Journal of Geophysical Research*, Vol. 106, No. C10, pp. 22559–22575, 2001.

Formation of Estuarine Turbidity Maxima in Partially Mixed Estuaries

H.M. Schuttelaars[1,2], C.T. Friedrichs[3] and H.E. de Swart[1]

1. Institute for Marine and Atmospheric Research, Utrecht University, Princetonplein. 5, 3584 CC Utrecht, The Netherlands.
2. Delft University of Technology, P.O.Box 5048, 2600 GA Delft, The Netherlands.
3. Viginia Institute of Marine Science, College of William and Mary, Va., USA.

1 Introduction

Estuaries are the connections between the marine and riverine environments where fresh river water and salty seawater meet. Vertical mixing processes, induced by e.g. tides and waves, cause the formation of a salt wedge. This results in an along–channel baroclinic pressure gradient which sets up a density–driven (also called gravitational) circulation, see e.g. *Hansen and Rattray* [1965]; *Nichols and Poor* [1967]. These models put emphasis on the convergence near the bed of the landward-directed gravitational circulation and seaward–directed river flow.

Another mechanism resulting in particle trapping is the occurrence of tidal velocity asymmetry and its interaction with the time–varying concentration field (see *Jay and Musiak* [1994]). The relative importance of these mechanisms has been studied numerically by *Burchard and Baumert* [1998]. They concluded that in the setting they choose the mechanism associated with tidal asymmetry was more important than the one resulting from the residual gravitational circulation.

The York river (VA.) seems to fit the conditions underlying the conceptual model of *Nichols and Poor* [1967] in some regards: the system is micro-tidal and partially mixed; the regions of highest turbidity are found above muddy deposits, near the transition from brackish to salt water. However, a second ETM is often located more seaward in the estuary, near the along–channel transition from stratified to mixed conditions (see *Lin and Kuo* [1999]).

In section 2 an idealized model is developed and analysed to gain more understanding about ETM dynamics. Approximate analytical solutions of the equations are constructed by making an expansion of the physical variables in a small parameter Z/H, the ratio of the amplitude of the vertical tide and the undisturbed water depth. Using these expressions, the leading order contributions to the convergence of net sediment fluxes can be separated in two distinct contributions, one related to the convergence of sediment associated with gravitational circulation and the other one associated with tidal velocity asymmetry. This is shown in section 3 where the results are discussed and the conclusions are given.

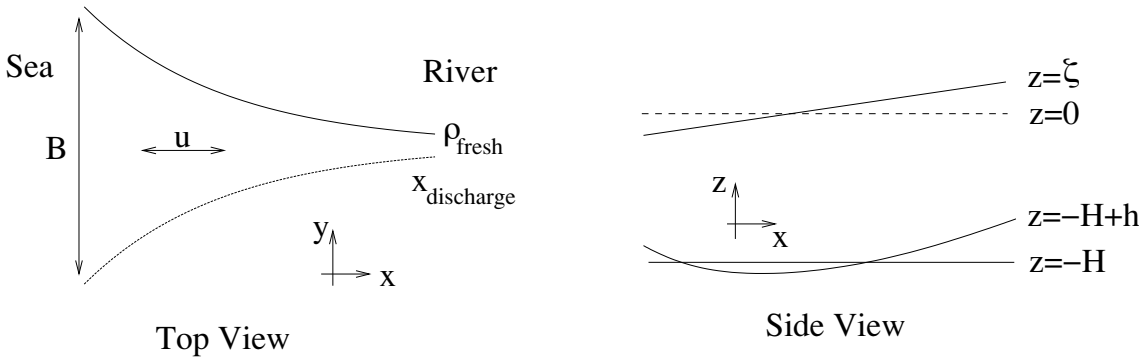

Figure 1: Geometry (left: top view, right: side-view) of the model estuary.

2 Model formulation

The geometry consists of an open channel with rectangular cross–section and a flat bed, whereas the width converges exponentially with a length scale L_b which is taken from observations. At the seaside the system is forced by a prescribed tidal elevation, whilst at the landside a river inflow is imposed. The water motion is modelled by the width–averaged shallow water equations. The width–averaged advection–diffusion equation is used to find the concentration profiles in the embayment. The density profile is prescribed diagnostically in both the horizontal and vertical direction. In estuaries with a significant river inflow the density is not constant in space and time. In order to model this behaviour in a diagnostic way the following density profile is used:

$$\rho = \rho_0(x) + \rho_1(z) + \rho_2(x, z, t) \tag{1}$$

Here the first contribution on the right-hand side describes the observed gradual decrease of density from the sea to the river, the second term reflects the observation that systems like the York river are always stably stratified, whereas the last term models the time–dependency of the density due to tidal effects. Since the stratification is depth–dependent, the eddy viscosity coefficients are influenced by it. Here we adopt formulations discussed by *Van de Kreeke and Zimmerman* [1988].

Our main interest is in finding the ETM locations in the estuary where a maximum in the concentration occurs. Besides we are interested in the locations where the convergence in the flux of suspended sediment is maximum. In order to find these locations the model, discussed above, is systematically investigated. The analysis is based on the fact that the parameter $\epsilon = Z/H$ (Z the tidal wave amplitude and H the water depth) which measures the relative influence of nonlinear terms with respect to linear terms in the equation of motion, is usually a small (for example in the York estuary $\epsilon \sim 0.05$). Hence approximate solutions can be constructed by expanding the physical variables in power series of ϵ and solving the equations at various orders of ϵ. It turns out that only at order ϵ^2 a net sediment flux is obtained. This net sediment flux consists of a part due to residual circulation and a part due to tidal asymmetry.

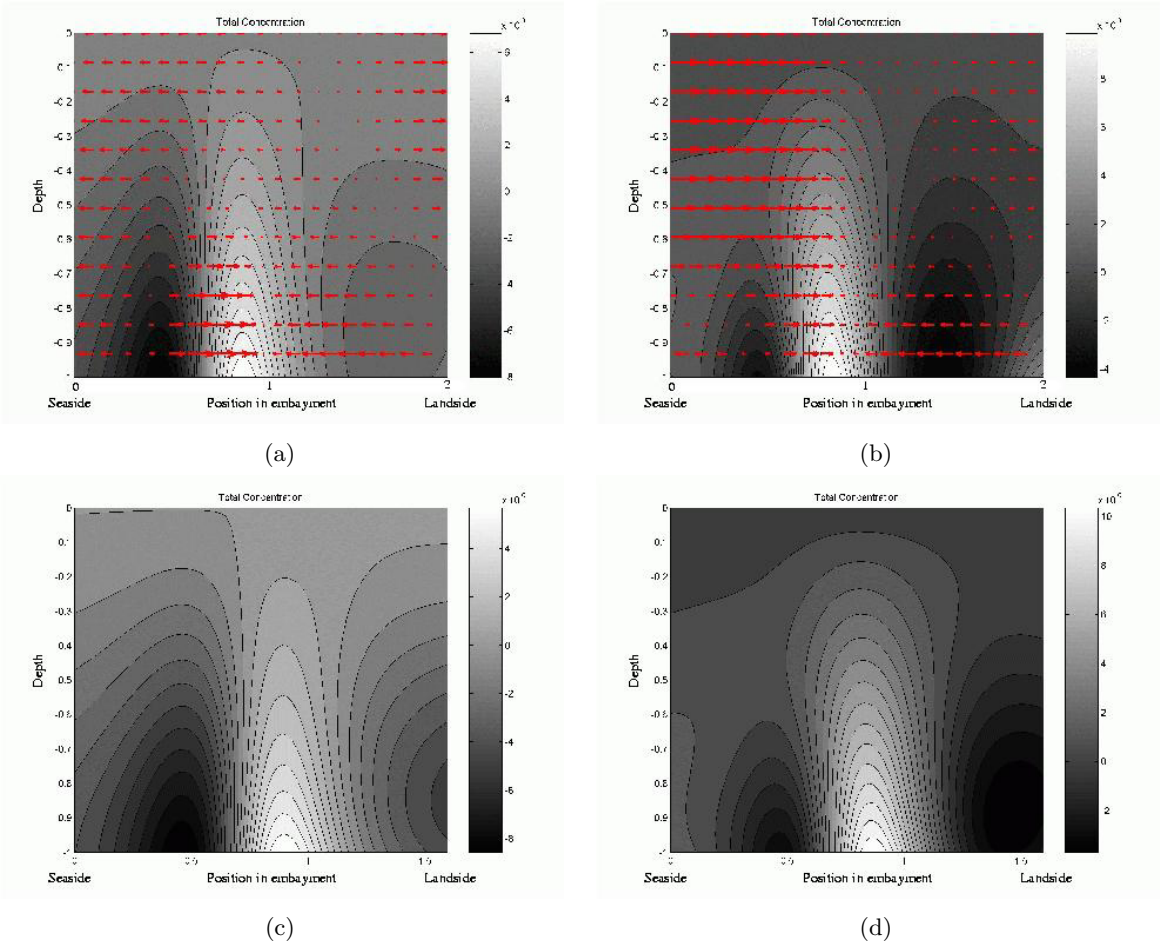

Figure 2: Time mean concentration for (a) and (c) a depth– and time–independent density field and (b) and (d) a depth– and time–dependent density field. Here the depth is scaled with $H = 10$ m and the length with convergence length $L = 70$ km. In figures (a) and (b) no river outflow is present, whereas in (c) and (d) a river outflow of $0.54B_0$ m^2 is prescribed with B_0 the width at the entrance of the embayment. In figures (a) and (b) the arrows indicate the direction of the net sediment fluxes. These sediment fluxes are omitted in figures (c) and (d) since no convergence–divergence patterns can be discerned (large outward sediment flux due to river outflow).

3 Results and Discussion

In figure 2 the time averaged concentration fields are plotted for two different diagnostically prescribed density fields. In figures 2(a)–2(b) no river outflow is prescribed, whereas in figures 2(c)–2(d) a river outflow is present. It turns out that to get an estuarine turbity maximum, it is essential for the density profile to have an inflection point, i.e. the along–estuary derivative of the density profile should have a maximum. This situation is shown in figure 2(a) where a density profile without any depth dependency and an inflection point around $L = 60$ km is prescribed. Here the mechanism is due to an along–channel

baroclinic pressure gradient which sets up a density–driven circulation. If a depth– and time dependency is added to the diagnostically prescribed density profile (so both ρ_1 and ρ_2 are unequal to zero in (1)), it is possible to find situations in which more than one ETM is observed. Hence another mechanism resulting in particle trapping is the occurrence of tidal velocity asymmetry and its interaction with the time–varying concentration field. Usually a strong ETM is found around $L = 60$ km and a weaker one near the entrance of the estuary.

From these and other numerical experiments it can be concluded that during generally stratified conditions, one near–bed ETM is found. If the density stratification is assumed to be time–dependent as well (influence of tide), situations occur where two distinct ETMs occur. Hence due to the phase lag between stratification and velocity another mechanism resulting in net convergence of suspended sediment is at work. The physical interpretation of this mechanism is presently under investigation. This seems to be consistent with field measurements where during more mixed conditions two instead of one ETMs are observed. However, the positions of the ETMs found in the model do not correspond very well with the observations. Therefore, the dependence of the stratification on time and place will be studied in more detail.

Furthermore, the strength of the ETMs is usually under–estimated. Therefore, an along–channel variable erosion will be studied in the near future as well.

References

Burchard, H., and H. Baumert, The formation of estuarine turbidity maxima due to density effects in the salt wedge. a hydrodynamic process study, *J. Phys. Oceanogr.*, *28*, 309–321, 1998.

Hansen, D., and M. Rattray, Gravitational circulation in straits and estuaries, *J. Marine Res.*, *23*, 104–122, 1965.

Jay, D., and J. Musiak, Particle trapping in estuarine tidal flows, *J. Geophys. Res.*, *99*, 445–461, 1994.

Lin, J., and A. Kuo, Downstream turbidity maximum in the york river, virginia, in *15th Biennial International Conference of the Estuarine Research Federation*, 1999.

Nichols, M., and G. Poor, Sediment transport in a coastal plain estuary, *J. Waterw. Harbors Div., ASCE*, *93*, 83–95, 1967.

Van de Kreeke, J., and J. Zimmerman, Gravitational circulation in well- and partially mixed estuaries, in *Physical processes in estuaries*, edited by J. Dronkers, and W. van Leussen, pp. 495–521, Springer–Verlag, N.Y., 1988.

Transport of particulate matter in the Elbe estuary by means of numerical simulations

Susanne Rolinski, (*Institut für Meereskunde, Universität Hamburg, Troplowitzstr. 7, D-22529 Hamburg, Germany*, rolinski@ifm.uni-hamburg.de[1])

1 Introduction

Investigations on riverine loads of dissolved and particulate substances have to deal with the complex hydrodynamic situation in the estuary. Transport of matter is influenced by hydrodynamic processes as tides, winds, the baroclinic circulation and the characteristics of the substances with the effect that the determination of fluxes is precarious even for dissolved substances. Regarding the transport of particulate matter of organic or mineral origin, deposition/resuspension as well as flocculation/deflocculation processes during the tidal cycle alter fluxes and net transport.
SPM composition in the Elbe estuary includes numerous algal classes, which can be assumed to be not autochthonous but transported into the estuary from the marine or limnic regions (*Wolfstein and Kies* [1999]). Enduring only a shallow euphotic zone and osmotic stress due to changing salinity, a high proportion of microalgae populations enters degradation processes.
Investigations on SPM dynamics so far have not established a congruent fate of the overall composition of SPM and its organic compounds, a substantial pool of food in the ecological cycle and a carrier of pollutants such as heavy metals. In spring and summer, *Wolfstein and Kies* [1999] found up to 90% of algal biomass associated to slow settling flocs (< 0.3 mm s^{-1}) and about 20 to 30% of algal pigments on faster settling flocs (> 1.9 mm s^{-1}). The latter also showed highest ratios of pheopigments to chlorophyll-a, indicating prevailing decay processes.
A distinct preference of organic material on the one hand and living algae on the other to sinking velocity fractions implies consequences for their transport behaviour. Hence, for this study it is distinguished between the sinking velocity of flocs of different size and composition and the amount of algal biomass, which is found to be connected to them.

2 Study area

The model area covers the estuary of the River Elbe from the weir at Geesthacht (km 589) to the outer estuary (km 745). The topography (Fig. 1) shows the deep waterway with depths of almost 30 m near Cuxhaven and wide shallow areas, which are flooded only during high tide. Characteristic for the River Elbe are its channel-like waterway with steep slopes on the sides.
In the partially mixed Elbe estuary (*Kappenberg et al.* [1996]) no salt wedge on the bottom can be observed but a vertical salinity gradient during part of the tidal cycle. The scale of the salt intrusion can be derived from Figure 2 which shows the tidal mean of the vertically integrated salinity calculated by the hydrodynamical model (*Krohn and Duwe* [1990]).

[1]current affiliation: Institut für Hydrobiologie, Technische Universität Dresden, Mommsenstrasse 13, D - 01062 Dresden, rolinski@rcs.urz.tu-dresden.de

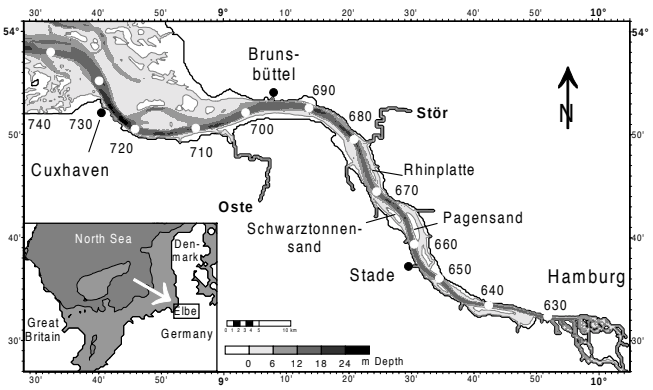

Figure 1: Topography of the tidal River Elbe; numbers denote river kilometer.

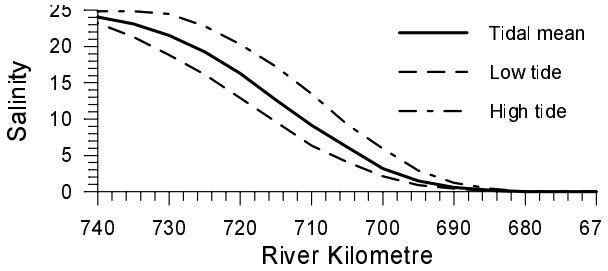

Figure 2: Tidal mean of the vertically integrated salinity distribution along the waterway.

3 Description of the Model

Currents and water elevations are calculated by a hydrodynamical baroclinic model for the Elbe Estuary (*Krohn and Duwe* [1990]). The grid resolution is 250 m horizontally and on average 3 m vertically with 6 layers at maximum.
SPM dynamics are simulated by a Lagrangian model transporting single particles according to current velocities (*Rolinski* [1999]). Initial properties of the particles are the release position, a mass, and a sinking velocity. The particulate material in the water column is represented by three fractions of different sinking velocities (as recommended by *Puls et al.* [1990]) with values of 0.3 (fast settling), 0.08 (medium) and 0.004 cm s^{-1} (slow) (*Wolfstein and Kies* [1999]). Deposition and resuspension at the river bottom are included as well as the in- and outflow from tributaries and the open sea.
The following investigations were carried out using a cycle of current velocities over one double tide, i.e. two subsequent tides, with a forcing of a constant discharge of 500 m^3 s^{-1} at the upstream boundary and uniform west winds of 7.8 m s^{-1}. The hydrodynamic situation does not correspond to a real episode of time but to a typical mean situation.
Using constant or variable sinking velocities, the influence of the relatively small vertical motions on the distribution of matter is studied. Released particles in set-up S belong to the slow sinking velocity fraction (0.004 cm s^{-1}) and in F to the medium sinking velocity fraction (0.08 cm s^{-1}); constant during the simulation. In set-up V, the sinking velocity alternates with the tidal phase, belonging to F during ebb and to S during flood tide; a

rather simple approach to include flocculation slack tides and deflocculation during the more turbulent flood. Simulations were carried out from two point sources and for two release times. Starting locations in the waterway are chosen upstream (U) at kilometre 690 as well as downstream (D) at kilometre 705 of the expected position of the estuarine turbidity maximum (*Kappenberg et al.* [1996]). Release of particles was either one hour after high water slack (E) or after low water slack (F) and simulations were run over four cycles.

4 Results

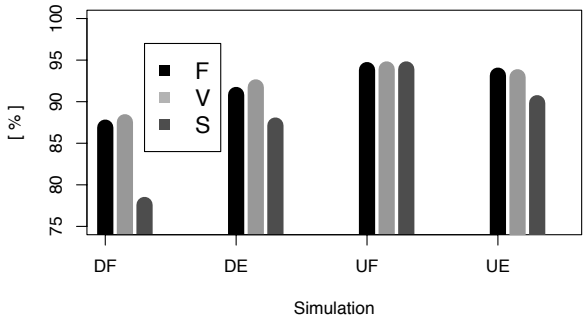

Figure 3: Percent of remaining particles after 4 tidal cycles.

Figure 3 gives the percentage of particles remaining in the model domain after 4 tidal cycles. The tendency to be washed out is high for fraction S and less for F. Starting at the downstream position, particles with variable sinking velocity (V) tend to remain longer in the domain than even the fast sinking fraction (F).

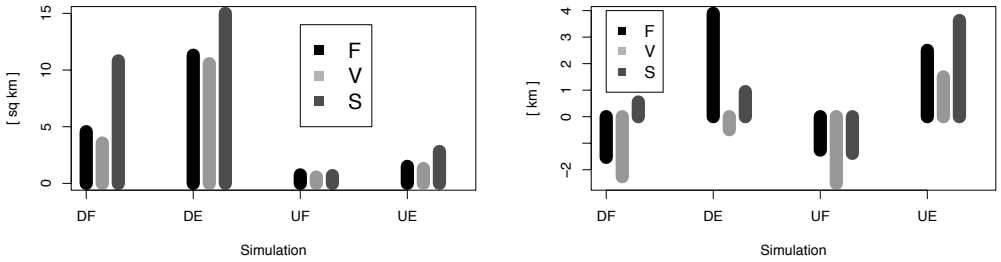

Figure 4: Extention of area with 50 % of the particles after 4 tidal cycles (left) and distance of their average from initial position; negative numbers denote upstream transport (right).

Dispersion of the particles can be estimated when looking at the area covered by 50 % of the particles (Fig. 4, left panel). Values are much less for U (0.6 to 2.8 km^{-2}) than for D

(3.5 to 15 km^{-2}). At both locations, the dispersion with beginning ebb tide outnumbers that for simulations with beginning flood (1.3 to 15 versus 0.6 to 10.8 km^{-2}). Comparing sinking velocity fractions, it can be stated that S spreads always further than the F (up to 2.3 times further). Even smaller is the extention for V (0.75 to 0.9 of the values for F). Considering the center of the cloud in relation to its initial position (Fig. 4, right panel), it is visible that the tidal phase of the release moment mostly determines the sign of the net transport; upstream for F and downstream for E. Exceptions are found for D with a net upstream transport for fraction V with beginning ebb of 0.5 km and fraction S with beginning flood of 0.55 km. Starting with flood, particles of F are found 2.5 to 3.9 km upstream from the initial position; starting with ebb 1.26 to 1.5 km downstream. Net transport for S is mostly directed downstream, highest for the upstream release at beginning ebb with 3.6 km and lowest for the downstream release at beginning flood with 0.55 km. Only at the upstream position starting with flood, the particles are transported upstream on average about 1.4 km. Fraction V has the highest retention capacity with 2.2 to 2.5 km net upstream transport for the simulations with beginning flood and only 1.5 km downstream transport for simulation UE.
Results suggest the sorting of organic material according to the sinking property and the resulting transport. Slowly sinking particles, where algal biomass is most abundant, seem to leave the estuary the earliest, whereas faster sinking ones, on which still living algae are found preferentially, are retained in the estuary. Though it is unlikely that these findings are fundamental for the development of algae populations in the very unfavourable environment, they may help in understanding transport paths of biological particles which play an important role as carrier of pollutants and fish food.

References:

Kappenberg, J., G. Schymura, H. Kuhn, H.-U. Fanger, Spring-neap variations of suspended sediment concentration and transport in the turbidity maximum of the Elbe estuary, *Arch. Hydrobiol., Spec. Issues Advanc. Limnol.*, *47*, 323-332, 1996.

Krohn, J., and K. Duwe, Mathematical modelling of hydrodynamics in the Elbe estuary, in *Estuarine Water Quality Management*, edited by Michaelis, W., pp. 35-40, Springer Verlag, Berlin, 1990.

Puls, W., M. Lobmeyr, A. Müller, M. Schünemann and H. Kühl, Investigations on suspended matter transport processes in estuaries and coastal waters. in *Estuarine Water Quality Management*, edited by Michaelis, W., pp. 165-171, Springer Verlag, Berlin, 1990.

Rolinski, S., On the Dynamics of Suspended Matter Transport in the Tidal River Elbe: Description and Results of a Lagrangian Model, J. Geophys. Res., *104*, C11, 26.043-26.057, 1999.

Wolfstein, K. and Kies, L., Composition of suspended particulate matter in the Elbe estuary: implications for biological and transportation processes, *Dt. Hydr. Z.*, *51*, 4, 453–463, 1999.

Bottom fine sediment boundary layer and transport processes within the turbidity maximum of the Changjiang Estuary, China

ZHONG SHI

(Department of Harbour and Coastal Engineering, School of Naval Architecture and Ocean Engineering, Shanghai Jiao Tong University, 1954 Hua Shan Road, Shanghai 200030, People's Republic of China, ZSHI@MAIL.SJTU.EDU.CN*)*

1. Introduction

A turbidity maximum zone has been found in many turbid estuarine environments (e.g., the Gironde Estuary, France, *Glangeaud* [1938]; the Chesapeake Bay, USA, *Schubel* [1968]; the Weser Estuary, Germany, *Wellershaus* [1981], *Grabemann et al.* [1995]; the upper Saint Lawrence Estuary, Canada, *Lang et al.* [1989]; the Tamar estuary, UK, *Uncles and Stephens* [1993]; the Hawkesburry River estuary, Australia, *Hughes et al.* [1998]; the Seine Estuary, France, *Brenon and Le Hir* [1999]). Several mechanisms govern the fine suspended sediment transport in the turbidity maximum: 1) flocculation, 2) estuarine circulation, 3) tidal pumping, 4) flood/ebb tidal asymmetry, 5) wind, and 6) turbulence suppressions of fine suspended sediment/salinity stratifications.

The Changjiang (Yangtze) is the fourth largest river in terms of both water and sediment discharge in the world. The Changjiang Estuary is a mesotidal estuary with mean tidal range of 2.8 m. More than 90% consists of fine sediments (<32 μm) in the Changjiang Estuary. It provides a good example of a well developed turbidity maximum (*Li and Zhang* [1998]; *Shi* [2002]). A number of questions need to be addressed regarding the generation and maintaining of the turbidity maximum in the Changjiang Estuary.

Aims of this paper are 1) to examine the spring/neap tidal, intratidal (flood/ebb), and burst-type structures of bottom fine sediment bounary layer; 2) to correlate those structures (average and instataneous) to dynamic processes such as tides, waves, and fine sediment density currents; and 3) to elucidate the dominant physical processes generating and maintaining the turbidity maximum at the mouth of the Changjiang Estuary, China.

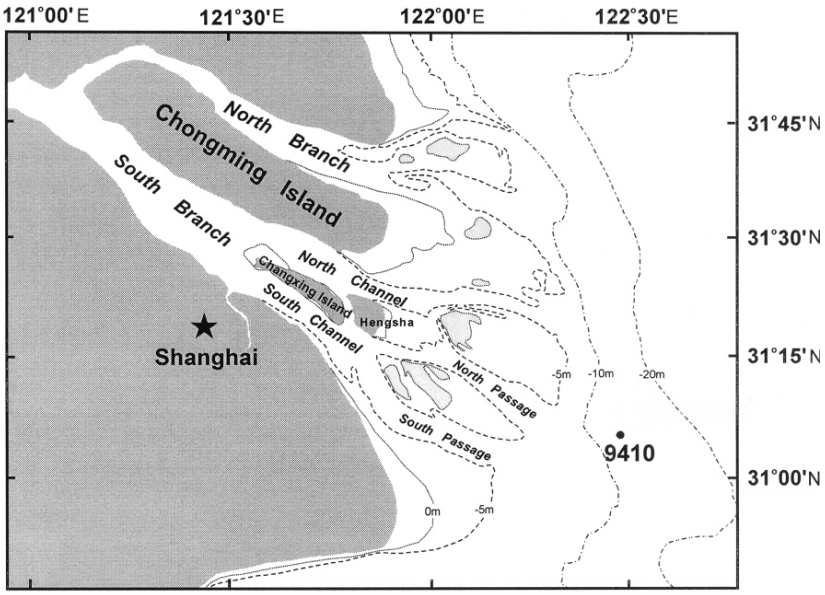

Figure 1: The Changjiang Estuary and monitoring station 9410.

2. Field Observations and Methods

Measurements (acoustic profiling) were also made at station 9410 (122°27'30"E, 310°5'36"N, Figure 1) during spring tide (0600 hr 07 October 1994_0700 hr 08 October 1994), moderate tide (1100 hr 13 October 1994_1500 hr 14 October 1994) and neap tide (1400 hr 15 October 1994_1700 hr 16 October 1994). Vertical profiles of fine suspension concentration were measured by an acoustic suspended sediment monitor (*Shi et al.* [1999]). Tidal current speed and direction were measured hourly at 0.1 D, 0.2 D, 0.4 D, 0.6 D, 0.8 D and 1.0 D (D: water depth above the bottom) using an electromagnetic current meter. Time series data of current velocity, salinity and suspended sediment concentration were measured at spring and neap tides in the Changjiang Estuary.

3. Results and Discussion

A turbidity maximum was consistently observed at the mouth of the Changjiang Estuary during spring tide (Figure 2). Those data were analyzed for (1) spring/neap tidal, (2) intratidal (flood/ebb), and (3) burst-type dynamic nature of fine suspended sediment transport processes within the turbidity maximum there.

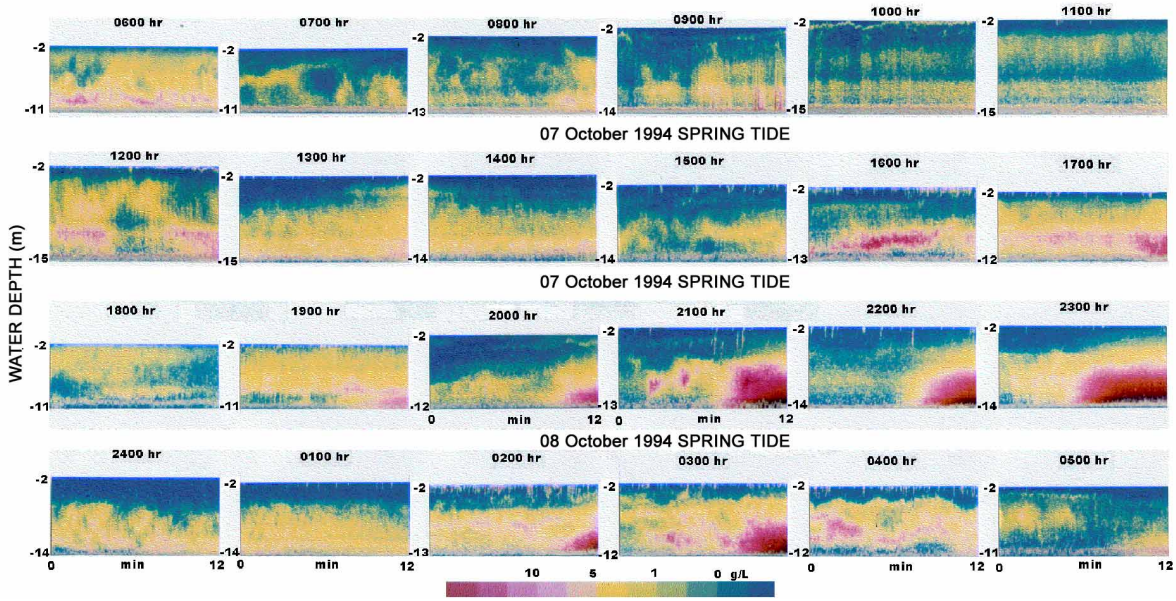

Figure 2: Acoustic images of burst-averaged concentration over a 12-min period for each hour during spring tide (0600 hr 07 October 1994_0500 hr 08 October 1994). Bottom bar: burst-averaged concentration.

Calibrated acoustic images (Figure 2) revealed that: (1) bottom fine sediment boundary layer; (2) the evolution of the fine suspension concentration profiles to tide-, wave- and fine sediment density-induced forcing; (3) turbulence suppression by salinity/concentration stratification is one of the important mechanisms for the formation of turbidity maximum; (4) impulsive fine sediment resuspension by bottom fine sediment boundary-induced currents; and (5) Kelvin-Helmholtz instability is one of the dominant processes responsible for the re-entrainment of the near-bed high concentration suspension. Furthermore, coherent structures were present in the fine sediment boundary layer (2400 hr, 08 October 1994). The structure of a bottom sediment boundary layer was studied in central Long Island Sound by *Bedford et al.* (1988). Fine sediment-induced density currents are responsible for fine suspended sediment transport processes (Figure 2). The coupling between fine sediment bed and fine suspension in the bottom boundary layer is important, as discussed by *Boudreau* [1997].

4. Conclusion

Field observations have been made to examine the spring/neap tidal, intratidal (flood/ebb), and burst-type dynamic natures of bottom fine boundary layer and suspended sediment transport processes at the mouth of the Changjiang Estuary. Fine sediment-induced density currents and others are responsible for fine suspended sediment transport processes in the turbidity maximum at the mouth of the Changjiang Estuary.

Acknowledgments: This research was funded by the National Natural Science Foundation of China (Estuarine and Coastal Program, No. 49806005).

References:

Bedford, K.W., Libicki, C., Wai, O., Abdelrhman, M. and Van Evra, R., The structure of a bottom sediment boundary layer in central Long Island Sound. In: J. Dronkers and W. van Leussen (Eds.), *Physical Processes in Estuaries*. Springer-Verlag Berlin Heidelberg, Germany, 1988, 446-462.

Boudreau, B.P., A one-dimensional model for bed-boundary layer particle exchange. *Journal of Marine Systems,* 11, 279-303, 1997.

Brenon, I. and Le Hir, P., Modelling the turbidity maximum in the Seine Estuary (France): identification of formation processes. *Estuarine, Coastal and Shelf Science,* 49, 525-544, 1999.

Glangeaud, L., Transport et sedimentation clans l'estuairc et a l'embouchure de La Gironde. *Bulletin of Geological Society of France,* 8, 599-630, 1938.

Grabemann, I., Kappenberg, J. and Krause, G., Aperiodic variations of the turbidity maximum of two German coastal plain estuaries. *Netherlands Journal of Aquatic Ecology*, 29 (3-4), 217-227, 1995.

Hamblin, P.F., Observations and model of sediment transport near the turbidity maximum of the upper Saint Lawrence estuary. *Journal of Geophysical Research*, 94 (C10), 14,419-14,428, 1989.

Hughes, M.G., Harris, D.T. and Hubble, T.C.T., Dynamics of the turbidity maximum zone in a micro-tidal estuary: Hawkesburry River, Australia. *Sedimentology*, 45, 397-410, 1998.

Li, J.F. and Zhang, C., Sediment resuspension and implications for turbidity maximum in the Changjiang Estuary. *Marine Geology,* 148: 117-124, 1998.

Schubel, J.R., Turbidity maximum of the Northern Chesapeake Bay. *Science,* 161, 1013- 1015, 1968.

Shi, Z., Dynamics of the turbidity maximum in the Changjiang Estuary, China, in J.C. Winterwerp and C. Kranenburg (Eds.), *Proceedings of the* 6^{th} *International Conference on Nearshore and Estuarine Cohesive Sediment Transport Processes,* September 4-8, 2000, WL/Delft Hydraulics, Elsevier Marine Sciences, The Netherlands, 2002: in press.

Uncles, R.J. and Stephens, J.A., Nature of the turbidity maximum in the Tamar estuary, U.K. *Estuarine, Coastal and Shelf Science*, 36, 413-431, 1993.

Wellershaus, S., Turbidity maximum and mud shoaling in the Weser estuary. *Archiva Hydrobiologica*, 92, 161-198, 1981.

Numerical simulation of Estuarine Turbidity Maxima in the Elbe estuary

Manuel Ruiz Villarreal, (*Institute for Oceanography, University of Hamburg, Troplowitzstr.7, D-22529 Hamburg, Germany*, ruiz@ifm.uni-hamburg.de)

Hans Burchard, (*Baltic Sea Research Institute Warnemünde, Seestr. 15, D-18119 Rostock, Germany*, hans.burchard@io-warnemuende.de)

1 Introduction

Transport of suspended particulate matter (SPM) in estuaries is a complex process where the interplay between hydrodynamics (mainly tidal movements and stratification effects) and the intrinsic dynamics of the particles determine the relevant spatial and time scales of variability. In some tidal estuaries, as a result of this interaction, Estuarine Turbidity Maxima (ETMs) appear. ETMs are characterised by high SPM concentrations, usually near the tip of the salinity intrusion. There are evidences of the biological effects of ETMs, that also have a significant influence on the distribution of contaminants in estuaries.

The Elbe estuary comprises the last kilometers of the Elbe river. The location of Hamburg harbor, the second biggest harbor in Europe, about 100 km upstream of the river mouth implies intensive traffic of containers and a great effort is devoted to keep the river navigable. At the outer zone, the estuary gets broader and an extense zone of tidal flats exists. The Elbe estuary can be classified as a mesotidal partially-mixed estuary. A zone of increased sediment concentration is found near the limit of the salt intrusion (usually near Brunsbütel). Apart from this main ETM, about 20 km upstream the salt wedge, there is another zone of SPM accumulation.

In this contribution, a series of numerical process studies of hydrodynamics coupled to SPM transport will be presented for the Elbe estuary with the main aim of claryfying the processes that influence the setting up of ETMs. Both process studies in simplified bathymetries and results in a high resolution realistic curvilinear grid will be presented

2 The model

The model we have applied (GETM, General Estuarine Transport Model, *Burchard and Bolding*, [2002]) is a 3D baroclinic mode-splitting model with generic vertical coordinates and a stable drying flooding algorithm. Few numerical studies of ETM formation with 3d models have been reported in the literature (for example, *Lang et al.* [1989] in the Weser, *Cancino and Neves*, [1999] in the Western Scheldt and Gironde or *Brenon and LeHir*, [1999] in the Seine). Although several physical mechanisms for the formation of an ETM have been suggested (see references for example in *Burchard and Baumert*, [1998]): the gravitational circulation, the tidal asymmetry of velocities due to the variation of stratification and the asymmetry of the tidal wave propagation; it is not yet clear their relative importance for given tidal forcing and stratification. The quoted 3d modelling studies have drawn conclusions from experiments in complex real bathymetries, where all processes interact non-linearly and also curvature effects and secundary flows make

it difficult to isolate the different contributions. In a process study in a simplified 2d bathymetry, *Burchard and Baumert*, [1998] could put forward that density effects are on the origin of ETMs, at least for mesotidal estuaries, as suggested by some previous works (*Jay and Musiak* [1994]). This also implies that the use of an adequate turbulence model closure might be necessary for an adequate description of ETM and for the evaluation of the effect of stratification on ETM formation. Contrastingly to the simple turbulence closures used in most of the previous studies, we will employ second-order closures from the extensively tested turbulence module in GOTM (General Ocean Turbulence Model http://www.gotm.net), which is coupled to GETM as the turbulence module. Another feature of the model we will show crucial for the performance of the model is the use of a high-resolution, monotonicity-preserving advection scheme for momentum and tracers.

Since we want to focus on the impact of hydrodynamics on sediment transport, a simple model for Suspended Particulate Matter (SPM) with a single class of noncohesive SPM particles that do not interact with the mean flow (no density effect of SPM) is considered. The SPM flux at the bottom is the result of erosion minus sedimentation:

$$-w_s C + -\partial_z(\nu_t'\partial_z C) = F_e - F_s \tag{1}$$

with C, the concentration of sediments and w_s their sinking velocity. Erosion and sedimentation fluxes (F_e and F_s) are modelled following *Krone,* [1962] as functions of the bottom shear stress τ_b. This parameterisation has been widely applied because its simplicity and because it requires only few empirical parameters. A pool B of nondynamic particulate matter is assumed in order to take into account the effects of depletion of erodible material at the bottom. Sedimentation and erosion fill and empty this pool, respectively, and the erosion flux is constricted by the availability of SPM from the pool.

3 Results

We have designed some idealised process studies to get insight into the physical mechanisms on the origin of ETMs and how they balance to create real ETMs. The first model set-up is based in the study by *Burchard and Baumert* [1998], and it is a 2d domain with dimensions and other relevant parameters (river run-off, sediment features...) set to those characteristic of the Elbe estuary. In this set-up, lateral effects are absent. A 2D channel of length L=100 km and constant depth of 15 m is closed at the left boundary where a weir in the real Elbe estuary exists. Tidal forcing at the open boundary is a M2 tide of amplitude 1.3 m and at the river boundary, a river run-off of 700 m^3s^{-1}, the most frequent value for the Elbe river, is imposed. Salinity is relaxed to 30 at the open sea boundary. The horizontal spatial steps are set to dx=dy=200 m, and 30 equidistant layers in the vertical are considered, which results in a vertical step of dz=0.5 m. This combination of tidal motion in a stratified environment induces the setting up of an ETM near the tip of the salt wedge. We find that advection and tidal variation of stratification induce a periodical evolution of SPM distribution for different phases of the tidal cycle (see figure 1). We will present some sensitivity tests of the results to different model assumptions (turbulence model, advection scheme...).

The second set-up is an idealised 3d domain, where we will consider lateral effects but in a symmetric domain without curvature effects. The domain is 100 km long and

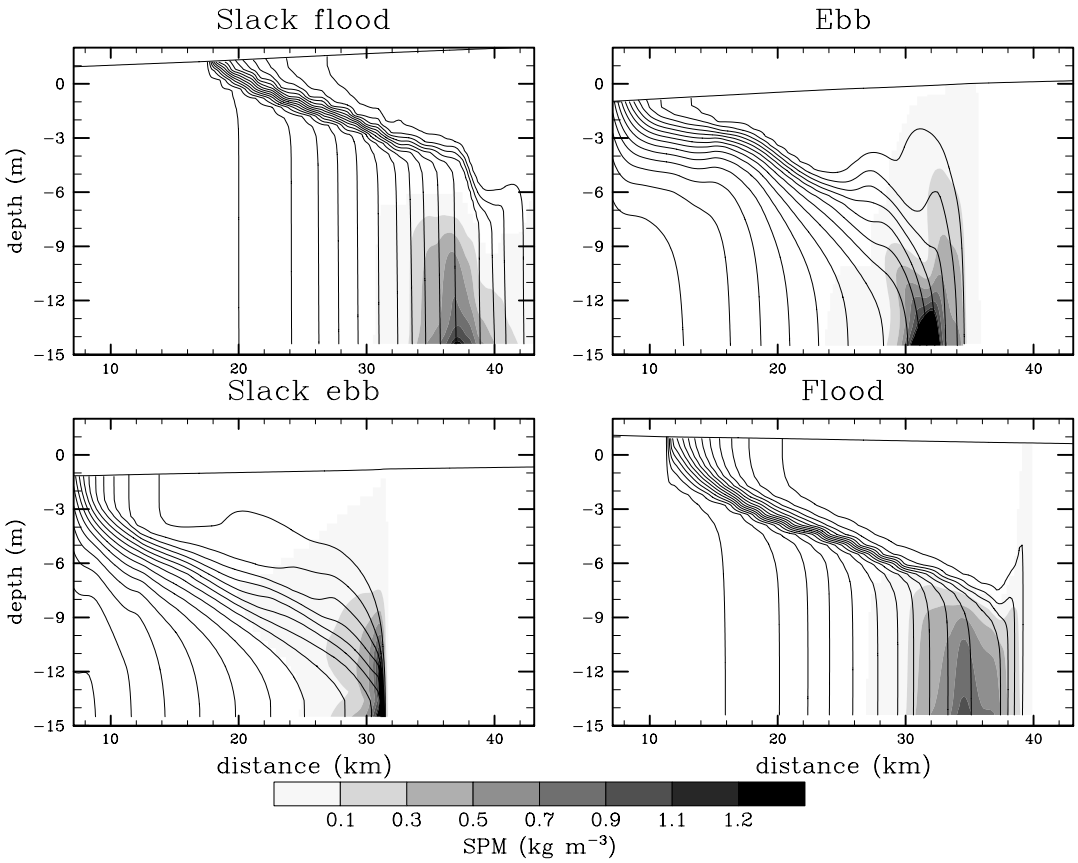

Figure 1: Salinity (contours from 2 to 30) and SPM concentration (shaded) on the first 50 km of the 2d domain for four tidal instants. A k-ϵ turbulence model and a Superbee advection scheme for momentum and tracers have been used.

broadens gradually from a width of 1 km at the river boundary to 8 km at the open sea boundary. In the across channel direction the section is symmetric with a maximum depth of 15 m at the center of the channel. Along the sides, intertidal zones are considered, and their extention is greater at the sea boundary, as in the Elbe estuary. The hydrodynamical model with the sediment module are ran in this set-up with similar choices as for the 2d set-up. In this case, lateral advection and intertidal zones also influence the dynamics. A stable ETM appears near the salinity intrusion, although not so intense as in the 2d case. The tidal evolution of SPM is also similar. Other interesting finding is that, for these dimensions of the domain, a two-cell structure appears in the across-channel direction during flood. This influences the spatial location of the ETM.

Finally, some preliminary results in a curvilinear bathymetry of the Elbe estuary will be presented. An idealised forcing forces the model and the predicted ETM dynamics will be discussed.

Acknowledgments: This research has been supported by a Marie Curie Fellowship of the Eu-

ropean Community Programme IHP under contract number HPMF-CT-2000-01037. Disclaimer: The author is solely responsible for information communicated and the European Comission is not responsible for any views or results expressed.

References:

Brenon, I. and LeHir, P., Modelling the Turbidity Maximum in the Seine estuary (France): Identification of formation processes, *Estuarine, Coastal and Shelf Sc.*, *49*, 525-544, 1999.

Burchard, H. and H. Baumert, The Formation of Estuarine Turbidity Maxima due to Density Effects in the Salt Wedge. A Hydrodynamic Process Study *J. Phys. Oceanog.*, *28*, 309-321, 1998.

Burchard, H., and K. Bolding, GETM, a general estuarine transport model. Scientific documentation. Tech. Rep. EUR 20253 EN, European Commission, 157 pp., 2002.

Cancino, L. and R. Neves, Hydrodynamic and sediment suspension modelling in estuarine systems. Part II: Application to the Western Scheldt and Gironde estuaries, *J. Mar. Systems*, *22*, 117-131, 1999.

Jay, D. and J. D. Musiak, Particle trapping in estuarine tidal flows, *J. Geophys. Res.*, *99*, 445-461, 1994.

Krone, R. B., Flume studies of the transport of sediment in estuarial shoaling processes. Final Report, Hydraulic Eng. Lab. US Army Corps of Eng., 110 pp., 1962

Lang, G., R. Schubert, M. Markofsky, H-U. Fanger, I. Grabeman, H.L.Kraseman, L.J.R. Neumann and R. Riethmüller, Data interpretation and numerical modeling of the mud and suspended sediment experiment 1985, *J. Geophys. Res.*, *94*, 14381-14393, 1989

Sediment flux and budget on tidal to decadal time scales in a sandy, macrotidal estuary

COLIN JAGO, SARAH JONES, GARRY REID, KADIR ISHAK

(School of Ocean Sciences, University of Wales Bangor, Marine Science Laboratories, Menai Bridge, Gwynedd, LL59 5EY, UK, c.f.jago@bangor.ac.uk)

1. Introduction

Estuaries on macrotidal coastlines are characterised by large sediment fluxes due to tidal currents and by net sedimentation resulting from differences in flood and ebb transports. Quantification of sediment budgets on time scales of years to decades is important for effective management with respect to, for example, ecosystem sustainability, water quality, and navigation. Appropriate datasets on such time scales are rare. However, the advent of technologies for high frequency measurement of currents and suspended sediment concentrations provides the potential for high resolution estimation of net sediment flux on short time scales and, hence, for extrapolation of sediment budgets on longer time scales. But, as emphasised by *McCave* [1979], the validity of net sediment fluxes determined from measurements is questionable since flood and ebb fluxes are very large numbers with large measurement error bars and the net flux is a relatively small number. Attempts to measure net sediment fluxes have been constrained by such uncertainties: see *Terwindt* [1967](Rhine), *Fleming* [1970] (Clyde), *Allen and Castaing* [1973] (Gironde), *Harris and Collins* [1988] (Bristol Channel), *Hardisty and Rouse* [1996] (Humber). Uncertainties become limiting where the net flux is a very small proportion of the gross flux – for example, 1% in the Humber estuary. Here we describe an attempt to quantify annual sediment budgets, independently measured on a decadal time scale, by short term measurement of sediment fluxes in an estuary where the net flux is about 10% of the gross flux.

2. Field site

The macrotidal Taf estuary in SW Wales, UK is 1.5 km wide at its mouth narrowing down to less than 10 m at the farthest intrusion of salt water, 15 km from the mouth. The estuary is dominated by tidal forcing (see *Jago* [1980]). The tidal range is large, reaching 10 m on a big spring tide. Tides show time-velocity asymmetry particularly on springs when the flood is < 3 hours and fast currents pulsing to 2.5 m s^{-1} are generated. On springs the ebb is about 4.5 hours long, after which the estuary is effectively void of salt water. The river Taf is small with a daily average discharge of 7 m^3 s^{-1}. The estuary is protected from swell waves due to a sand spit across its mouth.

The extended period (4.5 hours) when salt water is excluded from the estuary is characterised by a meandering channel (usually < 1 m deep) which cuts through extensive areas of intertidal sand flats bordered in places by narrow mud flats and saltmarsh. The sand flats are the most extensive physiographic unit and are characterised by well sorted, fine sand (mean grain size 130 μm) which shows little spatial variation. Mineralogical analysis proves that the estuarine sands are derived from offshore and not from the River Taf (see *Jago* [1980]). These sands are readily entrained by the tidal currents which generate shear velocities exceeding 0.15 m s^{-1} on big spring tides. The fine sands are entrained directly into suspension with little bed load transport.

3. Methods

Sediment budget

Ten transects were set up across the estuary in 1968 between temporary bench marks fixed in the

saltmarsh at both ends of each transect. Transects were spaced between the estuary mouth and the landward limit of the intertidal sand flats. Profiles along transects were determined by conventional levelling, at low tide when the estuary is traversable on foot, intermittently between 1968 and 1980, annually between 1981 and the present (35 surveys of each transect in total). Profile changes were spatially integrated to quantify gross changes between surveys and hence to determine the sedimentation rate on the sand flats (sand volume change/sand flat area).

Sediment flux

Short term flux measurements were made along two of the levelling transects across the estuary. Simultaneous measurements of velocity and suspended sediment concentration (SSC) were made at fixed stations, about 150 m apart, on the transects over several (up to 6) tidal cycles. Current velocities were measured using velocity gradient units (each with 10 impellors) at 2 sites on each transect; data were logged as 1 minute averages every 10 minutes. Velocities at other stations were measured with EM and impeller current meters deployed every 15 minutes in profiling mode from anchored boats.

SSC was measured using a 0.1 m path length SeaTech transmissometer linked to an Applied Microsystems STD-12, and was deployed in profiling mode from a fast inflatable boat which traversed a transect and visited each site every 10 minutes. Data were logged at 0.1 m depth increments. The transmissometer was calibrated in situ by comparison with 500 ml water samples filtered through washed, preweighed Whatman GF/C glass microfibre filters. Blank filters were used to determine the accuracy of the gravimetric procedures: the error was less than 0.3%.

4. Results

Sediment budget

While individual transects experienced variable sedimentation and erosion, integration of changes on all transects showed a progressive increase of sand in the estuary. During the period 1968-97, there was a gain of 2.94×10^6 m ^{3} of sand due to an annual influx of c. 0.10×10^6 m ^{3}. This gain gave rise to an annual mean sedimentation rate of 0.02 m. Given the mineralogical evidence, this represents a net input of marine sand from offshore and is the budget that has to be matched by the budget estimated from the flux measurements.

Sediment flux

There was a large variation in SSC at the sampling stations. High values, up to 1000 mg l $^{-1}$, occurred during peak flows but reduced to 10 mg l $^{-1}$around slack high water. Two orders of magnitude variation in SSC posed some problems with transmissometer calibration as there was a variation in particle size over a tidal cycle. Deployment of a LISST 100 laser sizer showed that suspended sediment was more than 80% fine sand during most of the flood and ebb, but at high water the sand fraction dropped out of suspension leaving finer particles (mode < 20 μm). Although the values of SSC around slack high water, after sand had been deposited, did not significantly impact on sediment flux estimates, separate calibration curves for sand and fine fractions were generated. Calibration coefficients (R^2) ranged 0.58-0.89 with lower R^2 values for sand because of the difficulties of obtaining simultaneous transmissometer readings and water samples in the rapidly changing conditions of the early flood and late ebb tides.

Much of the sediment flux during a tidal cycle occurred at the start of the flood tide (as the rapidly rising tide poured into the estuary) and towards the end of the ebb (as flow became confined to the main channel). Typical values of gross sediment flux per tide were 0.79×10^5 kg and 22.40×10^5 kg for

neaps and springs, respectively. While at some stations along transects, ebb sediment flux exceeded flood sediment flux (because flood and ebb channels did not coincide), overall flood sediment flux exceeded ebb sediment flux on all tides. Typical values of net sediment flux per tide were 0.19×10^5 kg and 1.88×10^5 kg for neaps and springs, respectively. Hence net flux, always landward, was an order of magnitude greater on springs than on neaps.

There were exponential relationships between sediment flux per unit width of transect and tidal range with R^2 values of 0.88 and 0.90 (95% confidence) for flood and ebb tides, respectively (Figure 1). These gave the following when data from both transects were combined:

$$F_{flood} = 19.20 \times 2.17^t$$

$$F_{ebb} = 9.67 \times 2.17^t$$

where F = sediment flux (kg m^{-1}) and t = tidal height above O.D. (m)

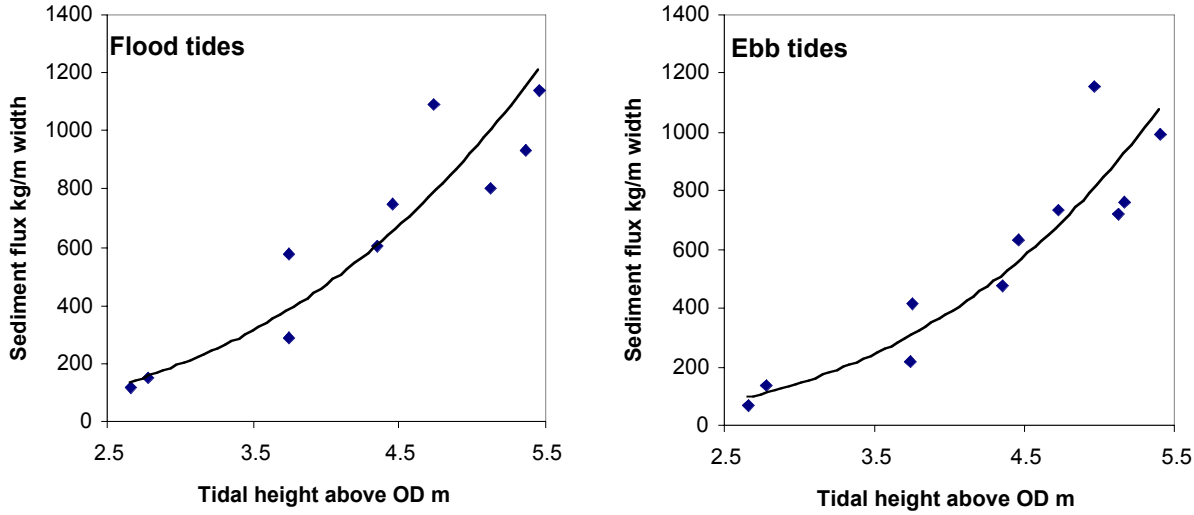

Figure 1: Relationships between sediment flux per metre width and tidal height

Errors were in part due to measurement errors: e.g. transmissometer calibration; water flux measurement (typically 0-5%). There was inherent variability during early flood and late ebb tides when measurement was most difficult due to problems of small boat handling in shallow, turbulent waters. Nevertheless, these errors were small. Further contributions to errors are the absence of any other processes (especially river discharge) in the algorithms. River discharge contributes to sediment transport during the period of sand flat exposure when river flow generates a seaward sediment flux.

The algorithms were used to compute total sediment fluxes over a year. And these fluxes were used to compute net sedimentation rate over the sand flats landward of each transect. With 40% porosity for the deposited sand, this gave sedimentation rates of 0.016 ± 0.046 m yr^{-1} and 0.012 ± 0.026 m yr^{-1} in each case. The error bars are 95% confidence limits around the defining algorithms. These estimates compare very favourably with the `true´ value (0.020 m yr^{-1}) given by the long-term levelling surveys.

5. Conclusions

The long-term levelling dataset provided an unusual opportunity for testing the validity of net sediment flux estimated from in situ measurements over short periods. While the experiment started

with the premise that short term measurements cannot be used to determine sediment budgets, for the reasons given by *McCave* [1979], in fact the annual sediment budget extrapolated from the flux measurements was remarkably close to the budget determined from the 30 yr levelling dataset. The conclusion must be that, for this estuary, the mean annual sedimentation rate can be realistically determined from flux measurements over a few tidal cycles. However, there are specific reasons why McCave's strictures have proved to be unfounded in this particular case. Bedload transport is negligible in the Taf estuary so that SSC is a valid parameterisation of sediment transport ; so sediment flux can be measured relatively easily. Furthermore, the uniformity of sand texture means that transmissometer calibrations are spatially and temporally robust. Finally, the time-velocity asymmetry of the tide gives rise to a large net sediment flux which is c.10% of the gross sediment flux. The net flux therefore lies outside the error bars of in situ measurement.

References

Allen, G.P., Castaing, P., 1973. Suspended sediment transport from the Gironde estuary (France) onto the adjacent continental shelf. *Mar.Geol.,* 14, M47-M53.

Flemming, G.,1970. Sediment balance of the Clyde estuary*J.Hydraul.Div.Proc.Amer.Soc.civil Eng.,* 96, 2219-2230.

Hardisty, J.G., Rouse, H.L., 1996. The Humber Observatory: Monitoring, modelling and management for the coastal environment. *J.Coastal Res.,*12, 683-690.

Harris, P.T., Collins, M., 1988. Estimation of annual bed load flux in a macrotidal estuary: Bristol Channel, U.K. *Mar.Geol.,* 83, 237-252.

Jago, C.F., 1980. Contemporary accumulation of marine sand in a macrotidal estuary, Southwest Wales. *Sediment.Geol.,* 26, 21-49.

McCave, I.N., 1979. Suspended sediment. In: Dyer, K.R. (Ed.), Estuarine Hydrography and Sedimentation. Cambridge Univ. Press, pp. 131-185.

Terwindt , J.H.J., 1967. Mud transport in the Dutch Delta area and long the adjacent coastline. *Neth.J.Sea Res.,* 3, 505-531.

Sediment Flux at the Mouth of the Humber Estuary

JACK HARDISTY

(Department of Geography, The University of Hull, HU6 7RX UK and NorthSea Software Systems Ltd. Barkers Mill, Beverley, HU17 0UJ, UK J.HARDISTY@NORTHSEANET.CO.UK)

1. Introduction

The Humber Estuary on the east coast of northern England drains some 24,000 km^2 and has a tidal prism in excess of 1.5km^3. Although recent work shows that the estuary has been accreting at a rate of about 1 MT a-1 throughout the last 5,000 years since sea level attained its current elevations, sediment transport processes at the estuary mouth are essentially symmetrical with some 100 kT of suspended solids carried inwards and outwards on each flood-ebb cycle (Hardisty, *et al*., 1998, Dyer, *et al.,* 2000). Results from the Humber Flux Curtain experiment are reported which describe the seasonal, inter- and intra-tidal variations in sediment flux and also quantify the effects of changing river discharge and demonstrate that net fluxes due to these processes are negligible.

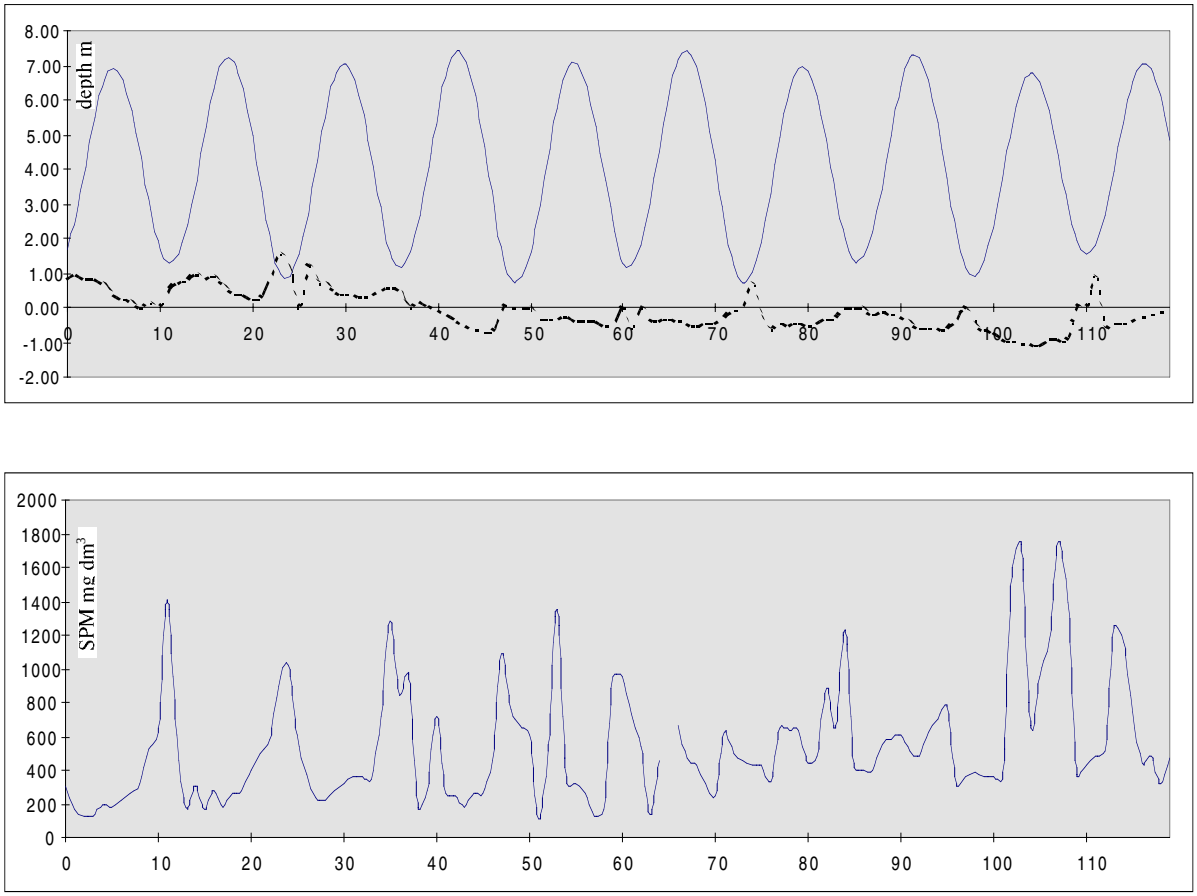

Figure 1: Water depth (upper diagram) and suspended particulate matter (lower diagram) at the mouth of the Humber Eastuary for the first five days of 1996.

2. Flux Curtain Experiment

Data were collected throughout 1995-1997 from radio linked instrument systems moored across the mouth of the Humber Estuary measuring water temperature, salinity, depth, suspended particulate matter (SPM) and flow velocities. The relationship between the SPM and tidal range and freshwater forcing is examined as shown in Figure 1.

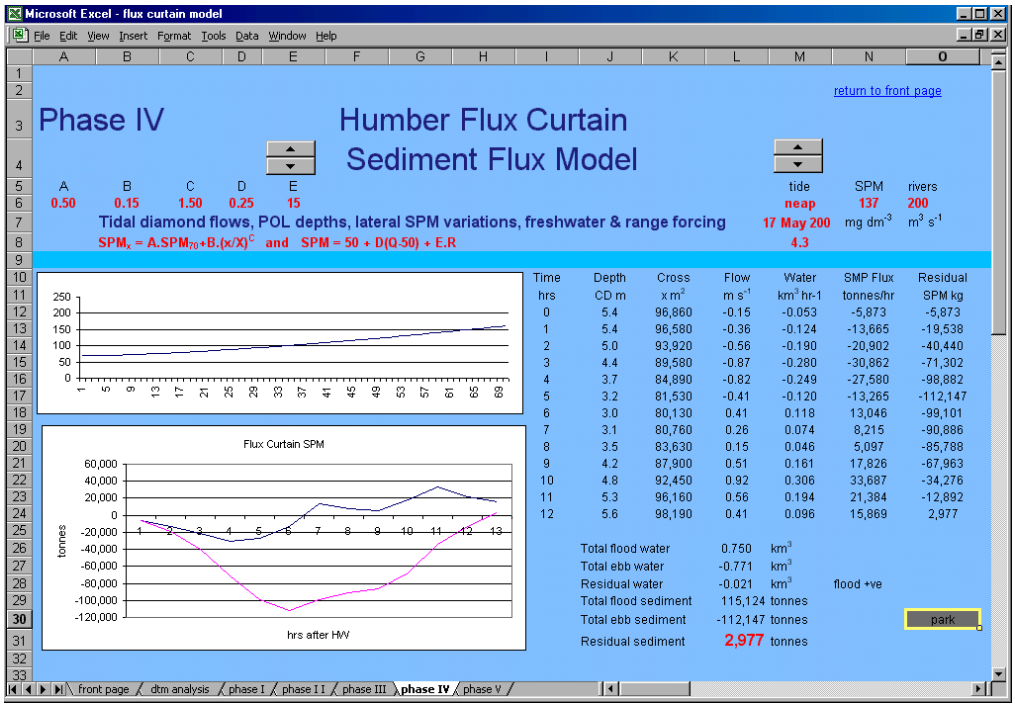

Figure2 : Typical model output for estuary mouth SPM

3. Modelling

A numerical model was constructed to simulate the estuary mouth sediment flux based upon the integration of local flow velocity and SPM

$$F = \int U_{x,z,t} C_{x,z,t}$$

As shown, typically, in Figure Two. The model was able to account for seasonal, inter- an intra-tidal variations in SPM but showed that the nett influx reported above could not be generated by these processes. The data do, however, demonstrate that massive in fluxes of sediment are associated with north easterly storm events when sediment is entrained from the coast of Holderness and transported into the estuary during the flood tide, settles and mixes and is not necessarily returned to the open sea during the subsequent ebb. Preliminary estimates indicate that this episodic process may be responsible for the observed accretion rates.

References:

Dyer, K.R., M.-C.Robinson and D.A. Huntley, 2000. Suspended sediment transport in the Humber Estuary. In : D.A.Huntley, G.J.L.Leeks and D.E.Walling (eds.) Land-Ocean Interaction: measuring and modelling fluxes from river basins to coastal seas. IWA Publishing, London. 169-183.

Hardisty, J., R.Middleton, D.Whyatt and H.L.Rouse, 1998. Geomorphological and hydrodynamic results from digital terrain models of the Humber Estuary. In : S.Lane, K.S.Richards and J.Chandler (eds.) Landform Monitoring, Modelling and Analysis. Wiley, Chichester 421-433.

Factors affecting longitudinal dispersion in estuaries of different scale

ROY LEWIS

(Brixham Environmental Laboratory, AstraZeneca UK Limited, Freshwater Quarry, Brixham, Devon, TQ5 8BA, U.K., roy.lewis@brixham.astrazeneca.com)

REG UNCLES

(Plymouth Marine Laboratory, Prospect Place, West Hoe, Plymouth, Devon, PL1 3DH, U.K., rju@pml.ac.uk)

1. Introduction

To assess the biological health of a given estuary, it is usual to compare the biological conditions with those in similar systems. This leads to the problem of deciding what aspects of the physical, chemical and biological characteristics make any two systems 'similar'. A key factor that indicates whether two estuaries are physically similar is the degree of dilution obtained by dissolved substances; this is not simply a measure of the overall capacity of the estuary but rather its ability to dilute and flush to sea any soluble substances entering the system.

The distribution of salinity of estuarine waters has long been used as an indicator of the diluting capability of the system. It is generally relatively easy to obtain salinity data for an estuary, especially if the salinity distribution can be measured without the need for anchored stations. Furthermore, the salinity distribution in an estuary is a useful overall indicator of the physical condition of the system because it represents the resultant effect of numerous complex processes - freshwater inflow, tidal range, velocity variations (spatial and temporal) and the degree of turbulence.

The approach adopted in this study is to develop a solution for the mass balance equation for salt under the assumption that estuaries tend to an equilibrium situation in which the loss of salt from the system by freshwater transport is matched by an upstream 'diffusive' flux due to non-advective processes. The model assumes that each estuary cross-section expands exponentially towards the sea and that, averaged over an appropriate period of time, the longitudinal dispersion coefficient is essentially constant in each system. In most instances, it is further assumed that this coefficient remains constant along the estuary length.

2. Data Sets

The data used in the analysis came from observations in five UK estuaries. These estuaries range in size and in cross-sectional form; for example, the reclamation and canalisation of the Tees estuary has greatly reduced the area of the intertidal mudflats, while the Tamar estuary retains extensive mudbanks at low water. Although the five estuaries were principally selected because of the quality of the data, it was seen as desirable that the systems should span a range of scales, so that any effects of scale differences could be noted.

The approach adopted for the analysis is really for well mixed systems in which the depth mean salinity deviates little from the surface and bed distributions. However, some of the data sets for partially- mixed estuaries, such as the Tees or the Tamar, were sufficiently sound and comprehensive as to merit their inclusion.

3. Analysis

For each estuary, the observed salinities were expressed as fractions of the salinity at the seaward end and plotted against distance along the estuary, the latter having been defined as a fraction of the full length. Fractional salinities were computed from the model for different values of a parameter m, which is used to characterise the dimensions and dispersion coefficient for the system. The value of m was adjusted to optimise the fit between the predicted and observed salinity distributions in each instance (Bassindale, 1943) (Fig 1).

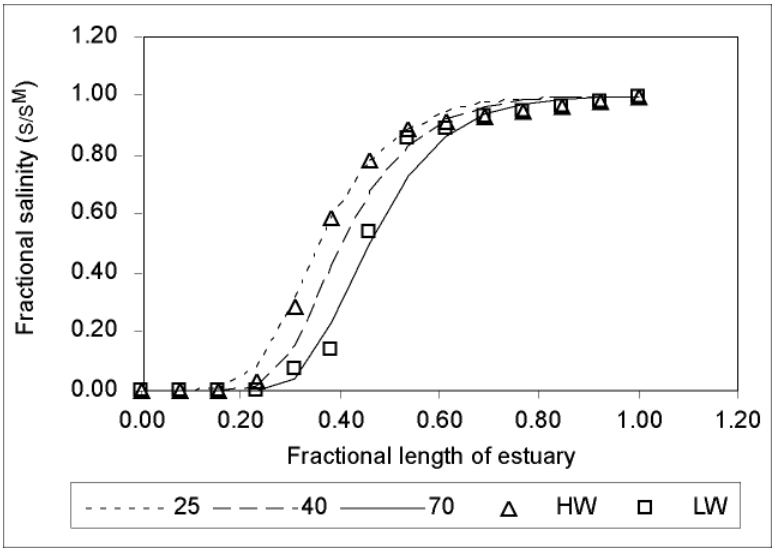

Figure 1: Predicted axial salinity distributions compared with observed salinities at high and low water in the Severn estuary for three different values of m.

The model indicated that the maximum flux of salt occurs at a similar longitudinal position to the maximum in the longitudinal gradient in salinity. Using the fitted values for m, the maximum fluxes of salt and the corresponding maximum salinity gradients were computed. Fluxes are shown plotted against salinity gradients for the five estuaries in Fig 2. The figure shows a linear regression line, forced through the origin, and the computed correlation coefficient. The slope of this line, which is a measure of the longitudinal dispersion coefficient, K_{xe}, resulted in a value of about 90 $m^2 s^{-1}$.

This plot of the maximum flux and salinity gradients suggests that a value of 100 $m^2 s^{-1}$ for K_{xe} is a reasonable first choice when setting up a simple estuary model. Perhaps more importantly, Fig 2 indicates that low salt fluxes are associated with low salinity gradients and high fluxes are associated with high gradients. The labels for the individual estuaries shown in the figure again show that it is the large, energetic systems, such as the Thames and Severn, which have smaller salt fluxes. These fluxes may be small because the vertical circulation flux, a major component of the net flux, is limited by the degree of turbulence. This is a likely explanation for the response shown in Fig 2 because the vertical circulation also aids the sharpening of the interface between the brackish and saline waters, and ultimately this mechanism tends to enhance the axial gradient in salinity.

The magnitudes of the individual flux components at eight stations along the Tees estuary have been calculated on each of five days of neap tides and five days of spring tides using data gathered in 1975 (Lewis and Lewis, 1983). The net fluxes were found to vary smoothly despite considerable spatial variation in the individual flux components. Fig 3 shows a comparison between these net fluxes and values computed from the model, based on the observed axial salinity distribution on tides of neap range. As the velocity and salinity measurements used to compute the fluxes were made along the central axis of the Tees, a factor of 0.6 was selected to correct for the cross-sectional mean to axis ratio of the fluxes. The tidal mean salinity distribution is shown in the plot.

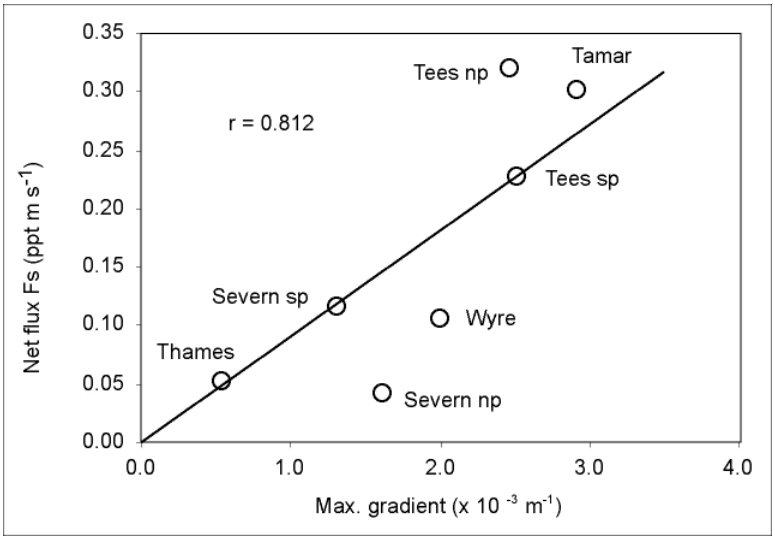

Figure 2: Plot of maximum net flux of salt against maximum salinity gradient.

In Fig 3 it can be seen that the predicted net flux from the model is of similar magnitude to the observed flux at the six most seaward stations in the diverging estuary; these span a distance of about 11 km. Only at the two landward stations does the difference between the observed and predicted fluxes become significant. This deviation is at least partially due to errors in the fluxes computed from the measurements because, at that part of the estuary, they represent relatively small differences between large terms.

The model was used to demonstrate that, allowing for a small increase in the freshwater flow, there was still a seaward shift in the depth mean salinity distributions between periods of neap and spring tides. This neap to spring change is associated with a reduction in the maximum landward flux of salt. As the model assumes an equilibrium between non-advective flux and freshwater advection, any reduction in the landward salt flux is balanced by a seaward shift in the overall salinity distribution. The displacement in the salinity distribution means that, for a given salinity, the cross-sectional area increases so that the seaward advective transport of salt per unit area decreases. The new location of the salinity distribution represents the location at which this transport again balances the non-advective transport of salt.

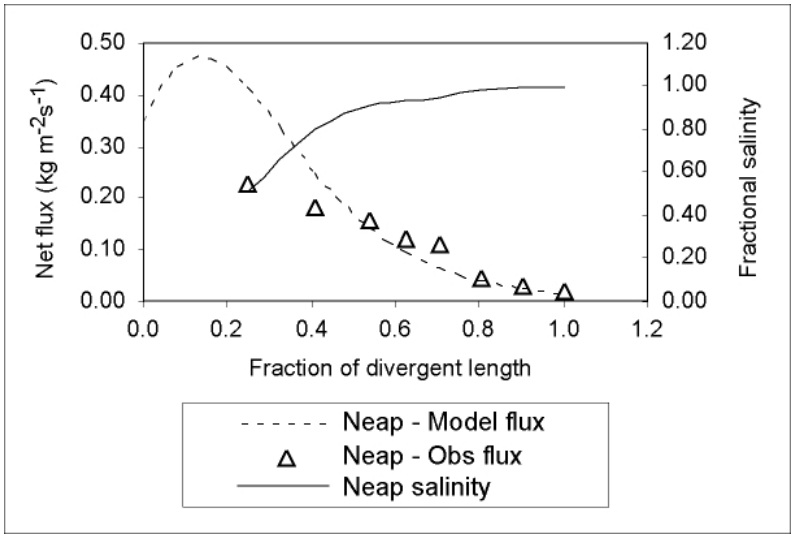

Figure 3: Comparison of the predicted net flux of salt with the observed fluxes along the Tees estuary. The corresponding observed tidal and depth mean salinities, expressed as fractions of the salinity at the estuary mouth are also shown.

4. Conclusions

A steady state model, that assumes an exponential increase in estuary area with distance towards the sea and a constant value for the longitudinal dispersion coefficient, indicates that the maximum landward flux of salt occurs in the vicinity of the maximum axial gradient in salinity.

Data sets selected for their quality were used to compute matching pairs of values for the maxima in salt fluxes and salinity gradients. A plot of these variables indicated that lower fluxes and salinity gradients were associated with the larger, more energetic, estuaries. A linear fit through the data suggested that a value of 100 $m^2 s^{-1}$ for the longitudinal dispersion coefficient, K_{xe}, is reasonable first estimate for estuary mixing problems.

Studies of the net fluxes associated with the salinity distributions for the Tees estuary indicated that, if the landward flux becomes too small to counter the seaward advection of salt by river flow, the salinity distribution shifts to a region of greater cross-section, so that the upstream 'diffusive' flux of salt again balances the freshwater advection per unit area.

References:

Bassindale, R., A comparison of the varying salinity conditions of the Tees and Severn estuaries. *Journal of Ecology*, 12 (1), 1-10, 1943.

Lewis, R.E. and Lewis, J.O. The principal factors contributing to the flux of salt in a narrow, partially stratified estuary. *Estuarine, Coastal and Shelf Science*, 16, 599-626, 1983.

Salt intrusions in Siberian River Estuaries -Observations and model experiments in Ob and Yenisei

INGO H. HARMS, UDO HÜBNER, JAN O. BACKHAUS

(Institute for Oceanography, University Hamburg, Troplowitzstrasse 7, 22529Hamburg, Germany, harms @ifm.uni-hamburg.de)

MIKHAIL KULAKOV, VLADIMIR STANOVOY

(Arctic and Antarctic Research Institute, Bering Strait 38, 199397 St. Petersburg, Russia, mod@aari.nw.ru)

OLEG STEPANETS, LUDMILLA KODINA

(Vernadsky Institute of Geochemistry, Kosygin Strait 19, 117975 Moscow, Russia, stepanet@geokhi.ru)

REINER SCHLITZER

(Alfred-Wegener-Institute for Polar and Marine Research, Columbusstrasse, 27568 Bremerhaven, Germany, rschlitzer@awi-bremerhaven.de)

1. Observations

Compared to other Arctic Shelf Seas, the Kara Sea receives large amounts of freshwater through the Siberian rivers Ob and Yenisei. Both rivers drain a catchment area in Siberia and Russia of more than 5 mill. km^2. The total annual amount of freshwater input into the Kara Sea equals roughly 1200 km^3/y of which 80% is discharged in spring (May - June) [*Pavlov and Pfirman,* 1995]. Peak discharge rates of more than 100.000 m_/s lead to a pronounced vertical stratification which is additionally enhanced by atmospheric warming and ice melting.

Historical data showed a permanently existing pycnocline in the estuary of Ob and Yenisei but recent CTD-profiles revealed that vertical salinity and temperature gradients in the Yenisei Estuary may be extremely strong and reach values of up to 5-10 psu per 10 cm and 1.5 – 2.0 °C per 10 cm (Fig. 1). These extreme situations can be observed when due to strong wind induced off-shore surface flow, high saline bottom water penetrates into the estuary, leading to so called 'salt intrusions'. The data show that salt intrusions occur most probably during summer, in August or September, when north-easterly winds prevail and the difference between upstream surface salinity and downstream bottom water salinity is most pronounced.

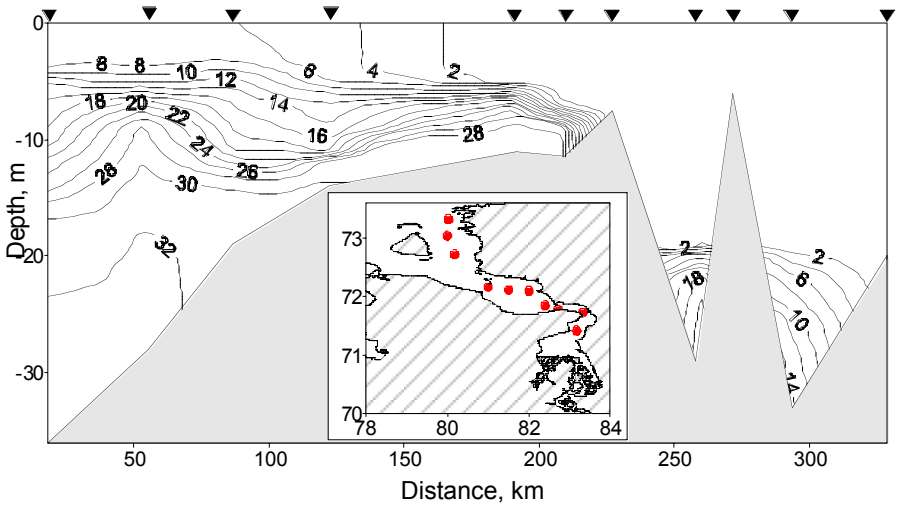

Fig. 1: Salinity section in the Yenisei estuary, summer 1995

2. Model application

At the *Institute for Oceanography, University Hamburg*, the shelf sea modelling group applies a high resolution baroclinic 3-d circulation and sea ice model to the Kara Sea. The horizontal grid resolution is 9.4 km. The model is based on the coding of the *Hamburg Shelf Ocean Model* HAMSOM, introduced by *Backhaus* [1985], and previously applied to the Barents and Kara Sea by *Harms* [1997a, b]; *Harms and Karcher* [1999] and *Harms et al.* [2000]. The circulation model is coupled to a thermodynamic and dynamic sea ice model, which calculates space and time dependent variations of ice thickness and ice concentration [*Hibler,* 1979].

Our present studies are forced with with realistic atmospheric winds, heat fluxes, river runoff and tides. In order to handle complex bathymetries and to reproduce more realistically topographic effects on circulation and hydrography, the coding was vectorised and supplied with a vertical adaptive gridding technique. The new coding is called *Vector Ocean Model* and got the acronym VOM [*Backhaus,* 2002]. The applied grid provides a high resolution in critical areas such as shallow estuaries, slopes and topographic obstacles. Surface and bottom following boundary layers are resolved uniformly in 4 m intervals. This allows for a better reproduction of estuary and shelf processes such as vertical stratification, stratified flows or current shear due to surface and bottom friction.

3. Results

Model results from summer reveal a general northward flow of river water at the surface out of the estuaries. Near the bottom however, a south-eastward transport of saline water from the Taymyr coast towards the estuaries prevails (fig. 2). A salt intrusion occurs during strong runoff when the direction of the wind induced offshore transport is aligned with the axis of the estuary. In this case, the enhanced surface flow has to be compensated by an onshore near bottom flow that may penetrate into the estuary.

Fig. 2: Simulated bottom flow near Ob and Yenisei estuaries for 12th of July climatological year

Since the simulated south-westward bottom current at the Taymyr coast is very persistent during summer, we assume that this flow brings saline water from the north-eastern Kara Sea towards the estuaries thus enhancing the vertical stratification and forming a pool of saline bottom water in front of the river mouths. This pool feeds the bottom flow that finally penetrates into the estuary leading to observed salt intrusions (fig. 3).

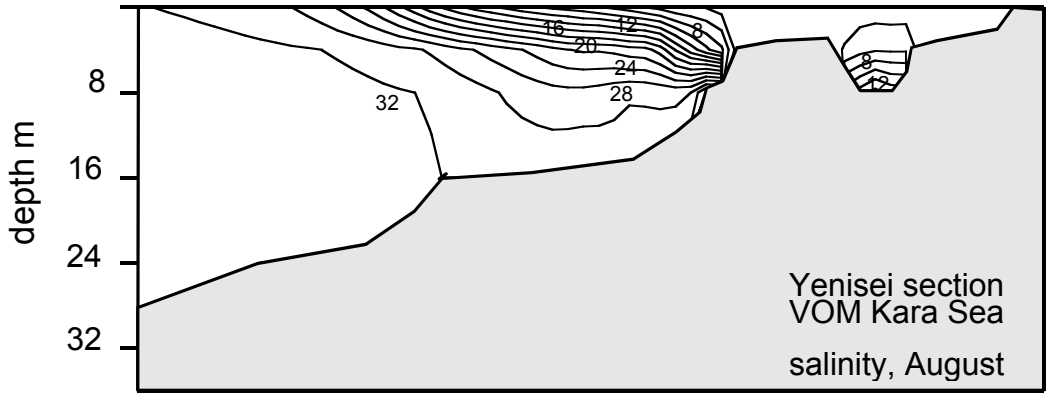

Fig. 3: Simulated salinity section in the Yenisei estuary (c.f. fig.1)

Salt intrusions occur frequently in the Yenisei estuary in connection with north-easterly winds, a prevailing wind direction in summer in the Kara Sea. In the Ob estuary, salt intrusions are almost absent and the haline stratification is weaker than in the Yenisei. This is due to enhanced tidal mixing in the Ob but also due to the orientation and depth profile of the estuary.

Acknowledgments: The work was funded by the BMBF through the bi-lateral German/Russian project SIRRO (Siberian River Runoff) and by the EU-project ESTABLISH.

References:

Backhaus J.O., A three-dimensional model for the simulation of shelf sea dynamics, Deutsche Hydrographische Zeitung, Z. 38, H4, 1985.

Backhaus, J.O., =V=O=M=>, a vector ocean model with a static adaptive grid, applied to the vertical co-ordinate. General model concept and grid adaptation. Manuscript in preparation, 2002.

Harms, I.H., Water mass transformation in the Barents Sea, ICES - J. Mar. Science, No. 54, 1997a

Harms, I.H., Modelling the dispersion of ^{137}Cs and ^{239}Pu released from dumped waste in the Kara Sea, J. Mar. Sys., 13, pp. 1-19, 1997b

Harms I.H. and M.J. Karcher, Modelling the seasonal variability of circulation and hydrography in the Kara Sea, Journal of Geophysical Research, Vol. 104, No. C6, 1999.

Harms I.H., M. J. Karcher and D. Dethleff, Modelling Siberian river runoff -implications for contaminant transport in the Arctic Ocean- Journal of Marine Systems, 27, pp. 95 – 115, 2000.

Hibler, W.D. III, A dynamic thermodynamic sea ice model, J. Phys. Oceanogr., Vol. 9, 1979.

Pavlov,V.K. and S.L.Pfirman, Hydrographic structure and variability of the Kara Sea: Implications for pollutant distribution, Deep Sea Res., Vol.42, No.6, 1995.

Lateral variability in a shallow, wind-driven estuary

JANELLE V. REYNOLDS-FLEMING

(Institute of Marine Sciences, 3431 Arendell St., Morehead City, NC 28557, janelle@email.unc.edu)

RICHARD A. LUETTICH, JR.

(Institute of Marine Sciences, 3431 Arendell St., Morehead City, NC 28557, rick_luettich@unc.edu)

1. Introduction

The study of lateral variability in estuarine waters is receiving greater attention since the initial studies of typial estuarine circulation which assumed lateral uniformity (Pritchard, 1956). The interactions between freshwater discharge, tidal and wind forcing and estuarine bathymetry can have profound effects on the lateral distribution of salinity, sediments and nutrients. Schroeder (1978) noted lateral variability in bottom salinity in Mobile Bay and related it to freshwater discharge rates. He also noted that winds played a role in the recorded variability. Wong and Moses-Hall (1998) completed a comprehensive study of the transverse salinity distribution at tidal and subtidal time scales in the Delaware Bay. Tidal variability was due to the interaction between tidal flows and variations in the bathymetry whereas subtidal variability was controlled primarily by local atmospheric forcing and secondarily by discharge.

Lateral variation can have significant effects on the distribution of nutrients, oxygen, and biomass. Malone et al. (1986) recorded tilts in the pycnocline along the main axis of the Chesapeake Bay that explained lateral variations in phytoplankton biomass, production and dissolved oxygen. Sanford et al. (1990) also recorded these tilts in the pycnocline in the upper Chesapeake Bay and attributed them to the local wind regime advecting saline, hypoxic water from below the pycnocline onto the flanks of the Bay and into the lower reaches of adjoining estuaries.

The Neuse River Estuary (NRE), located in North Carolina, USA, is a shallow, partially stratified, eutrophic, freshwater and wind-driven estuary whose density is mainly determined by salinity (Luettich et al. 2000). We document the lateral variability in salinity, circulation, and dissolved oxygen for a range of frequencies and show how freshwater discharge and local atmospheric forcing control this variability.

2. Methods

Field data

Two bottom-mounted, upward facing ADCPs were installed near the north and south shores of the NRE, approximately 32km downstream from the head of the estuary (figure 1). These ADCPs recorded flow data in 20cm depth bins every 3min semi-continuously from June 13, 1999 to September 27, 2000. Attached to each ADCP stand was a SeaBird Microcat 37-SM, which recorded conductivity, temperature and depth at a fixed point near the bottom. Approximately 25m shoreward of the ADCPs were deployed two vertically profiling platforms (profilers). The profilers lowered and raised a Hydrolab datasonde 4a with attached DO sensor through the water column every 15min (Reynolds-Fleming et al, 2002). The profilers were deployed for 30 consecutive days beginning June 24, 2000. Quarter hour near surface and near bottom salinity and DO was measured by the USGS at stations upstream of the ADCP (figure 1).

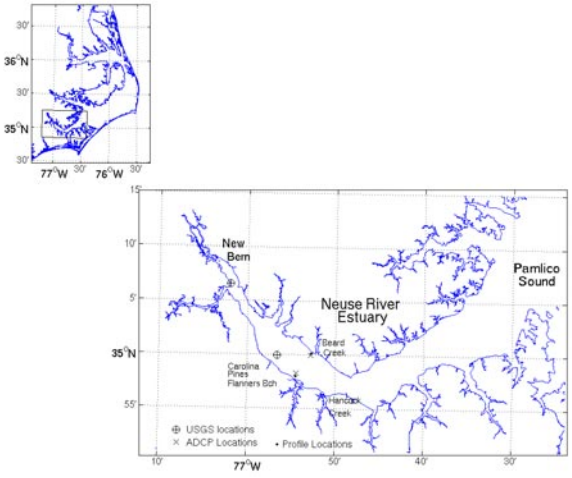

Figure 1. The Neuse River Estuary study site.

Hourly wind direction and speed and air temperature were collected from the Cherry Point Marine Corps Air Stations (CPMCAS) and distributed by the State Climate Office of North Carolina. The along and across channel wind directions are defined on coherence studies between wind, salinity and water level (Reynolds-Fleming and Luettich, submitted).

Model data

The hydrodynamics of the NRE were simulated using the mechanistic, three-dimensional, finite-difference model, Environmental Fluid Dynamics Code (EFDC). The EFDC model solves the three-dimensional, hydrostatic, free surface, turbulent averaged equations of motion for a variable density fluid. The model uses a stretched or sigma vertical coordinate system and Cartesian or curvilinear, orthogonal horizontal coordinate system. Dynamically coupled transport equations for turbulent kinetic energy, turbulent length scale, salinity and temperature are also solved (Hamrick, 1992).

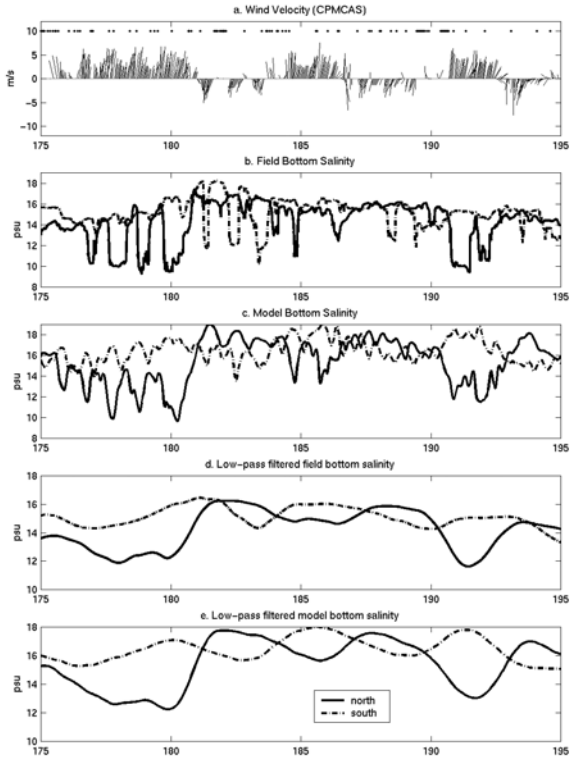

Figure 2. Bottom salinity along the shores from model and field data from summer 2000

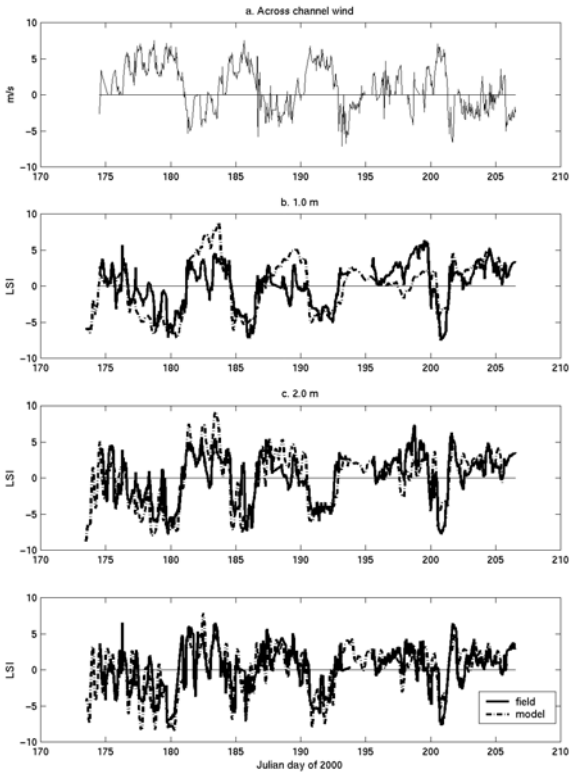

Figure 3. Across channel wind speed and the Lateral Salinity Index ILSI) of both field and model data.

The model was calibrated with 1998 water quality data collected as part of the MODMON (MODeling and MONitoring of the Neuse River Estuary http://www.marine.unc.edu/neuse/modmon.html) program (Luettich et al, 2000). Boundary conditions included freshwater discharge, atmospheric inputs like wind and solar radiation, and water level and salinity information at the open boundary located at the mouth of the estuary. We independently validated the model with the data collected during our field deployments and used the model to determine the physics surrounding fish kills that occurred during September, 2000.

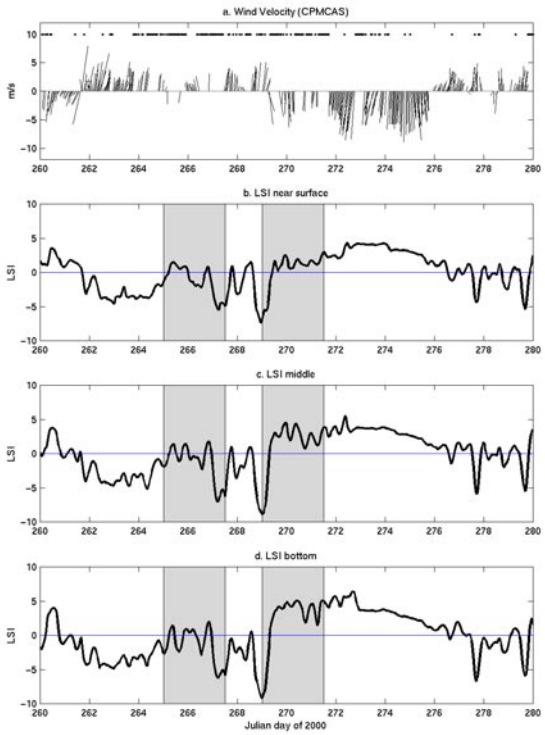

Figure 4. Simulated upwelling conditions during September 2000 (LSI> 0 implies upwelling along the N shore and LSI<0 implies upwelling along the S shore).

3. Results

The validated EFDC model was able to capture approximately 80% of the natural variability of near bottom salinity in the NRE. During a twenty day period of the summer of 2000, the model replicated diurnal and lower frequency variability. At periods of 2-4 days, the wind regime controlled lateral variability in bottom salinity evident in 30hr low-pass filtered bottom salinity from both the field and model data (figure 2 d and e). Specifically, winds blowing towards the NE caused less salty water to be downwelled along the north shore reducing bottom salinity. Concurrently, bottom salinity along the south shore increased. As winds blew towards the SW, the situation reversed and saltier water was upwelled along the north shore and fresher water was downwelled along the south shore. The unfiltered bottom salinity data showed higher frequency variability due to variations in wind speed. Here, winds often reduced in speed during the evening allowing the water column to equilibrate as bottom salinities adjusted to pre-upwelling values (figure 2 b and c).

Upwelling along the shores was quantified by defining a Lateral Salinity Index (LSI) and comparing that to the across channel wind speed. The LSI is the difference between demeaned salinities along the north and south shores. If the LSI was positive, upwelling occurred along the north shore. If the LSI was negative, upwelling occurred along the south shore. Profiler data increased the vertical resolution of salinity data and we focused our analysis on the near surface middle, and near bottom depths. The model replicated upwelling conditions (figure 3). Wind blowing towards the NE, positive across channel wind, led to upwelling conditions along the south shore that extended vertically to the near surface (figure 3). Negative across channel winds led to upwelling conditions along the north shore. Upwelling patterns were sensitive to decreases in wind speed as the nightly decrease led to a reversal in the LSI.

The EFDC model simulated salinity conditions during September 24-27, 2000 when two fish kills were reported. Wind-driven upwelling events were evident during the report and investigation of these fish kills (figure 4). We suggest that these upwelling events, which extended through the water column, were the cause of the fish kills.

References

Hamrick, J.M. 1992. A three-dimensional Environmental Fluid Dynamics Computer Code: Theoretical and Computational Aspects. Technical report, The College of William and Mary, Virginia Institute of Marine Sciences. Special Report 317.

Luettich, R.A., Jr., J.E. McNinch, H.W. Paerl, C.H. Peterson, J.T.Wells, M. Alperin, C.S. Martens, and J.L. Pinckney. 2000. Neuse River Estuary modeling and monitoring project stage 1: hydrography and circulation, water column nutrients and productivity, sedimentary processes and benthic-pelagic coupling, and benthic ecology. Report UNC-WRRI-2000-325B, Water Resources Research Institute of the University of North Carolina, Raleigh, NC, 172p.

Malone, T.C., W.M. Kemp, H.W. Ducklow, W.R. Boynton, J.H. Tuttle, and R.B. Jonas. 1986. Lateral variation in the production and fate of phytoplankton in a partially stratified estuary, MEPS, 32, 149-160.

Pritchard, D.W. 1956. The dynamic structure of a coastal plain estuary. J. Mar. Res., 15, 33-42.

Reynolds-Fleming, J.V., J.G. Fleming, and R.A. Luettich, Jr. 2002. A portable autonomous vertical profiler for Estuarine applications. Estuaries, 24(1):142-147.

Reynolds-Fleming, J.V. and R. A. Luettich, Jr. Wind-driven lateral variability in a partially mixed estuary and its influence on fish kills. *Sumbitted to Continental Shelf Research*.

Sanford, L.P., K.G. Sellner, and D.L. Breitburg. 1990. Covariability of dissolved oxygen with physical processes in the summertime Chesapeake Bay. J. Mar. Res., 48, 567-590.

Schroeder, W.W. 1978. Riverine influence on estuaries: A case study, *in* Estuarine Interactions, M.L. Wiley, Ed., Academic, San Diego, California, 347-364.

Wong, K-C and J.E. Moses-Hall. 1998. The tidal and subtidal variations in the transverse salinity and current distributions across a coastal plain estuary. J. Mar. Res., 56, 489-517.

Sediment Dynamics in a Submarine Canyon: a Case of River-Sea Interaction

JAMES T. LIU, JEFF C. HUANG, RAY T. HSU, HUI-CHEN CHANG, AND HUI-LING LIN

(Institute of Marine Geology and Chemistry, National Sun Yat-sen University, Kaohsiung, Taiwan 804-24, R.O.C., james@mail.nsysu.edu.tw)

1 Introduction

The dispersal and movement of suspended sediments within a river-sea system that consists of a river and a nearby submarine canyon on a micro-tidal coast in southern Taiwan was investigated. In this paper we report some of the findings from a one-month field experiment conducted during the flood season of 2000 to examine the sediment behavior and pathway from the standpoint of river-sea interaction.

2 Field Experiment Results

In this experiment, an instrumented tripod mounted with a CTD, and a directional wave, tide, and turbidity gauge, was deployed at the mouth of Kao-ping River (Fig. 1). A bottom-mounted, upward-looking ADCP was deployed on the shelf outside the submarine canyon. In the lower part of the Kao-ping Submarine Canyon, two sediment trap and RCM current meter sets (approximately 45 and 95 m above the canyon floor, respectively), a temperature and depth recorder, and a Laser In-Situ Scattering and Transmissometry (LISST-100) gauge (5 m above the canyon floor) were mounted on a taut-line mooring located approximately 8 km seaward of the river mouth. At the site, over 90% (by weight) of the sediment on the canyon floor is mud (silt and clay)[Liu et al., 2002]. Toward the latter part of the experiment, two significant river sediment discharge events occurred relating to the passage of a typhoon (Kai-tek) and an episodic extreme precipitation condition over the river catchment area.

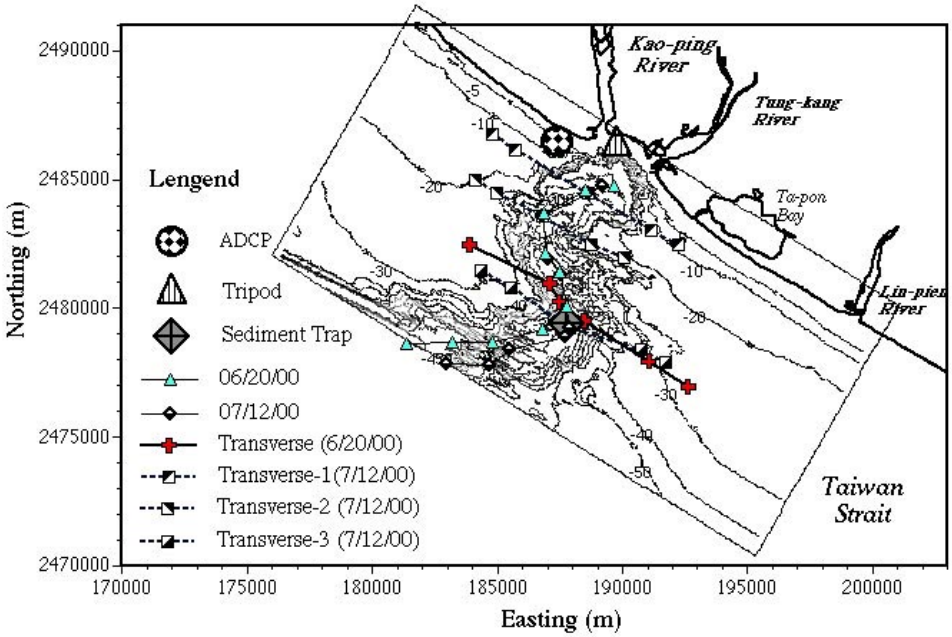

Figure 1: Locations of moored deployments and hydrographic stations. The bathymetric contours are in meters.

The flow field on the shelf outside the canyon is dominated by shore-parallel tidal signals at semidiurnal frequencies. The temperature and flow fields in the lower part of the canyon are highly coupled also at the semidiurnal tidal frequencies (Fig. 2). The flow primarily follows along the axis of the canyon, which brings cold offshore water toward the head of the canyon during the flood. The

largest size fraction captured by the two sediment traps is very fine to medium silt whereas near the canyon floor, the suspended sediment concentration (SSC) is dominated by sand. During the passage of Typhoon Kai-tek, the increase of the wave height observed at the river mouth correlates well with the amount of sand captured by the traps and the amount in the upper trap exceeds that in the lower trap (Fig. 3).

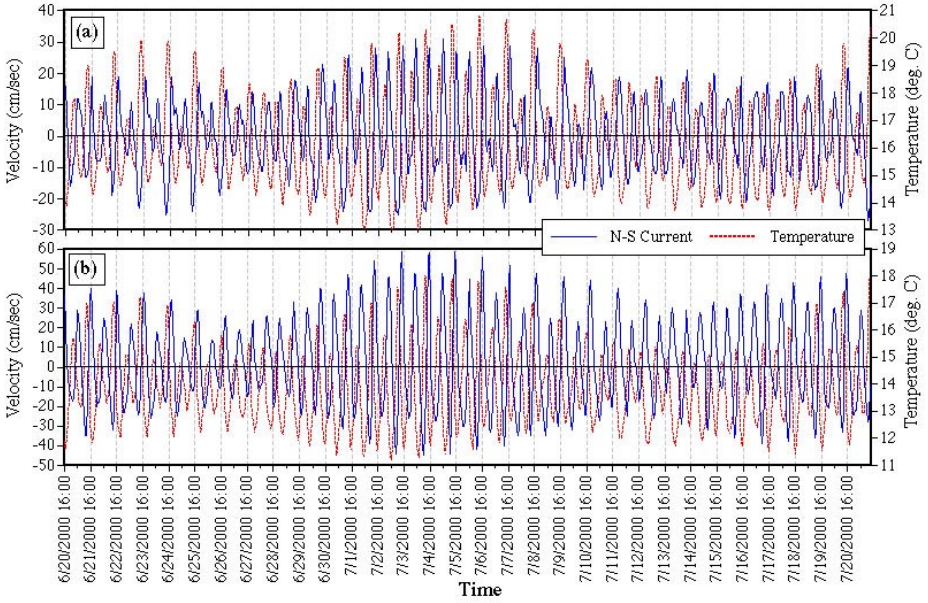

Figure 2: Observed N-S component of the flow and temperature located at (a) 95 m and (b) 45 m above the canyon floor.

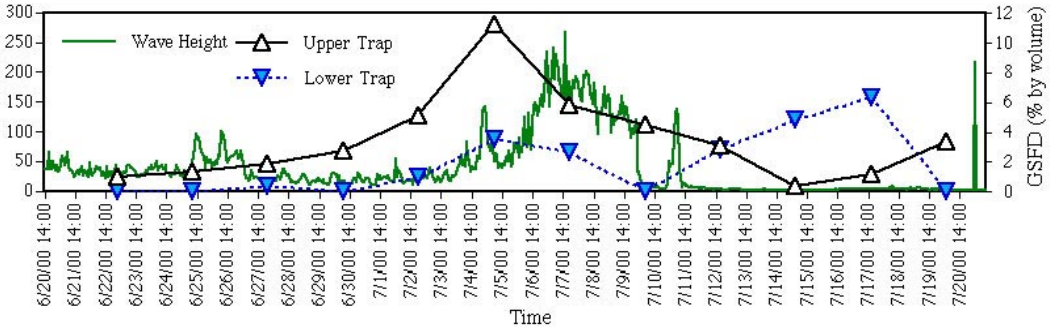

Figure 3: Significant wave height observed on the tripod and the grain-size frequency distribution (GSFD) of the sand fraction of the trap sediment samples measured by a Laser Particle Analyzer (Coulter LS100).

The 'behavior' of the 32 different grain sizes in the SSC near the canyon floor observed by LISST-100 can be differentiated into a coarse group (sand) and a fine group (mud) by using the empirical orthogonal (eigen) function (EOF) analysis technique. Each group has distinct spectral characteristics that show major energies at subtidal (about 10 days), diurnal, and semidiurnal frequency bands. The theoretical 'in-situ' settling velocity for quartz spheres of clay, very fine silt, coarse silt, and sand sizes were estimated based on a empirical equation [Gibbs et al., 1971], using the observed 'in-situ' density field from two cruises on June 20 and July 12, 2000. Due to the strong stratification in the canyon, the settling of suspended sediments becomes progressively slower as they fall deeper into the canyon. Subsequently, the time needed for the four grain sizes to fall from the sea surface to the canyon floor was estimated by dividing the water depth by the vertically averaged settling velocity. The results show that the time difference for sediment grains to settle through the canyon between the sand and the clay is on the order of hours and months (Fig. 4).

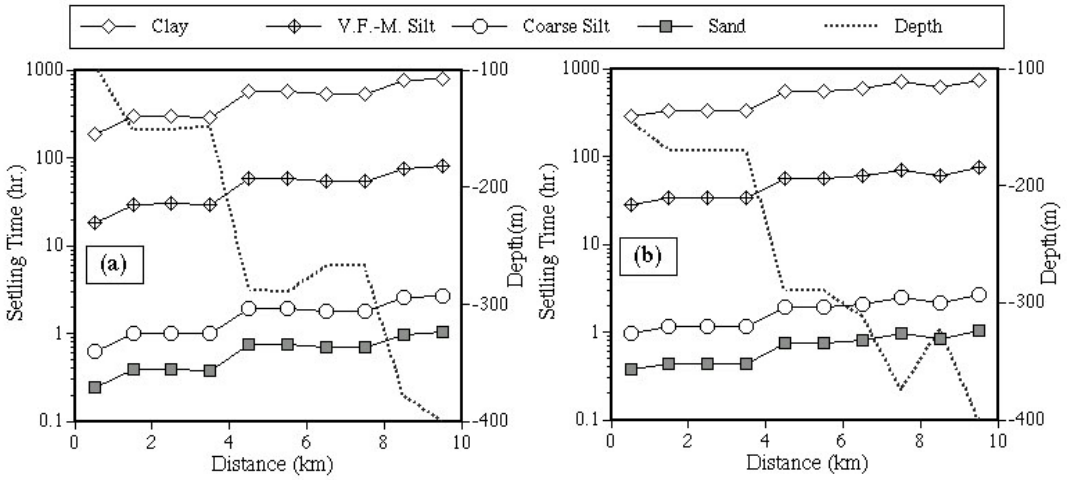

Figure 4: Depth-averaged settling time for the four grain sizes along the axis of the submarine canyon for the hydrographic condition surveyed on (a) June 20, and (b) July 12, 2000. The horizontal distance is relative to the most landward profiling station (zero distance).

Instantaneous suspended sediment fluxes for the above mentioned four grain-size groups at 5 m above the canyon floor were estimated by multiplying the total SSC measured by the LISST-100 and the N-S component of the flow measured by the RCM current meter at 45 m above the canyon floor assuming the flow field in the lower part of the canyon was spectrally coherent. Since the resulting flux showed strong tidal signals, each of the flux time series was then decomposed into the tidal and nontidal (residual). To estimate the accumulated (net) suspended sediment transport, the instantaneous total, tidal, and residual fluxes were multiplied by the observation time interval (1 hour), and incremented for the entire sampling period. The results show that tidal currents were the most important mechanism to transport suspended sediment in the lower part of the canyon whose net transport direction was landward (Fig. 5). However, the tidal transport was modulated by the spring/neap tide (Fig. 5b). The spring tide tends to transport sediment landward and the neap tide tends to transport sediment seaward. The net nontidal sediment transport in the lower part of the canyon was zero for the obsrevation period (Fig. 5c). Cross-spectral analyses among the SSC of 4 grain-size fractions measured near the canyon floor and the SSC measured at the river mouth indicate that the sand fraction near the canyon floor has the highest correlation with the SSC at the river mouth at subtidal frequencies, having zero time lag. Additionally, the patterns of the accumulated sediment discharge by the river and the total SSC near the canyon floor follow each other closely during the one-month long deployment.

3 Concluding Remark

These preliminary results indicate that the bottom nepheloid layer near the canyon floor consists of clay-to-medium-silt-sized 'standing' population, which are subject to subtidal and tide-related motions. Coarser sediments such as sand and coarse to medium silt are 'drop-ins'. They are either resuspended off the shelf floor by the wave field or exported by the river and subsequently fall into the canyon in a matter of hours. The drop-ins are more subject to the higher frequency semidiurnal motions of the currents inside the canyon. They contribute to the high value of measured downward mass fluxes (exceeding 700 g m^{-2} day^{-1}) in the lower part of the canyon.

References:

Gibbs, R.J., M.D. Mathews, and D.A. Link, The relationship between sphere size and settling velocity. *Journal of Sedimentary Petrology*, 41, 7-18, 1971.

Liu, J. T., K.-j. Liu, and J. C. Huan, The influence of a submarine canyon on river sediment dispersal and inner shelf sediment movements: a perspective from grain-size distributions. *Marine Geology*, 181 (4), 357-386, 2002.

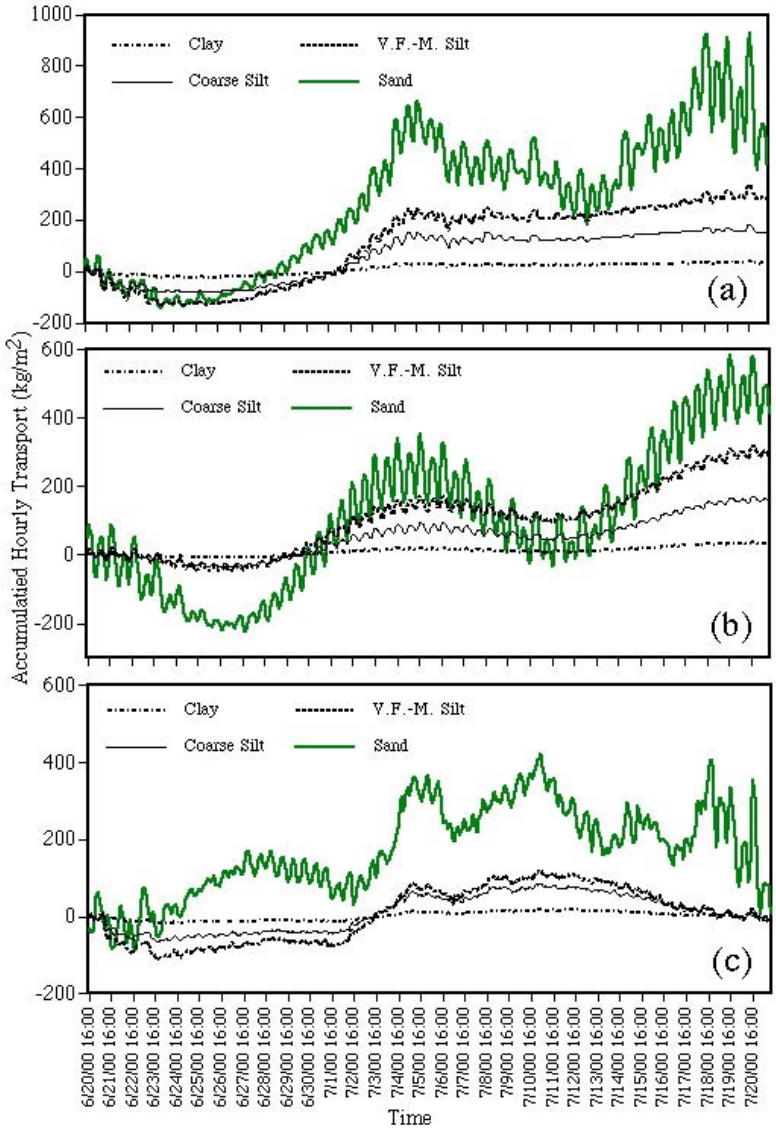

Figure 5: Cumulative hourly sediment transport of the four grain-size fractions near the canyon floor: (a) total transport, (b) tidal part of the transport, and (c) nontidal (residual) part of the transport.

The Influence of Asymmetries in Stratification on Sediment Transport in a Partially Mixed Estuary

MALCOLM SCULLY

(Virginia Institute of Marine Science, College of William & Mary, P.O. Box 1346, Gloucester Point, VA 23062, USA, mscully@vims.edu)

CARL FRIEDRICHS

(Virginia Institute of Marine Science, College of William & Mary, P.O. Box 1346, Gloucester Point, VA 23062, USA, cfried@vims.edu)

1. Introduction

In partially mixed estuaries, the presence of an estuarine turbidity maximum (ETM) is often attributed to the convergence of near-bed estuarine circulation with seaward-directed river flow. Fine sediments are thought to accumulate in a relatively low energy region near the limit of saltwater intrusion. In many estuaries, vertically sheared tidal currents interact with the along-channel salinity gradient leading to greater salinity stratification on the ebb phase of the tide. It has been suggested that this mechanism of tidal straining will lead to increased near-bed turbulence during the flood tide and contribute to the landward flux of salt (Simpson et al., 1990). Numerical modeling results demonstrate that asymmetries in bed stress caused by semi-diurnal changes in stratification may play an important role in the formation and maintenance of an ETM (Geyer, 1993; Lin and Kuo, 2001). Several data sets collected in the York River over the past six years were examined to evaluate the importance of asymmetries in stratification to sediment transport and provide direct observational evidence for the influence of stratification on near-bed Reynolds stress.

2. Results

During the springs of 1998 and 1999, observations were collected during 24-hour anchor stations in the main channel of the York River estuary. During the periods of observation, tidal straining of the along-channel salinity gradient resulted in greater density stratification during the ebb phase of the tide. Higher suspended sediment concentrations were observed during the flood tide, despite the fact that the near-bed current velocities and velocity shear were approximately equal. Net up-estuary sediment transport near the bed was observed despite the fact that tidally averaged residual near-bed currents were zero or slightly seaward directed (figure 1). We infer that greater salinity stratification on the ebb reduced the intensity of near-bed turbulent mixing, limiting fine sediment resuspension. While several indirect measurements suggest higher near-bed turbulence on the flood tide, no direct measurements were taken during the anchor stations.

In order to more conclusively link changes in stratification to near-bed turbulence and sediment transport, data collected during several additional experiments in the York River were examined. In each experiment, benthic boundary layer tripods were deployed equipped with acoustic Doppler velocimeters (ADVs) at several heights above the bed, so that direct measurements of turbulent Reynolds stress could be made. The most extensive of these experiments occurred in 2002, when S4 moorings were deployed to characterize top to bottom salinity differences. The results of these experiments highlight the conditions under which asymmetries in stratification are important to sediment transport.

Figure 2 plots the observed current magnitude against the measured Reynolds stress for more stratified and less stratified conditions observed in 2002. A least squares quadratic fit of the data suggests that for a given velocity, the Reynolds stress for stratified conditions was approximately 25% lower than the less stratified conditions, despite the fact that a relatively small difference in stratification was observed. Consistent with previous findings, the more stratified conditions corresponded to lower

energy neap tidal velocities, whereas the less stratified conditions were generally found during the more energetic spring tides. Preliminary evaluation of the data suggests that historically low river discharge resulted in incoherent patterns of tidal straining and low suspended sediment concentrations, which appeared to be the result of advection and not local resuspension of fine sediment. As a result, significant asymmetries in sediment resuspension were not observed.

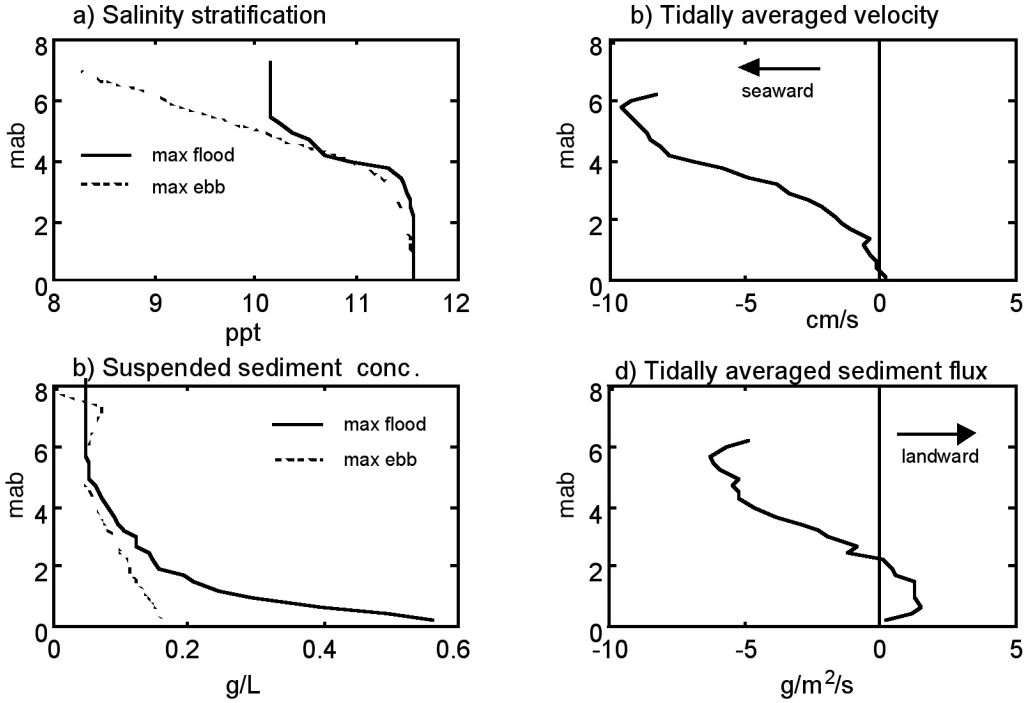

Figure 1. net landwart sediment flux due asymmetric sediment resuspension during April 1999.

In contrast, high suspended sediment concentrations were observed at a tripod deployed in the secondary channel of the York River for 10 days during April 1996. Although no concurrent measurements of salinity stratification were made, observations taken shortly after the end of the tripod deployment revealed significant tidal straining, with greater stratification developing during the ebb. As shown in figure 3, estimates of stratification based on the non-dimensional eddy viscosity, provide strong evidence for greater salinity stratification during the ebb. As a result, under low concentration conditions, estimates of Reynolds stress were significantly larger during the flooding tide, resulting in greater sediment resuspension and net up-estuary sediment flux. However, during high concentration conditions, sediment induced stratification appeared to significantly damp near-bed turbulence during the flood phase of the tide and play a more dominant role than salinity stratification in controlling near-bed Reynolds stress. For most of the deployment, the gradient Richardson number due to suspended sediment (Ri_s) during the flood tide was above the critical value of 0.25 with a median value of 0.53. However, significantly higher velocity shear during the ebb prevented significant sediment induced stratification from occurring, and the Ri_s approached, but seldom exceeded the critical value (median = 0.10). Thus, under high concentration conditions, the impact of sediment-induced stratification during the flood appeared to have a more dominant effect than salinity stratification, preventing preferential up-estuary sediment flux.

3. Conclusions

The data presented reveal how asymmetries in stratification can influence sediment transport. It is clear from these data sets that even slight changes in salinity stratification can have an important influence on the near-bed turbulent Reynolds stress. Thus, the changes in stratification due to tidal straining can lead to asymmetric sediment resuspension and increase the landward transport of sediment. This mechanism can effectively transport sediment up-estuary in the absence of a net residual current. However, when an abundant supply of fine sediment is available, sediment induced stratification can also play an important role in reducing near-bed turbulence. In the shallower secondary channel where the near-bed velocity shear was greater during ebb, sediment induced stratification damped turbulence on the flood and effectively reduced landward sediment flux.

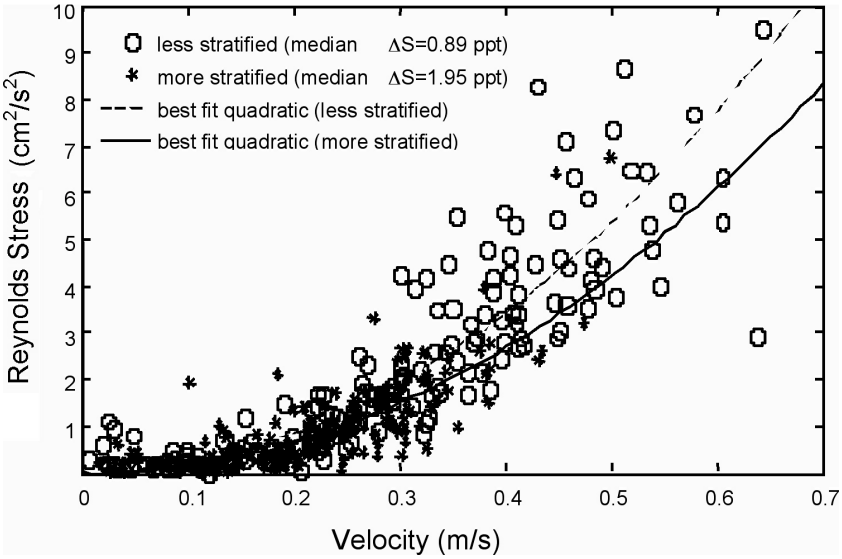

Figure 2. Impact of stratification on reynolds stress from ADV 105 cmab-spring 2002

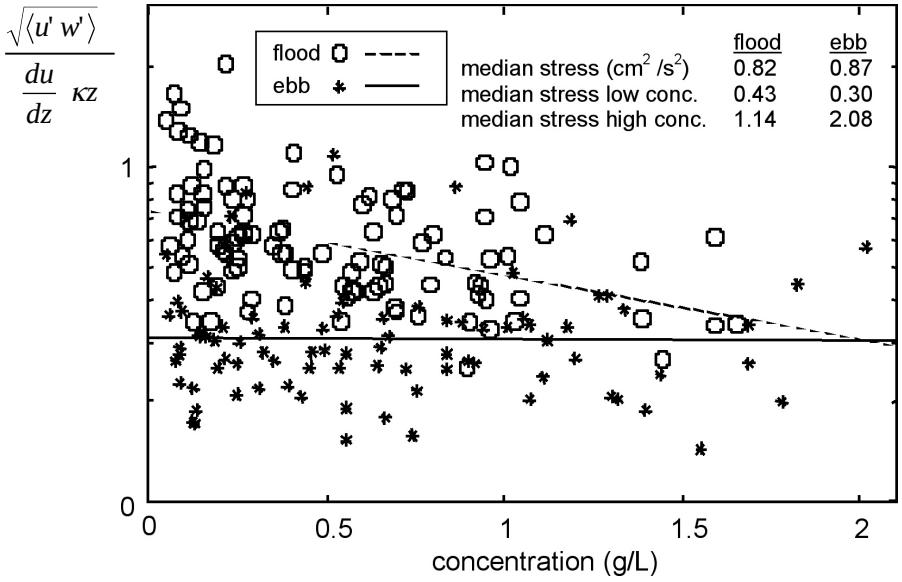

Figure 3. Influence of salinity and sediment-induced stratification on near-bed turbulence (Spring 1996)

References

Geyer, W.R. 1993. The importance of suppression of turbulence by stratification on the estuarine turbidity maximum. Estuaries, 16, 113-125.

Lin, J., and Kuo, A.Y. 2001. Secondary turbidity maximum in a partially mixed microtidal estuary. Estuaries, 24, 707-720.

Simpson, J.H., Brown, J., Matthews, J.P., and Allen, G. 1990. Tidal straining, density currents and stirring in the control of estuarine stratification. Estuaries, 13, 135-132.

Comparing lateral tidal dispersion with density-driven exchange in a highly unsteady, partially mixed estuary

NEIL BANAS AND BARBARA HICKEY

(School of Oceanography, University of Washington, Box 355351, Seattle WA 98195, U.S.A., neil@ocean.washington.edu)

1. Introduction

Willapa Bay, Washington, USA (Fig. 1) is among the largest in a system of coastal-plain estuaries in the Pacific Northwest United States, which (with the exception of the Columbia River) have received scant oceanographic attention. These estuaries border an Eastern Boundary ocean, and are forced by strong tides and strong wind-driven upwelling-downwelling fluctuations on event timescales (2-10 d). Here we uses three years of hydrographic time series and transects to examine the dominant salt balance in Willapa Bay on subtidal and longer timescales. We find that the dynamics of flushing and oceanic exchange fluctuate between control by gravitational circulation and control by lateral tidal stirring, on both the seasonal and the event scale. We find furthermore that the salt balance is frequently unsteady to lowest order, and that the steady-state assumption so common in analytical treatments of estuarine dynamics (e.g., *Hansen and Rattray* [1965]) seriously misrepresents the role of lateral stirring processes. We develop parameterizations which allow generalization to other macrotidal, highly unsteady systems.

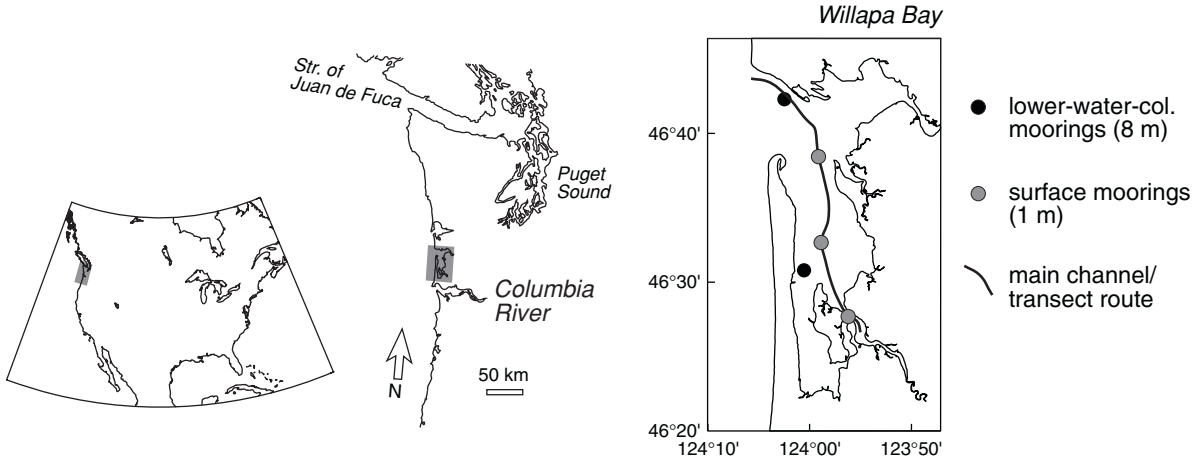

Figure 1: Willapa Bay, Washington, with a portion of the Pacific Northwest coast and North America shown for context. The locations of moored hydrographic and velocity observations are indicated.

The Pacific Northwest coast estuaries (again, with the exception of the Columbia River) receive weak-to-moderate river input, which peaks during winter storms and is negligible during late summer. Riverflow typically varies by a hundred-fold between these seasonal extremes (in Willapa, from 10 to 1000 $m^3 s^{-1}$). At the same time, tides on this coast are large (the mean diurnal range at the mouth of Willapa Bay is 2.7 m) and the estuaries tend to have extensive open intertidal areas (~50% surface area), so tidal prisms are in general 30-50% of total estuary volume (*Hickey and Banas* [2002]). Flushing and adjustment times are therefore relatively short: changes in ocean salinity take ~5 d to reach the head of Willapa Bay, 40 km from the mouth. Oceanic water properties show strong variability on the same timescale, driven by changes in the direction of the prevailing winds. Northerly, fair-weather winds produce upwelling of salty, nutrient-rich water, while southerly, foul-weather winds produce downwelling, lower salinities, and a depletion of nutrients in surface waters. Significantly, upwelling and not river input is the dominant source of nutrients for these estuaries (*Roegner et al.* [2002]). Thus the dynamics of bulk ocean-estuary exchange considered here (rather

than the dynamics of stratification and vertical mixing) form the prime physical control on estuarine ecology.

2. Riverflow and gravitational circulation

In winter and spring, when riverflow in Willapa is intermittent but high, evidence of an unsteady gravitational circulation can be seen in salinity and velocity time series. Residual, upstream velocities in the lower layer of the main channel show a linearly correlation with along-channel density gradient, and their magnitude is consistent with a simple balance between the baroclinic pressure gradient and vertical mixing, as in the canonical *Hansen and Rattray* theory [1965]. This density-driven flow, however, is superimposed upon spatially varying tidal residuals of similar or greater magnitude, which frequently oppose it (*Hickey et al.* [2002]).

Stratification appears to oscillate between two dynamical limits (Fig. 2). In the upper limit, stratification follows the 2/3-power-law relationship with riverflow which indicates an gravitational circulation in balance with flushing of salt by net river outflow (*Monismith et al.* [2002], others). In Fig. 2 a solid line marks this theoretical curve, and dashed lines mark 95% confidence limits on the constant of proportionality. This constant is determined empirically by regessing riverflow and baroclinic velocity to the along-channel salinity gradient.

In the lower stratification limit, intrusions of a strong, buoyant plume from the Columbia River, 50 km south, eliminate stratification and flatten the along-channel gradient for days or weeks at a time. These effects, which occur under downwelling conditions that bring the Columbia plume north and onshore, undermine density-driven exchange even when local riverflow is substantial. Thus the unsteadiness of the gravitational circulation is a result not just of unsteady river input, but more important, large and rapid fluctuations in ocean salinity. During a transition between plume-intrusion and upwelling conditions, salinity at the mouth can change several psu over one or two tidal cycles.

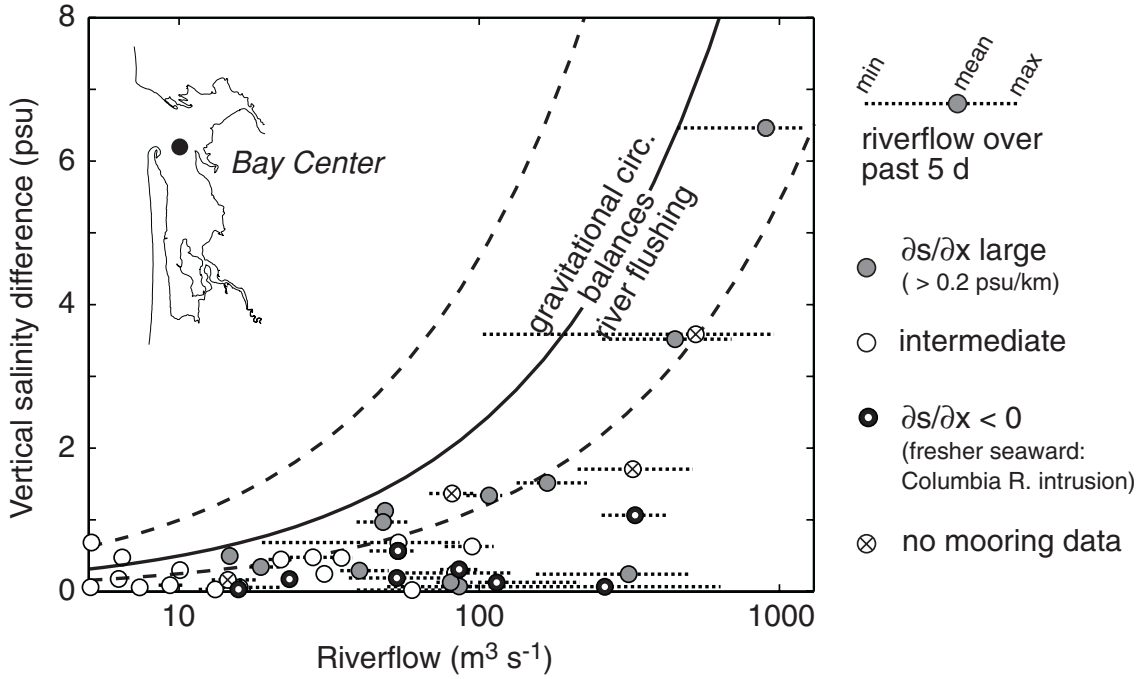

Figure 2: Relationship between stratification and riverflow at Bay Center, 18 km from the mouth. Stratification data is from 39 hydrographic transects over three years; these are instantaneous observations and thus tidally aliased. For each transect, symbol shading indicates the strength of the tidally averaged along-channel salinity gradient ($\partial s/\partial x$), from mooring data.

3. Tidal stirring and the low-flow regime

During summer in Willapa, local riverflows are negligible and stratification low (~0.1 psu over the water column), while ocean salinity, and thus the along-channel salinity gradient, continue to be highly variable on timescales of 3-10 d. Changes in ocean salinity have been observed to produce transient along-channel density gradients that drive gravity-current like exchange flows (*Hickey et al.* [2002]). Nevertheless, in the average over several wind events, salt transport by the mean gravitational circulation is very weak, because stratification is weak. Density-independent mechanisms of salt flux—lateral dispersion by tide- and wind-driven flows—thus dominate in low-flow conditions by an order of magnitude. We parameterize these mechanisms with a horizontal diffusivity K, which we allow to vary between mouth and head. The along-channel profile of K then can be calculated by finding the slope between the rate of change of salt storage and the along-channel salinity gradient at each of four time-series stations (Fig. 3).

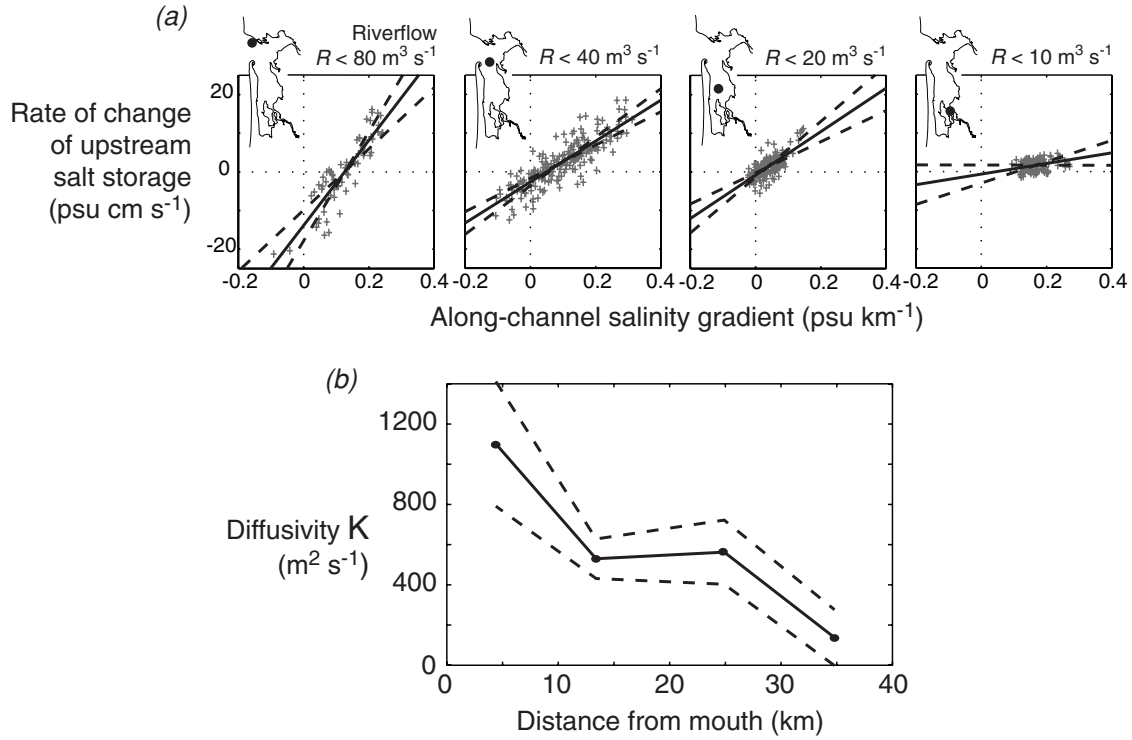

Figure 3: *(a)* Relationship between the rate of change of salt storage and along-channel salinity gradient at four stations along the main channel. Data shown are 5 d averages during low-riverflow conditions, where "low-flow" is defined, station by station, as flows for which density-driven salt fluxes are smaller than the scatter in the regressions above, and thus do not affect the estimate of K. The range of riverflows used is indicated for each station. *(b)* Along-channel profile of K from the four regressions shown in *(a)*.

The variation in K between stations, and over the spring-neap cycle at a single station, confirm the simple scaling $K \sim (0.1\text{-}0.2)\ U\ b$, where U is the tidal amplitude and b the channel width. This suggests that the dominant dispersion process here, in the absence of a strong gravitational circulation, is stirring by lateral tidal residuals tied to bathymetry. (The role of wind-driven circulations has not been quantified.) This is a natural conclusion in Willapa, where the intertidal zone accounts for over half the surface area, and nearly half the volume, of the estuary. *Zimmerman* [1986] proposes lateral dispersion in estuaries by "Lagrangian chaos," in which a deterministic but complex residual-current field randomizes and disperses the trajectories of water parcels. He estimates diffusivities for this process comparable to those observed in Willapa. This model of the tidal flushing mechanism is being

tested against results from a spatially explicit numerical model of Willapa, a version of ECOM-si, in which wetting and drying of the intertidal zone is resolved.

Flushing by tidal dispersion yields an inherently unsteady salt balance: that is, upstream diffusion of salt is balanced by a net change in salt storage rather than a downstream salt flux. Indeed, the downstream advection of salt by the mean riverflow ("river-flushing") is negligible in Willapa during low-flow, summer conditions. Significantly, however, even in very low-flow conditions the upper limit on stratification described above, the balance between gravitational circulation and river-flushing, continues to hold. A baroclinic feedback mechanism between riverflow and stratification (such as that described by *MacCready* [1999]) appears to be in effect, even when the overall salt balance of the estuary is controlled by other mechanisms.

4. Tide-controlled and density-controlled regimes

On the basis of 1) the along-channel profile of tidal diffusivity K and 2) the observed slope between the along-channel salinity gradient and baroclinic velocity, at each point along-channel we can define a *critical stratification*, above which salt transport by gravitational circulation exceeds that by tidal diffusion, and below which tidal diffusion dominates. In the seaward reach of the estuary this critical level is very high—a vertical salinity variation of 3-7 psu—so that tidal diffusion dominates during all but the largest storm events. At the head of the estuary, the critical stratification is much lower (~0.6 psu), and gravitational circulation dominates during all but the lowest flows of the year. The limiting relationship between stratification and riverflow described above allows us to rewrite this critical stratification as a *critical riverflow*. Thus this method provides a set of parameters that let us predict the dynamical balance in Willapa from its forcing alone, rather than from its hydrographic response, and without imposing the unrealistic assumption of a steady state. The method is general and presumably applicable to any estuary in which tidal and freshwater forcing compete closely.

Acknowledgments: This work was supported by the Pacific Northwest Coastal Ecosystems Regional Study (PNCERS) and Washington Sea Grant. Many thanks to Dr. Jan Newton and the Washington State Dept. of Ecology, who generously provided much of the data used in this analysis.

References:

Hickey, B.M. and N.S. Banas. 2002. Oceanography of the Pacific Northwest coastal ocean and estuaries with application to coastal ecosystems. *Estuaries.* Submitted.

Hickey, B.M., M. Zhang, and N. Banas. 2002. Coupling between the California Current System and a coastal plain estuary in low riverflow conditions. *J Geophys. Res.* In press.

MacCready, P. 1999. Estuarine adjustment to changes in river flow and tidal mixing. *J. Phys. Oceanogr.* 29: 708-726.

Monismith, S.G., W. Kimmerer, J.R. Burau, and M.T. Stacey. 2002. Structure and flow-induced variability of the subtidal salinity field in northern San Francisco Bay. *J. Phys Oceanogr.* In press.

Roegner, G.C., B.M. Hickey, J.A. Newton, A.L. Shanks, and D.A. Armstrong. 2002. Estuarine-nearshore links during a coastal upwelling-downwelling cycle: plume and bloom intrusions into Willapa Bay, Washington. *Limnol. and Oceanogr.* In press.

Zimmerman, J.T.F. 1986. The tidal whirlpool: A review of horizontal dispersion by tidal and residual currents. *Neth. J. Sea Res.* 20: 133-154.

Fluxes of salt and suspended sediments in a curving estuary

Jack Blanton[1] and Harvey Seim[2]

1. Skidaway Institute of Oceanography, 10 Ocean Science Circle, Savannah, GA 31406 USA. email: jack@skio.peachnet.edu

2. Department of Marine Science, University of North Carolina at Chapel Hill, CB# 3300, 12-7 Venable Hall, Chapel Hill, NC 27599, USA.
email: harvey_seim@unc.edu

1 Introduction

This study focuses on the transport of salinity and suspended sediments in a curving channel of the Satilla River estuary, a mesotidal estuary located in the southeastern U.S. We examine a month-long data set to describe the circulation and flux of salt and sediment over a limited reach that includes a sharp channel bend. We describe the low frequency changes in salinity, currents and optical backscatterance in the study area. Observations were obtained during a period of steadily decreasing river discharge that represents a period when transport of sediments to the ocean was negligible.

2 Observations

Spatial changes in *secondary* circulation has an effect on the along-channel flow ((Seim et al., 2002)) at the landward and seaward ends of the curving channel. During spring, flood currents were consistently stronger at the landward end while ebb currents were consistently stronger at the seaward end. This is attributed to the addition of momentum to bottom currents by the cross-axis secondary circulation acting throughout the channel bend (Seim and Gregg, 1997). Therefore, strong flood currents at spring tide would cause bottom stress to increase in the landward direction along the channel bend, and thereby account for significantly higher optical backscatterance observed at the landward station during spring tide.

Average current profiles measured half-way between the ends of the curving channel show export below mean low water (MLW) and import in the intertidal zone above MLW. The change to landward flow in the intertidal zone is consistent with tidally driven residual flow (Ianniello, 1977). There were pronounced differences in bottom current direction at the landward and seaward end of the curving channel. Bottom currents at the seaward end varied greatly between neap and spring tide, showing import during neap and export

during spring. The differences at the landward end were more of a degree - strong import at neap and weaker import at spring.

Curves representing cumulative salt fluxes at the bottom were calculated for both ends of the channel. Fluxes were landward and approximately equal throughout neap and approaching spring tide. This suggests that the channel was neither accumulating nor exporting a significant amount of salt along the bottom. At the approach of spring tide, cumulative flux at the landward end decreased slightly, but cumulative flux at the seaward end increased steadily until it became *seaward*, suggesting that bottom salt content in the channel decreased. From spring to the next neap tide, the curves become parallel only to diverge once again as the next spring tide approached.

Cumulative sediment fluxes at the landward and seaward sites indicated a net landward flux of suspended sediment. Throughout the period, there was more bottom flux during flood than during ebb, particularly at the landward site, substantiating the higher bottom stress during flood as described above. At the approach of spring tide, sediment flux at the landward site increased suddenly during flood tide. Since a similar increase was absent at the seaward end, suspended sediments were apparently evacuated along the thalweg somewhere between the landward and seaward ends of the channel.

3 Discussion

Weaker mixing at neap tide allows a clear gravitational mode to occur, with seaward flow above the middle of the water column and landward flow below. As spring tide approaches, an increase in strength of tidal pumping drives mass landward on the shallow flanks which requires seaward flow in the deep channel to balance the mass (Li et al., 1998). It would appear that the increased tidal flux at spring tide was sufficient to completely shut down the gravitational mode at the bottom at the seaward end of the study domain.

In order to maintain a salt balance in the presence of divergence along the bottom, tidal pumping must transfer salt vertically and laterally into the intertidal zone in order to maintain the landward flux of salt. Subtidal variations in bottom salt flux suggest a similar role for tidal pumping. However, tidal pumping cannot be as effective for sediments as for salt since sediments are not mixed as effectively upward into the water column.

We use a cartoon to visualize the observed fortnightly variations of the residual circulation in a channel bend (Fig. 1). We invoke conservation of volume transport in any given cross-section to complete the picture. Secondary circulation in a channel bend interacts with gravitational circulation and tidal pumping. Secondary circulation acting throughout channel bends overturn the water column as it travels around the bend (Seim and Gregg, 1997). During flood, secondary circulation adds momentum to the bottom current in the landward direction, while that of the ebb current adds momentum to the bottom current in the seaward direction. Secondary circulation at neap tide is too weak to interfere with the gravitational circulation mode. A well-developed gravitational mode at neap is illustrated by relatively strong bottom landward flow going through the deep

part of the channel (Fig. 1). This flow decreases in strength with distance from bottom and changes to seaward at the top of the intertidal zone. Within the intertidal zone, the flow is weakly landward due to tidal pumping. In order to achieve a neap-tide balance in a given cross-section, we infer a relatively strong seaward flow in shallow areas below mean low water to compensate for the predominantly landward flow over the deep channel.

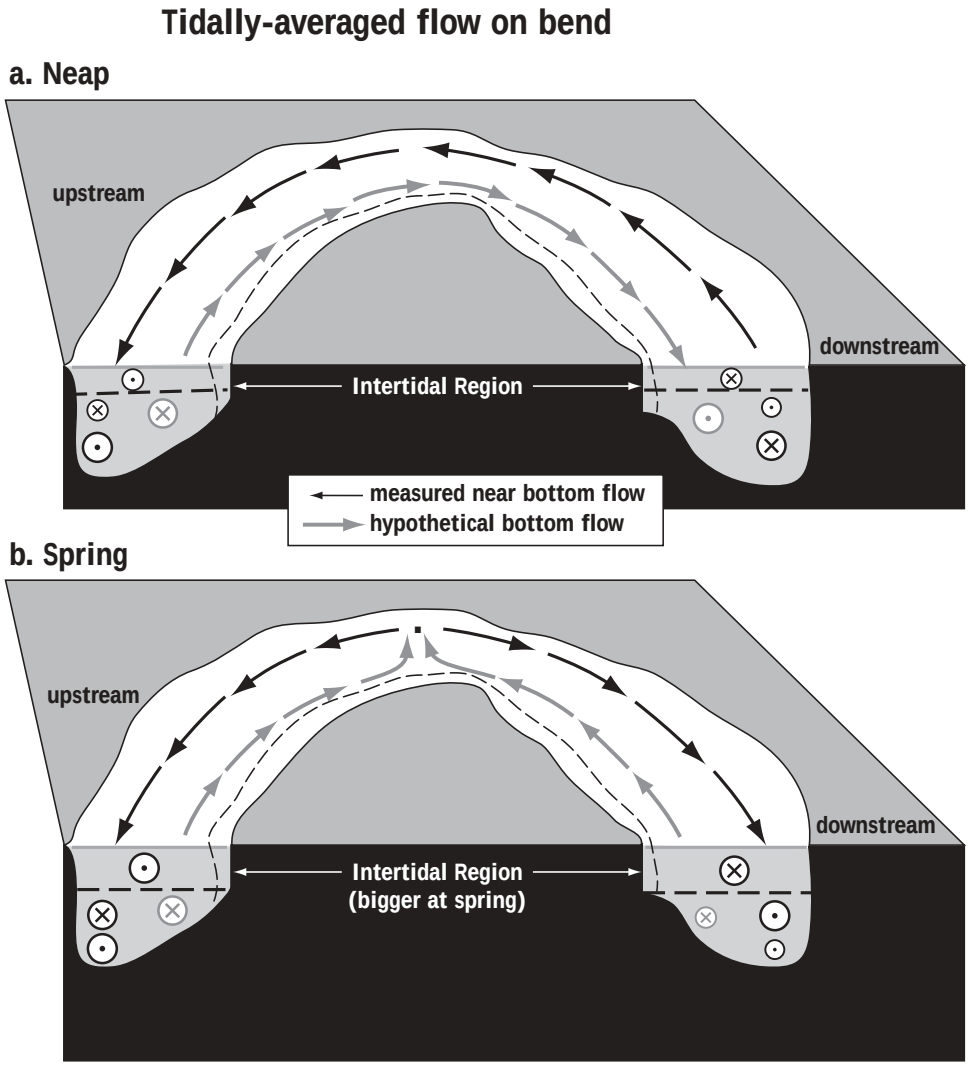

Figure 1: Tidally averaged flow on a channel bend. Neap Tide (top); Spring Tide (bottom)

At spring tide when tidal pumping is maximized, there is strong landward flow in the intertidal zone which is compensated by a seaward bottom flow that extends to mid-water levels in the deeper parts of the channel. However, as distance landward increases, the seaward bottom flow observed at the downstream end becomes weaker, eventually

stalls out, and finally reverses the seaward flow due to tidal pumping to landward flow. As a result, bottom stress from spring tide flood currents increases from downstream to upstream and accounts for significantly higher values of optical backscatterance observed during spring tide at the landward end of the channel bend.

Assuming our inferences are qualitatively correct, the neap near-bottom landward flow in the thalweg is more or less continuous throughout the axial extent of the channel and implies the presence of a seaward flow below MLW in the shallow areas. The spring-tide residual flow, however, has a gyre-like pattern (Fig. 1). The seaward flow in the straight part of the thalweg is replaced by landward flow in the bending thalweg. We speculate that the switch-over occurs somewhere in the zone of maximum curvature of the bend. To close this flow pattern, the bottom flow along the thalweg is compensated by seaward flow in the shallow areas thereby producing a counterclockwise gyre landward of the "switch-over point" and an clockwise gyre seaward of the point.

Our observations suggest the presence of a complex re-circulation of suspended sediments, driven by secondary circulation, that exists in curving channels and that complicates the traditional picture of a net landward transport of sediments. Large expanses of intertidal zones (marshes and mud flats) common to many estuaries play an important role in the transport of salt and sediments observed over the spring-neap cycle. The difficulty in obtaining measurements in estuarine intertidal zones makes the quantification of this role difficult.

References

Ianniello, J. P. (1977). Tidally induced residual currents in estauries of constant breadth and depth. *Journal of Marine Research*, 35:755–786.

Li, C., Valle-Levinson, A., Wong, K. C., and Lwiza, K. M. (1998). Separating baroclinic flow from tidally induced flow in estuaries. *Journal of Geophysical Research*, 103:10,405–10,417.

Seim, H., Blanton, J., and Gross, T. (2002). Direct stress measurements in a shallow sinuous estuary. *Continental Shelf Research*, in press.

Seim, H. and Gregg, M. (1997). The importance of aspiration and channel curvature in producing strong vertical mixing over a sill. *Journal of Geophysical Research*, 102:3451–3472.

Some aspects of the water quality modelling in the Ria de Aveiro lagoon, Portugal

ANA CRISTINA CARDOSO

(Universidade de Aveiro, 3810 Aveiro Portugal, fis15330@alunos.fis.ua.pt)

JOSÉ FORTES LOPES

(CESAM, Departamento de Física, Universidade de Aveiro, 3810 Aveiro Portugal, jflopes@fis.ua.pt)

JOANA MATZEN SILVA

(Departamento de Física, Universidade de Aveiro, 3810 Aveiro Portugal)

JOAO MIGUEL DIAS

(CESAM, Departamento de Física, Universidade de Aveiro, 3810 Aveiro Portugal, jdias@fis.ua.pt)

1. Introduction

Ria de Aveiro is a well mixed shallow water lagoon, situated in the Northwest coast of Portugal (40º 38' N, 8º 44'W), connected to the Atlantic ocean by an artificial bar, known as Barra de Aveiro, with a surface area of about 83 km^2, in high tide and 66 km^2, in low tide. Two major rivers, Antuã and Vouga, situated at the eastern side of the lagoon, with mean flows of 5m^3/s and 50m^3/s, respectively constitute the main freshwater input to the lagoon. In very rainy situations the freshwater input, from Vouga's river, may reach 820m^3/s (*Dias et al*., [1999]).

A long network of channels composes the lagoon, with four main branches radiating from the entrance: Mira, S. Jacinto, Espinheiro and Ilhavo channels (*Dias*, [2001]).

The tides at the mouth of the lagoon are predominantly semidiurnal, with a mean tidal range of about 2,0 m. Minimum and maximum tidal range are respectively 0,6 and 3,2m. The current speed has maximum values close to the lagoon mouth (1-2m/s) and decrease toward the end of the channels due to the bottom stress at the shallow areas.

The average depth of the lagoon is around 1 m, reaching 8m in the navigation channels that are frequently dredged.

The water quality of Ria de Aveiro results from a complex balance between pollutant emissions from natural and anthropogenic origin and its water auto-depuration capacity. The main anthropogenic sources of pollution are domestic and industrial discharges flows, as well as, contaminated water infiltration of agricultural and cattle raising activities. The seaweed catches abandon and microbiological pollution from domestic wastewater discharges (nutrient excess) also contribute to the organic and chemical contamination.

2. The Numerical Model

This work has the purpose to study the water quality in Ria de Aveiro lagoon, with the help of a two-dimensional numeric system model (*Mike21*, [1998]).

2.1 The water quality model

The water quality model solves the system of differential equations describing the chemical and biological evolution of coastal waters. The state variables of the model are the following: dissolved

BOD (BOD_d), suspended BOD (BOD_s), sedimentated BOD (BOD_b), ammonia (NH_3), nitrite (NO_2), nitrate (NO_3), Phosphorus (PO_4), dissolved oxygen (DO), chlorophyll-*a* (CHL), faecal coliforms (C_F) and total coliforms (C_T). The spacial and temporal evolutions of those variables are influenced by external factors, such as incident solar radiation (coliform bacteria decay), discharges, bottom and surface stresses, etc.

- **Oxygen processes (O_2)**

A number of chemical and biologic processes affect the oxygen concentration. The main processes related to the dissolved oxygen are described by the follow differential equation:

$$\frac{dDO}{dt} = +k_2\left(C_s - DO\right) - k_{d3}.BOD_d.\theta_{d3}^{T-20} - k_{s3}.BOD_s.\theta_{s3}^{T-20} - k_{b3}.BOD_b.\theta_{b3}^{T-20} - Y_1.k_4.NH_3.\theta_4^{T-20}$$

reaeration (1) dissolvedBOD(2) suspendedBOD(3) sedimentedBOD (4) nitrification (5)

$$- Y_2.k_5.NO_2.\theta_5^{T-20} - R_1.\theta_1^{T-20}.F(N,P) - R_2.\theta_2^{T-20} + P.F(N,P) - SOD.\frac{DO}{HS\_SOD - DO}$$

nitrification (6) respiration (7) and (8) photosynthesis (9) sedimented oxygen demand (10)

Where k_2 is a parameter dependent on the wind speed and flow velocities, C_s is a function of temperature and salinity, k_{d3}, k_{s3}, k_{b3} are degradation constants for BOD_d, BOD_s and BOD_b respectively, at 20ºC (1/day), k_4 is the nitrification rate at 20ºC, k_5 is the specific rate for conversion of nitrite to nitrate at 20ºC (1/day), $Y1$ and $Y2$ are yield factors describing the amount of oxygen used at nitrification, $R1$ and $R2$ are respectively the autotrophic and heterotrophic respiration (mg O_2/l/day), θ is the Arrenius temperature, T is the temperature, P is the actual production (mgO_2/l/day) and $F(N,P)$ is a limitation function by the potential nutrient limitation on photosynthesis.

A first order differential time equation for each one of the following state variables are also applied:

- **Biological oxygen demand process (*BOD*)**

The decay of different fractions of organic matter is derived from the descriptions of oxygen balance. The total BOD budgets include organic matter processes: dissolved organic matter process, suspended organic matter process and sedimentated organic matter process. Each one of these singular processes, which correspond to a first order differential equation, includes: BOD decay, resuspension and sedimentation.

- **Ammonia (NH_3), Nitrite (NO_2) and Nitrate (NO_3) processes**

The ammonium/ammonia process includes the balance of: BOD_d decay, nitrification and uptake by plants, as well as, by bacteria and heterotrophic respiration.

Nitrite process and nitrate process includes nitrification and denitrification.

- **Chlorophyll-*a* process (CHL)**

The production of chlorophyll-a includes carbon and oxygen production, as well as death and settling of chlorophyll-a.

- **Temperature processes (T)**

The temperature mode includes an exchange rate to account for the net surface heat transfer on air/water interface.

- **Bacterial processes (C_T , C_F)**

The spreading and fate of total coliforms (C_T) and faecal coliforms (C_F) includes the die-off of bacteria dependent of the light conditions in the water column.

2.2 The hydrodynamic and transport model

The water quality model is coupled to a hydrodynamic depth integrated model for mass and momentum, for shallow domains, and simulates unsteady two-dimensional flows (water levels and the current velocities).

The water quality model is integrated in the advection-dispersion module, which describes the physical transport processes at each grid point covering the area of interest. The integration of this system requires initial and boundary conditions for all the state variables.

The system solves the process equation using a rational extrapolation method in an integrated two-step procedure with the advection-dispersion module:

$$\frac{\partial}{\partial t}(hC) + \frac{\partial}{\partial x}(uhC) + \frac{\partial}{\partial y}(vhC) = \frac{\partial}{\partial x}\left(hD_x \frac{\partial C}{\partial x}\right) + \frac{\partial}{\partial y}\left(hD_y \frac{\partial C}{\partial y}\right) - FhC + S$$

Here C is the component concentration, u, v are the horizontal velocities components in x and y directions respectively, h is the water deep, D_x, and D_y are the dispersion coefficients in x and y directions, F is de decay coefficient, $S=Q_s*(C_s-C)$ and Q_s is the discharge of fonts/sinks and C_s is the component concentration of discharge of fonts/sinks.

3. RESULTS

Figure 1 shows temporal series for dissolved oxygen, nutrients, chlorophyll-*a* and bacteria, which evolution follows the tidal cycle with a diurnal and a forth-night periodicities. In particular, concerning nutrients it is observed that the nitrite (NO_2) is strongly reduced in nitrates (NO_3). Nitrate concentration increases in time towards a mean value around 0,06 mg/l. The ammonia (NH_3) concentration seems to be more sensitive to the tidal cycle fluctuating, with high amplitude around a mean value of 0,04 mg/l. The dissolved oxygen concentration tends to a stationary value around 9,5 mg/l in agreement with observed data (*Alcantara et al*., [1990] and *Projecto-QP0401/90* [1991]).

Figure 2 shows concentration maps of dissolved oxygen, nutrients, chlorophyll-a and bacteria. Dissolved oxygen and chlorophyll-a increase from the ocean towards the interior of the lagoon in accordance with the observations. Nutrients, in general, have a horizontal distribution corresponding to high concentration values close to the river's mouth and low concentration values close to the ocean boundaries.

Acknowledgements: This work was support by FCT through ModelRia and Proteu projects.

References:

ALCANT ARA, F., ALMEIDA,M. and PEREIRA, M., Qualidade Microbiológica da Àgua da Ria de Aveiro, Relat6rio POLA VEIRO, Universidade de Aveiro, Portugal, 1989-1990

DIAS, JOAO MIGUEL, Contribution to the Study of the Ria de Aveiro Hydrodinarnics, Universidade de Aveiro Portugal, pp 228,2001

DIAS, JOAO MIGUEL, LOPES, JOSE FORTES and DEKEYSER, IV AN, Hidrological characterisation of Ria de Aveiro, Portugal, in early summer, Oceanologica acta, 22 473-485, 1999

MlKE21, Water Quality Module, release 2.7, User Guide and Reference Manual, DHI software, 1998

Projecto-QP0401/90, Vigilância da Qualidade da Àgua da ria de Aveiro, rel. TF-QP02/9l,1990

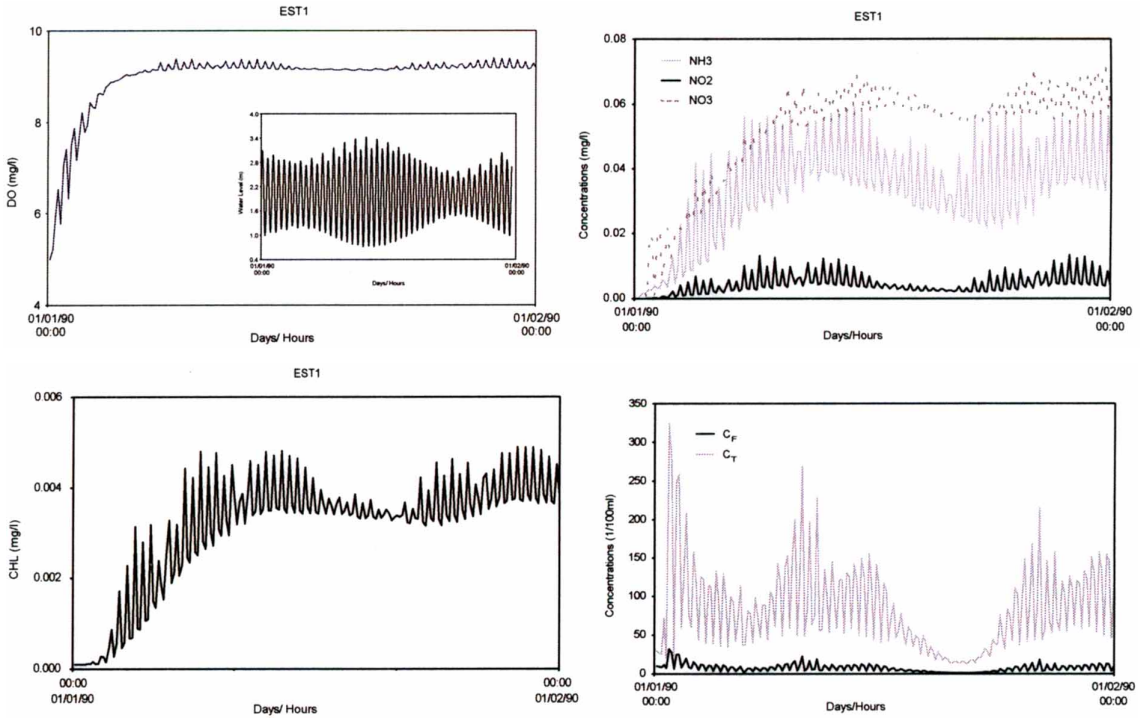

Fig. 1 Temporal series for simulated DO, Nutrients, Chorophyll-a and Coiform bacteria

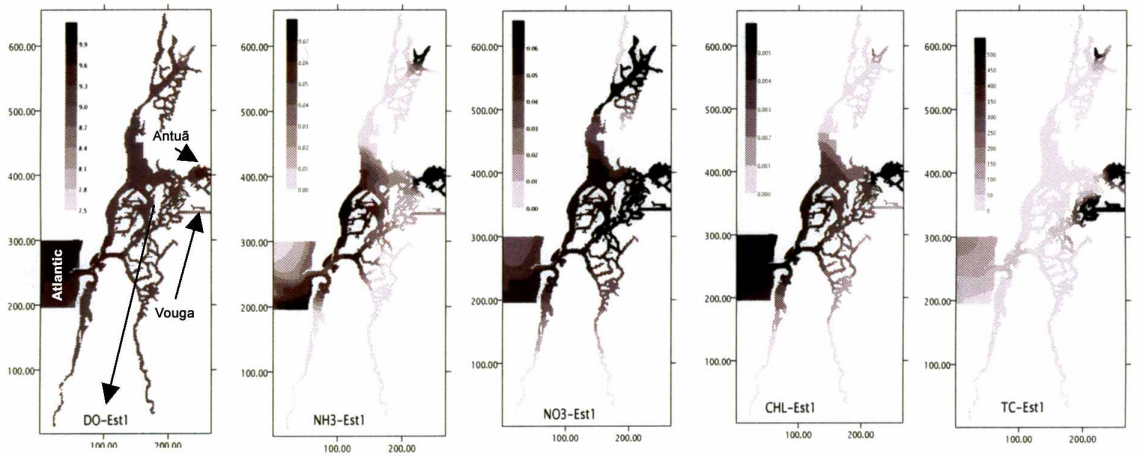

Fig. 2 Concentration maps for simulated DO, Nutrients, Chlorophyll-a and Coliform bacteria at 17/0 1/90 at 8hOOm.

Seasonal Variation of Flocculation on Tidal Flats, the Scheldt Estuary

MARGARET S. CHEN

(Department of Analytical and Environmental Chemistry, Free University of Brussels, Pleinlaan 2, B-1050 Brussels; Management of the Marine Ecosystem, Royal Belgian Institute of Natural Sciences, Rue Vautier 29, B-1000 Brussels, Belgium,
Margaret.Chen@naturalsciences.be)

STANISLAS WARTEL

(Management of the Marine Ecosystem, Royal Belgian Institute of Natural Sciences, Rue Vautier 29, B-1000 Brussels; Free University of Brussels, Pleinlaan 2, B-1050, Brussels, Belgium stanislas.wartel@naturalsciences.be)

1. Introduction

Flocculated fine-grained sediment transport in estuarine intertidal areas is a highly dynamic process strongly depending on the physical properties of suspended matter. As flocculation modifies the texture of suspended matter (SM), it thus affects its deposition. The hydrodynamic properties of cohesive sediment flocs in tidal waters and the resulting sediment transport depend on the strength of the flocs (see *Kranenbrug* [1999]). However, little is known about the true texture of SM, since the size of particles in suspension has been conventionally determined by granulometric analysis after destruction of inter-particle bindings. This study reviews a one-year biweekly measurement of SM on both freshwater and brackish water tidal flats in the Scheldt estuary. It evaluates the seasonal variation of sediment properties, organic matter (OM) content, and flocculation status of SM in the tidal water. The flocculation status includes floc's shape, sphericity and microfabric, which properties are believed to be significant in the sedimentary processes on the tidal flats.

2. Methods

SM was collected biweekly in siphon samplers for a one-year period (September 2000 – September 2001) from two tidal flats in the Scheldt, a freshwater tidal flat (FTF) and a brackish water tidal flat (BTF, with a yearly salinity range from 5 to 27). Short-term sedimentation rate was measured using a sediment trap which is a disc-shaped plastic dish (diameter of 23.3 cm and 4 mm in height) attached to the surface of the tidal flat. Every 14 days after a spring-neap cycle, the sediment trap was collected at neap tide and replaced. The dry weight of the deposited SM was determined in the laboratory. Sediment properties of SM were determined using a method described in *Wartel et al.* [1995], and the grain size distribution of the fine fraction (< 75 μm) was obtained using the Sedigraph 5100. Analyses of OM content were made using standard loss on ignition at 430°C for 24hrs method. Duplicate or triplicate samples were taken for the floc study, and the maximum particle size that can be sampled is 5000 μm due to the device's limitation. Natural floc material was retained on 0.2 μm pore-size filter using an experimentally tested optimal preparation procedure to acquire natural flocs that reflect the in situ state of the flocculation as closely as possible. Flocculation status was examined using Environmental Scanning Electron Microscope (ESEM) under the wet mode. The ESEM wet mode technique insures the examination of fresh wet natural sample and avoids accustomed arbitrary modification of the sample during procedures of critical point drying and coating. For each sample a minimum of 20 images was taken and at least 400 and up to 1000 flocs were measured.

3. Results

Sediments in the SM are fine-grained with a clay fraction (less than 4 μm) of more than 50 % of the total grain-size distribution on both tidal flats. Percentage sand on the FTF is relatively higher, around 10 % and up to 17 %, than on the BTF where it is about 2-3 % around the year. The mean diameter of the suspended sediments is below 3 μm on both tidal flats. Over this one-year period, high water discharge appears from November to April (winter and spring) with a maximum of 450 m^3/s in March, and low water discharge is from June to August (summer) with a minimum of 40 m^3/s in August. Short-term sedimentation rate is positively correlated to water discharge with average values of 950 and 1650 g/m^2/spring-neap cycle on the FTF and BTF respectively.

OM content is high on the BTF with an average value of 14 ± 5 %, compared to 9 ± 1 % on the FTF. OM varies generally in parallel with the change of clay content, however, a different trend is observed on the BTF in summer time, when a remarkable increase of OM appears together with a notable decrease of the clay fraction.

The average length of the flocs varies from 30 μm to 90 μm in different seasons over the year on both tidal flats. The average floc size is 50-70 % smaller and flocs are relatively denser during the winter and spring periods, than the considerably larger and looser flocs appear in summer. In winter and spring, sand-sized flocs (larger than 63 μm) are more abundant on the FTF (about 20 %) than on the BTF (about 4 %). It is also important to note that at least 5 % of the flocs are larger than 100 μm and reach up to 300 μm on the FTF. During the summer time, however, a remarkable phenomenon is observed on the BTF, where sand-sized flocs increase strongly to about 50 % of the total floc-size distribution, and over 5 % of the flocs are larger than 350 μm reaching up to 500 μm. Besides the seasonal variations in floc's size and microfabric, differences in floc's shape are also presented. ESEM examinations reveal more elongated flocs in winter and spring (November – April), while spherical flocs are dominant during the summer period (June – August). Furthermore, it appears that, with increasing floc size, flocs are not necessarily more elongated, but rather expand in three dimensions.

4. Discussion

Knowledge of the natural texture of SM is of primary importance to understand the sedimentary processes, and is essential to assess the sedimentation rate on tidal flats. ESEM wet mode technique has provided unique insight in SM texture. This one-year survey reveals some noteworthy relationships among physical aspects of the sediments, the amount of OM, the flocculation status and their effects on the sedimentary processes on the tidal flats.

High sand content observed on the FTF in the winter-spring period seems to indicate that high water discharge in the river basin brings an important sand supply to the FTF. It is also noted that the relatively high sand content on the FTF may influence floc's size and shape because of an abrasive effect of the sand grains in suspension. Collisions between the heavier sand grains and the fragile larger flocs may break up the latter ones into denser and smaller flocs. Indeed, ESEM observations present more relatively dense and small flocs in winter-spring time. Floc-size distribution at this period also shows that flocs rather tend to be elongated. Nevertheless, sand-sized flocs still represent about 20 % and, together with the high sand supply, contribute to the high sedimentation on the FTF in this period.

The abundance of larger than sand-sized flocs shows a parallel trend with the measured short-term sedimentation rate over this one-year period on both tidal flats. It suggests that fine-grained sediments transported as sand-sized flocs affect the sedimentation rate.

The changes in floc size and sphericity reveal a positive correlation with the change of OM from the winter and spring periods to the summer time. Larger and more spherical flocs are generated during summer time due to the existence of high OM, which at this time of the year is more degradable than in winter and spring. However, the increased amount of larger and more spherical flocs does not lead

to a high sedimentation rate in summer compared to the winter and spring periods. This implies that, although in summer OM is high favouring large floc formation on the one hand, OM decomposition catalyses floc's breaking up on the other. Deposition of these degradable-OM-flocs, which appear to be very loose, probably results in a more easily erodible sedimentation layer in summer.

5. Conclusion

The ESEM study has provided important textural observations of the flocculation status of SM. Floc texture and size exhibit clear seasonal variations and positively correlated with the measured short-term sedimentation rates on the tidal flats over this one-year survey. The changes in floc size and sphericity reveal a positive correlation with the change of OM. High OM increases floc size in a three-dimensional expanded way. Fine-grained sediments transported as sand-sized flocs have an important effect on the short-term sedimentation rate. It is deducted here that highly concentrated and relatively dense flocs contribute to fast sedimentation during winter and spring periods resulting in a compact sediment layer, while loosely formed flocs likely lead to an easier erodible layer in summer time. This deduction not only is in agreement with sedimentation measured on the tidal flats, but also matches the results of the suspended sediment concentration measurements in the flooding water on the two adjacent marshes for the same one-year period.

Acknowledgments: The authors sincerely thank J. Cillis for his great technical support in the ESEM work and S. Temmerman for providing the data of sediment traps. Thanks also go to F. Francken for his assistance in the fieldwork.

References:

Kranenburg, C., Effects of floc strength on viscosity and deposition of cohesive sediment suspensions, *Continental Shelf Research, 19*: 1665 – 1680, 1999.

Wartel, S., J. P. Barusseau and L. Cornand, Improvement of grain-size analyses using the automated SEDIGRAPH 5100. Documents de Travail de L'I. R. Sc. N. B., 80. Institut royal des Sciences naturelles de Belgique. Bruxelles, Belgique. 28 pp., 1995.

Hydrodynamic and particles transport in Ria de Aveiro lagoon, Portugal

João Miguel Dias, (*Departamento de Física, Universidade de Aveiro, 3810-193 Aveiro, Portugal*, jdias@fis.ua.pt)

José Fortes Lopes, (*Departamento de Física, Universidade de Aveiro, 3810-193 Aveiro, Portugal*, jflopes@fis.ua.pt)

Ivan Dekeyser, (*COM, université de la Méditerranée (Aix–Marseille II), 13288 Marseille cedex 9, France*, dekeyser@com.univ-mrs.fr)

1 Introduction

Ria de Aveiro is a remarkable shallow coastal lagoon on the Northwest Atlantic coast of Portugal (40°38'N, 8°45'W), and constituting a very sensible sub-system of the Portuguese coast. It is the most extensive lagoon of Portugal and the most dynamic in terms of physical and biogeochemical processes. It has a very irregular and complex geometry, characterized by narrow channels and by the existence of significant intertidal areas, namely mud flats and salt marshes, and it is connected with the sea through a single mouth.

In a lagoon like Ria de Aveiro the oceanic salt water is diluted by the freshwater coming from the terrestrial drainage, in a complex interaction under the action of tides. The water movements and the turbulent mixing resulting from the action of the different driving forces constitute interesting hydrodynamic problems.

This work presents the results of the numerical modelling studies concerning the hydrodynamic and particle transport in Ria de Aveiro. The hydrodynamic of the lagoon has been systematically studied, from both Eulerian and Lagragian point of view, in order to understand the overall circulation of the lagoon, to characterize the dynamic of its different channels, as well as to assess the particulate transport of matter.

This study focus on the Eulerian description of:
– the circulation in Ria de Aveiro, with the help of a two dimensional hydrodynamic depth integrated model, describing the tide-induced water level and depth mean current;
– the transport of suspended cohesive sediments in the lagoon, that is crucial to the understanding of the water quality of a complex system like Ria de Aveiro.

A Lagrangian description was also explored through the development and application of a particle tracking model.

2 Numerical Models

One of the objectives of this work is to develop a mathematical model able to simulate tidal flows and transport in Ria de Aveiro. As concluded in *Dias et al* [1999], Ria de Aveiro can usually be considered vertically homogeneous with generally shallow depths and a very complex geometry. For these reasons a 2DH model is considered to be the right choice to simulate the hydrodynamic of this lagoon.

2.1 Hydrodynamic Model

It was applied a classical two-dimensional vertically integrated hydrodynamic model, based on the *Leendertse and Gritton* [1971] model:

$$\frac{\partial U}{\partial t} + U\frac{\partial U}{\partial x_1} + V\frac{\partial U}{\partial x_2} = fV - g\frac{\partial \zeta}{\partial x_1} + \frac{\tau^s_{x_1} - \tau^b_{x_1}}{H\rho_0} + A_h\nabla^2 U \tag{1}$$

$$\frac{\partial V}{\partial t} + U\frac{\partial V}{\partial x_1} + V\frac{\partial V}{\partial x_2} = -fU - g\frac{\partial \zeta}{\partial x_2} + \frac{\tau^s_{x_2} - \tau^b_{x_2}}{H\rho_0} + A_h\nabla^2 V \tag{2}$$

where U and V are the depth integrated current speed components in the x_1 (eastward) and x_2 (northward) directions, respectively, H is water height, t is the time, f is the Coriolis parameter, g is the acceleration of gravity, ρ is the water density, A_h is the kinematic turbulent horizontal viscosity, τ^s and τ^b are, respectively, the magnitude of the wind stress on the water surface and the magnitude of the shear stress on the bottom caused by the flow of water over the bed. The horizontal diffusion term is of secondary importance, being kept only for numerical reasons. In this work a value of 20 m^2s^{-1} for A_h and a spatial step of 100 m in both x_1 and x_2 directions were adopted.

2.2 Sediments Transport Model

The sediments transport model adopted is based on a general transport model (*Clarke and Elliot* [1998]):

$$\frac{\partial(HC)}{\partial t} + \frac{\partial(HUC)}{\partial x_1} + \frac{\partial(HVC)}{\partial x_2} - \frac{\partial\left(HD_{ij}\frac{\partial C}{\partial x_i}\right)}{\partial x_j} = S_E - S_D \tag{3}$$

where C is the concentration of the suspended particles, D_{ij} represents the turbulent dispersion coefficients, and the source terms S_E and S_D characterize respectively the erosion and the deposition processes in the water column, as formulated by *Krone* [1962] and by *Hayter and Mehta* [1986], respectively.

2.3 Particle Tracking Model

In recovering Lagrangian information from an Eulerian currents data set, the purpose is to obtain Lagrangian particles trajectories, $\vec{X}_i^n$, given an Eulerian velocity field, $\vec{u}_i(\vec{X}_i^n, t)$, determined from the 2DV hydrodynamic model. To do this, the following equation has to be integrated:

$$\frac{d\vec{X}_i^n}{dt} = \vec{u}_i(\vec{X}_i^n, t) \tag{4}$$

where particles are identified as $i = 1, 2, \ldots$, and the vectors $\vec{X}_i^n$ and $\vec{u}_i$ give the 2D particle positions and velocities.

Therefore the two-dimensional trajectories of the simulated particles are computed using a Lagrangian approach, solving the equation:

$$\vec{X}_i(x_0, y_0)^{n+1} = \vec{X}_i(x_0, y_0)^n + \int_{t_0+n\Delta t}^{t_0+(n+1)\Delta t} \vec{u}_i(x_0, y_0, t)dt \tag{5}$$

at each time step. $\vec{X}_i(x_0, y_0)^{n+1}$ is the position at the instant $n+1$ of the particle released at the point $\vec{X}_i(x_0, y_0)^0$.

The computed trajectories can be quite sensitive to the details of the algorithm used to perform the integration. In this study the time integral is computed using a fourth-order Runge-Kutta scheme (*Hofmann et al* [1991]):

$$\vec{K}_{1i} = \Delta t \times \vec{u}_i \left[\vec{X}_i(x_0, y_0)^n, t\right] \tag{6}$$

$$\vec{K}_{2i} = \Delta t \times \vec{u}_i \left[\vec{X}_i(x_0, y_0)^n + \frac{\vec{K}_{1i}}{2}, t + \frac{\Delta t}{2}\right] \tag{7}$$

$$\vec{K}_{3i} = \Delta t \times \vec{u}_i \left[\vec{X}_i(x_0, y_0)^n + \frac{\vec{K}_{2i}}{2}, t + \frac{\Delta t}{2}\right] \tag{8}$$

$$\vec{K}_{4i} = \Delta t \times \vec{u}_i \left[\vec{X}_i(x_0, y_0)^n + \vec{K}_{3i}, t + \Delta t\right] \tag{9}$$

$$\vec{X}_i(x_0, y_0)^{n+1} = \vec{X}_i(x_0, y_0)^n + \frac{\vec{K}_{1i}}{6} + \frac{\vec{K}_{2i}}{3} + \frac{\vec{K}_{3i}}{3} + \frac{\vec{K}_{4i}}{6} \tag{10}$$

where $\vec{X}_i(x_0, y_0)^{n+1}$ represents the new location of a particle that is advected from its previous position $\vec{X}_i(x_0, y_0)^n$ by the velocity $\vec{u}_i = (u_i, v_i)$ in a time interval Δt, and $\vec{K}_{ji}$ represents the Runge-Kutta coefficients. In this study the time step of integration of the particle tracking model has the same value as the time step used to integrate the hydrodynamic model (40 s).

3 Results

After careful calibration and validation of the different models they were applied to study the hydrodynamic and transport of sediments and particles in Ria de Aveiro.

The main circulation features define the transport of suspended materials and the erosion or deposition that occurs in the lagoon. The distribution of suspended sediments characterizes the environment of the lagoon. The main areas of deposition and erosion were identified, and its origin understand by the analysis of the tidally induced residual circulation.

The lagoon dynamic is predominantly dominated by the tidal forcing, but the freshwater input from the main rivers during flooding situations has also important consequences in the establishment of the circulation and sediments patterns. The residence time determined using the lagrangian transport of particles is very low in the lagoon central area, revealing a very good water renewal. Its value increases toward the far end of the main channels. The main lagoon channels exhibit different characteristics, and maybe considered as almost independent systems.

Acknowledgments: This research was supported by FCT through projects ModelRia and Proteu.

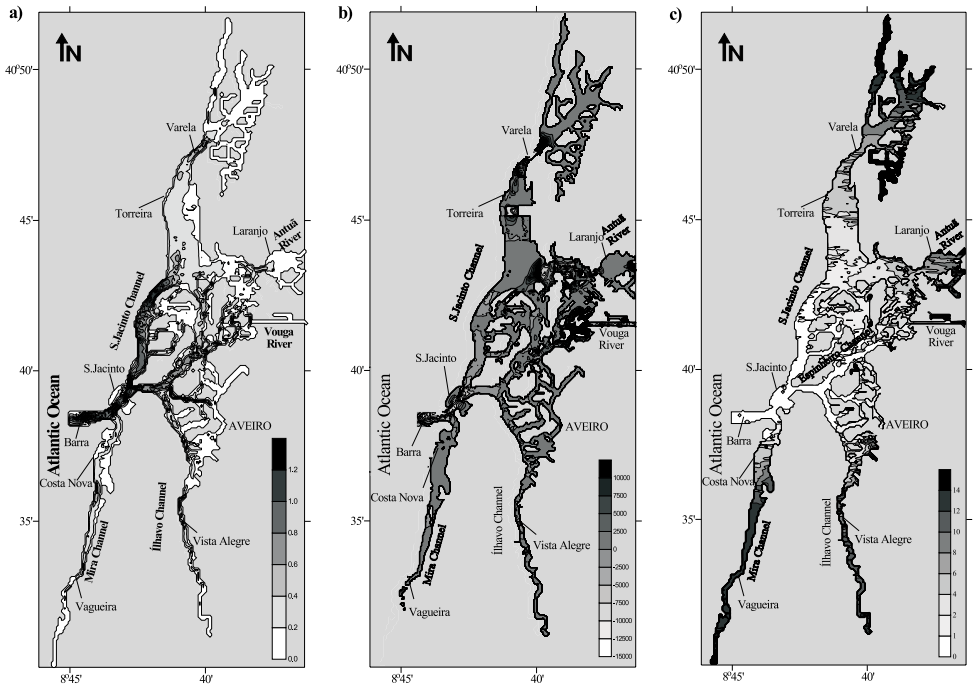

Figure 1: Simulated RMS speed distribution (a)(ms^{-1}) and net deposition field (b)(gm^{-2}) for spring tide conditions, and residence time (c) (days).

References:

Clarke, S., Elliot, A. J., Modelling suspended sediments concentration in the Firth of Forth, *Est. Coast. Shelf Sci.*, **47**, pp 235-250, 1998.

Dias, J. M., Lopes, J. F., Dekeyser, I., Hydrological characterization of Ria de Aveiro, in early summer, *Oceanologica Acta*, **22**, n°5, pp 473–485, 1999.

Hayter, E. J., Mehta, A. J., Modelling cohesive sediments transport in estuarine waters, *Appl. Math. Model.*, **10**, pp 294–303, 1986.

Hofmann, E. E., Hedström, K. S., Moisan, J. R., Haidvogel, D. B. and Mackas, D. L., Use of simulated drifter tracks to investigate general transport patterns and residence times in the coastal transition zone. *Journal of Geophysical Research*, **96**, C8, pp 15041–15052, 1991.

Krone, R. B., *Flume study of transport of sediments in estuarial processes*, Final Report, H.E.L.S.E.R.L.,Univ. of California, Berkeley, California, 1962.

Leendertse, J. J., Gritton, E. C., *A Water–Quality Simulation Model for Well–Mixed Estuaries and Coastal Seas: Volume II, Computation Procedures*, The Rand Corporation, Memorandum R–708–NYC, Santa Monica, 53 pp, 1971.

Sediment Dynamics in Tidal Flats and Salt Marshes of the Tagus Estuary, Portugal

PAULA FREIRE

(Laboratório Nacional de Engenharia Civil, Av. Do Brasil, 101, 1700-066 Lisboa, Portugal, pfreire@lnec.pt)

CÉSAR ANDRADE

(Centro e Departamento de Geologia da Faculdade de Ciências de Lisboa, Bloco C2, 5º Piso, Campo Grande, 1749-016 Lisboa, Portugal, candrade@fc.ul.pt)

1. Introduction

The Seixal bay is located in the southern bank of the inner Tagus estuary and consists of a shallow semi-enclosed system with extensive tidal mudflats and salt marshes (Figure 1), which formed and accreted during the last 500 years following the formation of the Alfeite sand spit (*Freire and Andrade* [1999]; *Freitas et al*. [1999]). The local mean tidal range in spring and neap tides is 3.2 m and 1.5 m, respectively, and the maximum tidal level above chart datum (MSL=2.2 m) is 4.3 m. The sediment forming the tidal flats and marshes in the Seixal bay is to a large extent cohesive (silty clay) with particulate organic matter content up to 9%. Sandy sediments are concentrated preferably in the deeper channels. The sediment dynamics inside the Seixal Bay is almost exclusively driven by tidal currents, in contrast with the exposed beach of the sand spit, which is essentially reworked by local generated waves.

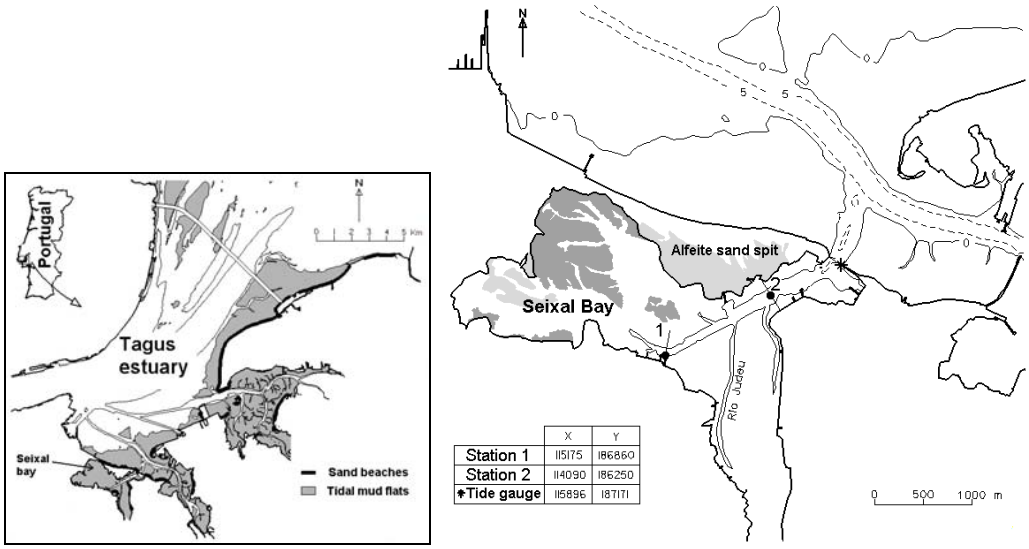

Figure 1: Location map of the field study area and surveyed stations.

Andrade et al. [1998], *Freire* [1999] and *Freitas et al.* [1999] studied the short to medium-term evolutionary trends of the Seixal intertidal areas using map comparison and field measurement of erosion/accretion. The results of theses studies pointed out a contrasting morphological behaviour between the subtidal and low-intertidal areas (net erosion) and the high-intertidal and supratidal region of flats and marshes (net vertical accretion and no appreciable surface change).

The results of two field surveys conducted to measure and describe the patterns of suspended sediment movement at the time scale of a tidal cycle are presented in this paper and the results discussed within the context of the evolutionary trends previous reported.

2. Methods

Two 13 hour-long field surveys were performed in February (neap waters) and March (spring waters) 1998 in two stations of the Seixal Bay (Fig. 1): station 1, positioned in the main thalweg of the Seixal channel (CD depth of 2 m) was equipped with one acoustic current meter RCM-9 with sensors of temperature, conductivity and turbidity; water samples were collected at regular intervals for later calibration of the conductivity sensor; station 2 lies 2 500 meters upstream, in the southern tidal flat (CD depth of 0.4m) and the equipment deployed consisted of a Braystoke current meter; water samples for conductivity and turbidity measurement were collected with a horizontal van Dorn-type bottle. During the surveys the local tidal level variation was monitored using a tide gauge (see Figure 1 for location). The meteorological conditions were similar during both surveys and are described in *Freire* [1999]. Bottom sediment mapping and hydrographical surveys of the intertidal and subtidal features were also performed.

The concentration of suspended sediment was determined in the laboratory following the gravimetric method and using Millipore 0.45μm mesh standard filters. Particle size analysis of the residual sediment in the filters was performed by laser diffraction.

3. Results and Discussion

The results obtained in the field surveys show that the estuary is the main source for the Seixal bay sediment bed load. The sand is transported mainly during the spring tide flood and is trapped into the bay, remaining in the deeper channel near the entrance. The results also reveal that there is no significant input of fine material in suspension from the estuary into the bay, being the local fluvial network the main source of silt-clay sediment.

Inside of the bay the resuspension of bottom sediments is particularly efficient during the spring tide ebb when maximum velocities (97 cms^{-1}) are observed (Figure 2). The finer sediment fraction (mean diameter of 10 μm), which includes most of the particulate organic matter (Figure 3), remains in suspension during the low water slack period. This promotes a flood-dominated net transport towards the higher intertidal flats and marsh banks. On the other hand, the coarser silt particles (mean diameter of 40 μm) are preferentially exported from the tidal flats during the ebb towards the lower flats and channels. In this way, the tidal currents promote a textural sorting of the suspended particles by size and the associated deposition of the finer inorganic silt fraction with the organic fraction, which has expression in the bottom sediment distribution.

The amount of suspended sediment transported during the tidal cycles was evaluated. The results show that in station 2 a residual amount of $5x10^3$ m^3 of material is transported during the ebb. Considering the total area influenced by the tide upstream the station 2, an average erosion rate of 0.3 $cmyear^{-1}$ was found.

These results suggest a contrasted morphological evolutionary short-term model for Seixal bay in which the accretion is dominant in the high-intertidal and supratidal flats while the subtidal and low-intertidal areas show an erosional tendency. The short-term evolutionary trends and rates deduced from the surveys are in agreement with the medium and long-term results for the Seixal bay achieved in other studies. *Freitas et al*. [1999], using radiometric dating, obtained a sedimentation rate for the salt marshes of the Seixal bay of 0.7 $cmyear^{-1}$. The results presented by *Freire* [1999], through chart comparison methods, show that the subtidal and low intertidal flats present an erosion tendency, with an average rate of -1 to -2 $cmyear^{-1}$.

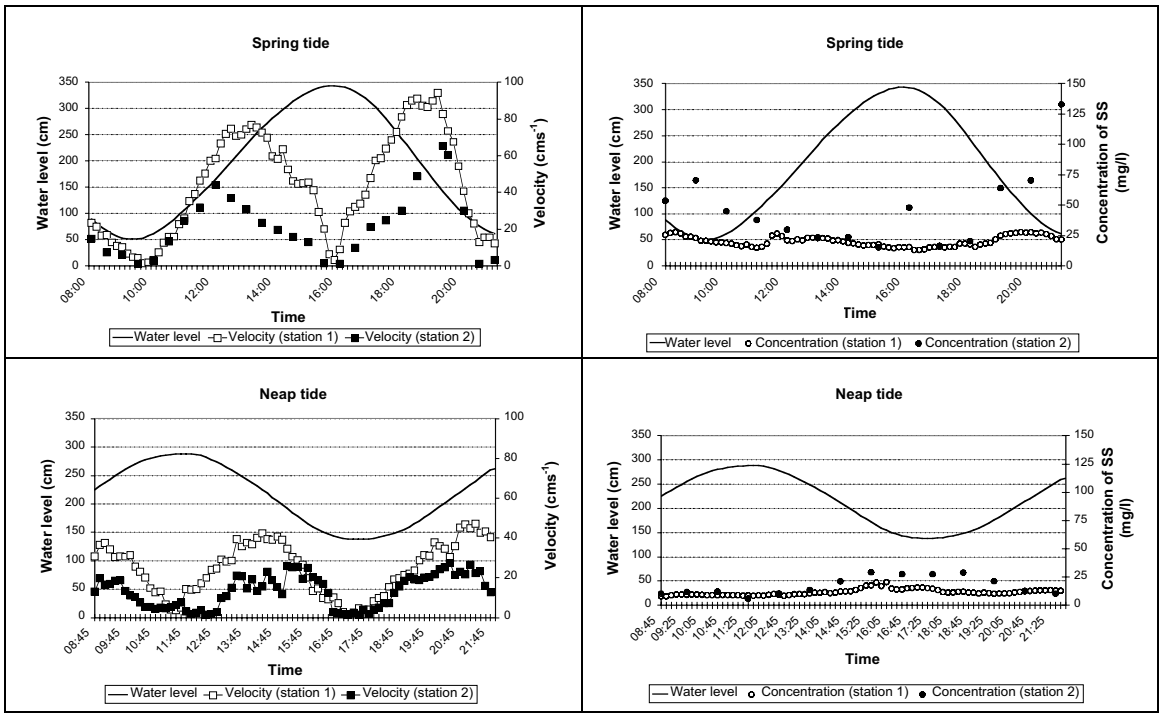

Figure 2: Measured time series of tidal currents velocity and suspended sediment concentration at Seixal bay.

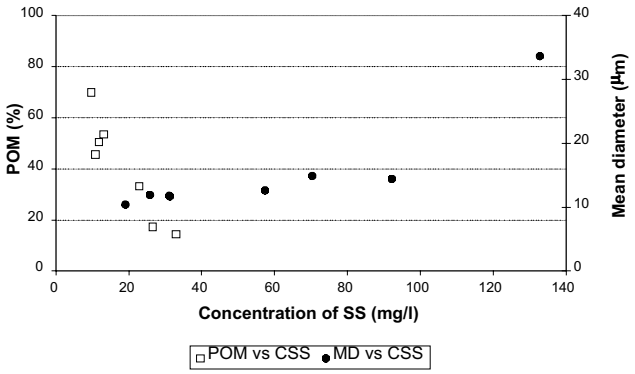

Figure 3: Suspended sediment concentration (CSS) plotted against sediment mean diameter and particulate organic matter content (POM).

The implications of the presented model for a long-term evolution of the Seixal bay are that this pattern of evolution must be interrupted by high-intensity and low frequency episodes of activity of the local fluvial network, that will bring important amounts of fine sediment into the system.

4. Conclusions

In order to characterize the composition and the short-term dynamics of the sediments in Seixal Bay, two field surveys were performed. The results show a contrasted morphological evolutionary trend of the subtidal and low-intertidal areas *versus* the high-intertidal and supratidal flats: the erosional behaviour is dominant in the former while the salt marshes show an accretionary tendency. The evolutionary trends and rates obtained in this study are in agreement with the medium to long-term results achieved by *Freire* [1999] and *Freitas et al*. [1999].

Acknowledgments: The first author was sponsored by Fundação para a Ciência e a Tecnologia under grant BD/2767/93-RN.

References:

Andrade, C., Freitas, M.C., Bastos, A., Abrantes, A. and A. Antunes, Micro-scale morphodynamics in salt marshes of Tagus estuary. An experimental approach. Actas V Congresso Nacional de Geologia. *Comum. IGM*, 84 (I), C67-C70, 1998 (in Portuguese).

Freire, P., *Morphogical and sedimentary evolution of estuarine banks (Tagus Estuary, Portugal),* PhD Dissertation, University of Lisbon, 320p., 1999 (in Portuguese).

Freire, P., and C. Andrade, Wind-induced sand transport in Tagus estuarine beaches. First results. *Aquatic Ecology*, 33, 225-233, 1999.

Freitas, M.C., Andrade, C., Moreno, J.C., Munhá, J.M. and M. Cachão, The sedimentary record of recent (last 500 years) environmental changes in the Tagus marshes, Portugal, *Geologie en Mijnbouw*, 77: 283-293, 1999.

Modelling of the seasonal dynamics of the water masses, ice and radionuclide transport in the large Siberian river estuaries

VLADIMIR MADERICH, NATALYA DZIUBA, VLADIMIR KOSHEBUTSKY, MARK ZHELEZNYAK

(Institute of Mathematical Machine and System Problems, Glushkov av. 42, 03187, Kiev, Ukraine, vlad@immsp.kiev.ua)

VLADIMIR VOLKOV

(Nansen International Environmental and Remote Sensing Center, 26/28, Bolshaya Monetnaya Str.197101 S.-Petersburg,Russia, vladimir.volkov@niersc.spb.ru

1. Introduction

The activities of several nuclear reprocessing plants (Siberian Chemical Combine (SCC), Mining, Chemical Combine (MCC) and Mayak Production Association (Mayak)) that are placed on the watersheds of large Siberian rivers Ob' and Yenisey may potentially cause contamination of the Arctic Ocean. Therefore, use of the models is necessary to assess the influence on potential radioactivity spreading location of these sources and impact of global warming on dispersion processes in the system river-estuary.

In frame of EU INCO-COPERNICUS project RADARC (*Johannesen et al.* [2002]) a linked chain of 1D river model RIVTOX and 3D model THREETOX was used to simulate impact of the previous and potential releases from the nuclear installations in the basins of Ob' and Yenisey rivers on the radioactive contamination of the Kara Sea and Arctic Ocean.

2. Model Chain

The model chain includes 1D river net model RIVTOX and 3D estuary model THREETOX. The THREETOX code (*Margvelashvili et al.* [1997] is intended for simulation of the transport and fate of the radionuclides and other contaminants in the stratified waterbodies. THREETOX includes a set of submodels: a hydrodynamics submodel, ice dynamics-thermodynamics submodel, suspended sediment transport and radionuclide transport submodels. The hydrodynamics is simulated on the basis of the three-dimensional, time-dependent, free surface, primitive equation model. The modified $\kappa - \varepsilon$ model (*Burchard and Pettersen* [1999]) is used. The dynamic-thermodynamic ice and snow model is based on the Hamburg Sea-Ice Model (*Stössel and Owens* [1992] that was modified by implementation of elastic-viscous-plastic rheology. Suspended sediment transport is described by the advection-diffusion equations, taking into account fall velocities of the sediment grains. The bottom boundary condition describes sediment resuspension or settling down depending on the ratio between the equilibrium and actual near bottom suspended sediment concentration. The thickness of the upper layer of the bottom deposition is governed by the equation of the bottom deformation. The equations of the radionuclide transport describe the concentration of the radionuclide in solute, the concentration in the suspended sediments and the concentration in the bottom deposition. The exchanges between these forms have been described as adsorption-desorption and sedimentation-resuspension processes. Adsorption and desorption of radionuclide between liquid and solid phases are described by the radionuclide exchange rates, and by the distribution coefficients.

The one-dimensional river model RIVTOX was developed at the IPMMS (*Zheleznyak et al.* 1992). It simulates the radionuclide and chemical pollution transport in networks of river channels. Sources can be a direct release into the river or the runoff from the catchment.The hydraulics part of the RIVTOX is based on the of Saint-Venant equations. The governing equations of the sub-model of suspended sediment and radionuclide transport model are derived from the 3-d model equations. They describe

advection-diffusion transport of the cross-sectional averaged concentrations of suspended sediments, toxins in solution, toxins in suspended sediments and in bottom depositions. The adsorption-desorption and diffusion contamination transfer in the systems "solution - suspended sediments" and "solution - bottom deposition" are treated also via the distribution coefficient approach.

3. Study area

The 1D model RIVTOX of river dynamics and radionuclide transport was adapted to the Ob' river path from Mayak and SCC and to the Yenisey River from MCC (see Figure 1). The river network was subdivided into a set of branches in compliance with the location of observation points and the main tributaries. The parameters of water cross-sections for observation points were used. The monthly tributary discharges values for 1949-1995 were used to simulate river hydraulics. The data on release from the radionuclide sources were collected in frame of RADARC project (*Johannessen et al.* [2002]). The THREETOX was customised for the Ob' and Yenisey estuaries using digitised navigational maps of estuaries. The horizontal grid resolution is 8x6 km in the Ob' and 3 km in the Yenisey. The 6hr fields of wind, air temperature, precipitation, humidity and cloudiness were used from NCEP reanalysis for the period 1949-1995. Daily mean discharges of rivers, suspended sediment and radionuclide concentrations were calculated by the RIVTOX model. In the estuary mouth, the temperature, salinity and velocity distributions and sea level computed by the Kara Sea model (*Johannessen et al.* [2002]) were used in the estuary model as outer boundary conditions. The simulations of the period 1949-1994 were carried out for the Ob' and period 1974-1994 for the Yenisey.

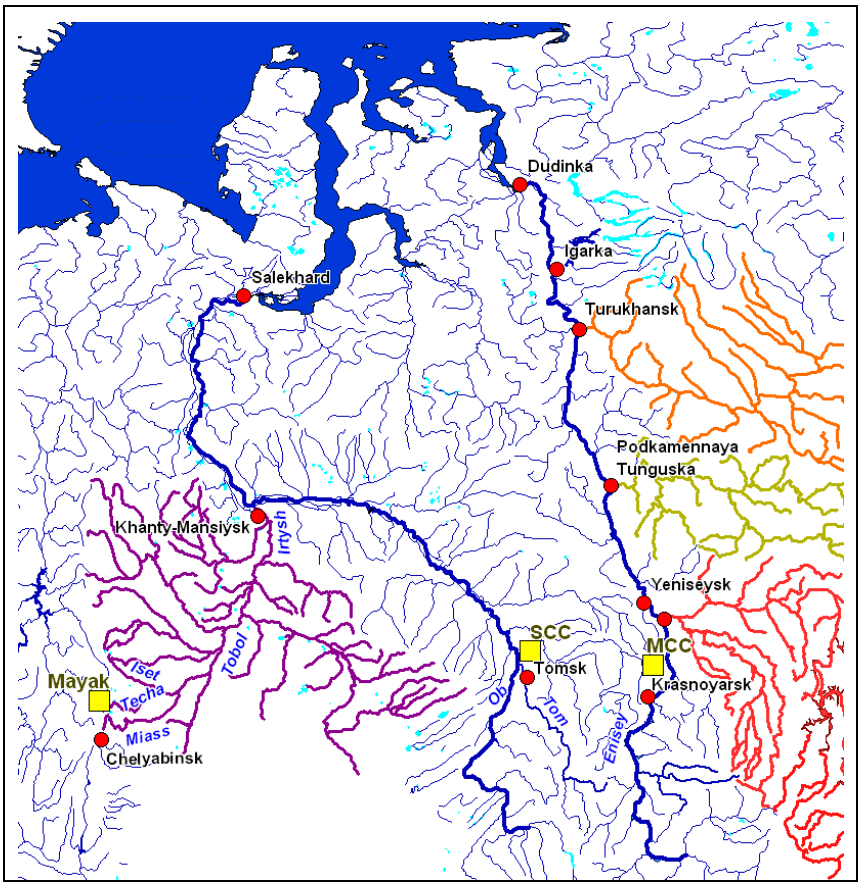

Figure 1: Ob' and Yenisey river system. The boxes correspond to the Mayak Production Association (Mayak), Siberian Chemical Combine (SCC) and Mining, Chemical Combine (MCC).

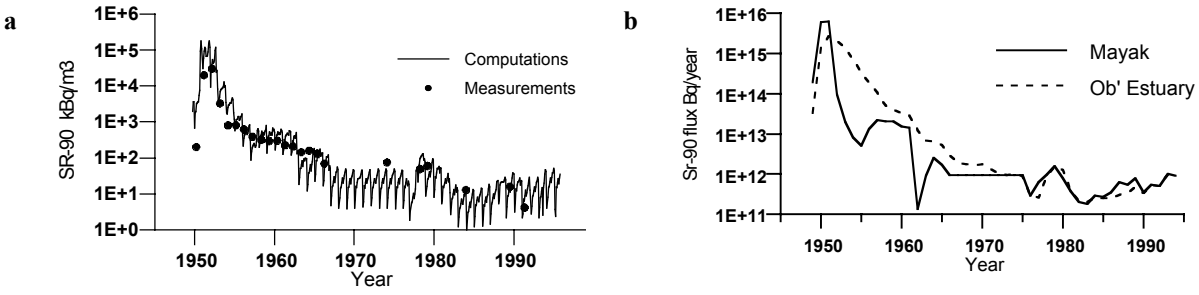

Figure 2: The computed and observed concentration of ^{90}Sr in the Musliumovo (Techa River) (a) and measured yearly mean release of ^{90}Sr from Mayak vs. computed flux from Ob' estuary to the Kara Sea.

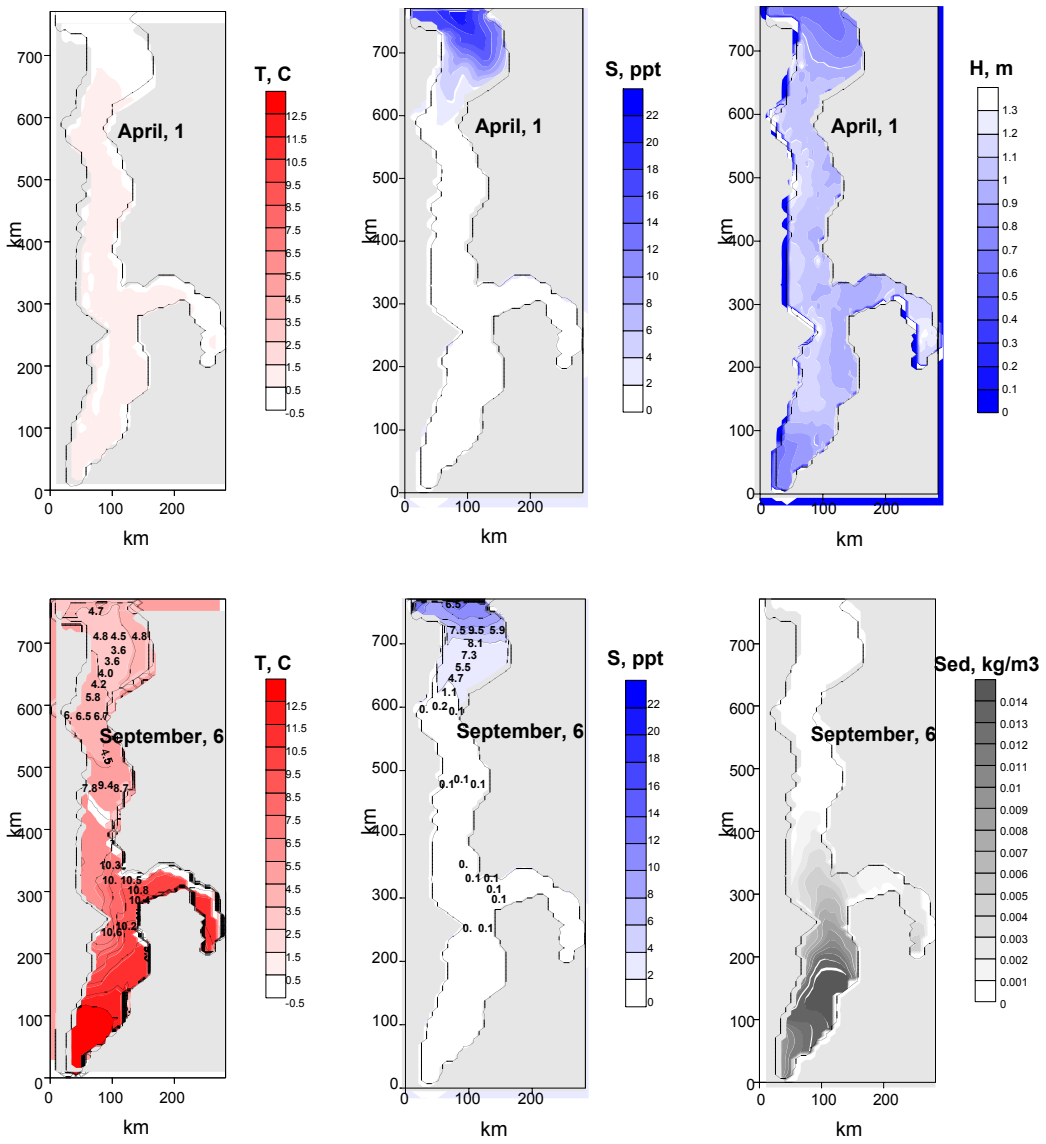

Figure 3: The computed surface fields of temperature, salinity and ice thickness in the Ob' Estuary in April 1994 and surface fields of temperature, salinity and near bottom distribution of suspended sediments in September 1994. The temperature and salinity are compared with KAREX-94 data.

4. Results and conclusions

The model chain was validated against the available data on river discharge, suspended sediment and radionuclide concentration, temperature, salinity and ice distribution in the estuaries. In Figure 2 the contribution of Mayak in ^{90}Sr contamination of the Ob' river system and the Kara Sea is presented. In Figure 2a the calculations are compared with ^{90}Sr measurements in Musliumovo (Techa River). As seen from figure the RIVTOX model reproduces transport of radionuclide quite well. In Figure 2b the fluxes of ^{90}Sr from Mayak and Ob' estuary mouth to the Kara Sea are given. This figure shows that after strong initial contamination in early 50th the sediments in the Ob' were sources for secondary contamination of river and estuary. Around 70% released in 1949-1994 ^{90}Sr reached the estuary mouth. The Yenisey River was contaminated the same way in 70th in result of washing up of contaminated sediments from the islands and flood plains. The numerical results agree quite well with the observations of the oceanographic fields. In Figure 3 the surface fields of temperature, salinity and ice thickness in the Ob' Estuary in April 1994 and surface fields of temperature, salinity and near bottom distribution of suspended sediments in September 1994 are presented. The computed temperature and salinity agree with the survey data from KAREX-94. The computed in other run the salt wedge in the relatively deep Yenisey Estuary is clearly visible.

The results of multi-year simulation of the water dynamics and radionuclide transport in the Ob' and Yenisey rivers and estuaries showed ability of the developed model chain to reproduce a seasonal dynamics of water mass. An important role of ice cover in the seasonal dynamics of the Ob' and Yenisey estuaries also was demonstrated. The developed model chain is used for assessment of the radionuclide spreading from inland sources.

Acknowledgments: This work was funded by EU INCO-COPERNICUS project RADARC (Contract ICA-CT-2000-10037) and project INTAS – 1997-31278.

References:

Burchard, H., Petersen O. Models of turbulence in the marine environment – a comparative study of two-equation turbulence models. *J. Marine Systems, 21*, 29-53, 1999.

Johannesen, O. M., Pettersson, L. H., Gao Y., Nielsen, S.P., Borghuis, S., Strand, P., Reiersen, L. O., Bobylev, L. P.,Volkov, V., Neelov, I., Stepanov, A., Bobylev, K., Zheleznyak, M., Maderich, V. Simulation for potential radioactive spreading in the 21 century from rivers and external sources in the Russian arctic coastal zone-RADARC, in *The 5th Int. Conf. on Environmental Radioactivity in the Arctic & Antarctic*, edited by P. Strand, T. Jølle and Å. Sand, Norway Radiation Protection Authority, Norway, 2002.

Margvelashvili, N., Maderich, V., Zheleznyak M., THREETOX - computer code to simulate three-dimensional dispersion of radionuclides in homogeneous and stratified water bodies. *Radiation Protection Dosimetry*, *73*, 177-180, 1997.

Stössel, A., and W. B. Owens, The Hamburg Sea-Ice Model. Report No. 3, DKRZ, 65 pp., 1992.

Zheleznyak, M., Demchenko R., Khursin S., Kuzmenko Yu., Tkalich P., Vitjuk N. Mathematical modelling of radionuclide dispersion in the Pripyat-Dnieper aquatic system after the Chernobyl accident. *The Science of the Total Environment*, *112*, 89-114, 1992.

Spring-neap variations in residual currents and bedload transport rates, associated with rectilinear and rotatory tidal current systems

ANA PAULA TELES

(Southampton Oceanography Centre, European Way, SO14 3ZH Southampton, U.K., anateles@soc.soton.ac.uk)

MICHAEL COLLINS

(Southampton Oceanography Centre, European Way, SO14 3ZH Southampton, U.K., mbc@soc.soton.ac.uk)

DAVID PUGH

(Southampton Oceanography Centre, European Way, SO14 3ZH Southampton, U.K., dtp@soc.soton.ac.uk)

1. Introduction

The Solent Estuarine System is an important estuarine system located along the south coast of the United Kingdom separating the Isle of Wight from the mainland (see *Collins and Ansell* [2000]). The system comprises the well-mixed Solent channel, the partially-mixed Southampton Water estuary, and the harbours of Portsmouth, Langstone and Chichester, together with other smaller estuaries. The Solent channel can be divided into two sections: the East Solent, 20 km long and 5.5 km wide; and the West Solent, 20 km long and 4 km wide, on average. Both sections contain a deep channel, with depths (related to Chart Datum) ranging mostly from 10 to 20 m; likewise, an extensive shallow area with depths less than 10 m, transitionally grading into the tidal flats. The East Solent entrance is wider (8 km) with depths in excess of 30 m in the narrow deep channel (1.5 km), whilst the West Solent entrance is very narrow (1.5 km) and deep (up to 60 m). The two entrances are connected to the English Channel; hence, they are affected by its tidal, wave and sediment dynamics regimes. These are examined in this contribution, in relation to potential sand transport.

2. Data Analysis

Data from (5) self-recording current meter locations in the West and East Solent are analysed here, in terms of residual currents and sediment transport rates. Residual currents have been measured around 5 m above the bed in the East Solent and 10 m above the bed in the West Solent (in water depths ranging from 11 to 20 m). Near-bed residual currents have been calculated at 1 m above the bed, based upon the assumption of a 'power law' on the vertical distribution of the currents (see *Dyer* [1970a]). Directionally-related (resolved into north, east, south and west components) mean and net bedload transport rates have been computed over neap and spring tidal cycles. Bedload transport has been calculated on the basis of the modified Hardisty equation (see *Hardisty* [1983]; *Wang and Gao* [2001]), for 'potential' sand (D_{50}= 0.14 mm (median diameter)) transport. Effectively, currents in the West Solent are rectilinear in character; those in the East Solent are rotatory, and under certain conditions influenced by wave activity. Under the influence of waves over the same region (see *Gao and Collins* [1997]), the magnitude of the directionally-related (qN, qE, qS and qW) transport rates varies, whilst the net transport remains relatively constant. This concept is examined here, in terms of spring-neap tidal cycles (approx. 7.5 days each) variability and in relation to rectilinear-rotatory current systems.

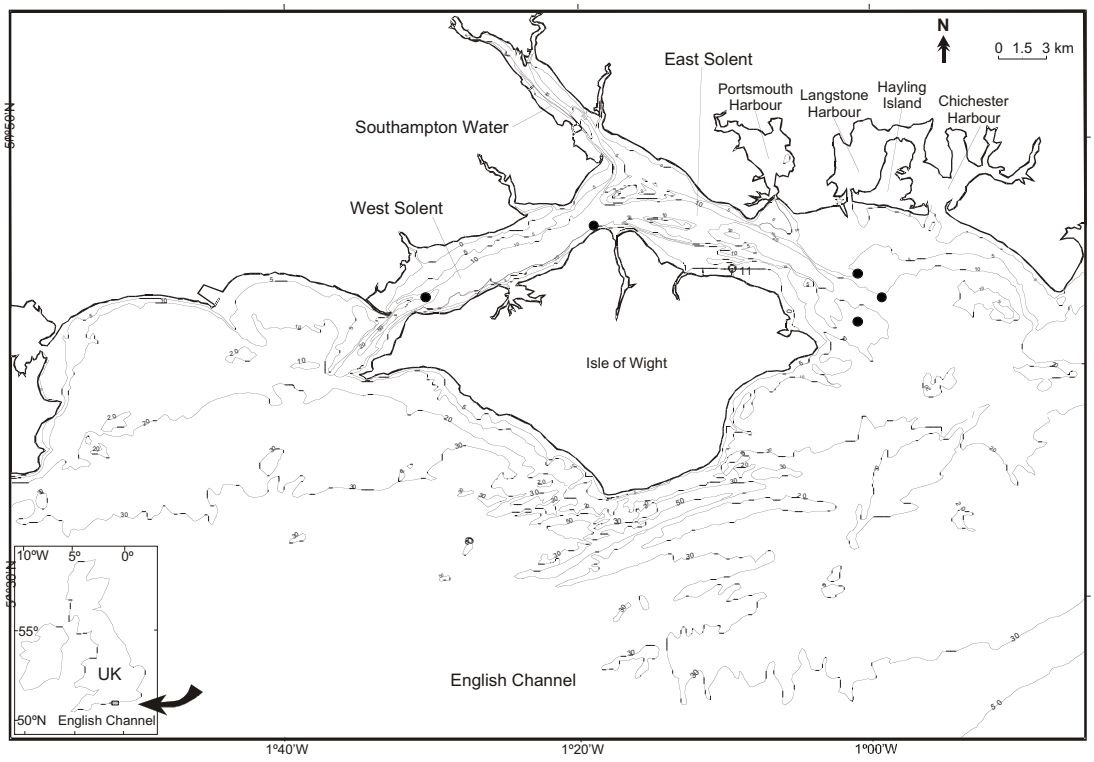

Figure 1: The Solent Estuarine System and the 5 current meter locations (•).

3. Summary and Conclusions

Mid-depth and near-bed residual currents

In terms of the mid-depth residual currents, those associated with rectilinear tidal current systems (West Solent) are larger in magnitude, on neaps (0.095 and 0.126 ms^{-1}) and springs (0.125 and 0.184 ms^{-1}) compared to rotatory locations (0.006 to 0.030,and 0.031 to 0.064ms^{-1}, respectively). Directional variability of the residual currents between springs and neaps ranged up to 8^o for the rectilinear stations and up to 74^o for the rotatory stations. In converting to near-bed residual currents, the directional values are slightly modified (generally, around 2 to 3^o) in response to resolution of the vectors (a high difference can be associated with a low residual current).

For all the stations, the rates ranged between 0.002 and 0.093 $kgm^{-1}s^{-1}$ on neaps and 0.001 and 0.135 $kgm^{-1}s^{-1}$ on springs. For the rectilinear current systems, the differences between near-bed residual current and net bedload transport directions ranged from 11 to 23^o, on neaps and springs; for rotatory, they ranged from 21 to 145^o. Hence, the direction of the net bedload transport is relatively consistent with the direction of the near-bed residual currents for the rectilinear current systems; it is not consistent for the rotatory currents.

Directional mean and net bedload transport rates

In all cases, the magnitude of the directionally-related mean bedload transport rates increased from neap to spring tidal conditions. In the case of the rotatory system, the rates show high variability, with an overall 78% to 783% increase on springs (in relation to neaps); for rectilinear, from 18% to 62% but at considerably higher transport rates. In comparison, the net rates showed similar increases (45%

to 61%) for the rectilinear currents; for the rotatory, they ranged from 198% to 812% (in a single case, a decrease).

Comparisons undertaken between the various directional components (qN, qE, qS, and qW), with the net rates demonstrate: (a) consistent contributions in the case of the various mean transport rate components at a particular station, on both neaps and springs, for the rectilinear currents (West Solent); and (b) highly variable contributions for each component, on neaps and springs and at the various stations, for the rotatory currents (East Solent).

Thus, particularly in relation to the rotatory tidal current systems, there is strong evidence of intensification of lateral transport under spring tidal conditions *cf* simulated 'stormy' conditions (see *Gao and Collins* [1997]). Similarly, there are variable contributions from the directional mean transport rates, to the net transport rates, at the same stations on both neap and spring tides.

Water circulation

In terms of mid-depth and near-bed Eulerian residual currents on neaps and springs, there is evidence of flow out of the West Solent, towards the East Solent. This is consistent with the eastward residual calculated previously from sea level differences (see *Blain* [1980]), and from current meter measurements on neap tides with high barometric pressure and northeasterly winds (see *Dyer and King* [1975]). On the other hand, it is not consistent with the westward residual occurred on spring tides with low barometric pressure and southwesterly winds. The southwestly residuals observed at the western end of the West Solent may be related locally to a topographically-induced eddy or even to systems of meanders-recirculating eddies identified {see *Dyer* [1970b]).

At the eastern end of the East Solent, there is a net water movement towards the southeast, with some evidence of divergence to both the north and south. Such patterns may be related to local bathymetric controls (large shoal area to the north and south of the stations). These residuals are similar to residuals computed for 1-month OSCR data sampled in 1995 during low wind activity.

Sediment fluxes

Within the rectilinear tidal system of the West Solent, the directional net (bedload) transport rates are similar to those of the residual currents. In the case of the rotatory systems, there are both similarities and dissimilarities between the two data sets.

Overall, the predicted mean transport vectors are indicative of sand movement out of the West Solent (see *Dyer* [1970a, b]; *Langhorne et al.* [1986]).

Overall, the predicted mean transport vectors are indicative of sand movement out of the East Solent and, possibly, towards the south. Such patterns are similar to those presented elsewhere on the basis of grain size trends and bedform asymmetries (see *Hydraulics Research* [1993]; *Paphitis et al.* [2000]). The mean directional component transport rates on neaps and springs appear, once again, to indicate predominant bedload movements out of the East Solent. Eventually, therefore, tidally-induced bedload transport is out of the system at the eastern limit; this is consistent with the direction predicted for prolonged storm activity, on the basis of time-asymmetry and wave activity (see *Gao and Collins* [1997]).

Acknowledgements: The authors of this extended abstract are grateful to the Brazilian Council of Scientific and Technological Development (CNPq) for a PhD scholarship to the first author, process no. 201052/97-0.

References:

Blain, W.R. *Tidal Hydraulics of the West Solent*. Ph.D. Thesis, University of Southampton. 3 volumes, 1980.

Collins, M. and Ansell, K. Preface, in *Solent Science- A Review,* edited by M. Collins and K. Ansell, pp. v-vi, Elsevier Science B.V., Amsterdam, 2000.

Dyer, K.R. Current profiles in a tidal channel. *Geophys. J.R. astr. Soc*. 22, 153-161. 1970a.

Dyer, K.R. The distribution and movement of sediment in the Solent, Southern England. *Marine Geol*., *11,* 175-187, 1970b.

Dyer, K. R. and King, H.L.The residual water flow through the Solent, South England. *Geophys. J.R. astr. Soc*. *42*, 97-106, 1975.

Gao, S, and Collins, M.B. Changes in sediment transport rates caused by wave action and tidal flow-asymmetry, *Journal of Coastal Research*, *13*, 198-201, 1997.

Hardisty, J. An assessment and calibration of formulations for Bagnold's bedload equation, *Journal of Sedimentary Petrology, 53,* 1007-1010, 1983.

Hydraulics Research, South coast seabed mobility study. Technical Report EX 2827, Summary Report EX 2795, HR Wallingford Ltd., 55pp, 1993.

Langhorne, D.N., Heathershaw, S.D. and Read, A.A. Gravel bedforms in the West Solent, Southern England. *Geo-Marine Letters*, 5, 225-230, 1986.

Paphitis, D. Residual circulation and associated sediment dynamics in the eastern approaches to the Solent, in *Solent Science- A Review,* edited by M. Collins and K. Ansell, pp. 107-109, Elsevier Science B.V., Amsterdam, 2000.

Wang Y.P. and Gao, S. Modification to the Hardisty equation, regarding the relationship between sediment transport rate and particle size. *Journal of Sedimentary Research, 71,* 118-121, 2001.

Estuary process research project linking hydrodynamics, sediments and biology (*EstProc*)

RICHARD WHITEHOUSE

(HR Wallingford, Howbery Park, Wallingford, Oxon OX10 8BA, UK, rjsw@hrwallingford.co.uk)
AND THE ESTUARY PROCESS CONSORTIUM

1. Introduction

A major research project into estuarine processes is underway within the UK's R&D framework of Fluvial, Estuarine and Coastal Processes. The *EstProc* project brings together a multi-disciplinary team to research estuarine hydrodynamics, sediments and biology and their interactions. The 3 year research project is being undertaken by a project team comprising 11 partners drawn from the UK and Netherlands:

HR Wallingford

Proudman Oceanographic Laboratory

Professor Keith Dyer / University of Plymouth

St Andrews University, Gatty Marine Laboratory (Sediment Ecology Research Group)

ABP Marine Environmental Research

WL | Delft Hydraulics

Plymouth Marine Laboratory, Centre for Coastal and Marine Sciences

University of Cambridge, Cambridge Coastal Research Unit

University of Southampton, School of Ocean and Earth Sciences

Digital Hydraulics Holland B.V.

Centre for Environment, Fisheries and Aquaculture Science

2. Project Overview

The project started in December 2001 and has the following stated objectives:

Innovative and fundamental research in estuarine hydrodynamics, sediments and biological interactions

Improved underpinning knowledge and sound scientific results for the estuary research community and end users

The research is being undertaken in an integrated fashion within three main themes of hydrodynamics, sediment processes and biology. Each one of the themes has a designated Theme Leader to oversee the conduct and delivery of the research, which tackles key issues related to the delivery of:

Improved understanding and modelling of hydrobiosedimentary processes

Improved understanding and modelling of sediment erosion and deposition and the resulting changes in estuary morphology

As part of this, the key question as to what time and space scales the assessment of the various estuarine processes and their linkages should be made is being addressed.

The individual scientific work is linked through a number of key integrating objectives to which all members of the team contribute:

Data task – interrogation of existing datasets for an improved understanding of hydrodynamic, sediment and biological processes and their interactions

Tidal flat sedimentation – a key environment in which the research results must be demonstrated to operate in a harmonious fashion

Mudflat-saltmarsh interactions – a key area of the estuary fringe for fluxes of water and sediment, and a role as high water storage

Integrated morphological modelling – a key tool for implementing the new research findings and assessing their suitability in the subtidal and intertidal reaches of estuaries. Morphological modellers are essentially one of the main 'end users' of the research.

The objectives and approach to the research are described in more detail in HR Wallingford (2002). The first research results will start to be disseminated towards the end of the first year of the project. The project web site has been created and will be updated throughout the life of the project (http://www.estproc.net/).

Acknowledgement: EstProc is funded in the UK within the joint DEFRA/EA Flood and Coastal Defence R&D Programme of Fluvial, Estuarine and Coastal Processes (Project FD1905).

3 Reference

HR Wallingford (2002). Estuary Process Research Project (EstProc): Inception Report. Report TR129 produced for DEFRA by the EstProc Consortium.

Evolution of Estuaries

DAVID PRANDLE

(Proudman Oceanographic Laboratory, Bidston Observatory, Merseyside, CH43 7RA, UK, dp@pol.ac.uk)

1. Objectives

Despite significant advances in the understanding of basic processes, observational technologies and simulation models, our ability to predict future estuarine functioning under various natural and anthropogenic scenarios is severely limited. In the era of 'total system science', end-users expect results from 'bottom-up', 'primitive equation' deterministic models of sediment transport to be explicable in terms of geological morphological theories.

Bridging all such gaps between physics-biology-chemistry-geology across the associated wide spectra of spatial and temporal scales can never be realised. However, further exploration of first-order coupling mechanisms seems timely-exploiting recent advances in both monitoring and modelling.

2. Illustration - Saline Intrusion

Saline intrusion is fundamental to the functioning of almost all estuaries. The concentration of many water quality indices are directly related to salinity (flushing times), the rate of vertical exchange is directly linked to salinity stratification and associated axial distributions are likewise often determined by the intrusion characteristics.

Prandle (1985) suggested the length of saline instructions, L can be expressed as:

$$L = \frac{A\,D^2}{k\,u_o\,\hat{u}}$$

where D is water depth, k bed stress coefficient, u_o residual current and $\hat{u}$ tidal current. Hence we might anticipate that L, and hence extent of saline intrusion, would increase for: increase in sea level, or decreases in k, Q (river flow) or $\hat{\xi}$ tidal elevation. Such results in laboratory flume tests provided the bases of the formula. However simple applications to (common place) funnel shaped estuaries suggest exactly opposite results! These applications suggest that whilst the formula may remain valid, the parameter perturbations result in axial migrations of the intrusion. Reproduction of such migrations in primitive equation models requires careful specification and 'relaxation' of both riverine and open-sea boundaries.

Assessing the likely spring-neap variation in L is likewise problematic. Tidal pumping complicates the specification of u_o and, in some cases, D. However, an initially surprising result from the simple applications was the heightened sensitivity to the bed stress coefficient k. In most (shallow) estuaries k determines the ratio $\hat{u}:\hat{\xi}$ as well as directly influencing turbulent intensity levels and hence L.

3. Challenge - satisfying stability

One of the most surprising aspects of many estuaries is their relative long-term morphological stability. Whilst 'hard-geology' is often significant, the long-term adjustments to changing climate, land-use, flora and fauna are generally less than specific perturbation analyses (as evidenced above) might suggest. An exciting challenge is to find stable feedback mechanisms linking specific processes and modulating and broadening their isolated spectral responses. These couplings might be

anticipated across the spring-neap and seasonal cycle and in relation to both extreme events and long term trends. Whilst the latter are likely to be complicated by their incorporation of biological and chemical phenomena, spring-neap modulations might involve more tractable dynamical-sedimentary linkages. In particular, we recall the sensitivity of saline intrusion to the bed stress coefficient, k, the value of which depends on surficial mud content. Then recognising the pronounced 15-day cycle of suspended concentration of fine sediments in many estuaries we might anticipate some self-stabilising relationship between k and û modulating the spring-neap variation in L. Derivation of such stability hypotheses and assessment of these against observational data appears a useful step-forward in bridging the gap between bottom-up and top-down models. Effective collaboration in collection and dissemination of the necessary wider-range of requisite observational data is an obviously corollary.

Physical controls on the dynamics of inlet sandbar systems

EDUARDO SIEGLE

(Institute of Marine Studies, University of Plymouth – Plymouth, PL4 8AA, United Kingdom, esiegle@plymouth.ac.uk) *Sponsored by CNPq – Brazil.*

DAVID A. HUNTLEY

(Institute of Marine Studies, University of Plymouth – Plymouth, PL4 8AA, United Kingdom, dhuntley@plymouth.ac.uk)

MARK A. DAVIDSON

(Institute of Marine Studies, University of Plymouth – Plymouth, PL4 8AA, United Kingdom, mdavidson@plymouth.ac.uk)

1. Introduction

Sedimentary processes at inlet systems are closely related to the combined action of a variety of driving forces that create unique hydrodynamic conditions. Understanding these physical processes and their interaction with sediments and sediment bodies provides important knowledge on the evolution of such coastal regions. In this study, the controlling processes of the complex sandbar dynamics at the Teign inlet (Teignmouth, UK) are identified and their relative importance is assessed through the combined application of a numerical model, field data and Argus video images.

The dynamic estuarine inlet of the river Teign is located in the southern portion of Teignmouth's beach (Figure1). This coastal region presents a three-dimensional nature, with a rocky headland (The Ness), an estuary mouth and nearshore sandbars all adjacent to the 2 km long beach, backed by a seawall. It has been suggested that complex interaction between waves and currents lead to a cyclic movement of sandbars systems in the mouth of the estuary (*Robinson* [1975]).

Tides are semi-diurnal with tidal range varying between 1.7 to 4.5 m. River discharge varies between less than 20 $m^3 s^{-1}$ in summer to 50-100 $m^3 s^{-1}$ in autumn and winter. The channel width varies from up to 300 m at high tide to just 80 m at low tide, funnelling the flow and generating significant differences in pressure gradients between the estuary and adjacent coastal region (*Siegle et al*. [2002]).

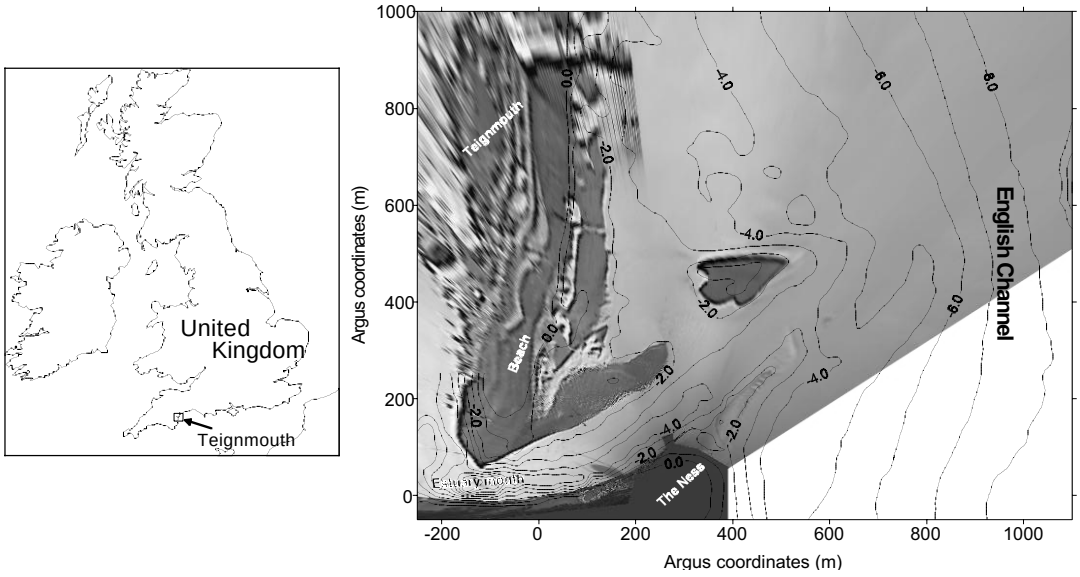

Figure 1: Study area. The nearshore bathymetry is plotted over a rectified Argus image.

2. Model setup and calibration

The numerical model applied in this study consists of the hydrodynamic (HD), nearshore spectral waves (NSW) and non-cohesive sediment transport (ST) modules of the well-known MIKE21 model (*DHI* [2001a, b, c]). Since these three modules work separately, it is necessary to run them independently and then apply each result as input for the next module. The rectangular model grid is the same for all modules and covers the whole estuary and approximately 3 km offshore and 4 km alongshore (Figure 2). The grid resolution is 10 m in x and y directions, resulting in approximately 180,000 water points.

The bathymetry used for the coastal region is the result of surveys carried out during the COAST3D project in October 1999. Bathymetry for the estuary was obtained from a 1979 digitised chart.

Boundary conditions applied to the HD module include river discharge, water level (offshore boundary) and flux (north and south boundaries). Water level and flux boundaries were obtained from a larger well-validated model (Delft3D – Continental Shelf Model – *Walstra et al.* [2001]). The wave module offshore boundary is the offshore measured wave data and water level. Results of hydrodynamics and waves simulations are used as input in the non-cohesive sediment transport module. The sediment data used as input in the sediment transport computations is specified as spatially varying, defined according to the data from sediment samples collected during the COAST3D project. MIKE21 ST uses a deterministic intra-wave sediment transport model STP to calculate the total transport rates of non-cohesive sediment. STP model accounts for the effects of waves propagating at an arbitrary angle to the current, breaking/unbroken waves, uniform/graded bed sediment, plane/ripple covered bed when calculating the local rates of total load transport (*Zyserman and Johnson* [2002]).

The model was calibrated and validated against field data obtained during the COAST3D project. The COAST3D datasets provide an excellent database for the calibration and validation of coastal area models (*Sutherland* [2001]; *Walstra et al.* [2001]). These data include accurate bathymetric surveys and a spatially dense array of instruments measuring neap/spring tides and calm/storm conditions. The model was calibrated through comparisons (measured against calculated) of water level and velocity time series at several locations at the region of interest. A more objective analysis of the quality of the model was also carried out through the determination of the Relative Mean Absolute Error (RMAE – *Sutherland* [2001]) values for the compared time series. Water levels and velocities are well predicted by the model, reproducing most of the rapid variations in the measured data. A detailed discussion of the model calibration and validation can be found in *Siegle et al.* (*in prep.*).

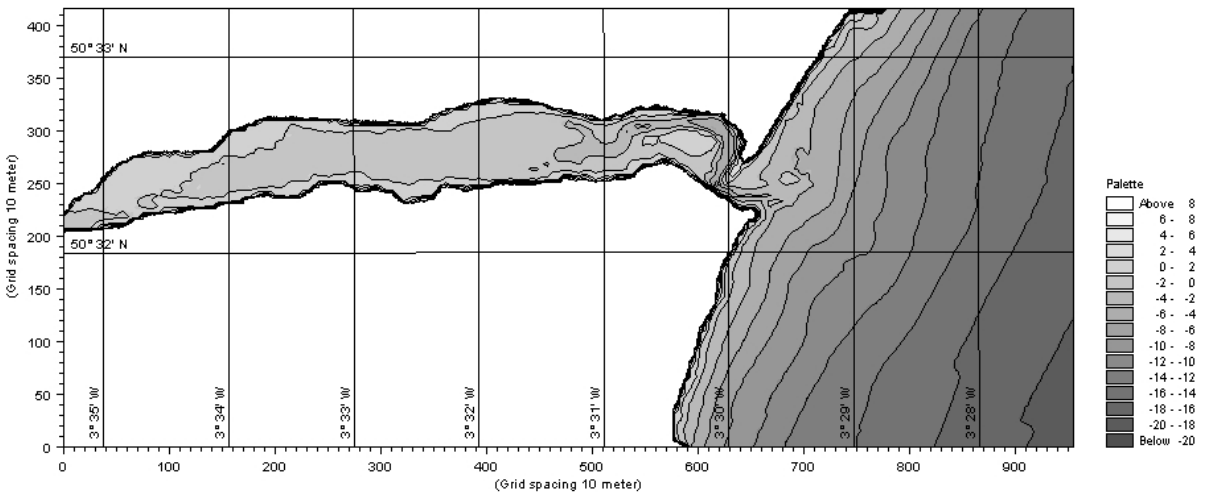

Figure 2: Model grid and bathymetry.

Using the calibrated and validated model, a series of experiments was conducted in order to quantify the relative importance of the physical processes in the sandbar dynamics. The design of the

experiments followed a sensitivity analysis on the response of sediment transport to the main processes acting at the inlet. So, experiments with different tidal range, wave conditions and river discharge were carried out to define the general transport paths and their physical controls.

3. Results and Discussion

Results of the modelling experiments show that the interaction between tidal motion and waves generate complex circulation patterns that drive the local sediment transport and sandbar dynamics. Both tidal currents and waves are shown to have large influence on sediment transport processes at this site, with tide dominated sediment transport in the inlet channel and wave dominated transport at the adjacent nearshore region. Tide only simulations show that tidal range drives sediment transport through the flow constriction in the main channel, with maximum transport during spring tide conditions associated with high flood and ebb currents (Figure 3a). Without the effect of waves, sediment transport is negligible outside the main channel and initial erosion/deposition rates show that sediment deposition takes place in the offshore end of the channel when tidal current velocity decreases. Assessment of wave effects in the simulations shows their key importance in the local sediment transport. Sediment transported as a result of wave generated currents adds sediment to the inlet system, through longshore transport from either sides of the channel (Figure 3b). Dependent on the angle of wave incidence, the onshore mean flow generated by wave radiation stresses combined with the tidal motion generates cells of sediment transport in the nearshore area, resulting in areas of sediment erosion and deposition. At low or no wave conditions sediment is transported directly offshore, while at periods at periods of intense wave action it is diverted into cell transport patterns that keep the sediment in the system.

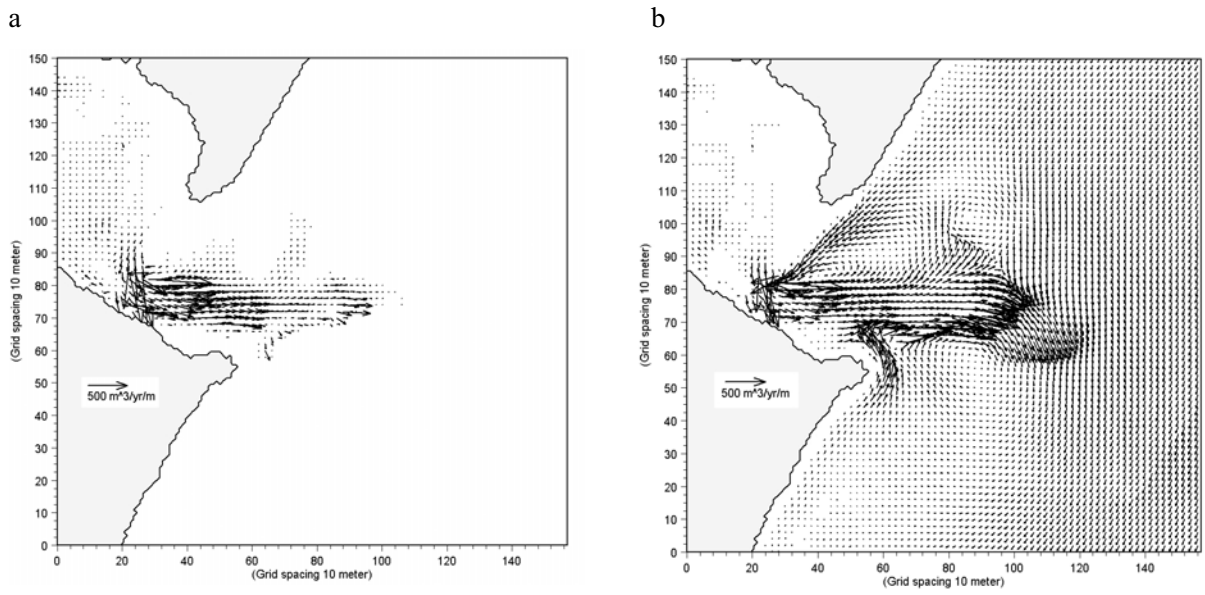

Figure 3: Calculated sediment transport rates for tide only (a) and tide and waves simulations (b) over two tidal cycles (25 hours).

The inlet channel presents flood dominance close to the estuary mouth and ebb dominance in the channel seaward to the inlet entrance. This is reflected in the sediment transport rates, which are divided into a main seaward transport and a secondary landward transport at the inlet mouth (Figure 3a, b). The flood dominance at the inlet mouth allows part of the sediment that reaches the channel to be transported into the estuary, providing sediment to the flood tidal delta. However, due to the predominant ebb dominance in the channel, the majority of sediment transported to the channel is redirected offshore and deposited on its offshore end. Transport rates and initial erosion/deposition

rates show that waves approaching the region from the predominant angle of incidence (120^{o} from true north) cause a northwards sediment transport and the deposition of sediment in the outer part and northwards of the main channel, adding sediment to the sandbar system. Through the analysis of video images and wave data over a period of two years (2000 – 2002), it is possible to verify that the most drastic changes in the sandbar system morphology occur during the winter period (December – March) coinciding with higher average wave energy periods.

Analysis of this complex sandbar system through the numerical model results and *in situ* data (video images and wave data) shows that the main physical process controlling the morphodynamics of the sandbars is the interaction between tidal currents and waves. Strong tidal currents in the inlet channel transport sediment to the estuary and offshore according to the flood/ebb dominance in the channel. Main sediment deposition is verified in the outer part of the main channel, where the action of waves redistributes sediment adding it to the sandbar system. Higher wave energy during winter period is responsible for the growth and onshore migration of the sandbars, causing drastic morphological changes.

Acknowledgements: The authors thank the partners of the EC COAST3D (MAS3-CT97-0086) project who collected the data used in this paper. Offshore boundary conditions for the modelled period was kindly provided by Dr Dirk-Jan Walstra (WL|DELFT). The authors are also thankful to the Danish Hydraulic Institute (Dr Pierre Regnier and Dr Hans J. Vested) for the opportunity to use the MIKE21 modelling system in this study through the collaboration in the EC SWAMIEE (FMRX-CT97-0111) project. The Argus video monitoring programme was established by Prof. Rob Holman (Oregon State University).

References:

Danish Hydraulic Institute, MIKE21 Hydrodynamic Module, *User Guide and Reference Manual*, 2001a.

Danish Hydraulic Institute, MIKE21 Nearshore Spectral Wind-Wave Module, *User Guide and Reference Manual*, 2001b.

Danish Hydraulic Institute, MIKE21 Sand Transport Module, *User Guide and Reference Manual*, 2001c.

Robinson, A.H.W., Cyclical changes in shoreline development at the entrance to Teignmouth Harbour, Devon, England, in *Nearshore Sediment Dynamics and Sedimentation*, edited by J. Hails and A. Carr, pp. 181-198, John Wiley, London, 1975.

Siegle, E., Huntley, D.A. and M.A. Davidson, Modelling water surface topography at a complex inlet system – Teignmouth, UK, *Journal of Coastal Research, SI36*, in press.

Sutherland, J., Synthesis of Teignmouth coastal area modelling. COAST3D Final volume of summary papers. *HR Wallingford Report TR 121*, 2001.

Walstra, D.J.R., Sutherland, J., Hall, L., Blogg, H. and M. van Ormondt, Verification and comparison of two hydrodynamic area models for an inlet system, *Proceedings of the Coastal Dynamics'01 Conference* (Lund, Sweden, ASCE), pp. 433-442, 2001.

Zyserman, J.A. and H.K. Johnson, Modelling morphological processes in the vicinity of shore-parallel breakwaters, *Coastal Engineering, 45*, 261-284, 2002.

Initial formation of rhythmic coastline features

M.van der Vegt[1], H.M. Schuttelaars and H.E. de Swart[1]

1. *Institute for Marine and Atmospheric research Utrecht(IMAU), Utrecht University, Princetonplein 5, 3584 CC Utrecht, The Netherlands.* E-mail: M.vanderVegt@phys.uu.nl

1 Introduction

Sandy coastlines show rhythmic variations with length scales ranging from several metres (beach cusps) to hundred kilometres (capes). The associated timescales are of the order of days to thousand years. Mesoscale features belonging to this class are sequences of barrier islands on a scale of 10 km and shoreline sandwaves (scale a few kilometres). Barrier islands can be found all around the world and have been studied intensively. It has been observed that the length of a barrier island is inversely related to the tidal range and that they hardly migrate, *Oost* [1995]. Longshore sandwaves, on the other hand, have a phase speed in the order of 100 m/year. They have been identified along the Dutch coast (*Verhagen* [1989]), but are also found along other sandy coasts in the world.

There are different potential forcing mechanisms generating coastline forms, which may e.g. involve wave action, tidal currents and net currents. Recently the presence of capes has been explained as the result of an inherent instability mechanism of the wave driven longshore sediment transport and coastline (*Ashton et al.* [2001]). In this paper it is investigated whether rhythmic coastline features can be the result of a positive feedback mechanism between tidal motion and coastline. This requires the formulation of a model in which coastline undulations develop as free instabilities of a basic state representing alongshore-uniform conditions. The procedure and results are discussed below.

2 Model description

The model distinguishes between two regions: the nearshore zone and the inner shelf, separated by a transition line. Sediment transport only occurs in the nearshore zone, thus in fact it is assumed that processes in the nearshore zone have much shorter timescales than processes on the inner shelf. It is assumed that the width of the nearshore zone is constant. The width-integrated sediment transport in nearshore zone is controlled by the shore-parallel velocity at the transition line and is linear in the velocity by a factor β. For wave-driven currents in the order of 1 ms^{-1} the width integrated volumetric sediment flux in the nearshore region is about 10^{-2} $\mathrm{m}^3\mathrm{s}^{-1}$ (*Komar* [1988]). This means that $\beta = 10^{-2}$ m^2. The velocity at the transition line is determined by the hydrodynamics on the inner shelf and is described by the 2DH shallow water equations. The water motion is forced by a prescribed alongshore pressure gradient which can have a constant and a tidal component. Changes of the shoreline (and hence of the transition line) position are due to alongshore variations of the width-integrated sediment transport.

The model allows for a basic state, describing longshore flow along a straight coastline. The magnitude and cross-shore structure is determined by a balance between inertia, longshore pressure gradient and depth dependent friction. As far as this aspect is concerned the model shows much resemblance with the model described by *Calvete et al.* [2001]. The

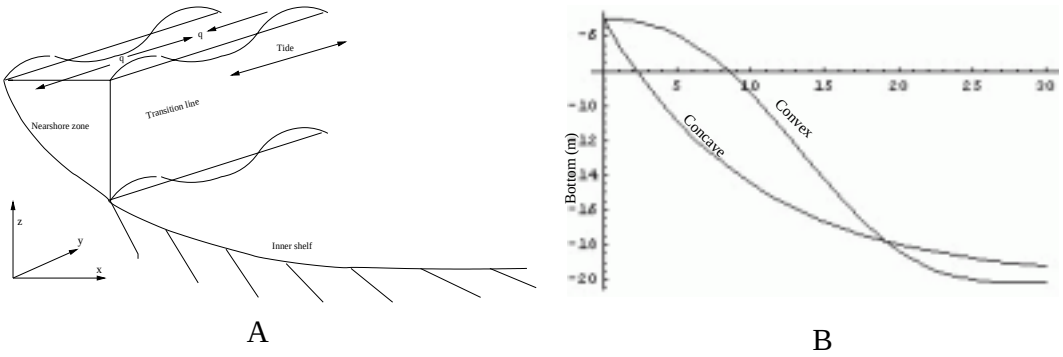

Figure 1: A) Geometry of the model. q is the volumetric sediment flux in the nearshore zone. For more information see text. B) Typical convex and concave bottom profile.

main difference is that they investigate stability with respect to bottom perturbations, while here stability with respect to coastline perturbations is studied. Thus, the straight coastline is disturbed by small rhythmic perturbations with wavenumber $k = 2\pi/\lambda$, with λ the wavelength of the perturbation. Because the normal velocity has to be zero at the coast, this coastline perturbation induces perturbed velocities and a perturbed sediment flux. Alongshore variations of this perturbed volumetric sediment flux causes changes of the coastline. The model yields growth rate ω and migration speed c as a function of wavenumber k. If $\omega > 0$ the initial perturbation is amplified and the perturbation grows. The mode with the largest ω is called the preferred mode.

3 Results

Experiments indicated that the growth rate curves strongly depend on whether the bottom profile is concave or convex. Typical examples of such profiles are shown in figure 1B. Figure 2 shows the growth rate versus wavenumber for the two profiles. Parameter values are representive for the Dutch coastal system. Here the basic state has no residual component and consists of only 1 (semidiurnal) tidal component. The wavenumbers are scaled with L^{-1}, where L=10 km is a typical length of the inner shelf. A growth rate of 1 corresponds to an e-folding timescale of 15 years. The curves of figure 2 indicate that for both profiles the growth rates can be positive, hence positive feedback. The preferred mode for the concave profile is at $kL = 20.6$, which implies that $\lambda = 3$ km. For the convex profile the preferred mode is at $kL = 3.6$, so that $\lambda = 17.5$ km. Note that the preferred mode for the concave profile is in the range of shoreline sandwaves, while for the convex profile it is in the range the distance between successive barrier islands. The phase speed is 23 m/year for the concave profile and 35 m/year for the convex profile. This phase speed is not forced by a pressure gradient, but induced by the Coriolis force. In the case of no Coriolis force, there is no movement of the perturbation, only growth. The residual flow for these two cases is shown in figure 3.

It is also possible to prescribe a residual pressure gradient which forces a residual flow in the basic state. A residual flow of $5 \cdot 10^{-2}$ ms^{-1} induces a phase speed of 175 m/year for the convex profile and 168 m/year for the concave profile. These phase speeds lie in

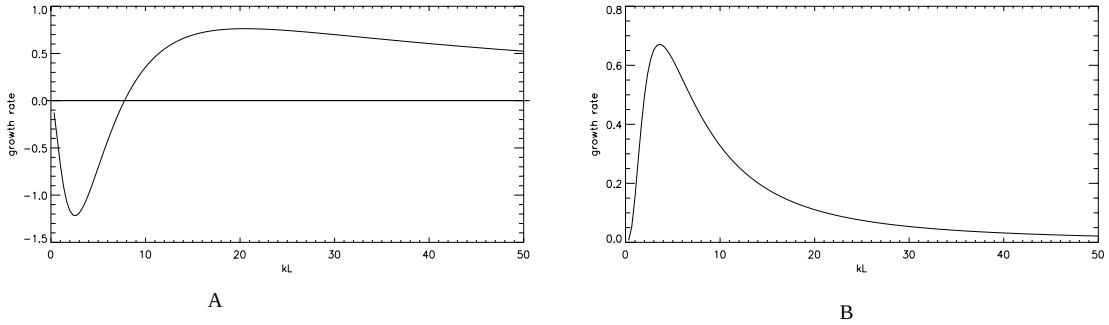

Figure 2: Growth rate for different wavenumbers. A: Concave bottom profile. B: Convex bottom profile.

the range of observed phase speeds for sandwaves.

The mechanism behind these model results is that interactions of basic tidal flow with the coastline leads to excitation of higher harmonics of the tide, but also to residual flow (tidal rectification). The spatial structure of the residual circulation cells is such that the maximum convergence of this flow is slightly to the right of a coastline feature (viewing in the seaward direction), see figure 3. This mechanism, which can be fully described in terms of vorticity dynamics, explains both the growth and migration of the coastline perturbations. A detailed analysis of the model results has revealed that the occurrence of different preferred modes for the different bottom profiles can be attributed to different cross-shore structures of the basic state tidal flow (different background vorticity distributions).

4 Discussion and conclusions

The present model describes the formation of coastline undulations, which resemble shoreline sandwaves and barrier coasts, as a free instability of a straight coastline under forcing by a tidal and residual flow. In case of the Dutch coast the bathymetry of the inner shelf has a concave bottom profile, thereby resulting in preferred wavelengths which are in the range shoreline sandwaves. With a small residual flow in the basic state the model seems to be capable in predicting the phase speeds of longshore sandwaves. To have preferred lengthscales in this model which are in the range of barrier island sequences, the bottom profile has to be convex.

Other experiments show that the characteristics of the preferred mode strongly depend on the steepness of the underlying bottom profile. A steeper profile results in shorter preferred wavelengths. This is due to the strong dependency of the basic flow on the depth by the depth dependent friction. The preferred wavenumber also depends on the velocity of the tidal flow: a stronger velocity results in longer wavelengths. Analysis of field data suggests that the length scale of barrier island sequences is inversely related to the tidal height. In this model a stronger tidal height also means stronger tidal velocities. So this model predicts that with stronger tidal height the lengthscale of barrier islands will increase.

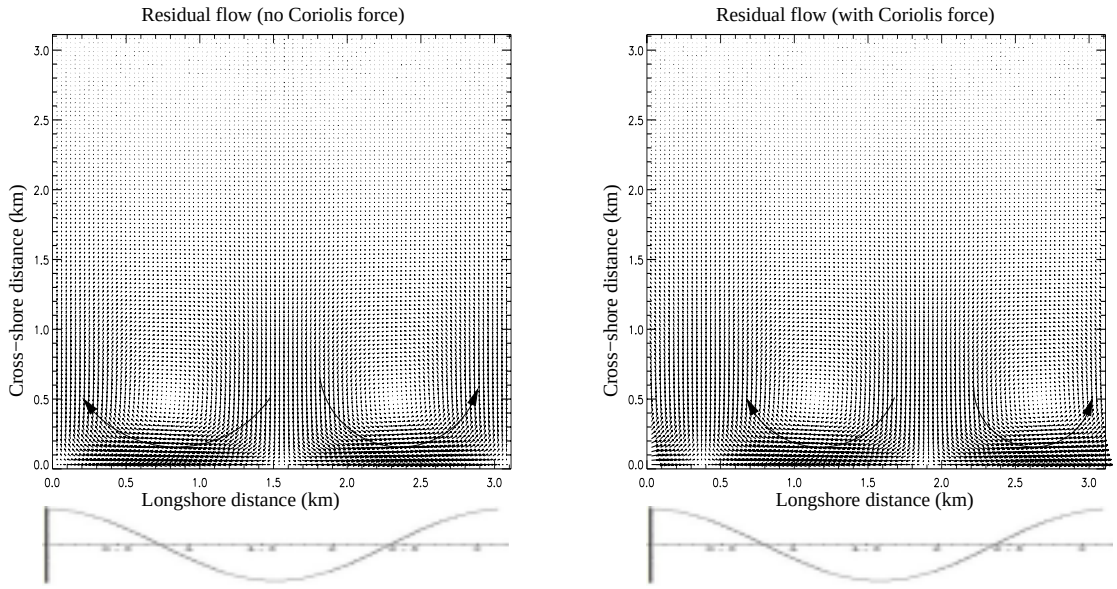

Figure 3: Left: residual flow pattern in the case of no Coriolis force. Two residual circulation cells (in the direction of the arrows) are noticeable which cause amplification of the coastline, which is shown beneath the subplot. Right: residual flow pattern in the case of realistic Coriolis force. Note that Coriolis force cause migration of the original perturbation. In both subplots the maximum velocity amplitude is about 10^{-2} ms^{-1}.

References:

Ashton, A., Murray, A.B. and O. Arnault, Formation of coastline features by large-scale instabilities induced by high-angle waves, *Nature*, *414*, 296-300, 2001.

Calvete, D., Walgreen, M., De Swart, H.E. and A. Falqués, A model for sand ridges on the shelf: effect of tidal and steady currents, *Journal of Geophysical Research C106*, 9311-9338, 2001.

Komar, P.D., *Beach processes and sedimentation*, Prentice Hall, Upper Saddle River, New Jersey, 1998.

Oost, A.P., Dynamics and sedimentary development of the Dutch Wadden Sea, with a special emphasis on the Frisian Inlet, PhD-thesis, *Geologica Ultraiectina*, *126*, 1995.

Verhagen, H.J., Sand Waves along the Dutch coast, *Coastal Engineering*, *13*, 129-147, 1989.

Migrating Sand Waves

Giovanni Besio, Paolo Blondeaux, Maurizio Brocchini & Giovanna Vittori, (*DIAm, Via Montallegro 1, Università di Genova, Genova 16145, Italy* giospud@diam.unige.it)

1 Abstract

Sand waves are large depositional coastal bedforms which appear typically in tide-dominated shallow seas, among which the North Sea is one of the most studied. They are characterized by wavelengths ranging from one hundred metres up to one kilometre while the typical heights are of the order of one to five metres. They are induced by tidal currents and one of the most striking characteristics of sand waves is that they are not static bed forms. Indeed they migrate, their crests almost orthogonal to the direction of the velocity oscillations caused by the tide, with migration speeds of the order of some tens of metres per year (*Terwindt* [1971]; *Bokuniewicz et al.* [1977]; *Fenster et al.* [1990]). Sand waves can be compared to other seabed features such as dunes or, at smaller scales, ripples. However, they differ from dunes induced by steady currents since the basic flow in which sand waves evolve has an oscillatory nature. Sand waves also differ from sea ripples, as the size of the former is such that they affect the whole water depth while the latter are only felt in the bottom boundary layer.

Sand waves growth and migration affect several human activities among which navigation and the oil and fishing industries. Finally, it has been recognited that nearshore, migrating sand waves might even affect shoreline evolution (*Verhagen* [1989]).

Sand waves appearance was first studied by means of depth-averaged approaches in which the effects of circulation motions taking place in the vertical plane are properly parametrized (*Hulscher et al.* [1993]; *De Vriend* [1990]; *De Swart & Hulscher* [1995]).

The first contribution aimed at a quantitative investigation of sand wave formation relying on a fully three dimensional approach is due to *Hulscher* [1996a], who formulated a model based on the three-dimensional shallow water equations and handled the turbulent stresses by means of the Boussinesq hypothesis. The eddy viscosity is assumed to be constant in time and over the water depth. Finally, the bottom time development is determined using the sediment continuity equation and a simple sediment transport predictor. The analysis predicts the temporal development of bottom perturbations of small amplitude (strictly infinitesimal) and determines the range of parameters for which the bottom perturbations amplify or decay.

The hydrodynamics of the problem is characterized by the presence of the parameter r, which is the ratio between the amplitude of the horizontal tidal excursion and the wavelength of the sand waves and turns out to be large for field conditions [i.e. $O(10^2)$]. More recently, *Gerkema* [2000] pointed out that under field conditions r is large, while *Hulscher's* [1996] approach is strictly valid only for moderate values of r. Hence, *Gerkema* [2000] solved the problem by using an asymptotic approach which is based on the assumption $r >> 1$ and is similar to that developed for the Orr-Sommerfeld equation in the case of large Reynolds numbers. However Gerkema's analysis assumes that the stress parameter s, relating the velocity and its derivative at the bed, is much larger than one.

As discussed in *Hulscher* [1996a,b], in the field s is of order one. Hence, the results obtained by *Gerkema* [2000] are not fully appropriate to describe field cases. An approach which holds for arbitrary values of both r and s has been developed by *Besio, Blondeaux and Frisina* [2002] (submitted for pubblication, BBF hereinafter) who consider the sea bed time development forced by an oscillatory current assumed generated only by the $M2$ tide constituent, the period of which is 12 hours. Therefore in BBF the tidal current is symmetric and unable to induce sand wave migration.

The model proposed by BBF forms the basis for the present analysis. The inclusion in the description of the phenomenon of a steady current ($Z0$) and a tide constituent characterized by a period of 6 hours ($M4$) is the main novelty of the present work which allows for the prediction of the migration of sand waves. Indeed both the steady current and the $M4$ tide constituent break the simmetry of the problem and induce sand wave migration. A first study of sand waves migration due to the presence of the steady current ($Z0$) only has been performed by *Németh, Hulscher & de Vriend* and has been submitted for publication in the early 2002. However, *Németh et al.'s* [2002] model predicts always a down-current migration of the sand waves while field cases exist of up-current migrating sand waves (down-current/up-current migrating sand waves mean bed forms moving in the direction of the steady current or in the opposite direction respectively).

The present model is based on a very simple turbulence closure scheme (constant eddy viscosity A combined with a partial slip parameter s) similar to that used by previous works on the subject. In order to model the flow induced by the propagation of the tidal wave, a forcing pressure gradient is considered which is the sum of two oscillatory components of angular frequency σ and 2σ ($M2$ and $M4$ constituents respectively) and a steady part which gives rise to the steady current $Z0$.

$$\frac{\partial p}{\partial x} = -\frac{\partial P_0}{\partial x} - \frac{1}{2}\frac{\partial P_1}{\partial x}\left(e^{i\sigma t} + c.c.\right) - \frac{1}{2}\frac{\partial P_2}{\partial x}\left(e^{2i\sigma t} + c.c.\right). \tag{1}$$

The model is based on the linear stability analysis of the flat configuration of the sea bottom subject to the tidal currents. Considering perturbations of small amplitude, we perform a normal-mode analysis. The dimensionless problem is characterized by the following dimensionless parameters

$$\delta = kH, \quad \hat{r} = \hat{U}_m/(\sigma H), \quad \mu = H^2\sigma/A, \quad s = \tilde{s}H \tag{2}$$

where δ is the wavenumber of the bottom perturbations, $\hat{r}$ is the ratio between the horizontal tide excursion and the water depth, μ is a reciprocal Stokes number and s is the already mentioned slip parameter (H=water depth, $\hat{U}_m$= amplitude of depth-averaged velocity oscillations due to the $M2$ tide constituent, A=costant eddy viscosity, σ=angular frequency of the tide, k=wavenumber of the bottom perturbations). Finally, the time development of the bottom perturbation is described by

$$\eta = \frac{\Pi_0}{2} e^{\Gamma_r \frac{\alpha \hat{U}_m^3}{H^2} t} e^{ik\left(x + \Gamma_i \frac{\alpha \hat{U}_m^3}{kH^2} t\right)} + c.c. \tag{3}$$

where Π_0 is the initial amplitude of the bottom waviness, α is a constant appearing in the sediment transport predictor, and the complex quantity $\Gamma = (\Gamma_r, \Gamma_i)$ is the growth rate of the bottom perturbations which is predicted by the analysis.

The steady current $Z0$ induces a distorsion of the recirculating cells originated by the interaction of the $M2$ tidal flow with the wavy bottom. Hence, the cells are not symmetric anymore with respect to crests and troughs of the bottom perturbations and this loss of symmetry leads to a net displacement of the sediment in the steady current direction, giving rise to a bedforms migration (see figure 1(b)). The model allows for the computation of the dimensional migration speed v which is related to the imaginary part of the amplification rate of the bottom perturbations as

$$v = \Gamma_i \frac{\alpha \hat{U}_m^3}{kH^2}. \tag{4}$$

These conclusions are also present in *Németh et al.* [2002], even though present results quantitatively differ from those of *Németh et al.* [2002] which are strictly valid for moderate values of the parameter r. We also show that, notwithstanding the basic flow obtained using $M2$ and $M4$ features a vanishing time average after a tidal cycle, it leads to a net migration of the bedforms because of the nonlinear relationship between the velocity field and the sediment transport rate Q

$$Q = \alpha |u|^3 \left(\frac{u}{|u|} - \gamma \frac{\partial \eta}{\partial x} \right). \tag{5}$$

A crucial model variable is the phase lag ϕ between the two oscillatory constituents. In fact the results concerning the migration speed are strongly conditioned by the value of ϕ which affects the sign of Γ_i and, hence, of the migration speed (see figure 2(b)). The sign identifies the direction of sand waves migration. In particular when ϕ falls between 30° and 180° an up-stream migration of the sand waves can be induced. This finding suggests that, if we consider a basic flow given by the sum of tidal constituents $M2$, $M4$ and $Z0$, when the effects of the oscillatory term $M4$ prevail on those induced by the steady current, an up-stream migration of the bedforms can be forced. Field data collected in the North Sea (Snamprogetti, Zeepipe Project) show, in fact, well shaped sand waves migrating upstream with a speed of the order of 3 metres per year.

It is also worth pointing out that the introduction of the steady current $Z0$ or of the tidal constituent $M4$ does not affect significatively the formation process of sand waves, and in particular the value of the amplification rate Γ_r is almost unaffected (compare figure 1(a) and 2(a)).

References:

Besio, G., Blondeaux P., Frisina, P. A note on tidally generated sand waves. *Submitted for publication to JFM*, 2002.

Bokuniewicz, H.J, Gordon, R.B. & Kastens, K.A., Form and migration of sand waves in a large estuary, Long Island Sound, *Mar. Geol.,* **24,** 185-199, 1977.

de Swart, H.E. & Hulscher, S.J.M.H., Dynamics of large-scale bed forms in coastal seas, in *Nonlinear Dynamics and Pattern Formation in the Natural Environment* (ed. A. Doelman and A. van Harten), pp. 315–331, Longman, 1995

de Vriend, H.J., Morphological processes in shallow tidal seas. In *Residual Currents and Long-term Transport* (ed. R. T. Cheng), pp. 276–301, Springer, 1990.

Fenster, M.S., Fitzgerald, D.M., Bohlen, W.F., Lewis, R.S. & Baldwin, C.T., Stability of giant sand waves in eastern Long Island Sound, U.S.A., *Mar. Geol.,* **91,** 207-225, 1990.

Gerkema, T., A linear stability analysis of tidally generated sand waves. *J. Fluid Mech.* **417**, 303–322, 2000.

Hulscher, S.J.M.H., Swart, H.E. de & Vriend, H.J. de, Generation of offshore tidal sand banks and sand waves. *Cont. Shelf Res.* **13**, 1183–1204, 1993.

Hulscher, S.J.M.H., Tidal-induced large-scale regular bed form patterns in a three-dimensional shallow water model. *J. Geophys. Res.* **101** (**C9**), 20727–20744, 1996a.

Hulscher, S.J.M.H., On validation of a sand waves and sand banks model. *Proc. 25th Int. Conf. Coastal Engng.* ASCE, September 2-6, Orlando, Vol. 3, 3574–3587, 1996b.

Hulscher, S.J.M.H. & van der Brink, G.M., Comparison between predicted and observed sand waves and sand banks in the North Sea. *J. Geophys. Res.* **106** (**C5**), 9327–9338, 2001.

Németh, A.A., Hulscher, S.J.M.H. & Vriend, H.J. de, Modelling sand wave migration in shallow shelf seas. *Submitted for publication*, 2002.

Terwindt, J.H.J., Sand waves in the Southern Bight of the North Sea. *Mar. Geol.,* **10,** 51-67, 1971.

Verhagen, H.J., Sand waves along the Dutch Coast, *Coast. Engng.,* **13,** 129-147, 1989.

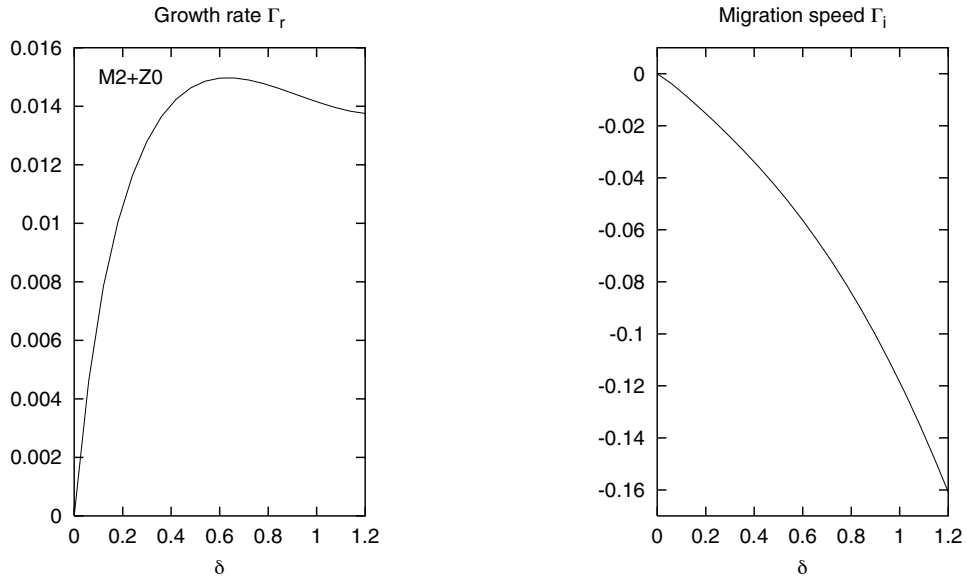

(a) (b)

Figure 1: Dimensionless amplification rate Γ_r (a) and dimensionless migration speed Γ_i (b) plotted versus the wavenumber δ in the case of tidal constituents $M2$ and $Z0$ only; $s = 0.84$, $\mu = 2.25$, $\gamma = 0.23$, $\hat{r} = 145$, $U_s/U_1 = 0.0559$.

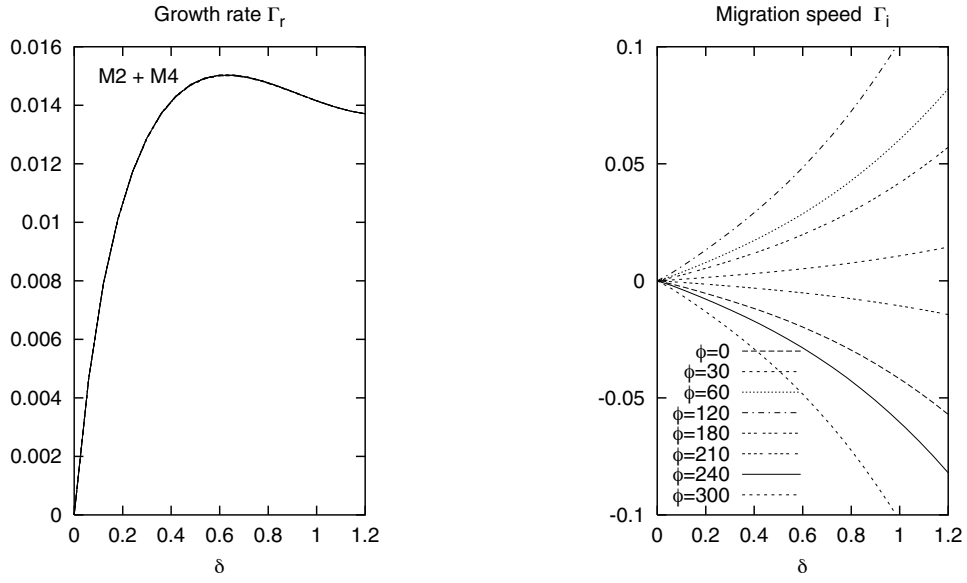

(a) (b)

Figure 2: Dimensionless amplification rate Γ_r (a) and dimensionless migration speed Γ_i (b) plotted versus the wavenumber δ in the case of tidal constituents $M2$ and $M4$ only; $s = 0.84$, $\mu = 2.25$, $\gamma = 0.23$, $\hat{r} = 145$, $U_2/U_1 = 0.0965$.

Sandwave generation: analytical and numerical approaches

Déborah Idier, (*Institut de Mécanique des Fluides de Toulouse, Allée Pr. Camille Soula, F-31400 Toulouse, France*, idier@shom.fr)

Attila A. Németh, (*University of Twente, Department of Civil Engineering, water engineering and management, P.O.BOX 217, NL-7500 AE Enschede, the Netherlands*,A.A.Nemeth@ctw.utwente.nl)

Dominique Astruc, (*Institut de Mécanique des Fluides de Toulouse, Allée Pr. Camille Soula, F-31400 Toulouse, France*, astruc@imft.fr)

Suzanne J.M.H. Hulscher, (*University of Twente, Department of Civil Engineering, water engineering and management, P.O.BOX 217, NL-7500 AE Enschede, the Netherlands*, S.J.M.H.Hulscher@ctw.utwente.nl)

Ruud M.J. Van Damme, (*University of Twente, Faculty of Mathematical Sciences, P.O.BOX 217, NL-7500 AE Enschede, the Netherlands*, vandamme@math.utwente.nl)

1 Introduction

Sandwaves are continental shelf rhythmic bedforms almost perpendicular to the tidal current direction whose wavelengths are several times larger than the water depth. Their migration rate can be up to 10-100 m/year. The origin of these bedforms may be related to free instabilities resulting from the interaction of the flow and the sandy seabed.

Huthnance [1982] was the first to look at a system consisting of depth-averaged tidal flow and an erodible seabed. Unstable modes comparable to tidal sandbanks were found, whereas smaller modes corresponding to sandwaves were not initiated. This work was extended by Hulscher [1996] using a model allowing for vertical circulations and found formation of sandwaves based on horizontally averaged symmetrical tidal motion (see also Gerkema [2000] and Komarova & Hulscher [2000]). The work showed that net convergence of sand can occur at the top of the sandwaves over an entire tidal cycle. Németh et al. [2002] extended the previous work by including a non-symmetric basic flow inducing sand wave migration.

This is far from the final objective, which is to understand and describe the entire process of sandwave evolution. Even if it has not been extensively used to study the behaviour of these bedforms, numerical methods could form a tool to overcome the linear stability analysis limitations and enable the study of the non-linear regime.

In this study, the linear stability properties of sandwaves are investigated from two viewpoints : analytical and numerical. We start with simulating a non-tidal situation, in which a constant current dominates in the x-direction thanks to a pressure gradient. The test case is based on the generation of sandwaves uniform in the transverse direction y. Then the system is 2DV. Herein we focus on simulating the vertical residual circulation cells enabling sandwaves to evolve.

2 Linear stability analysis

The analysis of Németh et al. [2000] gave insight in the initial evolution and migration under symmetrical tidal motion and a steady current inducing an asymmetry in the basic state. The order of magnitude for the migration rates and wavelengths found are 5-10 m/y and 600 m respectively for a tidal environment containing a small residual current. These values are in agreement with values reported in the literature. Here we apply a steady current (M0) induced by a pressure gradient on top of the seabed using the stability analysis. Its vertical structure ($u_r(z)$) is deduced from the basic state used in the stability analysis :

$$u_r(z) = P\left(\frac{1}{2}z^2 - \frac{A_v}{S}H - \frac{1}{2}\right) \tag{1}$$

The horizontal flow components at the bottom are described with the help of a partial slip condition, with S the resistance parameter :

$$\nu_z \frac{\partial u}{\partial z} = Su \tag{2}$$

and the sediment conservation equation reads :

$$\frac{\partial h}{\partial t} = -\alpha \frac{\partial}{\partial x}\left(|\tau_b|^b \left(\tau_b^{0.5} - \lambda' \frac{\partial h}{\partial x}\right)\right) \tag{3}$$

with λ' the bed slope term set at 8, τ_b the bed shear stress, t the time and h the seabed elevation above the reference level (located at $z_b = -H$). Positive growth rates appear for a range of wave numbers k (for the used Fourier transformation see Németh et al. [2002]). The wavelength having the largest growth rate is the mode we expect to find in nature. The dimensional wavelength follows from $L_{sandwave} = \frac{20H\pi}{k}$. The dimensional form of the migration rate can be found as follows $V_{sandwave} = \frac{10\omega_i H}{2\pi T_m}$ with ω_i the angular frequency of the bed forms.

3 Numerical model

The numerical model is based on TELEMAC software modules. It is composed of a 3D hydrodynamic submodel solving the shallow-water approximation of the flow equations coupled with a bottom evolution submodel. Both submodels rely on finite element formulation, which proved to be convenient to model sandbank stability properties (*Idier and Astruc* [2001]). The horizontal turbulence is modeled by a constant turbulent viscosity ν_H, whereas the vertical one is based on a mixing length model to determine the vertical turbulence viscosity ν_z : $\nu_z = l_m^2 \left|\frac{\partial u}{\partial z}\right|$ with $l_m = \kappa(z - z_b)$ for $z - z_b < 0.2d$, and $l_m = 0.2\kappa d$ for $z - z_b > 0.2d$, with z_b the bed level, d the water depth and κ the Karman constant. The seabed boundary condition follows the equation :

$$\nu_z \frac{\partial u}{\partial z} = \frac{u\sqrt{u^2 + v^2}}{C^2} \tag{4}$$

with $C = \frac{1}{\kappa}\ln\left(\frac{\Delta Z}{D_G}\right) + 4.9$ where ΔZ is equal to one tenth of the first bottom mesh (0.03 m in this paper) and D_G is the grainsize. To finish, the sediment conservation equation

reads :

$$\frac{\partial h}{\partial t} = -\alpha \frac{\partial}{\partial x}\left(|\tau_b|^{b+0.5} \left(1 - \lambda \frac{\partial h}{\partial x}\right)\right) \tag{5}$$

with $\lambda = 1/\tan(\phi)$ where ϕ is the repose angle of sediment (generally comprised between 30 and 40 ^{o}). The initial bedform amplitude h is equal to 0.3 m (i.e. 1% of the undisturbed water depth H). The domain length is equal to 8 wavelengths, and the Fourier transformation is computed over the 3 wavelengths at the middle of the domain. The physical duration of the bottom evolution simulations is 2 hours.

4 Test case

Parameters:

The test case is based on a flow forced by a free surface gradient such that the depth integrated velocity is equal to 1 m.s^{-1} with a water depth of 30 m. The model parameters are summarized in the table 1. The coefficient α is computed using the relation $\alpha = 8/[(s-1)g]$ with $s = \rho_{sediment}/\rho_{water}$, (*Komarova and Hulscher* [2000]). The corresponding morphological time scale T_m is about 4 years.

Parameter	Analytical model	Numerical model
Vertical viscosity	$\nu_z = 10^{-1}$ m^{2}s^{-1}	Mixing length model
Horizontal viscosity	$\nu_H = 10^{-1}$ m^{2}s^{-1}	$\nu_H = 10^{-4}$ m^{2}s^{-1}
α	0.49	0.49
b	1	1
Slope effect	$\lambda' = 8$	$\lambda = 1.3$
Resistance parameter	$S = 0.11$ m^2.s^{-2}	$D_G = 300$ μm

Table 1: Test case parameters.

Results:

The three main differences between the two models are : the turbulence closure model, the seabed boundary condition, and the bottom slope effect. Further more, the basic state is not uniform in the numerical model (there are free surface and velocity slopes) whereas it is uniform in the stability analysis. The theoretical correspondance between the parameters of the models are : $C = U_0\sqrt{2/S}$ and $\lambda' = \lambda/\tau_b$ with U_0 the depth-integrated velocity.

From a qualitative point of view, the two approaches show equivalent results (Fig.1). However there are numerical differences. Even if the growth rates are quite different, the fastest growing modes (FGM) are the same for the numerical model and the analytical one (300 m, i.e. k=6). However this value can only be achieved by increasing the value for the resistance parameter in the stability analysis with respect to the mixing length model, due to the difference in viscosity parameterization : the resistance parameter takes a value of $S = 0.11$ m^2.s^{-2} with a viscosity equal to 0.1 m^{2}s^{-1} being a depth averaged value of the viscosity profile used in the numerical model. Concerning the migration of the FGM, the analytical (4500 m) is much larger than the numerical (100 m).

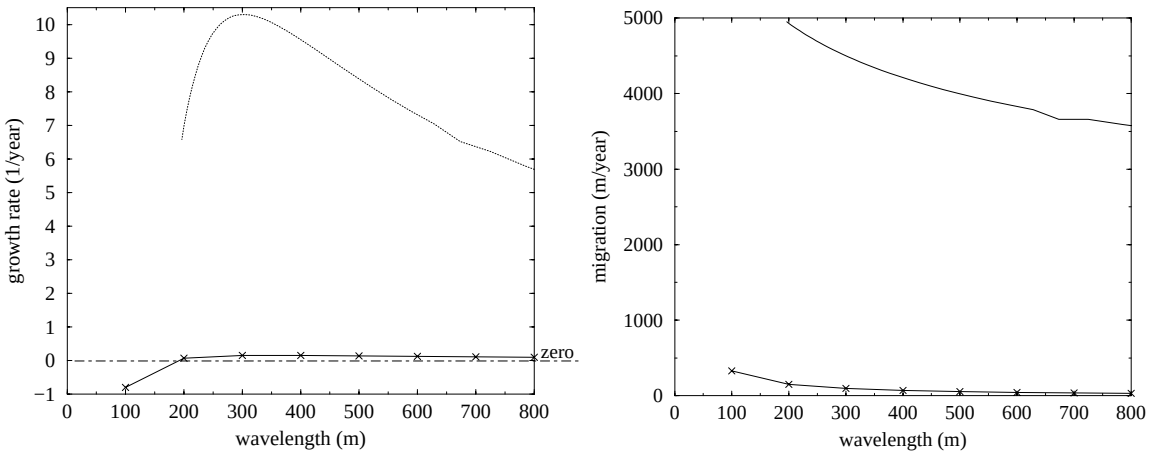

Figure 1: Growth rate (1/year) (left) and migration (m/year) (right) versus dimensional wavelength (m). Full-line: numerical results. Dotted line: analytical results.

The numerical differences in the values indicate that the viscosity formulation plays an important role in resolving the bottom shear stress, driving the sediment transport.

Acknowledgments: This research is supported by the Technology Foundation STW, the applied science division of NWO, the technology programme of the Ministry of Economic Affairs. This work is also sponsored by SHOM and CNRS and is performed in the framework of HUMOR.

References:

Gerkema, T., A linear stability analysis of tidally generated sand waves, *J. Fluid Mech. Vol. 417,* 303-322, 2000.

Hulscher, S.J.M.H., Tidal-induced large-scale regular bed form patterns in a three-dimensional shallow-water model, *J. Geophys. Res. Vol. 101, C9,* 20,727-20,744, 1996.

Huthnance, J.M., On one mechanism forming linear sand banks, *Estuarine and shelf science Vol. 14,* 79-99, 1982.

Idier, D. and Astruc D., Numerical modelling of large scale rhythmic bedforms in shallow water, *River, Coastal and Estuarine Morphodynamics*, IAHR, Obihiro, Japan, 565-574, 2001.

Komarova, N. and Hulscher S.J.M.H., Linear instability mechanisms for sand wave formation, *J. Fluid Mech. Vol. 413,* 219-246, 2000.

Németh, A.A., Hulscher, S.J.M.H. and Vriend, H.J. de, Sand wave migration in shallow shelf seas, Accepted at *Continental Shelf Research*, 2002.

Tidal and seasonal dependence of intertidal mudflat properties and currents in a partially mixed estuary

REG UNCLES & PML ECOH

(Plymouth Marine Laboratory, Prospect Place, The Hoe, Plymouth PL1 3DH, UK, rju@pml.ac.uk)

ROY LEWIS

(Brixham Environmental Laboratory, AstraZeneca UK Limited, Freshwater Quarry, Brixham, Devon, TQ5 8BA, UK, roy.lewis@brixham.astrazeneca.com)

1. Introduction

The Tamar Estuary is a strongly tidal, partially mixed estuary in which tidal currents play an important role in eroding and transporting suspended sediment as well as in shaping intertidal mudflats. Interplay between mudflat morphology, currents and other properties is complex, however, and it appears that the density of the surface mud, together with its chlorophyll concentrations (e.g. diatom mats) and other biological factors (e.g. bivalve numbers and species) can be important, although difficult to quantify. To investigate some of these processes, several tidal-cycle surveys were undertaken over a 750 m-wide cross-section of the central Tamar. The main channel at this section is approximately 7 m deep at HW (high water) springs and approximately 250 m wide at LW (low water) springs. The 500 m-wide intertidal areas are themselves flanked by salt marsh on their landward sides. The surveys were carried out at spring tides during June 1999 and January, April and July of 2000. Water column profiling of velocity, temperature, salinity, suspended particulate matter (SPM) concentrations, aggregate sizes and dissolved oxygen was carried out in the main channel. Mudflat properties of grain-size distributions and bulk wet and dry densities, loss on ignition, chlorophyll and carbohydrate (glucose equivalent) concentrations and critical erosion velocities were measured at sites across the intertidal areas. ADCP transect measurements of velocity were also obtained at approximately half-hourly time intervals over the section.

2. Hydrodynamics

The effects of channel shape on cross-estuary (i.e. transverse or lateral) spatial variations in the along-channel (longitudinal or axial) velocity are known to be significant in partially mixed estuaries (see *Friedrichs and Hamrick* [1996]). An example of strong lateral variations that occurred over the Tamar Estuary section close to HW on 20 January 2000 illustrates that currents on the flanking shoals began to ebb before those in the main channel (Figure 1). These data were obtained using an ADCP deployed with typical horizontal and vertical resolutions of 10 and 0.1 m, respectively. At HW the current was already ebbing slowly over the intertidal shoals, with faster currents flowing near the banks, Figure 1(a), whereas much of the main channel water was still slowly flooding. The ebb currents had increased in speed by HW+0.5h, Figure 1(b), although a central core of flooding water remained in the main channel, where a zone of intense lateral shear developed between it and the ebbing water to the west (left). Relatively fast ebb currents occurred in the upper 2 m and over the shoals by HW+1h, Figure 1(c), forming two 'jets' located over, and either side of, a deep core of slowly flooding water. These features are the result of enhanced density-driven flows in the channel and enhanced frictional drag over the shoals. The salinity distribution at HW+1h, Figure 1(d), was obtained during a different but similar spring tide and relies on just five stations located over the section. Nevertheless, it does demonstrate a 'doming' of salinity (> 27) in the channel, corresponding to the flooding core in Figure 1(c), and two 'bulges' of lower salinity (< 23) near-surface waters, corresponding to the two 'jets' in Figure 1(c). Similar results were obtained from ADCP measurements of velocity profiles across a section of the James River estuary (see *Valle-Levinson et al.* [2000]). A main and secondary channel separated by relatively narrow shoals characterized their observed estuarine reach. Transverse surface

flow convergence zones appeared over the edges of the channels and were produced by the phase lag of the channel flow relative to that over the shoals (e.g. Figure 1). In their measurements, flood convergence zones developed close to HW and those on the ebb appeared soon after maximum currents. Most of these convergence zones caused fronts in the density field as well as flotsam lines that appeared over the edges of the channel.

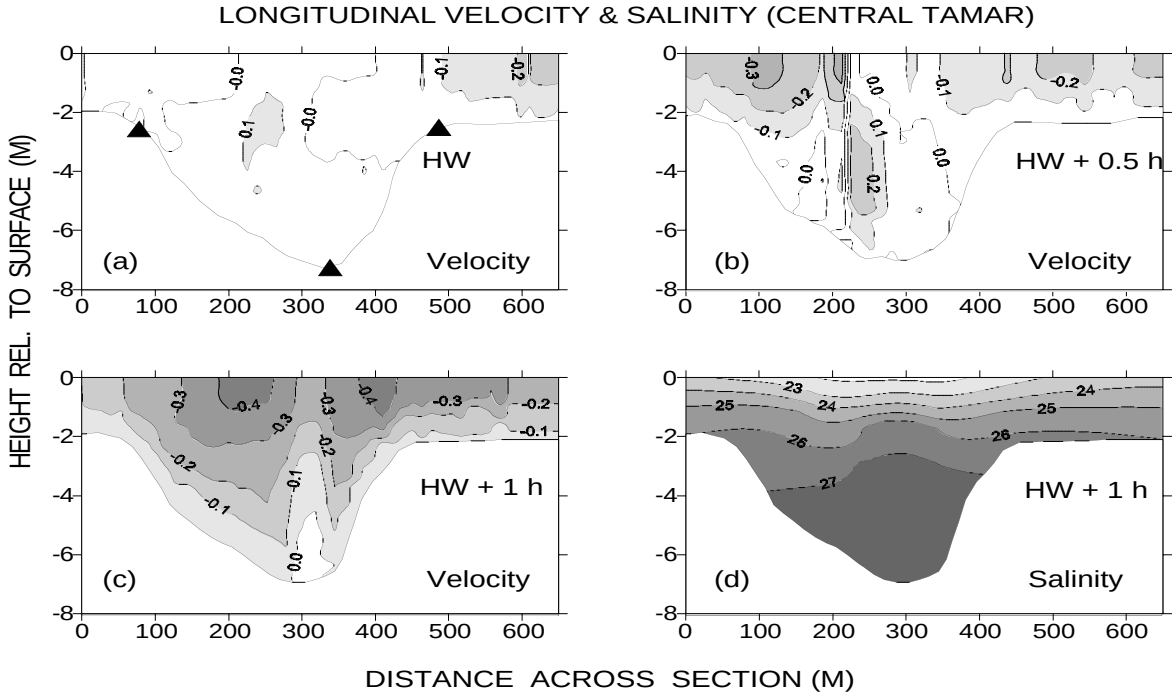

Figure 1: Spatial distribution of longitudinal currents (m s^{-1}, flood positive) across a 650 m-wide portion of the central Tamar Estuary section (looking up-estuary) during spring tides on 20 January 2000.

Analytical results (*Li and Valle-Levinson* [1999]; *Friedrichs and Hamrick* [1996]) also demonstrate that tidal velocities can have strong transverse shear over estuarine cross-sections and that tidal current speeds and depths are highly correlated, such that fastest, along-channel tidal speeds occur in the deepest water. This has been strikingly illustrated by *Cheng et al.*, [1993], using a 2-D hydrodynamic model. Phases of the along-channel velocity in shallow water led those in deeper water, which resulted in a delay of flood or ebb in the channel relative to the shallow regions (illustrated in Figure 1 for the Tamar).

3. Suspended Sediments

Variables were monitored throughout the water column of the main channel during each survey and at 0.25 m above the bed near the edges of the shoals (locations shown as filled triangles in Figure 1(a)). Currents were ebb dominant in the main channel and to the right of the channel during 20 January 2000 (Figures 1(a) and 2(a)) and ebb dominant on the shoulder to the left of the channel (Figure 1(a)), emphasizing the existence of transverse tidal current shears. Salinity was very low at LW (Figure 2(b)) and this was reflected in the large concentrations of SPM at that time, due to the down-estuary transport of sediments from the estuarine turbidity maximum (ETM). Having settled to the bed over LW slack, these sediments were subsequently suspended in the strong near-bed shears and concentrations close to the bed exceeded 1000 mg l^{-1} (Figure 2(c)). The sizes of suspended particles (i.e. aggregates) increased with increasing SPM concentration (Figure 2(d)) and reached 450 microns at maximum concentrations.

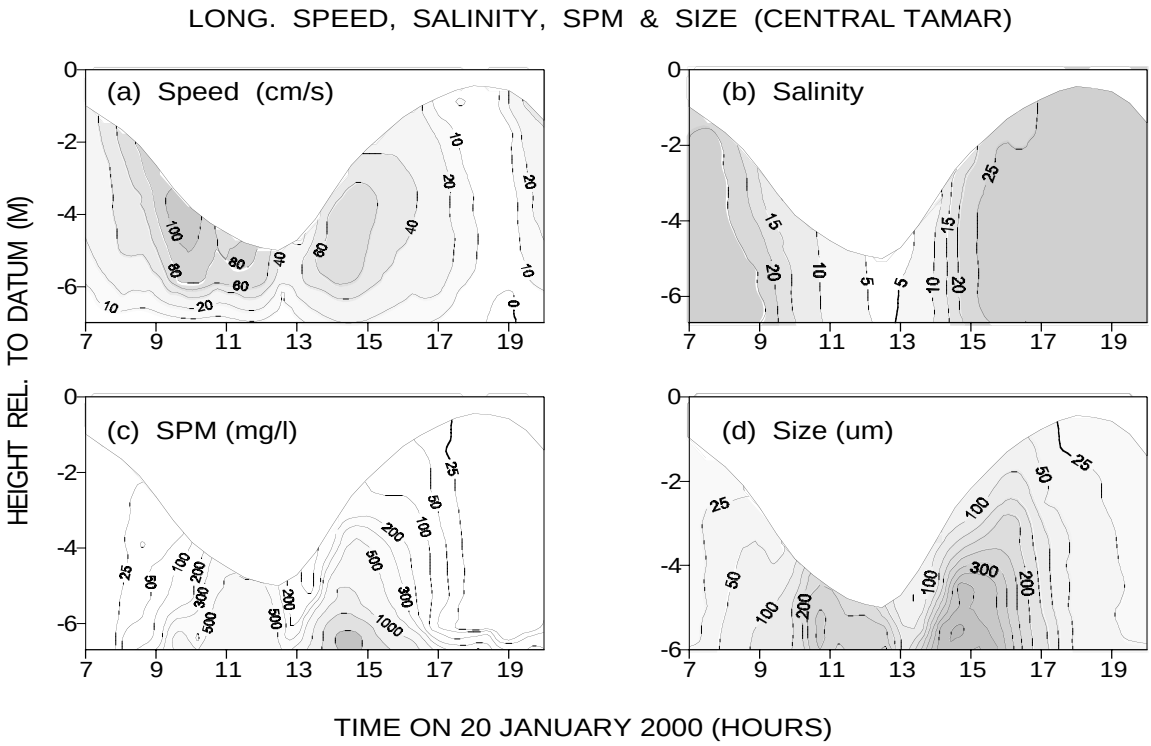

Figure 2: Depth-time contoured data for speed (a, cm s^{-1}), salinity, (b), SPM (c, mg l^{-1}) and size (d, microns) during spring tides on 20 January 2000.

The tidal dynamics therefore provide a strongly time-dependent environment of changing current speeds, shears, salinity and suspended sediment for the mud flats, once the water levels are sufficiently high to submerge them.

4. Mudflat Properties

During June 1999 the mean chlorophyll concentrations in the upper 1 cm of mudflat were 17 mg m^{-2} and the mean carbohydrate (glucose equivalent) concentrations were 470 mg m^{-2}. The mean bulk wet and dry densities were 1.25 g ml^{-1} and 0.43 g ml^{-1}, respectively. Loss-on-ignition (LOI) was 5.7% and the silt and clay fraction was 84% by weight (as opposed to 75% in the channel). In the upper 10 cm of mudflat, as opposed to the upper 1 cm, mean bulk wet density was 1.32 g ml^{-1} and mean dry density was 0.57 g ml^{-1}. LOI was 5.9% and the silt and clay fraction was again 84% and 75% in the channel. The mudflat densities were therefore somewhat higher when averaged over the upper 10 cm of mud column than over the upper 1 cm of column. In the water column, median particle (aggregate) sizes were typically 40 microns at HW (when suspended solids concentrations were approximately 10 mg l^{-1} and current speeds < 0.1 m s^{-1}) but exceeded 150 microns when current speeds were typically 1 m s^{-1} and suspended solids concentrations >300 mg l^{-1}. Particle sizes were larger near LW during winter conditions owing to the greater SPM concentrations then, but otherwise only relatively small differences occurred during the winter period (January 2000). Chlorophyll, carbohydrates and LOI were 5 – 15% less, densities were a few percent greater in the upper 1 cm and a few percent less in the upper 10 cm, suggesting some seasonal adjustment of the near-surface mudflat. Such an adjustment was anticipated in view of the seasonal mobility of sediment and the changes in mudflat bed heights during the year (Table 1).

date	d/m/y	upper shore		mid shore		lower shore	
from	to	mm change /month	S.E.±	mm change /month	S.E.±	mm change /month	S.E.±
23/11/99	03/02/00	-1.5	0.2	-2.2	0.3	-3.1	0.4
03/02/00	23/03/00	7.1	0.2	7.5	0.4	0.4	0.6
23/03/00	09/06/00	-3.0	0.4	-0.8	0.3	0.8	0.7
09/06/00	20/07/00	7.6	0.8	4.5	0.5	-1.4	1.0
20/07/00	28/09/00	3.2	0.5	3.5	0.7	-5.3	0.5

Table 1: Changes in bed heights (mm per month) between various dates at locations on the lower, middle and upper intertidal mudflats that are shown on the left side of the section in Figure 1.

Acknowledgements: The authors are grateful to Mr. J. Lewis of Astrazeneca's Brixham Environmental Laboratory, UK, for deploying the ADCP during this collaborative PML – Astrazeneca project. The PML ECoH (Estuarine and Coastal Function and Health) participants were: C. Turley, J. Widdows, J. Stephens, M. Brinsley, P. Frickers, C. Harris and the crew of RV Tamaris. We are grateful to former colleagues: R. Howland, P. Salkeld and N. Bloomer for their assistance during the fieldwork.

References:

Cheng, R. T., Ling, C.-H., Gartner, J. W. and P. F. Wang, Estimates of bottom roughness length and bottom shear stress in South San Francisco Bay, California. *Journal of Geophysical Research 104 (C4)*, 7715-7728. 1999.

Friedrichs, C. T. and J. M. Hamrick, Effects of channel geometry on cross sectional variations in along channel velocity in partially stratified estuaries. In: Buoyancy Effects on Coastal and Estuarine Dynamics (eds. D. G. Aubrey & C. T. Friedrichs), 53, American Geophysical Union, 283-300, 1996.

Li, C., and A. Valle-Levinson, A two-dimensional analytic tidal model for a narrow estuary of arbitrary lateral depth variation: the intratidal motion. *Journal of Geophysical Research 104 (C10)*, 23525-23543, 1999.

Valle-Levinson, A., Li, C., Wong, K.-C. and K. M. M. Lwiza, Convergence of lateral flow along a coastal plain estuary. *Journal of Geophysical Research 105 (C7), 17045-17061*, 2000.

Morphodynamics of muddy intertidal flats : a cross-shore modelling

PIERRE LE HIR

(IFREMER, centre de Brest, BP 70, 29280 Plouzané, France, plehir@ifremer.fr)

BENOÎT WAELES

(IFREMER, centre de Brest, BP 70, 29280 Plouzané, France, bwaeles@ifremer.fr)

RICARDO SILVA JACINTO

(IFREMER, centre de Brest, BP 70, 29280 Plouzané, France, rsilva@ifremer.fr)

1. Introduction

Considering the morphodynamics of muddy tidal flats in semi-enclosed bays, long-shore currents can be neglected, so that a cross-shore modelling is likely to describe dominant processes. This study aims to assess the conditions for a tidal flat to reach an equilibrium profile, either static, prograding or retreating landwards, and to relate these profile characteristics to physical and sedimentological parameters.

Assuming the peak shear stress was uniformly distributed across an equilibrium flat under tidal currents, *Friedrichs and Aubrey* [1996] derived an analytical profile, linear in the lower half of the tidal flat and convex-upwards in the upper half, with a sinusoidal dependence on the cross-shore distance. *Roberts et al.* [2000] used numerical models to calculate iteratively sediment transport and morphological change until a stable situation is achieved. They established relationships between the shape of the equilibrium profile and forcings (tidal range, wave amplitude and sediment supply) for a given sediment behaviour. Further on, *Waeles* [2001] demonstrated that the seawards shift of the shore does not stop under continuous sediment supply and tidal forcing only. On the other hand, wave effects are likely to change the profile shape and to lead to an equilibrium shore location after 10 to 20 years. Recently, *Pritchard et al.* [2002] carried on a numerical exercise on current alone effects. Independently of Waeles' work, they obtained a progradation of the shore in relation with the sediment supply. In addition, they investigated the consequence of tidal asymmetry and found that flood-dominance enhances the progradation and that ebb-dominance may lead to a flat which retreats landwards, both increasing the slope of the equilibrium profile.

By the means of similar numerical modelling, the present work aims to characterise the sensitivity of the cross-shore profile evolution to the sediment behaviour (settling velocity, critical erosion stress for erosion and erosion rate …) and to the tide and wave climate. The simulation of sediment sorting over a flat is slightly tackled by considering the cross-shore distribution of two particle classes, in relation with different wave and tide forcings.

2. Brief description of the model

The numerical model results from the adaptation of a depth-integrated sediment transport model (S*i*AM-2DH) to a one-dimensional geometry, with periodic adjustment of bottom elevation according to local sediment balances [*Waeles*, 2001].

The tidal wave propagation and associated currents are computed by solving shallow water equations, with non-linear advection terms and quadratic bottom friction. The wave heights distribution is deduced from a conservation equation for wave action density, accounting for current refraction. The Soulsby (1993) parametric expression of mean and maximum bottom stress over a wave period is used to account for wave and current interaction.

Dealing with mainly muddy flats, we only consider the transport in suspension mode of cohesive sediments, using classical deposition and erosion laws for water/sediment exchanges :

- erosion : $E = E_0.(\tau/\tau_e - 1)$, if $\tau > \tau_e$
- deposition : $D = W_s.C.(1-\tau/\tau_d)$, if $\tau > \tau_d$

In the case of wave + current forcing, τ in the settling law is represented by the peak bottom shear stress during the wave period, in order to prevent transient deposition within the wave period, whereas the erosion law is time-integrated over the wave period with a sinusoidal variation of the instantaneous bottom stress [*Waeles*, 2001].

The bottom elevation is deduced from erosion and deposition, assuming a uniform steady sediment dry density of 400 $kg.m^{-3}$, and is upgraded every 30 minutes.

At the sea boundary the tidal height as well as the wave height is given, whereas the suspended sediment concentration is specified during the flood period. Mean sea level is located at 3 m above datum. The computation grid is constituted by 110 cells of 100 m length.

3. Examples of result

Some illustration of the sensitivity study is given hereafter. As a first example, the effect of the neap-spring tidal cycle has been simulated by comparing the bed profile evolution for a sinusoidal M2 tidal forcing with a S2 wave superimposed (fig. 1b) or not (fig. 1a).

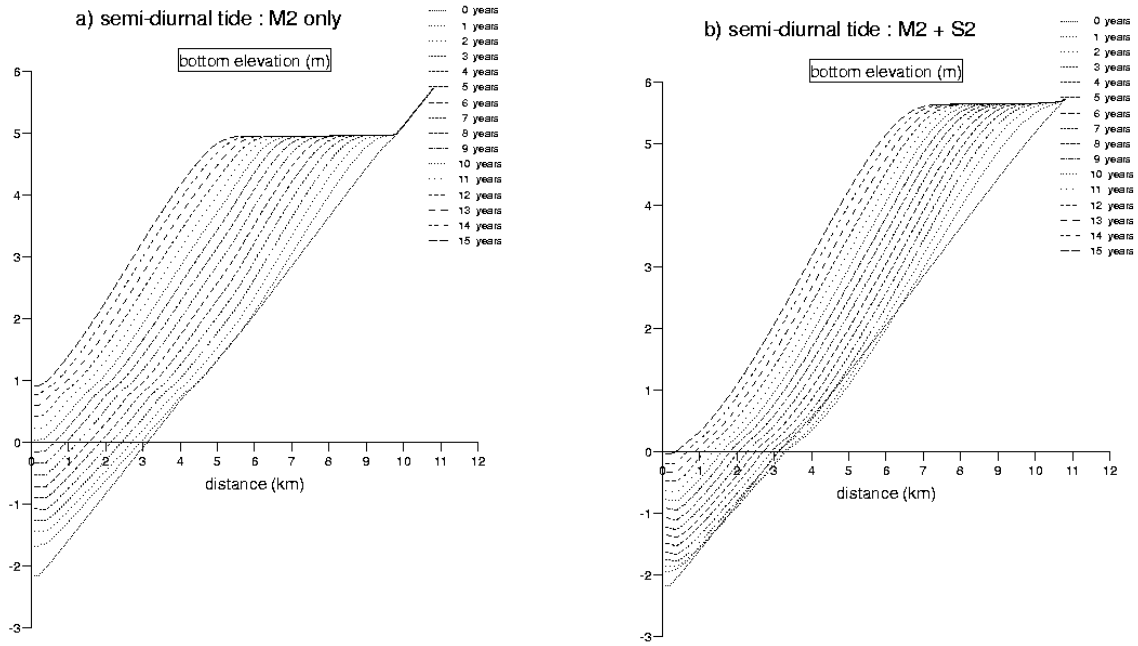

Figure 1: Bed profile evolution during 15 years for a tidal forcing. a) purely periodic semi-diurnal tide (4 m range). b) spring/neap amplitude variation (between 5.4 m and 2.6 m range).

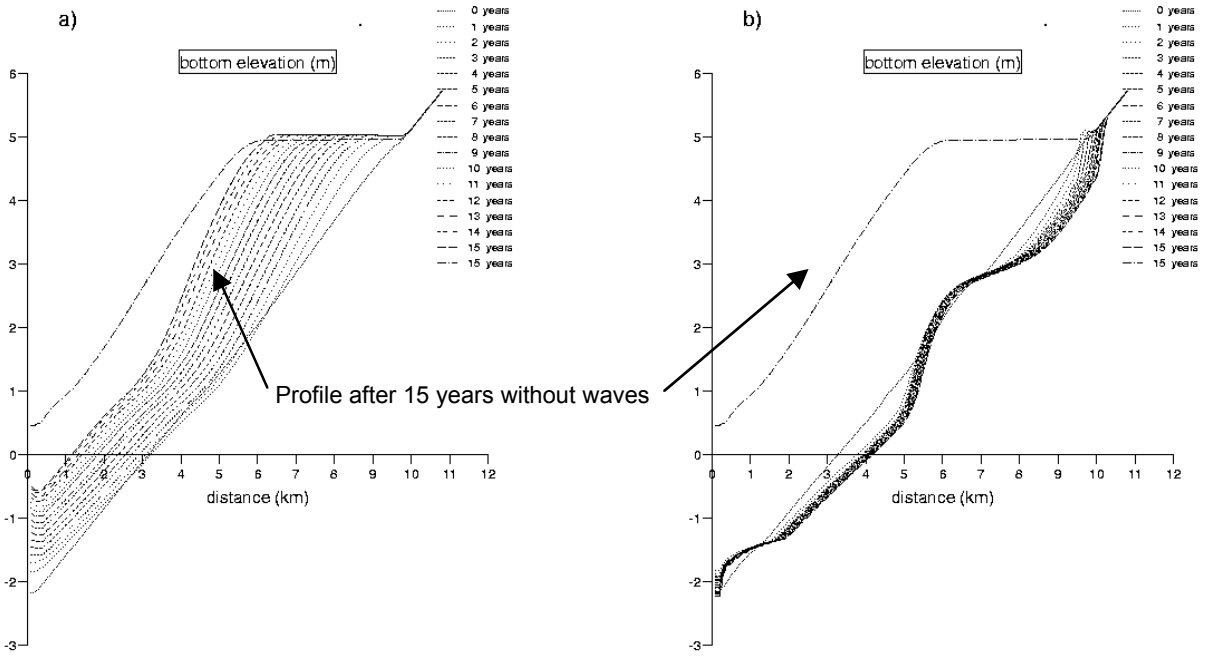

Figure 2: Bed profile evolution during 15 years for two combinations of wave regime and purely sinusoidal tidal forcing, with two particle classes.

a) waves (30 cm height) during 24 hours every week.

b) waves (10 cm height) continuously.

In each case the profile shape rapidly reaches an equilibrium (independent of the initial profile), but the shore advances seawards. In the case of a spring-neap cycle, the rate of progradation is reduced, but not as much as obtained by *Pritchard et al* [2002]. Also the equilibrium bed slope increases, which tends to maintain the mean flat width, that controls the maximum flow velocity [*Roberts et al*., 2000].

The figure 2 presents the bed profile evolution under wave + current forcing. While in the case of 30 cm height waves during 24 hours every week, the shore is still prograding with a steeper slope than without waves, in the steady case of 10 cm height waves added to a 4 m range tidal forcing, an equilibrium is reached after a few years. Erosion is dominant in the upper and lower parts of the flat, probably occurring around slack water when shallow depths last longer, while slight deposition can be observed in the middle.

The latter simulations were run with two particle classes, each of them being characterised by a fixed settling velocity (1 and 0.5 $mm.s^{-1}$). Both classes entered the domain at the same rate, but the initial sediment (4 m thick) was constituted of "heavy" particles only (*i.e.* with a 1 $mm.s^{-1}$ settling velocity). The figure 3 shows the increase of the "small" particle mean fraction in the sediment in the case 2b (10 cm waves + 4 m tidal range). Surprisingly, the inclusion of small particles is higher in the eroded section of the flat, which means that strong exchanges between water and sediment occur at each tide. It can be noticed that the small particles fraction is still increasing once the flat has reached its equilibrium.

Similar mixing processes could be observed in the case of a prograding flat, especially on its lower part. A possible sorting process along the flat is being investigated, by discretising the sediment into thin layers.

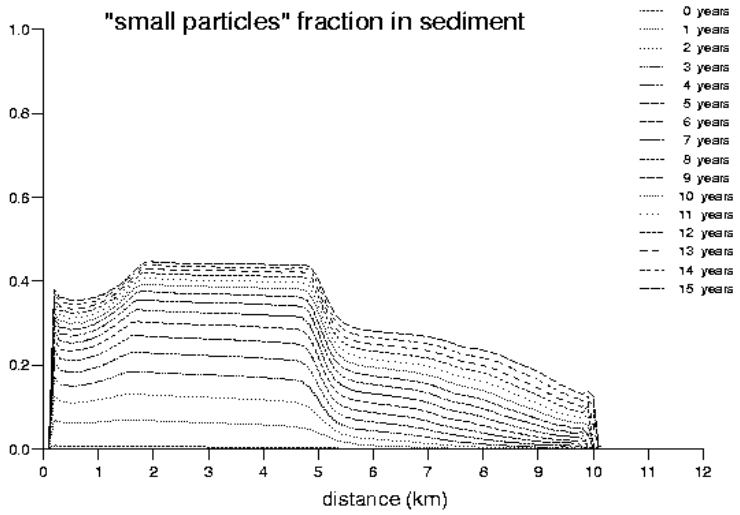

Figure 3 : Time evolution of the distribution of particles characterised by a small settling velocity, in the case of small waves + tidal current forcing (case 2b).

4. Conclusions

Many other tests are being conducted in order to give an overview of the model sensitivity to the sedimentological parameters and to the forcing climates. First results indicate the model is extremely sensitive to the latter, which increases the difficulty to assess a "representative" forcing, as often considered in morphological computations. Computed profiles are also analysed in relation with analytical profiles and the hypotheses on which the latter are funded, and a comparison with some observations in Europe is given.

Acknowledgments: This work is carried out in the framework of the Seine-Aval scientific program, funded by the French State, the Haute-Normandie Regional Council, and the Agence de l'eau Seine-Normandie.

References:

Friedrichs, C.T. and D.G. Aubrey, Uniform bottom shear stress and equilibrium hypsometry of intertidal flats, in Pattiaratchi, C. (Ed.), Mixing in Estuaries and Coastal Seas, vol. 50, American Geophysical Union, Washington D.C., 405-429, 1996.

Pritchard, D., Hogg, A.J. and W. Roberts, Morphological modelling of intertidal mudflats: the role of cross-shore tidal currents, *Continental Shelf Research* (in press), 2002.

Roberts, W., Le Hir, P. and R.J.S. Whitehouse, Investigation using simple mathematical models of the effect of tidal currents and waves on the profile shape of intertidal mudflats, *Continental Shelf Research*, 20, 1079-1098, 2000.

Waeles B., Modélisation morphodynamique cross-shore d'un estran vaseux. *Rapport de DEA Ifremer/DEL/EC-TP & UBO*, 46p., 2001.

Comparison of longitudinal equilibrium profiles of estuaries in idealised and process-based models

Anneke Hibma, (*Delft University of Technology, P.O. Box 5048, 2600 GA Delft, The Netherlands*, A.Hibma@ct.tudelft.nl)

Henk Schuttelaars, (*Delft University of Technology and Utrecht University, The Netherlands*, H.M.Schuttelaars@ct.tudelft.nl)

Zheng Bing Wang, (*Delft University of Technology and WL|Delft Hydraulics, The Netherlands*, Zheng.Wang@wldelft.nl)

1 Introduction

Morphological developments in complex areas such as estuaries result from complex interaction between water motion, sediment transport and the erodible bed. Various model approaches can be used to investigate the mechanisms behind the morphodynamic evolution (de Vriend, 1996; de Vriend and Ribberink, 1996). In this contribution two types of models, i.e. idealised and process-based models, will be compared.

In recent years much work has been done on width–averaged idealised models. These models give a good insight in the physics that underly morphodynamic processes. They have been used to determine long–term equilibrium profiles (Schuttelaars & De Swart, 1996; Schuttelaars & De Swart, 2000; De Jong, 1998; Van Leeuwen *et al.*, 2000; Lanzoni & Seminara, 2002). Additionally, linear stability analysis was adopted to study the initial formation of channels and shoals in tidal embayments (Schuttelaars & De Swart, 1999; Seminara & Tubino, 2001; Van Leeuwen, 2001). One of the drawbacks of idealised models, however, is that they are limited to idealised geometries. This limitation is absent in a process–based model (Hibma, 2001) using the numerical modelling system Delft3D (Wang *et al.*, 1991) to study the formation of channels and shoals with geometries similar to those used in the analytical models. However, a comparison of the model results appeared to be difficult due to the differences in model description and assumptions.

The objective of this study is to compare and explain the results of an idealised and a process-based model. This process-based model is an adapted version of Delft3D in which the differences between the model formulations are minimised. Step by step these adaptations in the process-based model will be removed. This will give more insight into the processes found in the process-based model on the one hand and into the influences of the assumptions in idealised models on the other hand.

2 Description of the model

Both models describe the water motion by depth averaged shallow water equations. The suspended sediment transport is calculated using an advection-diffusion equation. The formulation used in the process-based model is changed to resemble the model description of the idealised model as close as possible. The changes include the linearisation of the friction term, neglect of the bed-load transport and the formulation for the calculation of

equilibrium sediment concentration. The main difference in the description of the water motion concerns the higher order tidal components due to interaction of M_2 and M_4 components, which are neglected in the idealised model and will be maintained in de process-based model. The hydrodynamics and morphological development of basins of various lengths are simulated. In some experiments the initial bottom profile is a linear sloping bed, increasing from 10 m below MSL at the seaward boundary to around HWL at the landward end. In other experiments the equilibrium profiles resulting from the idealised models (see Fig. 1) are used. The lateral and landward boundaries are fixed and impermeable. On the seaward boundary a M_2 water level variation is imposed, with an amplitude of 1.75 m. The bed material consists of uniform sand with $D_{50} = 200\mu m$.

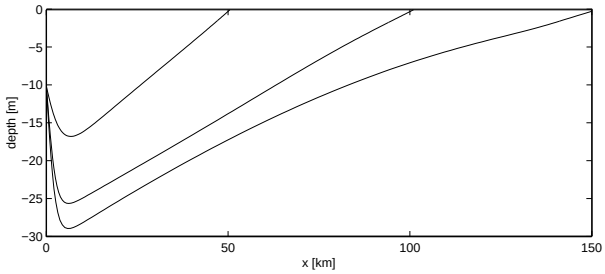

Figure 1: Equilibrium profiles for 50, 100 and 150 km basins.

3 Model results

3.1 Comparison of hydrodynamics

The hydrodynamics resulting from the idealised and process-based models are compared for three different basin lengths. These basins are shorter than (50 km), equal to (100 km) and longer than (150 km) the tidal resonance length (which is approximately 100 km). The M_2 and M_4 tidal components from the time series of the simulations are compared. Figure 2 shows the velocity and water level amplitudes and phases along the 50 km basin, resulting from the two models. For this as well as the larger embayments the hydrodynamics on identical bottom profiles in both models show very good agreement. Small deviations are found near the open boundary and in the shallow area of the basin. Deviations near the open boundary are due to different boundary conditions in the two models. Deviations in the shallow area can be explained by the slightly different formulations of the friction term, which become more significant for smaller depth.

3.2 Comparison of longitudinal profiles

Albeit small, differences in flow field imply that the sediment transport fields and therefore the morphological changes will also deviate. Thus the profiles of the idealised model will not be in equilibrium for the process-based model. For each basin a morphological simulation is made to investigate the tendency of the changes in the profile.
Starting from a linear profile strong erosion near the entrance of the embayment occurs for all embayments. The landward slope is linear for the short basin and becomes more convex for the longer basins. After the simulation period of approximately 1000 years, the

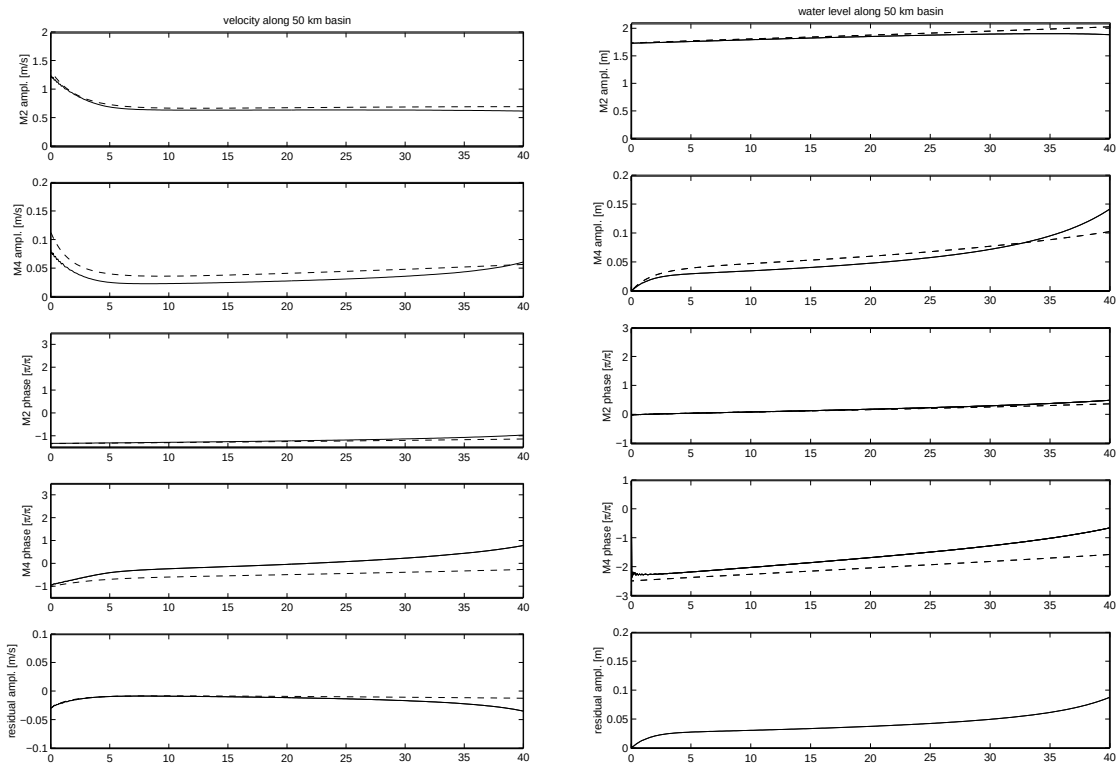

Figure 2: Amplitude and phase of the M_2 and M_4 tidal velocities (left panel) and water levels (right panel) along a 50 km long basin. Solid: process-based model; dashed: idealised model.

developing profiles resemble qualitatively the equilibrium profiles of the idealised model and also quantitatively for the 50 km basin. Starting from the equilibrium profiles of the idealised model, the morphological changes are much smaller, which implies that the deviation from a possible equilibrium profile is smaller. The main changes take place near the entrance of the basin, due to the differences in boundary description for the suspended sediment concentration. In the idealised model, a boundary layer is allowed for in the time-averaged part of the sediment concentration, but not in the time dependent concentration. In the process-based model no distinction is made between the time-averaged and time-dependent parts of the concentration field, and a boundary layer is allowed for the entire (time-dependent) concentration field.
In all cases the morphological changes decrease exponentially during the simulations. However, an equilibrium defined by zero net transport is not achieved during the simulation period.

3.3 Influence of model adaptations

To study the influence of the simplifying assumptions on the longitudinal profiles these assumptions are reversed in the process-based model. Linearisation of the friction term, neglect of the bed-load transport and the differences in formulation of the suspended sediment transport only have a minor influence on the development of the profiles. However, the difference in the boundary condition at the entrance of the embayment results in very

different equilibrium profiles. In the idealised model the bottom level at the entrance is fixed independent of the sediment transport direction, wheras in the process-based model the bottom level is only fixed if the residual sediment transport is inwards (Wang, 1990).

4 Conclusion

The results of the idealised and adapted process-based model show good agreement with respect to the water levels and velocities in a schematized estuary. The development of the longitudinal profiles in the process–based model resemble qualitatively the equilibrium profiles of the idealised model, although an equilibrium is not achieved in the strict sense of zero net sediment transport. Quantitative deviations in model result are caused by the different descriptions of the boundary conditions. Furthermore, the model adaptations have no qualitative influence, except for the fixation of bottom at the entrance.

References:

De Jong, K. (1998), Tidally averaged transport models. Ph.D. thesis, Delft University of Technology, The Netherlands.

Hibma, A., H. de Vriend and M.J.F. Stive (2001), Channel and shoal formation in estuaries. IAHR River, Coastal and Estuarine Morphodynamics, p. 463-472.

Lanzoni, S., & G. Seminara (2002), Long–term evolution and morphodynamic equilibrium of tidal channels. *J. Geophys. Res.*, 107, p. 1-13.

Schuttelaars, H.M. and H.E. de Swart (1996), An idealised long–term morphodynamic model of a tidal embayment. *Eur. J. Mech., B/Fluids*, 15(1), p. 55-80.

Schuttelaars, H.M. and H.E. de Swart (1999), Initial formation of channels and shoals in a short tidal embayment. *Journal of Fluid Mechanics*, vol.386, p. 15-42.

Schuttelaars, H.M. and H.E. de Swart (2000), Multiple morphodynamic equilibria in tidal embayments. *Journal of Geophysical Research*, vol.105, no. C10, p. 24,105-24,118.

Seminara, G. and M. Tubino (2001), Sand bars in estuaries. Part 1. Free bars. *J. Fluid Mech.*, 386, p. 15-42

Van Leeuwen, S.M., H.M. Schuttelaars and H.E. de Swart (2000), Tidal and morphologic properties of embayments: effects of sediment deposition processes and length variation. *Phys. Chem. Earth (B)*, 25, p. 365-368.

Van Leeuwen, S.M., and H.E. de Swart (2001), The effect of advective processes on the morphodynamic stability of short tidal embayments. *Phys. Chem. Earth (B)*, 26, p. 735-740.

Vriend, H.J. de (1996), Mathematical modelling of meso-tidal barrier island coasts. Part I: Empirical and semi-empirical models. In: P.L.-F. Liu (ed.), *Advances in coastal and ocean engineering (2)*, 115-149.

Vriend, H.J. de and J.S. Ribberink (1996), Mathematical modelling of meso-tidal barrier island coasts. Part II: Process-based simulation models. In: P.L.-F. Liu (ed.), *Advances in coastal and ocean engineering (2)*, 151-197.

Wang, Z.B. (1990), Some considerations on mathematical modelling of morphological processes in tidal regions, 5th Conference Physics of Estuaries & Coastal Seas.

Wang, Z.B., H.J. de Vriend, and T. Louters (1991), A morphodynamic model for a tidal inlet, The Second International Conference on Computer Modelling in Ocean Engineering.

Effect of grain size sorting on the formation of tidal sand ridges

Marianne Walgreen, (*Institute for Marine and Atmospheric research, Utrecht University, Princetonplein 5, 3584 CC Utrecht, The Netherlands*, M.Walgreen@phys.uu.nl)

Huib de Swart, (*same institute*, H.E.deSwart@phys.uu.nl)

1 Introduction

Tidal sand ridges are large-scale bed forms, found in the outer part of meso-tidal shelves. Characteristic spacings between the successive crests are 2-8 km and the ridges are rotated cyclonically with respect to the dominant tidal current. Field data show persistant spatial variations of the surficial sediments on the sand banks, of which the cause is not well known. An example is the Middelkerke bank along the Belgian coast (*Trentesaux et al.* [1994]), where the mean grain size pattern reveals coarse sediment on the crests and a fining trend towards the swales. At some locations this pattern is shifted seaward.

In this contribution a model is developed and analysed to gain understanding about the physical mechanisms responsible for the observed grain-size distribution over these ridges. Moreover, the influence of sediment sorting on the temporal and spatial characteristics of tidal sand ridges is investigated. In *Calvete et al.* [2001] the initial formation of tidal sand ridges was studied for the case of uniform sediment. A new aspect compared to this model is the inclusion of dynamic hiding effects in the transport of a sediment mixture. The approach is similar to that used by *Walgreen et al.* [preprint, 2002], who investigate the effect of sediment sorting for another class of large-scale bed forms found on coastal shelves, viz. the shoreface-connected sand ridges. These ridges are present on storm-dominated inner shelves and exhibit an oblique orientation with respect to mean alongshore current. Observations also indicate a clear relation between the mean grain size distribution and the ridge topography, with the finest sediment on the seaward (downcurrent) flank, and coarsest on landward (upcurrent) flank or in troughs. The present model for tidal sand ridges differs from the one presented in *Walgreen et al.* [preprint, 2002] in the sense that the dominant forcing is by tides, rather than by storms and that bed load instead of suspended load transport is considered.

2 Model

Following earlier work it has been hypothesized that tidal sand ridges form as a free instability of a morphodynamic system. A local model is used to investigate the flow-topography interaction on a tide-dominated coastal shelf, where bed forms develop as perturbations on an alongshore uniform reference state. The geometry of the model represents a semi-infinite domain, bounded on the landward side by the transition from the shoreface to the (sloping) inner shelf, which has a width of 12 km. Further seaward a flat bottom is used to represent the outer shelf. In the model the 2DH shallow water equations are used to describe the water motion, and they are mainly forced by the M_2

tide. Additional contributions of the M_4 tidal component or a steady current, both resulting in an asymmetry of the alongshore current, are also investigated. During these tide-dominated or fair weather conditions bed load transport is the dominant mode of transport and suspended load is neglected. A one-layer model for the bottom evolution, based on the concept of an active transport layer overlaying an inactive substrate (see *Seminara* [1995]), is used and two grain size classes (fine and coarse sand) are considered. The bottom and grain-size evolution are determined by the sediment fluxes of these two size classes. Dynamic hiding effects are included in the bed load transport of a sediment mixture, which causes the finer grains to feel the fluid drag less intensely than the coarser grains. The result is a reduced transport rate of the finer sizes. The initial feedback between currents and small bed forms is computed from a linear stability analysis of the reference state, resulting in growth rates and migration velocities, which depend on the longshore wavenumber k. The preferred mode gives the spatial patterns of the fastest growing bottom perturbations.

3 Results

In this section the influence of the non-uniformity of the sediment mixture on the initial formation of tidal sand ridges is investigated. This is done for different hydrodynamic situations, using a bimodal sediment mixture, and results are compared with the bottom response in case of a uniform sediment layer. The first case is where only a M_2 tidal contribution is considered. This means the tidally averaged longshore sediment transport is zero. Asymmetry in the flow is introduced by adding the M_4 component, resulting in a net alongshore (flood-dominated) current and a tidally averaged sediment flux along the coast. The total tidal current amplitude is constant in all experiments, with a characteristic value of 0.5 ms^{-1}.

The initial growth rates and migration velocities of the most unstable solutions are shown in figure 1 for different compositions of the sediment bed. The standard deviation σ_0 of the reference state is increased from zero (i.e. uniform sediment with $d = 0.35$ mm) to a bimodal mixture for a pure M_2 tide and a combined M_2, M_4 tide. The mean grain size is held constant at $d_m = 0.35$ mm and equal weight percentages of the two size classes in the reference state are assumed. Here $\sigma_0 = 0.5$ indicates a bimodal mixture consisting of the sediment classes $d_1 = 0.25$ mm and $d_2 = 0.50$ mm. Results indicate increased growth rates and migration speeds for a bimodal mixture, whilst the wavelengths ($= 2\pi/k$) of the bed forms for which maximum growth rates are attained remain unchanged. The relative increase in growth and migration due to a changing standard deviation is larger for asymmetrical flows than for symmetrical flows. Additional experiments (results not shown) indicate that growth rates and migration velocities increase if dynamic hiding effects become stronger. The bottom perturbations and the distribution of the mean grain size are shown in figure 2 for non-uniform sediment. Contour lines refer to the perturbation in the frequency of the finest grain size class, where solid lines (positive values) indicate an increase in the weight percentage of this sediment compared to the initial distribution and therefore locally a finer mean grain size. If a symmetrical tidal current is used, the grain-size distribution is in phase with the bed forms, with the finest sediments located in the troughs. Incorporation of an additional M_4 tidal component results in a phase shift

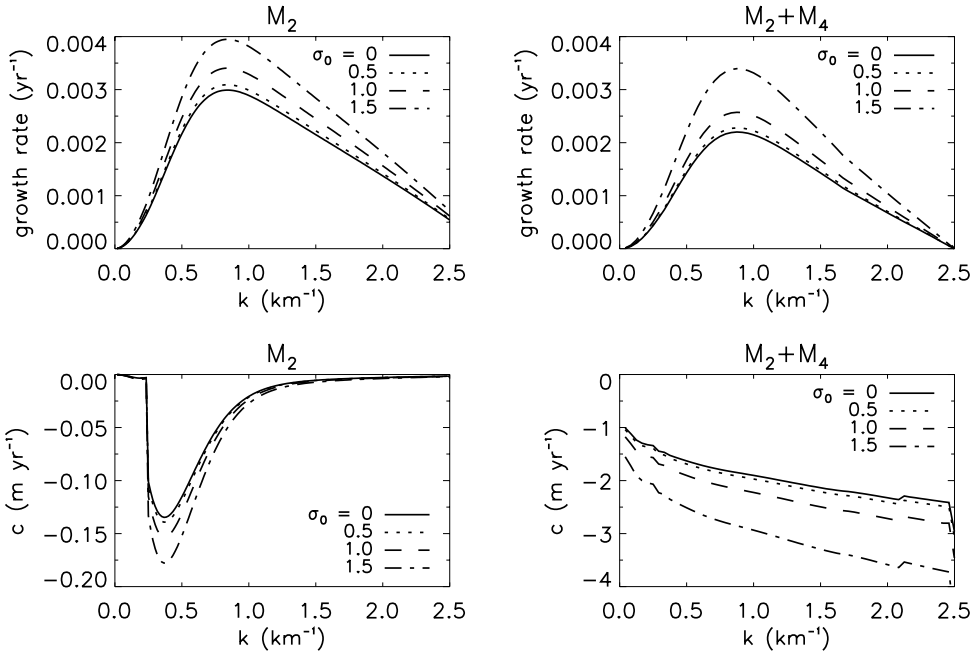

Figure 1: Growth rate and migration velocity of most unstable mode as a function of the longshore wavenumber k for different values of the standard deviation. Forcing due to (left) M_2 tide, and (right) M_2+M_4 tide

between the grain size and ridge topography. In the present case of a flood-dominant tidal current (i.e. residual transport towards the north) the finest sediments are found on the upcurrent (seaward) flank and on the crests of the ridges.

4 Discussion

In this model the bottom layer in which the sediment transport takes place is much smaller than the water depth. Therefore the grain-size distribution will develop on a much faster timescale than the formation of the ridges itself and the sediment pattern adapts almost instantaneously to changes in the bed topography. The difference in the sediment transport capacity of the two grain size classes, due to the so-called hiding effects, results in a local change in the size distribution of the surficial sediment. The reduced erosion and deposition flux for the finest sediment fraction results in a fining of the sediment in the erosion areas, and a sediment coarsening in the deposition areas. For the asymmetrical tide case, a northward migration of the ridges causes the sediment pattern to be shifted alongshore, with a fining on the upcurrent (southern/seaward) flank of the ridges.

The conclusion of the experiments is that a phase shift between the grain size and ridge topography can be introduced as a result of a net alongshore current (caused by an additional tidal component or steady current). Work done on the modelling of sorting effects for river bars and ripples generally attribute a phase shift between grain-size distribution and topography to the presence of the grain size in the formulation of the bottom

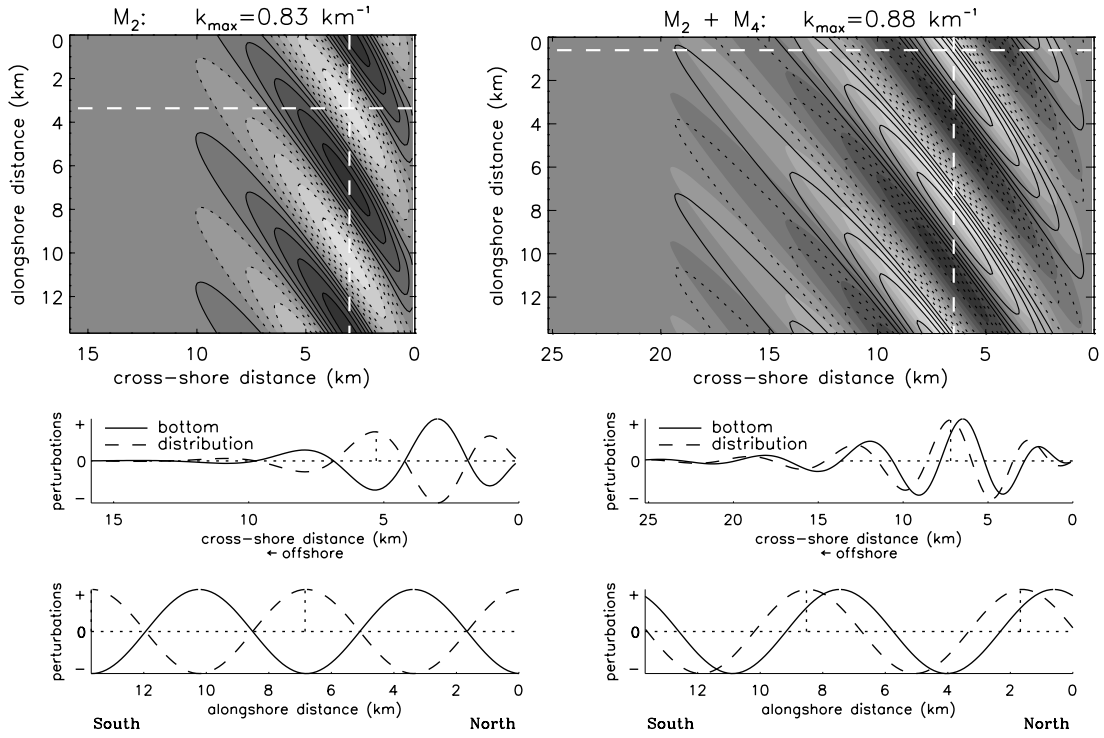

Figure 2: Bottom perturbations (colors; white: bars, black: troughs) and perturbations in the distribution of mean grain size (solid lines: finer; dashed lines: coarser). Also shown are cross-sections, where + indicates fining of the mean grain size and positive bottom elevations (crest) and − coarser and troughs. Bed forms are shown for $\sigma_0 = 0.5$ and forcing due to (left) M_2 and (right) $M_2 + M_4$.

friction (see *Seminara* [1995]). However, experiments with a grain-size dependent bottom friction in the momentum equations indicate that the pattern for tidal sand ridges is not influenced by this effect. Another aspect which is not included in the present model, but will influence the sediment pattern is selective suspended load transport. This introduces a mechanism for which the transport of fines is enhanced, as opposed to the reduced transport of fine sediment for bed load.

References:

Calvete, D., M. Walgreen, H.E. De Swart, and A. Falqués, A model for sand ridges on the shelf: effect of tidal and steady current. *Journal of Geophysical Research 106 (C5)*, 9311-9326, 2001.

Seminara, G., Effect of grain sorting on the formation of bedforms. *Applied Mechanics Reviews 48 (9)*, 549-563, 1995.

Trentesaux, A., A. Stolk, B. Tessier, and H. Chamley, Surficial sedimentology of the Middelkerke Bank (southern North Sea). *Marine Geology 121*, 43-55, 1994.

Sand-mud morphodynamics in a short tidal basin

MATHIJS VAN LEDDEN

(Delft University of Technology, Stevinweg 1, 2600 GA Delft, The Netherlands, m.vanledden@ct.tudelft.nl)

ZHENG-BING WANG

(WL|Delft Hydraulics, Rotterdamseweg 185, P.O. Box 177, Delft, The Netherlands, zheng.wang@wldelft.nl)

HAN WINTERWERP

(Delft University of Technology, Stevinweg 1, 2600 GA Delft, The Netherlands, h.winterwerp@ct.tudelft.nl)

HUIB DE VRIEND

(WL|Delft Hydraulics, Rotterdamseweg 185, P.O. Box 177, Delft, The Netherlands, huib.devriend@wldelft.nl)

1. Introduction

The bed composition in tidal basins is not uniform in general. For example, the following typical pattern in the short tidal basins in the Wadden Sea can be observed. Near their entrance, non-cohesive ('sand') deposits are predominant, while cohesive ('mud') deposits are found near their borders. Nutrients and pollutants tend to adhere to or be part of cohesive sediments and the distribution of sand and mud is an important habitat parameter for ecosystems. Therefore, understanding and predicting this phenomenon is of great practical importance.

Various authors investigated the morphological behaviour of short tidal basins previously [e.g. Van Dongeren & De Vriend, 1994; Schuttelaars & De Swart, 1996]. An important premise in these studies was that the bed consisted of sand only. Recently, a morphological model was developed for sand-mud mixtures [Van Ledden & Wang, 2001]. In the present paper, this model is applied to investigate the morphological behaviour when sand and mud are affecting the bed level and bed composition development in a short tidal basin.

2. Model set-up

Van Ledden & Wang [2001] proposed a set of equations for a process-based morphological model with two sediment fractions: a non-cohesive sand fraction and a cohesive mud fraction. Three major extensions can be dinguished compared to the present-day morphological models for sand only [Van Rijn, 1993]. Firstly, the bed level changes depend on the exchange of sand and mud. Secondly, the exchange of sediment between the bed and the water column depends on the bed composition at the bed surface. Thirdly, spatial and temporal variations of the bed composition are taken into account by applying the bed composition concept of Armanini [1995].

The basin is assumed to be rectangular with length L (Figure 1). The initial bed level z_b below the mean water level H is horizontal. The system is forced with an M_2-tide at the sea boundary (x = 0) and has a closed boundary at the land boundary (x = L). For inflow conditions, the sand concentration is set to its equilibrium value and the mud concentration is set at a constant value. For outflow conditions, a weak boundary condition is applied for both sediment fractions. The bed level is fixed for inflow conditions only.

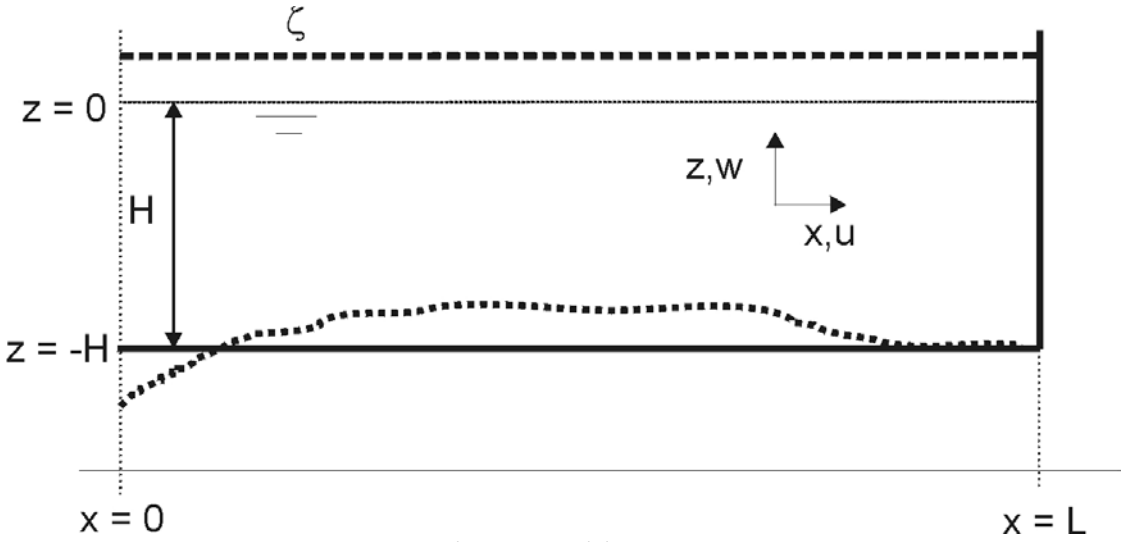

Figure 1: Model set-up.

The parameter settings are characteristic for the Wadden Sea tidal basins. The main settings are: length L = 20000 m, initial bed level H = 5 m, M_2-tidal amplitude ζ_2 = 1.5 m, sand grain size d_{50} = 120 μm, settling velocity mud w_m = 0.0005 m/s, mud concentration $c_{m,0}$ = 0.05 kg/m^3, erosion coefficient M = 10^{-4} kg/(m^{2}s), critical erosion shear stress τ_e = 0.25 N/m^2 and critical deposition shear stress τ_d = 0.10 N/m^2.

3. Results

The results show the following morphological behaviour (Figure 2a & b). Initially, two sedimentation waves are observed (Figure 2 at time t/T_m = 0.2 where the morphological time scale T_m = 115 years): a propagating sand wave near the sea boundary and a mud wave more landward. After some time, the mud wave is covered sand and mud is deposited more and more near the land boundary. A more or less linear bed level profile is obtained after 115 years (Figure 2 at time t/T_m = 1.0). The bed has a very sandy surface over almost the entire basin with only a very small muddy area near the head of the basin. A strict morphological equilibrium (i.e. zero bed level changes for the entire basin) is not reached, but the bed level changes are small compared to the initial bed level changes. The computed linear bed level profile can be regarded as a quasi-equilibrium which only changes on a very long time scale.

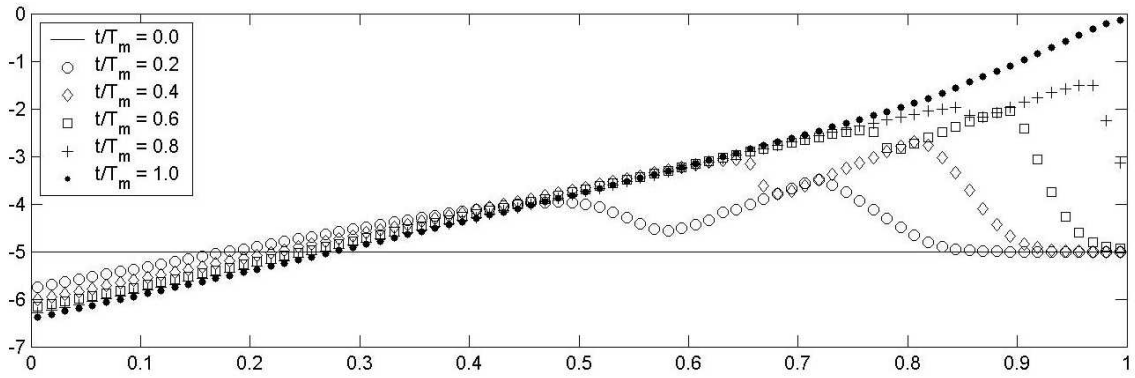

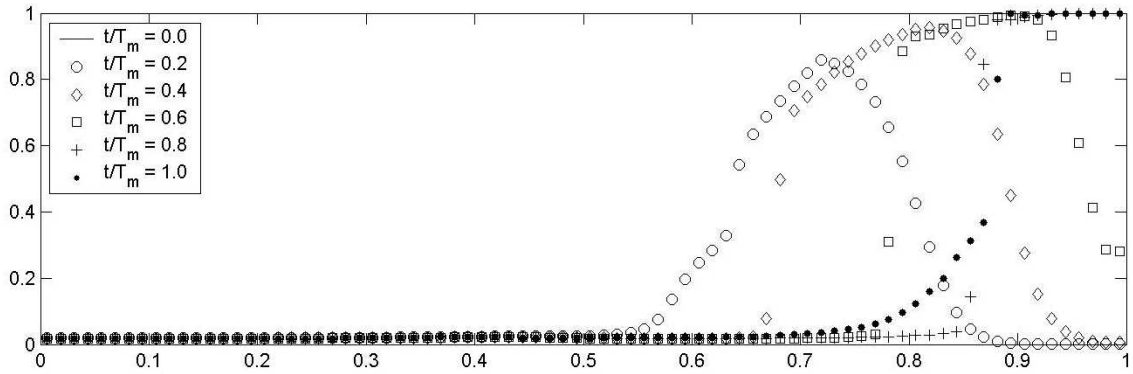

Figure 2: Development of bed level (a) and mud content at bed surface (b) along tidal basin with morphological time scale T_m = 115 years.

The analysis shows that the morphological behaviour can be understood by several dimensionless parameters. It turned out that especially the ratio between the mud deposition and erosion flux ($w_m\ c_{m,0}$ / M) is a distinguishing parameter for the morphological behaviour. When this parameter is smaller than unity, mud does not affect the (quasi-) equilibrium bed level profile significantly. The presence of mud only decreases the morphological time scale in which the system reaches this (quasi-) equilibrium.

4. Discussion

A comparison between the analytical results of Schuttelaars & De Swart [1996] for sand only and the above described numerical results is interesting because of the inclusion of mud in the present study. Schuttelaars & De Swart [1996] obtained a linear bed level profile for suspended sand transport. The obtained (quasi-) equilibrium bed level profile in the present study has an almost similar form, but is slightly concave. Schuttelaars & De Swart [2000] already showed for sand only, that a slightly concave profile results from the inclusion of non-linear effects in the momentum equation. However, the time scale for reaching this (quasi-) equilibrium bed level profile in case of sand and mud was 115 years, whereas the time scale for 'sand only' was more than 600 years. Thus, the morphological time scale of the system drastically decreases for the applied parameter settings when mud is included. The extra availability of sediment due to the introduction of mud explains the decrease in the morphological time scale of the system.

The model can further be validated against field data, even though the model contains numerous simplifications. Schuttelaars [1996] already mentioned that the often observed linear relationship between the tidal volume and the tidal prism is reproduced by the obtained linear bed level equilibrium for sand only. The present study shows that the presence of mud does not change this (quasi-) equilibrium bed level profile for the Wadden Sea basins and the same relationship is suggested in case of sand and mud. Furthermore, the mud distribution along the tidal basin in the (quasi-) equilibrium situation has a similar trend as the mud content in the various Wadden Sea basins [see e.g. De Glopper, 1967; Flemming & Ziegler, 1995]: the mud content is low for a large part of the tidal basin (< 10%) and suddenly increases near the dike at the head of the basin to high values (> 50%).

5. Conclusions

The morphological behaviour of a short tidal basin has been investigated with a process-based sand-mud model. A (quasi-) equilibrium bed level profile was found with a sandy bed surface over almost the entire basin and only a very small muddy area near the head of the basin. The dimensionless ratio between the deposition flux and erosion flux ($w_m\ c_{m,0}$ / M) turned out to be a crucial parameter for the

understanding of the observed behaviour. Comparison with previous studies on short tidal basins for sand only suggested that the presence of mud in a combined sand-mud model does not change the equilibrium bed level profile for the applied parameter settings herein, but drastically decreases the morphological time scale. Comparison between model results and field data of the Wadden Sea suggested that the obtained bed level and bed composition profile are realistic, indicating that the process-based sand-mud is a powerful tool for a better understanding and predictability of sand-mud distributions in tidal basins.

Acknowledgments: This research was supported by the Technology Foundation STW, applied science division of NWO and the technology programme of the Ministry of Economic Affairs.

References:

Armamini, A., 1995. Non-uniform sediment transport: dynamics of the active layer. Journal of Hydraulic Research, no. 33, 611-622.

De Glopper, R., 1967. Over de bodemgesteldheid van het waddengebied (in Dutch). In: Van Zee tot Land, no. 43, Tjeenk Willink, Zwolle.

Flemming, B.W. & Ziegler, K., 1995. High-resolution grain size distribution patterns and textural trends in the backbarrier environment of Spiekeroog Island (Southern North Sea), Senckenberg Maritima (26), 1 - 24.

Schuttelaars, H.M. & De Swart, H.E., 1996. An idealized long-term morphodynamic model of a tidal embayment. European Journal of Mechanics, B/Fluids, 15, 55-80.

Schuttelaars, H.M. & De Swart, H.E., 2000. Multiple Morphodynamic Equilibria. Journal of Geophysical Research, 105, 24105 - 24118.

Van Dongeren, A.R. and De Vriend, H.J., 1994. A model of morphological behaviour of tidal basins. Coastal Engineering, 22, 287-310.

Van Ledden, M. & Wang, Z.B., 2001. Sand-mud morphodynamics in an estuary. River, Coastal and Estuarine Morphodynamics Conference, IAHR-conference RCEM2001, Obihiro, Japan.

Van Rijn, L.C., 1993. Principles of sediment transport in rivers, estuaries and coastal seas. Aqua Publications, Amsterdam.

Nonlinear response of shoreface–connected sand ridges to interferences

H.E. de Swart, (*Institute for Marine and Atmospheric research, Utrecht University, The Netherlands*, h.e.deswart@phys.uu.nl)

D. Calvete, (*Department Física Aplicada, Universitat Politècnica de Catalunya, Barcelona, Spain*, calvete@fa.upc.es)

1 Introduction

An important variable quantifying the stability of sandy coastal systems is the volume of sand stored in the nearshore zone. Observations indicate that during storms this volume can decrease significantly because waves and wind-induced circulations cause sediment to be transported from the nearshore zone to the inner shelf (cf. *Harris and Wiberg* [2002]). It is plausible that the intensity of these exchange processes is influenced by the presence of shoreface-connected sand ridges (sfcr) on the inner shelf. These rhythmic bed forms have horizontal length-scales of the order of 5 km, amplitudes of a few metres and they migrate in the direction of storm-driven currents. The structure of these ridges themselves is affected by human interferences, for example by the dredging of navigation channels or by sand mining. As such activities can have large consequences for coastal stability it is important to study them from a model perspective. In this contribution a process-oriented morphodynamic model is used to analyse the response of sfcr to sudden interferences in the morphology, with specific emphasis on the exchanges of sand between inner shelf and nearshore zone.

2 The model

The model applied in this study describes the finite-amplitude behaviour of sfcr on a storm-dominated sandy inner shelf with a transverse slope, see the geometry in figure 1 (left). It is based on the supposition that these ridges initially form as inherent morphodynamic instabilities of a storm-driven current moving over such an inner shelf. The subsequent long-term behaviour of the ridges is determined by nonlinear processes. With regard to the initial growth of sfcr the validity of this hypothesis was already demonstrated by *Trowbridge*[1995].

The structure of the model is such that the water motion is governed by the depth-averaged shallow water equations. The sediment transport module includes both bed load and suspended load contributions. Bottom changes are computed from the sediment balance. Transport of sediment is assumed to take place only during storms and is due to the joint action of waves (stirring) and currents (transport). This model allows for a basic state describing a net storm-driven flow on the shelf. Upon analysing the linear stability of this state with respect to small perturbations (having a rhythmic structure in the alongshelf direction) the set of eigenmodes is obtained. The latter have different alongshelf and cross-shelf spatial patterns. The nonlinear model consists of equations

describing the time evolution of the the amplitudes of the different modes, for details about the method see *Calvete et al.* [2002].

The present version of the model accounts for the mode with an alongshelf-uniform structure (the so-called $k = 0$ mode, where k is the alongshelf wavenumber). This mode is linearly damped, but is excited by nonlinear processes, e.g. by self-interaction of a mode with wavenumber $k \neq 0$. Its incorporation is crucial for the present study because only the $k = 0$-mode can provide for net sand volume changes on the inner shelf. The model also allows for subharmonic modes; they have alongshelf wave-lengths which are larger than that of the initially fastest growing mode. A typical result of this model is shown in figure 1 (right), for parameter values which characterise the situation on the inner shelf of Long Island (USA).

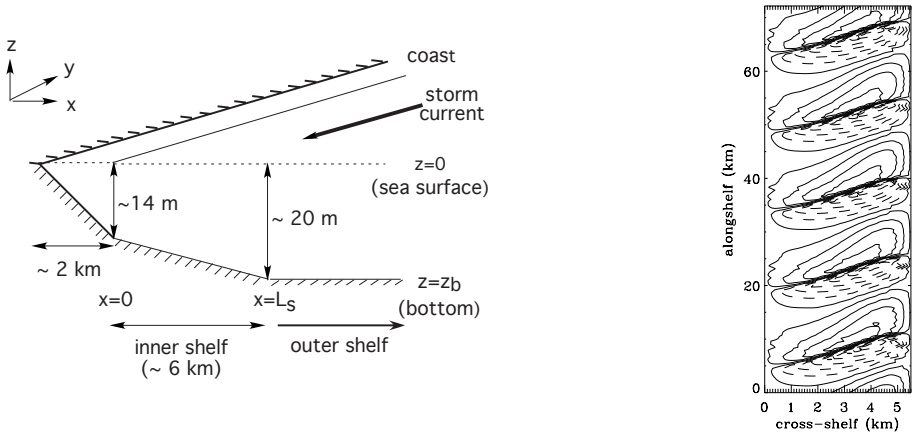

Figure 1: Left: Sketch of a storm-driven inner shelf. The model domain concerns the area $x \geq 0$. Values are representative for the Long Island inner shelf. In the computations a smaller bottom slope of the inner shelf is used. Right: contour plot of the bottom perturbation computed with the nonlinear model, $\sim$ 10000 yr after initial formation. Solid (dashed) contours represent ridges (troughs).

Here 7 subharmonic modes (choice based on field data) are included and the value of the transverse slope of the inner shelf is about 15% of its realistic value (otherwise numerical instabilities occur). The figure shows a contour plot of the bottom perturbation, about 10000 yr after initial formation. This is the fully saturated state in which all modal amplitudes have become constant and the ridges are steadily migrating (velocity of about 5 m yr^{-1}) in the downstream (negative y) direction. The spatial pattern (orientation of the crests, alongshelf length scales, asymmetrical profiles), height and migration speed are consistent with field data. The initially fastest growing has an alongshelf wave-length of about 8 km. The figure shows that in the saturated regime the bottom pattern is dominated by a subharmonic mode with a longer wave-length ($\pm$ 13 km).

The nonlinear model discussed above was used as a tool to study the response of sfcr to sudden interferences. The ridge field shown in figure 1 was taken as the undisturbed reference field.

3 Results

Below results are discussed of the case that sand is extracted from the ridge located between $y = 47$ km and $y = 63$ km. A total amount of $\pm 1.3 \times 10^6$ m^3 of sand was removed from the system. Figure 2 (top left) shows the bed level as a function of the alongshelf coordinate at the centre of the inner shelf immediately after the interference.

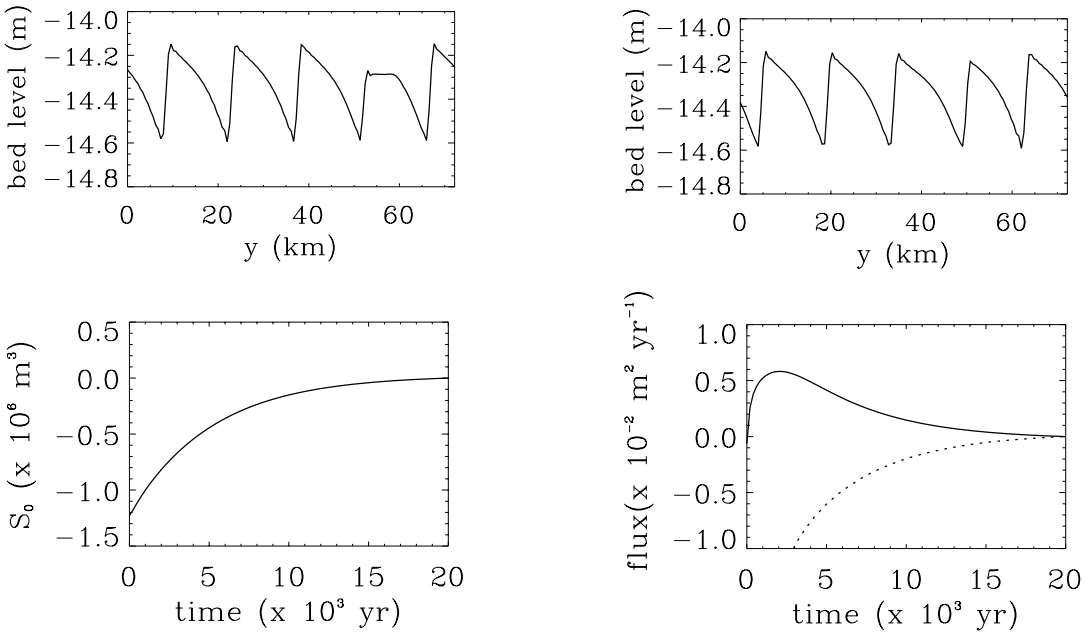

Figure 2: Top: along-shelf transect of the bed level at $x = 3$ km (centre of the inner shelf), immediately after sand extraction (left) and after 1000 yr (right). Bottom left: net sand volume S_0 stored in the inner shelf versus time. Bottom right: net cross-shelf component of the sediment flux induced by the sand extraction at the transition line $x = 0$ between inner shelf and nearshore zone (solid line) and at the transition $x = L_s$ between inner and outer shelf (dashed line).

The upper-right subplot of figure 2 shows the situation after about 1000 yr. It appears that the response of the system is such that it restores to its original situation. Thus the system does not tend to a new equilibrium, which could be present in such a highly nonlinear system. An important implication of the response is that the inner shelf must import sand. This is confirmed by the bottom-left subplot of figure 2 which shows that after the sand extraction the sand volume tends to its original value (corresponding to the undisturbed situation). The adjustment timescale in this case is of the order of 5000 yr, but it becomes shorter if smaller sand volumes are extracted or if larger values of the transverse bottom slope are considered.

The sand needed for the adjustment process is available in both the nearshore zone and the outer shelf. The exchange fluxes at the transitions inner shelf-nearshore zone and

inner shelf-outer shelf are shown in the bottom-right subplot of figure 2. It shows that sand is transferred both from the nearshore zone and outer shelf to the inner shelf, albeit that the largest contribution is from the outer shelf. This result suggests that extracting sand from sfcr has negative implications for the stability of the beach, because it causes a reduction of the sand volume in the nearshore zone.

Similar experiments have been carried out by applying different kinds of interferences, e.g. extracting sand from other ridges, adding sand to ridges and/or troughs and constructing navigation channels. The overall findings are that, at least for the presently studied settings, the system always restores to its original, undisturbed state, by either transferring sand from or to the inner shelf. In case of a sand surplus on the inner shelf almost all of the sand is moved to the outer shelf, so such a surplus has little effect on the stability of the beach.

4 Conclusions

The model results show that the response of sfcr to sudden interferences is such that the system restores to its original state of before the interference. So the natural equilibrium state, describing a field of migrating ridges with constant heights, is quite stable and no indications of the presence of multiple morphodynamic states within the present nonlinear model have been found. This adjustment process requires exchange of sand between inner shelf on one hand and the nearshore zone and outer shelf on the other hand. The net sand exchange is provided by the alongshelf-uniform mode, which is important during the adjustment process only. The response time depends on the amount of sand extracted (or added) to the inner shelf as well as on the transverse bottom slope of the inner shelf and is of the order of centuries. In case of sand extraction sand is transferred both from the nearshore zone and from the outer shelf to the inner shelf. This suggests that sand mining will have negative consequences for the stability of the beach. In case that sand is dumped on the inner shelf most of the surplus volume is transported to the outer shelf and not to the nearshore zone.

Acknowledgements: This work is part of the EU-funded HUMOR project (contract n. EVK3-CT-2000-00037).

References:

Calvete, D., De Swart, H.E, and Falqués, A., A model for sand ridges on the shelf: effect of tidal and steady currents, *Continental Shelf Research*, in press, 2002.

Harris, C.K. and Wiberg, P., Across-shelf sediment transport: interactions between suspended sediment and bed sediment, *Journal of Geophysical Research*, *C107*, 10.1029/2000JC000634.

Trowbridge, J., A mechanism for the formation and maintenance of shore-oblique sand ridges on storm-dominated shelves, *Journal of Geophysical Research*, *C100*, 16071-16086, 1995.

Towards a Modeling System for Long-Term Morphodynamics

ANDRÉ B. FORTUNATO

(National Laboratory of Civil Engineering, Estuaries and Coastal Zones Division, Av. Brasil, 101, 1700-066 Lisbon, Portugal, afortunato@lnec.pt)

ANABELA OLIVEIRA

(National Laboratory of Civil Engineering, Estuaries and Coastal Zones Division, Av. do Brasil, 101, 1700-066 Lisbon, Portugal, aoliveira@lnec.pt)

1. Introduction

A new 2DH coastal area modeling system for long-term morphodynamics, which couples an existing shallow water model with a new sand transport model, is described. We focus on the new model reduction techniques, that minimize computational time: 1) alternatives to the continuity correction, to update the velocity field without running the hydrodynamic model, based on assumptions on the behavior of friction; 2) hydrodynamic results provided in the frequency domain to avoid the concept of a "representative tide"; 3) an adaptive time step for the transport module; and, 4) a new criterion to determine when to run the hydrodynamic model.

2. Modeling system description

The general solution procedure is outlined in Figure 1. The flow field is computed with the finite element shallow water model ADCIRC (Luettich *et al.*, 1991). ADCIRC can harmonically analyze the model results during the simulation, thereby providing the output in the frequency domain (i.e., nodal amplitudes and phases of elevations and depth-averaged velocities). The evaluation of velocities and elevations through harmonic synthesis in the transport model simplifies their interpolation and allows their extrapolation in time, potentially reducing the length of the hydrodynamic simulations.

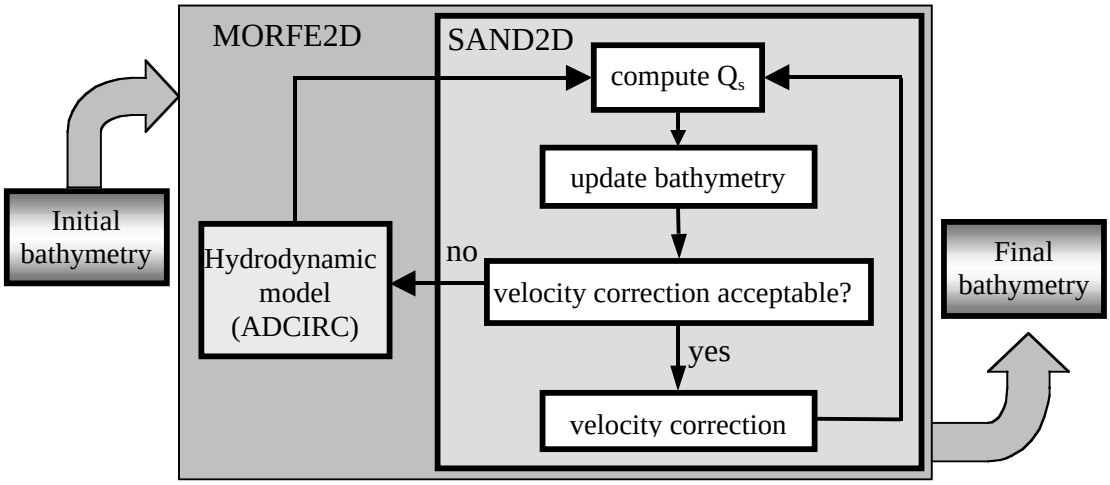

Figure 1: The modeling system MORFE2D: solution procedure.

The morphodynamics is governed by a depth-integrated sediment conservation equation:

$$\Delta h^i = \frac{1}{1-\lambda} \nabla Q_s^{\ i} \tag{1}$$

where i indicates the morphological time step, λ is the porosity and Q_s^i is the sediment flux integrated over the time step Δt_m^i. The morphological time step is taken as an integer number of tidal cycles in order to minimize the variability of Q_s. Equation (1) is solved with node-centered finite volumes, using the hydrodynamic model grid. This approach avoids averaging the bottom slopes, promoting the model stability, and guarantees local mass conservation.

The integration of Q_s^i can be performed with different intermediate time steps at each node since the residual fluxes at each morphological time step Q_s^i are evaluated separately at each location. The use of varying time steps is very useful because the instantaneous fluxes vary strongly both in space and in time. The integration is performed with a fourth-order embedded adaptive Runge-Kutta method, in which the time step is automatically adjusted to meet a user-specified criterion. Because the hydrodynamic model results are provided in the frequency domain, velocities at any time step are accurately interpolated through harmonic synthesis. Since ebb and flood fluxes may compensate each other to a large extent, the tide-averaged flux may be significantly smaller than the peak fluxes. Therefore, the morphological time step is set equal to an integer number of tidal cycles, to minimize the variability of Q_s.

3. Alternative methods for the velocity field update

To avoid calling the hydrodynamic model when bathymetric changes are "small", the velocity field is often updated with the *continuity correction* (e.g., Latteux, 1995), which states that the depth-integrated flow is unaffected by these changes:

$$(u_k^*, v_k^*) = \frac{H_i}{H_k}(u_i, v_i) = R_c(u_i, v_i) \tag{2}$$

where (u_i,v_i) is the depth-averaged velocity evaluated from ADCIRC results at the morphodynamic time step i, and the star represents an estimated value for the morphodynamic step $k>i$. Although this approach is simple and efficient, it produces unrealistically large estimates when the total depth H_k becomes very small.

When depth becomes small, velocities tend to grow only until friction prevents further increase. At this stage, friction dominates over the local acceleration, and the momentum equation becomes a balance between friction and the barotropic pressure gradient. This situation is crucial, because sediment transport occurs primarily where friction is large. Assuming, like in the continuity correction, that the surface elevation is unaffected by the bathymetric changes, the friction term is also unchanged. Mathematically, this *friction correction* is expressed as:

$$(u_k^*, v_k^*) = \sqrt{\frac{c_{fi}H_k}{c_{fk}H_i}}(u_i, v_i) = R_f(u_i, v_i) \tag{3}$$

When H_k tends to zero, R_c tends to infinity while R_f tends to zero. For Manning-type friction formulations, $R_f=(H_i/H_k)^{-2/3}=R_c^{-2/3}$.

As an alternative, the two approximations can be combined in a *mixed continuity-friction correction* as:

$$R_m = \sqrt{R_c R_f} = \left(\frac{c_{fi}H_i}{c_{fk}H_k}\right)^{1/4} \tag{4}$$

While R_m also tends to infinity when H_k tends to zero, it does so more slowly than R_c.

4. Criterion to determine the adequacy of the velocity correction

The criterion to determine when the velocity correction becomes unacceptable is established considering that the errors introduced by the velocity correction should be smaller than those associated with the sand transport formulae. It is usually accepted that sand transport formulae have errors up to 100%, i.e.:

$$\begin{cases} (q_{sn} - q_s)/q_s < 1 & if \quad q_{sn} > q_s \\ 2(q_s - q_{sn})/q_s < 1 & if \quad q_{sn} < q_s \end{cases} \tag{5}$$

where q_s is the exact sand flux, and q_{sn} is the computed flux. We therefore impose that:

$$\begin{cases} (\tilde{q}_{sn} - q_{sn})/q_{sn} < \varepsilon & if \quad \tilde{q}_{sn} > q_{sn} \\ 2(q_{sn} - \tilde{q}_{sn})/q_{sn} < \varepsilon & if \quad \tilde{q}_{sn} < q_{sn} \end{cases} \tag{6}$$

where the tilde indicates a flux where the velocity was updated with a velocity correction, and ε is a user-specified parameter representing the maximum acceptable error introduced by the velocity correction. This parameter should be as large as possible, for computational efficiency, yet small enough to avoid the introduction of errors that are large relative to those introduced by the sand transport formulae. The parameter ε should therefore be between 0.1 and 1.

Considering that sand fluxes are proportional to the cube of velocities, equation (6) can be written in terms of U^3. Also, given the good performance of the velocity corrections, we assume that velocity changes due to local effects dominate over those due to non-local effects, i.e.:

$$\begin{cases} U_i < U_k < U_i R^2 & if \quad R > 1 \\ U_i > U_k > U_i R^2 & if \quad R < 1 \end{cases} \tag{7}$$

where U_i and U_k are the velocity magnitudes computed with the old and new bathymetries, respectively, and R is the velocity correction ratio (R_c, R_f or R_m). Taking only the most stringent conditions necessary to satisfy equation (6), the criterion becomes:

$$(1-\varepsilon/2)^{1/3} < R < (1-\varepsilon/2)^{-1/3} \tag{8}$$

This criterion is similar to that proposed by Latteux (1995) and used in other modeling systems:

$$\left|(H_k - H_i)/H_i\right| < \varepsilon' \Rightarrow (1-\varepsilon')^{-1} > R_c > (1+\varepsilon')^{-1} \tag{9}$$

For ε'=0.1 (a commonly used value), R_c is approximately between 0.9 and 1.1. Taking R=R_c in equation (8) leads to a ε of 0.5-0.6. This value of ε is in the middle of the expected range (0.1-1), confirming the validity of the new approach.

5. Model assessment

The three velocity corrections and the criterion for velocity correction were assessed in the Guadiana, a long and narrow estuary in the south of Portugal, forced mostly by semi-diurnal tides and by river flow at the upstream boundary. Bottom sediments are predominantly sands, with mean diameters of

about 600 μm. The hydrodynamic model was forced by a river flow of 25 m^3/s and tides taken from a regional model. The computational grid has 11,000 nodes, and resolution of the order of 50 m near the mouth.

The three alternative velocity corrections were assessed and compared based on results from two hydrodynamic simulations. The first uses the original bathymetry (run A), while the second uses a bathymetry predicted by an early version of the modeling system after a six-month morphodynamic simulation (run B).

Velocities from run B during one tidal cycle were compared with those predicted using run A and the velocity corrections, at nodes where bathymetric changes were above 1 cm (Table 1). Results indicate that the mixed continuity-friction correction is the most accurate, followed by the friction correction. Average errors (not shown) are all below 1 cm/s, showing that all approximations are unbiased. A similar application to a different estuary confirmed these conclusions. The mixed continuity-friction correction is therefore retained.

	Continuity correction	Friction correction	Mixed continuity-friction correction
Minimum (m/s)	-1.55	-1.31	-0.90
Maximum (m/s)	3.52	1.12	0.76
Std. dev. (m/s)	0.06	0.06	0.05

Table 1 – Assessment of the velocity corrections: differences between model results and predictions.

To test the criterion to determine when the velocity correction becomes unacceptable, the errors associated with the sand transport formulae were estimated by comparing the discrepancies between the bathymetric predictions obtained with different formulae. One-year-long morphodynamic simulations were performed with the van Rijn, Engelund and Hansen, Ackers and White, and Karim and Kennedy sand transport formulae and a very small value for ε (0.1). This value of ε should ensure that the error associated with the velocity correction is negligible relative to the error due to the sand transport formulae. The comparison between the four formulae provides a baseline against which to compare errors associated with larger values of ε.

The results were analyzed based on the absolute difference between the depths predictions for each run and a reference run, scaled by the maximum depth variation during the reference simulation (2.4 m). The simulation with ε=0.1 and the van Rijn transport formula was used as reference. Discrepancies were then plotted against cumulative area fractions (Figure 2), using the elements where bathymetric variations in the reference simulation were larger than 1 cm.

For ε=1.0, the discrepancies associated with the velocity correction and those associated with the Ackers-White formula are similar. Decreasing ε induces roughly proportional reductions in the discrepancies (Figure 2), and increases the computational costs considerably. In practice, the choice of ε should therefore depend on the acceptable accuracy and on the computational costs.

6. Conclusions

The new morphodynamics modeling system presented here includes some innovations that can easily be introduced in similar systems. Among these innovations, the two new velocity corrections to estimate changes in the velocity field associated with small bottom variations were shown to be superior to the traditional continuity correction. In particular, the mixed continuity-friction correction reduced the maximum velocity error by 75% relative to the previous approach. Also, providing hydrodynamic model results in the frequency domain allows for their straightforward extrapolation and interpolation in time. The extrapolation can improve computational efficiency by reducing the duration of the hydrodynamic simulations, while the interpolation is useful if the time steps of the flow

and the sand transport models differ. In particular, this occurs when the transport model uses an adaptive time step to improve computational efficiency, an approach whose feasibility was also demonstrated herein. Finally, we propose a new criterion to determine when to run the hydrodynamic model.

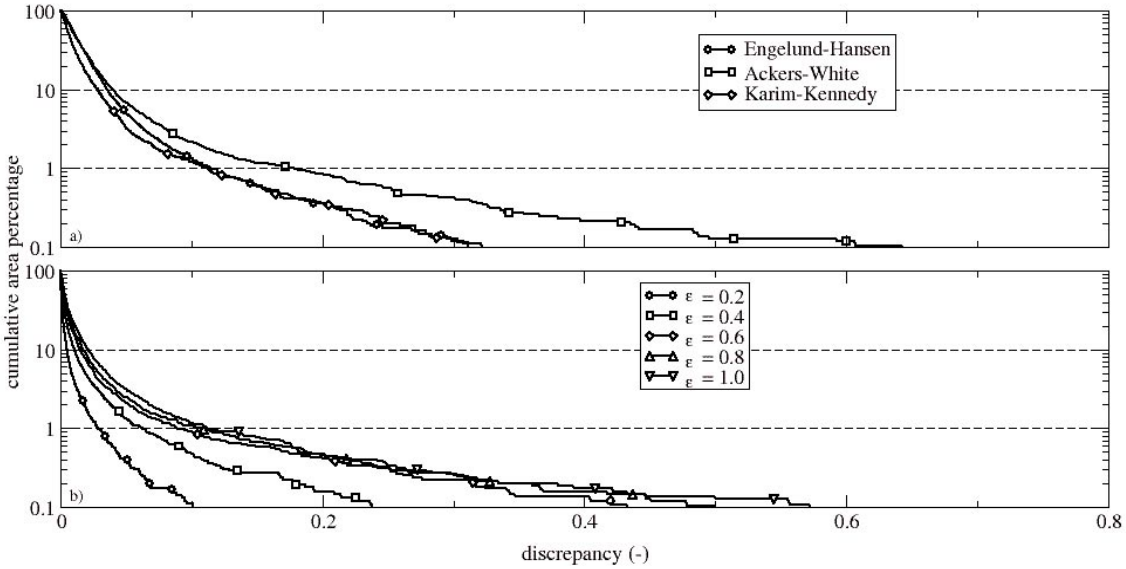

Figure 2 – Assessment of the velocity correction criterion: errors introduced by (a) the sand transport formulae, and (b) the velocity correction.

7. Conclusions

The new morphodynamics modeling system presented here includes some innovations that can easily be introduced in similar systems. Among these innovations, the two new velocity corrections to estimate changes in the velocity field associated with small bottom variations were shown to be superior to the traditional continuity correction. In particular, the mixed continuity-friction correction reduced the maximum velocity error by 75% relative to the previous approach. Also, providing hydrodynamic model results in the frequency domain allows for their straightforward extrapolation and interpolation in time. The extrapolation can improve computational efficiency by reducing the duration of the hydrodynamic simulations, while the interpolation is useful if the time steps of the flow and the sand transport models differ. In particular, this occurs when the transport model uses an adaptive time step to improve computational efficiency, an approach whose feasibility was also demonstrated herein. Finally, we propose a new criterion to determine when to run the hydrodynamic model.

Acknowledgements: This work was sponsored by LNEC, project *Morfodinâmica de Barras*. We thank Drs. R.A. Luettich, Jr. and W.W. Westerink for the model ADCIRC, and Mr. J.P. Fernandes for his assistance with the C-shell language.

References:

Latteux, B. (1995). “Techniques for long-term morphological simulation under tidal action.” *Marine Geology*, 126(1-4): 129-141.

Luettich, R.A., Westerink, J.J. and Sheffner, N.W. (1991). ADCIRC: An Advanced Three-Dimensional Model for Shelves, Coasts and Estuaries. Report 1: Theory and Methodology of ADCIRC-2DDI and ADCIRC-3DL, Department of the Army, US Army Corps of Engineers.

HYDRODYNAMICS AND SEDIMENT TRANSPORT ALONG SOUTH WEST COAST OF INDIA

FELIX JOSE*, N. P. KURIAN AND T. N. PRAKASH

Marine Sciences Division, Centre for Earth Science Studies, Thiruvananthapuram – 31, India

** Present Address: Dept. of Oceanography & Fisheries, University of Azores, PT-9901-862, Horta, Portugal. email: felix-jose@lycos.com*

1. Introduction

Concentrations of heavy sands (also known as black sand or placer deposits) occur along isolated patches along the south west coast of India (Mallik et al., 1987). The Chavara deposit extends for a length of 22.5 km as a barrier beach is the prominent one and the deposit is continuously being exploited for its commercial utilities. Though many studies are available on the distribution and other characteristics of these heavies, no significant effort has been made to study their transport and sorting processes in the innershelf with reference to the hydrodynamic processes. In this paper we have studied the seasonal transport characteristics of innershelf sediments along the Chavara coast and its resultant effects on the enrichment of heavy sand along the adjoining beaches.

2. Area of Study

The area of study (Fig. 1) is a stretch of the southwest coast of India encompassing Kollam and extending from Paravur in the south to Kayamkulam in the north. This coast is noted for a sharp change in the shoreline orientation from 290^{o} N to 350^{o} N at Thangassery headland. Change is also reflected in the bathymetry and bottom sediment characteristics. The innershelf south of Thangassery is steeper when compared to the northern zone. The Kallada River is a major river system debouching sediments into the Astamudi Kayal, which opens into the sea at Neendakara.

The shallow water wave regime in the study area is derived from deep-water wave data using a wave transformation model (Kurian et al., 1985). The deep-water wave data is compiled and supplied by National institute of Oceanography (Chandramohan et al., 1990). For preparation of bathymetric grid, the navigational charts for the area published by Naval Hydrographic Office are used. Also, the bathymetric data collected during the course of the study are used for fine scale computations.

3. Field Measurements

Waves and coastal currents are measured during the monsoon and post-monsoon seasons. Wave measurements are carried out using a wave gauge installed at a station 700 m offshore with a depth of 5 m. Current measurements using an S4 current meter are carried out at 1 m above the seabed during the months of May, September & December 1995 in a fixed location of water depth 11 m. Wave data are also collected from other wave monitoring programmes executed in the adjoining coastal locations. The textural and mineralogical characteristics of the beach and innershelf sediments are also studied for the different seasons.

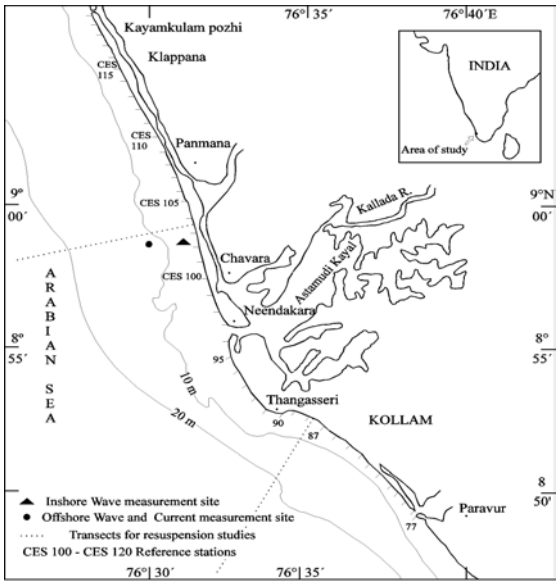

Fig. 1 – Study area

4. Sediment transport characteristics

Wave induced sediment re-suspension characteristics are studied by numerical computations. The threshold criteria for initiation of motion of different types of bed sediments of the region is given in Table 1. Monazite, the densest mineral, needs the highest shear stress and velocity for the initiation of motion whereas Quartz, the lightest needs less shear stress for its motion. Though Garnet has least density among the heavies studied, the initiation of motion characteristics is similar to the denser ones owing to its coarser size. The lightest Quartz also needs a comparable higher threshold shear stress owing to its coarseness. The percentage of exceedance of the threshold conditions for the initiation of motion of individual heavy minerals are also computed for the different seasons. The zone of re-suspension extends up to a distance of approximately 50 km from shore during the monsoon season.

Table 1- Threshold criteria for initiation of motion of different types of bed sediments along the Chavara coast

Name of heavy sand	Density Kg/m^3	Size (mm)		Threshold criteria	
		Mean	Median	Velocity (cm/s)	Shear stress $10^{-2}kgm^{-1}s^{-2}$
Monazite	5120	0.165	0.165	22.7	31.62
Ilmenite	4750	0.179	0.171	22.1	29.64
Zircon	4600	0.154	0.154	20.5	28.04
Rutile	4220	0.173	0.165	20.1	26.74
Garnet	4000	0.232	0.233	23.0	27.45
Quartz	2650	0.342	0.344	20.6	20.46

5. INNERSHELF SEDIMENT TRANSPORT

For the innershelf sediment transport studies, Soulsby (1991) and Grant and Madsen (1982) models, representing the two modes of transport viz; suspended load and a combined effect of bed load and suspended load, are used.

5.1 Inputs to the Model

Coastal Currents

The time series current measurements for the months of May, September and December 1995 are used for the sediment transport computations. The current observations are also presented as time series plots as well as alongshore and across shore components. The relative dominance of the different speed-direction components has been studied using the polar plots. During the onset of the southwest monsoon, in May, the onshore dominance of the monsoonal current regime along the coast is well manifested. During the fag end of the monsoon season, in September, the mean value of the current is 3.0 cm/s and the mean direction is southerly. The direction of the coastal current gives an indication of the persistent upwelling during the monsoon season. Also, during this period the dominance of monsoonal currents are impeded by the tidal components. From the polar plots it is inferred that the current directions are clustered in almost all the orientation.

Wave data

The wave data for the month of May are collected from Hameed et al., (1995). The zero crossing period ranges between 8-12 seconds with skewness towards lower values. The significant wave height shows a range of 1.25-2.0 m. These high waves can influence the bottom sediments, which results in the resuspension of sediments even in deeper waters. The measured wave data for the month of December shows that waves are long period with a significant wave height of 0.47-0.75 m. Because of the long periods, the waves can feel the bottom in deeper waters also. Due to lack of consistent time series wave data corresponds to the current measurement periods, the sediment transport computations are carried out with representative waves for the corresponding seasons.

Shelf sediments and bed characteristics

The bed and sediment characteristics of a coast are also discerning parameters in the computation of the sediment transport. The bottom bed form characteristics, viz, ripple height and length, which are still unknown for this coast, are assigned the values 7 and 20 cm respectively, after a comparison with similar coasts else where with identical wave and current regime. Also the sand entrainment coefficient and the bottom bed porosity are assumed to be 0.00025 and 0.65 respectively. The references in this regard were collected from Mathew (1997).

Transport Computations

The computed sediment transport rates are presented as time series plots along with other bottom frictional parameters. The Soulsby's model is applicable for a strong wave and current environment. Since Chavara coast comes under the moderate energy zones, the wave effect is dominant when compared to current. However, the simultaneous effect of wave and current results in bed load and suspended load transport of sediment along this coast. The Grant and Madsen (1982) model gives convincing transport estimates for the region. All the transport rates are computed for the quartz sediment with a mean size of 0.3422 mm. The transport rates computed using the two models for different seasons are discussed in the paper.

6. Conclusions

The wave and coastal current regime of the Chavara coast and its seasonal variability are discussed. The initiation of motion characteristics of the individual bed sediments are also computed. The innershelf sediment transport rates are estimated using different theoretical models. The wave data compiled from different sources as well as from the field measurements and measured current data are used for the computations. The sediment transport rates computed for the coast show variations between the measurement periods. Onshore-offshore transport computations for the monsoon season give a maximum transport rate of 0.028 g $cm^{-1}s^{-1}$ in the southerly direction with an onshore component. The dominant onshore-offshore transport during monsoon with a component towards coast helps in the transport of heavy sand from the submerged palaeo beaches in the offshore. During this onshore transport the individual sediments undergo different sorting processes, which ultimately results in the enrichment of heavies along the beaches. Also, the persistent erosion of the barrier island coupled with the seasonally reversing longshore sediment transport helps in the enrichment of heavy sand along the beaches.

Acknowledgements: The authors are thankful to Dr. M. Baba, Director, Centre for Earth Science Studies for all the support and encouragements for this work. FJ is thankful to CSIR, New Delhi, for the award of a Fellowship. The Financial support provided by the Department of Science and Technology, Govt. of India, under the project 23/159/92 is gratefully acknowledged.

References

Chandramohan, P., Kumar, V.S., Nayak, B.U. and Anand, M., "Wave Atlas for the India Coast". National Insitute of Oceanography, India, 1990.

Grant, W. D. and Madsen, O.S., "Combined wave and current interaction with a rough bottom." Journal of Geophysical Research, 84, 1797-1808, 1979

Kurian, N.P., Baba, M., and Hameed, T.S.S., "Prediction of nearshore wave heights using a refraction programme" Coastal Engineering, 9,347-356, 1985

Soulsby, R.L., Sediment transport by strong wave-current flows. Proc. Coastal Sediments' 91. American Society of Civil Engineers, Seattle, Washington, 405-417, 1991.

Mallik, T.K., Vasudevan, V., Verghese, P.A. and Terry Machado, The black sand placer depoits of Kerala Beach: southwest India. Marine Geology, 77, 129-150, 1987.

Some Aspects of Hydodynamic and Morphodynamic Modelling in Tidal Flat Areas

INGO JUNGE, HELGE HOYME, WERNER ZIELKE

(Institute for Fluid Mechanics and Computer Applications in Civil Engineering, Appelstr. 9A, D-30167 Hannover, Germany, junge@hydromech.uni-hannover.de)

1. Introduction

The prediction of morphological evolution in coastal zones is among the most important tasks of coastal engineering. The attempt to explain and predict morphodynamic processes in the Wadden Sea leads to a complex research field with various unresolved problems. Tides, waves and wind are the main cause for the relocation of sediment. A numerical model is able to consider only a limited number of physical processes, and the selection can be difficult due to the different spatial and time-scales and the interaction of processes. Tidal flat areas are very demanding on numerical models because one must consider the alternating tidal currents together with moving boundaries and open boundaries at the sea.

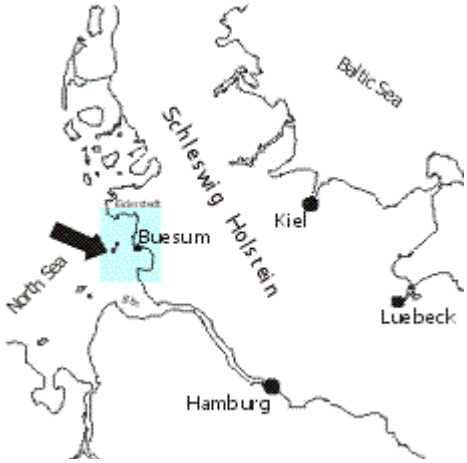

Figure 1. Location of the study area

Since January 2000, the Project PROMORPH deals with morphodynamic modelling with the final aim of predicting medium-term coastal morphology changes. The selected area of investigation is the Meldorf Bight located in the Wadden Sea in the State of Schleswig-Holstein, Germany.

Participants in the project are the Institute of Fluid Mechanics and the Institute of Meteorology of the University of Hannover, the Institute of Geology and Paleontology of the University of Kiel, the Research and Technology Centre West Coast in Büsum and the GKSS Research Centre in Geesthacht. The objective of this research is the coupling of climate models, wave models, hydrodynamical models, sediment transport, and morphodynamic models. An extensive on-site measurement program has been carried out in order to calibrate and validate the single models. These measurements (waves, water levels, currents, water properties, sediment properties, sediment transport, morphology, and meteorology) provide the opportunity to study multi-dimensional tide effects in selected parts of channels and their influence on sediment movement. Furthermore the high-resolution data give detailed information on formation and relocation of sandbanks and flooding processes on intertidal flats. This is remarkable because such detailed measurements are rarely available for other comparable areas.

This paper presents results of flow simulations in comparison with field measurements. Experiences of morphodynamic modelling in tidal flat areas in the Meldorf Bight are also provided.

In the context of the project different numerical models are used. All presented results in this paper were carried out with TELEMAC-2D and 3D numerical models developed at the Laboratoire National d'Hydraulique of Electricité de France, EDF *Galland*, [1991], Hervouet, [1992]

2. Open Sea Boundary Conditions and Nesting

The application of numerical models requires the declaration of conditions at the open model boundaries. Water levels or other hydrodynamic conditions that are needed to drive the simulations can be artificial, measured or computed values. A direct model forcing with measured data is only possible if enough measurements are available at the model boundary locations for the periods to be

simulated. Model boundaries then have to be placed near the measurement devices (water level gauges, etc.). This disadvantage of limited freedom in defining locations of model boundaries and arbitrary time periods is overcome by model nesting. Models are nested or coupled into larger models which turn over simulated boundary data at locations of smaller model boundaries.

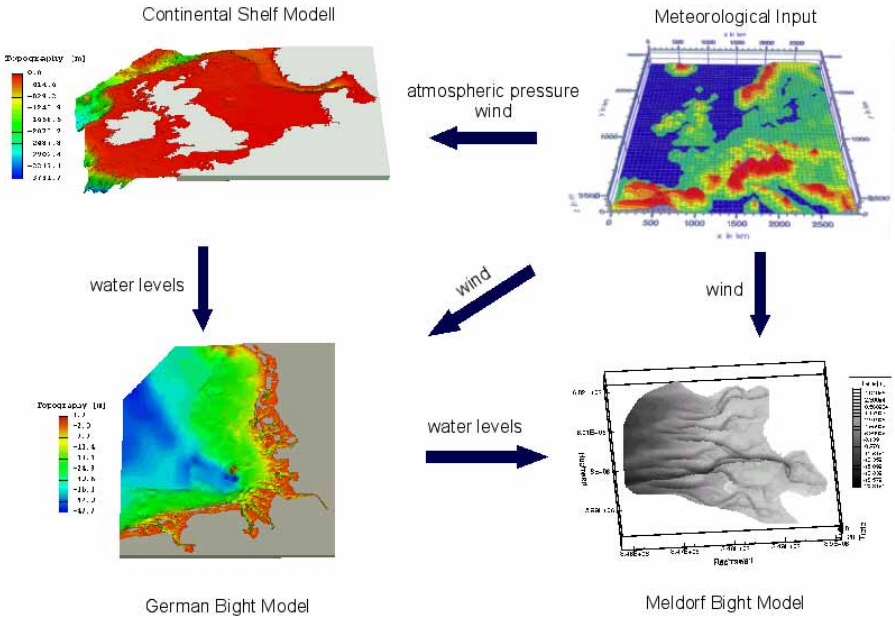

Figure 2: Model Nesting

The whole nested model family is shown in Figure 2. The free surface of the hydrodynamical models are calculated using a meteorological input, like wind data from *DWD* [2000], other projects like PRISMA *Luthardt* [1987] or meteorological models. The large model called CSM (Continental Shelf Model) *Verboom* [1987] covers the north-west European Continental Shelf area with grid spacing of about 9 km. It was developed at Delft Hydraulics in the Netherlands. The German Bight Model (GBM) *Stengel* [1994] is nested into the CSM. At the open boundaries of the GBM water levels are obtained from the CSM. PRISMA wind and pressure fields are used for meteorological forcing. In a last step the GBM generates the water levels for the boundary of the Meldorf Bight model which covers the investigation area.

3. Morphodynamic Modelling

The hydrodynamic behaviour within the investigation area can be efficiently reproduced by the above-mentioned Finite Element Model Telemac 2D, with consideration of the influence by wind and waves, *Zielke* et al., [2002]. The calculated vertically depth-averaged currents provide the input for the morphodynamic modelling. Therefore the modelling system TELEMAC contains a morphologic model named SISYPHE. In the context of the project PROMORPH for the aim of medium-term morphodynamic modelling a neap-spring tidal cycle was chosen. This cycle takes about 30 days and is split into 30 parts, each with a duration of 24 hours. For every 24 hours the hydrodynamic system values are computed by Telemac 2D. Afterwards a morphological computation with the flow field is carried out. This morphological computation is repeated up to seven times, so we receive a morphological time scale of seven days. Because of this strategy the saving in computational time is very high and also boundary conditions containing storm events are usable.

Figure 3 show sedimentation-erosion plots covering the entire model area respectively for the observed and modelled bathymetries. The plots are based on the differences in metres between final and initial bathymetries (observed: 1995/6 – 1990).

The simulation results (right) were obtained using the neap-spring simulation presented above and a total load formulation following *Engelund-Hansen* [1967].

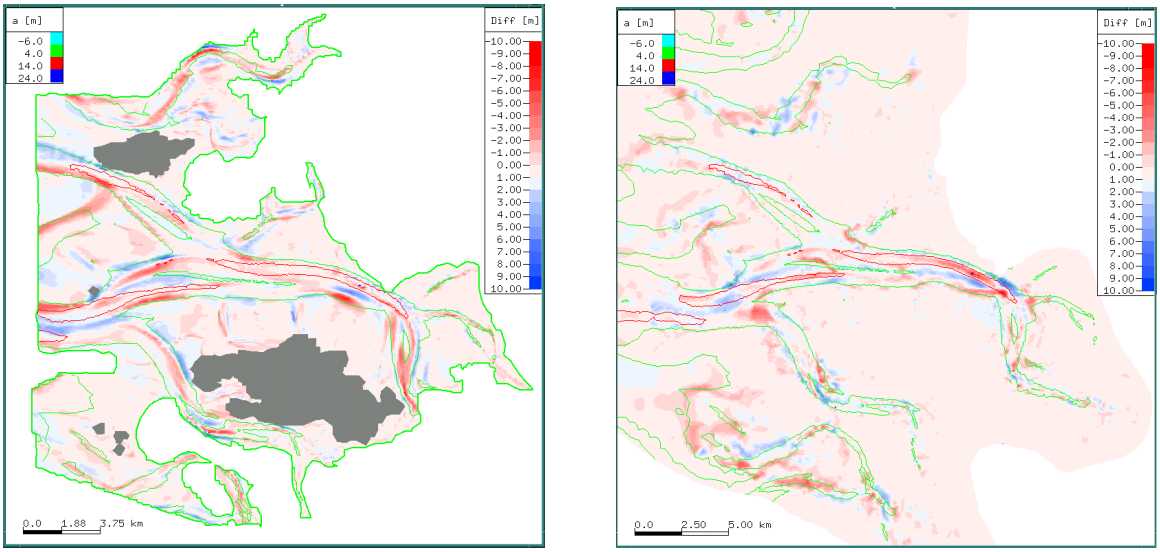

Figure 3: Observed (left) and modelled (right) sedimentation and erosion in meters between 1990 and 1995/6

In comparison with the measurements, many areas can be detected where the simulation shows the same tendencies as the measurements (for example near Büsum, westerly of D-Steert, south of Tertius, and the erosion of the Marner Plate easterly of Trischen). The minima and maxima of the erosion and accretion are the same as the measurements show.

4. 3D-Effects

The evaluation of morphologic simulation results, calculated with two dimensional models leads to the question to what extent 3D-effects impair the accuracy of these results, Cayocca [2000]. For example a ADCP measurement transection in the Norderpiep is displayed in Fig 4 (left). Simulation results in Fig. 3 show in this region explicit differences from the measurements. The main ebb currents measured during a measurement campaign by the FTZ- Büsum in December 2000 show in 1.5 and 12.0 m depth significant differences in their flow direction, see Fig. 4 (right). During the flood period this effect is only slightly recognized.

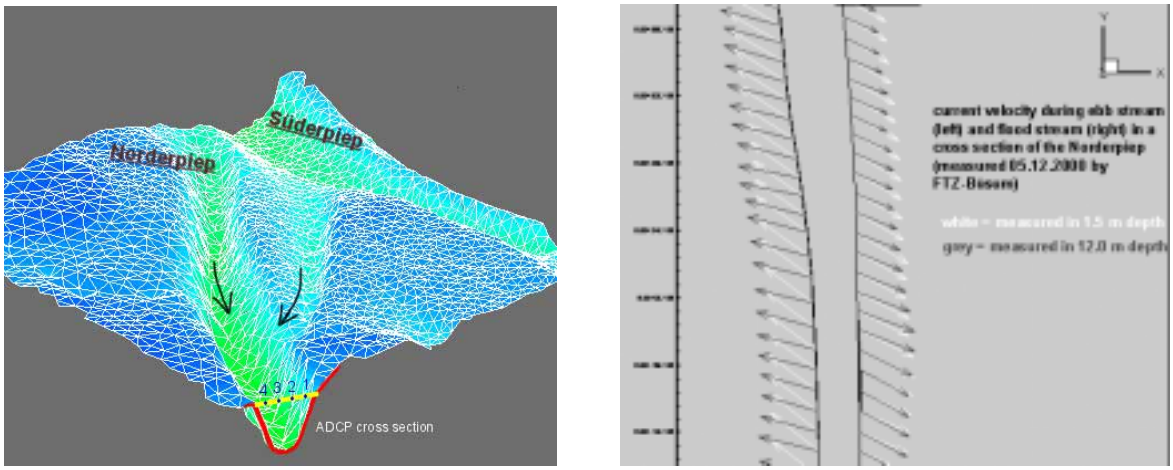

Figure 4: Measurment transection in the Norderpiep (left), currents in 1.5 m and 12.0 m depth during ebb and flood stream (right)

This behaviour is caused by the southern influx from the shallow channel into the deeper Norderpiep. The wind influence does not have an effect, because of a predominantly wind from north-west direction during the entire measurement campaign. In the same way the impact of curvature-induced secondary flows are not responsible. Following a formulation of *Engelund* [1974] the driftage of currents due to the impact of curvature-induced secondary flows can be roughly estimated at 2 degree under given conditions. Generally this effect has no significant influence in tidal flat areas. Thus it can be assumed that the driftage of currents near the surface result solely from the inflow of the lateral channel. Fig. 5 shows the difference of current directions near the bottom and the surface for an entire tidal cycle at four different points in the measurement cross section. It is obvious that during the main ebb stream the difference of current directions between the two levels can obtain angles between 15 and 30 degree whereas during flood period the values decrease to a maximum of 15 degrees. It can be noticed that the driftage of currents in different depth levels occur during a morphologic main active period. Around slack water the difference of current directions increase, but impact to the morphodynamic is not significant due to the low magnitudes of velocities (see Fig. 5). This complex hydrodynamic behaviour can also be recognized in results of other measurement campaigns.

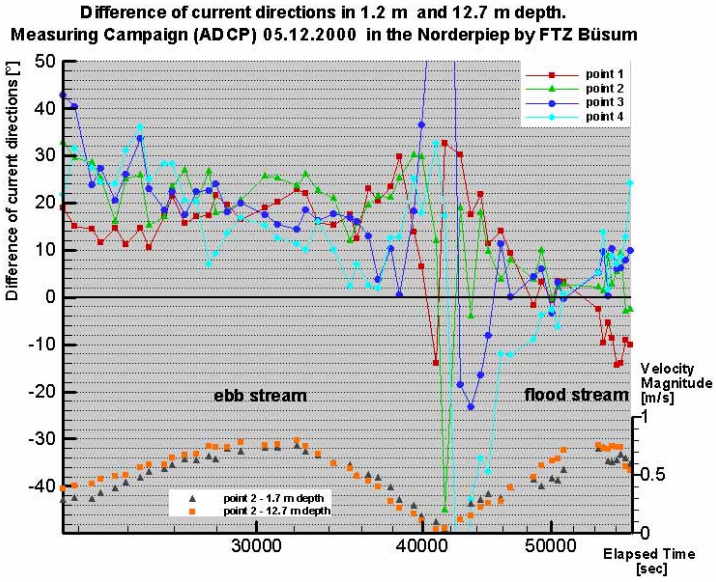

Figure 5: Difference of current directions near the bottom and the surface during a tidal cycle

First simulations with a 3D –finite element model (Telemac 3D) show that a high model discretization in vertical direction is required to reproduce the complex flow characteristic in this cross section. A higher resolution of the model leads on the other hand to an increasing computation effort and quickly in unfeasible limitations. Therefore it is necessary to examine how far small-scale flow effects affect the results of long-term morphologic simulations.

According to *Zielke* et al.,[2002] the tidal flats in the inner parts of the Meldorf bight are structured internally by gullies and tidal creeks. Taking these phenomena into account, further refining of the spatial model discretization is required. Due to the enormous computational effort this is impossible with three-dimensional models at present.

5. Conclusions

A 2D-morphodynamic model has been developed in view of carrying out medium-term simulations in the Meldorf Bight on the German Wadden Sea. Results of an ad hoc simulation over a period of five years has reproduced many characteristics and trends of observed morphodynamic behaviour. Further validation of the model against measurement data are currently in process to improve the predictive

qualities of the model. In this context the influence of small-scale three-dimensional processes and the possibility to set up a more refined modelling is presently being verified.

References

Cayocca, F., 2000. Long-term morphological modelling of a tidal inlet: the Arcachon Basin, France. Coastal Eng. 42, 115-142

DWD, 2000. Quaterly Report of the Operational NWP_Models of the Deutscher Wetterdienst. 1. September bis 30. November, No. 25, www.dwd.de

Engelund, F., Hansen, E., 1967. A Monograph On Sediment Transport in Alluvial Streams. Tekniks Forlag, Copenhagen, Denmark

Engelund, F., 1974. Flow and bed topography in channel bends. J. Hydr. Div., ASCE, 100(11):1631-1648, 21.1.3, 21.1.4, 21.2.4

Galland, J.-C., Goutal, N., Hervouet, J.-M., 1991. TELEMAC A new numerical model for solving shallow water equations. Adv. Water Resources, 14 (3), 138-148.

Hervouet, J.M., 1992 A two dimensional finite element system of sediment transport and morphological evolution. Computational Methods in Water Resources IX, Computational Mechanics Publications, Boston

Luthardt, H., 1987. Analyse der wassernahen Druck- und Windfelder über der Nordsee aus Routinebeobachtungen. Diss., Hamburger geophysikalische Einzelschriften, Reihe A, 83, FB Geowissenschaften, Uni Hamburg

Stengel, T., 1994, Änderungen der Tidedynamik in der Deutschen Bucht und Auswirkungen des Meeresspiegelanstiegs. Diss., Bericht Nr.38, Institut für Strömungsmechanik und Elektronisches Rechnen im Bauwesen, Uni Hannover

Verboom, G. K., Dijk, R.P. van, Ronde, J. G. de, 1987. Een model van het Europese Kontinentale Plat voor windopzet en waterkwaliteitsberekeningen. Rijkswaterstaat-Dienst Getijdewateren Waterloopkundig Laboratorium, GWAO-87.021,Z96.00

Zielke W. et al, 2002. Promorph - Prognosis of Medium-Term Coastal Morphology. - Interim Report 2001, Institut für Strömungsmechanik und ERiB, Universität Hannover

"Data analysis of sand waves"

Michiel Knaapen, (*Department of Civil Engineering, University of Twente, P.O. Box 217, 7500 AE Enschede, The Netherlands* , m.a.f.knaapen@ctw.utwente.nl)
Ruud van Damme, (*Faculty of Mathematical Sciences, University of Twente, P.O. Box 217, 7500 AE Enschede, The Netherlands* , r.m.j.vandamme@math.utwente.nl)
Suzanne Hulscher, (*Department of Civil Engineering, University of Twente, P.O. Box 217, 7500 AE Enschede, The Netherlands* , s.j.m.h.hulscher@ctw.utwente.nl)

1 Introduction

Little is known about the 2 dimensional patterns formed by sand waves. The available sand wave models (For example *Hulscher* [1996]; *Komarova and Newell*, [2000]; *Fredsøe, J., and Deigaard* [1992]) are based on analyses including only one horizontal dimension. Most data analyses so far been limited to rough estimates of the mean wavelength and height of the sand waves, in general based on human interpretation of 1 dimensional profiles.

To get better insight in the characteristics of the sand waves, the authors present an approach to get detailed information on the sand wave characteristics. This automated approach is based on the classical analysis of profiles, to determine the crest and trough, from a profile and deduce the height and length from bed level and positional differences, respectively. However, this approach is now applied on 2 dimensional data sets measured using multibeam echosounders.

The approach is applied on data from the entrance channel to IJmuiden harbour (see section 2) and near Noord Hinder, both situated in the North Sea. From these data the crests and troughs are determined in section 3. From the positions of the crests and troughs information is retained on the height and length of the sand waves. Finally, this information is analysed in section 4.

2 Determining the crest and troughs of sand waves

Using multibeam echosounders the sea bed has been measured over areas of 1 by 5 kilometre. Using a straightforward linear interpolation, these data are then stored in a regular grid with a spacing of 5 m. Figure 1 shows the bathymetry resulting from measurements near the entrance channel to IJmuiden Harbour. The accuracy of the data is high. Measurements and interpolation result in errors with a standard deviation less than 20 cm in the vertical, and about 1 m in the positioning. Most of the latter is a systematic error related to the DGPS positioning system and as such unimportant to this analysis.

The resulting bed levels are now analysed row by row. A low pass wavelet filter is used to reduce the noise caused by ripples and mega ripples. All remaining local maxima are related to the crests, while the sand wave troughs correspond to the local minima. Thus, the positions of crests and troughs can be determined easily from the gradients in the profiles.

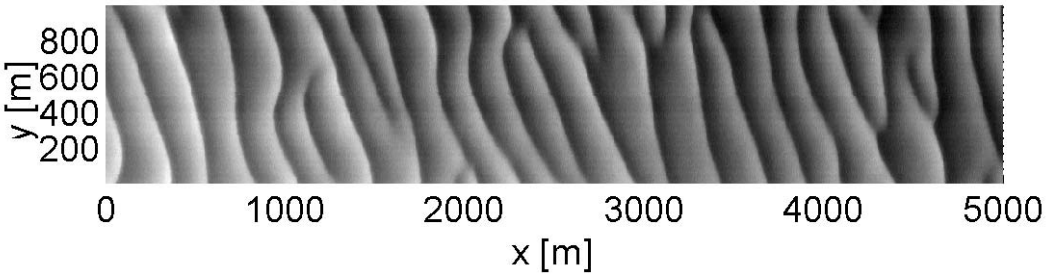

Figure 1: Sand waves as measured using a multibeam loading. The depth rages from 30 m (dark) to 25 m (light). The principal tidal direction is parallel to the horizontal axis.

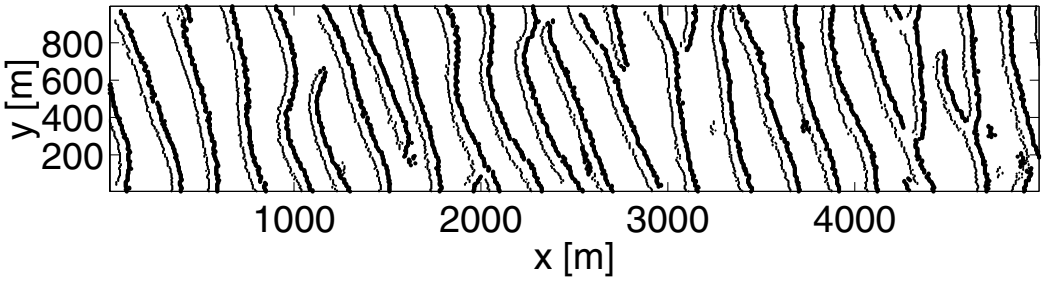

Figure 2: The troughs (wider lines) and crests (narrower lines) of the measured sea bed.

3 Characteristics of the sand waves

The main characteristics of sand waves, height and wavelength, can now be analysed in detail. The wavelengths are estimated using the spacing between two consecutive crests as well as the spacing between the troughs. This length value is then labelled with a position that is exactly halfway the crests (or troughs). Finally the resulting values are interpolated to a regular grid with a spacing of 25 m.

In general, the height of a wave is defined as the difference between a crest and a through. However, using this definition every crest (and trough) would be related to two height estimates. To avoid this, an extra step is used. The levels and positions of the crests and troughs are interpolated to the regular grid. The resulting values can be assumed to be the envelopes of the sand waves, similar to the envelope used in amplitude evolution models (*Komarova and Newell*, [2000]). The height is then determined by the difference between the higher and lower envelope.

4 Evaluation of the analysis

The Height of the sand waves (figure 4) is fairly regular, decreasing from about 3 m in the south ($x = 0$) to 2 m in the north of the area($x = 5km$) The dark spots, showing very low sand waves, coincide with the pitchforks of the sand waves.

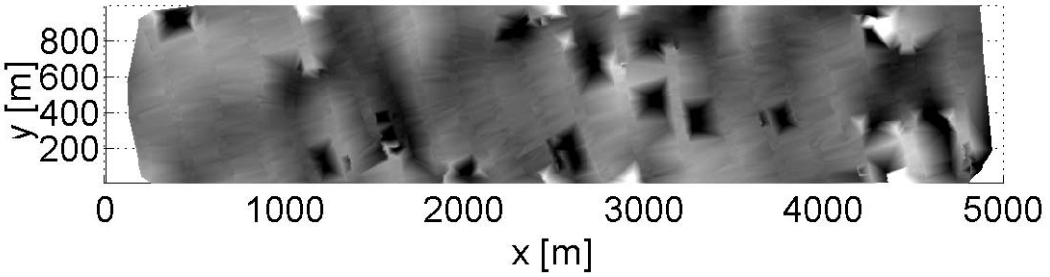

Figure 3: The wavelength distribution of the sand waves, values range from 100 (dark) to 400 m(light). Note that the distortions near the edges result from lack of information.

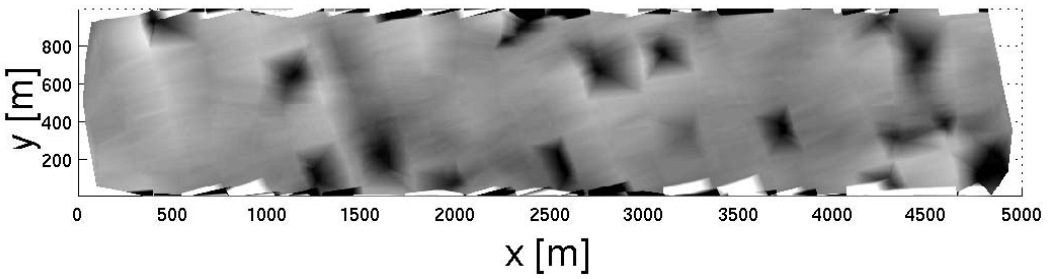

Figure 4: The height distribution of the sand waves, values range from 0 (dark) to 3 m(light). Note that the distortions near the edges result from lack of information.

The wavelength shows some rhythmicity with the wavelength varying from 350 to 400 m, with the pitchforks (again the dark spots) mostly present in areas with larger wavelengths. Apparently, in these areas the wavelength gets critically long resulting in splitting of the waves to reduce this length.

Acknowledgments: The research described in this paper is partly funded by the Technology Foundation STW, applied science division of NWO and the technology programme of the Ministry of Economic Affairs (TCT-4466). The bathymetric measurements are carried out in the framework of the Delft Cluster project Eco-morphodynamics of the seafloor

References:

Fredsøe, J., and Deigaard, R., *Mechanics of Coastal Sediment Transport*, Institute of Hydrodynamics and Hydraulic Engineering, Technical University of Denmark, 1992.

Hulscher, S.J.M.H., 1996, Tidal-induced large-scale regular bed form patterns in a three-dimensional shallow water model, *Journal of Geophysical research*, *101*, no.c9, 20727-20744.

Komarova, N.L. and Newell, A.C., Nonlinear dynamcis of sand banks and sand waves, *Journal of Fluid Mechanics*, *415, 285-312, 2000.*

Sand extraction and finite amplitude tidal sandbanks

Pieter C. Roos, (*University of Twente, Faculty of Engineering, P.O. Box 217, 7500 AE Enschede, The Netherlands*, p.c.roos@ctw.utwente.nl)

Suzanne J.M.H. Hulscher, (*University of Twente, Faculty of Engineering, P.O. Box 217, 7500 AE Enschede, The Netherlands*, s.j.m.h.hulscher@ctw.utwente.nl)

1 Introduction

Nowadays, the North Sea is used by man for a wide variety of purposes, such as navigation, fishery, sand mining, oil and gas extraction. Some of these activities are accompanied with morphological changes at the sea bed, e.g. navigation dredging, the creation of sand extraction pits or a locally subsiding sea bed due to gas mining. Besides these human influences, the seabed itself is dynamic, which results in the presence of rhythmic features, such as tidal sandbanks, sandwaves, megaripples and sand ripples. These dynamics are – despite considerable advances – not yet fully understood. As a result, the morphological fate of e.g. an offshore sandpit is hard to predict, as it may interfere with the natural dynamics of the seabed.

2 Offshore tidal sandbanks

In the present study we focus on sand extraction in relation to the largest of the patterns mentioned above: tidal sandbanks or, according the classification by *Dyer & Huntley* [1999], open shelf ridges. They can be up to 80 km long, and typically average 13 km width and tens of metres in height (*Dyer & Huntley* [1999]). The stability properties of equilibrium sandbank patterns are likely to be crucial in the study of the morphological consequences of offshore sand extraction. In the past, linear analysis (*Huthnance* [1982a], *De Vriend* [1990] & *Hulscher et al.* [1993]) have shown that the flat seabed is inherently unstable against small bottom perturbations and sandbank patterns are likely to develop. The underlying hydrodynamic mechanism, tidal rectification, is described in detail by *Loder* [1982], Zimmerman [1982], *Pattiaratchi & Collins* [1987] and the review by *Dyer & Huntley* [1999]. Limitation of the linear theory is that it does not contain a saturation mechanism which determines the final shape and height of the banks. In the present study we therefore investigate the finite amplitude behaviour of the linearly most unstable mode. We note that our approach differs from the nonlinear part of the study by Huthnance [1982a], with respect to both hydrodynamics (role of $k = 0$-mode) and sediment transport (we consider also suspended load).

3 Model ingredients

Analogously to *Huthnance* [1982a], *De Vriend* [1990] and *Hulscher et al.* [1993], we consider an offshore part of the seabed and we assume a topography that varies in one direction only, say $h = h(x)$.

The model consists of a hydrodynamic module, a sediment transport module and a seabed update module. The hydrodynamic part describes tidally forced shallow water flow, both in the cross-bank direction x and the along-bank direction y. We include Coriolis effects, adopt a linear friction law and apply a rigid lid. The hydrodynamic equations are solved on the 'fast' tidal timescale t, in which tidal flow is represented as the average of two steadily forced flows in opposite directions, inclined at an arbitrary angle θ with the direction of topographic variations. Sediment transport is modelled as both bedload and suspended load, the former as a power of the depth-averaged flow velocity with a bedslope correction, the latter satisfying an advection-diffusion equation with the entrainment modelled as a power of the depth-averaged flow velocity. The seabed evolves on a 'slow' morphodynamic (tidally averaged) time scale τ as a result of divergences in the bedload flux, and the net difference between deposition and entrainment of suspended matter. Slope effects on suspended load transport are taken into account (see e.g. *Talmon et al.* [1995] and *Parker* [1978]).

4 Solution method

The model is solved using a pseudospectral Fourier approach, where we consider a one-dimensional box of length $2\pi/k_{\mathrm{fgm}}$ in which k_{fgm} is the wavenumber of the linearly most unstable mode. Furthermore we set the tidal flow angle accordingly at $\theta = \theta_{\mathrm{fgm}}$. Next, we expand the state of the system is as a sum of Fourier modes, truncated at the M-th superharmonic of the FGM and including the $k = 0$-mode. We consecutively derive the cross-bank flow velocity, the along-bank flow velocity, the sediment transport. Finally, the morphodynamic time-stepping is implicit in the linear terms and explicit in the nonlinear ones. Typical values of the numerical parameters are: $M = 20$, $\Delta\tau = 0.01$.

5 Results

Numerical experiments, starting from a flat seabed with a small perturbation show the following behaviour: (i) exponential growth of the FGM according to the linear theory, (ii) growth and deformation of the result of nonlinear mode interactions, (iii) saturation towards equilibrium profiles, that express a balance between drag and slope effects on sediment transport. The equilibrium shapes strongly depend on the type of transport: bedload transport leads to sharply peaked profiles that touch the water surface, whereas suspended load gives banks with flattened crests taking up 90% of the (undisturbed) water column. Even though the former profile touching the water surface is obviously unrealistic, the tendencies of both bedload and suspended load appear to agree qualitatively with observations of flat crests in shallow water and sharp crests when water is deep enough to limit wave effects (*Dyer & Huntley* [1999]).

It turns out that, as the bank grows, the increased friction experienced by the flow diverts the spatially uniform part of the flow in the along-bank direction. Hence, the cross-bank flux is reduced by frictional effects, with the Coriolis force affecting the spatially uniform part of the along-bank flux. Note that, in the nonlinear part of his analysis, Huthnance [1982a] kept the cross-bank flux constant. In contrast with the present study, this effectively requires the tidal forcing to be adjusted continuously to the changing

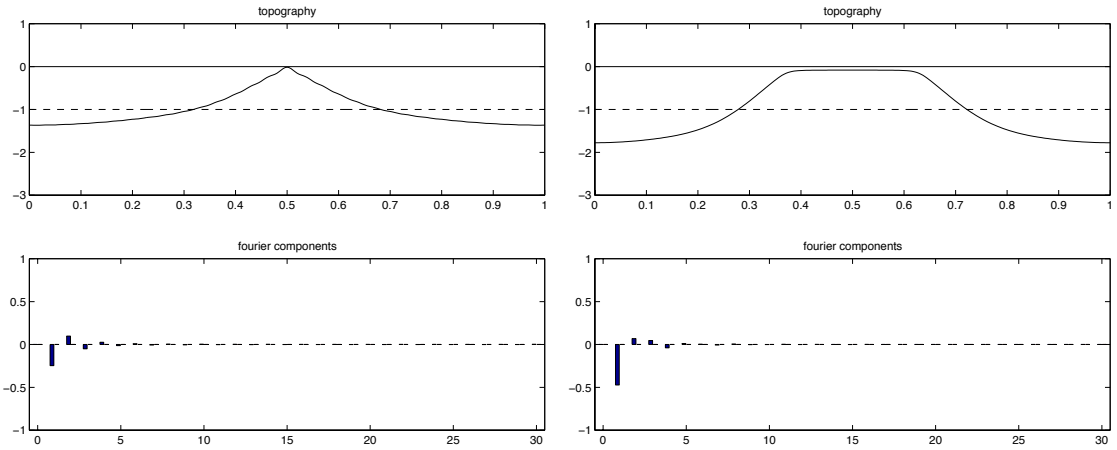

Figure 1: Typical equilibrium profiles as a function of normalized horizontal coordinate x/ℓ_{fgm} (with ℓ_{fgm} the FGM-wavelength) for bedload (left) and suspended load transport (right). The solid line shows the equilibrium bed profile, the dashed line the undisturbed water depth, whereas the bars (bottom) indicate the corresponding Fourier components.

friction conditions.

6 Conclusions and outlook

The main result of the present study is the existence of finite amplitude sandbank equilibria. This finding sheds new light on the process-based modelling of offhore morphodynamics, in relation to human intervention such as sand extraction. The stability properties of the actual North Sea morphology namely determines the consequences of sand extraction in a sea where sandbank patterns are present. Other topics for future research are therefore the stability properties of the obtained equilibria (both with respect to subharmonic and superharmonic perturbations), but also the ramifications of extending this model to two-dimensional topographies $h = h(x, y)$ (which enables e.g. a comparison with *Huthnance* [1982b] and the characteristics analysis by *De Vriend* [1987]). Moreover, a comparison with North Sea bathymetric data will be useful to compare the qualitative findings of the present idealized model with reality. This will be the first step towards providing practical recommendations, concerning the – morphodynamically speaking – optimal locations for sand extraction, relative to the sandbank pattern.

Acknowledgment: This research was carried out within the EU-project HUMOR, contract number EVK3-CT-2000-00037.

References:

De Vriend, H.J. Analysis of Horizontally Two-dimensional morphological evolutions in shallow water. *J. Geophys. Res.* **92**, 3877-3893, 1987.

De Vriend, H.J. Morphological processes in shallow tidal seas, in *Residual currents and long term transport, Coastal and estuarine studies, vol. 38,* edited by R.T. Cheng, 276-301, Verlag, 1990.

Dyer, K.R., & D.A. Huntley. The origin, classification and modelling of sand banks and ridges, *Cont. Shelf Res.* **19**, 1285-1330, 1999.

Hulscher, S.J.M.H., H.E. De Swart & H.J. De Vriend, The generation of offshore tidal sand banks and sand waves, *Cont. Shelf Res.* **13** (11), 1183-1204, 1993.

Huthnance, J.M., On one mechanism forming linear sand banks, *Est. Coast. and Shelf Science* **14**, 74-99, 1982a.

Huthnance, J.M., On the formation of sand banks of finite extent, *Est. Coast. and Shelf Science* **15**, 277-299, 1982b.

Loder, J.W. Topographic rectification of tidal currents on the sides of Georges Bank. *J. Phys. Ocean.* **10**, 1399-1416, 1982.

Parker, G. Self-formed straight rivers with equilibrium banks and mobile bed. Part 1. The sand-silt river. *J. Fluid Mech.* **89**, 109-125, 1978.

Pattiaratchi, C., & M. Collins, Mechanisms for linear sandbank formation and maintenance in relation to dynamical oceanographic observations, *Prog. Oceanog.* **19**, 177-176, 1987.

Talmon, A.M., M.C.L.M. Van Mierlo & N. Struiksma, N. Laboratory measurements of the direction of sediment transport on transverse alluvial slopes. *J. Hydr. Res.* **33**, 495-517, 1995.

Zimmerman, J.T.F., Dynamics, diffusion and geomorphological significance of tidal residual eddies, *Nature* **290**, 549-555, 1981.

Morphodynamic behaviour of the Meghna Estuary in the northern Bay of Bengal

MUSTAFA ATAUS SAMAD

(Department of Civil and Environmental Engineering, University of Western Ontario, London, Ontario, N6A 5B9, Canada, msamad@uwo.ca)

M. MAHBOOB-UL-KABIR

(Surface Water Modelling Centre, House 476, Road 32, New DOHS, Mohakhali, Dhaka 1206, Bangladesh, muk@swmcbd.org)

MIR HAMMADUL AZAM

(Externally Funded Office for Research and Science, UAE University, Al-Ain, UAE, mirazam@hotmail.com)

HITOSHI TANAKA

(Department of Civil Engineering, Tohoku University, Aoba 06, Aoba ku, Sendai 980-8579, Japan, tanaka@tsunami2.civil.tohoku.ac.jp)

1. Introduction

The Bengal delta is one of the largest and most active deltas in the world comprising three of the great rivers in Southeast Asia, the Ganges, the Brahmaputra and the Meghna Rivers. Drainage from huge catchments of these rivers takes place through a single outlet, the Meghna estuary, to the Bay of Bengal (Figure 1). The estuary consists of a number of deltaic islands, generally densely populated, and exposed to extreme meteorological and hydrological conditions.

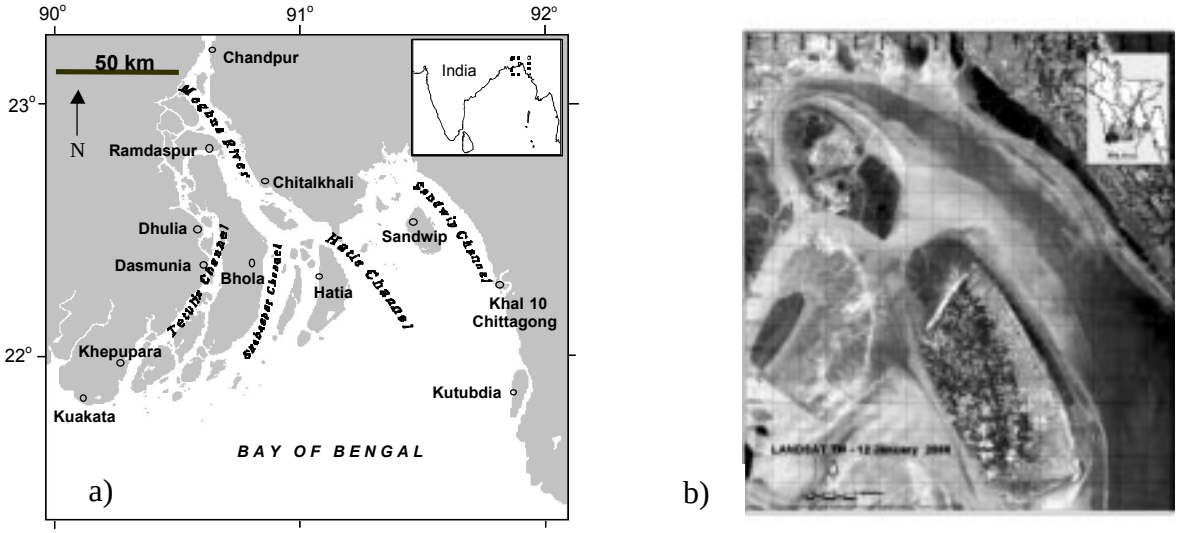

Figure 1: a) Meghna estuary and location of major islands in the northern Bay of Bengal; and b) LANDSAT image of the study area around Sandwip on January 12, 2000

The lower-Meghna River carries one of the highest amount of sediment load (*Coleman* [1969]) and flow discharges (*Milliman and Syvitsky* [1992]) to the Bay of Bengal. The tidal range varies from an extreme of over 6.0m in the eastern part of the estuary to about 2.0m in the west (*Samad et al.* [2001]). Although the influence of waves could not be quantified precisely, generally a wave height in excess of ~1.0m can be observed during monsoon in the eastern part. Tropical cyclones formed during pre-

and post-monsoon periods cause severe cyclonic surges resulting in widespread flooding and possibly in considerable redistribution of sediment in the estuary. Over the years although accretion in the estuary saw extinction of some of the channels, severe erosion affected most of the islands, especially Sandwip, Hatia and Bhola.

In the present study the morphodynamic behaviour of the estuary, with emphasis on Sandwip Island located in the east, has been analysed. The analysis has been based on satellite images, recent bathymetric and sediment measurements and on the results form a two-dimensional hydrodynamic model of the Bay, developed by Surface Water Modelling Centre (SWMC) (*SWMC* [2001]). It was observed that unlike other islands in the Bay, Sandwip is eroding in the south and west and depositing in the north. The erosion pattern in the west is governed by the interaction of tidal currents and river inflow, and in the south by monsoon waves. The residual circulation around the island is believed to be responsible for transporting the eroded materials and depositing in the north.

2. Recent Morphological Development

The lower-Meghna River provides over 10^9 tons of sediment annually to the Bay of Bengal. Recent studies have shown that the delta is prograding (*Allison* [1998] etc.), although previous researchers reported relative shoreline stability in the Bengal basin (*Coleman* [1969] etc.). It is estimated that (*Goodbred and Kuhel* [1999]) about 30-40% of the total sediment load is deposited in the river system and its flood plains with the remaining transported to the sea. *Kudrass et al.* [1998] estimated only about 20% of the total sediment load depositing in the submarine delta annually with the rest (~ 40%) moving further to the offshore depocenters bypassing the sub-aqueous delta. The large amount of sediment trapped in flood plains and riverbeds along with those bypassing the delta-front resulted in slow progradation rate of the sub-aqueous delta. However, while the net change in the estuary is relatively small, individual islands present in the estuary undergo considerable changes in its sub-aerial shapes even at an annual time-scale.

Recent shoreline position data obtained from satellite images (1973-2000) indicate relatively higher morphological activities in the estuary especially in the region between Hatia and Sandwip (Fig.2). Except in the case of Sandwip, erosion in the estuary mainly takes place along the lower-Meghna river and in the northern tip of the islands. Considerable deposition can be observed along the central-mainland region and along the southern part of the islands. In case of Sandwip the phenomenon is reversed; while severe erosion has been observed along the west and the south coast, heavy sedimentation resulted in the development of huge land areas attached to the north of the island.

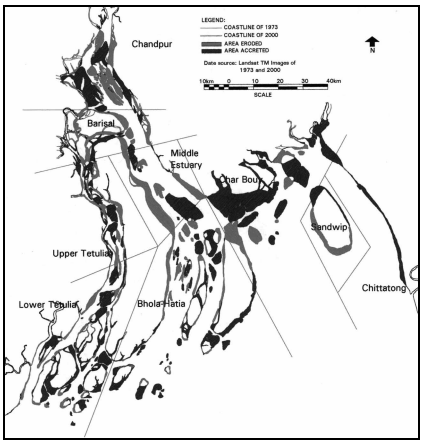

Figure 2: Erosion and deposition patterns between 1973 and 2000 (after *MES* [2001]).

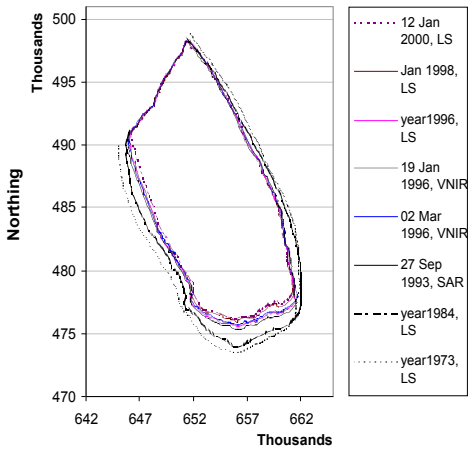

Figure 3: Shoreline position around Sandwip in different years (1973,'84,'93,'96,'98 and 2000).

Figure 3 shows shoreline positions of Sandwip island obtained from satellite images from 1973, 1984,

1993, 1996, 1998 and 2000. As can be observed, during this period the island has undergone considerable erosion along its western and southern coasts with average annual erosion rates exceeding 65m and 80m respectively. The east coast has maintained relative shoreline stability. Considerable land has accreted in the north somewhat offsetting the net erosion effect over the island (Fig.2). Development in the north, however, has not been included in this analysis mainly due to the uncertainties in defining the extent of inter-tidal flat under extremely high tidal range (~6.0m) present in this area.

3. Factors Affecting Morphological Processes

Change in morphological development around the island and erosion of its shoreline is governed by the relative importance of river inflow, tidal forcing and wave actions etc. *Samad et al.* [2001] has indicated a trapped residual tidal circulation around Sandwip. This interacts with the tidal currents, amplified due to shallow and wide bottom topography, to produce a complex flow pattern between Sandwip and Hatia islands.

The coastal profiles along Sandwip have been studied from measured bathymetry data collected during 2000. Figure 4 shows the cross-shore profiles along the west, east and the south coastlines at selected locations. It can be seen that a deeper channel section prevails along the west coast forming a sharp cliff-like formation (Fig.4.a). The channel is mainly governed by the tidal current flowing in the north-south direction and eroding the coastline through erosion of the channel bed. The freshwater flow during monsoon through the north Hatia Channel pushes the tidal channel eastward causing more erosion in the Sandwip coast.

In the east the profiles follow a gentle convex shape representative of a muddy cohesive coast (Fig.4.b). Morphological change in the east coast is more governed by characteristics of the tidal volume in the Sandwip channel. Such that the cross-sectional properties as well as the coastline position along this coast has not changed considerably over the period of data availability. In recent years it shows trends of accretion in the south and central parts, which can be related with increasing erosion pattern along the south coast and with decreasing freshwater flow through the north Hatia channel.

In recent years the south coast showed the most severe erosion in Sandwip. Unlike that of the west, majority of its eroded materials remained in place forming a shallow pool just off the coast (Fig.4.c). This can clearly be identified from the satellite images. Formation of 'berm' observed in the profiles is probably indicative of wave breaking in this region. In the absence of any wave measurement this was compared with the results from near-shore spectral wave modeling carried out during the study. Model results indicated that the significant wave height during monsoon could be of the order of 2.0m close to the south coast. The estimated wave height is in general agreement with the cross-shore profile presented in Fig.4.c

Increased erosion due to wave action in the south may also indicate reduced influence of fresh water flow through the north Hatia channel that may result in northward progress of the breaker line. Also this may have considerable influence on residual circulation resulting in significant morphological development in a relatively shorter time span. The hydrodynamic model results have indicated a similar declining flow ratio through the north Hatia channel (*SWMC* [2001]).

The development of the new land in the north of the island is probably favoured by the sediment supply from the eroded coasts in the south and the west. The rapid development through deposition generally follows the time with increased erosion in the south coast. The sediment brought into suspension moved to the north due to the residual circulation and deposited at areas with relatively smaller tidal currents between the islands of Sandwip and Urir Char.

4. Conclusions

The morphodynamic behaviour of the Meghna estuary has been investigated based on satellite images, bathymetric survey and sediment sampling data, and the results from a two-dimensional

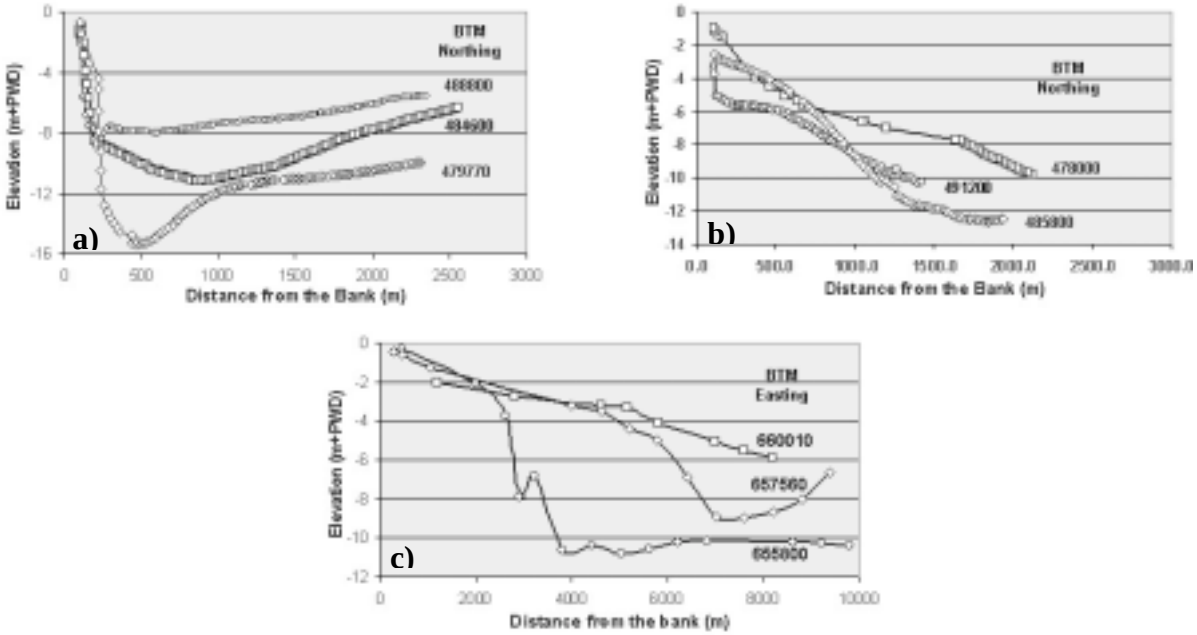

Figure 4: Cross-shore profile along Sandwip coast at selected locations from bathymetry data surveyed in 2000; a) west coast, b) east coast, and c) south coast

hydrodynamic model of the Bay of Bengal. The study was especially concentrated around the Sandwip island located northeast in the Bay. Although the estuary is prograding with a relatively smaller rate, islands in the estuary could be affected due to erosion or deposition even in an annual time scale. Although the islands are eroding at the north and depositing in the south, Sandwip shows an opposite trend. Analysis of collected data indicate that while the erosion in the west coast is mainly due to strong tidal current, erosion in the south is due to monsoon waves. The properties of tidal wedge in the Sandwip channel are responsible for relative stability of the east coast.

Acknowledgments: The authors gratefully acknowledge the contribution from Nissan Science Foundation, Japan for partially supporting the study.

References:

Allison, M.A., Geologic framework and environmental status of the Ganges-Brahmaputra delta, *J. Coast. Res.*, *14*(3), 826-836, 1998.

Coleman, J.M., Bhrahmaputra river, channel processes and sedimentation, *Sed. Geol.*, *3*, 129-239, 1969.

Goodbred, S.L. and S.A. Kuehl, Floodplian processes in the Bengal basin and the storage of Ganges-Brahmaputra river sediment: an accretion study using ^{137}Cs and ^{210}Pb geochronology, *Sed. Geol.*, *121*, 239-258, 1998.

Kudrass, H.R., K.H. Michels, M. Wiedicke and A. Suckow, Cyclone and tides as feeders of a submarine canyon of Bangaldesh, *Geol.*, *26* (8), 715-718, 1998.

Milliman, J.D. and J.P.M. Syvitski, Geomorphic/tectonic control of sediment discharge to the oceans: The importance of small mountainous rivers, *J. Geol.*, *100*, 525-544, 1992.

Samad, M. A., H. Tanaka, M. H. Azam and M. Mahboob-ul-Kabir, Flow and Salinity Modelling in the Meghna Estuary, Bangladesh, *Proc.* 8^{th} *Int. Sym. Flow Modeling and Turb. Measurements*, Tokyo, Japan, 2001. (in press)

SWMC, *Maintenance of 2-D general model of the Meghna estuary*, Dhaka, Bangladesh, 2001.

Evolution of sand waves in the Messina Strait, Italy

VINCENZA CINZIA SANTORO

(Department of Civil and Environmental Engineering, University of Catania, Viale A. Doria, 6 – 95125 Catania, Italy. Ph: +390957382707. Fax: +390957382748. email: csantoro@dica.unict.it)

ELENA AMORE

(Department of Civil and Environmental Engineering, University of Catania, Viale A. Doria, 6 – 95125 Catania, Italy. Ph: +390957382711. Fax: +390957382748. email: eamore@dica.unict.it)

LUCA CAVALLARO

(Department of Civil and Environmental Engineering, University of Catania, Viale A. Doria, 6 – 95125 Catania, Italy. Ph: +390957382711. Fax: +390957382748. email: lcavallaro@dica.unict.it)

MASSIMO DE LAURO

(GEOMARE SUD, INSTITUTE OF CNR, VIA A. VESPUCCI, 9 – 80143 NAPOLI, ITALY. FAX: +390815979222. PH: +390815979211. EMAIL: DELAURO@GMS.01.GEOMARE.NA.CNR.IT)

Abstract

In the present paper the morphodynamics of sand waves in the Messina Strait, Italy, is analysed, through a comparison between data gathered during two different surveys carried out in 1991 and 2001 respectively. Particularly a morphometric analysis on the most recent data and a qualitative analysis of the differences in time between bed-form patterns, have been carried out. As a result, it was observed that the planimetric configuration of the field has not changed during the considered ten years, i.e. crest orientation and wavelength practically coincide. On the opposite, wave height has significantly grown; an explanation of such a change, based on a comparison with a theory based on a linear stability analysis of ripple formation, is provided, as a possibility.

1. Introduction

Sand waves are regular patterns in marine non-cohesive bottoms mainly caused by tidal currents, characterized by a wavelength of the order of few hundreds meters and a height of five to ten meters. Besides their intrinsic interest from a geophysical point of view, these sedimentary structures are deeply studied because of their engineering relevance, mainly related to their evolution in time (see, for example, Freds↵e and Deigaard, 1993; Hulsher, 1996; Blondeaux et al., 1999; Gerkema, 2000). As a matter of fact, translation and reorientation of such bed-forms can cause severe problems to buried pipelines and/or cables, as detected in the Messina Strait (Italy) during several bathymetric campaigns. In particular, it was observed that sand waves exist there in three different areas (Santoro et al., 2002). The attention of the present paper has been focused on the area lying outside the northern part of the Messina Strait in order to detect their morphodynamics.

2. The study area

During several bathymetric campaigns, three areas have been identified in the Messina Strait (Italy) as sand waves fields and have been studied by some of the writers within a wide research program. The first area (area no. 1 in figure 1), lying just outside the northern part of the Messina Strait, was investigated in 1991 for a new gas pipeline; southward, sand waves in the second area (area 2 in figure 1), have been detected through measurements taken in 1979 for sake of designing a bridge crossing; a third area, going beyond the Sill, in front of Messina (area no. 3 in figure 1), was investigated during a survey made in 1992 for a tunnel crossing design. The attention of the present work has been focused

on area no. 1, also by the light of a new measurement campaign carried out in 2001 by the present research group.

The area under study lies, then, in the south-eastern part of the Tyrrenian Sea, between Sicily and Calabria regions, in particular in the southern part of the Scilla Valley, a narrow U-shaped channel, WSW-ENE directed, with depth ranging between 150 and 400 m; the Valley has rough steep flanks (10° northward - 30° southward) and a smooth bottom where the sand waves exist. In the area under study depth varies between 200 m and 240 m. In spite of its relatively small dimensions, the Strait of Messina is nevertheless of particular importance since it is characterised by irregular hydrodynamic conditions. It is possible to observe very high marine current velocities as well as an exceptionally developed semidiurnal tidal current (over 220 cm/s on average). Combined with other factors of meteoclimatic and oceanographic nature the total current velocity can reach 500 cm/s (10 knots), though it is rare and occurs in isolated areas only.

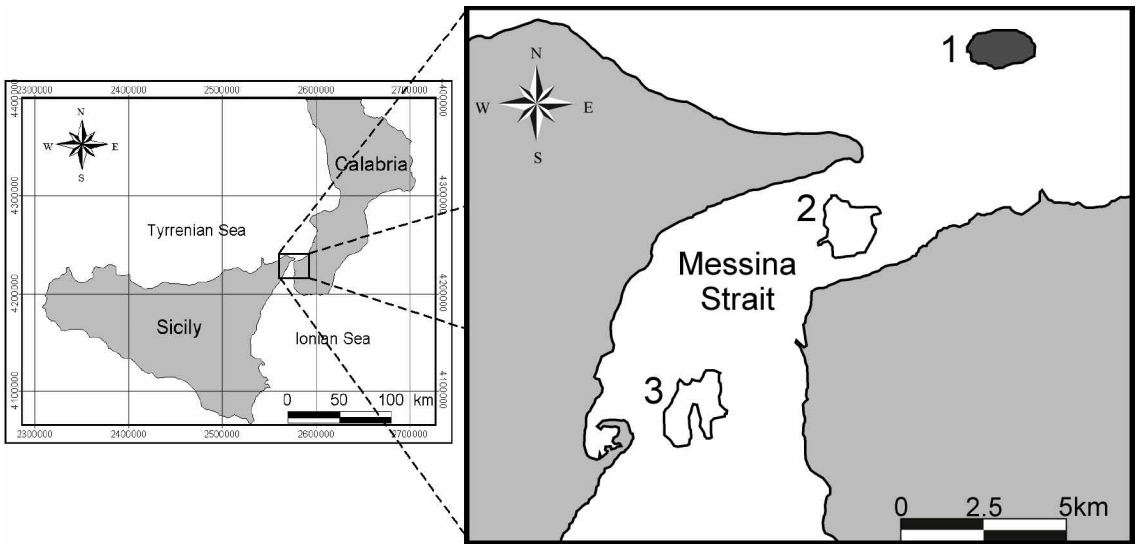

Figure 1: Location of the study area (the coordinates are referred to Gauss-Boaga system). In the zoomed frame, the areas where sand waves were detected during different surveys are shown.

2.1 The survey of 1991

In 1991 within an investigation campaign for a new gas pipeline crossing, a bathymetric survey was carried out using echo-sounders both from the sea surface and mounted on a ROV, the latter in order to improve the quality of data, particularly on steep slope bottoms. Results of measurements show that sand waves extend for approximately 850 m in the W-E direction, verge to N-NW and show megaripples on the current-prone side, which verge transversally. Their crests are discontinuous and slightly diverging westward. Furthermore, both in the western and in the eastern side megaripple fields exist.

During the survey, an existing pipeline, which in the past had been laid on the sea-bed, was seen to be suspended among two successive crests (i.e. partially floating with respect to the bottom), thus proving the bed-forms had changed their geometry in time. Sandy and gravelly sediments are present with a relative density Dr = 80-100 % and a friction angle of 40°, lying on a 5 m deep rocky sublayer.

In the survey, also climatic and oceanographic characteristics were measured. In particular, with reference to tidal currents, the stations recorded the highest values approximately at 0° N, ranging between 1.2 and 1.4 m/s.

2.2 The survey of 2001

In collaboration with Geomaresud – CNR, the Department of Civil and Environmental Engineering of the University of Catania carried out a bathymetric campaign on 09/27/2001.

A 100 kHz Multibeam Echosounder (MBES) System was used, which measures the relative water depth over a wide area across a vessel's track.

The maximum selectable scale is 1400 m; however, maximum measuring span typically occurs at water depth of 150 m. At depths grater than 150 m, accurate bottom surveys are still possible, but with a corresponding decrease in measuring width. The echosounder covers an area on the sea bottom that is 150° wide across the track by 1.5° along the track. The area consists of 101 individual 1.5° by 1.5° beams, with a bottom detection range resolution of 3.7 cm. The most external beams at depths greater than 200 m have been excluded through filter processing. Measurements were carried out on a 5m x 5m grid, chosen on the basis of the beam projection, that is about 5 m.

3. Data analysis

In order to perform a detailed comparison between data gathered during different surveys, all kinds of available data (i.e. cartographic, hydrodynamic and geomorphological) were georeferenced through a Geographical Information System. In particular, maps of bathymetry were used to determine sand wave orientation and to extract 13 bottom profiles, approximately perpendicular to sand wave crests. Profiles were tracked over a DTM grid (cells 5m x 5m) obtained on the basis of the two campaign databases through IDW interpolation method. Figure 2 shows profiles tracks as obtained from the two campaigns.

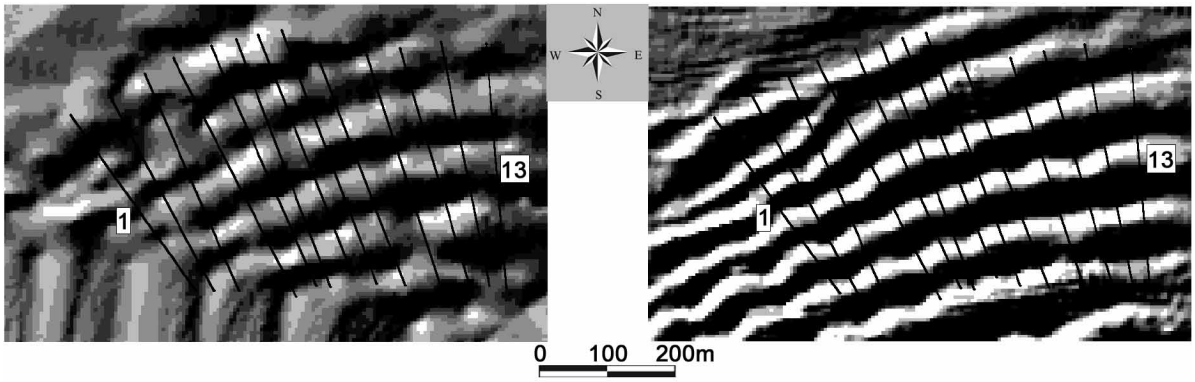

Figure 2: Profile tracks: (a) 1991 survey; (b) 2001 survey.

3.1 Morphometric analysis

Analysis of profiles has been performed by first eliminating the mean slope, which was estimated through a least-squares method. Then, a traditional zero up-crossing method used in oceanography for determining wave characteristics has been here adopted in order to obtain sand wave morphometry. Values of average wavelength (L), wave height (H), and steepness (s) for each profile are reported in table 1.

It can be noted that for sand waves detected during the 1991 survey there is a likely low effect of flow separation(s ranges between 0.01 and 0.02); on the contrary for those detected during the 2001 survey this effect is significant, so that it can influence hydrodynamic characteristics.

Table 1: Sand wave geometric parameters as detected during the two campaigns.

Profile	1991 survey			2001 survey		
	H (m)	L (m)	s = H/L	H (m)	L (m)	s = H/L
1	0.71	56.15	0.013	2.46	55.58	0.044
2	1.67	114.62	0.015	2.93	61.23	0.048
3	1.18	79.65	0.015	1.98	62.48	0.032
4	1.29	77.48	0.017	3.49	75.45	0.046
5	1.44	75.22	0.019	2.84	73.63	0.039
6	1.04	77.03	0.013	2.57	76.44	0.034
7	2.08	80.20	0.026	4.16	81.19	0.051
8	1.48	84.16	0.018	3.54	82.18	0.043
9	0.96	80.75	0.012	2.44	81.19	0.030
10	2.14	103.22	0.021	3.26	83.11	0.039
11	2.27	87.17	0.026	3.50	85.18	0.041
12	1.63	84.96	0.019	3.59	87.39	0.041
13	1.52	93.36	0.016	3.70	93.81	0.039

3.2 Comparison between field measurements

The examined sand wave fields, as obtained from measurements taken in 1991 and in 2001, show surprisingly similar planimetric patterns, in the sense that the position and the orientation of their crests practically coincide. As a conclusion, it must be noted that wavelength in the field corresponds to an equilibrium value, as also stated by the results of the application of a hierarchic theory (Amore et al., 2002).

On the contrary, wave height has changed, in the sense that it has significantly grown in time. As an example, the old profile, together with the new one, along track no. 7, is shown in Figure 3, being such a track representative of any of the other ones. In fact, as it can be noted in Figure 3, trend laws for both campaign profiles are almost equal. An explanation could be found supposing the validity of an analogy between sand wave and rolling grain ripple (O 10 cm) formation, as provided by Blondeaux (1990). The mentioned theory is based on a linear stability analysis of a flat sandy bottom subject to a viscous oscillatory flow. If sand waves form according to a mechanism similar to the one of rolling grain ripples, then their wavelength corresponds to the most unstable component of bottom perturbation which triggered their formation.

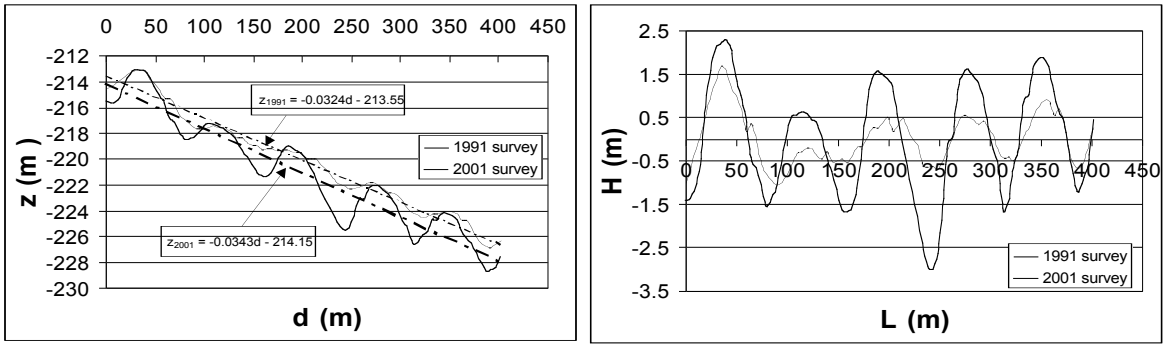

(a) (b)

Figure 3: Example of bottom profile as gathered in the two field campaigns: (a) original form with trend laws; (b) de-trended profile.

4. Conclusions

In the present work the results of two surveys carried out ten years from each other, aimed to recover sand wave characteristics, have been presented. In particular, a data comparison regarding sand wave geometry showed that, surprisingly, their position remained the same; indeed the only detected

changes regard bed-form height which increased about twofold. This also implies a dramatic change in sand wave steepness, which, in turn, seems to influence the hydrodynamics. In fact, assuming an analogy with wave generated small scale bed-forms, while at the time of the first survey flow separation probably didn't play a important role, the steepness at the time of the second survey, being in the range 0.03-0.04, could deeply influence the hydrodynamics and then bed-form evolution.

The assumed analogy with ripple formation is also substantiated by sand wave crest location. Indeed, since the wavelength didn't changed over ten years, it could be guessed that, as for ripple formation (Blondeaux, 1990), sand wave pattern is forced by the wavelength of the most unstable component of the disturbance which triggers bed-form formation.

Finally, according to the data of the two surveys, it could be stated that sand waves are characterized by a stable configuration, that is their migration is almost null. However, since the mentioned surveys have been performed by means of very different instruments, a definitive answer about sand wave morphodynamics cannot be given. For this reason a new field campaign is already planned for August 2002 using the same instrumentation as for the 2001 survey.

Acknowledgements:
The present work has been carried out in the framework of the 5RTD Programme (European Commission Research Directorate-General, Contract n. EVK3-CT-2001-00056). The Italian Minister of the Research (project Cofin 2000 "Idrodinamica e Morfodinamica di ambienti a marea") is also acknowledged.

References:

Amore, E., Cavallaro, L., Cozzo, G., Foti, E., and V. C. Santoro, Il ruolo dei parametri morfodinamici nella formazione e nella evoluzione delle sand waves nello Stretto di Messina, Proc. of XXVIII Convegno di Idraulica e Costruzioni Idrauliche, Potenza (Italy), 16-19 September 2002, accepted for publication (in italian).

Blondeaux, P., Sand ripples under sea waves. Part 1. Ripple formation, *J.of Fluid Mechanics*, 218, 1-17, 1990.

Blondeaux, P., Brocchini, M., Drago, M., Iovenitti, L., and G. Vittori, Sand waves formation: preliminary comparison between theoretical predictions and field data, Proc. I.A.H.R., Symposium on River, Coastal, and Estuarine Morphodynamics, 1, 197-206, Genova 1999.

Fredsoe, J., and R. Deigaard, Mechanics of coastal sediment transport, *World Scientific*, 3, 260-289, 1993.

Gerkema, T., A linear stability analysis of tidally generated sand waves, *J. of Fluid Mechanics*, 417, 303-322, 2000.

Hulsher, S. J. M. H., Tidal-induced large scale regular pattern in three-dimensional shallow water model, *J. of Geophysical Research*, 101, C9, 20727-20744, 1996.

Santoro, V. C., Amore, E., Cavallaro, L., Cozzo, G. & E. Foti, Sand Waves in the Messina Strait, *J. of Coastal Research*, accepted for publication, 2002.

Nonlinear channel-shoal dynamics in tidal basins

G.P. Schramkowski [1], H.M. Schuttelaars [1] and H.E. de Swart [1]

1. *Institute for Marine and Atmospheric research, Utrecht University, PO BOX 80005, 3508 TA Utrecht, The Netherlands*, G.P.Schramkowski@phys.uu.nl

1 Introduction

This paper focuses on the finite-amplitude behaviour of bed forms in well-mixed long embayments. Such basins have lengths comparable to the tidal wave-length; an example is the Dutch Western Scheldt (WS). Field observations (*see Van den Berg et al.* [1997]) indicate that the WS exhibits a complex system of channels and shoals that vary on several length scales. On length scales of a few tidal excursion lengths or less (herafter called "local"), the most prominent tidal channels show meandering behaviour. Often these channels are linked by smaller-scale *connection channels* which are usually migrating. At regions where different main channels meet or appear to be relatively straight, *thresholds* are observed: these are regions of enhanced deposition.

In order to gain more fundamental understanding about the dynamics of these features, idealized models have been analyzed by *Seminara and Tubino* [1998] and *Schramkowski et al.* [2002]. Such models adopt several symplifying assumptions regarding, e.g., basin geometry and bottom friction parameterization. In these studies a linear stability analysis was used to demonstrate that the formation of local bed forms may be viewed as a result of a generic instability of the interaction between water motion, sediment transport and erodible bottom. *Schramkowski et al.* [2002] focused on wide and moderately frictional embayments, with the WS as a prototype example. They demonstrated that the critical mode is an *alternating bar* mode and it occurs when the friction parameter r exceeds a critical threshold $r_{\rm cr}$. Such a mode may be viewed as describing the rudimenary begin of meandering behaviour. Physically, the instability is related to the fact that frictional tide-topography interactions induce currents that set up destabilizing net advective sediment fluxes, viz. directed towards shoals or away from troughs.

Although a linear analysis yields insight into the onset of bed forms, their ultimate fate cannot be captured since linear theory always predict indefinite exponential growth. To determine the long-term morphodynamics, nonlinear effects need to be incorporated. Here, we present first results regarding the finite-amplitude behaviour of alternating-bar forms. These finding are confined to the so-called weakly nonlinear regime, i.e. to magnitudes of bottom friction which are still close to the critical value $r_{\rm cr}$.

2 Model setup

The model setup has been discussed in detail in *Schramkowski et al.* [2002] and will be briefly outlined now. Since the model describes local bathymetry, the channel geometry is represented by an infinitely long channel with straight non-erodible side-walls at $y = 0, B$ (see Fig 1). The local water depth is $H - h(x, y)$ and only the bed is allowed to erode. The water motion is described by the depth averaged shallow water equations (velocity components u and v) which are forced by an external pressure gradient. In the present

model, only an along-channel directed M_2 tide is forced. A linear bottom friction formulation is used: this gives similar qualitative results as a fully nonlinear parameterization (*see Schramkowski et al.* [2002]). Sediment transport is modelled as suspended load and is computed by solving an equation for the depth-integrated sediment concentration C. The flux is corrected for the presence of bed slopes which is required to prevent unrealistic formation of very small-scale bottom patterns. The bottom, finally, results from the tidally-averaged divergence of the sediment flux.

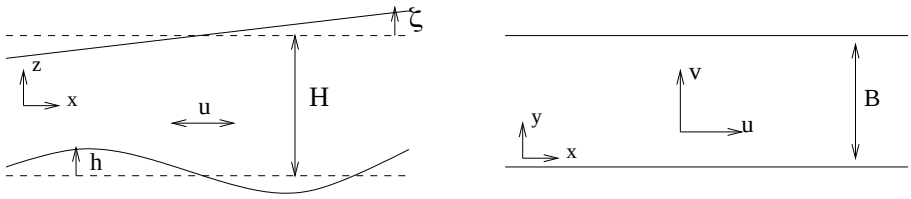

(a) Side View (b) Top View

Figure 1: Sketch of model geometry and definitions of several quantities. For the WS, $B \sim 4$ km and $H \sim 10$ m.

3 Method

The model allows for a morphodynamic equilibrium which corresponds to a spatially uniform along-channel directed tide over a horizontal bed. This basic state is expressed by the state vector $\Psi_{\rm eq} = (u, v, \nabla\zeta, C, h)_{\rm eq} = (U\cos(\sigma t), 0, \nabla\zeta_{\rm eq}, C_{\rm eq}, 0)$, with $\sigma = 1.4 \times 10^{-4}$ s^{-1} the M_2 tidal frequency. Bottom patterns arise as perturbations $\Psi'(x, y, t)$ of this basic state and are expanded in known eigenfunctions of the linear stability problem with as yet unknown amplitudes. For example, the expansion for the bottom perturbation thus reads

$$h' = \sum_{\rm m=0}^{\rm M} \sum_{\rm n=0}^{\rm N} h_{\rm mn}(t) \cos(l_{\rm n} y) \exp(imk_{\rm cr} x) \quad + \quad \text{c.c.} \,, \tag{1}$$

with $h_{\rm mn}$ the time-dependent amplitude of mode (m, n), $l_{\rm n} = n\pi/B$ the cross-channel wavenumber, $k_{\rm cr}$ the longitudinal wavenumber of the critical mode and M, N truncation numbers. Equations for the modal amplitudes are obtained by substitution of solutions of the form $\Psi = \Psi_{\rm eq} + \Psi'$ into the model equations, followed by a Galerkin projection onto the linear modes.

Results

Hereafter, we will consider stationary, non-linear equilibria for varying bottom friction r. Such equilibria are obtained by setting all time derivatives zero in the amplitude equations. The results below refer to typical WS parameter values except for the control parameter r. The basis that was used to span Ψ' was truncated at $M = N = 5$. Furthermore, only residual and M_2 tidal components of flow and sediment concentration were considered.

Figure 2a shows the so-called *bifurcation diagram* which gives the height of the bed form as the control parameter r is changed. This plot indicates the existence of *multiple*

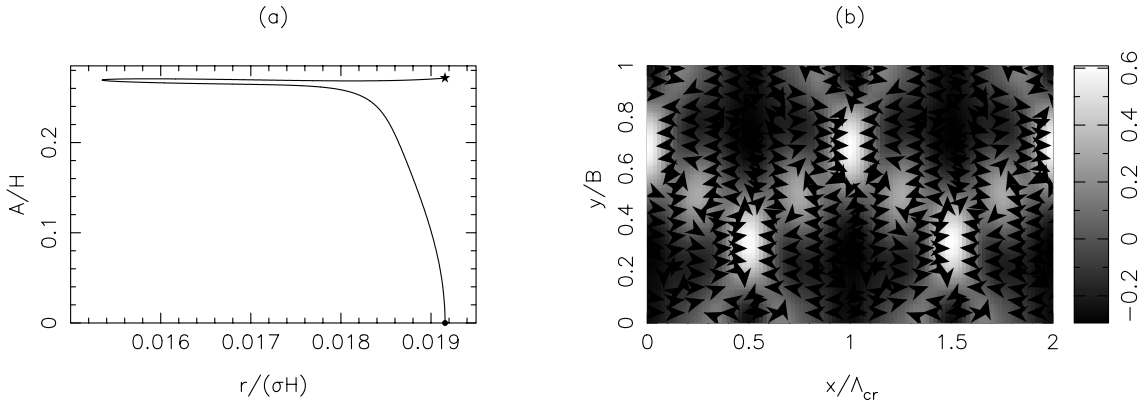

Figure 2: Panel (a): bifurcation diagram. Here, $A = \sqrt{\sum\sum \|h_{\rm mn}\|^2}$. Panel (b): image plot of bed perturbation h'/H at $\star$ in panel (a). Positive (negative) values indicate shoals (troughs) and $\Lambda_{\rm cr} \sim 45$ km denotes the critical wavelength. Arrows indicate the residual velocity pattern.

equilibria below the critical value of bottom friction, as will be explained now. Below $r = r_{\rm cr}$, there is a stable zero-amplitude equilibrium, which represents the reference state. At $r = r_{\rm cr} \approx 0.019\sigma H$ ($\bullet$ in Fig. 2a), two branches of equilibria are generated: these branches coincide in Fig. 2a and the corresponding solutions only differ by a reflection across the channel's central axis $y = B/2$. As r is decreased further along the branch, the characteristic height of the bottom profiles increases. At $r/(\sigma H) \approx 0.0153$, the branch turns and the friction parameter increases along the branch. Thus, for $0.0153\sigma H < r < r_{\rm cr}$ there exist five solutions, with two pairs that are obtained by reflection across the central axis. The stability of these paired equilibria is still under consideration. The existence of finite-amplitude equilibria below $r = r_{\rm cr}$ is referred to as *subcritical behaviour*.

Figure 2b shows the equilibrium bed profile of the finite-amplitude equilibrium near $r/(\sigma H) = 0.01915$ ($\star$ in Fig 2b). The longitudinal extend of the image is twice the critical wavelength $\Lambda_{\rm cr} = 2\pi/k_{\rm cr} \sim 45$ km. Also, the residual flow pattern is displayed. Note that several small-scale features are present: for instance, a total of eight distinct banks is observed. Such features are mainly due to self-interaction of the alternating bar mode which is the dominant source of nonlinearity for dynamics near criticality. The along-channel residual flow is mostly directed towards the most pronounced banks and away from deep regions: this is reminiscent of the flow pattern that underlies the linear instability mechanism (*see Schramkowski et al.* [2002]).

The net divergences of the dominant sediment fluxes for the equilibrium of Fig. 2b are shown in Fig. 3. These contributions are due to (a) advection of perturbed sediment concentration by the background tide, (b) bed slope effects and (c) the advection of background concentration by the perturbed velocity. These quantities have been multiplied by $-h'$ before displaying them so that positive (negative) values indicate destabilizing (stabilizing) contributions. The main balance is between (a) and (b), which reflects the underlying "linear" mechanism in that this balance holds exactly at criticality ($r = r_{\rm cr}$). Due to nonlinearity, however, a considerable part of the equilibrium is also mediated by advection of background concentration by perturbed velocity (c). Note that the latter contribution is predominantly destabilizing, so that the saturation of the growth of bed

forms from the horizontal equilibrium bottom is primarily governed by bed slope effects.

4 Final remarks

The results presented above give insight into the finite-amplitude behaviour of bed forms under weakly nonlinear circumstances. Several nonlinear effects (finite height of bed forms, excitation of small-scale patterns) are clearly visible while the underlying equilibrium appears to contain several properties that are characteristic of the critical mode. Also, some features (e.g., the small near-bank troughs at $x/\Lambda_{\rm cr} = 0,\ 0.5,\ 1, \dots$) may be the rudimentary begin of connection channels. However, the formation and meandering of tidal channels was not reproduced. This may be due to the low friction that was considered so far. The next step will be to extend the results to values of $r/(\sigma H)$ that are representative for the WS (typically $0.1 - 1$).

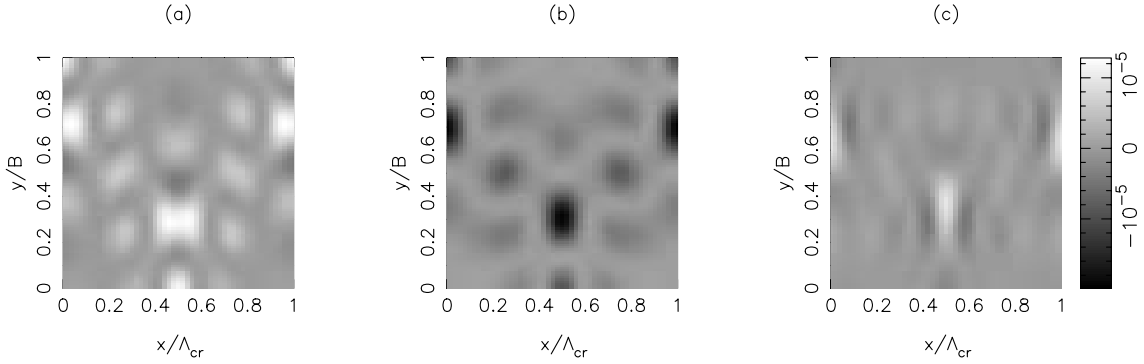

Figure 3: Contributions of sediment fluxes that constitute the nonlinear equilibrium near $r/(\sigma H) = 0.0195$ ($\star$ in Fig. 2a). Positive and negative values refer to destabilizing and stabilizing contributions, respectively.

References

Schramkowski, G. P., H. M. Schuttelaars, and H. E. de Swart, The effect of geometry and bottom friction on local bed forms in a tidal embayment, *Continental Shelf Research*, *in press*, 2002.

Seminara, G., and M. Tubino, On the formation of estuarine free bars, in *Physics of Estuaries and Coastal Seas*, edited by J. Dronkers and M. Scheffers, pp. 345–353, PECS 96, Balkema, Rotterdam, 1998.

Van den Berg, J. H., M. C. J. L. Jeuken, and A. J. F. van der Spek, Hydraulic processes affecting the morphology and evolution of Westerschelde estuary, in *Estuarine shores: evolution, environments and human alterations*, edited by K. Nordstrom and C. Roman, pp. 157–184, John Wiley and Sons Ltd., Chichester, 1997.

Preliminary hydrodynamic results of a field experiment on a barred beach, Truc Vert beach on October 2001

NADIA SÉNÉCHAL[1], PHILIPPE BONNETON AND HÉLÈNE DUPUIS

Department of Geology and Oceanography, University of Bordeaux I, avenue des Facultés, 33405 Talence, France

[1]corresponding author, n.senechal@epoc.u-bordeaux.fr, tel: +33 5 56 84 83 81, fax : +33 5 56 84 08 48

A field experiment has been carried out on October 2001 during one week at Truc Vert beach, situated on the southern part of the French Atlantic coastline. Three cross-shore sensor lines have been deployed along a ridge and runnel system with high energy incident swell. This allowed us to investigate the influence of the offshore incident energy level for a same incident wave period on the energy dissipation in the surf zone and also to consider the influence of the nearshore bar on the wave dissipation.

1. Introduction

Much effort has been devoted to investigate the role of waves in the formation of nearshore bars but less has been done to improve our knowledge on the effect of the nearshore bars on wave dissipation. An yet it has been shown that the incoming wave field can be strongly modified during propagation over submerged bars (Elgar et al., 1997; Masselink, 1998, Sénéchal et al., 2002) and that this can lead to a delay of the energy dissipation on the beach face (Sénéchal et al., 2002).

The subject matter of this study is to report observations of wave dissipation on a barred beach in case of a high energy incoming swell.

2. Field experiment

The study area

This study is based on data collected during one fieldwork carried out during six days in October 2001. The data described in this paper were collected at Truc Vert beach, which is situated on the southern part of the French Atlantic coastline (for further informations on the study area see Sénéchal et al., 2001). Truc Vert beach, situated in a meso-macro tidal environment (tidal range is 4.5 m at spring tides), is of the intermediate type 2e (following Masselink and Short, 1993) and exhibits a ridge and runnel system in the dissipative lower intertidal domain (figure 1). This coast is exposed to almost continuous moderate energy swell.

Instrumentation

Figure 1 illustrates the study area and the sensor deployment on the first day of the fieldwork. Pressures were measured at fifteen locations in the intertidal zone using thirteen bottom-mounted piezoresistive pressure transmitters (black round), one bottom mounted Directional wave current meter from InterOcean system (black star) and one Acoustic Doppler Velocimeter (ADV Vector) from Nortek (black square).

A wave rider (TRIAXYS) was also moored in about 56 m water depth at about 10 miles offshore of the study area and served as the reference gage for the incident waves (not shown on figure 1). During the field experiment, the beach was exposed to high energy and long incoming swell with significant wave heights ranging from 1.20 m to 2. 90 m and significant wave periods ranging from 7.5 s to 13.5 s in about 56 m water depth

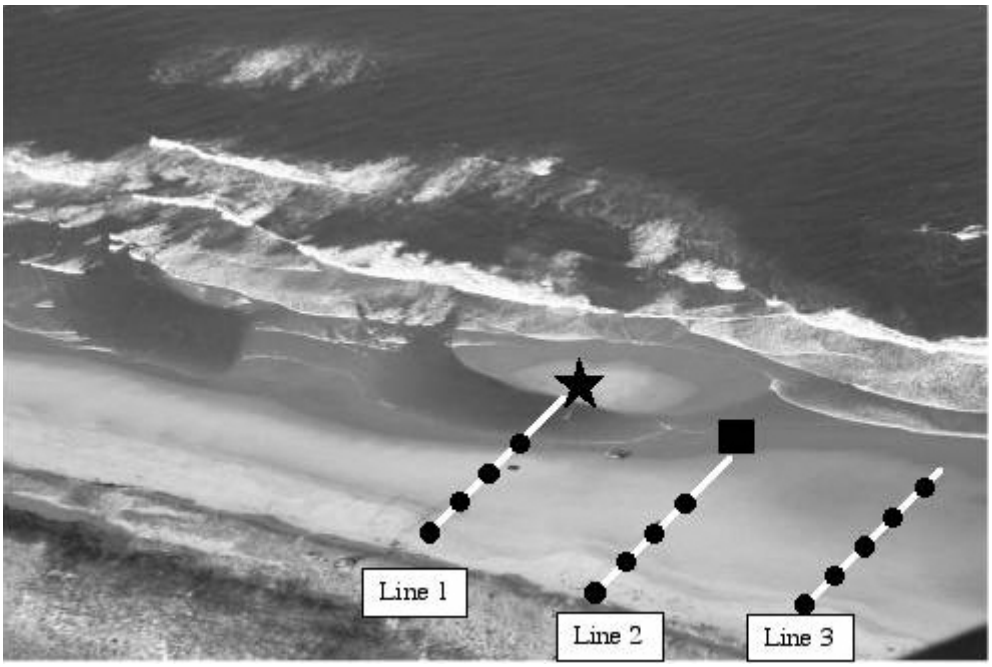

Figure1: aerial view of the study area and sensor deployment at low tide

3. Results

Although data were collected during four days, the measurements presented in this study were taken over two high tide cycles with same offshore significant wave periods but different offshore significant wave heights. Figure 2 illustrates the wave spectra (computed over 30 mm) for these two high tide cycles.

On October 17th, the significant wave height was about 1.7 m and the significant wave period was about 11.5 s whereas on October 18th, the significant wave height was about 2.7 m and the significant wave period was about 12 s.

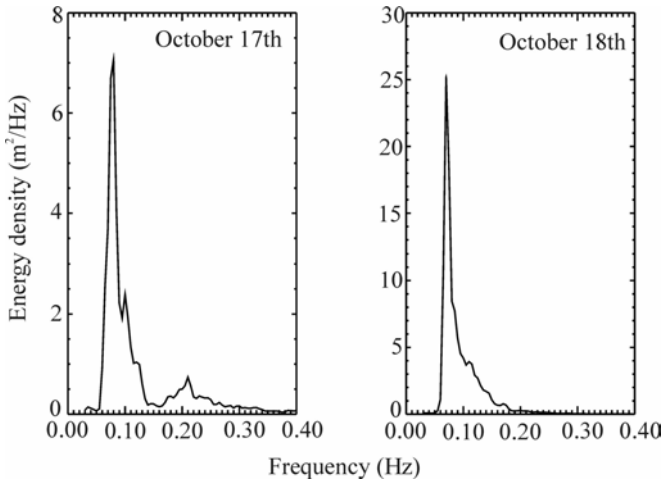

Figure 2: incident wave spectra as measured in 56 m water depth at TRIAXYS buoy

Figure 3 illustrates the wave height decay as observed at line 1 (onshore the ridge and runnel system) and at line 3 (outside the influence of the ridge an runnel system) in the surf zone. The different symbols correspond to each sensors on the sensor line (from offshore to onshore for both lines : star, cross, square, triangle).

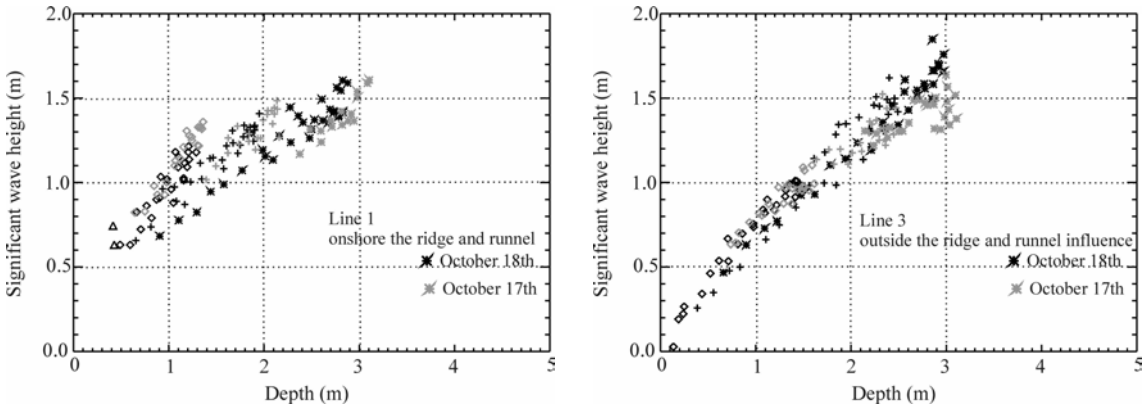

Figure 3: Wave height decay in the surf zone at line 1 (left) and line 3 (right)

Figure 3 clearly shows that the wave heights are locally driven. For a same incident wave period, the wave heights observed in the surf zone at each sensor are quite similar although the offshore energy levels for both days are very different as testified by the energy density spectra (figure 2).

On the other side, the presence of the bar (figure 3, left panel) appears to scatter the data of each sensor. Indeed, whereas at line 3 (right panel) the wave height decay at each sensor appears to be similar, at line 1 (left panel) it seems to be different.

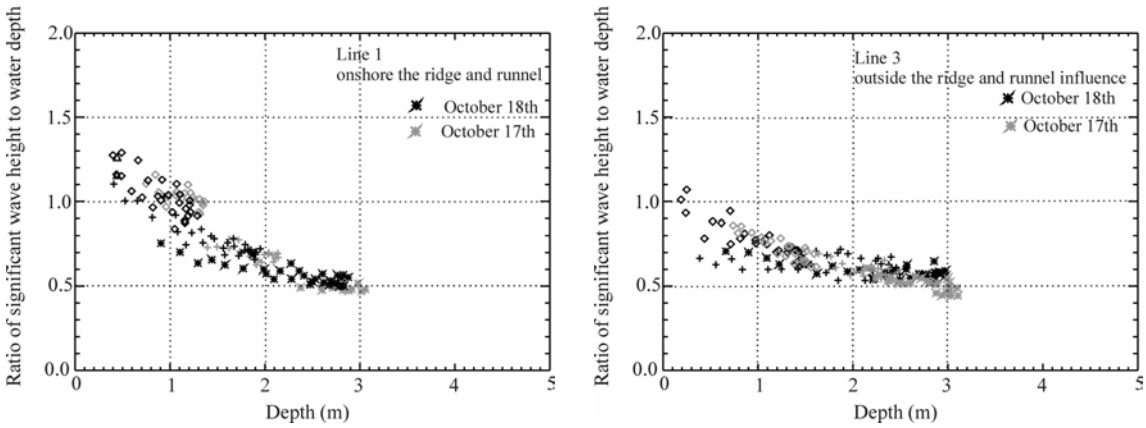

Figure 4: ratio of wave height to water depth in the surf zone at line 1 (left) and line 3 (right)

Figure 4 clearly illustrates that the ratio of wave height to local water depth (nominally the γ parameter) is not constant in the surf zone along a cross-shore transect, consistent with previous works (Raubenheimer et al., 1996; Sénéchal et al., 2001 and many others). We observe an increase of the γ parameter shoreward. This increase is stressed by the bar (figure 4, left panel), consistent with the observations made above in figure 3.

4. Conclusions

In this paper, data collected on a barred beach with sensors deployed along three parallel cross-shore lines along a ridge and runnel system allowed us to investigate the influence of the incident wave energy level and the influence of the nearshore bar on the wave dissipation in the surf zone. The measurements presented in this study were taken over two high tide cycles with same significant wave periods but different significant wave heights (figure 2).

Wave energy dissipation appears to be locally driven and relatively independent of the offshore energy level (figure 3). On the other side, the presence of the bar seems to scatter the data (figure 3, left

panel). Furthermore, in presence of a bar, the wave height decrease on the beach face is more important (figure 4, left panel). The analysis of the other days of the fieldwork should allow us to investigate the influence of the offshore significant wave period.

Acknowledgments : This study was performed within the framework of the Programme National d'Environnements Côtiers, project "Hydrodynamique sédimentaire en zone côtière" sponsored by CNRS/INSU. Partial support was also received from the European community under MAST contract n° MAS3-CT-0106. We would like to thank Mr S. Abadie, C. Brière, R. Butel, R. Capobianco, B. Castelle, G. Chapalain, A. De Resseguier F. Desmazes, C. Dulou, P. Larroude, P. Maron, D. Malengros, D. Michel, M. Mory, G. Oggian, R. Pedreros, V. Rey, D. Rihouey and Miss H. Howa for their contributions during the field experiment

References :

Elgar, S., Guza, R.T., Raubenheimer, B., Herbers, T.H.C. and Gallagher, E.L., Spectral evolution of shoaling and breaking waves on a barred beach. *J. of Geophys. Res.*, 102 (C7):15,797-15,805,1997.

Masselink, G., Field investigation of wave propagation over a bar and the consequent generation of secondary waves. *Coastal Eng*., 33:1-9, 1998.

Masselink, G. and Short, A.D., The effect of tide range on beach morphodynamics : a conceptual model. *J. of Coastal Res*., 9:785-800, 1993.

Raubenheimer, B., Guza, R.T. and Elgar, S., Wave transformation in the inner surf zone. *J. Geophys. Res*., 101: 25,589-25,597.

Senechal, N., Dupuis, H., Bonneton, P. , Howa, H . and Pedreros, R., Observation of irregular wave transformation in the inner surf zone over a gently sloping sandy beach on the French Atlantic coastline. *Oceanologica Acta*, 24(6):545-556, 2001.

Senechal, N., Bonneton, P. and Dupuis, H., 2002. Field experiment on secondary wave generation on a barred beach and the consequent evolution of energy dissipation on the beach face. *Accepted with modifications in Coastal Eng*.

Effect of velocity veering on sand transport in a shallow sea

GEORGY I. SHAPIRO

(University of Plymouth, UK, and Institute of Oceanology, Moscow, Russia , g.shapiro@plymouth.ac.uk)

JOHAN VAN DER MOLEN

(Institute of Marine and Atmospheric research Utrecht (IMAU), Utrecht University, Princetonplein 5, 3584 CC Utrecht, Netherlands, j.vandermolen@phys.uu.nl)

HUIB E. DE SWART

(Institute of Marine and Atmospheric research Utrecht (IMAU), Utrecht University, Princetonplein 5, 3584 CC Utrecht, Netherlands,h.e.deswart@phys.uu.nl)

1. Introduction

Understanding and predicting sand transport in shallow shelf seas is an important issue for scientists and coastal zone managers. In the last decades a variety of formulations for sand transport under different hydrodynamic conditions have been developed. They require knowledge of the shear stress acting at the sandy seabed. Nowadays, these formulations are implemented in many process-oriented morphodynamic models. Since the practical applicability of full three-dimensional morphodynamic models is still in its infancy most models use a prescribed vertical structure of the current without taking into account the veering of the velocity vector over the vertical. Besides, in the case of time-varying currents, also temporal phase differences between velocities at different vertical levels are neglected. Thus, in shallow areas with a sandy bottom and where currents experience veering over the vertical, such models yield incorrect magnitudes and directions of the sand transport. Consequently, deviations also occur in the computation of erosion and deposition areas of sediment, which are determined by the spatial divergence of the net sand flux.

This study focuses on meso-scale currents (spatial scales > 10 km, timescales > 1 day) on the shelf (depths > 10 m). Such currents are subject to Ekman veering due to earth rotation effects (Coriolis force). Analysis of field data and model studies by *Niedoroda and Swift* [1991] demonstrate that already in depths of 20-30 m Ekman veering can be significant and can cause depth-averaged currents and net sand fluxes to have different directions. The aim of the present work is to quantify the role of Ekman veering on both the sand transport rates and the location of erosion/deposition areas. The study is carried out using two different models. The first model is the standard formulation of *Bailard* [1981] for suspended sand transport which neglects velocity veering. The second is a new semi-analytical 2.5 dimensional boundary layer model based on the sediment transport model by *Shapiro et al.* [2000] in which velocity veering due to earth rotation is taken into account.

2. The sand transport models

The formulation of *Bailard* [1981] is based on a logarithmic velocity distribution over the vertical. Thus the magnitude of the current changes with depth, but its direction is fixed. Furthermore, it uses a prescribed bottom roughness and assumes steady-state conditions (suspended particulate matter, hereafter called SPM, concentration is always in equilibrium with the current velocity). It then calculates horizontal fluxes of suspended sediment at a fixed location independently of the neighbouring points (One-Point model) and preceding conditions (no memory), see *Molen*, [2002].

The new 2.5D model uses the vertical structure of the current from a shallow-water version of Ekman model. The main difference with the classical Ekman formulation is that the present model has a vertical eddy viscosity coefficient that depends on the current velocity (*Shapiro et al.,* 2000). The model uses a prescribed drag coefficient at the seabed, typically C_d= (1-3)*10^{-3} to calculate both turbulent viscosity and diffusivity coefficients at each grid point given the velocity of the surface current. This results in changes of both the magnitude and direction of the current with depth. The thickness of the nepheloid layer is also calculated at each grid point given the current velocity and SPM settling velocity.

The model calculates the SPM load taking into account the time lag between changes in the magnitude/direction of main current and in the SPM concentration within the nepheloid layer. The erosion/deposition rates at a fixed location on the sea floor are computed via the divergence of horizontal sediment fluxes and suspension load tendency due to time lag. In the experiments the formulation for the erosion function at the bed was chosen such that, for coarse sand, it yields the same SPM load as that obtained with the *Bailard* [1981] formulation.

3. Results

Below results of first experiments are discussed which illustrate the potential importance of Ekman veering for net sand transport patterns in coastal seas. The first case concerns a straight jet in a domain of 100x100 km with a water depth of 50 m. The jet has a width of 30 km and a maximum velocity of 50 cms^{-1}. The Coriolis parameter is taken to be 10^{-4} s^{-1}, the grain density 2650 kgm^{-3} and the porosity

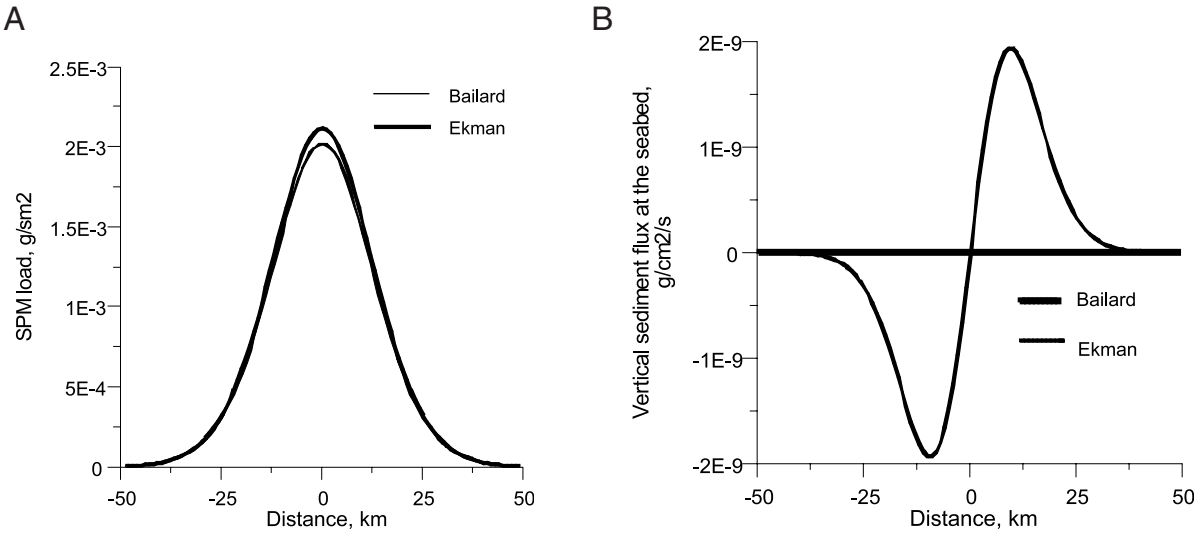

Figure 1: Spatial pattern of SPM load (A) and erosion-deposition flux near the seabed (B) in case of a straight coastal jet. Grey curve: Bailard model, dark curve: Shapiro et al. model.

of the bed is 0.4. In figure 1A the distribution of the SPM load (depth-integrated sediment concentration) is shown for sediment with a settling velocity of 2 cms^{-1}. The diagrams of SPM distribution do not show any significant differences between the two models. However, the distribution of the erosion-deposition flux near the bed is quite different, as is shown in figure 1B: the model without Ekman veering does not predict any difference between erosion and deposition, whereas the second model shows net deposition (erosion) to the left (right) of the centre of the jet.

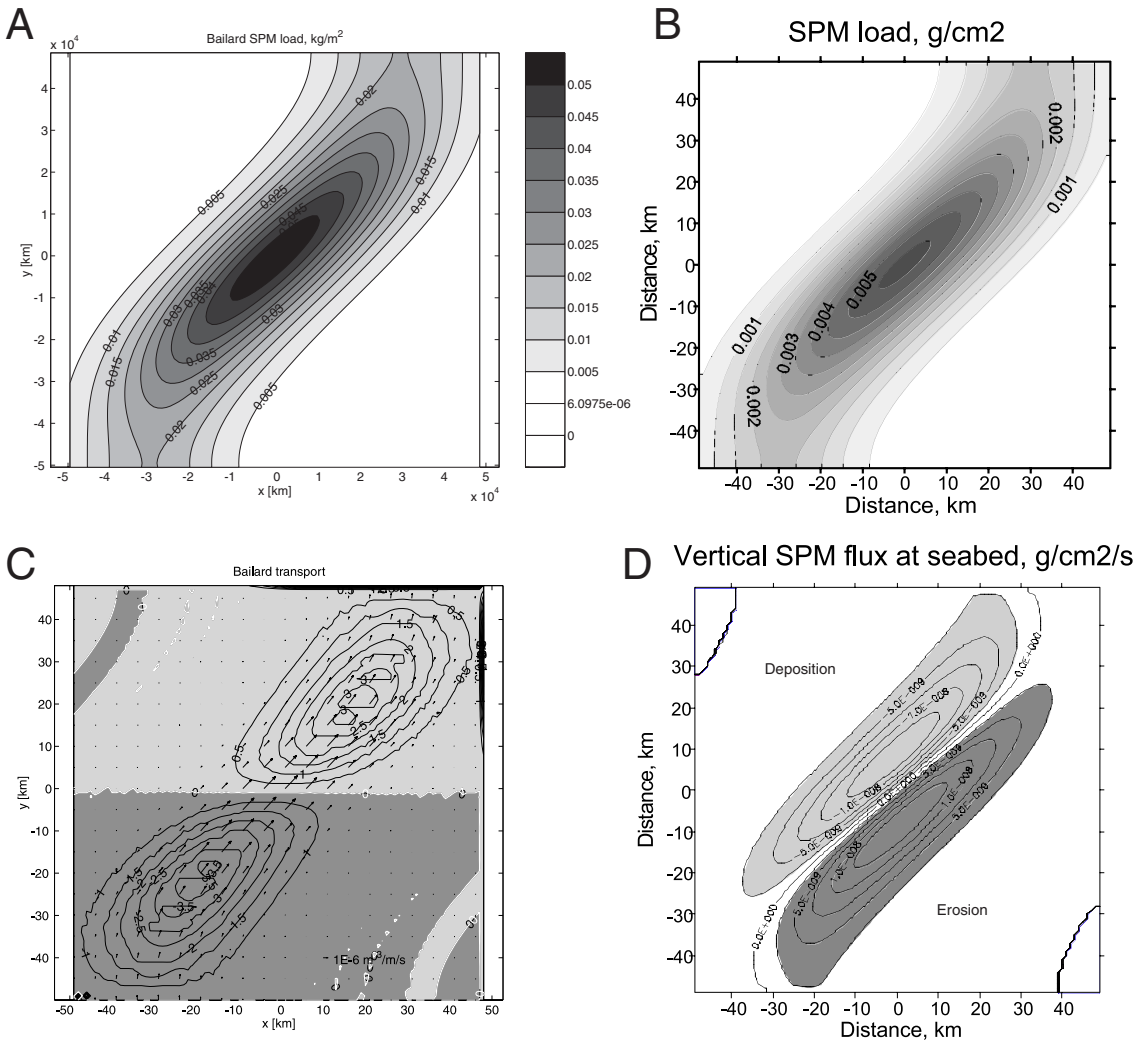

Figure 2. Suspended matter load for Bailard (A) and Ekman (B) model, and associated erosion/deposition patterns (C, D).

The second example concerns a meandering coastal jet. Parameters are as in the previous experiments, except for the maximum velocity in the jet (here 70 cms^{-1}) and the meander wave-length is 200 km. Characteristic results of the experiments are summarised in the Table. The results for the distribution of the SPM load and erosion-deposition flux near the seabed are shown in figure 2. For this set of experiments, the SPM loads are similar. The erosion/deposition fluxes near the seabed, however, are again very different: while the Bailard model shows erosion in the lower half of the basin and deposition in the upper half, the Ekman model predicts erosion to the right of the jet, and deposition to the left.

4. Conclusions and outlook

An intercomparison has been made of two sand transport models which neglect and account for velocity veering due to earth rotation effects, respectively. The two models use a matching set of parameters to provide identical values for the bottom stress and suspended load for a uniform steady current at any given surface velocity. The models were tested in a range of sand grain sizes 50-500 μm and current speeds up to 1 ms^{-1} for an idealised square region (100x100 km) of a shelf sea of constant depth. The erosion/deposition patterns and suspension load distribution was examined for two illustrative cases: a straight jet and a meandering jet. The results show that velocity veering causes the

direction of the sediment flux to be generally different from the direction of the surface flow. Both the rates and spatial distribution of the areas of erosion/deposition differ significantly between the models in both cases. This difference can be attributed mainly to additional flux divergence due to velocity veering. Furthermore, time lags between current velocities and SPM concentration occur during the period that the concentration adjusts to the current, which are particularly significant in case of smaller grains.

Table. Model comparison.

Run	Ws, cm/s	SPM load, g/sm2, Bailard	SPM load, g/sm2, Ekman	Maximum erosion/deposition depth, mm/year,	
				Bailard	Ekman
Z21	5	2.16e-3	2.2e-3	1.3	0.38
Z22	2	5.4e-3	5.6e-3	3.4	2.2
Z23	1	1.08e-2	1.1e-2	6.7	8.3
Z24	0.5	2.16e-2	2.25e-2	13.4	27

At the conference results of additional experiments will be presented and it will be shown how the model can be modified to account for currents that are predominantly driven by tides.

Acknowledgments: This work was supported by the Dutch Organization of Scientific Research (NWO) through grant nr. 811.33.005.

References:

Bailard, J.A. An energetics total load sediment transport model for a plane sloping beach. *J. Geophys. Res., 86*, 10938-10954, 1981.

van der Molen, J. The influence of tides, wind and waves on the net sand transport in the North Sea. *Continental Shelf Res.*, in press, 2002.

Niedoroda,.A.W., and Swift, D.J.P.. Shoreface processes, in *Handbook of coastal and ocean engineering, v.2*, edited by J.B. Herbich, pp. 735-770, Gulf Publ. Co., Houston, 1991.

Shapiro, G.I., Akivis, T.M., Pykhov, N.V. and Antsyferov, S.M. Transport of fine sediment with mesoscale currents in the shelf-slope zone of the sea. *Oceanology, 40*, 305-311, 2000.

Theoretical Investigation of Bed Form Shapes

RICHARD STYLES

(Marine Sciences Program, and Department of Geological Sciences, University of South Carolina, Columbia, South Carolina, 29208, USA7, rstyles@geol.sc.edu)

SCOTT M. GLENN

(Institute of Marine and Coastal Sciences, Rutgers University, New Brunswick, New Jersey, 08901, USA, glenn@imcs.rutgers.edu)

1. Introduction

The deformation of movable boundaries under the action of an applied turbulent shear stress is well known. Examples from fluvial systems include sand ridges, sand dunes, and wave-formed sand ripples (see *McLean et al*. [1999]). Forms produced in sandy environments often are highly organized and nearly 2-dimensional. This makes them an intriguing focus of study considering that they are generated in both steady and oscillatory turbulent flows. Current generated bed forms are often asymmetric, with gently sloping back faces and steep forward faces (see *Wiberg and Nelson* [1992]; *McLean et al*. [1999]). Wave-formed ripples are generally sharp crested with symmetric forward and back faces that are separated by a broad flat trough (see *Inman* [1957]). In oscillatory flow, the height and length of the bed forms generally scale with the orbital amplitude of the fluid motion (see *Inman* [1957]; *Wiberg and Harris* [1994]) For steady flows, no such scaling parameter exists, but a correlation between the non dimensional wavelength and the Froude number has been determined theoretically and verified experimentally (see *Kennedy* [1963]; *Engelund* [1970]).

Because bed forms evolve in response to the overlying flow and have wavelengths that are scaled to the local flow properties, a number of studies to describe their formation and evolution have been conducted in the past (see *Kennedy* [1963]; *Engelund* [1970]; *Foti and Blondeaux* [1995]). Most of these studies share a common strategy in which an infinitesimal perturbation of variable amplitude is prescribed, and the resulting growth or decay patterns are examined. In this approach, the initial state consists of a flat bed with a superimposed oscillatory current, an infinitesimally perturbed bottom, or a combination of both. The governing equations for fluid mass and momentum are solved under the constraint of these prescribed initial states. The dynamics are simplified by prescribing a no-0slip condition at the sediment water interface, allowing for a positive current at the point of sediment contact. Although perturbation analysis has been able to accurately predict bed form wavelength and the conditions for bed change (i.e., anti dunes to dunes or flat bed to rippled bed), it does not provide a theoretical prediction of equilibrium bed form geometry. Only the maximum height and wavelength of the resulting bed forms are obtained.

2. Methods

An alternative approach is suggested here in which the forcing terms (pressure and Reynolds stress) are prescribed and the governing equations for fluid mass and momentum are solved for the flow speed and the associated boundary deformation. To simplify the dynamics yet retain the non-linear advective terms, the bottom boundary layer is divided into an arbitrary number of finite layers (Figure 1). *Smith and McLean* [1977] also used a layered approach to investigate boundary shear stress over a wavy surface. By dividing the bottom boundary layer into finite regions, a pair of coupled equations is produced that predict the flow speed and interface height between each layer. The horizontal dependence of the interface at the lowest boundary is presumed to mimic the equilibrium profiles of a deformable bed. This is similar to the approach adopted by *Kennedy* [1963], who replaced an arbitrary streamline beneath a wavy surface to represent the moving bottom boundary. Unlike some of the previous models (see *Smith and McLean* [1977]; *Kennedy* [1963]), the horizontal velocity within each layer is independent of height. Although somewhat simplified in a

bottom boundary layer where the flow is highly sheared, this constraint leads to analytical solutions for the horizontal current and bed profile for simple forcing functions. The simplified layered model is able to predict interface profiles that are qualitatively similar to observed bed forms.

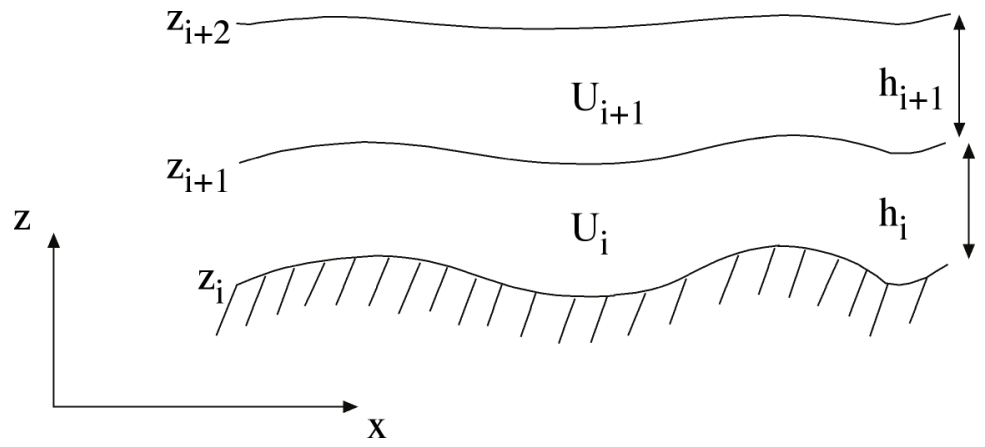

Figure 1 Schematic illustrating the layered model. The thickness of each layer is denoted by h. The horizontal velocity, U,3 within each layer is independent of height but varies with x.

3. Preliminary Results

With the water column divided into finite layers, only the stress divergence at the interface between adjacent layers has to be prescribed. This eliminates the need for an eddy viscosity closure. The prescribe fields include the vertical stress divergence across each layer and the fluid pressure. Both of these fields can depend on the horizontal coordinate and time within each finite layer. To highlight the theoretical approach presented here, the analysis focuses on the current and interface height for one layer only under steady forcing conditions. Figure 2 shows the contour of an arbitrary layer with zero stress divergence and sinusoidal pressure forcing [$p = 9\ p_0 \sin(kx)$]. This is similar to the pressure distribution measured by *McLean et al*. [1999] over fixed duned-shaped bed forms. The current vectors represent the depth-averaged flow field over the layer. For the prescribed conditions, the vertical velocities are significantly enhanced along the rising and falling side of the layer interface. These strong velocities may enhance vertical mixing and contribute to observed spatial variability in the stress field and turbulent kinetic energy. There is also a weak flow reversal near the 0centerline of the trough. This produces convergence on the lee side of the ridge and divergence on the front face. In terms of sediment transport, this configuration favors horizontal migration of the interface in the direction of the ambient current. Interestingly, the resulting profile shape, which is generated under a steady flow, is qualitatively similar to symmetric ripples found under waves. Other cases to be discussed will include forcing by an applied stress divergence and a phase lag between the stress and pressure. A similar model is applied to the mass conservation equation for sediment, and the resulting spatial transport patterns will be discussed.

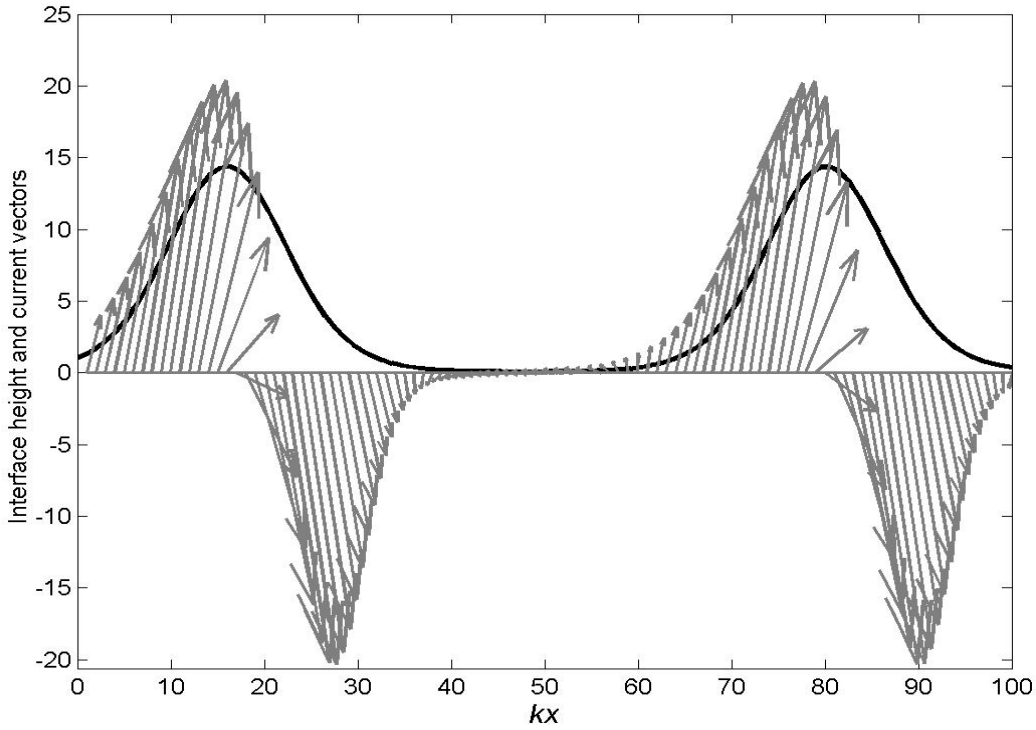

Figure 2 Current vectors (arrows) and interface height for an arbitrary layer, h (solid line). Feather plot denotes the current speed and direction at each point along the contour of h. Mean flow direction is from left to right.

Acknowledgments: Support for this project was provided by the National Oceanographic and Atmospheric Administration/National Undersea Research Program (NOAA/NURP) under grant number NA06RU0139.

References:

Engelund, F., Instability of erodible beds, *J. Fluid Mechanics, 42*, 225-244, 1970.

Foti, E. and P. Blondeaux, Sea ripple formation: the turbulent boundary layer case, *Coastal Eng., 25,* 227-236, 1995.

Inman, D. L., Wave-generated ripples in nearshore sands, Tech. Memorandum, No. 100, Dept. of the Army Corps of Eng., 42 pp., 1957.

Kennedy, John F., The mechanics of dunes and antidunes in erodible-bed channels, *J. Fluid Mechanics, 16,* 521-544, 1963.349

Smith, J. D. and S. R. McLean, Spatially averaged flow over a wavy surface, *J. Geophys. Res., 82*, 1735-1746, 1977.

McLean, S. R., S. R. Wolfe and J. M. Nelson,798 Spatially averaged flow over a wavy boundary revisited, *J. Geophys. Res., 104*, 15,743-15,753, 1999.

Wiberg, P. and J. M. Nelson, Unidirectional flow over asymmetric and symmetric ripples, *J. Geophys. Res.*, 97, 12,745-12,761, 1992.

Wiberg, P. and C. K. Harris, Ripple geometry in wave-dominated environments, *J. Geophys. Res., 99*, 775-789, 1994.

Spatial variation of diurnal tidal asymmetry around a protruding delta front

BAS VAN MAREN

(Institute for Marine and Atmospheric Research Utrecht / IMAU, Utrecht University, Heidelberglaan 2, 3508 TC Utrecht, The Netherlands, b.vanmaren@geog.uu.nl)

PIET HOEKSTRA

(Institute for Marine and Atmospheric Research Utrecht / IMAU, Utrecht University, Heidelberglaan 2, 3508 TC Utrecht, The Netherlands, p.hoekstra@geog.uu.nl)

1. Introduction

The Red River delta is the largest delta system in north Vietnam, and debouches in the Gulf of Tonkin by a number of distributaries of which the Ba Lat river mouth is the largest (Fig. 1). The morphological evolution of the Ba Lat delta is characterised by periods of coastal accretion, alternating with periods of coastal erosion and a redistribution of sediment due to reworking by waves and currents. Van Maren and Hoekstra (2003) presented a conceptual model that explains this pattern with the internal dynamics of the system, rather than by periodically varying boundary conditions such as river discharge or wave power. This concept is presently being implemented and tested in a numerical model that is able to simulate the morphological developments of the subaquous delta in response to waves, currents and river discharge. Together with field data, this model is applied to test hypothesis about the morphologic evolution of the delta.

At present, the southern part of the delta front is rapidly accreting, while the northern part is eroding (Van Maren and Hoekstra, 2003). The reasons for this southward growth were observed to be a southward sediment transport driven by tidal asymmetry, and southward advection of the turbid river plume. In this paper we focus on the potential role of alongshore tidal currents for redistribution of delta front sediments by means of a numerical tidal model.

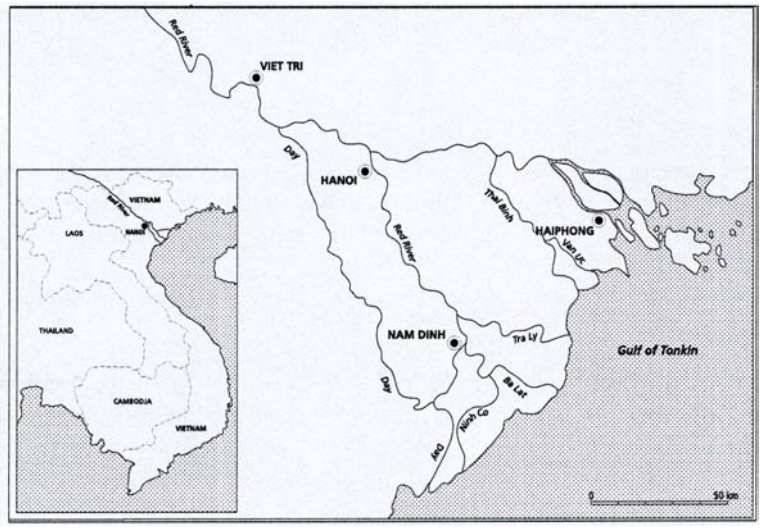

Figure 1 Distributaries of the Red River delta

2. Field methods and observations

Current velocities were measured in front of the river mouth during three 25-hour stations; one at neap tide and two during spring tide conditions. Water level variations were measured in the river mouth,

and supplemented with sparse available data from literature. The dominant tidal constituents in the Gulf of Tonkin are O_1, K_1, and M_2 (Fang et al., 1999) with amplitudes of about 50, 50, and 15 cm, respectively near the Red River Delta. The co-tidal lines of O_1 and K_1 in these regions of the Gulf of Tonkin are widely spaced due to resonance of the diurnal constituents (Fang et al., 1999). Therefore the phase differences between the northern and southern part of the Red River Delta are only small for the diurnal constituents, and the corresponding tidal wave celerity equals a value of approximately 30 m/s. The M_2 co-tidal lines are less widely spaced near the Red River delta, and related to a tidal wave propagating with a speed of about 10 m/s.

The measured velocities in front of the river mouth were asymmetrical and diurnal during spring tides, with a short period of strong southward flow and a longer period of weak northward flow (see Fig. 2a and 2c). Nearly symmetrical semi-diurnal currents characterize the flow pattern during neap tide. This difference in flow conditions is attributed to interaction of the O_1, K_1 and M_2 tidal constituents, which are able to induce a tidal asymmetry with a distinct periodicity (e.g. Hoitink et al., 2003). As the sediment transport capacity of the tidal currents is commonly proportional to the third power of flow velocity, this asymmetry favours southward sediment transport. The tidal asymmetry is an important mechanism that has to be reproduced correctly by the numerical model.

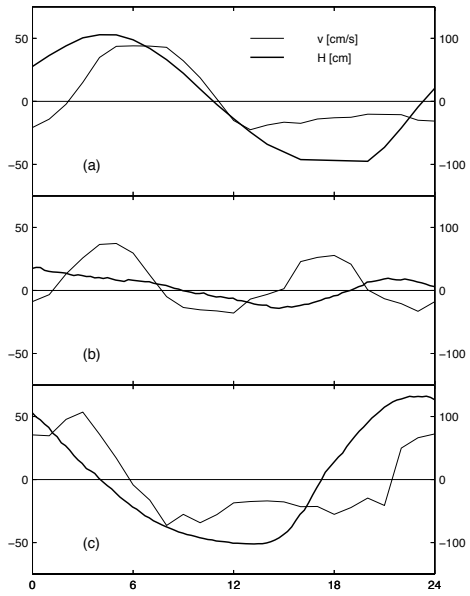

Figure 2. Three 24-hour measurements of water level (right y-axis, in cm) and near-bottom current velocity (left y-axis, cm/s, flood current positive) in front of the river mouth (for location; see panel (a) of Fig. 4). Panel (a) and (c) show spring tide measurements while neap tide measurements are given in (b). The flood current is directed towards the south.

3. Modelling: setup and preliminary results

The current field is computed with the flow module of the Delft3D software package for morphodynamic modelling. The flow module, run in 2DH mode, is solving the non-linear shallow water equations. The computational grid is curvilinear with 300*150 grid points, covering an area of 30 km cross-shore by 70 km alongshore. Water level variations are prescribed on the northern open boundary and the southern open boundary as progressive tidal waves; the shore-parallel sea boundary is closed. The 'free' parameters are the phase lag of the M_2 constituent on the diurnal constituents, and the propagation velocity of the semi-diurnal tidal wave and diurnal tidal wave. These three parameters can be estimated and fine-tuned to reproduce the flow pattern in front of the river mouth. Using the

propagation velocities of 30 m/s for the diurnal components and 10 m/s for the semi-diurnal component, only the phase lag of the semi-diurnal component relative to the diurnal component has to be iterated until the flow patterns of Fig. 2 are reproduced. The resulting water level variation and current velocities over two tidal cycles (spring tide and neap tide), at the same location were the measurements took place, are shown in Fig. 3.

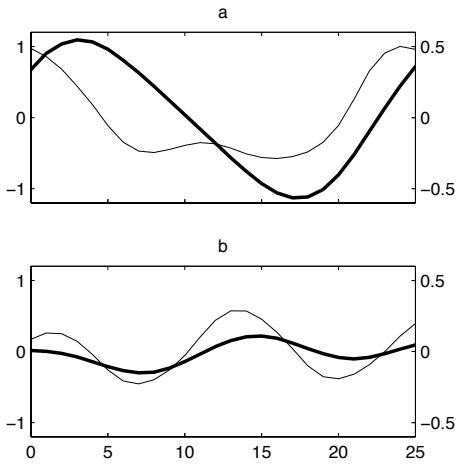

Figure 3. Model results in front of river mouth showing water level (thick line, left y-axis, in m.) and depth-averaged current velocity (right y-axis, m/s, flood current positive) in front of the river mouth (for location; see panel (a) of Fig. 4). Panel (a) shows a spring tide simulation, and panel (b) a neap tide simulation.

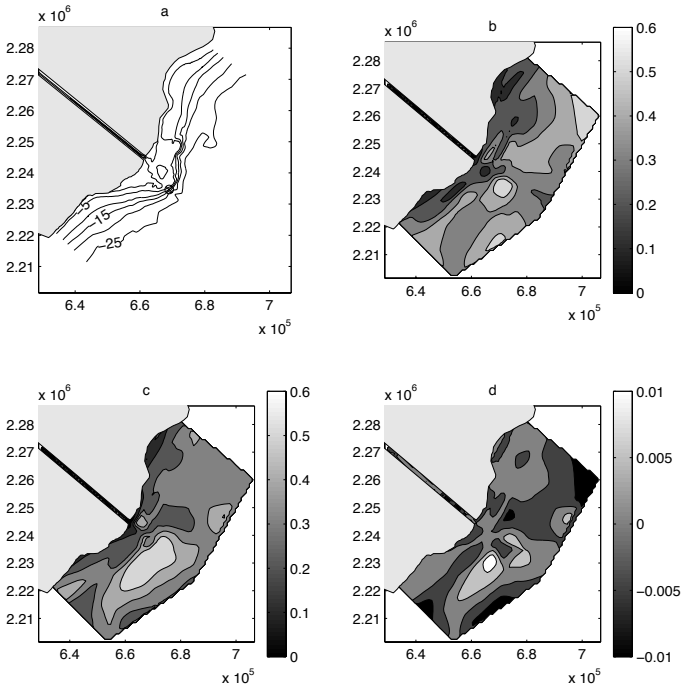

Figure 4. Model results for an M_2 tidal wave travelling at a speed of 10 m/s and O_1 and K_1 tidal waves travelling at a speed of 30 m/s. The bathymetry is shown in panel (a), while maximum ebb (northward) and flood (southward) velocities are given in (b) and (c) respectively (m/s). The transport capacity, defined as $< u^3 >$, is given in panel (d); positive values are directed towards the south.

The southward current (positive) is stronger than the northward current, and the period of southward flow is shorter, both agreeing with the results shown in Fig. 2. However, the propagation of a diurnal tidal wave and a semi-diurnal tidal wave is different due to e.g. bathymetric and frictional effects. Therefore the phase lags of the M_2 currents on the O_1 and K_1 currents will spatially vary. The result is a spatially varying asymmetry, which is depicted in fig. 4b and 4c: areas with higher flood velocities alternate in an alongshore direction with areas were ebb velocities are higher. This spatially varying dominance of ebb- and flood currents has implications for the sediment transport capacity of the tidal currents.

Erosion and deposition result from gradients in sediment transport. Flow contraction over the delta front (see Fig. 4b and 4c) results in deceleration of the flow velocity, and therefore sediment transport capacity, downstream of the deltafront. Therefore the southward tidal asymmetry on the delta front (Fig. 2 and 3) promotes deposition in the southern part of the subaqeous delta. The spatially varying tidal asymmetry complicates this pattern. The transport capacity is parameterised by averaging u^3 (the southward flood current as positive) over two tidal cycles (Fig. 4d). The strong spatial variation in this transport capacity is indicative of sediment transport divergences and convergences, and therefore, of spatial alternations of erosion and deposition. Southwest of the measurement location, where strong south-westward currents where measured, the model predicts stronger north-eastward currents. This implies that sediment transport paths converge on the southern part of the delta front. North of this point ebb-currents dominate as well, producing a divergence of the sediment transport capacity. Therefore, the spatial variability of O_1-K_1-M_2 tidal asymmetry may be another mechanism that contributes to the southward growth of the Ba Lat delta, in addition to the southward advection of suspended river plume sediments as described by Van Maren and Hoekstra (2003).

4. Discussion and conclusions

As a first order estimate, boundary conditions are prescribed by progressive tidal waves. Although the asymmetry of the current pattern is reasonably reproduced, the phase lag of water levels on the currents is not correct. While the currents lead the water levels according to the numerical model (due to frictional effects on the enforced progressive wave), the opposite was observed. The currents lag the water levels in Fig. 2, which is caused by resonance of the diurnal components in the northern parts of the Gulf of Tonkin. This will affect river outflow patterns, residual transports by the Stokes drift, and the spatial distribution of the flow asymmetry. Implementation of standing waves is part of future research.

Tidal asymmetry and flow contraction on the delta front favour a southward growth of the delta front. In addition, spatially varying tidal asymmetry results in alongshore alternations of sediment transport capacity divergence and convergence, which might result in erosion and deposition patterns. Although the spatially varying asymmetry of the tidal currents is highly sensitive to the imposed phase lags in the boundary conditions, a spatial varying pattern does arise for every calculated scenario. The result is that a large disturbance, in this case a delta front, can affect the O_1, K_1 and M_2 constituents in such a way that the resulting asymmetry further promotes or counteracts the growth of the disturbance.

References

Fang, G., Kwok, Y. K., Yu, K., and Zhu, Y. (1999), Numerical simulation of principal tidal constituents in the South China Sea, Gulf of Tonkin and Gulf of Thailand. Continental Shelf Research, 19(7), pp. 845-869.

Hoitink, A. J. F., Hoekstra, P., and Van Maren, D. S. (2003), Flow asymmetry associated with astronomical tides: implications for the residual transport of sediment. Journal of Geophysical Research C: Oceans, Submitted
Van Maren, D. S. and Hoekstra, P. (2003), A model for cyclic delta growth; the Ba Lat delta, Vietnam. Journal of Asian Earth Sciences, submitted.

Hydrodynamics across a channel-shoal slope in the ebb tidal delta of Texel, the Netherlands.

SANDRA VERMEER

(Utrecht University, P.O. BOX 80.115, 3508 TC Utrecht, the Netherlands, s.vermeer@geog.uu.nl)

AART KROON

(Utrecht University, P.O. BOX 80.115, 3508 TC Utrecht, the Netherlands, a.kroon@geog.uu.nl)

1. Introduction

Ebb tidal deltas are highly dynamic morphological features on the seaward side of tidal basins. They play an important role in the exchange of water and sediment between the tidal basin and the coastal zone. The interaction between the hydrodyamic conditions in and outside the inlet (waves, tides, winddriven currents, etc.) and the morphology of the ebb tidal delta provide for the sediment bypassing over the outer delta and thereby affect the stability of the adjacent barrier islands.

Sediment by-passing in ebb tidal delta systems is a well studied phenomenon (e.g. Bruun and Gerritsen, 1959; Bruun, 1966; Oertel, 1972; Nummedal and Penland, 1981; Hanisch, 1981; FitzGerald, 1982, 1988). However, these studies focus on the large scale behaviour of sediment paths but neglect the detailed sediment movement processes.

The aim of this research is to increase our knowledge of small scale hydrodynamics and sediment transport processes in a channel-shoal transition area on an ebb tidal delta. The hydrodynamic conditions are studied on a monthly time scale, twice a year in 2001 and 2002. The morphological changes are investigated over a period of 10 years, showing the morphological development of the channel-shoal transition area at the southern part of the Noorderhaaks shoal.

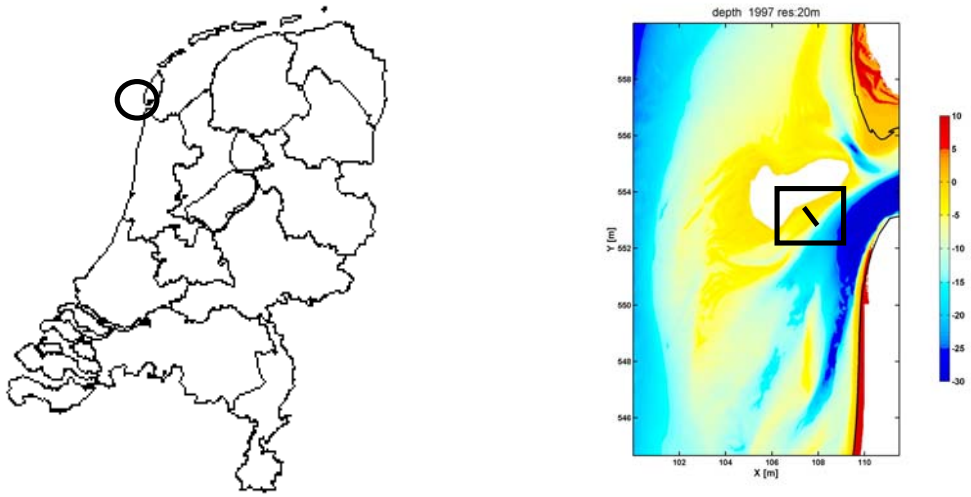

Figure 1: Left panel: Location of the ebb tidal delta of Texel, Right panel: Depth contours of the ebb tidal delta of Texel with the location of the channel-shoal area (box) and cross-channel transect (line).

2. Setting

The study area is situated on the ebb tidal delta of Texel, the Netherlands (Figure 1, left panel). The location of the experiments is south of the shoal Noorderhaaks and on the upper slope of the channel Schulpengat (Figure 1, right panel). This area is indicated as the channel-shoal transition area, from

–10 m to –2.5 m depth, where tidal and wave processes act upon and interact. The local morphology is separated in two zones: an upper slope and a lower slope area. The upper slope of the transition area, which is the deeper part of the shoal Noorderhaaks, inclines mildly around 1-2%. Mega ripples are the main bottom structures (height about 40-60 cm and length over 100 m, from local observations). The lower slope is steeper (up to 7%) and coincides with the upper slope of the channel Schulpengat. This part is situated in the outer channel bend. Bed forms mainly consist of oblique sand waves.

3. Morphological development 1986-1997

Figure 2 (left panel) shows the accretion and erosion patterns on the ebb tidal delta of Texel during the period 1986-1997. The black to gray colours indicate erosion and the gray to white accretion.

The middle supratidal part of the Noorderhaaks moved southward and expanded to the north and south at the western end. The situation is more complicated on the eastern side. The northern part of the channel Molengat migrated towards the east, thereby eroding the beach of Texel, while the southern part of the channel branched off to a northwestern direction. The southern part of the Noorderhaaks shows alternating stripes of erosion and accretion. For instance, the northern fringe of the Schulpengat channel eroded, while the Westgat was filled with sediment.

Figure 2 (right panel) shows two transects south of the Noorderhaaks in detail. The dynamic area is indicated by the box. The lower slope of the shoal Noorderhaaks, at a depth of about –3 to –5 m below mean sea level, increases in height by 0-0.5 m/yr, while the upper channel slope at a level of –10 m erodes at a rate of 12-13m/yr. This implies an overall increase of the channel slope. The field experiments are executed in this area.

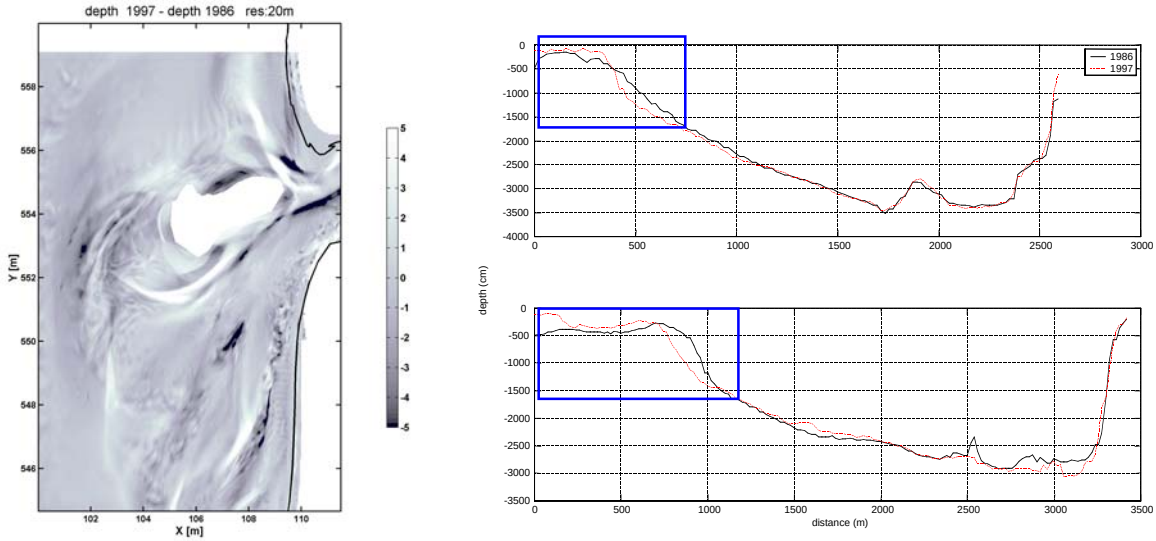

Figure 2: Left panel: Accretion – erosion patterns (in meters) in the ebb tidal delta of Texel, 1986-1997; Right panels: Transects from Noorderhaaks and the channel Schulpengat, orientated northwest-southeast. Top panel is the eastern transect, the lower panel the western transect, tripod transect (see Figure 1) is situated in between.

4. Hydrodynamics

Currents

The tidal wave on the North Sea travels from south to north along the Dutch coast and propagate into the tidal inlet from southwest. The tidal current ellipses in the study area have a bidirectional character with a northeast – southwest direction.

The hourly averaged mean currents as observed at –10 m depth (Figure 3, left panels; for location see Figure 1) show a barchan shaped cloud of dots. Each dot represents averaged velocity measurements which were sampled each hour with a frequency of 2 Hz over 34 minutes. The shape indicates a downslope directed (secondary) current, which can be associated with the secondary downslope directed current in the outer bend of a river channel (personal communication Van Aken, 2002; Van Rijn, 1994).

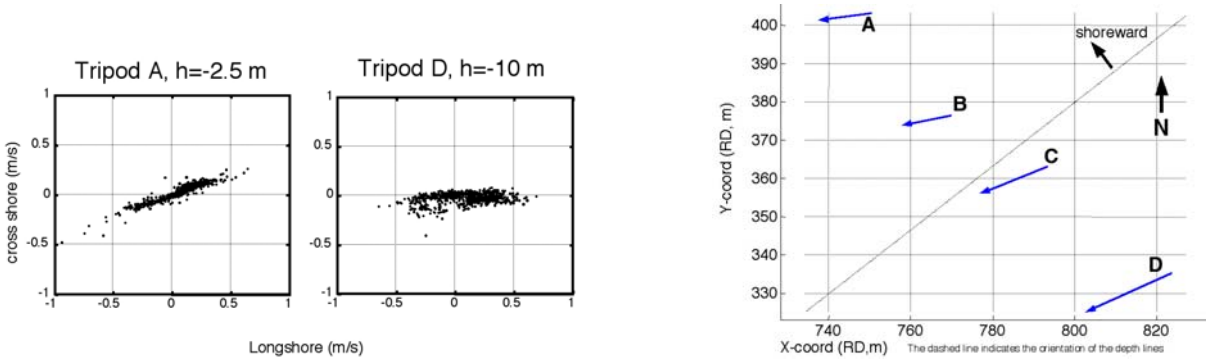

Figure 3: Left panel: mean current during June 2001 and October 2001 at –2.5 m (left panel) and –10 m depth (right panel). The x-axis represents the longshore direction, the y-axis the cross shore direction, Right panel: tidally averaged mean current (25 hours), conditions indicated in Figure 4; Depths: –10 m (D), -7.5 m (C), -4.5 m (B) and –2.5 m (A).

The tidally averaged mean current (25 hour resultant vectors) over the cross-shore profile show a spatial pattern (Figure 3, right panel) with an increase of the velocity direction towards the slope from deep water (tripod D at –10 m) towards the shore (tripod A at –2.5 m). However, the velocity decreases from 0.24 m/s at deep water (tripod D) to 0.18 m/s at shallow water (tripod A). The net velocity vectors point at an ebb dominance in the channel-shoal transition area. The difference in direction of the mean current between tripod A and D (see also Figure 3, left and middle panels) is theoretically due to the generation of vorticity by bottom friction and the Coriolis force (Van de Meene, 1994).

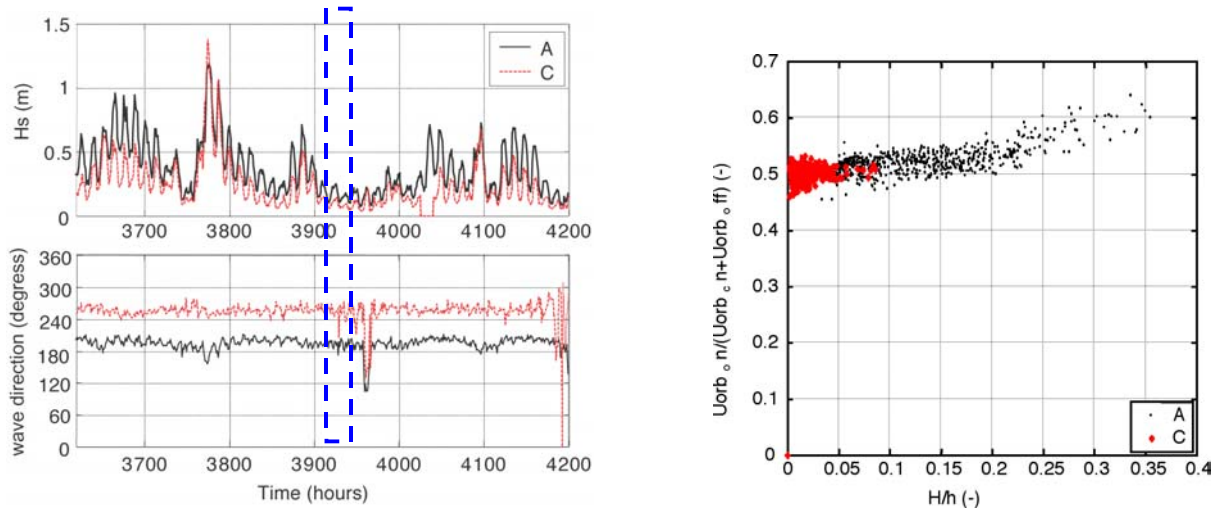

Figure 4: Upper left panel: significant wave height (A,C), lower left panel: wave direction (A,C) during June 2001. The box indicates the conditions for Figure 3, right panel. Right panel: wave asymmetry at –7.5 m (C) and –2.5 m (A) depth.

Waves

Figure 4 (upper en lower left panels) shows the wave conditions during June 2001. In this period of one month, higher wave energy conditions with local significant wave heights over 0.5 m alternate

with lower wave energy periods. The dominant wave direction during this month is south-southwest. This direction often differs from the wind direction. This is caused by refraction and the sheltering effect of the Noorderhaaks in the North and West, the coast of North-Holland east of the tripods and the location of the tidal inlet in the northeast.

The waves on the channel-shoal transition zone transform when they propagate from deep to shallow water.

Firstly they refract on the depth contours and tidal currents and secondly they become asymmetrical.

The refraction of the waves is shown in Figure 4, lower left panel. The waves refract from a west-southwestern direction at a water depth of 7.5 m (tripod C) towards a southern direction at a water depth of – 2.5 m (tripod A). The asymmetry of the waves is expressed by the velocity ratio:

$$A = \frac{U_{orb,on}}{(U_{orb,on} + U_{orb,off})}$$

Where $U_{orb,on}$ is the significant onshore component of the orbital velocity and $U_{orb,off}$ is the significant offshore component of the orbital velocity.

The asymmetry of all measured bursts is presented in Figure 4, right panel, where it is plotted against the local relative wave height, defined as the local wave height (H) divided by the local water depth (h). The waves near tripod C are almost symmetrical, whereas they become more asymmetric in shallow water dephts (tripod A). This asymmetry clearly increases with an increase of the local relative wave height.

5. Conclusions

The results from the hydrodynamic measurements and the erosion-accretion map indicate that processes involved with curved flow in a channel bend, provide for the morphological development in the lower part of the channel-shoal transition area.

In addition, the wave asymmetry, the dominant wave direction and the tide averaged currents indicate to provide for the observed accretion on the higher part of the channel-shoal transition area.

Further analysis of ADCP data, deployed in the channel-shoal transition area should give more indications for the processes as described in this paper.

Acknowledgements: This research is part of the `Outer Delta Dynamics'-project, initiated by the Netherlands Centre for Coastal Research (NCK) and financed by NWO/ALW (the Netherlands Organization for Scientific Research). Shipping time was provided by the NIOZ (Netherlands Insitute for Sea Research) and also partner in this project. The tripods were supplied by the Direction North Holland of the Ministry of Transport, Public works and Water management.

References

Bruun, P. (1966) Tidal inlets and littoral drift. Universiteitsforlaget, Trondheim, Norway.

Bruun, P. and Gerritsen (1959) By-passing of sand by natural action at coastal inlets and passes. Proc. ASCE, J. Waterways and harbour Div., Vol. 85, WW4.

FitzGerald, D. M. (1982) Sediment bypassing at mixed energy tidal inlets. Proceedings of the Eighteenth Coastal Engineering Conference(November 1982), Cape Town, South Africa. ASCE, p 1094-1118.

FitzGerald, D. M. (1988) Shoreline erosional-depositional processes associated with tidal inlets. Vol 29, New York, Springer-Verlag. Lecture notes on Coastal and Estuarine studies, p 186-225.

Hanisch, J. (1981) Sand transport in the tidal inlet between Wangerooge and Spiekeroog (W. Germany). Special Publs.Int.Ass.Sediment 5, p 175-185.

Nummedal, D. and Penland, S. (1981) Sediment dispersal in Nordeneyer Seegat, West Germany.Special Publs.Int.Ass.Sediment 5, Oxford, Blackwell Scientific Publications, p 187-210.

Oertel, G. F. (1972) Sediment transport of estuary entrance shoals and the formation of swash platforms. Journal of Sedimentary Petrology 42 No. 2, p 857-863.

Van de Meene, (1994) The shoreface-connected ridges along the central Dutch coast. Thesis, KNAG / Netherlands Geographical Studies, 222 p.

Van Rijn, L. C. (1994) Principles of fluid flow and surface waves in rivers, estuaries, seas and oceans. Aqua Publications, Oldemarkt, 335 p.

Effect of wind wave breaking on the eddy viscosity profile to understand large-scale morphology in tidal seas

H.P.Viduragomi Vithana and Suzanne J.M.H.Hulscher

July 17, 2002

University of Twente, Postbus 217, 7500 AE Enschede, The Netherlands email: h.p.v.vithana@ctw.utwente.nl, s.j.m.h.hulscher@ctw.utwente.nl

1 Introduction

The generation mechanisms of offshore large-scale bed features in the North Sea such as sand waves and sand banks have been modelled using the shallow water equations with the aid of a depth averaged eddy viscosity profile. One simplified way of accounting for the influence of enhanced turbulence due to wind wave breaking in the upper ocean layer is to reflect it in a parabolic z-dependent eddy viscosity profile via viscosity variation parameter, ε which will determine the shape of the profile in relation to a change in strength of wave breaking. The relationship of this parameter with other important model variables like wind speed, fetch and significant wave height coupled via a $k-\epsilon$ model reasonably mimics the general behaviour of the upper ocean turbulence (or eddy viscosity) in response to a development stage of the wind waves.

1.1 Linking wind waves and offshore morphology

More sophisticated $k-\epsilon$ models to determine the wave breaking induced turbulence and hence eddy viscosity in a more realistic manner is available in the literature [Burchard (2001); Burchard & Petersen (1999); Ly (1996)]. Nevertheless, this study was undertaken to bring-in the main effect of wave breaking induced turbulence in a simple way via an eddy variation paramter ε inside the parabolic eddy viscosity profile in the form $\tilde{\nu}_t = \kappa \hat{u}_* \tilde{z}\,[1-(\varepsilon \tilde{z}/h)]$ for the more limited objective of morphological modelling using shallow water equations. Presently no plausible method exists to translate the magnitude of the wind wave stirred turbulence into a parameter like ε ranging between 0.5$\sim$1.0.

Hulscher's (1996) model predicts the occurance of large scale seabed patterns like sand waves and sand banks quite well via two parameters. That is, stokes parameter $E_v = \frac{2A_v}{\sigma h^2}$ and ressistance parameter, $\hat{S}$ defined such that $\tau = A_v\left(\frac{\partial u}{\partial z}\right) = Su$ and $\hat{S} = \frac{2S}{\sigma h}$. Here, A_v is the depth averaged eddy viscosity , h is water depth and σ is tidal frequency. A schematic diagram of the Hulscher (1996) bed form

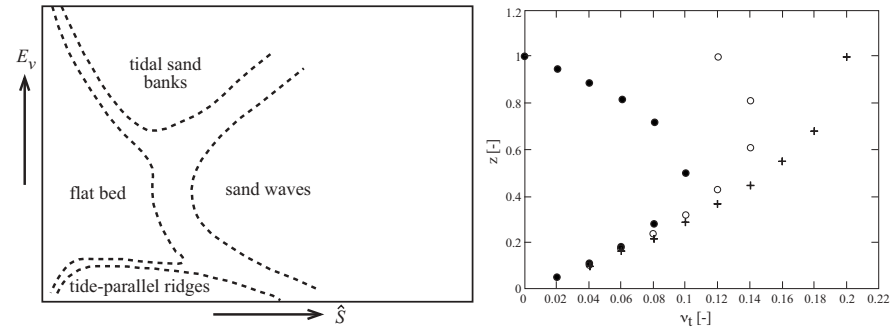

Figure 1: (a) Morphology prediction model of Hulscher (1996) [**left**] (b) The normalised eddy viscosity ν_t, plotted against normalised depth for $\varepsilon = (+)\ 0.5$, $(\circ)\ 0.7$ and $(\bullet)\ 1.0$ [**right**]

prediction model is given in Figure 1. The stokes and the resistence parameters have been interpreted via ε parameter and bed roughness z_0 for the ease of physical estimation (Hulscher & Van den Brink, 2001).

2 Modelling dissipation rate

The pattern of the TKE dissipation over the water column has been found to follow three layered structure according to Terray *et al.* (1996). The top layer whose thickness is in the order of a one wave height is considered to be directly stirred and is assumed to have a constant dissipation rate. The intermediate layer below has been found to obey the following power law, $\tilde{\epsilon}_w H_s/\alpha_0 u_{*a}^2 c = \beta \tilde{Z}^{-2}/H_s^{-2}$, where $\tilde{Z}$ measured downwards from water surface. Here $\tilde{\epsilon}_w$ is the dissipation due to wave breaking, $\alpha_0 = \rho_a/\rho_w$, ρ_a and ρ_w are mass densities of air and water respectively, u_{*a} is the wind shear velocity, c is an *equivalent phase speed*, H_s is the significant wave height, $\beta = 0.3$. Let us define $\alpha_a = \alpha_0 u_{*a}^2 H_s^{-1} c$. In this case for the ease of manipulation an exponential form, i.e., $\tilde{\epsilon}_w H_s/\alpha_0 u_{*a}^2 c = \beta \exp(Kz)$ for the dissipation rate was used without loosing general trends. It is assumed that the total TKE dissipation is the sum due to shear flow (wall layer close to bottom) and the wave energy dissipation, i.e., $\tilde{\epsilon} = (\hat{u}_*^3/\kappa\tilde{z}) + \alpha_a \beta e^{K\tilde{z}}$ where $K \sim 1.0$.

3 Formulation

A relation for the energy balance of the turbulence in the upper ocean could be given as follows [Burchard and Petersen (1999), Burchard (2001)]:

$$\frac{\partial k}{\partial \tilde{t}} - \frac{\partial}{\partial \tilde{z}}\left(\nu_k \frac{\partial k}{\partial \tilde{z}}\right) = P + B - \tilde{\epsilon} \tag{1}$$

k denotes the square root of the turbulent kinetic energy per unit mass. The second term on the left hand side in (1) is represented by a turbulent kinetic energy diffusion term $\tilde{D}_v \partial^2 \tilde{u}/\partial \tilde{z}^2$ with a vertical diffusion coefficient $\tilde{D}_v$. The vertical buoyancy flux term B has been neglected assuming an unstratified ocean

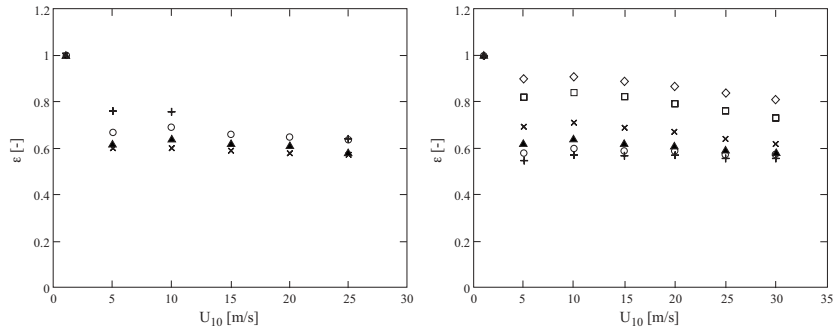

Figure 2: (a) ε parameter vs different wind speeds for four different fetches at 30m water depth ; (+) 100 km, (∘)250 km, (▲) 500 km and (×) 1000 km [**left**] (b) ε parameter vs wind speed for different water depths at a fetch X=500km ; + h=10m, ∘ h=20m, ▲ h=30m, × h=50m, □ h=100m, ⋄ h=150m [**right**]

and $P = \nu_t \left(\frac{\partial \tilde{u}}{\partial \tilde{z}}\right)^2$. It is also assumed that the turbulence is steady, i.e., $\partial k/\partial \tilde{t} = 0$. Substituting a constant stress relationship $\tilde{\nu}_t(\tilde{z})\, \partial \tilde{u}/\partial \tilde{z} = u_{*w}^2 \approx 8\hat{u}_*^2/3\pi$ in (1) for the relatively thin upper ocean layer we get a quadratic equation for the eddy viscosity variation parameter, ε

$$\varepsilon^2 + \left(\frac{n}{\kappa m z^2} - \frac{2\lambda}{\kappa m z^3} - \frac{2}{z}\right)\varepsilon + \left(\frac{1}{z^2} - \frac{n}{\kappa m z^3} + \frac{\lambda}{\kappa m z^4}\right) = 0 \qquad (2)$$

where $m = \epsilon/D_v$, $n = \lambda^2/D_v$. The horizontal velocity is scaled using the maximum shear velocity, $\hat{u}_*$ of the tidal flow. The vertical coordinate is scaled using the water depth, h and the eddy viscosity by $\hat{u}_* h$. The tildes represent the dimensional parameters. Here, $\lambda = 8/3\pi$. The normalisation $(\tilde{u}, \tilde{z}, \tilde{\nu_t}) = (\hat{u}_* u, zh, \hat{u}_* h \nu_t)$ is used in this formulation throughout. It was found that the wind shear stress and the significant wave height are the most appropriate scales to model the diffusion coefficient. The dimensional and experimental evidence and the intuitive considerations led to the following scaling $\tilde{D}_v = \mu_0 (H_s/L)^{\frac{1}{2}} u_{*a}^2 H_s$. Here $\mu_0 = 10$ is a constant.

4 Results and Discussion

The model retains the important property that for a particular fetch distance there is a particular wind speed which will give the maximum wave development. Beyond this critical wind speed however much the wind speed is increased the value of ε will remain almost constant. The parameter values corresponding to maximum and minimum wind wave turbulence are computed to be $\varepsilon \approx 0.5$ and 1.0 [*see Figure 1(b)*]. It further shows that for lower values of ε not only the full development but also the magnitude of the significant wave height is important. The transformation of wind speed and fetch into wave parameters was done via the JONSWAP spectrum.

If we look at the Table 1 for fetch X=500 km the bigger waves which can make a significant impact on morphology occur when wind speed say, $U_{10} >$ 10 m/s, representing storm conditions. If we observe Figure 2(a) it could be noticed that value of ε falls in a narrow region between $0.6 \sim 0.75$ for a wide

Table 1: The change of eddy viscosity variation parameter with the wind speed for 500 km fetch and 30m water depth

U_{10} (m/s)	$\frac{U_{10}}{c_p}$	H_s (m)	T_s (sec)	H_s/L	$\overline{\varepsilon}$
1	0.14	0.4	4.5	0.01	1.00
5	0.42	1.8	7.6	0.02	0.62
10	0.72	3.6	9.6	0.03	0.64
15	1.00	5.4	11.0	0.03	0.62
20	1.29	7.2	12.0	0.038	0.61
25	1.57	9.1	13.0	0.043	0.58

range of fetch distances at a constant depth of 30 m. This is about 30% of the maximum possible variation of 0.5. The Figure 2(b) describes the change of the parameter against wind speed for different water depths for a constant fetch distance of 500km. For such wave conditions it can be seen broadly that the value of ε parameter for lower water depths say upto 50m, lies in a narrow region between $0.55 \sim 0.7$. For intermediate depths, say 50m$> h >$100m, the parameter broadly lies between $0.65 \sim 0.85$. For deeper water, say h>100m, the values may vary between $0.85 \sim 1.00$.

5 Conclusion

The assumption of steady turbulence in the upper ocean with constant shear stress and no density stratification has yielded a solution for the eddy viscosity variation parameter ε in which the effect of wind wave breaking could be reflected in a simple way for the specific purpose of morphological modelling using shallow water equations. The results lead to following conclusions.

[1] The parameter could be generally assumed constant within certain depth ranges for morphologically significant wind conditions if sufficient fetch is available.
[2] The parameter does not show a sensitivity for higher fetch, say, above 250km suggesting its spatial variation is not important for open shelf seas.
[3] For depths upto $O(50m)$ where the wind wave breaking influenced stirring of the water column is important an overall parameter value of 0.65 is appropriate.
[4] These evidence suggests that variations in wind wave breaking in the upper ocean layer do not contribute to significant variations in eddy viscosity profile to be able to effect variations in generating the type of large-scale bedforms, i.e., sand banks and sand waves.

References

[1] Burchard, H., 2001, Simulating the wave-enhanced layer under breaking waves with two equation turbulence models, *J. Phys. Oceanogr.*, **31**, 3133-3145

[2] Hulscher, S.J.M.H. & van den Brink, G.M., 2001, Comparison between predicted and observed sand waves and sand banks in the North Sea, *J. Geophys. Res.*, **106**, C5, 9327-9338

[3] Terray, E.A., Donelan, M.A., Agrawal, Y.C., Drennan, W.M, Kahma, K.K., Williams III, A.J., Hwang, P.A., & Kitaigorodskii, S.A. , 1996, Estimates of kinetic energy dissipation under breaking waves, *J. Phys. Oceanogr.*, **26**, 792-807

Forced oscillations near the critical latitude for diurnal-inertial resonance

JOHN.H.SIMPSON, PAT HYDER, TOM.P. RIPPETH

University of Wales, Bangor, School of Ocean Sciences, Menai Bridge, Anglesey, LL59 5EY; UK.,

Extended Abstract

Oscillations at, or close to, the inertial frequency are widely observed in shelf seas where frictional damping is weak. In the vicinity of latitudes 30 deg. Nand S, such motions may become significantly enhanced by a resonance in which the local inertial frequency coincides with that of diurnal forcing. Under these conditions, regular daily variations in wind stress tend to produce large anticyclonic motions which may extend throughout the water column. In this presentation we shall examine new observations from a location close to the critical latitude on the Namibian shelf in the southern hemisphere

The observations, covering the period March 1998 to April 1999, were made by Fugro Geos for Shell Exploration and Production Namibia B. V. at the Kudu field on the Namibian shelf. Here we shall consider the results from a single ADCP mooring deployed at a location (28.6° S, 14.6 °E) which is ≈133 km from the coast at the outer edge of the shelf in water of depth 175m. This location is at the southern end of the Benguela upwelling system. Time series of the current structure were obtained using a pair of ADCP instruments (RDI Workhorse 300kHz) mounted- in midwater on a single mooring. The instruments, one looking upward, the other downwards, measured the current profile throughout the water column except for immediate near-surface and near- bed shadow zones (≈12 m thick) where side lobe effects prevent valid measurements. The vertical bin size was set to 8m and the instruments recorded ensemble means over periods of 10 minutes. Our initial analysis concentrates on a continuous data series from both instruments for the period 9/3/98 to 15/4/98 but we shall also make use of the full annual cycle of data to draw further conclusions about the nature and origin of the observed diurnal-inertial oscillations.

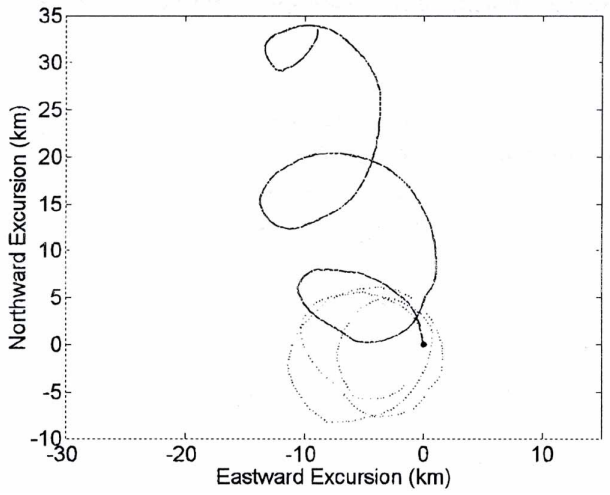

Figure 1 Progressive vector diagram at 21 m depth (----) and with mean flow removed (. . . .)

At all depths there is clear evidence in the progressive vector diagrams (fig 1) of a pronounced anticyclonic component of current rotating once per day. In many cases these diurnal currents exceed the mean flow and cause the flow direction to reverse. This dominance of the circular motions is most apparent during the period March 15-23 when the mean flow was generally weaker. The vertical structure of the diurnal currents is presented in fig.2 as the amplitude and

phase of the anti-clockwise component which dominates over the almost negligible clockwise flow. The oscillations have the greatest amplitude in the surface layer but energetic motions (speed > 0.2 m/s) occur in the bottom layer where the flow is ~180 degrees out of phase with the upper layer. This phase change which occurred progressively between ~40 and ~ 110m depth was a persistent feature of the flow and was associated with a minimum amplitude at around 80m depth.

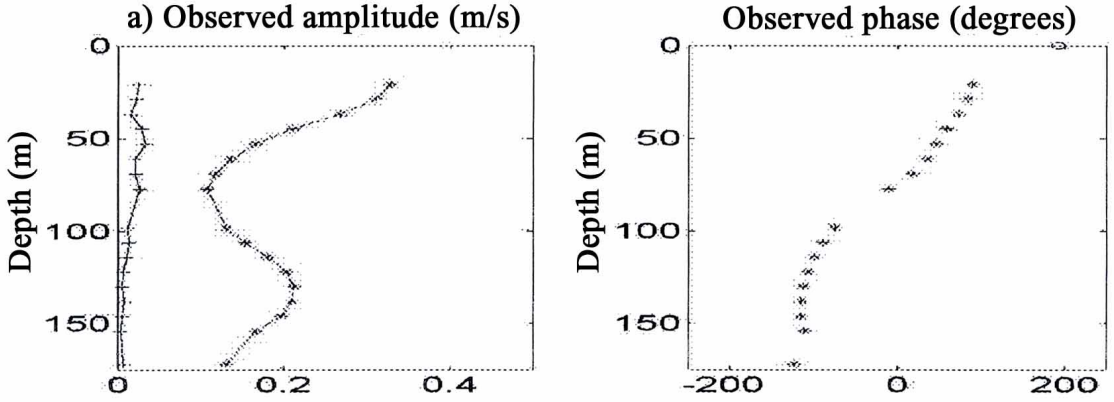

Figure 2.Vertical structure of (a) the amplitude of the anti-clockwise (*) and clockwise (+) diurnal current components and (b) the phase of the anticlockwise component

Unfortunately wind data were not recorded at the mooring location. The nearest source of wind data is the airport at Oranjemund which is close to the Namibian coast but ~ 150 km from the current meter mooring. Time series from this source provide clear evidence of marked diurnal variations in the windstress associated with the sea breeze regime which is a well known feature of this coast. The mean stress at oranjemund is mostly directed to NE with values up to 0.04 Pa but considerably stronger stresses are associated with the high frequency variations. Cross-shore and along shore components have maxima of comparable amplitude in mid-late afternoon (1500-1800) with peak stresses exceeding 0.1 Pa. and much weaker offshore stresses at night. The cross-shore and along shore diurnal components of the wind vector are almost in phase so the motion is approximately rectilinear at 45^{o} to the coast, i.e. N-S, and consists of nearly equal clockwise and anticlockwise components.

The picture that emerges from the observations is of a current system in which strong diurnal-inertial oscillations are superimposed on a weaker mean flow to the north. The vertical structure of the diurnal motions consists of two layers oscillating with comparable kinetic energy but ~ 180 degrees out of phase. This form of vertical structure and the intensity of the current response may be understood in terms of a simple analytical model. . We consider flow in a shelf region bounded by a coastline extending in the y direction at x=O and with a depth profile H (x). The layers are assumed to be uniform but decoupled from each other by a frictionless interface while the motion is forced by an oscillatory windstress (τ_x , τ_y) at the diurnal frequency ω. The momentum equations may be written for the upper and lower layers respectively as:

$$\frac{\partial u_1}{\partial t} - fv_1 = \frac{\tau_x}{\rho h_1} - g\frac{\partial \eta}{\partial x}\ ; \qquad \frac{\partial v_1}{\partial t} + fu_1 = \frac{\tau_y}{\rho h_1} \tag{1}$$

$$\frac{\partial u_2}{\partial t} - fv_2 = -g\frac{\partial \eta}{\partial x}\ ; \qquad \frac{\partial v_2}{\partial t} + fu_2 = 0 \tag{2}$$

where η is the surface elevation. Providing that the shelf width L is small in relation to the barotropic wavelength $2\pi(gH)^{1/2}/\omega$, we may employ the lowest order vertically-integrated solution (Craig 1985) in order to determine the surface slope as:

$$\frac{\partial \eta}{\partial x} = \frac{\tau_x + i\left(\frac{f}{\omega}\right)\tau_y}{\rho g H} \tag{3}$$

Because of the no-normal-flow condition at the coast, the diurnal cross-slope stress τ_x induces an opposing surface slope. Similarly the along-shore windstress τ_y drives a coast-parallel, depth uniform current V= i $\tau_y/(\omega gH)$ which, in geostrophic balance, requires a surface slope component of amplitude $(f/\omega)\ \tau_y$. Substituting equation (3) into (1) and (2) and defining the complex velocity $w=u+iv = We^{i\omega t}$, we have the steady state solutions for anti-clockwise motion as:

$$W_1 = \frac{\gamma T_x + i(\gamma + f/\omega + 1)\,T_y}{i\rho H(f+\omega)}\ ; \qquad W_2 = \frac{-(T_x - if/\omega T_y)}{i\rho H(f+\omega)} \tag{4}$$

where $\gamma = h_2/h_1$. Close to the resonant latitude in the southern hemisphere $f/\omega \Rightarrow -1$ so that

$$W_1 \approx \frac{\gamma(T_x + iT_y)}{\rho H(f+\omega)} \approx -\gamma\, W_2 \tag{5}$$

This result indicates that the phase of the motion will differ by 180 degrees between the two layers and that the ratio of the velocity amplitude in the two layers will be γ which is of order unity in the present case so that upper and lower layer motions will be of comparable magnitude. While the anticlockwise response will be enhanced at latitudes close to 30 degrees South where f= -ω, the response to cyclonic forcing (ω = f) at the diurnal frequency is considerably weaker by a factor of $|(f+\omega)|/|(f-\omega)|$. This ratio has a value of ≈47 for latitude 28.6 degrees south so that, for equal forcing, anti-clockwise motions should be minimal as observed. The ratio of the depth mean current amplitudes in the upper and lower layers is ≈ 1.7 (figs 5 and 10) which is consistent with a value of *y* based on layer thicknesses h_1 = 65m and h_2 = 110m.

Because the wind data was not recorded locally, it is not possible to demonstrate unequivocally that these unusually large oscillations are due to local wind forcing alone. An interesting, alternative mechanism which might account for the enhancement of energy near the critical latitude is the turning of near inertial internal waves (Fu 1981). Such waves of diurnal frequency, having been generated by wind forcing in lower latitudes, propagate polewards to be arrested at their "turning latitude" of30 degrees with a consequent peak in energy in the diurnal band at this latitude. Three results from our analysis of the full data series of ~400 days are against such non-local generation:

i) The annual cycle of the diurnal windstress at the coast is reflected to a significant degree in the current amplitude

ii) The phase of diurnal oscillations, determined daily, shows a considerable degree of consistency throughout the year but particularly during the summer period when diurnal wind forcing is greatest.

iii) The consistent vertical structure over the annual cycle does not show indications of the phase and energy propagation commonly observed in deep-ocean observations of inertial motions.

The near-resonant response observed in this case involves an efficient transfer of momentum and energy from the wind field to the current system with the diurnal motions dominating the kinetic energy spectrum. The anti-phase motions in top and bottom layers involve substantial vertical shears which will tend to promote dissipation and vertical mixing through the water column. In shelf areas with significant diurnal winds and located close ($\pm 10^{o}$) to the critical latitude, this energy source may be an important mechanism for inducing mixing between upper and lower layers. Where, as in the case considered here, tidal forcing is weak, motions in the diurnal-inertial band may be the dominant mechanism for vertical exchange through a stratified water column.

References

Craig P.D. (1989a) Constant eddy-viscosity models of vertical structure forced by periodic winds Continental shelf Research 9(4), 343-358.

Craig, P.D. (1989b) A model of diurnally forced vertical current structure near 30° latitude. Continental Shelf Research, 9 (11), 965-980.

Fu L.L. (1981) Observations and models of inertial waves in the deep ocean. Rev. Geophys. Space Phys. 19, 141-170

First results of a study on the turbulent mixed layer in the Baltic Sea

HANS ULRICH LASS

(Baltic Sea Research Institute Warnemünde, Seestr. 15, D-18119 Rostock, Germany, lass@io-warnemuende.de)

HARTMUT PRANDKE

(ISW Wassermesstechnik, Lenzer Straße 5, D-17213 Petersdorf, Germany, prandke@t-online.de)

HANS BURCHARD

(Baltic Sea Research Institute Warnemünde, Seestr. 15, D-18119 Rostock, Germany, hans.burchard@io-warnemuende.de)

1. Introduction

An understanding of turbulence is a key goal of the dynamics of the surface layer of the ocean since turbulent processes are crucial in controlling the exchange of momentum, dissolved and particular matter between the atmosphere and the ocean. Until recently our knowledge of turbulence in the surface mixed layer has been severely limited by the difficulties of making measurements of the fluctuating velocity components near the sea surface remote from a disturbing platform (ship) carrying the necessary equipment.

Using free falling dissipation profiler the high wave number range of the turbulence was accessible. Oakey and Elliott (1982) could show that a constant fraction of the energy flux in the atmospheric boundary layer, namely $8u_*^3$, appears as dissipation in the mixed layer. Measurements below breaking surface waves revealed a layer of enhanced dissipation where dissipation could not be scaled by the wall-layer scaling, Agrawal et al. (1992). Anis and Moum (1995) observed by means of a rising dissipation profiler vertical profiles of dissipation in the surface boundary layer. They observed a depth dependence of the dissipation close to exponential with a decay rate on the order of the inverse wave number of the waves, suggesting wave-related turbulence in the upper part of the ocean surface boundary layer. Moreover, they suggest that high levels of turbulent kinetic energy are produced in a thin surface layer with thickness of the order of the height of the breaking waves.

Shallow (50 m deep) banks in the central parts of the tide less Baltic Sea provide a suitable site for performing reliable turbulence measurements with bottom mounted instrument carrier. This gives a good opportunity to study the surface mixed layer dynamics in relation to surface gravity waves in a stratified water body remote from the shores.

2. Methods and data

Measurements have been performed in the central Baltic Sea, from 30 August to 7 September 2001 aiming at the estimation of the turbulent energy balance of the surface mixed layer. Time series of profiles of turbulent kinetic energy dissipation were measured by a rising dissipation profiler. The profiler was positioned with bottom mounted idler pulley outside the area where the ambient turbulence is disturbed by the anchored ship, see Figure 1 (for details, see Prandke et al., 2000). The dissipation profiler started from a depth well below the seasonal thermocline and rose up to the sea surface. Six profiles were taken every hour in a burst mode. Complementary measurements comprised time series of hourly CTD profiles extending from the sea surface to close to the bottom, of hourly current profiles measured with a bottom mounted ADCP, of hourly wave spectra measured with a pressure recorder SBE 26 moored in about 5 m below the sea surface, of momentum and of buoyancy

fluxes through the sea surface calculated from continuous time series of the corresponding meteorological parameters measured on board the research vessel.

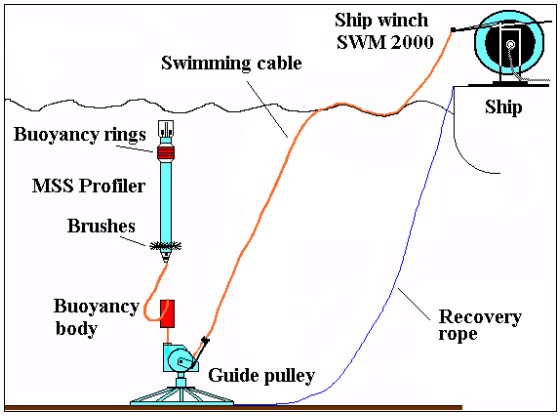

Figure 1: Scheme of dissipation measurements with a rising dissipation profiler from the anchored R/V Prof. A. Penck

3. Observational results

The wind forcing at the sea surface was characterised by a sequence of calm phases followed by wind events of moderate strength during the observations. The typical summer stratification of the Baltic Sea consisted of 17°C warm brackish surface water and 4°C cold intermediate winter water. Both layers were separated by a strong thermocline located at about 25 m depth. A special wind event forced a group of inertial waves at 4 September 2001, while weak inertial oscillations where prevailing before this event.

Two physically different dissipation regimes could be observed, see Figure2. The first, the internal dissipation regime, was quite independent of the local wind speed. It featured a maximum located in the seasonal thermocline and was most intense after the wind event that generated strong inertial waves. The second, the surface dissipation regime, was closely correlated to the local wind speed. It had a maximum at the sea surface. An injection layer of turbulent energy was observed near the sea surface which was roughly one significant wave height thick. About one third of the total turbulent energy flux through the sea surface was dissipated within the injection layer.

A transport layer of turbulence was observed below the injection layer. The dissipation rate of turbulent energy decayed exponentially with depth within the transport layer. The decay rate depends on the local wind. The dissipation rate of the transport layer decreased to values of the internal dissipation regime at a depth $z_i=2U^2/g$, where U is the wind speed at 10 m above the sea surface and g is the gravity of the earth.

The vertical integrated dissipation rate of the surface dissipation regime is balanced by the flux of turbulent kinetic energy through the sea surface ($8u_*^3$ according to Oakey and Elliott, 1982). This flux was found to be not significantly different from the energy loss of surface waves by wave breaking according to Longuett-Higgins (1969).

The surface dissipation regime can be described by the relation $\varepsilon(z) = \varepsilon_o e^{kz}$, where $\varepsilon_o = \frac{8u_*^3}{3H_{sig}}$ and k is the characteristic wave number of the wind waves $k = \frac{g}{U_{10}^2}$. H_{sig} is the significant wave height,

$u_*^2 = \frac{\tau}{\rho_o}$ with the wind stress τ and the density of sea water ρ_o and the wind velocity at 10 m height above the sea surface U_{10}.

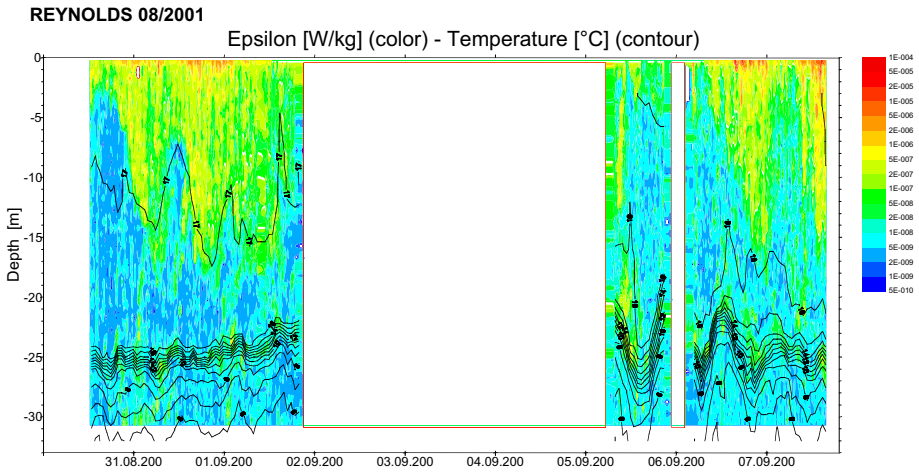

Figure 2. Isopleths of dissipation of turbulent kinetic energy (grey scale coded) and water temperature (contour lines) during the cruise. The gaps are due to technical problems with the stern anchor of the research vessel.

The normalised dissipation rate measured in the surface regime is shown in Figure 3.

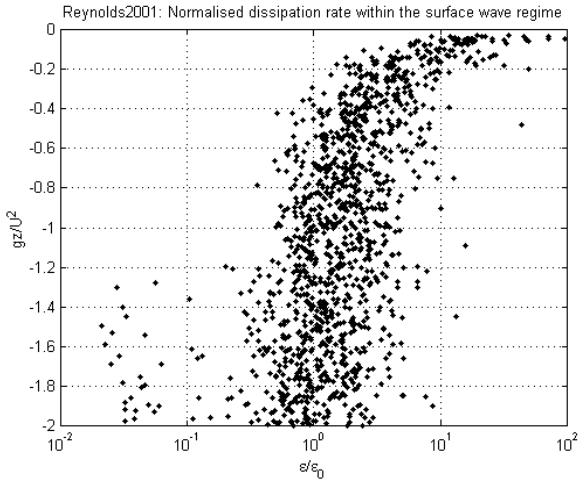

Figure 3. Profiles of turbulent kinetic energy dissipation normalised with respect to depth and dissipation.

4. Numerical Modelling

In order to better interprete the observed dissipation rates, a simulation with a 1D water column model will be performed. Initial and surface boundary conditions will be taken from observations as well as the vertical velocity which will be analysed from CDT-casts. The model includes a generic two-equation turbulence closure model recently suggested by Umlauf and Burchard (2002) which is able to resolve the transport layer and the underlying shear layer, but parameterises the injection layer which is calculated by means of a surface roughness length depending on the wave height.

Acknowledgments: The authors are grateful to the captain, the officers and the crew of the research vessel Prof. A. Penck who supported us during the field measurements. This work was supported by the Federal Ministry of Research and Education of Germany under contract number 01LD0025.

References:

Agrawal, Y. C., E. A. Terray, M. A. Donelan, P. A. Hwang, A. J. Williams III, W. M. Drennan, K. K. Kahma, and S. A. Kitaigorodskii, Enhanced dissipation of kinetic energy beneth surface waves. *Nature*, 359, 219-220, 1992.

Anis, A. and J. N. Moum, Surface Wave – Turbulence Interactions: Scaling ε(z) near the sea surface. *J. Phys. Oceanogr*., 25, 2025 – 2045, 1995.

Longuett-Higgins, M. S., On wave breaking and the equilibrium spectrum of wind-generated waves. *Proc. Roy. Soc. A.*, 310, 151-159, 1969.

Oakey, N. S. and J. A. Elliott, Dissipation within the surface mixed layer. *J. Phys. Oceanogr.*, 12, 171-185, 1982.

Prandke, H., K. Holtsch, and A. Stips, MITEC technology development: The microstructure/turbulence measuring system MSS. Tech. Rep. EUR 19733 EN, European Commission, 2000.

Umlauf, L., and H. Burchard, A generic length-scale equation for geophysical turbulence models, *J. Phys. Oceanogr*, 2002, submitted.

Wind- and tidally-driven fluctuations of the thermocline in the North Sea

Patrick Luyten

Management Unit of the Mathematical Models (MUMM),
Gulledelle 100, B-1200 Brussels, Belgium.
P.Luyten@mumm.ac.be

Observations

Measurement campaigns in the deeper parts of the North Sea showed the presence of large amplitude oscillations in the thermocline during the summer and autumn (e.g. Van Haren et al., 1999). Basic harmonics are the inertial and semi-diurnal frequencies arising from wind- and tidally-forced horizontal and vertical motions. The observational data, considered in the present study, were collected from three mooring sites. The first two are the central North Sea stations DM ($54^0 20'$N, $24'$E) and CS ($55^0 31'$N, $54.5'$E) of the North Sea Project for which high-frequency temperature data are available during the summer of 1989. The third one is located in the northern North Sea ($59^0 20'$N, 1^0E) where measurements were taken of microstructure parameters, currents, temperature and salinity in the autumn of 1998 during the PROVESS campaigns (Howarth et al, 2002).

The temperature variability at the stations DM and CS is mainly driven by the M_2-tide with inertial modes appearing during strong wind events. The oscillations induce vertical up- and downward displacements of the thermocline upto 5 to 10 m and with amplitudes varying during the semi-monthly spring-neaps cycle. A similar behaviour, although with lower amplitudes, is observed during the PROVESS 1998 period (Fig. 1). A common feature seen in both the 1989 and the 1998 data is the absence of a vertical phase shift in the temperature oscillations. The ADCP current data at the PROVESS site show, on the other hand, an important phase shift across the thermocline. This is due to a higher dominance of inertial modes in the surface mixed layer compared to the tidal bottom layer below the thermocline. The different behaviour seen in the temperature and current data is remarkable if advection

is considered as the only forcing mechanism and can only be explained by taking account of vertical turbulent diffusion, further discussed below.

Modelling aspects

A series of numerical simulations was conducted for the 1989 period with the three-dimensional COHERENS model (Luyten et al., 1999). Results were validated against the NSP data (Luyten et al, 2002b). A general trend, observed in the model results, is that stratification is underestimated in the thermocline and overestimated in the surface and bottom layers. The discrepancy is not necessarily related to the turbulence closure scheme but also due to an improper resolution of advective processes (Fig. 2). On the other hand, the model was generally able to simulate the semi-diurnal temperature oscillations, as seen in the data, although the amplitudes are lower compared to the observations. The model solutions show however an important vertical phase shift not seen in the data.

To analyse the separate roles of advection and diffusion two numerical experiments were performed at the PROVESS site. The first one solves the momentum and temperature equations without advective terms and with surface forcings derived from the data. In the second one, temperature and salinity are not calculated but directly implemented from the data using a simple data relaxation scheme. Details of the study are found in Luyten et al. (2002a). Both runs use however the same turbulence scheme which is a 2-equation $k-\varepsilon$ scheme with limiting conditions for background diffusion in the thermocline.

The results of the experiments are compared with the turbulence profile data from 21 to 24 October (Fig 3). The tidally-averaged profiles for ε, obtained from both runs, show a similar good agreement with the data (Fig. 3a). The non-averaged time series, as given in Figs. 3b–d for the temperature diffusion coefficient, do show important differences between models and data. The sharp, high-amplitude oscillations in the turbulence data are mainly semi-diurnal and in alignment with those seen in the temperature data. The abrupt changes from a mixing to a stratifying regime are well presented in the second run but obviously not in the first one. This can explain the absence of a vertical phase shift in the temperature measurements and the anomalous behaviour of the 3-D model where the temperature oscillations, and hence the associated mixing processes, are not accurately resolved.

Conclusions

The combined roles of advection and diffusion processes occurring on a semi-diurnal time scale have important consequences for the longer term temperature evolution since they (1) prevent shallowing of the thermocline, (2) preserve the stratification in the thermocline and (3) retard the erosion of the thermocline in late summer and autumn.

To resolve these processes accurately this implies that 3-D models must use (1) a resolution covering the appropriate tidal length scales (1–2 km in the horizontal, 1–2 m in the vertical), (2) an appropriate mixing scheme in the thermocline, (3) a non-diffusive scheme for advection and (4) high-resolution data for the surface forcing.

References

Howarth, M.J., Simpson, J.H., Sündermann, J., Van Haren, H., 2002. Processes of vertical exchange in shelf seas (PROVESS). J. Sea Res, in press.

Luyten, P.J., Jones, J.E., Proctor, R., Tabor, A., Tett, P., Wild-Allen, K., 1999. COHERENS – A coupled hydrodynamical-ecological model for regional and shelf seas: User Documentation. MUMM Report, Management Unit of the Mathematical Models of the North Sea, Belgium, 911 pp.

Luyten, P.J., Carniel, S., Umgiesser, G., 2002. Validation of turbulence closure parameterisations for stably stratified flows using the PROVESS turbulence measurements in the North Sea. J. Sea Res., in press.

Luyten, P.J., Jones, J.E., Proctor, R., 2002b. A numerical study of the long- and short-term temperature variability and thermal circulation in the North Sea. J. Phys. Oceanogr., in press.

Van Haren, H., Maas, L., Zimmerman, J.T.F., Ridderinkhof, H., Malschaert, H., 1999. Strong inertial currents and marginal internal wave instability in the central North Sea. Geophys. Res. Lett. 26, 2993–2996.

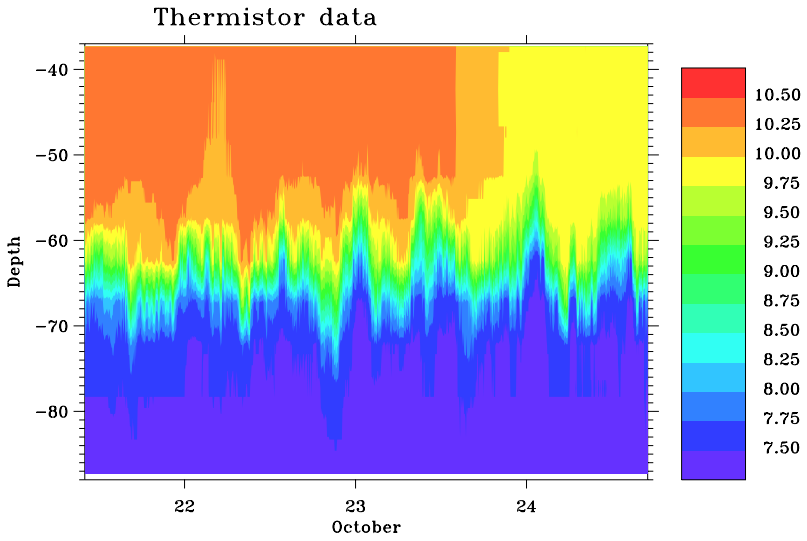

Figure 1: Thermistor data at the PROVESS site from 21 to 24 October.

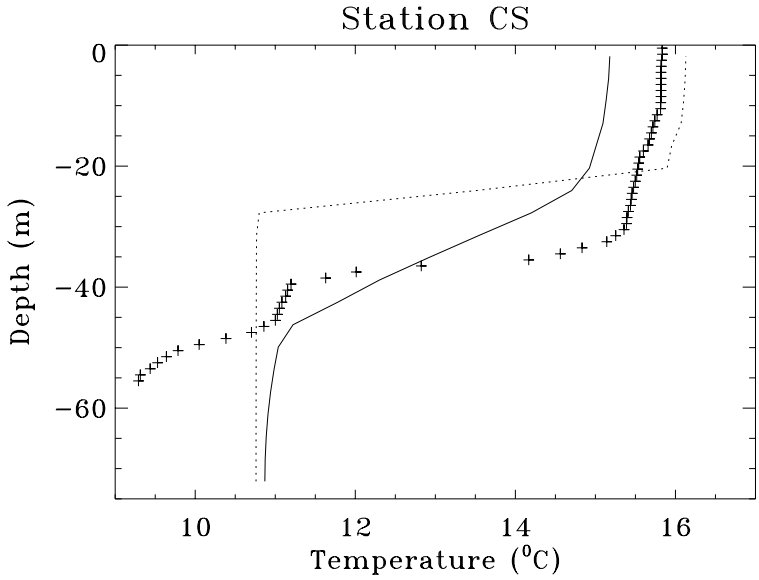

Figure 2: Temperature profile at station CS on 30 August 1989: observations (plus signs), full model (solid curve), model without advection (dots).

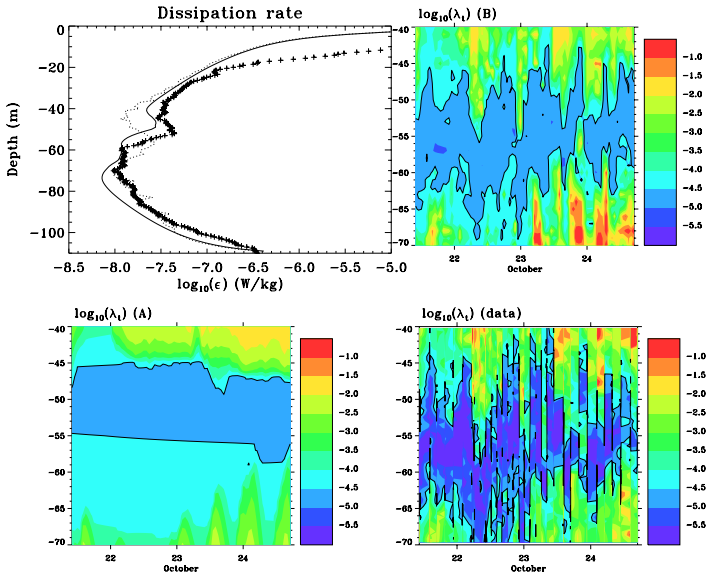

Figure 3: PROVESS site from October 21 to 24. (Upper left) tidally-averaged profiles of dissipation rate: observations (plus signs), first run (solid), second run (dots). Time series of the temperature diffusion coefficient: first run (lower left), second run (upper right), data (lower right).

Basin-scale interaction between tides and bathymetry in a shelf sea: morphodynamics of Taylor's problem

JOHAN VAN DER MOLEN

(Institute for Marine and Atmospheric Research Utrecht (IMAU), Utrecht University, Princetonplein 5, 3584 CC Utrecht, The Netherlands, j.vandermolen@phys.uu.nl)

TACO MULDER

(same address, t.mulder@phys.uu.nl)

JEROEN GERRITS

(same address, j.gerrits@phys.uu.nl)

HUIB DE SWART

(same address, h.e.deswart@phys.uu.nl)

1. Introduction

Numerical simulations of sand transport in the southern bight of the North Sea have indicated that a feedback mechanism exists between the tidal hydrodynamics and the basin-scale bathymetry (Van der Molen & De Swart, 2001). This feedback mechanism results in a co-evolving bathymetry and associated tidal system on a time scale of thousands to tens of thousands of years. Results are presented of a numerical study of the behaviour of this system. In particular, the question is addressed whether this feedback process leads to morphodynamic equilibria equivalent to those that have been found for tidal basins of a size of tens of kilometers.

Equilibria between hydrodynamics and sea-bed topography, characterised by vanishing average divergence in the displacement of sediment, have been demonstrated to exist in tidal basins (e.g., Schuttelaars & De Swart, 2000). Such equilibria arise from positive feedback between water motion and bottom topography during the initial stage of development, followed by a stabilising mechanism during the final stage. If morphodynamic equilibria exist for tidal basins, it is worthwhile to investigate the possible existence of equilibria for larger basins like tidal shelf seas. Indeed, numerical model results of sand transport for the southern bight of the North Sea show overall smaller tide-averaged sand transports for the actual large-scale bathymetry when compared with results of a model run where all bathymetrical features within the southern bight were removed by assuming a flat bottom at average depth. This result indicates that the present southern bight may be in an intermediate stage of development towards a large-scale morphodynamic equilibrium. Geological observations seem to support this presumption, they indicate large-scale marine erosion and deposition of 5 to 20 m following the large-scale flooding of the North Sea as a result of the last deglaciation. These bottom changes will have interacted with the hydrodynamics, because they are of the same order of magnitude as the present-day mean water depth (~25 m).

The present study was carried out by using fully non-linear numerical models of the tidal hydrodynamics applied to an idealised basin with a geometry that represents the main dimensions of the southern bight of the North Sea. Local sand-transport formulations were used to compute the redistribution of sediment. Two morphodynamical models were applied: the existing Delft-3D-Mor model of Delft Hydraulics (Wang et al., 1995), and a newly developed morphodynamical model (UMORPH) that uses the HAMSOM ocean circulation model (Backhaus, 1985) to calculate the hydrodynamics.

2. Models

Both morphodynamical models calculate changes in the bathymetry from the divergence of calculated sand transport rates, and recompute the hydrodynamics for this changed bathymetry, and so on. Both models were used in the 2-dimensional depth-averaged mode. The most essential difference between the morphodynamical routines of the two models is discretisation of the computation of sediment transport and bottom evolution.

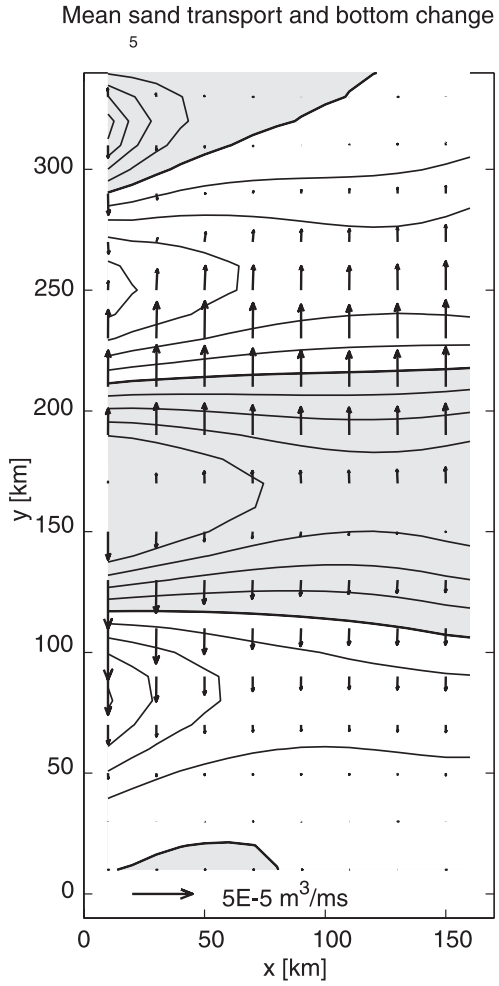

Figure 1. Initial sediment transport and bed-level change pattern. Gray: erosion, white: deposition. Contour interval 0.1 m.

The Delft-3D-Mor model (see, e.g., Wang et al., 1995) uses a central scheme that is stabilised using a LAX relaxation method. The computations were carried out using the Engelund-Hansen sediment-transport relation. The parameters of the stabilisation method were chosen to interfere in the computation only in regions where instability may occur.

For simplicity, the UMORPH model was supplied with the Bagnold bedload transport relation. At a later stage of the research, other transport relations will be implemented. Sediment transport rates and bottom evolution were computed using an explicit upwind discretisation. The resulting model satisfies the physics of morphological evolution down to a grid-size scale. The model is conditionally stable, subject to a CFL type criterion for bottom evolution. The morphodynamical part of the model was tested on several simplified 1D examples, including stationary and oscillating flow over a step in the bathymetry, downstream motion of a sand bank in uniform flow, and infilling of a semi-closed basin forced with a rigid-lid approximation of tides. In these simplified examples, the water motion is described by the continuity equation only. The full model was tested on a 1D morphodynamical equilibrium in a long tidal basin, similar to the equilibria found by Schuttelaars & De Swart (2000).

To investigate the presence of morphodynamical equilibria in the North Sea, computations were carried out with both models, using an idealised basin geometry inspired on the Taylor model (Taylor, 1921) for tidal propagation. The idealised basin consists of two connected rectangular basins: one basin with dimensions resembling those of the southern bight of the North Sea (width 160 km, length 360 km, depth 25 m), and one basin mimicking the behaviour of the northern North Sea (width 160 km, length 540 km, depth 75 m). The southernmost basin is the one in which the largest bathymetrical changes take place, the deeper northern basin is used to supply proper boundary conditions for the southernmost basin. Both basins have the average width of the southern bight, and have lengths selected to accommodate a full tidal amphidromic system each. The northern boundary of the combined basins was forced with an incoming Kelvin wave with an amplitude of about 1.5 m, and an outgoing Kelvin wave with 20% of the amplitude of the incoming one.

3. Results

The initial pattern of sediment transport and bottom change for a flat bottom in the southernmost basin is shown in Figure 1 for the Delft-3D-Mor model. Results of a similar model run with the UMORPH model are comparable, except for local details. The large-scale pattern is similar to that found with a numerical model of the North Sea (Van der Molen & De Swart, 2001), and shows a sediment-erosion zone with transport to deposition areas in the north and south. The bottom-change pattern is periodic in the north-south direction, and features exponential decay in the east-west direction towards a line east of the center of the basin. This pattern resembles that of a stationary Kelvin wave, where the wave patterns along the eastern and western boundaries are approximately in phase in a spatial sense but have different amplitudes. Figure 2 shows the bathymetry resulting from a 7200 year run of the Delft-3D-Mor model. The chosen stability coefficients did not allow longer simulations. The results show that the bottom wave pattern has grown substantially, while the general shape has remained more or less the same. The changes in bottom geometry cause an increase in the mean bottom friction which results in a shift of the amphidromic system towards the east. The amphidromic system is also shifted slightly to the north, which may result from a change in resonance characteristics of the basin caused by the depth changes. The current amplitudes are closely related to the changing bottom geometry and have decreased in the erosion area and increased in the deposition areas.

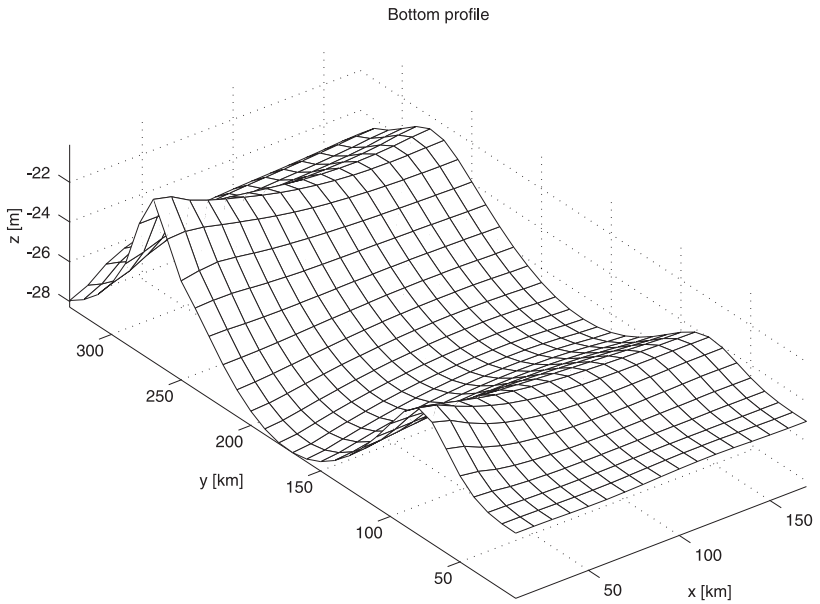

Figure 2. Sea-bed topography after 7200 years in the southern basin, Delft-3D-Mor model.

In Figure 3, results of the UMORPH model are shown after 320,000 years. The time spans of the two models cannot be compared directly because a total-load formulation was used in the Delft-3D-Mor model, whereas a bedload formulation was used in the UMORPH model, resulting in a faster rate of evolution for the Delft-3D-Mor model. The large-scale evolution of the UMORPH model is similar to that of the Delft-3D-Mor model: erosion in the center and deposition in the north and south. At approximately the stage where the Delft-3D-Mor simulation was discontinued, linear bars are formed (not shown) that connect to evolve into the large-scale ridges shown in Figure 3 in the western part of the basin. At this stage of the model evolution, the ridges are near dynamic equilibrium with the water motion: their shape has become more or less constant, although they do show some migration. In the eastern part of the basin, a complex pattern of banks evolves. Meanwhile, the larger scale basin evolution is continuing. Analysis of the water motion showed that flow velocities have a maximum over the ridges in the west, with major axes of the current ellipses oriented across the ridges and along the troughs between the ridges. Clockwise residual circulation cells exist around the ridges. The amphidromic systems of the principle tide M_2 and the overtide M_4 are affected by the basin evolution, in particular those of the currents, that clearly reflect the sand-bank pattern. Net sediment transports are largest at the crests of the banks, and show circulation of sediment around the banks, as well as net transport across the crests that results in the migration.

More results of the UMORPH model will be presented at the conference, such as simulations with different initial bottom topographies and computations with modified sediment-transport formulations.

4. Conclusions

The following results were obtained:

- The initial bottom features which form in a shelf-sea basin with a geometry similar to that used by Taylor (1921) and with a flat bottom have the characteristics of stationary Kelvin waves.
- These large-scale features have the tendency to grow.
- At an early stage in the morphodynamic development of the model basin, local bedforms develop. These bedforms most likely represent conditions that are closer to local equilibrium than a nearly flat basin floor, and (quite suddenly) evolve into larger-scale features as time progresses, while the total system continues to evolve. It is expected that this step like process will repeat itself until full equilibrium is obtained.

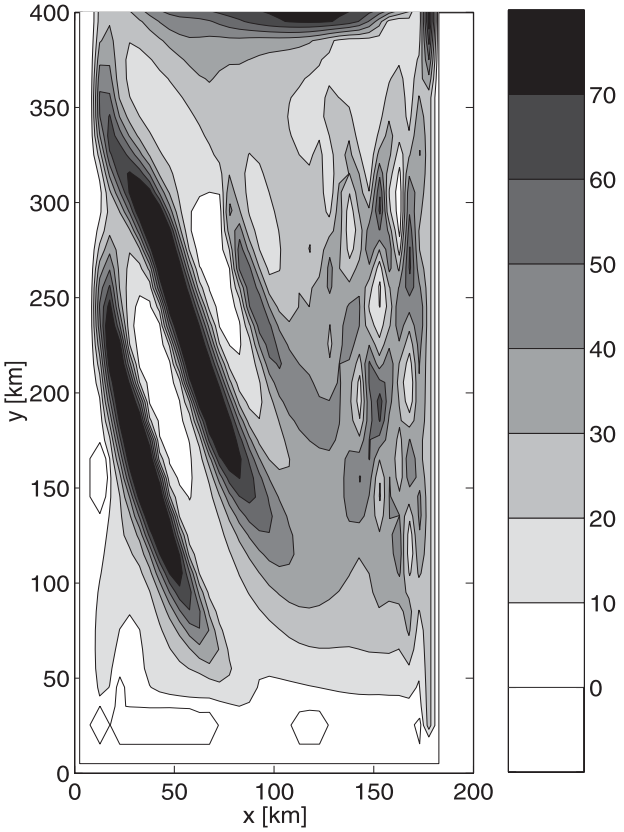

Figure 3. Sea-bed topography in southern basin of the UMORPH model after 320,000 years. Depths in m.

Acknowledgments: The authors would like to express their gratitude to Prof. dr. Jan Backhaus for making the HAMSOM model available. WL | Delft Hydraulics is thanked for permission to use the Delft-3D model. The research was funded by the Netherlands Geosciences Foundation (GOA) with financial aid of the Organization for Scientific Research (NWO) (NWO-grant 811.33.005).

References:

Backhaus, J.O., 1985. A three-dimensional model for the simulation of shelf sea dynamics. Deutsche Hydrographische Zeitschrift 38, 165-187.

Schuttelaars, H.M., de Swart, H.E., 2000. Multiple morphodynamic equilibria in tidal embayments. Journal of Geophysical Research 105 C10, 24105-24118.

Taylor, G.I., 1921. Tidal oscillations in gulfs and rectangular basins. Proceedings of the London Mathematical Society 20, 148-181.

Van der Molen, J., de Swart, H.E., 2001. Holocene tidal conditions and tide-induced sand transport in the southern North Sea. Journal of Geophysical Research 106 C5, 9339-9362.

Wang, Z.B., Louters, T., de Vriend, H., 1995. Morphodynamic modelling for a tidal inlet in the Wadden Sea. Marine Geology 126, 289-300.

Modelling the influence of artificial degassing on the stratification and the safety of Lake Nyos

MARTIN SCHMID, ANDREAS LORKE AND ALFRED WÜEST

(EAWAG, Seestrasse 79, CH-6047 Kastanienbaum, Switzerland, martin.schmid@eawag.ch)

1. Introduction

Lake Nyos is one of several crater lakes in the north-western part of Cameroon (Kling, 1988). The lake has an infamous reputation since August 1986, when it released a large cloud of carbon dioxide (CO_2), which flowed down the neighbouring valleys and asphyxiated 1700 people (Kling et al., 1987). With the exception of a similar gas burst of smaller scale at nearby Lake Monoun (Sigurdsson et al., 1987), this volcanological hazard had not been previously known. The disaster was followed by an intense scientific discussion about the origin of the gas burst. Two main hypotheses were set up (Sigvaldason, 1989). Following the limnic eruption hypothesis, high CO_2 concentrations had slowly built up in the lake column, and a large part of the CO_2 was released after a trigger mechanism led to local oversaturation. The volcanic eruption hypothesis, on the other hand, ascribed the gas burst to a sudden injection of CO_2 from beneath the lake. The slow recharge of CO_2 to the bottom water of the lake after the eruption (Kusakabe et al., 2000; Evans et al., 1994; Nojiri et al., 1993) strongly supports the limnic eruption hypothesis. Our work therefore is based on this hypothesis. Nevertheless it should be kept in mind that sudden volcanic activity leading to similar disasters cannot be excluded in this region.

Since the renewal of high CO_2 concentrations in the lake column could lead to a new disaster within decades, a plan was set up to degas the lake. In January 2001, after several experimental tests in preceding years, a first polyethylene pipe was installed in Lake Nyos. Water is taken in at a depth of 203 m and released as a fountain on the lake surface. Due to the high CO_2 pressure in the bottom water, the water flow through the tube is self-sustaining, driven by the expansion of gas bubbles. A detailed description of the degassing procedure can be found on the Lake Nyos degassing homepage (Halbwachs, 2002). However, there is concern that the degassing procedure, by lifting heavy bottom water to the surface, could lower the stability of the lake column and impose the risk of a new eruption during the degassing process (Pickrell, 2001). Previous simulation results have suggested that the water column below the epilimnion should remain stable during the degassing process (McCord and Schladow, 1998). However, this model did not include the effect of the geochemical cycling on water density with the exception of CO_2. The bottom water of Lake Nyos contains also large amounts of dissolved reduced iron and other minerals. Transported to the surface, the iron will be oxidized and transformed to amorphous iron hydroxide particles (Davison, 1993). The influence of the minerals and the iron hydroxides on the density stratification is included in the model presented in this study.

2. Model Description

We developed a one-dimensional model of Lake Nyos with a vertical resolution of 1m. The model is implemented within the lake module of the software AQUASIM 2.0 (Reichert, 1994; Reichert, 1998), which is designed to concurrently simulate physical and biogeochemical processes in natural and technical aquatic systems. The simulation is driven by weather data (irradiation, wind speed, temperature, water vapour pressure, and precipitation). Figure 1 gives an overview of the main processes included in the model which are shortly described below.

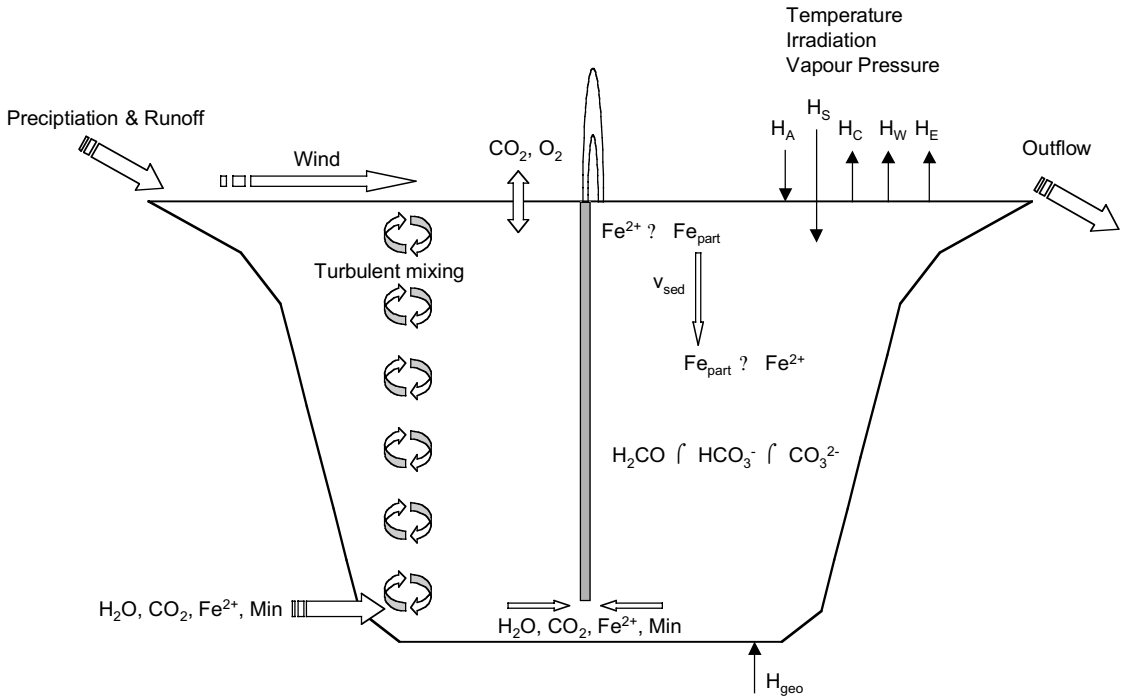

Figure 1: Overview of the processes included in the simulation of Lake Nyos.

Water balance

The water balance includes precipitation to the lake surface, runoff from the lake catchment, and an exchange with a warm subsurface reservoir with higher concentrations of CO_2, Fe and minerals. This exchange is considered the source for the observed increase in mineral concentrations and heat (Kusakabe et al., 2000) in the bottom waters of Lake Nyos. Whereas in reality the lake surface drops below the outflow level during the dry season, the lake surface is assumed to be constant in the model by closing the water balance with the surface outflow. The water flow through the degassing pipe is parameterized depending on the intake depth z_{in} and on the partial pressure of CO_2 at z_{in}. The currently installed pipe has an intake depth of 203 m, a diameter of 14.5 cm, and an average water flow of 65 l/s. However, it is planned to install further pipes within the next years.

Heat balance

The heat exchange between the lake surface and the atmosphere includes short-wave irradiation (H_S), infrared radiation from the sky (H_A), infrared radiation from the water surface (H_W), latent heat flux (H_E), and convection (H_C) (Goudsmit et al., 2002; Henderson-Sellers, 1986; Imboden and Wüest, 1995). The observed increase in temperature in the bottom water is simulated with the high temperature of the water reservoir that exchanges with the bottom water. The exsolution of the CO_2 in the pipe leads to a heat loss of c. 20 kJ/mol CO_2.

Turbulent mixing

The physical mixing of the lake is simulated with a buoyancy-extended k-epsilon turbulence model (Goudsmit et al., 2002; Burchard and Petersen, 1999; Rodi, 1980). Turbulent mixing is driven by the energy introduced into the system by surface shear stress from wind forcing, and by negative buoyancy due to heat loss to the atmosphere, the heat input to the lake bottom, and the uplifting of heavy bottom water to the lake surface with the degassing pipe. The model includes the energy transfer from internal seiches to turbulent kinetic energy in the bottom boundary layer, because the contribution of this mixing on sloping boundaries to diapycnal transport has been shown to be important (Gloor et al., 2000). The water density is calculated depending on temperature and the concentrations of carbon dioxide, minerals, and dissolved and particulate iron.

Geochemistry

The observed annual inflow of 100-200 Mmol CO_2 to the bottom waters of Lake Nyos (Kusakabe et al., 2000) is the reason for the risk of a new eruption. The three species carbon dioxide, bicarbonate and carbonate are supposed to be in equilibrium. At the lake surface, the CO_2 concentration equilibrates with the atmosphere. The pH is assumed to be in equilibrium with the partial CO_2 pressure and the alkalinity defined by the mineral concentration.

Dissolved iron (Fe(II)) is transported to the surface with the degassing pipe where it is oxidized and transformed to particulate iron hydroxide. The particles sink down and are resuspended in the anoxic zone below the thermocline.

Minerals, simulated with one state variable for the sum of Mg, Ca, K, and Na, as well as temperature, are also introduced into the lake from the subsurface reservoir and transported to the surface with the pipe. Altogether the degassing reduces density at the bottom (gas, minerals) and increases density in the surface water (minerals) and below the thermocline (resuspension of particulate iron). Oxygen is set to saturation at the lake surface and is used up in the sediment in proportion to the estimated biological primary production.

3. Simulations and safety assessment

Simulations are performed for several years before the degassing of the system. The results of these simulations are compared with observed CTD and CO_2 profiles to check the applicability of the model. A mooring was deployed in November 2001 in Lake Nyos with 11 thermistors and 4 sediment traps. The mooring will be retrieved after one year, and the results together with new CTD profiles will be used to check the consistency of the model during one year of lake degassing.

To assess the safety of the degassing of Lake Nyos, the energy is estimated, which is needed to move water from anywhere below the thermocline to a level where it is supersaturated with CO_2, which is a necessary but not sufficient requirement for a limnic eruption to occur. This energy depends on the vertical distance between a water parcel and its level of supersaturation, and on the difference between the potential densities at these two levels. It can be compared to the energy contained in the internal waves in the lake observed with the moored thermistors. These simulations and energy calculations will allow to identify the safest of a variety of possible degassing scenarios.

Sensitivity analyses are conducted to check the sensitivity of the simulations to parameters that have either a large natural variability (e.g. precipitation) or are only imprecisely known for Lake Nyos (e.g. CO_2 input rate at the lake bottom, biological productivity).

At the PECS conference, we present the model structure and the model validation with available data of temperature, CO_2, mineral and iron concentrations. Figure 2 shows a preliminary result of a first simulation run. The simulated total CO_2 concentrations after 10 months of degassing show a mixed epilimnion with a depth of slightly more than 50 m and a mixed bottom boundary layer (BBL). Both these features of the lake column could be observed in the CTD data measured in November 2001, even though the epilimnion was slightly less deep, and the BBL was less pronounced. These results indicate that the mixing is well reproduced by the k-epsilon model.

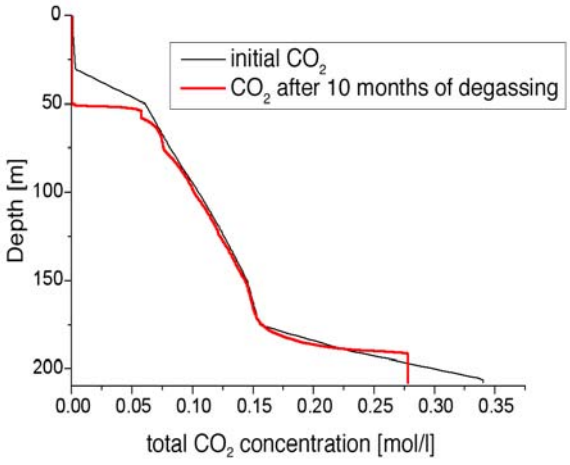

Figure 2: Total CO_2 concentrations simulated in a preliminary model run after 10 months of degassing.

References

Burchard, H. and Petersen, O., 1999. Models of turbulence in the marine environment - a comparative study of two-equation turbulence models. Journal of Marine Systems, 21: 29-53.

Davison, W., 1993. Iron and manganese in lakes. Earth-Science Reviews, 34: 119-163.

Evans, W.C. et al., 1994. 6 Years of Change at Lake Nyos, Cameroon, Yield Clues to the Past and Cautions for the Future. Geochemical Journal, 28(3): 139-162.

Gloor, M., Wüest, A. and Imboden, D., 2000. Dynamics of mixed bottom boundary layers and its implications for diapycnal transport in a stratified, natural water basin. Journal of Geophysical Research, 105(C4): 8629-8646.

Goudsmit, G.-H., Burchard, H., Peeters, F. and Wüest, A., 2002. Application of k-ε Turbulence Models to Enclosed Basins - The Role of Internal Seiches. Journal of Geophysical Research, in press.

Halbwachs, M., 2002. Degassing Lake Nyos project. http://perso.wanadoo.fr/mhalb/nyos/nyos.htm.

Henderson-Sellers, B., 1986. Calculating the Surface Energy Balance for Lake and Reservoir Modeling: A Review. Reviews of Geophysics, 24(3): 625-649.

Imboden, D. and Wüest, A., 1995. Mixing mechanisms in lakes. In: A. Lerman, D. Imboden and J. Gat (Editors), Physics and chemistry of lakes. Springer, Berlin, pp. 83-138.

Kling, G.W., 1988. Comparative Transparency, Depth of Mixing, and Stability of Stratification in Lakes of Cameroon, West-Africa. Limnology and Oceanography, 33(1): 27-40.

Kling, G.W. et al., 1987. The 1986 Lake Nyos Gas Disaster in Cameroon, West-Africa. Science, 236: 169-175.

Kusakabe, M., Tanyileke, G.Z., McCord, S.A. and Schladow, S.G., 2000. Recent pH and CO2 profiles at Lakes Nyos and Monoun, Cameroon: implications for the degassing strategy and its numerical simulation. Journal of Volcanology and Geothermal Research, 97(1-4): 241-260.

McCord, S.A. and Schladow, S.G., 1998. Numerical simulations of degassing scenarios for CO2-rich Lake Nyos, Cameroon. Journal of Geophysical Research-Solid Earth, 103(B6): 12355-12364.

Nojiri, Y. et al., 1993. An Estimate of CO2 Flux in Lake Nyos, Cameroon. Limnology and Oceanography, 38(4): 739-752.

Pickrell, J., 2001. Scientists Begin Taming Killer Lake. Science, 291: 965-967.

Reichert, P., 1994. AQUASIM - A tool for simulation and data analysis of aquatic systems. Water Science and Technology, 30(2): 21-30.

Reichert, P., 1998. AQUASIM 2.0 - User Manual. EAWAG, Dübendorf, 214 pp.

Rodi, W., 1980. Turbulence Models and their Application in Hydraulics, International Association for Hydraulic Research, Delft.

Sigurdsson, H. et al., 1987. Origin of the Lethal Gas Burst from Lake Monoun, Cameroun. Journal of Volcanology and Geothermal Research, 31(1-2): 1-16.

Sigvaldason, G.E., 1989. International-Conference-on-Lake-Nyos-Disaster, Yaounde, Cameroon 16-20 March, 1987 - Conclusions and Recommendations. Journal of Volcanology and Geothermal Research, 39(2-3): 97-107.

3D numerical modelling of sediment disposal

ANTOINE GARAPON

(Laboratoire National d'Hydraulique et Environnement de l'EDF, 6 quai Watier, 78400 Chatou, Antoine.Garapon@edf.fr)

CATHERINE VILLARET

(Laboratoire National d'Hydraulique et Environnement de l'EDF, 6 quai Watier, 78400 Chatou, Catherine.Villaret@edf.fr)

ROLAND BOUTIN

(S.T.T.I.M., 15 rue de Laborde,00309 Armées, Roland.Boutin@wanadoo.fr)

1. Introduction

Sediments can be transported along the coastline either by the residual tidal currents or by the wave induced longshore current. Littoral transport can be responsible for the sedimentation of fine particles in sheltered areas, like harbour entrances or navigation channels. Maintenance dredging operations are often necessary to prevent these effects.

The total volume of dredged material is estimated to about 40 to 50 millions m^3/year for the maintenance of french harbours. The dredging material is generally released in the ocean, either by pumping into the main current in order to facilitate its mixing and transport, either directly from a barge opening above a disposal area.

After release, the behaviour of the settling material can be decomposed into a settling phase followed after impact on the bed, by the formation of a turbidity current. Characteristics of the deposit material, horizontal dimensions, height and porosity, are important in order to predict the long term fate of the material, and related impact of pollutants on the marine environment.

Despite its importance for environmental issues, there is still today little understanding of the fundamental physical processes that govern the short-term fate of sediments released in the ocean (short-term fate). In this study, laboratory experiments and numerical modelling have been combined in order to study the dispersion of sediment disposal at sea. We present in part 2 the experiments that have been carried out by R. Boutin (2000) using natural cohesive sediments, and in part 3, we introduce the 3D numerical model. Part 4 gives a comparison between model results and experimental data both in a flow at rest and in a steady current. Finally, we will present applications of the model to predict the characteristics of a deposit, under typical field conditions.

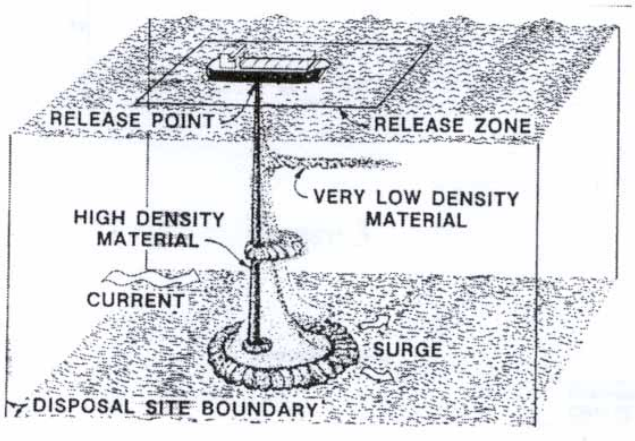

Figure 1 General overview of the disposal of dredged material, (Truitt, 1986)

2. Experiments

Series of experiments have been performed in a large flume (80m x 1.5m x 1.5m) by R.Boutin (2000), in order to study the settling phase and the development of a turbidity current on the bottom. The mud was marked with radioactive tracers. The time-varying concentrations were measured at various positions along the flume, using scintillation probes and OPCON turbidity probes. At the end of the experiment, a radioactive probe was moved along the bed to map the density of the deposit.

At t=0, an initial volume of mud was mixed with water to obtain any desired concentration, and released at about 15 cm under the water surface, from a settling device piloted by a PC. Observations were made using series of 4 cameras taking synchronised pictures. Experimental conditions were designed in order to reproduce in-situ conditions at scale 1/25th.

Complementary experiments were performed at LNHE in order to observe the settling of fine sand and mixtures of sand and mud. The different experimental programs are described in a database[1], which has been constructed as part of the LITEAU project.

We will present underneath a comparison with experiment CLAP18, which has been performed in a flow at rest, with initial volume V=43.3 l and concentration C=348.1 g/l. The water depth is h=1m.

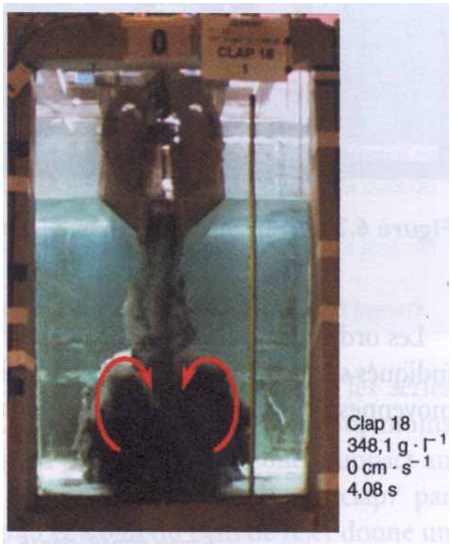

Figure 2: Experiment Clap 18 -Boutin (2000)

3. Numerical model

In the numerical approach, we are using the LNHE finite element Navier Stokes Reynolds solver, TELEMAC 3D, to model the *settling phase, the turbidity current development* and the *formation of the deposit* on the bed. The descending phase is extremely rapid and generates large vertical velocities. The non-hydrostatic version has been used here in order to account for the effect of those large vertical velocities on the pressure distribution. Model equations are written below using the Boussinesq approximation.

$$\frac{\partial \vec{u}}{\partial t} + (\vec{u}.grad)\vec{u} = \frac{1}{\rho} div\overline{\overline{\sigma}} + \vec{g} \qquad (1)$$

$$div(\vec{u}) = 0 \qquad (2)$$

[1] http://www.cetmef.equipement .gouv.fr

$$\rho_m = \rho_{wat} + C\left(\frac{\rho_{sed} - \rho_{wat}}{\rho_{sed}}\right) \quad (3)$$

$\vec{u}$ represents the velocity vector, $\vec{g}$ the acceleration of gravity, $\overline{\overline{\sigma}}$ the stress tensor, ρ_{sed} the sediment density, ρ_{wat} the water density and ρ_m the resulting density.

The transport of suspended sediment is described by the following advection-diffusion equation:

$$\frac{\partial C}{\partial t} + (\vec{u}.grad)C + \frac{\partial(W_c C)}{\partial z} = div(\nu_T gradC) + S \quad (4)$$

where C is the concentration of suspended sediment, u, v and w are the cartesian velocity components, ν_T is the eddy diffusivity coefficient, and W_c, the vertical settling velocity, and S the source term.

The model equations are solved by means of fractional steps method (an advection step, a diffusion step, pressure is found by solving a Poisson equation and a velocity correction step that makes the velocity field satisfy equation 2. The spatial discretization is achieved using prisms duplicated along the vertical direction. For the advection of velocities a characteristics scheme is used whereas for the tracer it is a specially developed scheme : the murd PSI scheme (Janin, 1995).

The release is represented in the model by a distribution of several source points placed in the domain and characterized by a given concentration and vertical velocity. The source term S of in the transport-diffusion equation (eq. 4) is proportional to the local concentration C and the fixed concentration of the source C_s, Δt being the time step it can be written:

$$S = (C - C_S) / \Delta t \quad (5)$$

The concentration of the sources is set equal to the initial concentration of the released material and the velocity of the sources was chosen in order to speed up the settling process.

Different turbulence models have been tested for the turbulent eddy viscosity coefficient. Best results have been obtained during the settling phase by applying a modified mixing length model derived from the algebraic Balwin-Lomax model, where the mixing length is assumed proportional to the sediment cloud diameter. This turbulence model has been validated in comparison to small-scale experiments made in the case of a spherical release by Burel and Garapon (2002). This new turbulence model has been extended here to simulate this new and more complex case.

4. Numerical results

We show here a numerical simulation of CLAP18. In order to save computer time, we have modelled only a 3D slice of 0.09m width of the experimental channel. The 3D grid is made of 30 vertical planes and a number of 384 grid points in the horizontal. The horizontal grid is refined near the release points while the vertical spacing is kept constant.

The effect of the sources is turned off once the total mass of sediment has been reached.

According to the observations, 90% of the material should be released in less than about 1s. Best results are obtained by putting about 32 sources, located between the water surface and the release point (z=-0.15 m under the surface). We present here (fig. 5) an example of numerical results obtained at t= 5s, after release. The sediment cloud has reached the bottom and the turbidity current is propagating along the bed. A preliminary comparison of the model final deposit on the bottom with the experiment is presented in fig.5. The maximum deposit appears slightly under estimated by the model, the mass difference is found along the width and the predicted deposit appears a little too wide.

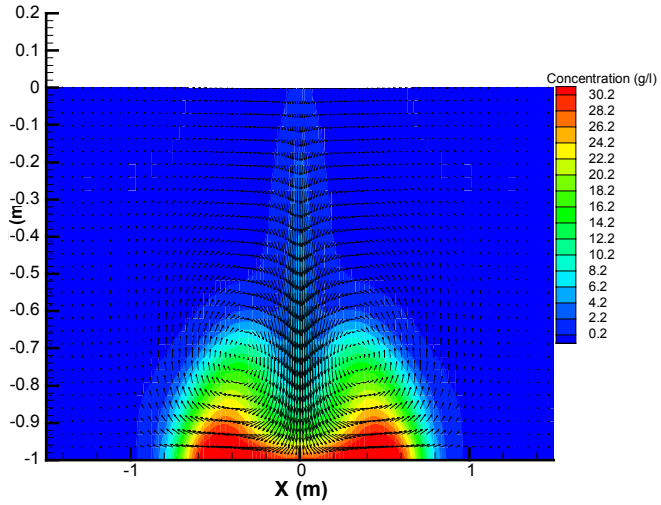

Figure 3: Concentration and velocity field at t= 5s after release (Exp. Clap18)

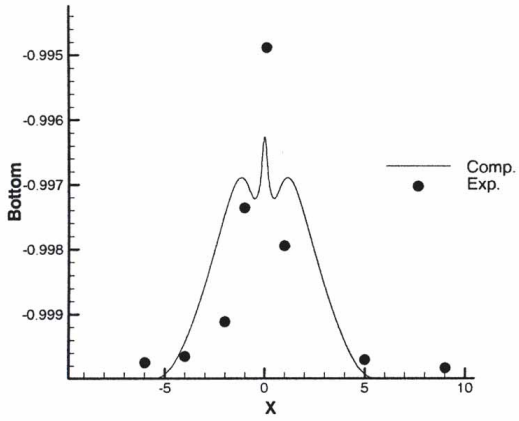

Figure 4: Comparison of model and experimental sediment deposits (Exp. Clap18)

5. Conclusions

The 3D numerical model has been validated against experimental data. The model is able to reproduce the vertical descent of the material, the development of the turbidity current and formation of a deposit.

Applications of the model to in-situ conditions (Le Kannick) will be presented at the conference. Model results will be discussed in order to show the effect of hydrodynamic conditions on the formation of the deposit.

Acknowledgments: This work is part of a National Project LITEAU, funded by the French Ministry of Environment and Transport (contrat n°2000/1213601).

References:

R.Boutin, 2000: Dragage et rejets en mer, Presse de l'école nationale des ponts et chaussées.

D.Burel and A.Garapon , 2002: 3D numerical modelling of dredged material descent, ICCE.

Janin, J.M. : Conservativité et positivité dans un module de transport scalaire écrit en éléments finis - Application à TELEMAC-3D. Rapport HE-42/95/054/A. 1995.

The use of $\delta^{18}O$ as a tracer for river water in Arctic shelf seas

DOROTHEA BAUCH

(GEOMAR Research Center, Wischofstr. 1-3, D-24149 Kiel, Germany, dbauch@geomar.de)

INGO HARMS

(Institute for Oceanography, University of Hamburg, Troplowitzstr.7, D-22529 Hamburg, Germany, harms@ifm.uni-hamburg.de)

HELMUT ERLENKEUSER

(Leibniz Laboratory, Max-Eyth Str. 11, D-24103 Kiel, Germany, herlenkeuser@leibniz.uni-kiel.de)

UDO HÜBNER

(Institute for Oceanography, University of Hamburg, Troplowitzstr.7, D-22529 Hamburg, Germany huebner@ifm.uni-hamburg.de)

1. Introduction

The Kara Sea is the second largest arctic shelf area which receives about 1/3 of the total arctic river runoff [*Pavlov and Pfirman,* 1995] and large amounts of sea-ice are produced in flaw leads in winter [*Dethleff et al.,* 1998]. Information on the formation of water masses, transport paths and budgets of freshwater are necessary in order to better understand the sedimentological processes on the southern Kara Sea shelf and to evaluate the transport of water masses and fluvial matter into the Arctic Ocean.

The isotopic composition of river water is highly depleted in ^{18}O relative to marine waters and sea-ice. Therefore the $\delta^{18}O$ composition of the water is a good measure for the amount of river runoff within the water column. In combination with salinity the additional freshwater sources of sea-ice melting and freezing can be deduced and quantified, because these processes cause only minimal isotopic fractionation [*Melling and Moore,* 1995] and therefore these waters have a distinctively different isotopic signature relative to the waters which are a mixture of river water and marine water only.

In this paper we will discuss the isotopic characteristics and budgets of water masses and freshwater sources in the southern Kara Sea.

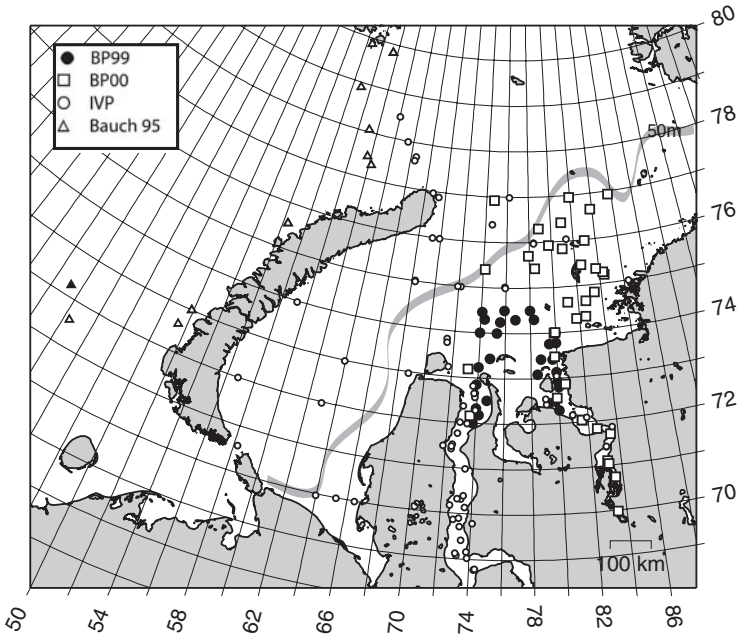

Figure 1: Geographic position of stations taken during "Boris Petrov" expedition in 1999 (BP99) and 2000 (BP00). Also indicated are stations taken in the Barents Sea (open triangles; Bauch [1995]) and stations from Brezgunov et al. [1980, 1983] (open dots, IVP data). Grey line indicates the approximate position of the 50m isobath.

2. $\delta^{18}O$/salinity correlation

The southern Kara Sea is strongly influenced by river runoff during summer resulting in a pronounced two-layer structure near the estuaries. The influence of river water is reflected in the mixing line between marine high $\delta^{18}O$ water and riverine low $\delta^{18}O$ water (Fig. 2). But the deviation of single data points from the linear regression line is up to 1‰ in $\delta^{18}O$ and up to 5 in salinity and thereby far beyond the analytical uncertainty (0.07‰ for $\delta^{18}O$ and 0.1 for salinity) and has to be interpreted in terms of additional salinity or freshwater sources.

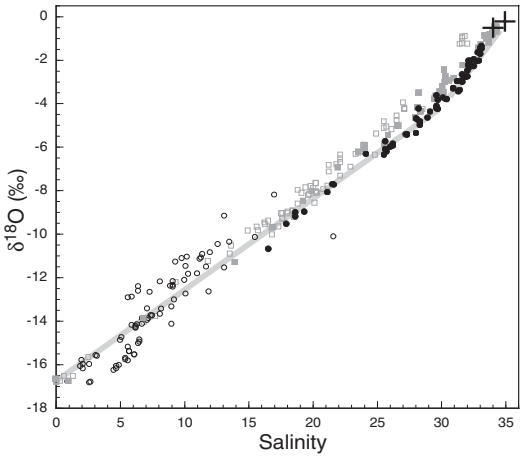

Figure 2: $\delta^{18}O$ versus Salinity for all stations of BP99 (circles) and BP00 (squares). All data divided by surface layer (open symbols) and bottom layer (closed symbols). The crosses indicate the values of Atlantic Inflow water and Barents Sea Inflow water. The lines indicate the assumed mixing lines.

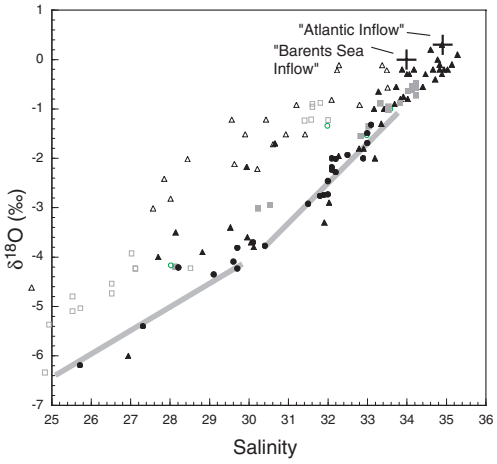

Figure 3: Same as Fig. 2 for salinities above 25. Additional stations from deeper parts of the Kara Sea are also included (triangles; IVP data; Brezgunov et al. [1983, 1980]).

When ice forms from sea water most of the salt is rejected and brines are injected into the sea, while the $\delta^{18}O$ composition of the water is preserved with a small fractionation factor only. The influence of sea-ice melting and formation is thereby seen in a shift to lower and higher salinities, respectively at about constant $\delta^{18}O$. The contributions of sea-ice and river runoff to a given sample can be modeled as a mixture of marine water (m), river water (r) and sea-ice meltwater (i) from a mass balance and the balance of salinity and $\delta^{18}O$. The balance is governed by the following equations:

$$f_m + f_r + f_i = 1$$

$$f_m * S_m + f_r * S_r + f_i * S_i = S_{meas}$$

$$f_m * O_m + f_r * O_r + f_i * O_i = O_{meas}$$

Where f_m, f_r and f_i are the fractions of marine water, river-runoff and sea-ice meltwater in a water parcel, and S_m, S_r, S_i, O_m, O_r, and O_i are the corresponding salinities and $\delta^{18}O$ values. S_{meas} and O_{meas} are the measured salinity and $\delta^{18}O$ values of the water samples. This concept was applied in several studies to Arctic Ocean halocline waters [e.g. *Östlund and Hut,* 1984; *Bauch et al*., 1995; *Ekwurzel et al*., 2001]. Specific endmember values have to be chosen for the Kara Sea:

River water $\delta^{18}O$: Slightly different river water $\delta^{18}O$ values are observed for Ob and Yenisey and during BP99 and BP00. During BP99 $\delta^{18}O$ endmember values (S=0) for the Ob and Yenisey are –16.8‰ (r^2=0.996) and –18.1‰ (r^2=0.991), respectively. During BP00 $\delta^{18}O$ endmember values for the Ob and Yenisey are about 1‰ higher in $\delta^{18}O$ with –16.1‰ (r^2=0.995) and –17.0‰ (r^2=0.998), respectively.

Sea-ice meltwater component: Within the Kara Sea most of the sea-ice is first year ice and therefore more saline and highly variable compared to multi-year ice. For the fraction calculation salinity of sea-ice is set to (6* S_{meas})/35 to account for the salinity of the water from which the sea-ice forms. The $\delta^{18}O$ value of sea-ice is set to the measured $\delta^{18}O$ value multiplied with a fractionation factor of 1.0021 [*Melling and Moore,* 1995]. The sea-ice meltwater component can have positive and negative solutions representing net meltwater and brine formation, respectively.

Marine water $\delta^{18}O$ endmember value: Atlantic water enters the southern Kara Sea only indirectly via the Barents Sea and is already slightly modified (Fig. 3). "Atlantic Inflow" (AI) is set to 34.92 salinity and 0.3‰ in $\delta^{18}O$ and is defined as the least modified Atlantic water within the Arctic Ocean, i.e. in the southern Nansen Basin [*Bauch et al,.* 1995]. We use AI, because the modification in the Barents Sea is not well defined and only small.

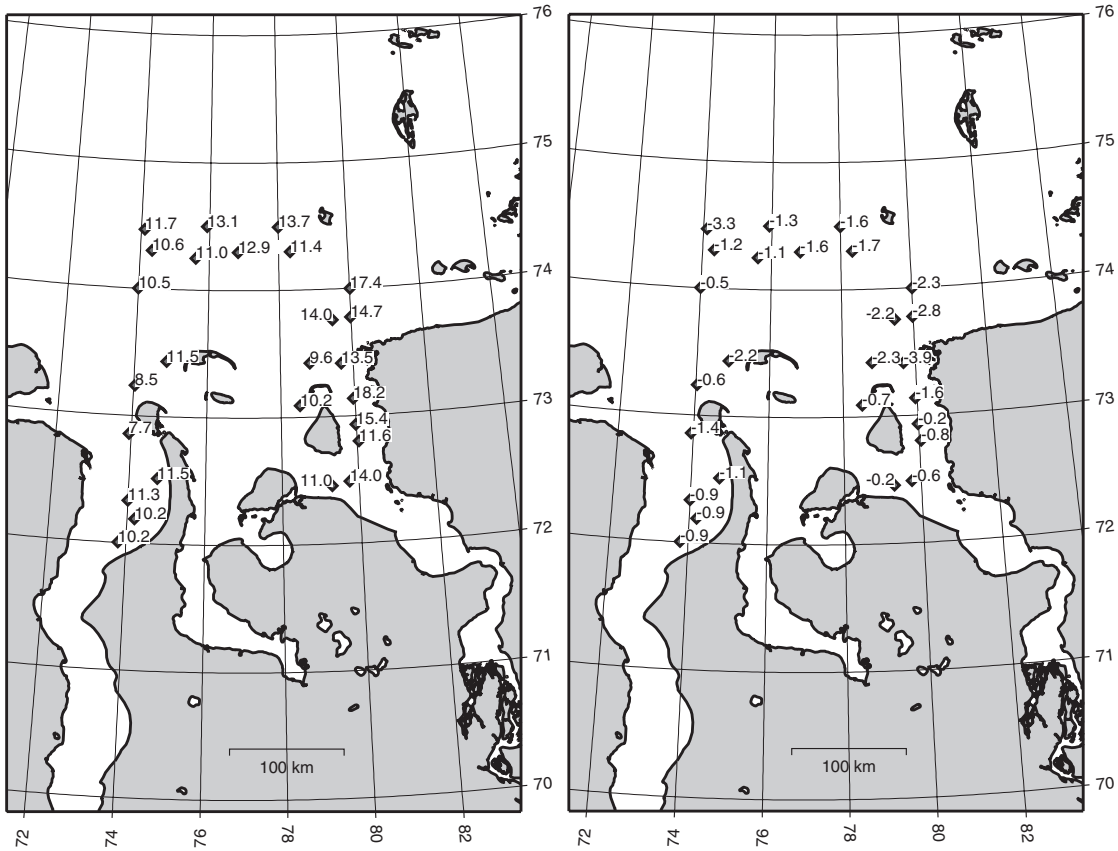

Figure 4 : Integral values of river water (left panel) and sea-ice meltwater (right panel) contained in the water column. Data are given in meters and shown for station sampled during BP99.

Quantitative freshwater fractions are calculated and integrated over the whole water column. For BP99 ~10 to 15 m of pure river water are observed (Fig. 4). The integral river water values near the Yenisey estuary are slightly higher than near the Ob estuary and there is no south to north trend.

Integral values of sea-ice meltwater are between –0.5 to –1.0 m near the Ob and Yenisey estuaries and decrease to about –2 to –3 m for stations in the north (Fig. 4). Negative values have to be interpreted as water removed from the water column by sea-ice formation. All stations sampled during BP99 reveal the signature of net sea-ice formation – despite sampling during a period of local sea-ice melting. Because the fraction calculation is relative to Atlantic Inflow this values represent net values for the residence time of the waters in the southern Kara Sea.

3. Shelf derived Polynya Winter Water

At higher salinities a discontinuity in the S/δ^{18}O correlation in the bottom layer is observed (Fig. 3). This is most clearly seen for stations taken north of 74°N during BP99, when the sampling density was highest in this region (Fig. 1). During BP00 δ^{18}O values are generally less depleted and a discontinuity in the S/δ^{18}O correlation is observed at higher δ^{18}O values.

Relative to a direct mixing line between the marine source and river water the bottom layer in the Kara Sea has higher salinities. This means that salt has been added during formation of sea-ice in winter. Sea-ice formation can occur repetitively, especially in flaw polynyas, which are kept open by offshore winds and produce large amounts of sea-ice and brines [*Dethleff et al.,* 1998]. It is not possible, according to the available salinity and δ^{18}O data from outside the Kara Sea, to ascribe the changing slopes of the S/δ^{18}O correlation to an external water mass. Thus we interpret the value of this "bend" to represent the remnant of a water mass formed in winter during enhanced sea-ice formation in a flaw polynya. This "Polynya Winter Water" (PWW) constitutes most or all of what is generally called Kara Sea Bottom Water.

According to the average winter position of the flaw polynya along the southeastern Kara Sea shelf [*Pavlov et al.,* 1996] PWW might be formed locally or advected from the northeast. Results from the HAMSOM Kara Sea model [*Harms et al.,* 1999, 2002 this volume] suggest a transport of PWW from the northeast within the counter current typical for the summer month (Fig. 5; compare also Fig. 2 in *Harms et al.,* this volume) running from the northeast to southwest on the shallow part of the Kara Sea shelf.

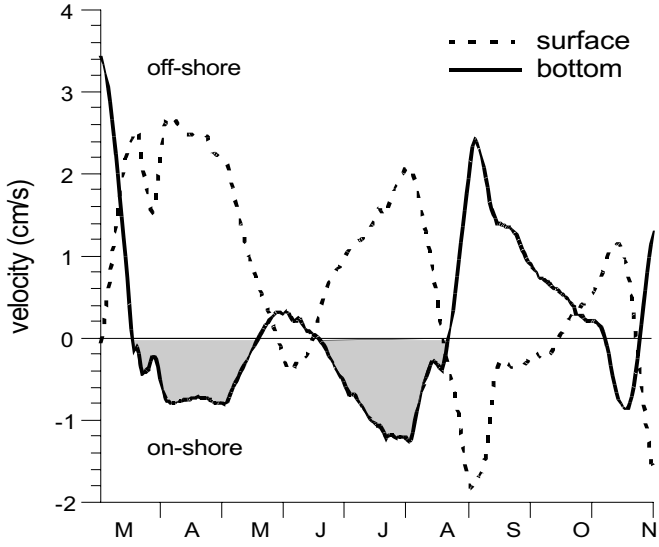

Figure 5: Time series of de-tided bottom and surface flow in the outer Yenisei Estuary, near Dikson, from 1. March to 30. November , climatological year (HAMSOM/VOM). Shaded areas denote periods and strength of on shore bottom flow.

References:

Bauch, D., 1995. The distribution of δ^{18}O in the Arctic Ocean: Implications for the freshwater balance of the Halocline and the sources of deep and bottom waters. Berichte zur Polarforschung, 159: 144 pp.

Bauch, D., Schlosser, P. and Fairbanks, R.F., 1995. Freshwater balance and the sources of deep and bottom waters in the Arctic Ocean inferred from the distribution of $H_2{}^{18}O$. Progress in Oceanography, 35: 53-80.

Brezgunov, V.S., Debolskii, V.K., Mordasov, M.A., Nechaev, V.V. and Yakimova, T.V., 1980. in russian: Study of the conditions of formation of salinity of waters in the mouth regions of Arctic seas by means of natural stable oxygen isotopes. Vodnye Resursy (in russian), 2: 101-105.

Brezgunov, V.S., Debolskii, V.K., Nechaev, V.V., Ferronskii, V.I. and Yakimova, T.V., 1983. Characteristics of the formation of the oxygen isotope composition and salinity upon mixing of sea and river waters in the Barents and Kara Seas. Water Resour. (Transl. of Vodnye Resursy, No. 4, 3-14, 1982), 9(4): 335-344.

Dethleff, D., Loewe, P. and Kleine, E., 1998. The Laptev Sea flaw lead- detailed investigation on ice formation and export during 1991/1992 winter season. Cold regions science and technology, 27: 225-243.

Ekwurzel, B., Schlosser, P., Mortlock, R. and Fairbanks, R., 2001. River runoff, sea ice meltwater, and Pacific water distribution and mean residence times in the Arctic Ocean. Journal of Geophysical Research, 106(C5): 9075-9092.

Harms, I.H., Hübner, U., Backhaus, J.O., Kulakov, M., Stanovoy, V., Stephanets, O. Kodina, L., 2002. Salt intrusions in Siberian River Estuaries -Observations and model experiments in Ob and Yenisei , this volume.

Harms, I.H. and Karcher, M.J., 1999. Modeling the seasonal variability of hydrography and circulation in the Kara Sea. Journal of Geophysical Research, 104(C6).

Melling, H. and Moore, R., 1995. Modification of halocline source waters during freezing on the Beauford Sea shelf: Evidence from oxygen isotopes and dissolved nutrients. Cont. Shelf Res., 15: 89-113.

Östlund, H. and Hut, G., 1984. Arctic Ocean water mass balance from isotope data. JGR, 89(C4): 6373-6381.

Pavlov, V.K. and Pfirman, S.L., 1995. Hydrographic structure and variability of the Kara Sea: Implications for pollutant distribution. Deep-Sea Research II, 42(6): 1369-1390.

Pavlov, V.K. et al., 1996. Hydrometeorological regime of the Kara, Laptev and East-Siberian Seas. Technical Memorandum Applied Physics Laboratory, University of Washington, TM 1-96: 179pp.

North Sea/Baltic Sea 3D-model comparison using either cartesian or curvi-linear coordinates.

Karsten Bolding[1], Hans Burchard[2], Johan Mattsson[3], Carsten Hansen[3] and Peter Gylling Jørgensen[3]

1. Joint Research Centre, I-21020 Ispra, Italy. email: karsten.bolding@jrc.it
2. Baltic Sea Research Institute Warnemnde,Institute for Oceanography, Seestr. 15, D-18119 Rostock, Germany.
3. Farvandsvæsenet, 1023 København K, Denmark.

1 Introduction

This paper presents some of the results obtained in a comparative study of the influence of different computational grids on model simulation results for the North Sea/Baltic Sea area. All simulations have been done with the same numerical model 'getm' - see [1] and have used the same data sources for initial conditions and forcing functions and - hence - the differences between the simulations can be attributed to the model grid differences only. Two principle different grid types have been used - the cartesian grid with a constant grid size (in terms of meters) and the curvi-linear grid where the orientation of the individual gridcells and their dimensions varies (under the constraint that the grid is orthogonal). Here only the results from a 3x3 nm cartesian grid and a curvi-linear grid will be presented.

The main motivation of the study was to find an operational feasible model setup which still reproduces the important physical processes for the area. The major problem simulating the North Sea/Baltic Sea is to - sufficiently well - resolve the Danish Belt Sea area to get the exchange of water and salinity between the Baltic Sea and the North Sea correct.

In addition to the two methods investigated here two other methods exists for resolving narrow straits and belts in large model setups. The traditional approach is to use nesting where a finer resolution model is embedded in a coarser model. Another approcah is the use of un-structured grids. In both these cases high spatial resolution can be achieved in desired areas with greater flexibility than for the curvi-linear grid.

2 Bathymetry and computational grid

Both the cartesian and the curvi-linear grid are based on the same 'master' bathymetry. The master bathymetry was produced as part of the EU MAST-II project DYNOCS (DYNamics Of Connecting Seas) and has a spatial resolution of 1 nm x 1nm. The bathymetry covers the North Sea - Baltic Sea area - see [5] and [4].

In this study it was found that the averaging procedure used to go from the fine 1x1 nm grid to a coarser resolution grid had a pronounced influence on model results. This was tested by runing the model in 2D and 3D barotropic mode as pure tidal simulations where a comparison to a number of tide-gauge stations were done to evaluate the quality of the simulations. We investigated 4 different methods 'max', 'min', 'mean' and 'sqrt'.

The first 3 takes the max, min or mean value of the 1x1 nm grid boxes in side the coarser grid. The 'sqrt' uses the square of the mean of the square roots - to reproduce the wave propogation speed. The overall best performance was obtanied for the 'max' method, especially in the North Sea region. All cartesian results in this paper will be based on the 'max' generated bathymetry. The size of the grid is 350x316 but only about 25 % - e.g. 28000 - of the points are actualy water points. With the large variations between the different methods in mind a comprehensive study of the 'optimal' bathymetry should be done.

The curvi-linear grid has been constructed using the 'SeaGrid' package developed by Charles A. Denham (`http://crusty.er.usgs.gov/~cdenham/seagrid/seagrid.html`) and based on the 'gridpak' package developed by Kate Hedstrom (`http://marine.rutgers.edu/po/gridpak.html`). The complete grid is composed of a number of single orthogonal grids which have been matched together. The grid dimension is 88x138 and about 70 % of the points are water points. The resolution varies from around 100 km down to around 100 m. For this grid no sensitivity studies have been made with regard to the averaging procedure to get the water depth for a specific grid box.

The two different grids are shown on Figures 1 and 2

3 Initial conditions and forcing

Model simulations are started from rest - i.e. velocity and sea surface elevation are 0 - and spun up over one month with frozen density field. Initial conditions for salinity and temperature are based on the climatological data set compiled by [2]. The monthly climatology is given on a sperical grid with a resolution of $\frac{1}{10}$ by $\frac{1}{6}$ of a degree and have 18 vertical levels. As preperation for the present simulations the climatology is horizontally (linearly) interpolated to the model grid. The vertical interpolation to the model grid is done as part of the model initialisation.

At the open boundaries the model is forced by specified sea surface elevations and specified climatological temperature and salinity data. At the air/sea interface momemtum and heat fluxes are calculated.

The elevation boundaries have been calculated using the altimetry data from TOPEX/POSEIDON - a total of 13 constituents have been included and the data have been interpolated to the model grid with a temporal resolution of 1 hour. The open boundaries are situated in the English Channel and between Scotland and Norway.

The salinity and temperature boundaries are extracted from the climatology described above. The boundary values are linearly interpolatad from the monthly values to the actual model time.

The atmosperic forcing is based on the ECMWF re-analysis project and comprises six-hourly values on a 1^o by 1^o grid of 10 meter wind, air pressure, relative humidity, 2m temperature and cloud cover. Using these variables together with the modelled sea surface temperature momentum fluxes as well as latent and sensible heat fluxes and long wave radition has been calulated as part of the model simulation using the [3] bulk formulae. Short wave radiation is included and distributed over the depth according to a specified Jerlov water class.

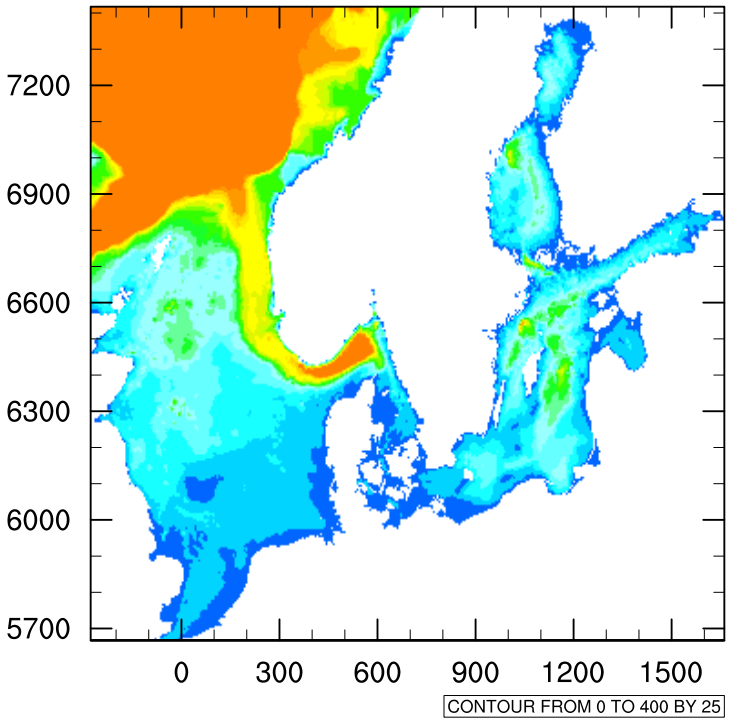

Figure 1: Cartesian (3nm) bathymetry of the North Sea and Baltic Sea

References

[1] Hans Burchard and Karsten Bolding. GETM – a general estuarine transport model. Scientific documentation. Technical Report EUR 20253 EN, European Commission, 2002.

[2] Frank Janssen, Corinna Schrum, and Jan O. Backhaus. A climatological data set of temperature and salinity for the Baltic Sea and the North Sea. *Dt. Hydrogr. Z.*, Suppl. 9:1–245, 1999.

[3] J. Kondo. Air-sea bulk transfer coefficients in diabatic conditions. *Bound. Layer Meteor.*, 9:91–112, 1975.

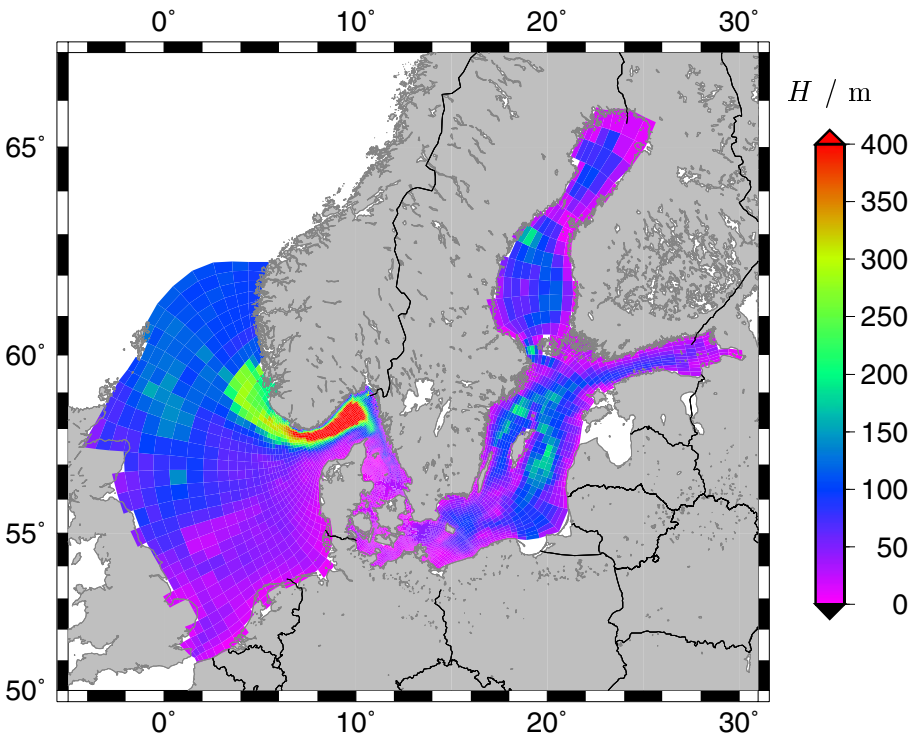

Figure 2: Curvilinear bathymetry of the North Sea and Baltic Sea. The depths are taken from the DYNOCS data set.

[4] T. Seifert and B. Kayser. A high resolution spherical grid topography of the Baltic Sea. *Meereswiss. Ber., Warnemünde*, 9:73–88, 1995.

[5] J. Weiergang and M. Jønsson, editors. *DYNOCS technical data report.* Danish Hydraulic Institute, Hørsholm, Denmark, 1996.

Sensitivity studies of sea ice formation in the Kara Sea

UDO HÜBNER, INGO H. HARMS, JAN O. BACKHAUS

(Institute for Oceanography, University Hamburg,Troplowitzstrasse 7, 22529Hamburg, Germany, huebener@ifm.uni-hamburg.de)

Sea ice formation is an important process in Arctic shelf seas because it determines environmental conditions in the whole Arctic, in particular at the coasts. Arctic shelf seas receive large amounts of freshwater which has a significant impact on ice formation and which could be affected by climate change.

In order to study the direct and indirect influence of river runoff on sea ice formation, a high resolution baroclinic 3-d circulation and sea ice model is applied to the Kara Sea. The model is forced with climatologic atmospheric winds, surface heat fluxes, river runoff and tides. A vertical adaptive grid is used which provides high resolution in critical areas such as shallow estuaries, slopes or topographic obstacles. The surface following boundary layer is resolved uniformly in 4 m intervals in order to resolve the strong vertical stratification.

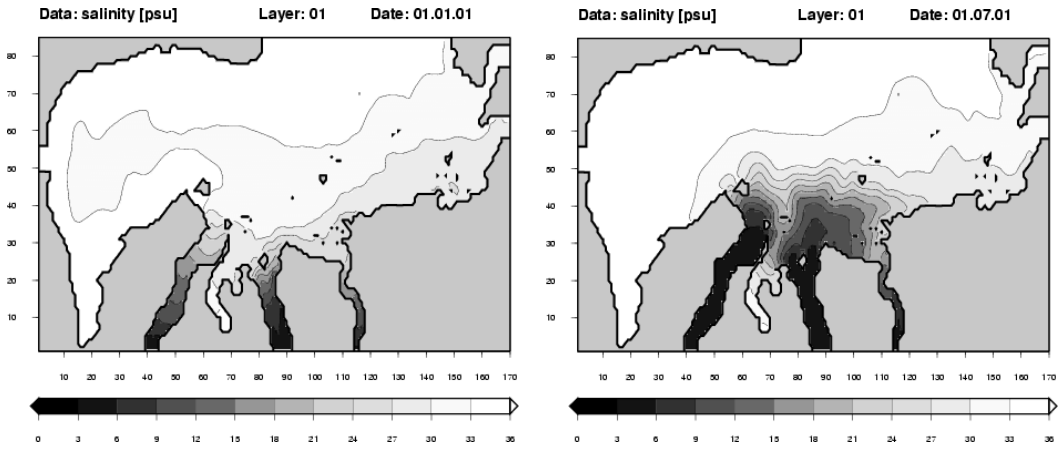

Fig. 1: computed salinity distribution at surface in the Kara Sea, january(left), july(right).

Peak runoff rates in the Kara Sea in spring might exceed 100.000 m_/s which causes high suspended loads in the water column and reduces the shortwave penetration depth considerably compared to ambient Arctic waters. The distribution of salinity is driven by the discharge of the 3 major rivers (Jenisei, Ob and Piasina). In summer a large plume of low saline water spreads into the Kara Sea (upper right figure) while in winter the low saline water is located next to the coast (upper left figure).

Jerlow has proposed a sheme for classifying oceanic (typ: I, IA, IB, II, III) and coastal (typ: 1, 3, 5, 7, 9) water according to its clarity. For the parameterization of absorption of shortwave radiation a bimodal exponetial scheme after Paulson and Simpson is used.

The simulated melting rates are sensitive to the penetration depth of shortwave radiation into the water column. To investigate the influence of shortwave penetration into depth some experiments were carried out and the ice parameters were compared to each other.

Figure 2 (left) shows the ice compactness computed with deep penetration depth (watertyp: OT I). In figure 2(right) a case with penetration depth depending on salinity is shown.

As a result, coastal sea surface temperatures rise and ice melting is significantly enhanced. The main differences occur in summer in the region of the river estuaries. The sea surface temperature shows deviations of up to 1.3°C. The maximum difference in ice thickness is up to 0.8m.

Our sensitivity studies show, that the indirect influence of river runoff on ice melting could play an important role in future studies on climate variability in the Arctic.

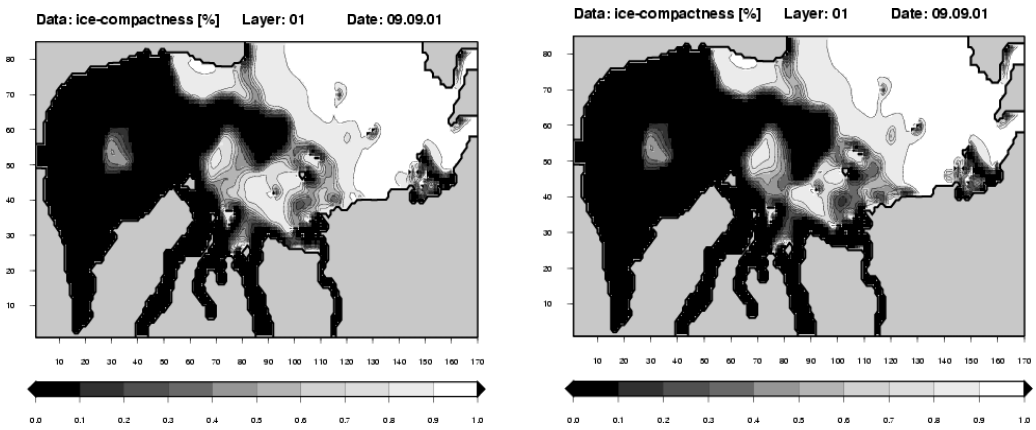

Fig. 2: computed ice concentration in the Kara Sea in september, deep shortwave penetration (left), shortwave penetration depending on salinity(right)

The model results are in good agreement to the ice concentration derived from satellite data, in spite of the fact, that the model forcing is climatologic.

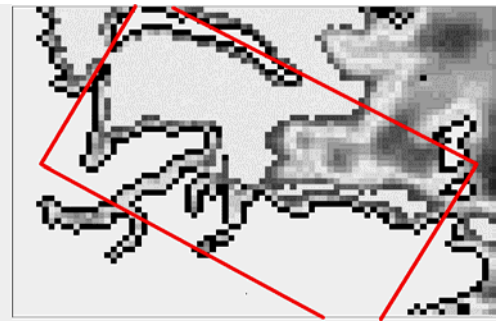

Fig. 3:observed ice concentration in the Kara Sea, 9.09.1996 (SSMI-data from NASA team)

Acknowledgments: The work was funded by the BMBF through the bi-lateral German/Russian project SIRRO (Siberian River Runoff) .

References:

Backhaus, J.O., =V=O=M=>, a vector ocean model with a static adaptive grid, applied to the vertical co-ordinate. General model concept and grid adaptation. Manuscript in preparation, 2002.

Hibler, W.D. III, A dynamic thermodynamic sea ice model, J. Phys. Oceanogr., Vol. 9, 1979.

Frontal zones in the Kara Sea: observation and modeling

MIKHAIL KULAKOV

(Arctic and Antarctic Research Institute, 38, Bering str., 199397, St. Petersburg, Russia, mod@aari.nw.ru)

VLADIMIR STANOVOY

(Arctic and Antarctic Research Institute, 38, Bering str., 199397, St. Petersburg, Russia, mod@aari.nw.ru)

1. Introduction

The Kara Sea has one of the largest regions of fresh water influence (ROFI) in the world. Horizontal salinity and temperature gradients can reach values 1.5 ppt and 0.2^{o}C per 1 km, and vertical 1^{o}C and 5 ppt per 1 m in the open sea and 8 ppt and 2^{o}C per 10 cm in the estuaries. Data analysis has shown that the characteristics of the frontal zones in the Kara Sea have the significant spatial and temporal (interannual, interseasonal and seasonal) variability. About 60% of the annual discharge of the combined Ob' and Yenisey rivers occurs during the three months (May, June, July). This pulsing of the Kara Sea inflow suggests that pooling of fresh water formed before the shipboard survey could take place by the time of ice-free conditions in September. The difficulty of making in-situ observations in this ice-covered sea makes the combined use of in-situ observations and modeling particularly advantageous for the solution of problem of frontal zones formation.

2. Method and data

The Kara Sea model is based on the coding of the S-Coordinate Rutgers University Model (SCRUM, see *Hedstrom* [1997]). This model use high order advection scheme that is very important for frontal zones modeling. The SCRUM was applied to the Kara Sea with spatial resolution equal about 10 km. The vertical scale was resolved with 10 layers. The model has been validated to observed sea level elevation at some coastal stations and some other kinds of field and laboratory experiments. The SCRUM was run with different scenarios of forcing (river runoff, atmospheric forcing) in prognostic mode for spring-summer period in the Kara Sea.

For the investigation of the frontal zones variability in the Kara Sea and model validation all available data of expeditions for period from 1950 till 2001 were used. More than 20000 CTD-stations were involved in this analysis.

3. Results

In the first experiment, spreading of river water in the absence of wind and mean multiyear river discharges as only forcing was simulated. The calculated buoyancy-forced currents and salinity at the surface for August 30 are presented in Fig. 1. The strongest currents agree with the secondary frontal zone (isohaline 25) and direct along the tangent to it. The location of this frontal zone in our experiment is in good agreement with a 60 m isobath. This depth is probably sufficient for the currents to attain a quasi-geostrophic character. These currents do not practically have a component perpendicular to the front and do not transport river water towards the open sea. An insignificant plume increase mainly occurs due to turbulent diffusion. When the frontal zone reaches a depth of 60 m, the plume of river water stops increasing in size and achieves a dynamic equilibrium while the excess of continuous freshwater from rivers flows through the eastern boundaries of the Kara Sea. The buoyancy-forced current velocity in the frontal zone can reach 35 cm/s. Our results show good agreement with the results of laboratory simulation (see *McClimans et al.* [2000]).

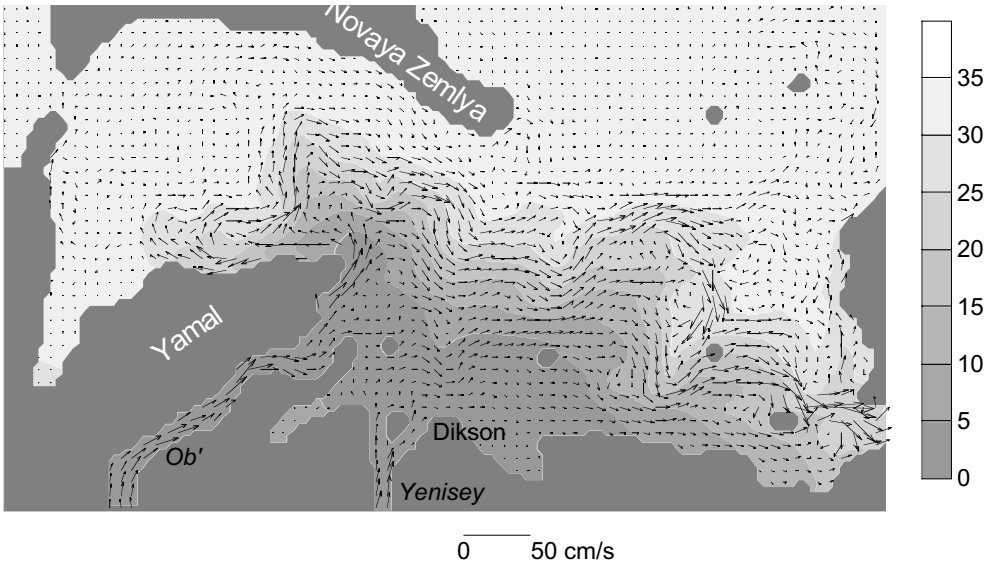

Figure 1: Surface salinity and currents in the Kara Sea.

There are numerous meanders, eddies and squirt like features generated by baroclinic instability in the frontal zone. They have different sizes and directions of rotation. For example, a tongue of freshwater along the coast of the Yamal Peninsula spreading southwestward from Beliy Island (Fig. 2). The presence of this structure is confirmed by *in-situ* observations. It is clearly traced on a satellite image of sea surface temperature of the Kara Sea (Fig. 2b). The calculations show that this tongue is formed by a set of several quasi-geostrophic rings in frontal zone with an anticyclonic rotation in the river water area and a cyclonic rotation in the sea water area (Fig.3a). The radii of these rings have dimensions of order of 40-50 km.

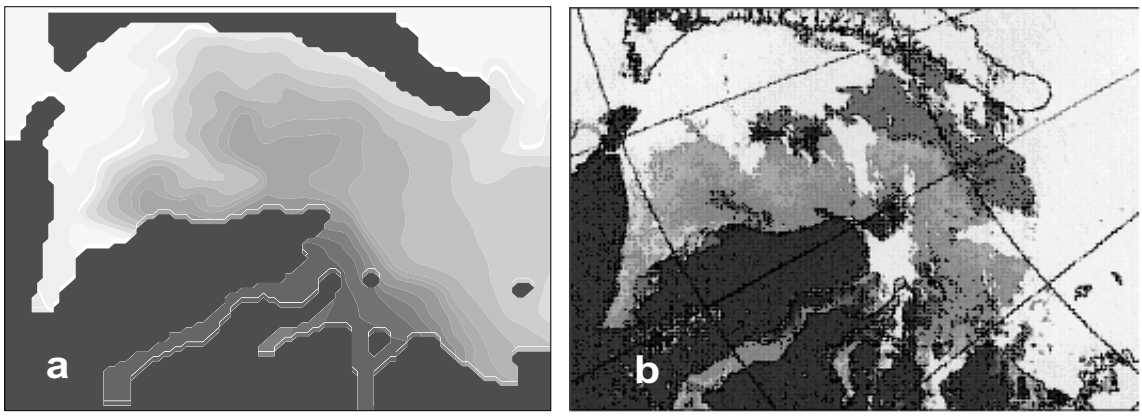

Figure 2: Calculated surface salinity (a) and satellite image of sea surface temperature (b).

Such eddies are typically for the frontal zone of the Kara Sea. In Figure 3b sea surface salinity along section from Dikson toward Novaya Zemly is presented. Section was carried out in frame of Norwegian expedition in 1994 (see *Johnson et al*. [1997]). This section shows salinity front, with about 14 ppt difference over 65 km. The feature just west of the front with lower salinity then the surrounding water is most likely formed by an outflow of surface water from the delta region. The ADCP velocity section, corrected for tidal phase, shows (Fig. 3c) the biderictional velocity with

almost clear anticyclonic character. The size of this eddy with the brackish core is equal 54 km. Such eddy contains about 10 km^3 river water or about one day of river flux. These anticyclonic eddies can migrate off ROFI, transporting large quantities of river water to the ocean currents in the deeper basin.

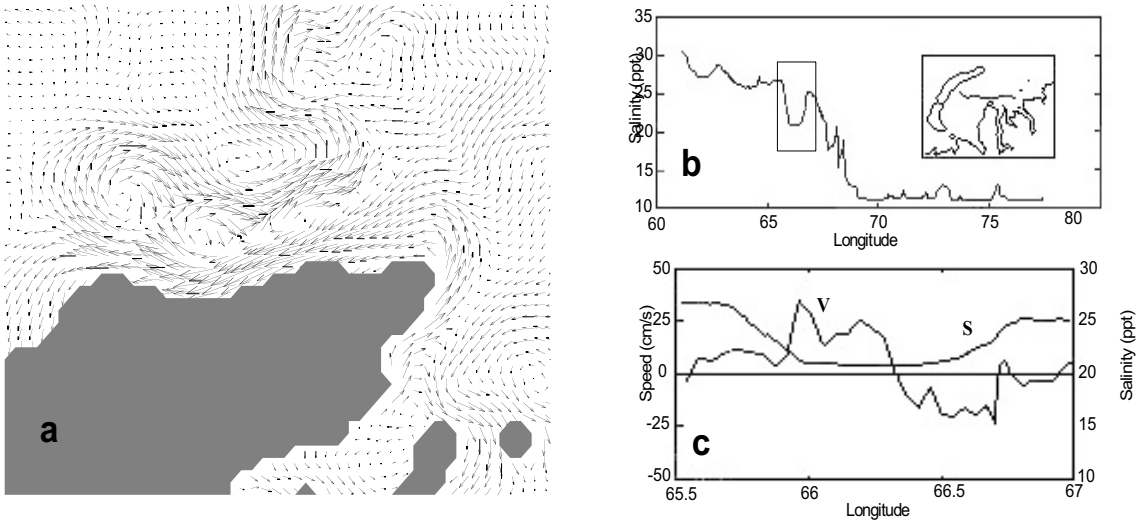

Figure 3: Calculated surface currents (a), sea surface salinity along section (b) and surface salinity and current speed normal to the ship's track on passage through the anticyclonic structure (c).

One of the most important reasons of the pycnocline gradients changing, vertical diapicnal mixing and entrainment processes is the breaking of the internal waves. Analysis of the all available data of multi-hour and multi-day CTD stations in the Kara Sea shows the pronounced amplification of the water temperature and salinity oscillations in pycnocline with periods from 3 hour to inertial (see *Pavlov et al.* [1996]). Observations of the summer surveys 1997 and 2001 demonstrated well-pronounced high-frequency internal waves with periods from 2 to 15 minutes at the background of the more long-periodic oscillations (see *Stanovoy and Shmelkov* [2002]). Amplitudes of the internal waves in the Kara Sea can reach several meters and the changing of salinity can reach 15 units per several hours and 0.3-0.5 (in estuaries – up to 6-8) per 10 minutes. In the coastal zone of the Kara Sea the nonlinear internal waves were observed. But all estimations of the internal waves breaking probability were based on the approximated estimations of the current shear or on the modeling results.

Only in summer 1995 two stations with ADCP were deployed within the frontal zone for two weeks. Analysis of the obtained records has shown the predominance of the oscillations with tidal period at the all horizons. In Figure 4a the vertical distributions of the salinity in one ADCP station at the moments of deployment and recovery and the standard deviation of meridional current component are presented. Also the spectra of the meridional current component oscillations at the different horizons of this station are presented (Fig. 4b). The amplification of the oscillations in the pycnocline is shown well. These oscillations are twice as much the barotropic tidal current. The increasing of the inertial oscillations at the second half of record period results in shear instability of the internal waves (Richarson number was less than 0.25) and increasing of entrainment. As sequent, the changing of vertical salinity distribution, deepening of the mixing layer boundary and strengthening of the pycnocline were observed (Fig. 4a).

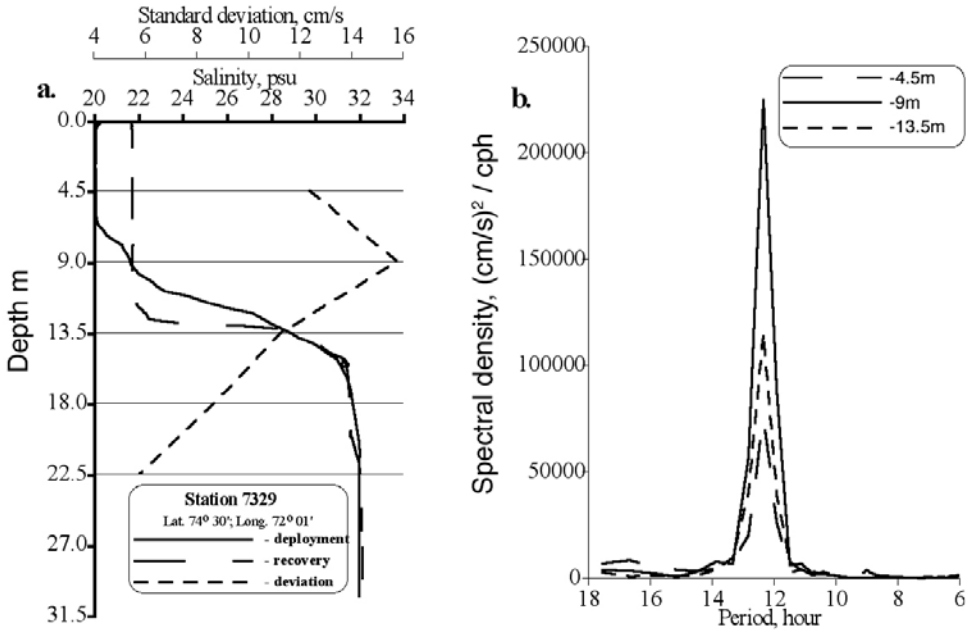

Figure 4. Vertical distribution of the salinity and standard deviation of the meridional current component (a) and spectra of the meridional current component at the horizons 4.5, 9 and 13.5 m (b) at the ADCP station in summer 1995.

4 Summary

We describe the some processes inherent in the frontal zones of the Kara Sea. These processes are very important for frontal zones behavior. Ob' and Yenisey rivers tend to form frontal zones structures under strong topographic steering throughout spring and summer. Eddies and internal waves well developed in frontal zones of the Kara Sea enhance mixing and weaken the cross-front gradients of different water properties and can transport dissolved and suspended material carried by rivers for a long distance.

Acknowledgments: The work was made within the frame of the Russian-German project *'Siberian River runoff'*, ***SIRRO*** (BMBF and Russian authorities) and the EU-project ***ESTABLISH*** (contract No. ICA2-CT-2000-10008).

References:

Hedstrom, K.S., User's Manual for an S-Coordinate Rutgers University Model (SCRUM). Version 3.0, *Institute of Marine and Coastal Sciences at Rutgers University,* 116 p., 1997.

Jonson, D.R., T.A. McClimans, S. King, O. Grenness, Fresh water masses in the Kara Sea during summer, *J. Of Mar. Syst*., *12*, 127-145, 1997.

McClimans, T.A., D.R. Jonson, M. Krosshavn, E.E. King, J. Carrol, and O. Grennes, Transport processes in the Kara Sea, J. of Geoph. Res., 105, C6, 14,121-14,139, 2000.

Pavlov, V.K., Timokhov L.A.,. Baskakov G.A.,. Kulakov M.Yu.,. Kurazhov V.K., Pavlov P.V., Pivovarov S.V., and Stanovoy V.V., Hydrometeorological regime of the Kara, Laptev and East-Siberian Seas. Technical Memorandum APL-UW TM 1-96, 179 pp., 1996.

Stanovoy, V.V., and B.S. Shmelkov., Short-period internal waves in the Kara Sea. *Berichte zur Polar and Meeresforschung*, 2002 (in press).

A Consistent Derivation of the Wave Energy Equation from Basic Hydrodynamic Principles

ANDREAS MALCHEREK, (*Federal Waterways Engineering and Research Institute (BAW), Coastal Department, Wedeler Landstr. 157 D-22559 Hamburg, Germany,* malcherek@hamburg.baw.de)

1 Introduction

Wave energy defined as the square of the wave height H or amplitude A is advected by the mean flow and the group velocity. It is dissipated by bottom shear stresses, viscous and turbulent damping. Wave energy is lost also through breaking in shallow and white capping in deep water. When the wave energy spectrum is regarded, it is believed that quadruplet nonlinear interactions transfer energy within the spectrum.

For the description of these processes several wave energy equations can be found in literature. The most fundamental equation starts from the conservation of wave action density $N(\vec{x},t) = 2|A(\vec{x},t)|^2/\omega$ given as:

$$\frac{\partial N}{\partial t} + \text{div } \left((\vec{\overline{u}} + \vec{c_g})N\right) = 0$$

where $\vec{\overline{u}}$ is the mean flow and $\vec{c_g}$ the group velocity. This equation is derived from the classical kinematic wave theory which analyzes the behavior of a harmonic function dependent on a arbitrary phase function [10], [1], [2].

The same derivation process leads to the spectral wave energy equation when the wave energy is assumed to be a function of the wave number too, $N(\vec{k}(\vec{x},t),\vec{x},t) = 2|A(\vec{k}(\vec{x},t),\vec{x},t)|^2/\omega$ [11], [7]. Introducing source and sink terms this kind of models is one of the most successful approach for ocean wave modeling.

The main characteristics of this approach is the fact that it is originally a kinematic and not a hydrodynamic approach. Therefore sources and sinks for the energy of surface waves do not appear in the derivation of the wave action density equation and have to be taken into account heuristically i.e. they are postulated as right hand side terms.

A second approach for the derivation of a wave energy equation starts from analyzing the wave energy e^w as the sum of kinetic and potential energy integrated over the wave period T and water depth

$$e^w = \frac{1}{T}\int_0^T \int_{z_B}^{z_S} \left(\frac{1}{2}u^{\vec{w}}u^{\vec{w}} + gz\right) dzdt \tag{1}$$

where z_B and z_S are the vertical coordinates of the bottom and the free surface respectively and $u^{\vec{w}}$ is the orbital wave velocity. By taking into account the related fluxes a wave energy equation is obtained which contains the transport by the mean and the group velocity as well as the exchange of energy with the mean flow field by radiation stresses [3], [5]. For the integration over the water depth boundary conditions are needed whereby wind and bottom shear stresses as source and sink terms are introduced straightforward. Milbradt

[6] also added a sink term for wave breaking and showed that the resulting model is capable to cope with large scale coastal wave modeling.

Independent of wave energy modeling several attempts were made to study wave dynamics using a Reynolds decomposition of the flow field into a mean flow, the periodic wave motion and turbulent fluctuations. Svendsen and Lorenz [8] used this decomposition to improve the theory of undertow and long-shore currents. They neglected viscous effects and they did not proceed to an wave energy equation. Also very often a decomposition into the mean and the turbulent components is found whereby the mean flow is identified with the wave motion. In this way Teixera and Belcher [9] for example showed how kinetic wave energy is transformed into turbulent kinetic energy as the wave propagates.

In this paper a decomposition of the full Navier-Stokes-equations into mean, turbulent and wave motions is presented. The decomposition is consistent with the original equations i.e. when adding the resulting momentum equations for the three components the original Navier-Stokes-equations are re-obtained.

From the momentum equations of the wave field three dimensional kinetic and total wave energy equations can be derived straightforward. Double averaging over the wave period and water depth leads to an equation for the wave energy with some unknown correlation terms. After closing these terms using linear wave theory the kinematic wave energy equation is obtained where the energy is propagated in a velocity field being the sum of mean and group velocity. In contrast to wave action density models energy dissipation processes due to viscosity, turbulence and bottom shear stress as well as wind input are clearly identified in this derivation. Again parameterizations using linear wave theory lead to well known formulations for these processes.

Although the presented theory just confirms the correctness of well known equations it provides a unique approach to turbulence and wave theory. It is able to identify especially turbulence-wave interaction in the dynamic equations. It leads the way how to extend the wave energy equation to describe further processes: Non-linear wave theories can be used to close unknown correlations as well as a spectral wave energy theory can be derived.

2 Consistent Reynolds Decomposition of the Velocity Field in Average Currents, Waves and Turbulence

For the following derivation the Navier-Stokes-equations are written in their conservative form

$$\frac{\partial \vec{u}}{\partial t} + \text{div } (\vec{u} \otimes \vec{u}) = -\frac{1}{\varrho}\text{grad } p + \text{div } \nu \text{ grad } \vec{u} + \vec{f}$$

where ϱ is the fluid density, ν its molecular viscosity and $\otimes$ denotes the tensor product. The velocity field $\vec{u}$ and the pressure p are decomposed to the average flow field, periodic waves and turbulent fluctuations:

$$\vec{u} = \overline{\vec{u}} + \vec{u}' + \vec{u}^w$$

$$p = \overline{p} + p' + p^w$$

The equations are time averaged over a period which is long compared to the wave periods i.e. it contains fluctuations due to turbulence and waves. As a result the dynamics of the average currents are described by the equations

$$\frac{\partial \vec{\overline{u}}}{\partial t} + \text{div } \left(\vec{\overline{u}} \otimes \vec{\overline{u}}\right) = - \text{ grad } \overline{p} + \frac{1}{\varrho} \text{ div}(\overline{P} + T_l + R + S) + \vec{f} \tag{2}$$

with the molecular viscosity tensor of the average flow field

$$\overline{P} = \nu \text{ grad } \vec{\overline{u}},$$

the long term Reynolds stress tensor

$$T_l = -\overline{\vec{u'} \otimes \vec{u'}},$$

the radiation stress tensor

$$S = -\overline{\vec{u^w} \otimes \vec{u^w}},$$

and another nameless tensor

$$R = -\overline{\vec{u'} \otimes \vec{u^w}} - \overline{\vec{u^w} \otimes \vec{u'}}$$

which describes the interaction between turbulence and waves. Therefore the average flow field is affected by what turbulence and waves do with each other and the tensor R can be characterized as a jealous one.

Subtracting the average flow field from the Navier-Stokes-equations and averaging a second time over the turbulent time scales results in an equation for wave motion:

$$\frac{\partial \vec{u^w}}{\partial t} + \text{div } \left(\vec{u^w} \otimes \left(\vec{\overline{u}} + \vec{u^w}\right)\right) = -\frac{1}{\varrho} \text{grad } p^w + \text{div } \left(P^w - R - S - T_l + T_s - \vec{\overline{u}} \otimes \vec{u^w}\right) \tag{3}$$

with $P^w = \nu \text{ grad } \vec{u^w}$ and the Reynolds Stress Tensor T_s related to the short term averaging of the nonlinear advection terms. When this distinction between a long and a short term averaging is not made, i.e. $T_l = T_s$, the wave energy equation will not contain a mechanism for the dissipation of wave energy by turbulence.

When the dynamic equation for the wave motion is subtracted from the equation for wave and turbulent fluctuations an equation for the turbulent fluctuations is left:

$$\frac{\partial \vec{u'}}{\partial t} + \text{div } \left(\vec{u'} \otimes \vec{u}\right) = -\frac{1}{\varrho} \text{grad } p' + \text{div } \left(\nu \text{ grad } \vec{u'} - T_s - \vec{\overline{u}} \otimes \vec{u'} - \vec{u^w} \otimes \vec{u'}\right) \tag{4}$$

Turbulent fluctuations are advected with the total velocity consisting of average, wave and turbulent components. The last two terms on the right hand side describe turbulence production by currents and waves respectively.

3 Derivation of the Wave Energy Equation

Following equation (1) an dynamic equation for this quantity is obtained by multiplying eq. (3) with the wave velocity vector, adding the potential energy and averaging over the wave period. After closing unknown correlations where it is possible using linear wave theory the following wave energy equation can finally be obtained:

$$\frac{\partial e^w}{\partial t} + \text{div } ((\vec{u} + \vec{c_g})e^w) = -\sum_{i,j} \overline{S_{ii}} \frac{\partial \overline{u_i}}{\partial x_j} + \frac{\overline{u_S^w \tau_S^w}}{\varrho} - \frac{\overline{u_B^w \tau_B^w}}{\varrho} - 4e^w \nu k^2 + \overline{\vec{u^w} \text{ div } T_s}$$

This equation contains the radiation to the mean flow, the free surface and bottom stresses as well as the viscous and turbulent dissipation of wave energy as source and sink terms on the right hand side. It extends the other wave energy equations cited introduction by a further term for the turbulence wave interaction.

In the paper a path to obtain a spectral wave equation will also be presented.

References

[1] Bretherton, F.P. and Garrett, C.J.R. Wavetrains in Inhomogeneous Moving Media. *Proc. Roy. Soc.*, Ser. A, 302:529–554, 1969.

[2] Hayes, W.D. Kinematic Wave Theories. *Proc. Roy. Soc.*, A 320:209–226, 1970.

[3] Johnson, R.S. *A Modern Introduction to the Mathematical Theory of Water Waves.* Cambridge University Press, Cambridge, N.Y., 1997.

[4] Longuet-Higgins, M.S. and Stewart, R.W. The Changes in Amplitude of Short Gravity Waves on Steady Non-Uniform Currents. *J. Fluid Mech.*, 10:529–549, 1961.

[5] Mei C.C. *The Applied Dynamics of Ocean Surface Waves.* World Scientific, Singapore, New Jersey, London, Hong Kong, 1989.

[6] Milbradt, P. *Zur mathematischen Modellierung grosräumiger Wellen- und Strömungsvorgänge.* Veröffentlichung 1/95, Institut für Bauinformatik der Universität Hannover, Universität Hannover, Hannover, 1995.

[7] Schneggenburger, C. Spectral Wave Modelling with Nonlinear Dissipation. Technical Report GKSS 98/E/42, GKSS-Forschungszentrum Geesthacht, Geesthacht, 1998.

[8] Svendsen, I.A. and Lorenz, R.S. Velocities in Combined Undertow and Longshore Currents. *Coastal Engineering*, 13:55–79, 1989.

[9] Teixeira, M.A.C. and Belcher S.E. On the Distortion of Turbulence by a Progressive Surface Wave. *J. Fluid Mech.*, 458:229–267, 2002.

[10] Whitham, G.B. A General Approach to Linear and Nonlinear Dispersive Waves Using a Lagrangian. *J. Fluid Mech.*, 22:273–283, 1965.

[11] Willebrand, J. Energy Transport in a Nonlinear and Inhomogeneous Random Gravity Field. *J. Fluid Mech.*, 70:113–126, 1975.

Modeling the oceanic response to episodic wind forcing over the West Florida Shelf

STEVEN L. MOREY

(Center for Ocean – Atmospheric Prediction Studies, The Florida State University, Tallahassee, FL, USA, 32306-2840, morey@coaps.fsu.edu)

MARK A. BOURASSA

(Center for Ocean – Atmospheric Prediction Studies, The Florida State University, Tallahassee, FL, USA, 32306-2840, bourassa@coaps.fsu.edu)

XUJING JIA

(Center for Ocean – Atmospheric Prediction Studies, The Florida State University, Tallahassee, FL, USA, 32306-2840, jia@coaps.fsu.edu)

JAMES J. O'BRIEN

(Center for Ocean – Atmospheric Prediction Studies, The Florida State University, Tallahassee, FL, USA, 32306-2840, obrien@coaps.fsu.edu)

WILLIAM W. SCHROEDER

(Marine Science Program, The University of Alabama, Dauphin Island Sea Lab, 101 Bienville Blvd., Dauphin Is., AL, USA, 36528, wschroeder@disl.org)

JORGE ZAVALA-HIDALGO

(Center for Ocean – Atmospheric Prediction Studies, The Florida State University, Tallahassee, FL, USA, 32306-2840, zavala@coaps.fsu.edu)

1. Introduction

Shallow seas and wide continental shelves respond dramatically to local energetic episodic wind forcing, such as atmospheric fronts and tropical storms. High-resolution ocean models show great promise in simulating the ocean environment at these regional scales, but are often limited by the availability of gridded wind fields for surface fluxes that have high enough spatial and temporal resolution to adequately capture these strong events. Numerical weather prediction products are typically too coarse and the fields can be too smooth to adequately resolve these energetic systems. Winds measured by the Seawinds scatterometer aboard the Quikscat satellite have admirable quality and spatial resolution, but the bandlike sampling can lead to large temporal gaps at some locations, which complicate the representation of moving weather systems. In this study, comparisons are made between results of a numerical model of the Gulf of Mexico (GoM) forced by objectively gridded satellite scatterometer winds, Eta-29 atmospheric model forecast data, and a hybrid of the satellite and numerical weather prediction products. Validation of the model results with in-situ observations shows the strengths and weaknesses of using the different gridded winds for modeling the region. Particular attention is paid to episodic weather events, such as tropical systems and atmospheric fronts. The West Florida Shelf (WFS) region is chosen for the focus of this study as a testbed for examining how best to use satellite derived winds to force regional-scale ocean models.

2. The Model

This study evaluates the solution from simulations of the GoM using the Navy Coastal Ocean Model (NCOM). The NCOM is a three-dimensional primitive equation hydrostatic ocean model developed at the Navy Research Laboratory (see *Martin* [2000]). The model's hybrid sigma (terrain following)

and z (geopotential) level vertical coordinate is useful for simulating upper ocean processes in domains encompassing both deep ocean basins and very shallow shelves. The NCOM is set up to simulate the entire GoM and Caribbean north of Honduras (15° 30' N) to 80° 36' W with 1/20° between like variables on the C-grid, 20 sigma levels above 100 m and 20 z-levels below 100 m to a maximum depth of 4000 m (Figure 1). The model is forced by discharge from 30 rivers, transport through the open boundary (with monthly climatology temperature and salinity) yielding a mean transport through the Yucatan Strait of approximately 30 Sv, monthly climatology surface heat flux, and twelve-hourly winds. A surface salinity flux has the effect of uniformly evaporating an amount of water at a rate equal to the sum of the annual average discharge rates of the 30 rivers. The model is spun up from rest using DaSilva monthly climatology wind stress for approximately five and one-half years before the twelve-hourly wind stresses are applied.

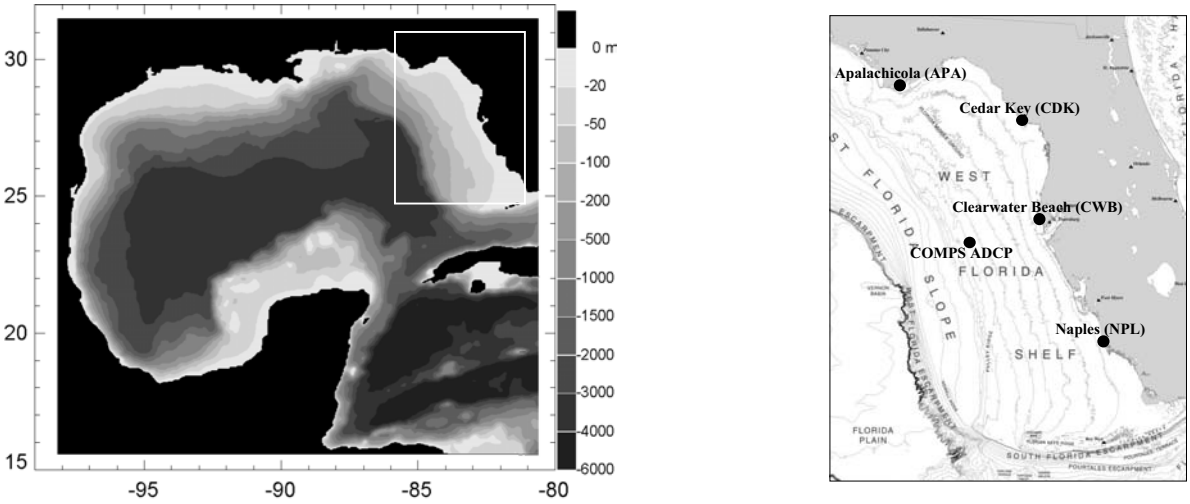

Figure 1: Left: NCOM GoM simulation domain and topography. Right: Bathymetric chart of the WFS region (shown by the white box to the left) with the locations of the in situ data used for model validation.

3. The Wind Fields

Three gridded wind products are used to force the ocean model: the 29 km resolution Eta-29 model 10 m winds, winds derived from the SeaWinds scatterometer aboard the QuikSCAT satellite objectively mapped to a 1/2° grid using winds from the same scatterometer data to create a background field, and another mapping of the QuikSCAT winds using the Eta-29 winds as the background field (these three wind fields will be termed ETA, QSCAT, and QSCAT/ETA, respectively, for convenience). Wind stress fields are prepared to force the ocean model from July 21, 1999 through the end of 2000. The starting date corresponds to the beginning of the QuikSCAT observations.

To form the two gridded scatterometer wind products, the pseudostress is objectively gridded using the variational method described by *Pegion et al.* [2000]. The functional

$$f = \sum_{i,j}^{I,J} \left\{ \beta_a \sigma_{P_o}^{-2} \left[\left(P_x - P_{x_o}\right)^2 - \left(P_y - P_{y_o}\right)^2 \right] + \beta_d L^4 \left[\nabla^2 \left(P_x - P_{x_{bg}}\right) \right]^2 + \beta_d L^4 \left[\nabla^2 \left(P_y - P_{y_{bg}}\right) \right]^2 + \beta_e L^2 \left[k \cdot \nabla \times \left(\vec{P} - \vec{P}_{bg}\right) \right]^2 \right\}$$

is minimized for the solution pseudostress (P_x, P_y). Here, the terms with the small 'o' subscripts are the observations from the satellite, and the terms with the small 'bg' subscripts are the background field. The betas are weights, sigma is the uncertainty of the observational average within a grid cell, and L is a grid-spacing dependent dimensionless length scale. The first term represents the misfits to the scatterometer observations, the second and third terms comprise a penalty function to smooth with respect to the background field, and the last term is the misfit to the vorticity of the background field.

For the QSCAT gridded wind product, the background field is constructed from 3-day binned QuikSCAT wind data, Gaussian smoothed over a five degree radius. For the QSCAT/ETA product, the background field is the Eta-29 wind field.

Observations collected within a twelve-hour window centered on 0:00Z or 12:00Z are treated as the observations at the middle of the time window. Therefore, twelve hourly gridded wind pseudostress fields are produced. For consistency, the Eta-29 wind fields from the same twice-daily times are selected for the model experiments. The wind stress is computed from the bulk formula with the drag coefficients computed using a quadratic function of the wind speed. The resultant wind stress is interpolated to the ocean model grid using bicubic splines.

4. Results

The ocean model solutions are compared to data collected over the WFS. The WFS is chosen as a testbed for evaluating the impact of the different wind stress fields as forcing for coastal and regional scale ocean models because it has been shown that the circulation on the inner and middle WFS is primarily driven by local winds (See Weisberg, et al. [2001]). The region is also subject to episodic energetic forcing from tropical and extratropical storms. It is useful to study the response of the ocean model forced by the various wind products during these periods of energetic forcing. Data are collected from coastal sea level (SL) stations and from a moored acoustic doppler current profiler deployed as part of the Coastal Ocean Monitoring and Prediction program at the University of South Florida. Only the SL comparisons will be discussed here.

SL time series from the NCOM experiments are compared to in situ data at four stations along the WFS: Naples, Clearwater Beach, Cedar Key, and Apalachicocla (Figure 1). The observational and model data are filtered to form sets of daily SL values. SL root mean square error (RMSE) scaled by the standard deviation (of the observational data computed over same time record used for computing RMSE) is used as one metric for evaluating the model performance. SL can be thought of as a function of the wind stress (alongshore) integrated along the characteristics of the coastally trapped waves, propagating counterclockwise around the GoM. The Florida Keys to the south of the shelf serve approximately as an insulating boundary.

The results are similar for all stations studied; Cedar Key is used as an example here. The standard deviation of the observations is 13.1 cm for the full time record studied at this location. The scaled RMSEs are 0.88, 0.75, and 0.73 for the simulations forced by ETA, QSCAT, and QSCAT/ETA, respectively. To study the different behavior of the ocean model response to energetic wind forcing versus the more typical conditions, the time record is decomposed into two parts. The first consists of all data within a 7-day window centered around any day with observed SL fluctuations greater than two standard deviations (26.2 cm, in this case) of the mean. This record comprises approximately 20% of the data. Most of this subset of data is from the late fall through early spring months when there are frequent passages of cold fronts through the region, with occasional tropical cyclones (three passed during this period) during the summer and early fall months. The second part of the decomposed record consists of the remaining data, and contains more moderate or weak SL fluctuations. The results show that during weak or moderate events the simulations perform similarly with scaled (now by a standard deviation of 9.5 cm) RMSEs of 0.91, 0.92, and 0.91 corresponding to the ETA, QSCAT, and QSCAT/ETA forced simulations, respectively. However, during the part of the record corresponding to energetic SL fluctuations (and, thus, more energetic forcing), the simulations forced by the scatterometer derived gridded wind products perform much better. Scaled (by a standard deviation of 20.2 cm) RMSEs are 0.88, 0.62, and 0.60 for the simulations as ordered above. That is, using this metric, the model solution shows significant improvement when the QSCAT and QSCAT/ETA gridded wind stress fields are used during periods of energetic wind forcing, however, the model performance is similar under all conditions when forced by the ETA wind stress fields.

5. Discussion

The large errors in the model solution when forced by the ETA wind stress fields are primarily due to the fact that the ETA wind fields are smooth and weak, a trait often found in numerical weather prediction products. The scatterometer observations are better able to represent the intensity and spatial patterns of energetic weather systems. Comparisons of the wind stress from the gridded products to the wind stress computed from National Data Buoy Center measurements show that the average ETA wind stress is approximately 50% of the magnitude of the observations, whereas the scatterometer derived wind stress fields have quite similar magnitudes to the observations in this region. It is not clear, however, whether simply multiplying the ETA wind stress vectors by a scalar is an appropriate solution, as the spatial structure of QSCAT and QSCAT/ETA fields is often quite different from the ETA fields. An example from each of the three fields during the passage of Tropical Storm Harvey illustrates this fact (Figure 2).

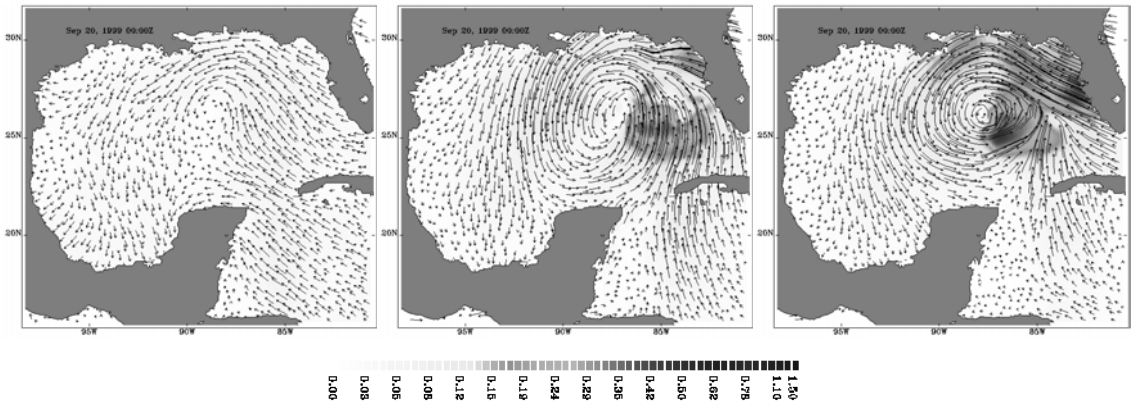

Figure 2: Wind stress (Pa) fields from the gridded ETA (left), QSCAT (middle) and QSCAT/ETA (right) wind stress fields on September 20, 1999, just prior to T.S. Harvey passing eastward over the WFS.

Acknowledgments: The authors thank Drs. Paul Martin, Alan Wallcraft, and others at the Navy Research Laboratory for their development of and assistance with the Navy Coastal Ocean Model. Drs. Robert Weisberg and Mark Luther at the University of South Florida graciously provided the COMPS ADCP data. Simulations were performed on the IBM SPs at Florida State University and the Naval Oceanographic Office. Computer time was provided by the DoD High Performance Computing Modernization Office. This project was sponsored by funding provided by the DoD Distributed Marine Environment Forecast System, by the Office of Naval Research Secretary of the Navy grant awarded to Dr. James J. O'Brien, by a NASA Office of Earth Science grant to the COAPS authors and through NASA funding for the Ocean Vector wind Science Team. Frank Wentz at Remote Sensing Systems produced the scatterometer data.

References:

Martin, P., A description of the Navy Coastal Ocean Model Version 1.0. NRL Report NRL/FR/7322-009962, Naval Research Laboratory, Stennis Space Center, MS, 39 pp., 2000.

Pegion, P.J., M.A. Bourassa, D.M. Legler, and J.J. O'Brien, Objectively derived daily "winds" from satellite scatterometer data. *Mon. Wea. Rev.,*128, 3150-3168, 2000.

Weisberg, R.H., Z.J. Li, and F. Muller-Karger, West Florida Shelf response to local wind forcing: April 1998, *J. Geophys. Res., 106*, 13239-262, 2001.

Transport over a Narrow Shelf: Exuma Cays, Bahamas

NED P. SMITH

(Harbor Branch Oceanographic Institution, Fort Pierce, Florida 34946, U.S.A., nsmith@hboi.edu)

1. Introduction

The Exuma Cays separate the western side of Exuma Sound from the eastern margin of Great Bahama Bank (Fig. 1). The cays extend 130 km from Norman Cay (24° 39.3'N, southeast to Rat Cay (23° 44.2'N) at the northern end of Great Exuma Island. Thirty major tidal channels and numerous smaller channels, exchange significant amounts of water between the sound and the bank. For example, at peak flood and ebb, current speeds through Adderley Cut, at the northern end of Lee Stocking Island, reach 80-100 cm s^{-1} (Smith 1996), and transport commonly reaches 1000-1500 m^3 s^{-1}. Cumulative half tidal cycle flood and ebb volumes average 16.3 and –26.1 x 10^6 m^3, respectively.

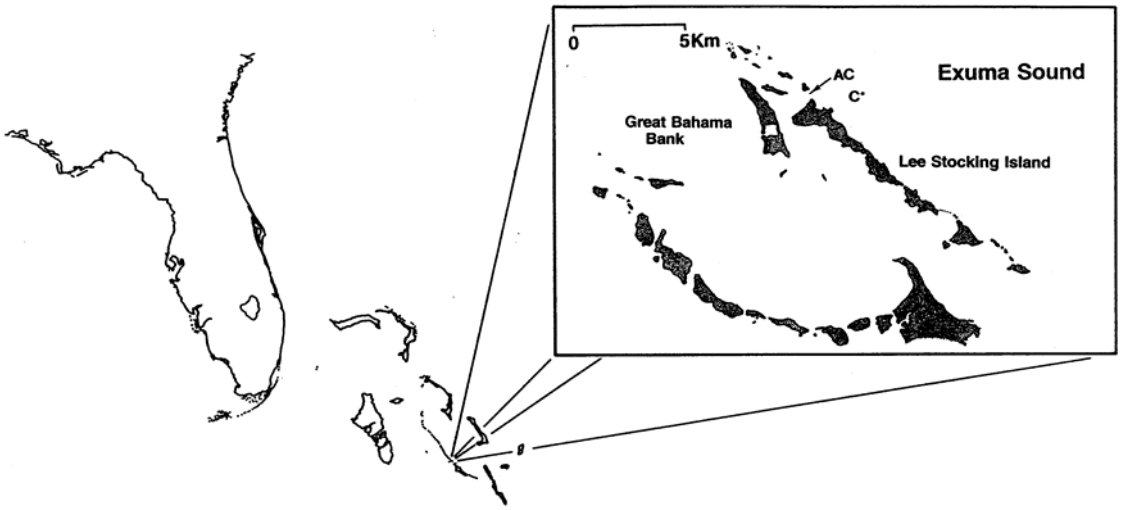

Fig. 1. Map of study area off the northern end of Lee Stocking Island, Exuma Cays, Bahamas. C shows the location of the current meter. The AC arrow points to the mouth of Adderley Cut, which connects shelf waters of Exuma Sound with the shallow waters of Great Bahama Bank.

The continental shelf on the Exuma Sound side of the Exuma Cays is generally between 1 and 2 km wide, and the shelf break is the top of a "wall," at a depth of 25-30 m. Water depth increases abruptly to approximately 200 m, and from the base of the wall the slope of the sea floor is approximately 60°. Water depths of 1000 m occur within just a few kilometers of the Exuma Cays. Because of the narrow width, across-shelf transport occurs over unusually short time scales. For example, Stoner and Smith (1997) showed that the location of highest concentrations of larvae in surface layers across the shelf correlated most highly with wind stress over the preceding 6-8 hours.

Shelf circulation is responsive to wind forcing, but coherence is reduced because of the vigorous tidal exchanges. Ebb tide plumes can extend across the entire shelf and interrupt the wind-driven along-shelf movement of water. Near-bottom current observations from the outer shelf directly seaward of the mouth of Adderley Cut have across-shelf components at tidal periodicities that are commonly between -5 (shoreward) and +20 cm s^{-1} (Smith 1996). Even as ebb tide plumes perturb along-shelf wind-driven transport, however, they also serve to enhance across-shelf turbulent transport as mesoscale eddies are generated by alternating landward and seaward deflections. This paper focuses on the across-shelf transport of heat and momentum by turbulent transport over time scales ranging from a few hours to a few days.

2. Data

Current meter data were recorded hourly for 402 days at an outer shelf study site off the northern end of Lee Stocking Island (Fig. 1). A General Oceanics Mark II current meter was moored 13 m above the bottom in 22 m of water from October 22, 1991 to November 27, 1992. Speed and direction accuracies are ±1 cm s^{-1} and ±2°, respectively. Bursts of 8 samples taken every 2 seconds were vector-averaged to reduce high-frequency noise in the data. Water temperature was recorded by the current meter with an accuracy of ±0.25° C.

Wind speed and direction, air temperature and humidity were measured at a study site at the northern end of Lee Stocking Island, 300 m from the coast on the Exuma Sound side of the island and approximately 1 km from the current meter. Wind was recorded 3 m above the surface, and temperature and humidity were recorded 2 m above the surface. The weather station is on the southwest side of a landing strip, and there are no nearby topographic features when winds are out of the northern and eastern quadrants (landward). Weather variables were recorded hourly from July 7 through November 27, 1991. During this 143-day time period, winds were landward 81% of the time.

3. Methods

Water temperatures are combined with across-shelf current components to track the across-shelf transport of heat, and along-shelf (v) and across-shelf (u) current components are used to quantify across-shelf momentum transport. Current and temperature data are high-pass filtered to focus on meso-scale turbulence generated by semidiurnal tidal exchanges, and perturbation analysis is used to investigate across-shelf transport of heat and momentum over time scales ranging from hours to seasons. Perturbation quantities for the ith observation of the across- and along-shelf component current speed and water temperature (t) are defined by

$$u_i' = u_i - U_i,\ v_i' = v_i - V_i \text{ and } t_i' = t_i - T_i,$$

where the prime notation refers to the high-frequency deviations of the hourly observation (u_i, v_i and t_i) from the low-pass filtered value (U_i, V_i and T_i) (Bloomfield, 1976). With this filter, 90% of the input variance is retained at a period of 30 hours, 50% at 37 hours and 10% at a period of 48 hours. To focus on the longer-term effects of tide-induced across-shelf transport, perturbation products are accumulated. Thus, for hours 1 through m of the time series, the cumulative heat flux, F_h, is given by

$$F_h = \sum_{i=1}^{m} u't',$$

and the cumulative momentum flux is

$$F_m = \sum_{i=1}^{m} u'v'.$$

Quadratic wind stress was quantified using the drag coefficient suggested by Wu (1980). Air density was calculated using the virtual temperature, but no adjustment was made to approximate a 10-m level over-water wind speed.

4. Results

a.Response to wind forcing

Results of spectral analysis of wind stress and unfiltered along-shelf current speed are not shown, but two points are noteworthy. First, highest coherence occurred with the 300-120^{o} and 315-130^{o} wind stress components, and for periodicities longer than about one week. Given the 310-130^{o} orientation of the coastline, this confirms the expected low-frequency response to along-shelf wind forcing. Second, however, highest coherence values were only 0.32. It is likely that this is largely a result of the perturbing effect of local tidal exchanges through Adderley Cut.

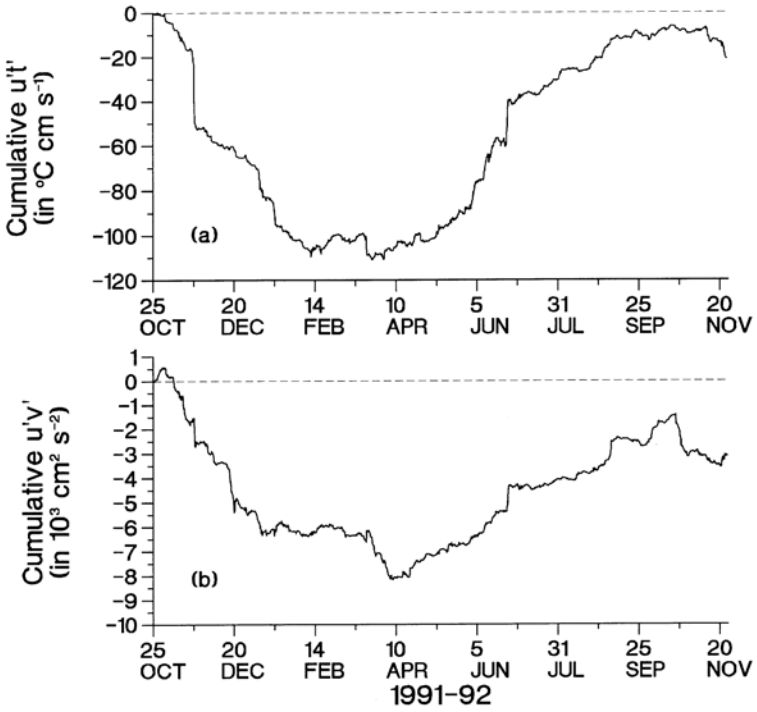

Fig. 2. Cumulative u't' (a) and u'v' (b) perturbation products, calculated from outer shelf current and temperature measurements, October 25, 1991 to November 25, 1992.

b. Across-shelf heat flux

The plot of cumulative u't' perturbation products is shown in Fig. 2a. Negative u't' products, and a descending curve result when relatively warm water is transported landward and when relatively cool water is transported seaward. Results indicate a net landward heat flux from the start of the study in late October through mid February. Little net across-shelf heat transport is recorded from mid February to late March. The ascending curve from late March to late August indicates net seaward transport of relatively warm water. From mid February to late March, and again from late August to mid November, heat transport across the shelf is minimal.

Infrequent, transient events throughout the study account for a significant fraction of the seasonal net landward and seaward heat transport. The sudden drop in the curve in late November is a result of large positive u' coinciding with negative t', followed by large negative u' coinciding with positive t'. The event lasted less than one day. Two similar, though smaller events occur in early and mid January, and a final brief period of landward across-shelf heat flux interrupts the start of the seaward heat flux in early March. Only one prominent seaward heat flux event occurs in the record. In late June, the curve ascends sharply when a landward transport of relatively cool water is followed immediately by a seaward transport of relatively warm water. Again, the event lasts less than one day. At the end of the study, the cumulative heat transport is landward, but the net effect is a small fraction

of the landward transport during fall and early winter, or the seaward transport during spring and early summer.

c. Across-shelf momentum flux

The plot of cumulative u'v' perturbation products is shown in Fig. 2b. Negative perturbation products occur when $\Delta v'/\Delta x > 0$, e.g., when positive v' perturbations increase seaward, or when negative v' perturbations decrease seaward. From the start of the record through mid April the curve descends irregularly. Most of the decrease occurs before mid January and from late March through the first half of April. The ascending curve from mid April to late October is produced by $\Delta v'/\Delta x < 0$, viz., some combination of positive v' perturbations decreasing seaward and negative v' perturbations increasing seaward. Taken together, these two components of Fig. 2b suggest, that $\Delta v'/\Delta x$ reverses at about the same time the across-shelf temperature gradient reverses. Relatively weak positive v' perturbations (or relatively strong negative v' perturbations) move seaward from the inner shelf during fall and winter, when warm water is imported onto the inner shelf. Then relatively strong positive v' perturbations (or relatively weak negative v' perturbations) move seaward during spring and summer, when heat is being exported from the inner shelf.

References:

Bloomfield, P. 1976. Fourier Analysis of Time Series: An Introduction. John Wiley & Sons. New York. 258 pp.

Smith, N.P. 1996. The effect of hyperpycnal water on tidal exchange. Pp. 107-116 *in:* Buoyancy Effects on Coastal and Estuarine Dynamics (D. Aubrey and C. Friedrichs, eds.). Coastal and Estuarine Studies, vol. 53. American Geophysical Union, Washington, D.C.

Stoner, A.W. and N.P.Smith. 1997. Across-shelf transport of gastropod larvae in the central Bahamas: rapid response to local wind conditions. J. Plankton Res. 20:1-16.

Wu, J. 1980. Wind-stress coefficients over sea surface near neutral conditions—a revisit. Journal of Physical Oceanography 10:727-740.

Modelling flow, water column structure and seasonality in the Rockall Slope

ALEJANDRO J. SOUZA[1], SARAH WALKELIN[1], JASON T. HOLT[1], ROGER PROCTOR[1] AND MIKE ASHWORTH[2]

[1]*Proudman Oceanographic Laboratory, Bidston Observatory, Bidston Hill, Prenton CH43 7RA, UK*

[2]*CLRC, Daresbury Laboratory, Warrington, WA4 4AD, UK*

1. Introduction

The accurate simulation of currents, water quality parameters and plankton variability in shelf seas requires a physical model that includes the effects of vertical and horizontal density variations. This is necessary since the former introduces horizontal transports while the latter controls vertical fluxes critical for biological production (Holt and James, 2001). Furthermore, shelf sea fronts (both thermal and haline) affect both the horizontal and vertical transfer of momentum and tracers. To accurately model this we need the development of fine resolution 3-dimensional hydrodynamic models.

This is why the Proudman Oceanographic Laboratory Coastal Ocean modelling system (POLCOMS) has been developed to tackle multidisciplinary studies in the coast/shelf and shelf edge environments (figure 1).

The central core is a sophisticated 3-dimensional hydrodynamic model that provides realistic physical forcing to interact with, and transport, environmental parameters. Integrating from ocean to coast and vice versa, biological production and the fate of contaminants can be determined.

The objective of this work is to show a fine resolution application of POLCOMS to the Rockall shelf-edge region and to show that the model has been successful in reproducing the dynamics of this area.

2. The hydrodynamic model

The hydrodynamic model is a 3-dimensional model with temperature and salinity treated as prognostic variables, developed at the Proudman Oceanographic Laboratory using an Arakawa B-grid discretisation. The original model was produced by James (1986) and has subsequently being developed to include, the Piecewise Parabolic Method (PPM), non-diffusive advection scheme (James, 1996). The advantage of having a non-diffusive B-grid model for shelf seas is that the B-grid prevents the dispersion of velocity features associated with fronts and the PPM advection scheme avoids diffusion of momentum and scalars making it an ideal tool to model typical baroclinic shelf features such as river plumes (James, 1997) and fronts (Proctor and James, 1996). These two characteristics are what particularly distinguish the model

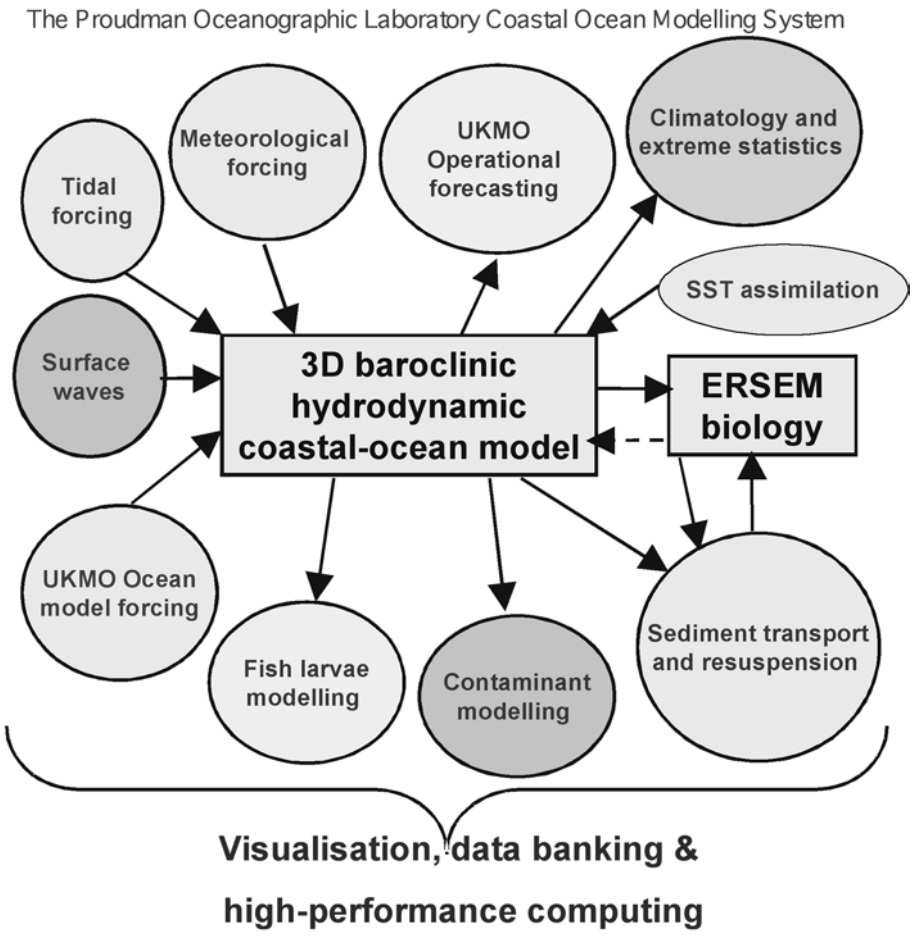

Figure 1. The POLCOMS paradigm

from other shelf sea model such as the Princeton Ocean Model (POM) (Blumberg and Mellor,1987).

The model is formulated in spherical polar sigma coordinates: λ (eastward), ϕ (northward) and σ (vertical), with $\sigma = (z - \zeta)/(h + \zeta)$, where z is the Cartesian vertical coordinate, h is the water depth relative to the reference sea level ($z = 0$) and ζ is the elevation above this.

The incompressible, hydrostatic, Boussinesq equations of motion are solved using time splitting between barotropic and baroclinic components. Baroclinic pressure gradients are computed on horizontal planes with spline interpolation through the vertical σ grid point distribution. Vertical mixing is parameterised using the Mellor-Yamada 2.5 turbulence closure scheme. Horizontal diffusion of momentum and scalars can be included with a linear or shear-dependent (Smagorinsky form) coefficient of diffusion. For detail explanation of the model see Holt and James (2001).

3. Model application

This particular application uses a horizontal resolution of 1 nautical mile with 34 S-levels. It attempts the most realistic simulation possible, so it uses realistic meteorological forcing supplied by the UK met-offices and the initial and lateral boundary conditions are provided from a 12 km shelf-wide version of POLCOMS, which is it self forced by the UK Met-office FOAM.

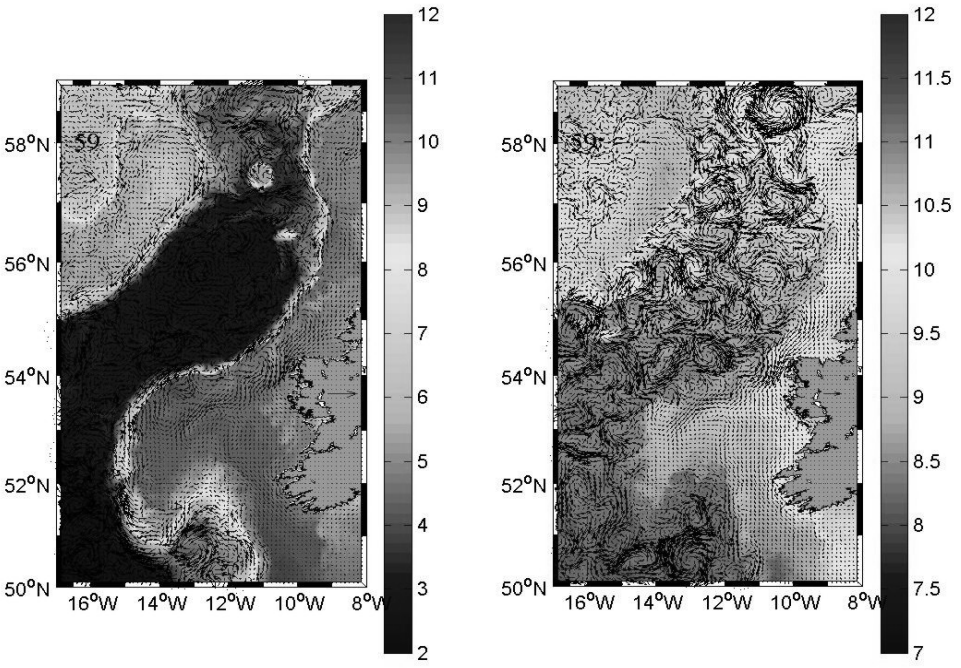

Figure 2. Example model output showing bottom (left) and surface (right) temperature and currents, velocity vectors show only a fifth of the model resolution.

4. Model Results

The preliminary results show consistency with previous observations in the Roackall shelf-edge (Souza *et al,* 2001), with a warm Northward slope current of about 20 cms^{1} with strong variability due to eddies. The eddy field reproduced by the model resembles that observed by satellite imagery (figure 2). The model also reproduces the seasonal variability shown by the UK Shelf Edge Study (Souza et al, 2001).

References.

Blumberg, A.F. and G.L. Mellor (1987). A description of a three-dimensional coastal ocean model. In three Dimensional Coastal Ocean Models, Coastal and Estuarine Studies, vol4, edited by N.S. Heaps, pp1-16, AGU, Washington, D.C.

Holt, J.T. and James, I.D. (2001) An S coordinate density evolving model of the northwest European shelf 1, Model description and density structure. Journal of Geophysical Research, 106, C7, 14015-14034.

James, I.D. (1986). A front-resolving sigma coordinate model with a simple hybrid advection scheme. Appl. Math. Modell., 10, 87-92.

James, I.D. (1996). Advection schemes for shelf se model. J. Mar. Sys., 8 237-254.

James, I.D. (1997). A numerical model of the development of anticyclonic circulation in a gulf-type region of freshwater influence. Cont. Shelf Res.,17, 1803-1816.

Patsch, J. and Radach, G. (1997). Long-term simulation of the eutrophication of the North Sea: temporal development of nutrients, chlorophyll and primary production in comparison to observations. *J. Sea Res*., 38 (3/4) 275-310.

Proctor, R. and I.D. James (1996). A fine-resolution 3-D model of the southern North Sea. J. Mar. Sys., 8, 285-295.

Souza, A.J., J.H. Simpson, M. Harikrishnan and J. Malarkey (2001). Flow structure and seasonality in the Hebridean Slope Current. Oceanologica Acta,24, S63-S76.

Simulating the North Sea using different models and methods

Adolf Stips, (*Institute for Environment and Sustainability, CEC - Joint Research Centre, I-21020 Ispra, Italy*, adolf.stips@jrc.it)
Karsten Bolding, (*Institute for Environment and Sustainability, CEC - Joint Research Centre, I-21020 Ispra, Italy*, karsten.bolding@jrc.it)
Thomas Pohlmann, (*Institute for Marine Research, University of Hamburg, Troplowitzstr. 7, D-22529 Hamburg, Germany*, pohlmann@ifm.uni-hamburg.de)
Hans Burchard, (*Baltic Sea Research Institute Warnemünde, Seestr. 15, D-18119 Rostock, Germany*, hans.burchard@io-warnemuende.de)

1 Introduction

The aim of this study is to compare two different models, using the same NOMADS2 (North Sea Model Advection Dispersion Study) setup for both models, by extracting various integral parameters from the 3D model output. We want to compare here the HAMSOM model (Hamburg Shelf Sea and Ocean Model), which is an original NOMADS2 participant, with the newly developed GETM model (General Estuarine Transport Model), which is described in *Burchard and Bolding* [2002].

Further we want to investigate how different advection schemes influence the model results. For doing so, the same horizontal grid, the same number of vertical layers, the same forcing data and the same flux calculation routines were applied.

2 Model Domain

The model domain was chosen to coincide as much as possible with the setup of the HAMSOM model for the NOMADS2 model comparison study. It covers the North Sea from the channel to $61{,}5^o$ N, with a horizontal resolution of 20 km. The bathymetry used for both models is shown in figure 1.

To compare different integral parameters derived from the model output data, the so called common area (CA) between 51^o N and 57^o N was selected by the NOMADS2 consortium and is also used here.

3 Some remarks on the models

Both models solve the 3D baroclinic shallow water equations in the hydrostatic approximation. For the horizontal discretization, we selected spherical coordinates in this case, but GETM prinicpally allows for different horizontal and vertical coordinates. HAMSOM is implemented in such a way, that it guarantees a second order stability for the Coriolis term and applies the Kochergin approach for the vertical turbulence closure. GETM allows the selection of different order scalar advections schemes, as e.g. UPSTREAM and SUPERBEE scheme, which were used here. The turbulence scheme of GETM is chosen via the GOTM (General Ocean Turbulence Model) turbulence model. In this study we used the k-ε turbulence closure.

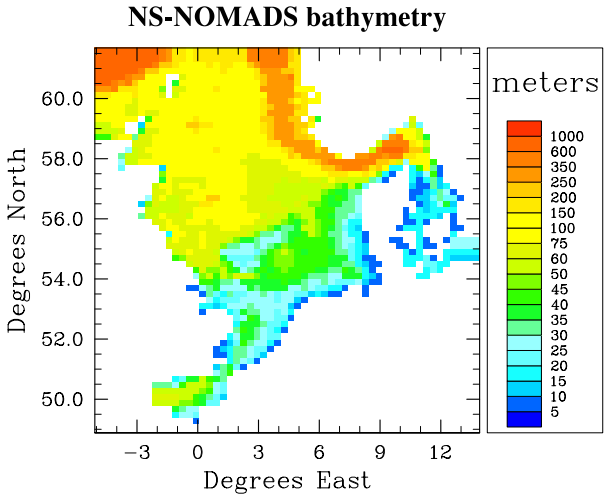

Figure 1: Used bathymetry (depth in meters) for both models of the North Sea area.

4 Results

The first investigated integral parameter is the total potential energy of the common area, which is presented in figure 2. During winter both models predict a quasi well mixed water column. Substantial differences show up during summer stratification and autumn destratification. The largest amount of potential energy is created with the SUPERBEE scheme, whereas the UPSTREAM scheme has about 30% less potential energy during peak stratification. This delays the following mixing of the water column in autumn by more than 4 weeks, in better agreement with reality. Interesting to note that during the spring restratification HAMSOM and GETM-SUPERBEE agree very well.

The temporal evolvement of the heat content of the common area, can be seen in figure 3. The mean temperatures derived from GETM and HAMSOM follow each other relatively close, having maximum differences of less than 0.5 K. These maximum differences appear during winter and summer. The used advection scheme has quasi neglectable influence on the total mean temperature of the common area. Also shown is the eman tmeprature of the upper 20 m and the layer from 20 m down to the bottom. Because the volumes of the upper and the lower layer are comparable, the total mean temperatures fall nicely between these two extrem temperatures. Using higher order advection schemes, leads to a much stronger pronounced stratification of the water column. For both GETM simulations the same turbulence closure was used, so this stronger stratification is in this case not caused by the turbulence closure.

The vertical temperature field during the NOMADS2 annual simulation at a selected Station A (68 m depth) is presented in figure 4. It can be seen that the maximum and minimum temperatures of the HAMSOM model during the year exceeding the respective

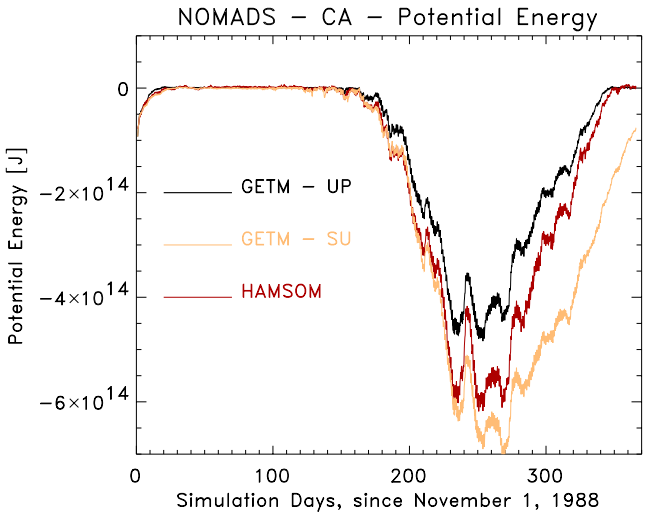

Figure 2: Potential energy of the NOMADS common area. HAMSOM - red line, GETM-UPSTREAM - black line, GETM-SUPERBEE - mellow line.

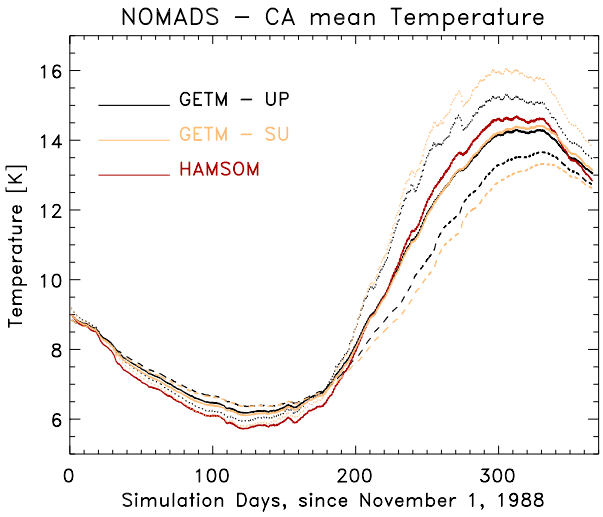

Figure 3: Heat content of the NOMADS common area, expressed as mean temperature. The bold lines show the mean temperatures of the total water column, the dotted lines represent the upper 20 m, whereas the dashed lines represent the part from 20 m to the bottom.

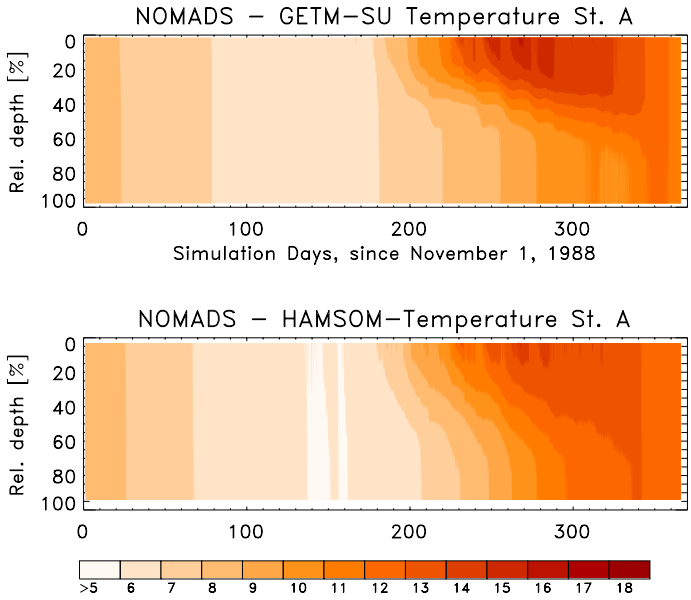

Figure 4: Temporal evolvement of the temperature fields at the NOMADS2 station A (stratified) for the two models.

GETM extrem values. The vertical stratification during summer is more pronounced in the GETM results, the thermocline is nearer to the surface and sharper, in better agreement with the available measurements. This is not only caused by the better turbulence closure used within GETM, because the GETM-UPSTREAM simulation (not shown) is also more diffusive.

5 Conclusions

The agreement between the model results obtained from simulations of the North Sea dynamics using GETM and HAMSOM is quite promising and especially much better, than the differences found between different models during the NOMADS2 study.

Higher order advections schemes lead not only to stronger horizontal gradients but also to a much stronger pronounced vertical stratification in the North Sea. The use of advanced turbulence closures is necessary for a more realistic simulation of the vertical stratification, resulting in a shallower a sharper pycnocline.

Acknowledgments: The authors of this extended abstract are grateful to the NOMADS2 consortium.

References:

Burchard, H., and K. Bolding, GETM, a general estuarine transport model. Scientific documentation. Tech. Rep. EUR 20253 EN, European Commission, 157 pp., 2002.

Sediment Flocculation and Flow in a Tidal Marsh Environment.

GEORGE VOULGARIS

(Marine Science Program, Department of Geological Sciences, University of South Carolina, Columbia, SC 29208, USA, gvoulgaris@geol.sc.edu)

SAMUEL T. MEYERS

(Marine Science Program, University of South Carolina, Columbia, SC 29208, USA, meyers@msci.sc.edu)

1. Introduction

Salt marshes are invaluable ecological resources along the Southeast coast of the United States. The survival of these resources is dependant on their ability to import and accumulate sediment at a rate sufficient to keep pace with the regional rise in sea level. Sediment erosion, transport and deposition in these environments are important from both geomorphological and geochemical points of view. While the morphology reflects the age, maturity and tidal characterstics of the marsh, the sediment characteristics (i.e., size, concentration, properties) affect the ability for chemical pollutants to be transported and accumulate in the marsh. The traditional theory for sedimentation in the intertidal zone is that of settling and scour lag effects that assume a single particle size that remains constant through the tidal cycle. In this study the variability in particle size as a function of flow strength is examined and the implications in sediment transport are discussed.

2. Background

Suspended sediment in estuaries is predominantly found in flocculated form (Van Leussen 1997). The coalescence of charged clay particles occurs in saline water when numerous cations are free to interact with the particles. Mucous biofilms from algae, bacteria and higher plants also cause the aggregation of particles to occur upon collision with other particles. This process of flocculation has a significant effect on the behavior of particles in suspension that varies from the behavior of their constituent particles. Flocculated particles will continue to increase in size as particle collision continues, due to settling or turbulent mixing, until shear becomes strong enough to prevent aggregation or cause disaggregation. Increased turbulence will often promote flocculation at first through particle-to-particle collision, but then reaches a critical level when the flocs can no longer retain their shape and start to break apart (Van Leussen 1997). The ability to define these critical levels offers a better understanding and prediction capability of the mode by which sediment is transported throughout various stages of the tidal cycle

3. Location

Velocity and suspended sediment concentrations were collected during three deployments at a location in the upper region of Bly Creek, a terminal tidal creek basin comprising a portion of the North Inlet salt marsh near Georgetown, South Carolina (USA). The North Inlet marsh is a back-barrier environment composed of meandering channels with an approximate area of 32 km^2. The primary exchange of water in the marsh is with the Atlantic Ocean through North Inlet to the east with very little fresh water influence from the neighboring uplands and Winyah Bay estuary to the south. The marsh has astronomical tides that are semidiurnal with an average range of 1.4 m and has a slight diurnal inequality. The Bly Creek basin is ebb-dominant with a well-developed channel and steep banks. The dominant vegetation in the marsh is *Spartina Alterniflora*, which covers the entire marsh surface above the creek banks, with small patches of *Juncus* in the high marsh. The surface sediment

of the vegetated marsh is composed primarily of silt while the channel beds are composed of silt and sand.

4. Methods

Experiments were performed to define the relationship between turbulence, flocculation, particle size distributions, and suspended sediment characteristics. A 10 MHz Sontek acoustic Doppler velocimeter (ADV) measured 3-D velocities at a single point and was used to calculate the turbulent characteristics of flow. An optical backscatter (OBS) turbidity sensor was mounted in-sync with the velocimeter to measure the total suspended sediment concentration, while a laser particle size analyzer (LISST) was used to measure the size distribution in the range of 1.25-250 um. A hand-powered bilge pump was also used to collect water samples that were filtered and weighed for total suspended sediment concentration. A galvanized steel frame supported the instrumentation and was placed in the thalweg of the channel. The sample volumes for the instruments and pump were 15 cm above the bed. The ADV, OBS, and LISST were programmed to sample continuously for 12 minutes every half hour ranging from 2 to 8 days. The third deployment captured the longest time series and was the only deployment in which all of the instruments collected valid data simultaneously.

5. Results

Friction velocity was calculated using the covariance method, turbulent kinetic energy method, and inertial dissipation method. Similarity of all three values established the accuracy of the estimates. A mean of the three friction velocity estimates was calculated and used for data analysis. Results show that as the mean current flow and friction velocity increase flocs size increase. The effective density and settling velocity of the flocs were found to be in agreement with published data, from the ocean environment (Dyer and Manning 1999, Manning and Dyer 1999, Mikkelson and Pejrup 2001). Effective density of the flocs decreased with increasing floc size while the settling velocity increased with floc size (Fig. 1). By calculating the Kolmogorov microscale (η), the upper limit on floc size can be estimated. While the limit of floc growth was never surpassed during the third deployment, measurements from the OBS during the second deployment imply that the limit was surpassed and the flocs actually may have begun to disaggregate. Unfortunately, no LISST data from the second deployment was retrieved to confirm this notion. Fresh water discharge was neglogible during the experiments thus all results are attributed to changes in turbulence levels rather to changes in water salinity

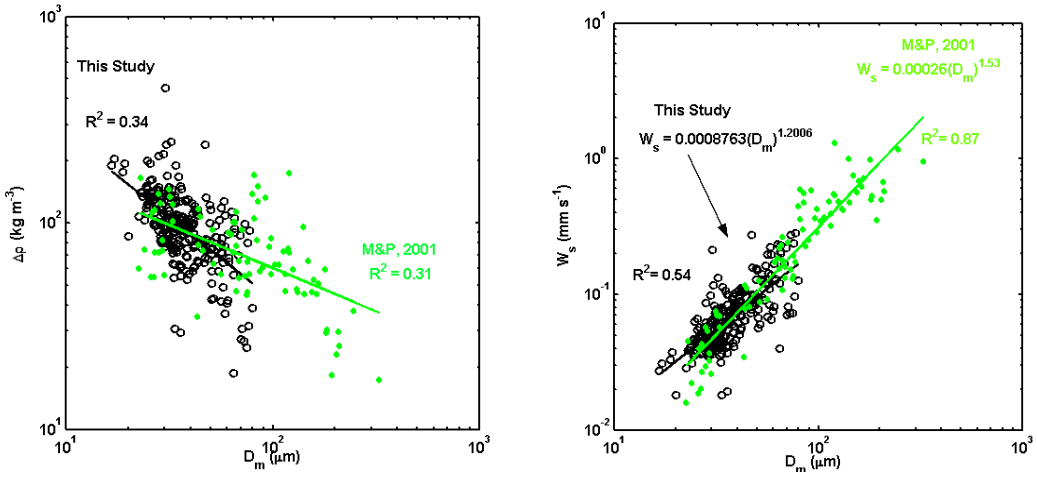

Figure 1. Effective density ($\Delta\rho$) and fall velosity (Ws) of suspended sediment vs mean grain size, Dm (left and right panels, respectively) from this study compared with the results from Mikkelson and Perjup (M&P, 2001)

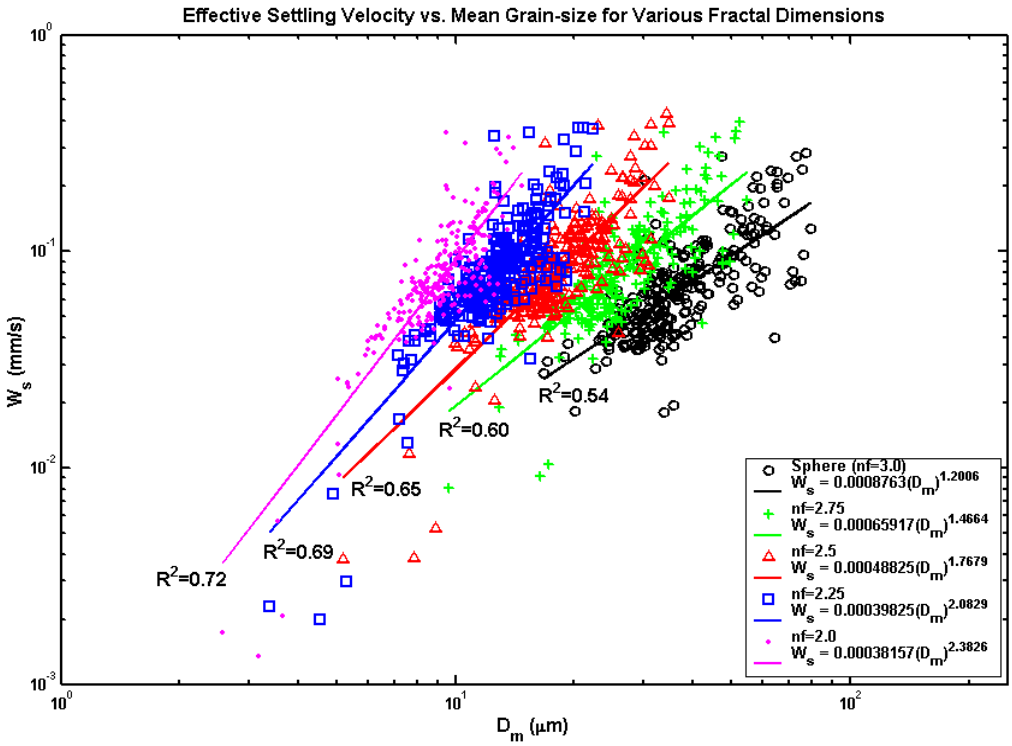

Figure 2. Effective settling velocities (mm s^{-1}) of suspended sediment estimated assuming various fractal dimensions vs. mean grain size D_m. Fractal dimensions (nf) from 3 (spheres) to 2 are plotted in order to observe the change in settling velocity due to decreased diameters.

Various fractal dimensions (nf) were applied to the LISST data to determine the effect of particle geometry on settling velocity. Results show that the settling velocity of most of the flocs in suspension does not change with different values of nf, indicating that in similar environments, the settling velocity is not sensitive to the true shape of the flocs. As the fractal dimension decreases, the effective density of the particles must increase. As larger flocs usually have greater settling velocities than smaller flocs, the increase in density with smaller fractal dimensions balances this change in floc size and no great variation in settling velocity is revealed (Fig. 2). Since problems may arise when the LISST assumes all particles are spherical, it is important to determine the effects this has on actual particle density and settling velocities.

The results of testing various fractal dimensions on flocculated particles reveal that the LISST provides very good estimates for the parameters concerned. However, this only holds true for flocculated particles (Mikkelson and Pejrup 2001) and within turbulent regimes that do not surpass the floc growth limit. As soon as shear stress increases to the level of particle disaggregation, the above relationship is no longer valid.

6. Conclusions

Accurate estimates of friction velocities using the covariance, turbulent kinetic energy, and inertial dissipation methods combined with particle size and concentrations of sediment in suspension enabled us to relate flow with sediment dynamics in a tidal creek environment. It was found that:

- Increased velocity and turbulence cause increases in particle size through the process of focculation while still within the limits of the Kolmogorov scale.
- As floc size increases, effective density was shown to decrease while settling velocity increased.

- As the fractal dimension of particles changes, there was little variation in the settling velocity of focculated sediment. This confirms the ability of the LISST to provide good estimates of the volume concentration of suspended sediment in similar environments.

In the final paper we will present some numerical results indicating the implication of the floculation processes in salt marsh sedimentation processes.

Acknowledgments: The authors would like to acknowledge Belle W Baruch Institute for Marine Biology and Coastal Research for providing access to the site. Funding for this work was provided through a University of South Carolina Research and Productive Scholarship awarded to G. Voulgaris. Additional funding was provided to S. Meyers through a John Hodge Summer Research Fellowship.

References:

Dyer, K.R., and Manning, A.J., Observation of the size, settling velocity and effective density of flocs and their fractal dimensions. *Journal of Sea Research*, 41, 87-95, 1999.

Manning, A.J., and Dyer, K.R., A laboratory examination of floc characteristics with regard to turbulent shearing. *Marine Geology*, 160, 147-170, 1999.

Mikkelson, O., and M. Pejrup., The use of a LISST-100 in-situ laser particle sizer for in situ estimates of floc size, density and settling velocity. *Geo-Marine Letters*, 20, 187-195, 2001.

Van Leussen, W., The Kolmogorov microscale as a limiting value for the floc sizes of suspended fine-grained sediments in estuaries. In: Burt, N., Parker, R., Watts, J. (eds), Cohesive Sediments. John Wiley & Sons Ltd., pp.45-62, 1997.

GIS-Based Sediment Transport Study in Kyunggi Bay, Korea

CHANG S. KIM, HAK SOO LIM, SUE HYUN LEE, SUN JEONG KIM, JONG-CHAN LEE

(COASTAL ENGINEERING DIV, KOREA OCEAN R&D INSTITUTE 1270 SA 1 DONG ANSAN 425-744 SOUTH KOREA , surfkim@kordi.re.kr)

1. Introduction

The Kyunggi Bay (125-128E, 36-38N) is a macro-tidal bay in the western central port of Korean Peninsula (Fig.1). The Bay characterizes its feature as wide tidal flats, deep tidal channels and tidal sand ridges running in parallel to tidal flows. The macro-tidal range (up to approximately 8.6m) and consequent strong tidal currents erode the bottom sediment and selectively transport to the low-energy area forming tidal ridges or tidal flats.

The tides in the Bay are mostly of semi-diurnal types with increasing tidal range toward the shoreline. The main flows of flood direct toward north-east while the ebb currents flow south-westward. Relatively strong currents occur along the spatially distributed channels, implying spatial nonhomogeneity in sediment characteristics.

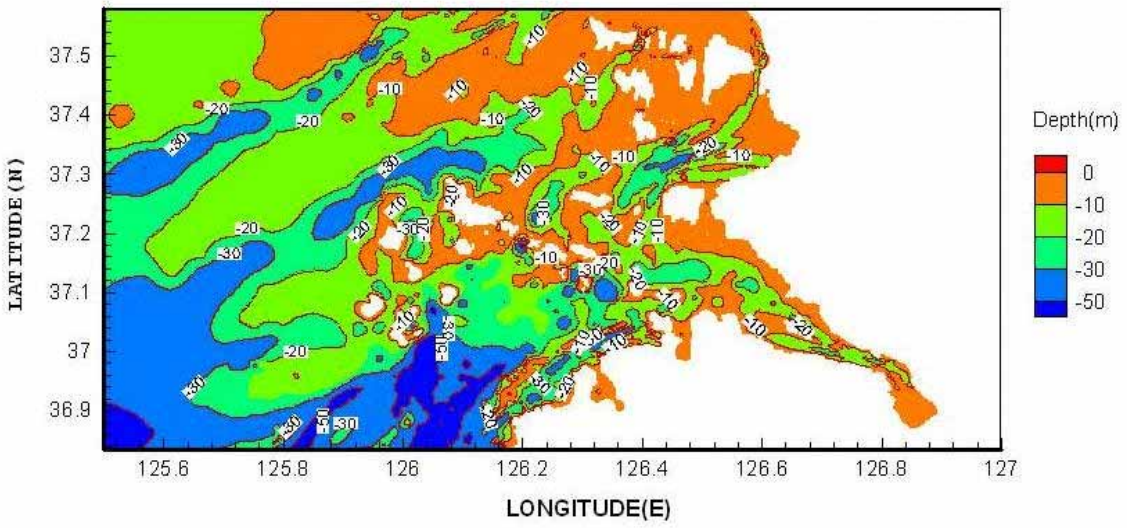

Figure 1: Study area map ; the bathymetry was reproduced by using the digital navigation chart.

2. Motivation

Due to the public awareness and fishermen's interest, the potential environmental impacts of undersea sand mining has been drawn attention. The motivation of the study is how we could balance the positive and negative impacts arising from the undersea sand mining in the Bay.

3. Goals of the study

The goals of the study is to quantity the sediment transport processes due to the undersea sand mining, to predict the recovering processes of the sand pits, and to provide time-varying distributions of environmental parameters in the GIS system that is coupled with ecological impact assessment.

4. Field Observation and Estimation of Co.

A prototype field experiment has been conducted in an undisturbed area where the sediment types are favored by dredging company. The purpose of setting the test site is to measure the major hydrodynamic and sediment parameters affected by the mining operations, and their progressive variation in time and space, including the dispersion of surface benthic plumes, and the recovery status of the pit in the seabed. Through the filed experiment, the sediment flux (source concentration at the source cell) and the sediment size has been measured for modeling control parameters. The temporal variation of the mining pit has been observed to estimate the recovering rate of the disturbed seabed.

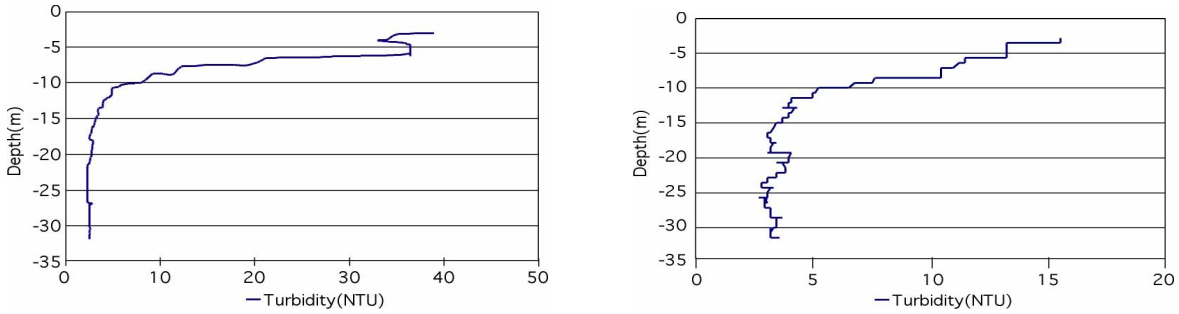

Figure 2: Observed concentration profiles of suspended materials sampled at different points away from the mining site.

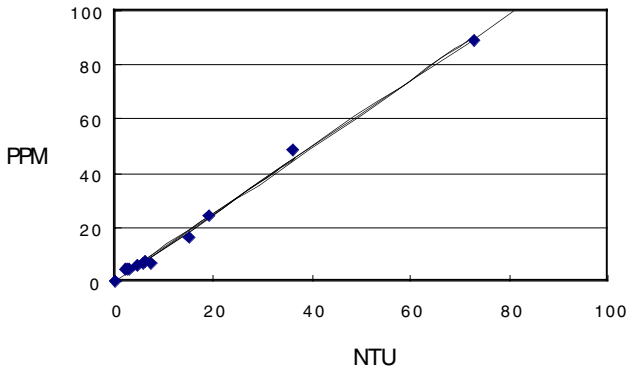

Figure 3: Comparison of directly sampled concentration(PPM) and YSI measured concentration(NTU) : y=0.2987+1.2317x, R^2=0.997.

5. Mathematical Modelling

The Mathematical description of the physical and sediment transport processes are performed by means of 1-D, 2-D and 3-D models. The 1-D model is to estimate the vertical variation of concentration profile due to the surface and benthic plumes. The 2-D and 3-D models predict the tides and tidal currents and dispersion of suspended materials released in the surface and benthic boundary layer.

The model grid was set at horizontal dimension of approximately 150 meters to resolve the strong tidal currents along narrow channels in the model area. The very fine bathymetric map was compiled by using the digital navigation chart of the NORI. An example application was presented for continuous release of suspended materials of 0.1308_/_ in concentration and of 0.0625mm in grain size at the source cell.

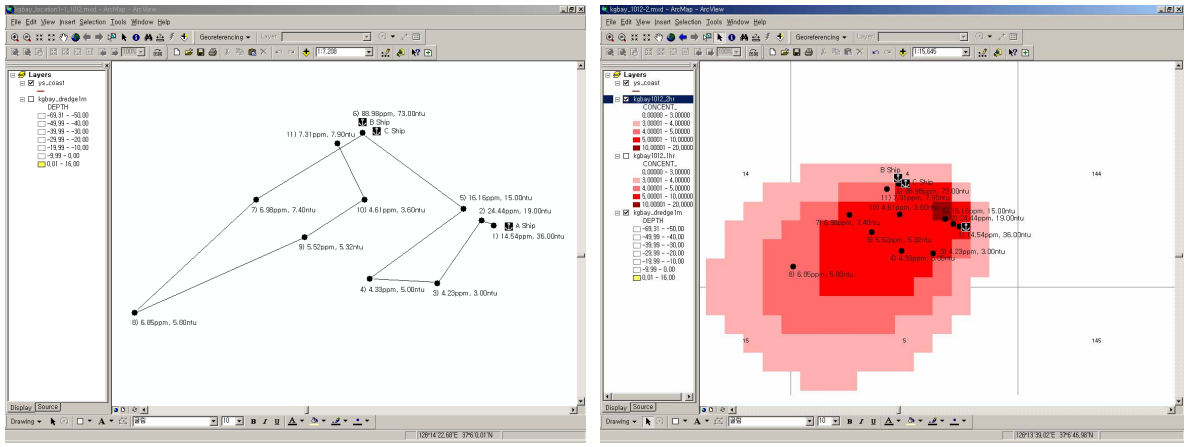

Figure 4 : YSI measured SS concentration(left) and concentration estimated(right) by numerical modeling .

6. Integration of ArcGIS with Hydrodynamics & Sediment Transport Model

The spatial accuracy in the application of 3-D environmental models has increased dramatically over the past decade due to the benefits of high computational resources, and accurate location of input /calibration data obtained through field measurement using DGPS, and immediate data transmit through the internet. So it seems extremely advantageous to handle the spatial data associated with environmental models with georeferencing tool such as ArcGIS 8.1.

In this study, the integration of hydrodynamic and sediment transport models is accomplished with the use of the ArcGIS 8.1 and the ArcIMS3.1.

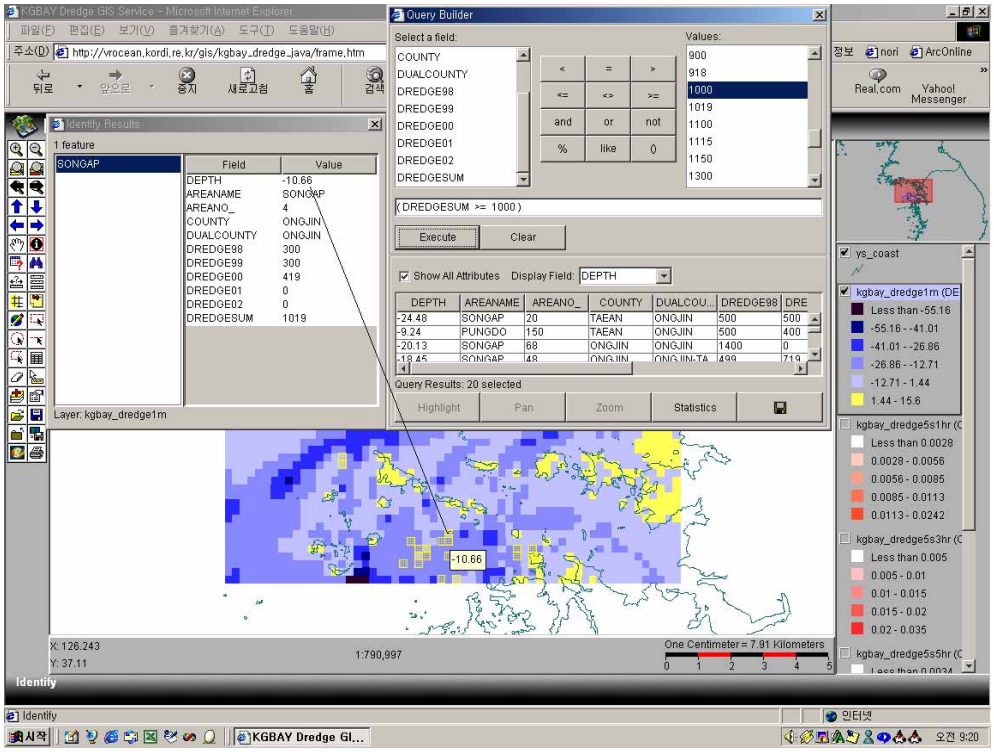

Figure 5: A sample application of GIS Internet Map Service showing model results and general environmental parameters. A user can interact with the ArcIMS on-line.

7. Conclusion

1. Digital navigation charts benefits the preparation of high resolution bathymetry data for fine scale mathematical models.
2. The continuous monitoring and measurement of changing seabed due to undersea sand mining are essential part of sediment transport study.
3. Prediction of hydrodynamic and sediment transports models is easily enhanced by more field observed data.
4. Interfacing the ArcGIS to hydrodynamic models benefits the pre - and past – processing and decision making tasks.
5. Further improvement of more robust and accurate models to predict the change in seabed features.

Acknowledgments: The authors of this paper are grateful to the RRC program operated by Inha University, Incheon Korea.

References:

Blumberg, A. and G. Mellor, 1987. A description of a three-dimensional coastal ocean circulation model. Three-Dimensional Coastal Ocean Models, edited by N.S. Heaps, *American Geophysical Union*, Washington, D.C. 1-16.

Haidvogel, D.B., H.G. Arango, K. Hedstrom, A. Beckmann, P. Malanotte-Rizzoli, and A.F. Shchepetkin, 2000. Model Evaluation Experiments in the North Atlantic Basin: Simulations in Nonlinear Terrain-Following Coordinates, *Dyn.Atmos. Oceans*, 32, 239-281.

Hamrick J.M., 1992. A three-dimensional Environmental Fluid Dynamics Computer Code: Virginia Institute of Marine Science, *Special Report* 317, 63 pp.

Luyten P.J., Jones J.E., Proctor R., Tett P. and Wild-Allen., 1999. COHERENS – A coupled Hydrodynamical Model for Regional and Shelf Seas: *MUMM Report*, 914 pp.

Lee, J.C., C.S. Kim and K.T. Jung. 2001. Comparison of bottom friction in formulations for single-constituent tidal simulations in Kyunggi Bay. *Estuarine, Coastal and Shelf Science*. 53, 701-715.

Recovery of Yanbu (Red Sea) Coral Reefs -Hydrodynamic features at Thermal out falls.

JOSEPH SEBASTIAN PAIMPILLIL

(Envirosolutions, 37/1387, Elemkulam Road, Cochin 17, Kerala, India, 682017, Email daj@vsnl.com)

MUNIR DAHALAWI

(Environmental Monitoring Project, Royal Commission for Jubail & Yanbu, Saudi Arabia.)

1. Introduction.

The Royal Commission of Yanbu (Saudi Arabia) tried to set up an example to industrialists in the field of pollution control by establishing a respected enforcement and monitoring program; with five areas of concern (air quality, water quality, solid and hazardous waste management, industrial waste water quality and conservation areas management). The most extensive coral reef formations north of Tropic of Cancer found in Yanbu (Red Sea) were subjected to destruction by the industrial infrastructure developments, especially the coral blasting and land filling for the King Fahd Port construction.

2. Results and Discussion.

The dominant coral forms in the region had changed from the branching to the massive form. The health of the coral system, particularly in the Port Barrier Reef that protects the harbor from storm waves was assessed during the coastal ecosystem studies sponsored by Royal Commission of Jubail and Yanbu. The main components of the studies were a coral recruitment, coral growth and percentage cover, coral fishes population diversity and biomass studies.

A natural protection is provided by the Port Barrier Coral Reef to King Fahd Industrial Port of Yanbu, but coral structure can easily be altered by chemical or thermal pollution. The major role of monitoring of the coastal ecosystem is to provide protection to the corals from the effluents from three perto-chemical plants, six oil refineries and from the municipal sewage. The relatively young coral reef formation and other marine and coastal ecosystem at Yanbu (Red Sea) are under stress due to intensive industrial activity. The treated effluents from the industrial waste treatment plant (IWTP) at Yanbu are discharged into Red Sea, along with the industrial cooling water of 10 C higher than ambient level, through a common the discharge canal. The monitoring of the chemical composition of the treated watewater had revealed a high degree of efficiency of IWTP with percentage reduction in chemical concentrations of the following magnitude: Sulfide (43), sulfate (88), Reactive phosphate (88), oil (7), Phenol (18), BOD (11), COD (14), TSS (12), NH4 (21), Co (59), Cu (31), Fe (18), Mn (70), Zn (39). But few violations of pollutant levels were also detected at the IWTP outlet with the following frequency of occurrence for TSS (3.2%), BOD (1.1%), TDS (21.3%), Sulfide (14%), Sulfate (19%), COD (5%), Oil (3%), Phenol (11%), NH4 (16%), Fe (0.6%), Ze (0.6%). The concentration of nitrate and nitrites increased considerably in the treated effluent, but were below the pollution limit. The chemical characteristics of the pollutants in the coastal waters in the vicinity of the outfall channel had shown violations for TSS, PO4 and for the trace metals (Cu, Pb, Co, Cd, Ni, Mn &Zn). The enrichment of PO4 in the coastal water was attributed to the release of PO4 from the re-suspended fine sediments from the shipping channel, which were deposited during its construction phase.

Most of this coral reef formation is in lagoon type enclosure with restricted water movements and circulation. A small portion of the barrier reef is exposed to the prevailing monsoon weather and with a far greater circulation. Water circulation in this coral region can play the key role on larval attachment and metamorphosis, while temperature is a limiting factor. The distribution of the treated industrial waste water (350000 Cu m /day) from IWTP plant along with the non contact cooling water with 10 C elevated temperature than ambient condition, discharged through a common channel in the

vicinity of barrier reef is controlled by the bathymetery and by other hydrodynamic features. The cooling water moves as a surface layer of 3 to 4m thick with a well-marked thermal boundary. The average current speed in the region is around 7cm/s with in northwest direction. The thermal and current patterns in the barrier reef have shown no positive evidence of the thermal flow reaching the barrier reef.

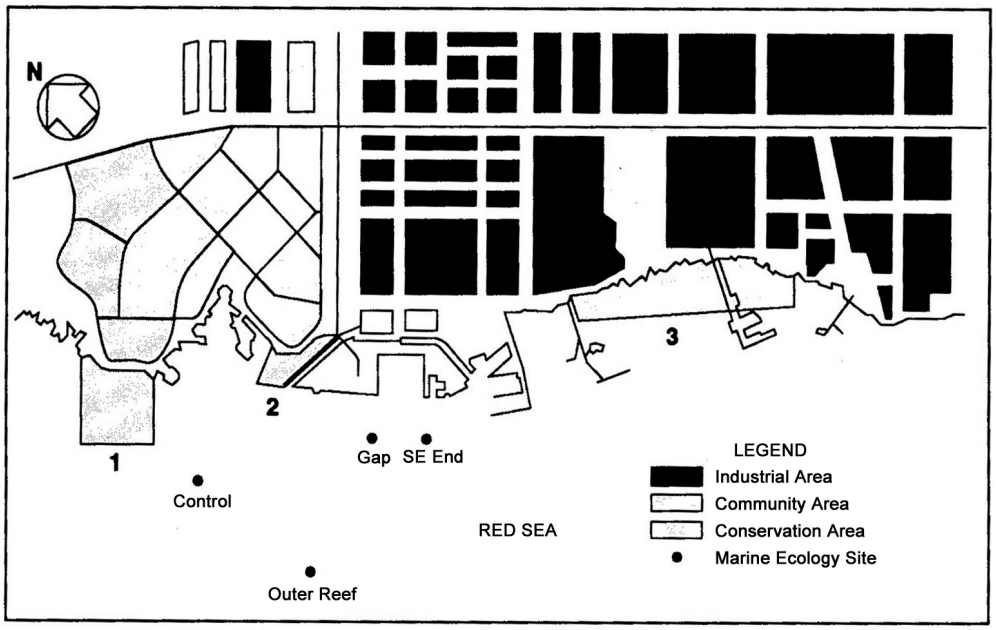

Fig.1 Port Barrier Reef and sampling locations.

The gradual and slow accumulation of thermal stress in the Port Barrier Reef vicinity off Yanbu during the past 15 years had shown a sharp rise in the recent summer months with a surface temperature higher by 3 C than the ambient level. This rise in thermal stress seems to be not detrimental to coral survival as the thin surface layer with this heat stress accumulation had a spatial distribution, which carried away the heat from the coral vicinity. The nutrient level, another factor controlling coral growth, remained the same in the water column for the years though high nutrient input from industrial discharges were frequent, but the nutrient balancing mechanism is not yet clear. The health and species diversity of corals in the Port Barrier Reef vicinity as revealed by three independent studies (coral growth / recruitment, Butterfly fish diversity, coral coverage) had shown that the relative influence of thermal stress is less compared to the combined effect of nutrient loading and siltation, as certain portions of the Port Barrier Reef much away from the thermal discharge had shown much less growth potential. These studies had also shown that the pioneering coral species had not re-established itself even after a decade since the initial physical disturbances in the locality. There are good signs that coral reef is recovering, although it is still in an unstable stage. The dominant corals in the region (Pocillopora verrucosa, Stylophora pistillata) are the branching types with high tolerance for stress such as siltation. The proliferation of corals which are more opportunistic and highly tolerable to stress and the elimination of corals sensitive to physical, chemical and thermal stress are still going on and the region will eventually harbor resistant and opportunistic coral species and its stability as a community may take some more time.

During study period, reasonable coral recruitment rates were observed at three selected localities (Fig 1.) of varying different degrees of industrial impacts. The competition for living space due to the excessive growth of filamentous algae triggered by the supply of dissolved nutrients had restricted the coral development in the Port Barrier reef. The low species diversity of the butterfly fish and the high Damsell fish association at the coral sites stressed by human impacts clearly indicates the possibility of these fish populations as indicators of coral health and of the water quality. The poor coral health condition at the Barrier reef sites was attributed to the discharges of treated industrial wastewater. The

discharge of industrial cooling water , the re-suspension of the fine grained sediments from the navigational channel and the poor water movement in the Barrier reef region were also contributing to the poor health of the corals

The coral growth, coral recruitment and coral fish diversity in the barrier reef region hind towards the recovery stage of the corals from industrial stress inhibited by the King Fahd Port development. The details of thermal and current structure of the region are also discussed and the natural protection to King Fahd Industrial Port of Yanbu from strong swell and currents action by the Port Barrier Reef is highlighted. The possibility of the coral structure to be easily altered by chemical or thermal pollution is also warned from the findings of the coral growth studies.The impact of excessive sediment and phosphate load on the reduction of coral recruitment and live coral coverage, excessive growth of filamentous algae, changes in population diversity of coral reef fishes such as butterflyfishs and damsel fishes were also highlighted.

3. Conclusion

By the stringent pollution regulatory measures of RC, the coral reefs in the region had shown some signs of improvement, but they are still in an unstable state. This study had clearly established the need of proper checking of any irreversible or irretrievable commitment of resources that might result from the human action that would curtail beneficial use of coastal environment.

Modelling the tracer flux from the Mururoa lagoon toward the Pacific

ERIC DELEERSNIJDER

(Institut d'astronomie et de géophysique Georges Lemaître, Université catholique de Louvain, 2 Chemin du Cyclotron, B-1348 Louvain-la-Neuve, Belgium, ericd@astr.ucl.ac.be)

1. Introduction

Mururoa Atoll is located in the tropical Pacific at 138°55' W and 21°50' S. It is a cone of volcanic rocks emerging from the ocean bottom, at a depth of approximately 3,500 m. The volcanics are topped by a layer of carbonates several metres thick. The boundary between the Pacific and the lagoon is delineated at sea level by a coral rim which is impermeable except for the hoas (Figure 1). The latter are channels allowing the oceanic swell to enter the lagoon. The main connection to the Pacific is a 5 km-wide and 8 m-deep pass. The mean depth and volume of the lagoon are about 33 m and 4.5 km^3, respectively. The water flow in the lagoon is forced by oceanic tides, wind stress and hoa inflow, and is affected by stratification (see *Tartinville et al.* [1997]).

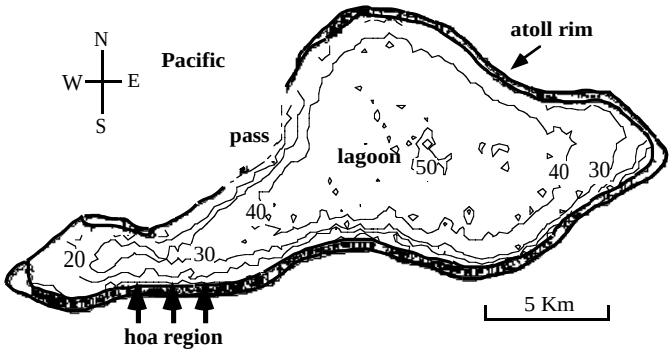

Figure 1. Bathymetry of Mururoa Atoll lagoon. The contour interval of the isobaths is 10 m.

From 1976 to 1996, the French army detonated nuclear weapons at Mururoa. Most of the tests took place in the volcanic rocks, so that a significant amount of radioactive material is now stored in this rock layer. The carbonates and the volcanics are porous. Thus, radioactive elements are in contact with water, which progressively dissolves some of them, turning them into "tracers". Water circulation in the rocks is mostly upwards, so that radioactive tracers are released, through the lagoon bottom, into the lagoon water, in which they are transported by advection and diffusion. Eventually, tracers are exported toward the Pacific through the pass.

Herein, modelling studies are reviewed which addressed tracer transport in the lagoon and toward the Pacific. The role of the various flow forcings is examined in the next Section. Next, the importance of the mean residence time for estimating tracer flux toward the Pacific is assessed. Finally, future research work is suggested.

2. Hydrodynamics

Tartinville et al. [1997] carried out a sensitivity analysis consisting of four three-dimensional model runs. The sole difference between these simulations lied in the selection of the forcings. In the first numerical experiment, only the M2 tidal forcing was taken into account. Then, the wind stress — due

to the trade winds, which are blowing from the east —, the hoa inflow and a simplified buoyancy forcing were successively included as steady state processes. The buoyancy fluxes at the lagoon-atmosphere interface, the lagoon mouth and the hoa are poorly known, which is why no attempt was made to resolve the heat and salt equations. Instead, the Brunt-Vaisala frequency was assumed to be a constant, which affected the Mellor-Yamada level 2.5 turbulence closure scheme and, hence, the vertical eddy viscosities and diffusivities. The circulation averaged over a tidal cycle was seen to be negligible in the simulation in which the tide is the sole forcing. The other three model runs clearly indicated that the wind stress is the dominant forcing of the long-term water motions, i.e. the hydrodynamic processes that are believed to be responsible for the transport of tracers inside the lagoon and the flux toward the Pacific. The wind-induced horizontal circulation was analysed in depth by *Mathieu et al.*

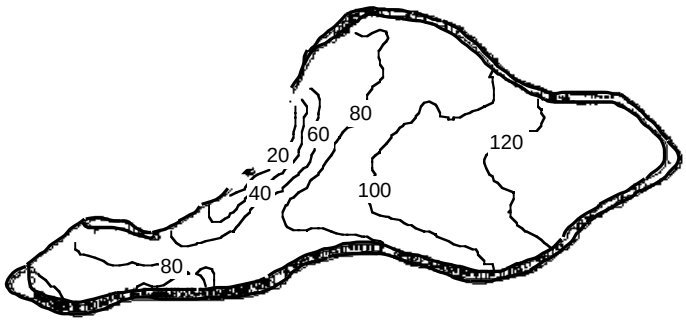

Figure 2. Average over all numerical simulations of *Anonymous* [1998] of the depth-mean of the residence time. As vertical diffusion is by far the "fastest" transport process in the lagoon, the residence time depends weakly on the vertical coordinate, so that little information is lost by displaying only the depth mean of the residence time. The contour interval is 20 days.

For each of the model runs mentioned above, maps of the residence time were produced by tracking Lagrangian particles, which at the initial instant were homogeneously distributed in the lagoon. By ascribing to the initial position of every particle the time at which it left the lagoon, the residence time field was constructed. The lagoon-averaged residence time, θ, was found to be much larger than one year for the tide-only simulation, and was between 3 to 4 months for the simulations in which the wind stress was taken into account. Using the model of *Tartinville et al.* [1997], *Anonymous* [1998] carried out the most comprehensive sensitivity analysis so far, which yielded $\theta = 98 \pm 37$ days (Figure 2). On the other hand, assuming that the global warming-induced rise of the ocean level will progressively lengthen the hoa region in the southern rim of the atoll, *Lousse* [1998] found that the variation of the residence time resulting from the increase of the hoa inflow would be much smaller than a simple water budget would suggest.

3. Tracer model

The tracer flux entering the lagoon through the bottom is considered as a forcing to be prescribed in accordance with appropriate geological data sets. On the other hand, the outgoing tracer flux depends on the tracer concentrations and the flow in the lagoon. Assuming that the lagoon is sufficiently well mixed that the tracer concentration is almost homogeneous throughout the lagoon, the flux ϕ toward the Pacific may be estimated as (see *Deleersnijder et al.* [1997]) $\phi = m/\theta$, where m is the tracer mass contained in the lagoon. This parameterisation, though very simple, if not simplistic, was validated by model-data and model-model comparisons (see *Deleersnijder et al.* [1997], *Anonymous* [1998]). This is illustrated in Figure 3.

For most impact studies, it is reasonable to assume that the tracer field is a steady state, implying that the outgoing tracer flux is equal to the tracer flux entering the lagoon through the bottom — if the

tracer under consideration is passive or decays sufficiently slowly. If the latter may be estimated from geological data, it is then possible to estimate the tracer content of the lagoon as $m = \theta\phi$. If, on the other hand, the tracer content of the lagoon is determined from a suitable amount of lagoon water samples, then the outgoing tracer flux may be evaluated by the formula $\phi = m/\theta$.

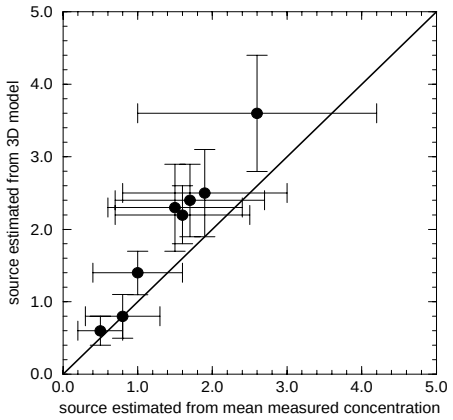

Figure 3. Plot of the Mururoa lagoon bottom source of tritium estimated by means of the three-dimensional model against its equivalent estimated as the ratio of the lagoon content of tritium — estimated from in situ observations — to the residence time. The flux are expressed in 10^{13} Becquerel year^{-1}. The error bars (see Anonymous [1998]) associated with each method are also displayed.

4. Future work

There are additional sensitivity studies to be carried out so as to understand the impact on the residence time of parameters or processes that have not been considered so far, such as the sill at the lagoon mouth. Though the lagoon seems to be widely open, its mouth is very shallow. Does this increase the residence time? The answer is not necessarily positive, since it may be argued that the outgoing water flux is largely determined by the tidal range and the lagoon surface which are independent of the section of the lagoon mouth. This issued may be investigated by computing numerically the residence time for various sill geometries.

Because the surface wind stress is the key forcing of the lagoon hydrodynamics, the surface velocity is generally downwind near the surface and upwind close to the bottom (see *Tartinville et al.* [1997], *Mathieu et al.*). Does this imply that the paths of tracer parcels are of a "conveyor belt" nature? This may not be the case, because vertical diffusion is the "fastest" transport process in the lagoon. A Lagrangian model, with random walks for representing diffusion, should be used to simulate particle trajectories, and a criterion should be set up to assess the relative influence of advection and vertical diffusion on trajectories.

The external sides of the atoll exhibit very steep slopes. In the vicinity of the atoll large wavelike displacements of the ocean thermocline several tens of metres in amplitude have been observed and modelled, to a certain extent, by means of a two-layer model (see *Garrigues et al.* [1993]). The impact of these motions on the outgoing tracer flux and tracer dispersion in vicinity of the atoll is unknown. A coupled lagoon-ocean model should be developed, which should be able to simulate the hydrodynamics of both the shallow lagoon and the deep ocean surrounding Mururoa Atoll.

Acknowledgments: The author is a research associate with the Belgian National Fund for Scientific Research (FNRS).

References:

Anonymous, The radiological situation at the atolls of Mururoa and Fangataufa, Technical Report, Volume 5: Transport of radioactive material within the marine environment, Report by an International Advisory Committee (Working Group 5) IAEA-MFTR5, International Atomic Energy Agency, Austria, 140 pp., 1998.

Deleersnijder E., B. Tartinville and J. Rancher, A simple model of the tracer flux from the Mururoa Lagoon to the Pacific, *Applied Mathematics Letters, 10 (5),* 13-17, 1997.

Garrigues L., E. Deleersnijder and J. Rancher, Modélisation bi-dimensionnelle à deux couches de la circulation autour d'îles: application aux atolls de Fangataufa et Mururoa, Service Mixte de Sécurité Radiologique, Montlhéry, France, 85 pp., 1993.

Lousse I., Modélisation de l'impact des hoa sur le temps de résidence des traceurs radioactifs dans l'atoll de Mururoa, Mémoire de second cycle, Département de physique, Université catholique de Louvain, Louvain-la-Neuve, Belgium, 65 pp., 1998.

Mathieu P.-P., E. Deleersnijder, B. Cushman-Roisin, J.-M. Beckers and K. Bolding, The role of topography in small well-mixed bays, with application to the lagoon of Mururoa, *Continental Shelf Research* (in press).

Tartinville B., E. Deleersnijder and J. Rancher, The water residence time in the Mururoa atoll lagoon: sensitivity analysis of a three-dimensional model, *Coral Reefs, 16*, 193-203, 1997.

Trace metal dispersion and uptake in the Gulf of Cadiz

Jean-Marie Beckers and Alexander Barth, (*University of Liège, Sart-Tilman B5, B-4000 Liège, Belgium*, JM.Beckers@ulg.ac.be)

Eric Achterberg and Charlotte Braungardt, (*Department of Environmental Science, University of Plymouth, Drake Circus, Plymouth PL4 8AA, UK*, C.Braungardt@plymouth.ac.uk)

1 Introduction

A nested high resolution 3D primitive equation model is used in the Gulf of Cadiz in order to understand the trace metal dispersion behaviour in this region. The local model operates at a 1.3km resolution embedded into a 4 km resolution model of the Gulf of Cadiz and the Gibraltar Strait.

The nested model takes into account the discharges from the main rivers in the region (Tinto-Odiel, Guadalquivir and Guadiana). The model setup is designed so as to verify if the river discharge of trace metals (Cu, Ni, Zn, Cb, Cu and Zn, measured at high resolution during the TOROS project *Elbaz-Poulichet et al* [2001]) can be modelled by a passive tracer and if not which kind of source/sinks could account for the difference.

To help diagnosing the tracer dispersion, several tracer origins are differentiated (sediments and individual rivers) as well as the age of the tracers when reaching a given location.

To analyse the age, the theory of *Deleersnijder et al* [2001] is used, which needs the calculation of the evolution of a tracer C ($\boldsymbol{u}$ is the velocity field, $\boldsymbol{K}$ the diffusion tensor, $\boldsymbol{\nabla} = \sum_i \boldsymbol{e_i} \frac{\partial}{\partial x_i}$ the Nabla operator and $P - D$ source and sink terms of material)

$$\frac{\partial C}{\partial t} = P - D - \boldsymbol{\nabla} \cdot \left(\boldsymbol{u} C - \boldsymbol{K} \cdot \boldsymbol{\nabla} C \right), \tag{1}$$

and the calculation of the so-called age-concentration α:

$$\frac{\partial \alpha}{\partial t} = \pi - \delta + C - \boldsymbol{\nabla} \cdot \left(\boldsymbol{u} \alpha - \boldsymbol{K} \cdot \boldsymbol{\nabla} \alpha \right), \tag{2}$$

from which the age a of the tracer can be calculated:

$$a = \frac{\alpha}{C}. \tag{3}$$

For the present study, if trace metals behaved conservatively, all production-destruction (P, D, π, δ) terms would be zero.

Though the theory of the age was investigated in depth (e.g. *Beckers et al.* [2001], *Deleersnijder et al.* [2002], *Delhez and Deleersnijder*, [2002]) applications of the new theory to the understanding of transit times for trace metals are not yet analysed and will be the purpose of the presentation. The presentation will thus focus on the diagnostic possibilities of the tracers in view of a better understanding of the circulation processes and the shelf-opean sea exchanges.

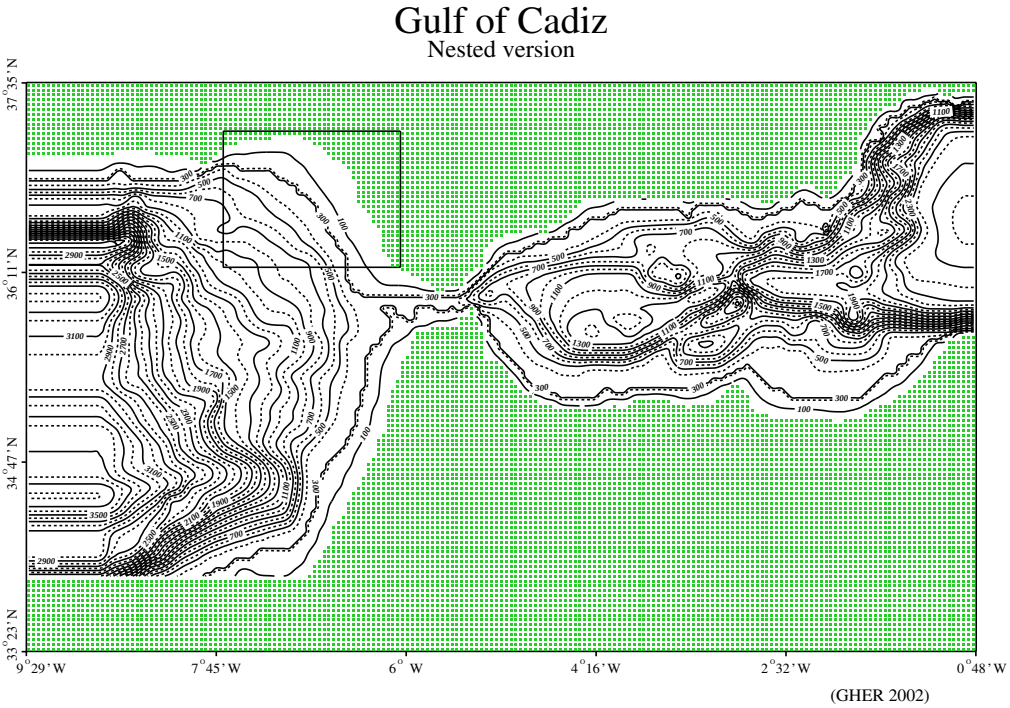

Figure 1: Gulf of Cadiz Nested model with coarse resolution model grid and location of the nested model

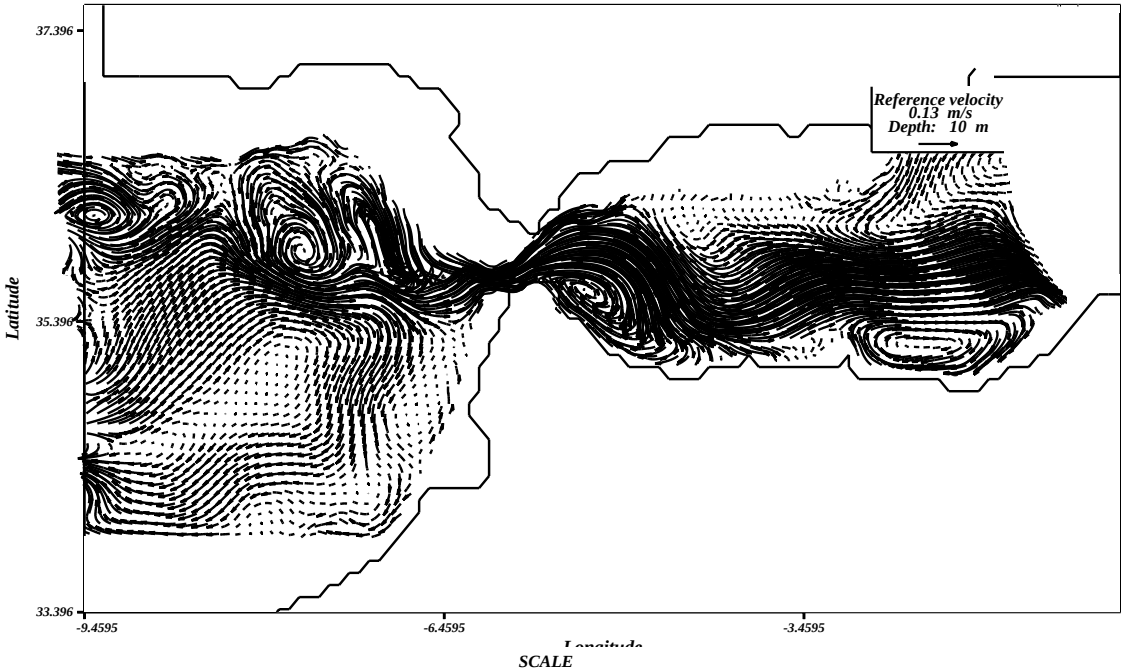

Figure 2: Circulation pattern of the coarse grid model

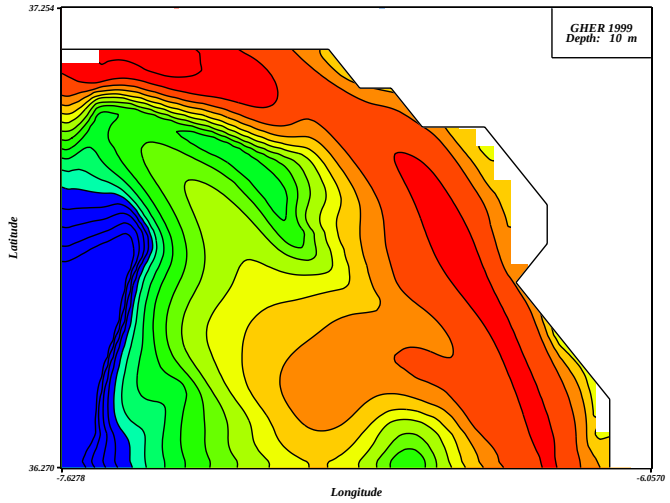

Figure 3: Tracer distribution in the fine grid model, logarithmic scale

Acknowledgments: The National Fund for Scientific Research, Belgium is acknowledged for the financing of a supercomputer and the position of the first author.

References:

Beckers J.-M., Delhez E.J.M., Deleersnijder E., Some properties of generalised age-distribution equations in fluid dynamics. *SIAM Journal on Applied Mathematics*, 61(5) : 1,526-1,544, 2001

Deleersnijder E., Campin J.-M. and Delhez E.J.M., The concept of age in marine modelling : I. Theory and preliminary model results. *Journal of Marine Systems*, 28 : 229-267, 2001

Deleersnijder E., Mouchet A., Delhez E.J.M. and Beckers J.-M., On the Transient Behaviour of Water Ages in the World Ocean. *Mathematical and Computer Modelling* . Accepted, 2002

Delhez E.J.M. and Deleersnijder E., The concept of age in marine modelling : II Concentration distribution function in the English Channel and the North Sea. *Journal of Marine Systems*, 31 : 279-297, 2002

F. Elbaz-Poulichet, Ch. Braungardt, E. Achterberg, N. Morley, D. Cossa, J.-M. Beckers, Ph. Nomerange, A. Cruzado, and M. Leblanc. Metal biogeochemistry in the Tinto-Odiel rivers (southern Spain) and in the Gulf of Cadiz. A synthesis of the results of TOROS project. *Continental Shelf Research*, 21:1961–1973, 2001.

Measurements of sediment diffusivity under regular and irregular waves

PETER D. THORNE

(Proudman Oceanographic laboratory Bidston Observatory,Bidston Hill, Prenton, Merseyside, CH61 7RA, UK, pdt@pol.ac.uk)

ALAN G. DAVIES

(School of Ocean Sciences, University of Wales(Bangor), Menai Bridge, Anglesey, LL59 5EY, a.g.davies@bangor.ac.uk)

JON J. WILLIAMS

(Proudman Oceanographic laboratory Bidston Observatory,Bidston Hill, Prenton, Merseyside, CH61 7RA, UK, jjw@pol.ac.uk)

1. Introduction

Vortex shedding above ripples in oscillatory flow provides a highly effective mechanism for the entrainment of sediment into suspension (Nielsen, 1983). Although this process is complex in both space and time, it is helpful for practical purposes to develop simplified, horizontally- and temporally-averaged, descriptions of the near-bed velocity and suspended concentration fields which allow, in turn, the behaviour of derived quantities such as the vertical profile of cycle-mean sediment diffusivity to be established. While different representations have been presented for the form of the one-dimensional vertical (1DV) diffusivity above ripples (Van Rijn, 1993; Lee and Hanes, 1996), there has been no general consensus as to the precise vertical structure. Moreover, descriptions of the suspended sediment distribution with height above the bed have been based not only upon disorganised turbulent diffusion processes, but also upon coherent convective and combined convection-diffusion formulations (Thorne *et al*, 2002).

The aim of the present work is to contribute new measurements of the suspended sediment concentration beneath waves, based upon which detailed profiles of the sediment diffusivity have been obtained. The measurements were made under regular and irregular waves, over a sandy bed, in a large-scale flume facility (330 m long, 5 m wide and 7 m deep). The size of the facility allowed the generation of waves at full-scale, under laboratory controlled conditions. To investigate the form of the diffusivity with height above the bed, experiments were conducted with regular waves of height 0.6 m- 1.3 m and period 4 s– 6 s, and irregular waves (Jonswap spectrum) with significant heights and peak periods in the ranges 0.5 m- 1.2 m and 4.9 s- 5.1 s. To estimate the sediment diffusivity, a combination of pumped sampling and multi-frequency acoustic backscattering were used. Acoustics was specifically employed for the diffusivity measurements because it provided high spatial resolution, 0.01 m, suspended concentration profiles above the bed, which were linked to the bed location by utilisation of the bed echo. This combination of knowing the precise location of the bed, and its variation with time (as ripples migrated past the observation point), and high resolution concentration profiles directly referenced to the varying bed height, is unique to the acoustic approach and essential for obtaining accurate sediment diffusivity profiles. From the acoustics data, sediment diffusivity profiles have been derived and the results interpreted in terms of underlying convective and diffusive mechanisms. The implications of the results for sediment transport modelling are discussed.

2. Instrumentation

The large-scale flume facility used in the present study was the Deltaflume of Delft Hydraulics, The Netherlands. Regular and irregular waves were propagated over a medium size, quartz sand bed (d_{50}=330μm) of thickness 0.5 m and of length 30 m located midway along the flume in water of mean

depth 4.5m. To collect the measurements an instrumented tripod platform STABLE (Sediment Transport And Boundary Layer Equipment) was used. The platform and the instrumentation are shown in figure1. To measure the suspended sediment diffusivity profiles a triple frequency (1.0 MHz, 2.0 MHz and 4.0 MHz) acoustic backscatter system, ABS, was employed. This provided measurements of the concentration at 0.01m intervals from the bed up to the location of the acoustic transducers mounted at a mean height of 1.24 m above the bed. To augment and calibrate the ABS measurements, pumped samples were collected at ten heights above the bed, between 0.05 m-1.55 m. As well as using the ABS to locate the bed position, an acoustic ripple profiler, ARP, (Bell et al, 19**) was used to make measurements of ripple height and wavelength along a 3 m profile of the bed over time. To measure the hydrodynamics, three pairs of electromagnet current meters, ECM, were located at heights of 0.30 m, 0.60 m, and 0.91 m above the bed.

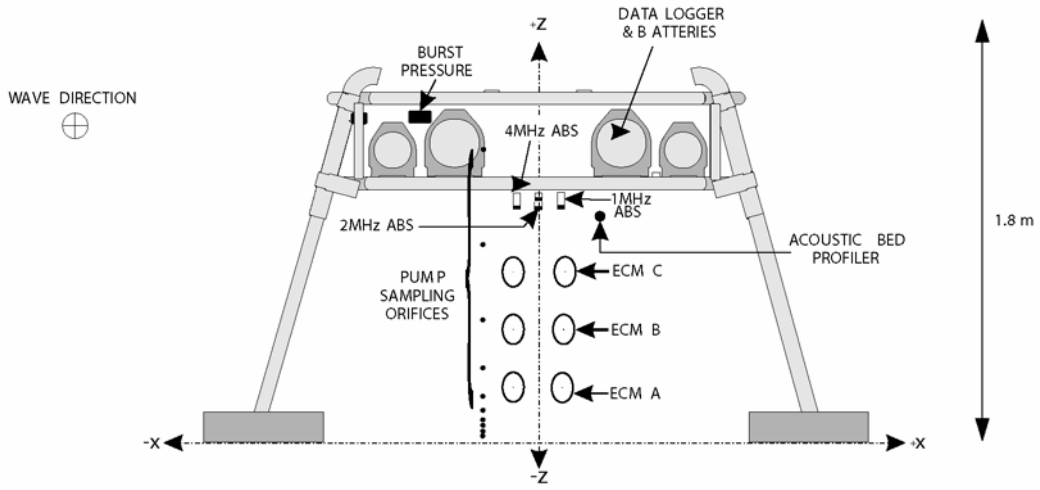

Figure 1: Instrument platform STABLE showing the location of the ABS, ARP, ECMs and pumped samples

3. Measurements and analysis

To obtain estimates of the sediment diffusivity, ε_s, the standard formulation based on the cycle-mean concentration and it vertical gradient (C and dC/dz, respectively) was adopted (e.g. Nielsen, 1983):

$$\varepsilon_s = \frac{-w_o C}{dC/dz} \tag{1}$$

where w_0 is the mean settling velocity of the sediment in suspension and z is the height above the bed measured from the ripple crest For purposes of interpretation, the data has been plotted in a normalised form based on the following parameterisation:

$$\varepsilon_{sn}=\varepsilon_s/(\kappa u_* h) \tag{2a}$$

$$z_n=z/h \tag{2b}$$

where κ is von Karman's constant ($\approx$0.4), h is the mean water depth and u_* is the peak value of friction velocity in the wave cycle given by

$$u_*= \sqrt{f_w/2}A_w\omega \tag{3}$$

where f_w is the wave friction factor, for which Swart's (1974) formula has here been used, A_w is the orbital amplitude of the fluid just above the boundary layer and ω is the angular frequency of the wave. The respective terms are given by

$$A_w = \frac{H}{2\sinh(kh)} \tag{4}$$

$$f_w = \exp\left\{5.213\left(\xi / A_w\right)^{0.194} - 5.977\right\} \tag{5}$$

$$\xi = 8\eta_r^2 / \lambda_r + 5\theta' d_{50} \tag{6}$$

where H (or H_s) is the wave height, k is the wave number, η_r is the ripple height, λ_r is the ripple wavelength, θ' is the grain roughness Shields parameter and d_{50} is the median grain diameter of the bed.

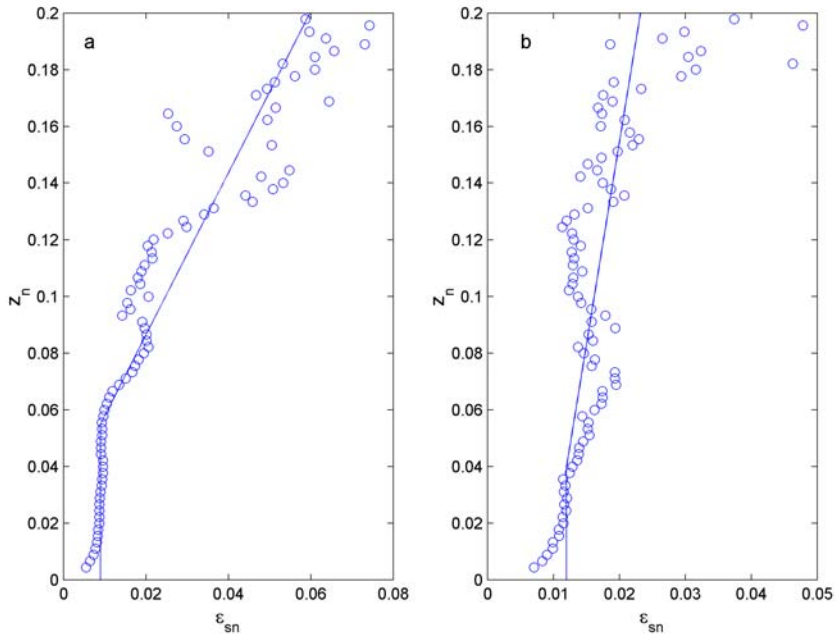

Figure 2: Measurements of sediment diffusivity under a regular wave (a) and irregular wave (b)

Two examples of sediment diffusivity profiles measured in the Deltaflume are show in figure 2. Figure 2a shows an example for regular waves, of height H = 1.047 m and period T = 5 s, and figure 2b for irregular waves with significant height H_s = 1.006 m and peak period T_p = 5.1 s. The water depth in each case was h = 4.50 m. The ripple heights and wavelengths in the respective cases were η_r =0.061 m, λ_r =0.409 m and η_r =0.046 m, λ_r =0.395 m.

For the regular wave case, the profile of diffusivity is relatively uniform near the bed, z_n = 0.01-0.055, though there is some reduction below z_n = 0.01. The thickness of the vortex-affected layer in which the diffusivity remains constant corresponds to about 5 ripple heights in this case. Above approximately z_n = 0.055 the diffusivity starts to increase linearly with height, though there is significant scatter in the data and the presumption of linearity requires further justification. For the irregular wave case, a 'uniform+linear' description for the sediment diffusivity is possible, but somewhat less convincing. The diffusivity decreases below z_n = 0.02, has an approximately linear region between z_n = 0.02 and 0.04 (corresponding to a vortex layer thickness of 3 – 4 ripple heights), and then increases above z_n =

0.04, though with a reduced gradient as compared with the regular wave case. Importantly, what is clear in both cases is that the sediment diffusivity remains approximately constant in a layer extending upwards from the level of the ripple crest to a level corresponding to about 3 to 5 times the ripple height. This is in contrast to the generally accepted picture for plane beds, above which the sediment diffusivity increases linearly with height from the bed level itself.

To represent the present data, a simple, tentative, two-parameter model (c.f. Van Rijn, 1993) is explored here, namely:

$$\varepsilon_{sn} = \alpha \qquad z_n \le z_{no} \tag{7a}$$

$$\varepsilon_{sn} = \alpha + \beta(z_n - z_{no}) \qquad z_n \ge z_{no} \tag{7b}$$

The straight lines in figure 2 correspond to equation (7) with α=0.009, β=0.35 for the regular wave case and α=0.012, β=0.07 for the irregular wave case. Physically, equation (7) is interpreted as corresponding to a lower vortex-dominated layer ($z_n \le z_{no}$), of thickness a few ripple heights, in which the process of eddy shedding gives rise to efficient, vertically uniform, mixing of sediment (and also of momentum; see Davies and Villaret, 1997). Above height z_n, the vortices break down, and normal turbulent diffusion concepts become dominant. In this upper turbulent layer ($z_n \ge z_{no}$), the mixing length scale is expected to increase with height (possibly linearly), and the sediment diffusivity (and eddy viscosity) are therefore expected to increase with height also. These fundamental points underlying the structure of the sediment diffusivity profile will be discussed more fully, and with reference to the complete Deltaflume data set, in the full length paper.

Acknowledgments: The work was jointly supported by the EU contract MAS3-CT97-0106, NERC, UK .

References

Bell, P.S., Thorne, P.D. and Williams, J.J. Acoustic measurements of sand ripple profile evolution under controlled wave conditions. Fourth European Conference on Underwater Acoustics, held September 21-25, 1998, in Rome, Italy. Edited by A. Alippi, Università di Roma "La Sapienza" and G. B. Cannelli, Instituto die Acustica "O.M. Corbino", CNR, Roma, 353-358. 1998

Davies, A. G. and Villaret, C.,. Oscillatory flow over rippled beds: Boundary layer structure and wave-induced Eulerian drift. In: Gravity Waves in Water of Finite Depth, Advances in Fluid Mechanics, ed. J. N. Hunt, Computational Mechanics Publications, Southampton, UK, 215-254 1997.

Lee, T.H., and Hanes, D.M Direct inversion method to measure the concentration profile of suspended particles using backscattered sound. *Journal of Geophysical Research*, 100, 2649-2657. 1995

Nielsen, P. Entrainment and distribution of different sand sizes under water waves. Journal of *Sedimentary Petrology*, 86(2), 423-428 1983.

Swart, D.H., (1974). "Offshore sediment transport and equilibrium beach pro-files." Publ. 131, Delft Hydrol. Lab., Delft, Netherlands.

Thorne, P.D., Williams J. J, and Davies A. G. Suspended sediments under waves measured in a large-scale flume facility. *Journal of Geophysical Research*, In Press 2002.

Van Rijn, L.C., (1993). Principles of sediment transport in rivers, estuaries and coastal seas. Aqua Publications, Amsterdam

Investigations of sediment transport in the Jade Bay

SIGRID PODEWSKI

(Institut für Meereskunde, Troplowitzstr. 7, 22529 Hamburg, Germany, present address: Plöner Str. 10, 24148 Kiel, Germany, spodewski@web.de)

THOMAS WEVER

(Forschungsanstalt der Bundeswehr für Wasserschall und Geophysik, Klausdorfer Weg 2-24, 24148 Kiel, Germany, wever@fwg-kiel.de)

Abstract

A number of experiments was performed in the Jade Bay in the southern North Sea, to study bedform migration and the controlling processes.

The use of burial registration mines (mine bodies with three rings of light bridges that measure in 1 hour intervals the sand coverage) revealed an extremely strong small-scale heterogeneity of mega-ripple migration rates which reached up to 2 meters per day. In one extreme event the migration rate was even higher.

A scanning sonar, mounted on top of a 5 m high tower was used to monitor changes of seafloor morphology. During subsequent slack water periods clear differences of backscatter resulting from the overall re-orientation of megaripples in response to the tidal currents are visible. This re-orientation of the megaripple crests at 6 hour cycles was also sampled with the burial registration mines.

Continuous turbulence measurements were performed at two different sites in the outer Jade Bay. At both locations water depths varied with the tides between 12 m and 16 m. The site *Explosionsreede* is characterised by a flat seafloor and fine sand to mud sediments while the other site (*Schillig Reede*) is dominated by medium sand megaripples. At both sites turbulence increased pronouncedly near the seabed with increasing tidal current and rose into the upper water column continuously. During the mid-tide cycle a minimum of turbulent dissipation rates occurred at mid-depth. This characteristic vertical distribution of turbulence in the water column occurred at both study sites and indicates a reduced vertical exchange of heat, salt, and suspended particulate matter (SPM) between the sea surface and the seabed.

At *Explosionsreede* concentrations of SPM varied pronouncedly and occasionally reached about two times the ones at *Schillig Reede*. In addition, the generation of turbulence due to thermal convection was more intense here. Nevertheless, the dissipation rates at the same maximal tidal mean currents were found to range about one order of magnitude lower than at the study site *Schillig Reede*. Both effects, the enhancement of turbulence due to a complex topography and the damping of turbulence due to SPM cannot be treated separately. The analysis clearly indicates that the complex bottom topography dominated the generation of turbulent kinetic energy as a function of the mean tidal currents.

Effect of advective and diffusive sediment transport on the formation of bottom patterns in tidal basins

Sonja van Leeuwen, (*Institute for Marine and Atmospheric research Utrecht, Princetonplein 5, 3508 TA Utrecht, the Netherlands*, s.m.vanleeuwen@phys.uu.nl)

Huib de Swart, (*same institute*, h.e.deswart@phys.uu.nl)

1 Introduction

This paper focuses on tide-dominated embayments, such as those found in the Dutch Wadden Sea. The morphology of a tidal embayment is usually quite complex. Analysis of field data has revealed that often two classes of bed forms can be distinguished: a fractal-like pattern of channels and shoals throughout the basin and tidal sand bars that are found near the entrance of the embayment. It is important to understand more about the physical processes which determine these bottom profiles, both from a scientific and a coastal management point of view. Many different ways of studying this problem have been applied. Recently, the formation of channels and shoals in tidal embayments has been successfully simulated with state-of-the-art complex numerical morphodynamic models. These results motivated further studies on analysing the underlying mechanisms responsible for the occurrence of these features. For this purpose idealised models were designed and analysed, which attempt to include only the dominant physical processes. *Schuttelaars and De Swart* [1999] used such an idealised model and found global bottom patterns (covering the entire basin area) that comprises channels and shoals. *Seminara and Tubino* [1998] on the other hand found local bottom patterns (with length scales of the order of the basin width) which resemble tidal sand bars. However, it is hard to compare these results as the two models are widely different. In the first study a semi-enclosed basin with weak bottom friction and only diffusive sediment transport was considered, whereas in the second study an open channel with frictionally dominated tidal flow and only advective transport of sediment was examined. In order to bridge this gap *Van Leeuwen and De Swart* [2001] extended the model of *Schuttelaars and De Swart* [1999] with advective transport of sediment. Using weak bottom friction they found global patterns for equal magnitudes of advective and diffusive sediment fluxes. Here, this extended model is analysed for both strong and weak bottom friction in order to see what determines the presence of local or global bottom patterns.

2 Model Description

The basin is represented by a rectangular geometry with fixed side walls and an erodible bottom. The length and width of the basin are $L \sim 20$ km and $B \sim 2$ km, respectively. The depth at the entrance ($x = 0$) is $H \sim 10$ m, see figure 1. The model consists of the depth-averaged shallow water equations, a concentration equation and a bottom evolution equation. Only suspended load transport is considered. The bottom evolution is determined by the tidally averaged sediment flux because the morphological timescale (~ 10 years) is much larger than the tidal timescale (~ 12.5 hours). Boundary conditions

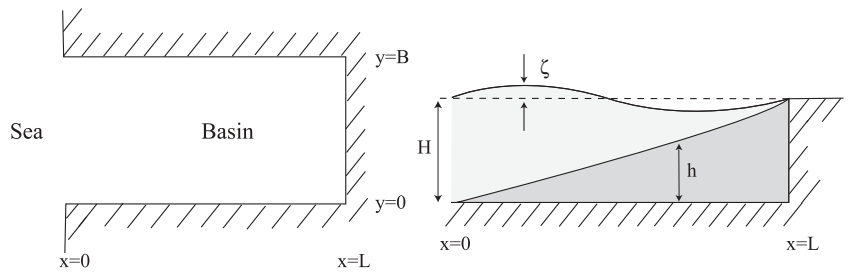

Figure 1: Model geometry; left : top view, right : cross-sectional view.

consist of a prescribed free surface elevation at the entrance (M_2 tide with an amplitude of 1.5 m), no water or sediment flux through solid boundaries and no diffusive boundary layer in the time-varying part of the concentration. The bed level at the entrance is kept fixed. The model is applied to short basin, i.e. the basin length is short compared to the tidal wave length. This assumption reduces the momentum equations, which then in a first approximation state that the free surface is spatially constant. In order to solve the two-dimensional model the vorticity equation is needed to close the system. The strength of the advective fluxes is measured by the Strouhal number ϵ, which is the ratio of the tidal amplitude over the depth at the entrance. The parameter values are representative for the main channel of the Frisian Inlet, located in the Dutch Wadden Sea.

The model allows for a basic state which is characterised by a spatially uniform tidal motion over a linearly sloping bottom. *Schuttelaars and De Swart* [1999] showed that two-dimensional perturbations superimposed on this basic state can have positive growth rates, resulting in the excitation of channel/shoal-like bottom patterns. The same procedure is applied here. The perturbations consist of an along-channel structure, which is continued in the cross-channel direction with a cosine profile. The number of half cosines which fit in the basin width is given by n, which determines the lateral wave number $l(n) = n\pi B/L$. The temporal behaviour of the perturbations is determined by an eigenvalue of the problem. The real part of this eigenvalue indicates growth (when positive) or decay (when negative) of the corresponding bottom pattern. The imaginary part specifies the migration rate. The bottom pattern with the largest positive growth rate will be dominant over other patterns.

3 Results

First, the use of realistic values of the bottom friction is considered. Figure 2 shows on the left the scaled growth rates of the fastest growing modes for increasing lateral wave numbers. A growth rate of 1.0 corresponds to an e-folding time scale of decades. Two different modes are found. The first mode ($m = 1$) is a diffusively generated mode, i.e. it is controlled by diffusive sediment fluxes. This mode corresponds with a global bottom pattern as shown in figure 2 in the right top plot. The second mode ($m = 2$) shows very different characteristics, although its maximum growth rate is equal to that of the diffusive mode. The corresponding bottom pattern is shown in figure 2 in the right bottom plot. A local pattern is found here. Analysis showed that this pattern grows due to divergence of

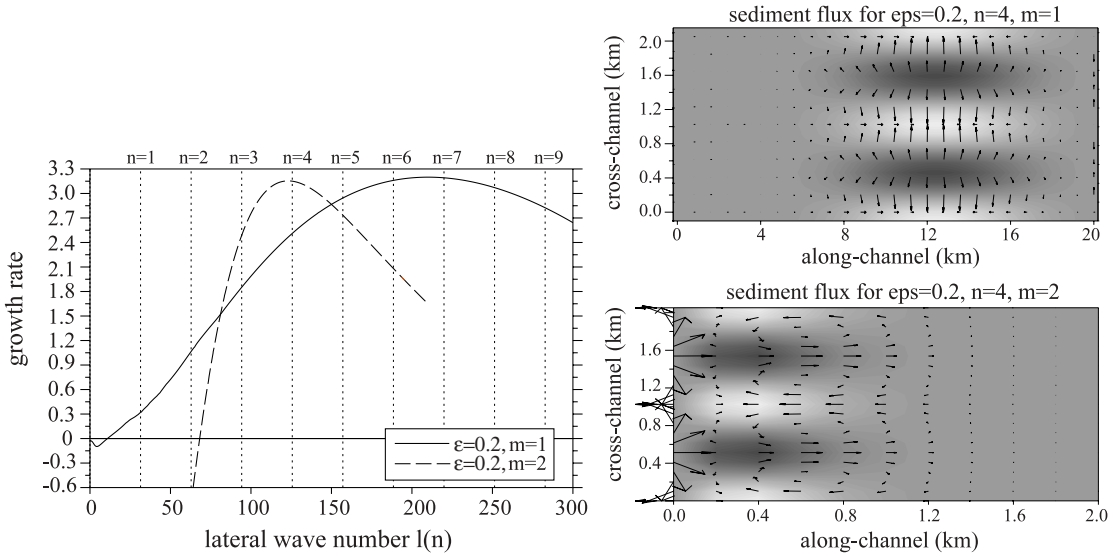

Figure 2: Left: scaled growth rates of the perturbations for equal magnitudes of diffusive and advective sediment fluxes. Different curves represent different along-channel modes and the dashed vertical lines indicate the discrete values of the lateral wave number $l(n)$ which can be obtained in this basin. Right: the most preferred bottom modes for $n = 4$, top: $m = 1$, the diffusive mode, bottom: $m = 2$, the advective mode. Note the different along-channel length scale for the bottom figure. Dark areas are troughs and white areas are bars. The arrows indicate the direction and relative magnitude of the tidally averaged sediment flux.

the along-channel advection of the mean concentration by the residual current. Therefore, this mode is called an advective mode and it corresponds to the tidal sand bars found by *Seminara and Tubino* [1998]. The appearance of the advective mode only occurs when the advective fluxes are at least of the same order of magnitude as the diffusive fluxes.

In order to further examine the effect of advective processes on the pattern formation process the diffusion coefficient is reduced by a factor 4. Here a low value of the friction parameter is chosen to allow comparison with the model of *Schuttelaars and De Swart* [1999]. The case of weak bottom friction is near critical conditions when perturbations first become unstable. Figure 3 shows on the left the largest scaled growth rates for increasing strength of advective processes. The curves show that the second mode becomes dominant when advective processes are strong. The bottom pattern corresponding to mode $m = 1$ is shown in figure 3 in the upper right plot where the dominant mode for $\epsilon = 0.1$ is plotted. This is a global pattern which will decay in time, as can be seen by the negative growth rate. The bottom pattern of the second mode is shown in the lower right plot of figure 3 (dominant mode for $\epsilon = 0.2$) and is defined by a local pattern. The growth rate of this mode is positive and its mechanism of growth is the same as described in the previous section for the advective mode.

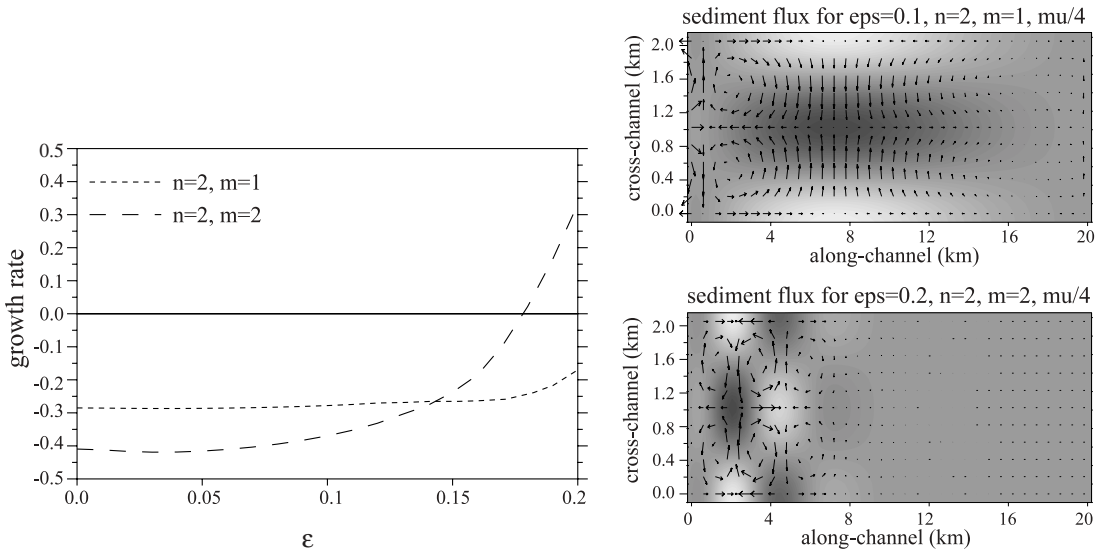

Figure 3: Left: scaled growth rates as a function of the Strouhal number. Right: bottom patterns and corresponding sediment fluxes for $n = 2$ and top: $\epsilon = 0.1$, the dominant mode is $m = 1$, bottom: $\epsilon = 0.2$, the dominant mode is $m = 2$.

4 Conclusions

The conclusions drawn from the presented research are that the long timescale for bottom pattern growth found by *Schuttelaars and De Swart* [1999] and *Van Leeuwen and De Swart* [2001] (order of centuries) can be attributed to the use of a weak bottom friction coefficient. When realistic values are applied the timescale of bottom pattern growth becomes of the order of decades, which is consistent with field data. Both local and global bottom modes were found here, the first resembling tidal sand bars and the latter resembling channel/shoal patterns. The local profiles form when advective sediment fluxes are dominant over diffusive fluxes. Their growth is caused by divergence of the along-channel advection of the mean concentration by the residual current. The effects of internally generated overtides and settling lag effects are of minor importance.

References:

Schuttelaars, H.M., and H.E. De Swart, Initial formation of channels and shoals in a short tidal embayment, *J. Fluid Mech., 386*, pp. 15-42, 1999.

Seminara, G., and M. Tubino, On the formation of estuarine free bars, in *Physics of Estuaries and Coastal Seas*, edited by J. Dronkers and M. Scheffers, pp. 345-353, Balkema, Rotterdam 1999, Proc. of the int. PECS conference, Den Haag, the Netherlands, 1996.

Van Leeuwen and H.E. De Swart, The effect of advective processes on the morphodynamic stability of short tidal embayments, *Phys. and Chem. of the Earth, 26*, pp. 735-740, 2001.

Sediment Transport and Coastline Development Along the Caspian Sea "Bandar Nowshahr Area"

M. F. NIYYATI

(Head of Coastal Supervision Dept., Ports and Shipping Organization, #751 Enghelab Islami Ave., Tehran, Iran, M_F_NIYYATI@ir-pso.com)

ALIREZA MARAGHEI

(*Head of Basic Ports and Marine Research Dept., Ports and Shipping Organization, #751 Enghelab Ave., Tehran Iran, A_R_MARAGHEI@ir-pso.com)*

SEYED MAJID NIYATI

(*Head of Hydraulic Structure Design Office, Serat Omran Engineering Co. , Flat 8, #6, Garrous st., Soleyman Khater st., Motahhari Ave., Tehran, Iran, S_M_Niy@yahoo.com)*

1. Introduction

The harbor area of the Bandar Nowshahr is about 400,000 m^2 and there is no natural protection at the region, hence the harbor depends entirely on two breakwaters. The two breakwater are rouble mound with the lengths of 480 m and 700 m. The breakwater gap is 200 m. The access channel is maintained to 120 m wide and 6.5 m deep. Only that part of the channel and basin is maintained that is required to reach the berths. The depth in the harbor is maintained at 6.5 m at the quays and 7 m in the center. The annually dredging volume is some 100,000 m^3 of and from the access channel and some 40,000 m^3 of silt from the basin.

Port authorities are suffering from inundation due to sea level rise of the Caspian Sea and wave penetration inside the basin. In order to solve wave penetration problem, there is a plan for extension of the western breakwater (350 m). Port authorities also encounter with siltation inside access channel and port basin. Moreover they intend to develop the port basin by calling bigger vessels, therefore, it is important to determine rate of siltation after deepening the access channel and port basin. This study is focused on sediment transport, rate of siltation before and after extension of the breakwater and effect of sea level rise on coastline development in the port area.

2. Available existing data

2.1 Wind and Wave records

Available existing windroses are related to Nowshahr and Ramsar area. No wave measurements have been carried out in the off-shore area of the Bandar Nowshahr. In view of the available data of the wind along the southern shore of the Caspian Sea, it can be assumed that the predominant wind and wave direction is northwest, although occasionally high waves from more northerly direction also occur.

2.2 Currents

No current measurements have been carried out in the area of the Bandar Nowshahr. In general, in the Caspian Sea, currents are North-South along the west coast from the Volga river in Russia to Anzali. The main portion of the current stream the south coast from Anzali to an area north of Babolsar, 110km east of Bandar Nowshahr, where it is deflected to the N by shallower water. In the Caspian Sea no tides is perceivable and probably the currents are mainly governed by the winds. A limited number of observations carried out at Neka, 160 km east of Bandar Nowshahr, in May and June 1976. Those observations show rather low velocities, usually less than 0.15 m/s.

2.3 Water level variations

There is good reason to believe that the lowering of level from 1932 to 1974 has been due to impounding of the Volga on which there are at least 8 dams. It was not a big surprise, therefore, when in the early 1970s, the Caspian Sea level following a period of relative stability, dropped again, reaching its lowest recorded level of 29 m below sea level in 1977. Then the situation in the Caspian fishery became critical. Biologists predicted that if the Caspian Sea level dropped to -31 m, it would result in almost total collapse of the sturgeon stock and other anadromous and semi-anadromous species.

Meanwhile, quite unexpectedly, the sea level began to rise after 1977. Notwithstanding, the sea level continued to rise and by 1992 it rose to almost 2 m above the level of 1977.

3. Wave climate

To find out wave characteristics in deep water, the existing wind data of the Nowshahr are used. In order to compute the wave height in deep water, (depth = 75 m), the WATRON (wave generation and propagation model) and SCATTER models are applied. To provide the required input data for the WATRON, the relevant area of the Caspian Sea which causes maximum fetch length in different directions for the Bandar Nowshahr, is schematized. Then WATRON computes the wave parameters at the defined location 75 m water depth, using a Bretschnieider method, predicting the wave growth under the constant wind duration and defined fetch length.

To compute the wave propagation from deep to shallow water the refraction module of WATRON was used. As the bathymetric map shows, the depth contours in Nowshahr area are almost straight and parallel. Hence, the ENDEC model could be applied there. To determine the reliability of ENDEC computations the wave condition in the nearshore was modeled using a 2D-wave model called HISWA. The results show good agreement between HISWA and ENDEC.

4. Current

There is no tide in the Caspian Sea, therefore there is no tidal current in the area. The greatest overall determinants of current velocity and direction are surface winds, river inflows, the earth rotation and water density gradients. Due to lack of field data a general the literature study was carried out. For the wind-induced current a rough calculation was carried out resulting in current velocity values in the upper layer below 0.2 m/s in moderate and storm wind conditions. The general current circulation in the southern part of the Caspian Sea has a counter-clock wise rotation. The currents are north-south along the west coast from Volga to Bandar Anzali. A limited number of observations has been carried out at Bandar Anzali and at Neka power plant (160 km east of Nowshahr), showing rather low velocities, usually less than 0.15 m/s.

To find the annual current pattern in the nearshore area of Nowshahr, a quadratic combination of wind-induced current and wind-driven longshore current was used. To determine the effect of wind-induced alongshore current near the access channel and harbor area, the 2DH TRISULA model was used. To set up the TRISULA model, the rectilinear grid was used. One computation using a curvilinear grid was carried out with the available bathymetry and no sea-level rise condition. Comparison of the results of the rectilinear grid computation (grid space = 50*50) and curvilinear grid shows that the flow velocities with the rectilinear grid are in the order of 35% more than those of the curvilinear grid. This difference may mostly be due to difference in bathymetric schematization. The curvilinear result shows much more detailed flow parameters. The curvilinear grid has a much finer grid specially near the harbor entrance, i.e.15 cells, where the rectilinear grid has 3 cells only.

To estimate the wave-driven longshore current, two approaches were applied. As a first approach the longshore current was determined using the Komar formula (1979). The results show rather high

current velocities in the order of 2 m/s in the predominant direction and storm conditions which seems very conservative particularly for waves incident with angle of 45° with respect to coast normal.

The computed longshore current velocity mostly varies from 0.4 to 1 m/s for storm conditions. By deepening the channels to 7 m and 8 m, the current velocity decreases by about 10% and 15%.

The effect of extension of the breakwater on the current pattern in the harbor area was determined by using TRISULA model. The computational results show that the current velocity near the tip of the extended breakwater will be about 15% to 25% more than in the present situation, but it decreases dramatically downstream of the extension and along the access channel. This means that after extension of the breakwater, scouring at the tip of the breakwater will be more than in the present situation. The effect of extension of the breakwater on easterly flow was computed resulting in a 10% to 15% increase of the flow velocity at various locations. Finally, the resulting current condition is separately determined for the present situation, after deepening the channel to 7 m and 8 m depth, and after extension of the breakwater using a quadratic combination of wind-induced currents and wave-driven currents:

$$U = (U_1^2 + U_2^2)^{0.5}$$

5. Sedimentation in the access channel

To determine the rate of sedimentation in the existing access channel, 2DV-SUTRENCH model (developed by Delft Hydraulics) using the stream tube approach was applied. The available wind observation data were schematized in three main classes; calm, moderate and storm condition. The channel extends up to about 360 m far from the basin entrance.

The current velocity along the stream tubes was derived from the quadratic combination of wind-induced currents (TRISULA) and wave-driven current (ENDECV). The results of the computations for the present situation show an annual deposition of approx. 110,000 m^3 which is in a good agreement with the reported annual maintenance dredging (105,000 m^3). The results show that 87% of the sedimentation is due to sediment carried by currents from west to east, mostly in storm situation. .

The computational results show that by deepening of access channel to 7 m and 8 m, the annual sedimentation will increase to about 210,000 m^3 and 300,000 m^3, respectively. The results show that the increase of access channel depth and length both will lead to larger sedimentation volumes.

6. Sediment deposition inside the basin

To study the deposition problem in the basin of Nowshahr harbor, the annual rate of deposition was computed using SILTHAR program (developed program by Delft Hydraulics). The deposition due to horizontal eddy in the harbor entrance was considered in three wind situation; calm, moderate and storm. The computation was carried out for sand and silt separately. The sand concentration in front of the entrance was derived from SUTRENCH computations. The results of the computations show that the sand deposition is in the order of 6,000 m^3/year.

Computational results show that the deepening of the access channel does not have severe effect on deposition inside the harbor but from economical point of view the total increase of deposition in the harbor area has to be studied in more detail.

7. Coastline development

To study coastline development in the Nowshahr area Unibest model (LT module) was used. Firstly, the longshore sediment transport was determined using Bijker and Van Rijn formula in the model. The computational results show a net longshore sediment transport for initial coastline (before harbor construction) of about some 470,000 and 300,000 m^3/year from west to east by Bijker and Van Rijn

formulas respectively. The computational results show a net longshore sediment transport for present situation of about some 370,000 and 230,000 m^3/year from west to east by Bijker and Van Rijn formulas respectively. The littoral drift is mainly from west to east, which is generated by the waves in the sector of west to north due to severe storms in this sector. The littoral drift from east to west is about 12% of the westerly littoral drift.

7.1 Future situation of coastline development

To have an idea of future coastline development, the coastline model (UNIBEST, developed by Delft Hydraulics) was run from present situation up to 2020and the computational results of sediment bypass for each 5 years were determined (Figure 5). Based on crude computation it is concluded that the rate of annual sediment by-pass may decrease dramatically (from about 250,000 to 100,000 m^3/year) after extension of the breakwater and then it may decrease more due to severe coastline retreat of sea-level rise. The computations show that the effect of extension of the breakwater on sediment transport is considerable and makes high accumulation west of the breakwater resulting high erosion east of the harbor. The computational results show that the effect of sea-level rise in the area on longshore transport and coastline changes is significant.

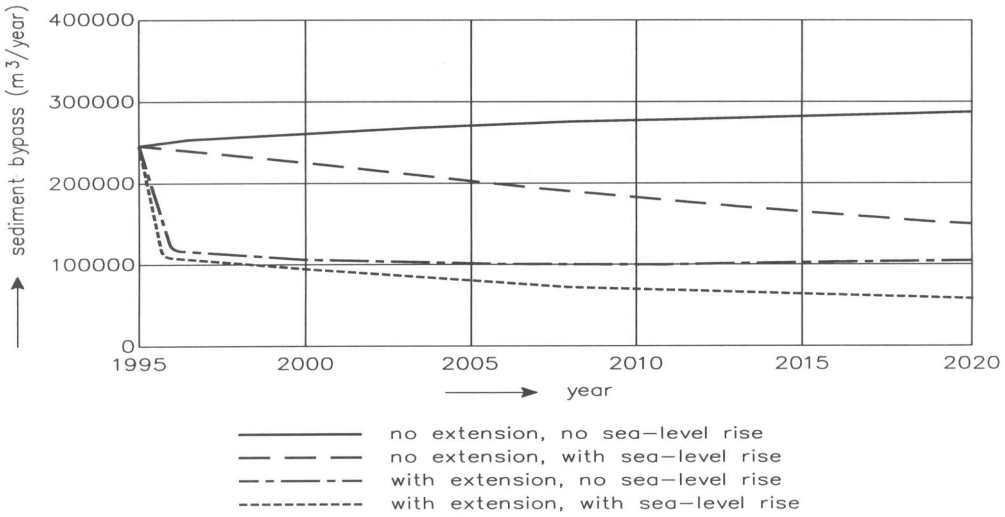

Figure 6: Prediction of future coastline development

8. CONCLUSI ONS & RECOMMENDATIONS

As the deepening of the channel to 7 and 8 m depth makes extra maintenance dredging in the order of 2 to 3 times as in the present situation, hence, deepening of the channel has to be studied very carefully from economical point of view.

The extension of the breakwater can cause a large volume of scouring at the tip of the breakwater, therefore, it is strongly recommended to make a toe protection near the tip of the western breakwater.

The extension of the breakwater will decrease the rate of the maintenance dredging in the channel and basin but in will cause more accumulation west of the breakwater and corresponding coastline changes, hence, these two effects should be considered for future study.

After extension of the breakwater it is to be expected that in future recession of the coastline will occur east of the harbor if no adequate protection will be done.

To do detailed studies for the future sedimentationand coastline development, the required mathematical models like Hiswa, Sutrench and Unibest, etc should be used.

The calibration of two or three-dimentional models is very essential.

Long term wind observations and a wide range of relevant measurements for salinity, river discharge, sea-level rise, water temperature, etc. are required

The required field measurements are proposed below:

1- continious wave measurements in deep water area using wave rider (H, T, etc)
2- Wave measurements in shallow water (at least one year) using wave rider bouy (H, etc)
3- Bed level sounding around the harbor area (5000 m *4000 m).
4- Bed sampling in some locations inside and outside the harbor and along the channel
5- Flow track measurements, atleast at one station near the tip of the breakwater
6- River discharge and sediment discharge of river in different seasons
7- Sediment concentration in somelocation particularly in front of the entrance

Reference:

Bialard, J.A., 1981: An energetics total sediment transport model for asloping beach. J. Geophys. Res., Vol. 86, no. C11, pp, 10, 938-10, 954.

Bakker, W.T., 1968: The dynamic of a coast witha groyne system, Proc. 11th Coastal Eng. Conf., ASCE, pp. 492-517.

Berg, L. S., 1934. Caspian Sea level foe the historical period. Problemy Fizicheskoi Geogray, No, 1, p. 11-46

Bijker, E. W., 1980. Sedimentation in channels and trenches. Proc. 17th Conf. On Coastal Eng., Sydney, Australia, pp. 299-300.

Bruun, P., 1962. Sea-level rise as a cause of shore erosion. Journal of the Waterways and Harbors Division. ASCE, Vol. 88, No. WW1.

Delft Hydraulics, 1987. Neka Power Plant Project.

Eysink, W.D., 1989. Sedimentation in harbour basins. Small density deifferences may cause serious effect. Report H417, Delft Hydraulics.

Herbich, J.B., 1992. Handbook of Coastal and Ocean Engineering, Vol. 3, Harbors, Navigational Channels, Estuaries, Environmental Effects, Houston Gulf Publishing Company.

Komar, P.D., 1979. Beach slope dependence of longshore currents. Journal of waterway, Port, Coastal and Ocean Division, Vol.105, WW4.

NEDECO Report, 1973. Master plan study of Iranian Harbors.

Rodinov, S.N., 1994. Global abd regional climate interaction: The Caspian Sea Experience. Water Science and Technology Library, Volume 11, Kluwer Academic Publishers, The Netherlands.

Rijn, L.C. van, 1985. Two-deimentional vertical mathematical model for suspended sediment transport by currents and waves. Report S488-IV, Delft Hydraulics, The Netherlands.

Water Exchange between Tokyo Bay and the Pacific Ocean during Winter

TETSUO YANAGI* AND HIROFUMI HINATA**

** Research Institute for Applied Mechanics, Kyushu University, Kasuga 816-8580, Japan*

*** Institute for Infrastructure and Harbor, Ministry of Infrastructure and Transportation, Yokosuka 239-0826, Japan*

Abstract:

Variability in water exchange time between Tokyo Bay and the Pacific Ocean is investigated based on the results of intensive field observation during winter from 2000 to 2001. Variability in water exchange time between Tokyo Bay and the Pacific Ocean during winter mainly depends on the variability in northerly monsoon. When the warm water mass approaches to the mouth of Tokyo Bay through the eastern channel of Sagami Bay, which connects Tokyo Bay and the Pacific Ocean, water exchange time becomes longer because the warm water mass is blocked in the surface layer at the bay mouth. On the other hand, when the warm water mass approaches to the mouth of Tokyo Bay through the western channel of Sagami Bay, water exchange time becomes shorter because the warm water mass intrudes into the middle or lower layers of Tokyo Bay. Such different behavior of warm water mass from the Pacific Ocean is due to the difference of water temperature of approaching warm water mass, that is, water temperature of warm water mass through the eastern channel is higher than that through the western channel.

1. Introduction

Water exchange between Tokyo Bay and the Pacific Ocean during winter, when the sea surface cooling and the northerly monsoon dominate, is affected not only by the meteorological variability but also by the variability of oceanic condition in the Pacific Ocean. Yanagi et al. (1989) showed that a thermohaline front was developed at the mouth of Tokyo Bay during winter and Yanagi and Sanuki (1991) showed that the intrusion of warm water mass from the Pacific Ocean to Tokyo Bay is blocked by this front. On the other hand, Hinata et al. (2000) showed that the thermohaline front at the mouth of Tokyo Bay was developed only when the warm water mass approached to the bay mouth from the Pacific Ocean and the approaching warm water mass from the Pacific Ocean intruded into the middle or lower layers of Tokyo Bay.

The blocking or intrusion of approaching warm water mass depends on the relation between the density of the surface water in Tokyo Bay and that of the warm water mass from the Pacific Ocean. As the density of the surface water in Tokyo Bay during winter depends on the river discharge and the sea surface cooling, and the density of the warm water mass from the Pacific Ocean depends on the Kuroshio variability (Yanagi and Isobe, 1992), both phenomena of Yanagi and Sanuki (1991) and Hinata et al. (2000) may occur at the mouth of Tokyo Bay. Such variability of the oceanic condition at the mouth of Tokyo Bay may affect the variability of water exchange time between Tokyo Bay and the Pacific Ocean.

We conducted an intensive field observation in and out of Tokyo Bay to elucidate the variability of water exchange time between Tokyo Bay and the Pacific Ocean during winter from 2000 to 2001. The results of this intensive field observation and obtained new information are shown in this paper.

2. Field observation

An intensive field observation was conducted in and out of Tokyo Bay from November 2000 to March 2001.Water temperature and salinity 0 m, 5 m, 10 m, 20 m, 30 m and 50 m below the sea surface at Stns.1-7 (Fig.1) were observed by thermister and salinometer every 10 minutes from 29 November 2000 to 10 March 2001.Current every 1 m at Stn.6 were observed by ADCP (Acoustic Doppler Current Profiler) every 20 minutes during the same period. Two HF radars (24.515 MHz and 100 W, distance of 84 km, resolution of 1.5 km and 7.5 degree) were deployed at Chigasaki and Mera in Fig.1 and surface currents in Sagami Bay were observed every one hour during the same period.

3. Results

Low-passed northward current variations 10 m, 25 m and 50 m below the sea surface at Stn.6 are shown in Fig. 2 with the low-passed northward wind velocity at Daini-kaiho. In average, low-passed current 10 m below the sea surface is directed southward but those 25 m and 50 m below the sea surface northward at Stn. 6 of the mouth of Tokyo Bay. This means that an estuarine circulation, which flows offshoreward in the upper layer and landward in the lower layer, was dominant in Tokyo Bay even in winter from 2000 to 2001. Moreover, southward current 10 m below the sea surface and northward current 50 m below the sea surface are strengthened when the northerly wind is developed. This means that the wind-driven current by the northerly monsoon intensifies the strength of estuarine circulation in Tokyo Bay during winter. WC and EC show the periods of warm water mass approaching to the mouth of Tokyo Bay through the western channel and the eastern channel of Sagami Bay, respectively. When the warm water mass approaches through the western channel, it intrudes into the middle or lower layers of Tokyo Bay because the density of approaching warm water mass is a little heavier than that of the surface water of Tokyo Bay. On the other hand, when the warm water mass approaches through the eastern channel, it is blocked at the mouth of Tokyo Bay because the density of approaching warm water mass is nearly the same as that of the surface water of Tokyo Bay.

4. Discussion

Water exchange time between Tokyo Bay and the Pacific Ocean is estimated from the average northward residual flow speed in the lower layer at Stn. 6 in each case depending on the northerly wind speed and with or without the warm water mass approaching. The results are tabulated in Table 1. We can understand that the water exchange time becomes shortest when the strongest northerly monsoon blows. When the warm water mass approaches through the western channel, water exchange time becomes shorter but when the warm water mass approaches through the eastern channel, water exchange time becomes longer.

Table 1 Vertically average northward residual flow speed in the lower layer at Stn. 6 and water exchange time in different cases.

	Strong N wind without intrusion (27 Jan. 2001)	Weak N wind without intrusion (10 Feb. 2001)	Weak N wind with intrusion through E Ch. (25 Jan. 2001)	Weak N wind with intrusion through W Ch. (12 Jan. 2001)
Northward flow (cm/s)	7.1	3.5	3.1	4.6
Exchange time (days)	8.3	17.1	18.8	12.9

5. Conclusions

Variability of water exchange time between Tokyo Bay and the Pacific Ocean depends on the variability of northerly monsoon and warm water mass approaching from the Pacific Ocean to the mouth of Tokyo Bay.

Water exchange time becomes shortest when the strongest northerly monsoon blows and it becomes shorter when the warm water mass approaches from the Pacific Ocean to the mouth of Tokyo Bay through the western channel of Sagami Bay but it becomes longer when the warm water mass approaches through the eastern channel of Sagami Bay. This is due to that the densities of approaching warm water mass through the western and eastern channels of Sagami Bay are different.

References

Hinata, H., H.Yagi, K.Yoshioka and K.Nadaoka (2000): Flow structure, heat and material flux at the mouth of Tokyo Bay during warm water intrusion originated from the Kuroshio. Contribution of the Civil Engineering Society of Japan, 656-II-52, 221-238 (in Japanese with English abstract and captions)

Yanagi,T. Isobe,A., T.Saino and T.Ishimaru (1989): Thermohaline front at the mouth of Tokyo Bay in winter. Continental Shelf Res., 9, 77-91

Yanagi,T. and T.Sanuki (1991): Variation of the thermohaline front at the mouth of Tokyo Bay. J. Oceanogr. Soc. Japan, 47, 105-110

Yanagi,T. and A.Isobe (1992): Generation mechanism of thermohaline front in shelf sea. In "Oceanic and Anthropogenic Controls of Life in the Pacific Ocean", ed. by V.I.Ilychev and V.V.Anikiev, Kluwer Academic Publisher, Amsterdam, 11-33

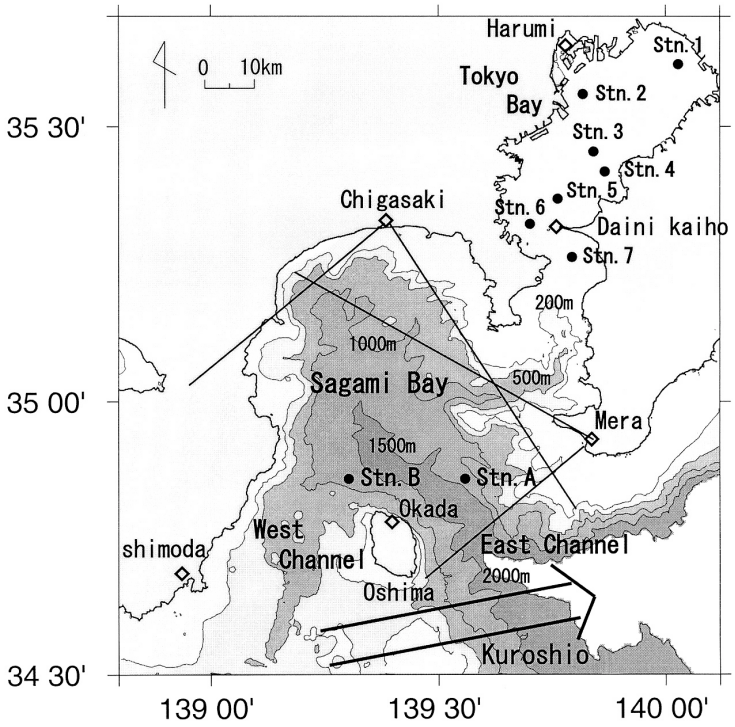

Fig.1 Observation stations in Tokyo Bay and Sagami Bay.

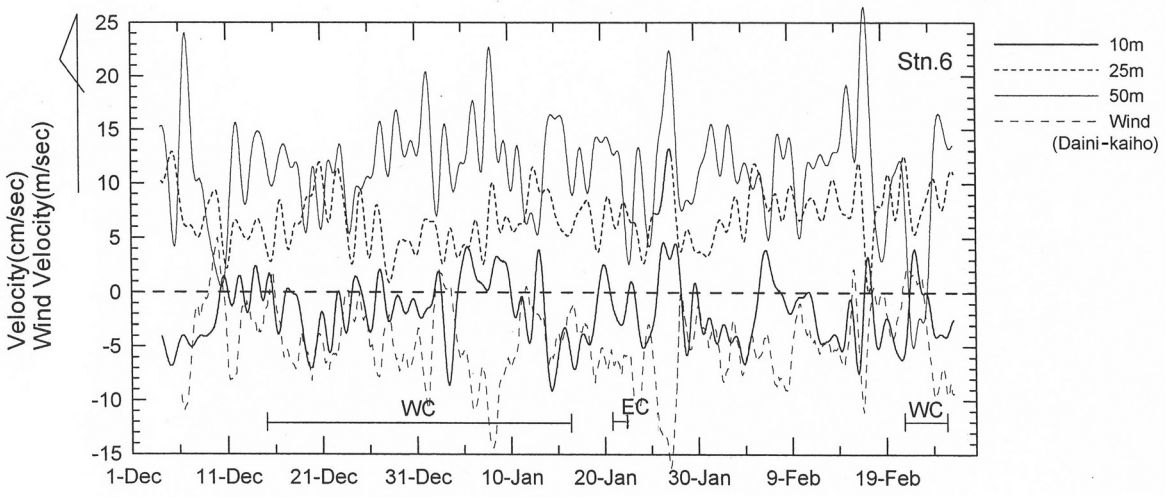

Fig.2 Temporal variations in daily mean northward wind velocity at Daini-Kaiho and northward residual current velocity in the lower layer at Stn.6.

Sand Transport around a Coastal Headland: Portland Bill, Southern UK.

ALEX BASTOS

(School of Ocean and Earth Science, Univ. of Southampton, Southampton Oceanography Centre, SO14 3ZH, Southampton, UK, acb4@soc.soton.ac.uk)

MICHAEL COLLINS

(School of Ocean and Earth Science, Univ. of Southampton, Southampton Oceanography Centre, SO14 3ZH, Southampton, UK, mbc@soc.soton.ac.uk)

1. Introduction

The interaction between coastal headlands and oscillating rectilinear tidal currents results in the formation of tidal eddies (Pingree, 1978; Wolanski et al., 1984; Signell and Geyer, 1991). The significance of coastal headland-eddies on the associated sedimentary processes has been pointed out by different authors, in terms of sandbank formation and/or facies and bedform distribution around headlands (Pingree, 1978; Ferentinos and Collins, 1980; Signell and Harris, 2000; and Bastos et al., in press). However, the effects of transient eddies on the instantaneous patterns of sediment transport still require investigation.

Using a numerical simulation of the real environment, this investigation examines sand transport processes around a coastal headland (Isle of Portland, Southern UK, Fig.1). Likewise, the response of these processes in relation to the formation and evolution of tidal eddies. The inner shelf area under investigation is subject to semi-diurnal tides, with amplitudes of 2.4 m at Portland during spring tides. Overall over the region, the tidal currents tend to increase offshore and towards Portland Bill. Maximum spring current speeds, near the water surface, reaches up to 3.60 m s^{-1}, at the tip of Portland Bill.

The principal objective is to study the potential patterns of sand movement (as bedload) and seabed mobility during the development of headland-associated eddies. Further, to examine how comparable are the final results of net (bedload) sand transport, with the tidally-induced residual circulation, in terms of sandbank formation and sedimentary facies distribution.

2. Methods

The study was undertaken using a 2-D finite element hydrodynamic model (TELEMAC, provided by HRWallingford (Hervouet, 1991)) combined with a sediment transport model (SEDTRANS, provided by the Geological Survey of Canada (Li and Amos, 1995)). Results from TELEMAC were provided, to the authors, by HR Wallingford in the form of original TELEMAC output files. These files correspond to two tidal cycles (25 hours) during spring and neap tides. The results are referred to the tidal signature only, with no consideration given to wind-driven currents.

SEDTRANS is an ANSI standard FORTRAN-77 numerical model. The model calculates bottom shear stress (for currents alone or under combined (wave and current) flows) and sediment transport rates, for input data of depth, current, wave, bed roughness and grain size. For the present study, the simulations were carried out assuming a uniform grain size distribution over the inner shelf, due to the complex patterns of sediment distribution (including coarse lag deposits and bedrock outcrops (Bastos et al., in press). Three types of seabed were investigated: a coarse sand bed (D_{50} = 1 mm); a medium sand bed (D_{50} = 0.5 mm); and a fine sand bed (D_{50} = 0.25 mm).

Threshold of sediment movement were calculated using SEDTRANS and compared with results obtained by flume experiments. The potential for bedload transport is investigated every 15 minutes (time-step).

Depth-averaged current data were input from the results obtained from TELEMAC. Bed shear stress and sediment transport rates were calculated by SEDTRANS, at each point of the original grid (triangular element mesh) imported from TELEMAC. Near-bed currents (1m above the seabed) were calculated using SEDTRANS, by assuming a logarithmic velocity profile law. The bed shear stress under currents alone was calculated by applying a quadratic friction law, using a friction factor (f_c=0.006) based upon the field experiments of Sternberg (1972).

$$\tau_b = 0.5\rho f_c u_{100}^2$$

Where, τ_b is the bed shear stress, ρ water density and u_{100} is the current speed 1 m above the seabed. Potential bedload transport rates were predicted/calculated, using the algorithm proposed by Gadd et al. (1978), for currents alone.

$$q_s = \left(\beta / \rho_s\right)(u_{100} - u_{cr})^3$$

Where q_s is the bedload transport rate, β is an empirical coefficient (1.73 x 10^{-3}), ρ_s is sediment density, and u_{cr} is the critical velocity for the initiation of bedload transport.

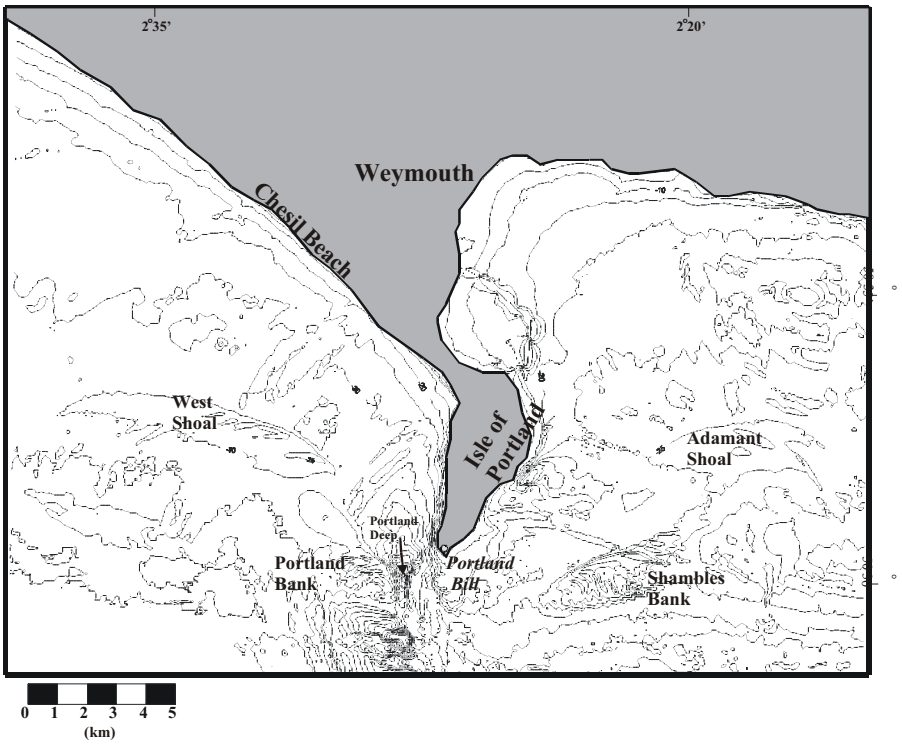

Figure 1: Area under investigation, showing main bathymetric features (Note: bathymetry in meters, relative to Chart Datum).

3. Sand Transport

By simulating the potential bedload sand transport around a coastal headland, the non-linear nature of sediment transport is taken into consideration i.e. instead of assuming that residual water circulation represents patterns of sediment transport. Because sand transport rates are calculated here based upon the excess shear stress (where a critical threshold value must be reached before sediment initiates movement), instantaneous sand transport patterns do not necessarily follows the same transient pattern as that of the tidal flow. Herein, this concept is observed clearly during the formation and evolution of

tidally-induced transient eddies. Analysis of the hourly time steps during the tidal cycle, has revealed that during the formation of the tidally-induced transient eddies, no current-induced bedload eddy is formed for either of the sand beds. The simulation of instantaneous sand transport over the tidal cycle has shown that most of the bedload transport process occurs during the period of maximum flood and ebb flows. At such times, gradients in bed shear stress and transport rates are also at maximum.

The significance of this pattern, to the understanding of sand dispersal around the headland, relies upon the fact that these instantaneous gradients in transport rates occur upstream and downstream of the headland during the same part of the tidal cycle. Nevertheless, considering that currents, shear stress and bedload transport rates are at maximum at the tip of the headland, over the entire tidal cycle, a reverse in the transport rate gradient is observed as the flow passes the headland.

Thus, net sediment transport around a coastal headland represents instantaneous gradients in bedload transport rates, during flood and ebb flows, rather than the average flow. These gradients in transport rates lead to the formation of two distinct sand-mobile zones:

a) The *inner sand transport zone*. This zone is characterised by resultant sand transport towards the tip of the headland i.e. southward on both sides of the headland, followed by a downstream increase in the transport rate gradient. Ebb and flood currents are constrained by the coastal geometry; they flow parallel to the coastline, then veer towards the south (with increased velocities), to follow the headland coastline. This zone is associated with the sand transport enhanced by the maximum ebb and flood currents; these flow parallel to coastline on the eastern and western sides, respectively.

b) The *outer sand transport zone*. This zone is situated offshore from the tip of the headland; it is defined by sand transport away from the headland, with a downstream decrease in the transport rate gradient. At the tip of the headland, the currents reach their maximum speed and a bottom frictional torque is induced, producing vorticity. When the flow leaves the tip of the headland, vorticity is advected away into the flow, which starts veering towards the north. Because of these increased speeds at the tip of the headland, the currents leaving the headland are very strong and bedload transport rates are high. This process forms the outer sand transport zone, which is characterised by a veering in the sand transport vectors towards the north.

The boundary between the inner and outer zones defines a zone of bedload convergence. Consequently, this zone can be recognised on both sides of the headland, coinciding with the presence of sandbanks (the Shambles and Portland Banks, Fig. 1). At the tip of the headland, a zone of maximum erosion occurs.

Furthermore, the occurrence of a suite of bedforms and sedimentary facies, described elsewhere (Bastos et al., in press) reinforce the results obtained here i.e. that the residual circulation is not appropriate to be used as a net sediment transport indicator. The sand transport pathways, indicated by the asymmetry of large and very large sandwaves, corroborates the prediction of net bedload transport, as well as the occurrence of sandbanks associated with the bedload convergent zones.

4. Conclusions

The instantaneous bedload sand transport patterns do not necessarily follow the same transient pattern as that of the tidal flow; this is because sand transport rates are derived here on the basis of the excess shear stress, i.e. a critical threshold value must be reached, before the initiation of sediment movement. The numerical simulation has revealed that, during the formation of the tidally-induced transient eddies, no current-induced bedload eddy is formed for either of the sand beds.

Local characteristics and irregularities, in coastal and seabed morphology around the headland should be considered as a parameter for modelling tidal and sand dispersal around headlands. Despite the same magnitude of different length-scale parameters (such as tidal excursion, headland dimensions and bottom friction), net sand transport rates do not follow the pattern of residual (water) circulation

over the study area. Neither could the concept of sandbanks occurring in the centre of residual eddies be verified.

Sediment transport and erosion around coastal headlands is defined by the presence of a zone of maximum erosion at the tip of the headland (maximum transport rates) and by occurrence of two distinct zones of sand transport: (a) an *inner zone* showing sand transport towards the headland, following an increase gradient in the sand transport rates; and (b) an *outer zone* showing sand transport away from the headland, following a decrease in the transport rate gradient.

Acknowledgments: During the research, the first author (ACB) was supported by a Scholarship awarded by the Conselho Nacional de Pesquisa (CNPq, Brazil). The authors would like to acknowledge: HR Wallingford and Wessex Water Authority, for providing the output data from TELEMAC; and the Geological Survey of Canada, for providing the SEDTRANS92 model.

References:

Bastos, A.C., Kenyon, N.H. and Collins, M.B., Sedimentary processes, bedforms and facies, associated with a coastal headland: Portland Bill, Southern UK. *Marine Geology*, *in press*

Ferentinos, G. and Collins, M. B.,. Effects of shoreline irregularities on a rectilinear tidal current and their significance in sedimentation processes. *Journal of Sedimentary Petrology, 50(4)*, 1081-1094, 1980

Gadd, P. E., Lavelle, J. W., and Swift, D. J., Estimate of sand transport on the New York shelf using near-bottom current meter observations. *Journal of Sedimentary Petrology, 48*, 239-252, 1978.

Hervouet, J. M., TELEMAC, a fully vectorised finite element software for shallow water equations. HE43/91-27, Electricite de France, 1991.

Li, M. Z. and Amos, C. L., SEDTRANS92: A sediment transport model for continental shelves. *Computers & Geosciences, 21(4),* 533-554, 1995.

Pingree, R. D., The formation of the Shambles and other banks by tidal stirring of the seas. *Journal of the Marine Biological Association U K, 58*, 211-226, 1978.

Signell, R. P. and Geyer, W. R., Transient eddy formation around headlands. Journal of *Geophysical Research, 96(C6)*, 2561-2575, 1991.

Signell, R. P. and Harris C. K., Modeling sandbank formation around tidal headlands. In *Proceedings 6th International Conference Estuarine and Coastal Modelling*, edited by Spaulding, M.L. and Blumberg, A.F., New Orleans, LA, November 1999. ASCE Press, 2000.

Sternberg, R. W., Predicting initial motion and bedload transport of sediment particles in the shallow marine environment: In *Shelf sediment transport, processes and pattern*, edited by Swift, D. J., Duane, D. B., and Pilkey, O. H., Dowden, Hutchison and Ross, Inc., Stroudsburg, Pennsylvania. pp61-83, 1972.

Wolanski, E., Imberger, J., and Heron, M., Island wakes in shallow coastal waters. *Journal of Geophysical Research, 89*, 10553-10569, 1984.

Modeling Sediment Dynamics at the Outer Delta of the Texel Tidal Inlet

Hans Bonekamp, (*Faculty of Civil Engineering and Geosciences, Delft University of Technology, P.O. Box 5048, 2600 GA Delft*, j.g.bonekamp@ct.tudelft.nl)

Sandra Vermeer, (*Department of Physical Geography, Utrecht University, P.O. BOX 80.115, 3508 TC Utrecht*, s.vermeer@geog.uu.nl)

1 Introduction

Ebb tidal delta's are key elements of a barrier coastal system. They have the capacity to distract or to provide large amounts of sand to the adjacent coastal system and the tidal basin. Despite these important functions, ebb tidal delta's belong to less well studied coastal environments. The main reason is the complexity of the wave and current action. The focus of the Dutch research program "Outer Delta Dynamics" is to enhance the scientific understanding of the morphology of ebb tidal delta's. The program consorts observational and numerical research, the latter with both idealized and quasi-realistic models.
The goal of this particular study is to identify the main mechanisms for sand transport at the well-observed ebb tidal delta of the Texel Inlet. Measured decadal displacements of sand banks and channels are compared with simulations of transports from a quasi-realistic numerical model.
The analysis in this first study is restricted to tidally driven motions. Depth-averaged sand transports are modeled with the transport model of *Groen* [1967] on the basis of an harmonic analysis of the flow. The area of consideration is confined to the Northern Extension of the Texel Outer Delta (NETOD, see Figure 1, top left panel). This area is separated from the remainder of the outer delta by a large shoal called the *Noorderhaaks* (see bottom of Figure 1, top right panel). The main morphological developments of the NETOD are discussed.

2 Observed Shoal and Channel Developments

Every three years, the Dutch National Institute of Coastal and Marine Management publishes high-resolution (20 m) two-dimensional data of the measured nearshore depth. In Figure 1 some recent bathymetries of the NETOD area are plotted. The corresponding erosion and sedimentation pattern (Figure 2, top left panel) summarizes the morphological changes. One can distinguish three important developments: (1) an eastward movement of the large bar in the North, (2) a new ebb channel marked by a large ebb chute, (3) the development of channel just northward of the *Noorderhaaks*. These developments may form a threat to the coast of Texel island and the nearby marine pathways.

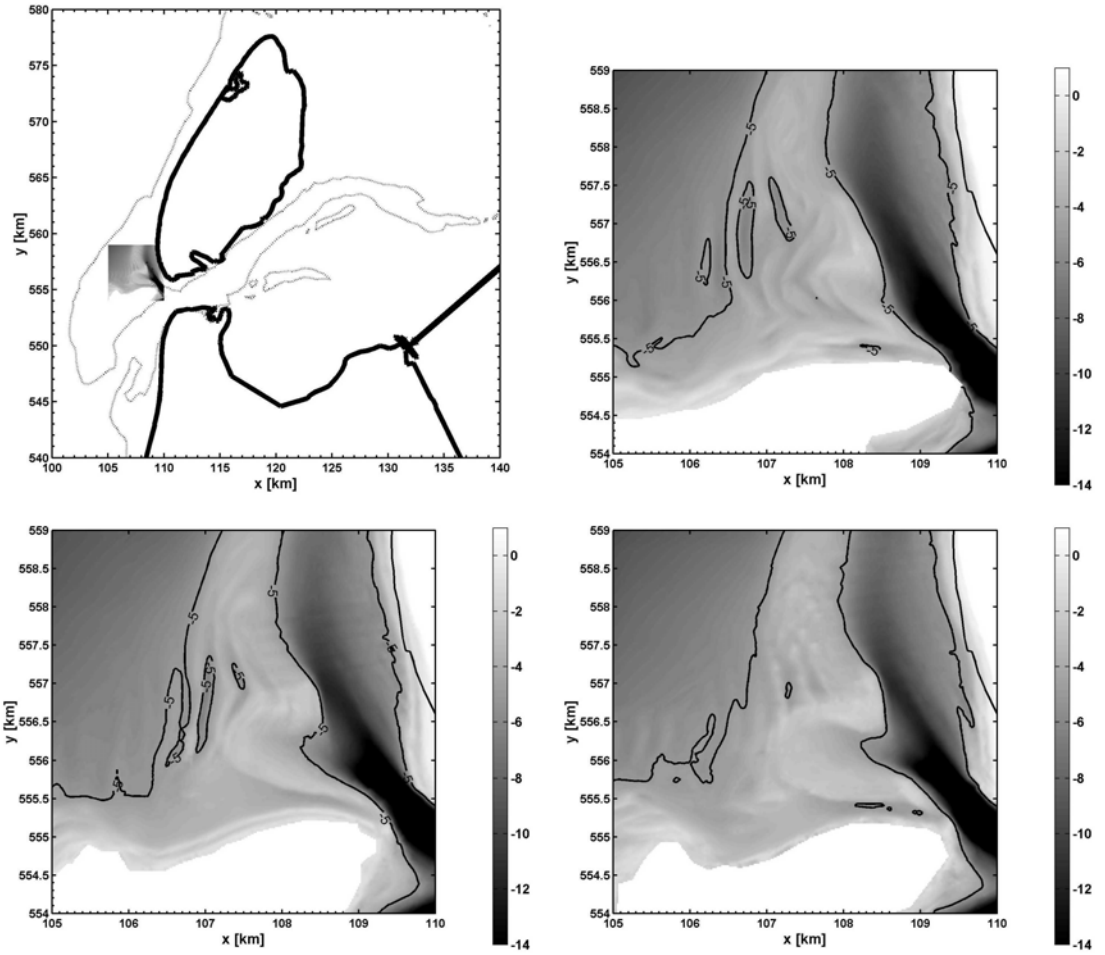

Figure 1: Top left panel: Area of consideration. In addition, the bathymetry of the Northern extension of the Texel Outer Delta measured in the years 1991 (top right panel), 1994 (bottom left panel), and 1997 (bottom right panel).

3 Flow Simulations

To obtain realistic simulations of the flow at the Texel Inlet and its outer delta, nested model runs for the Southern North Sea, the Western Wadden Sea and the Texel Inlet have been performed with the DELFT3D system (see, e.g., *Roelvink & van Banning* [1994]). The DELFT3D-FLOW module solves the shallow water equations. It is run in a depth-averaged mode.

Specific attention has been paid to the calibration of the tides in the flow simulations. Not only water levels measurements at observing stations in the vicinity have been used, but, importantly, also the long-term flow measurements by an Acoustic Doppler Current Profiler (ADCP) attached to the ferry of Texel [*Ridderinkhof et al.* 1999]. The latter have been applied to correct the amplitudes and the phases of the main tidal constituents (e.g. M2, M4, M6, S2) at the model boundaries. Details of the model runs and the calibration

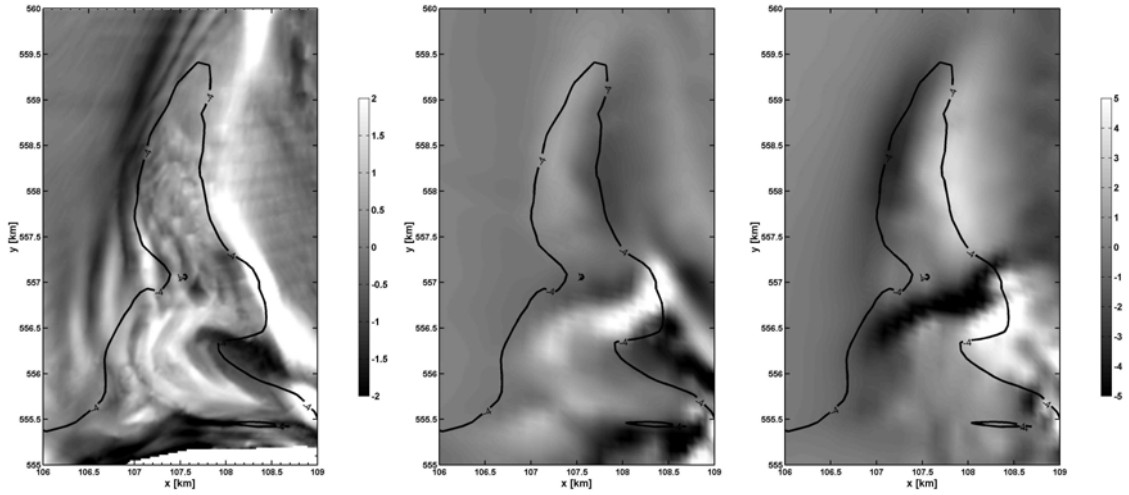

Figure 2: Left Panel: Observed erosion (black) and sedimentation (white) over the years 1991-1997. Middle Panel: Calculated erosion (black) and sedimentation (white) due to the M0-M2 tidal asymmetry in the bed load transport. Right Panel: See middle panel but for the M2-M4 tidal asymmetry in the suspended transport. NB. the middle and right panel are rescaled. Therefore, the absolute magnitude of transports are meaningless.

are presented in *Bonekamp* [2002].

4 Analysis of Sediment Transport

The morphological developments of the NETOD will be strongly influenced by both the wind- (surface wave) and the tide-driven motion. To appreciate their relative importance both influences should be investigated. This study, however, concentrates on the tide-driven sediment transports. In particular, the effects of tidal asymmetries (e.g. *van de Kreeke & Dunsbergen* [2000]) are investigated.
The analysis of sediment motion is based on the simple model of *Groen* [1967]. In this model the concentration of suspended material is given by

$$\beta \dot{c}/\omega + c = c_{equi}, \qquad \beta \geq 0, \tag{1}$$

where $c_{equi} = |\boldsymbol{u}|^2$, ω the angular frequency of the main (M2) tide. The tidally averaged transport of sediment is given by $\boldsymbol{q} =< c\boldsymbol{u} >$. The factor β determines the relative importance of the settling lag of fine sediment. As in the study of *Ridderinkhof* [1997] for the Ems-Dollard Estuary, β is set to 1 for suspended transport. For $\beta = 0$, the concentration adjusts instantaneously with the flow. In this way bed load transport is modeled by just an u^3-law. Analytical approximations for the tidally averaged bed load and suspended transports are obtained by considering only the rest current (M0), the M2, and M4 constituents of the flow. In this way, the main tidal asymmetries (M0-M2 and M2-M4) are evaluated.

5 Results

Figure 2, middle panel, demonstrates that, on the one hand, bed load transports (in particular the M0-M2 interaction), may explain the development of the ebb chute of the new channel in the NETOD area, but, on the other hand, may counteract the eastward movement of the northern bar. For suspended transports (in particular, the M2-M4 interaction, see right panel) the argument is just opposite. Calculated transports are equivocal with respect to the development of the channel just northward of the *Noorderhaaks*. This channel is possibly poorly captured by the model. Further work will include comparisons with full morphological calculations and a model analysis of wind (wave) driven effects.

References:

Bonekamp J.G., Comparisons of Observed and Process-Oriented Modeled Water Motion and Sediment Transport in Tidal Inlets, *Proceedings of International Conference on Coastal Engineering 2002, Cardiff*, 2002 (to appear).

Groen, P., On the residual transport of suspended matter by an alternating tidal current, *Neth. J. Sea Res.*, *3*, 564–674, 1967.

Ridderinkhof, H., The effect of Tidal Asymmetries on the Net Transport of Sediments in the Ems Dollard Estuary, *Journal of Coastal Research,25*, 41–48, 1997.

Ridderinkhof H., Van Haren H., Eijgenraam F., and Hillebrand T. Ferry observations on temperature , salinity and currents in the Marsdiep tidal inlet between the North Sea and the Wadden Sea, *Proceeding of the EUROGOOS conference 1999, Rome*, Elsevier, 1999.

Roelvink, J. A. and G. K. F. M. van Banning, Design and development of DELFT3D and application to coastal morphodynamics, *Hydroinformatics 1994*, Balkema, Rotterdam, 451–455,1994.

Van de Kreeke, J. and D. W. Dunsbergen, Tidal asymmetry and sediment transport in the Frisian inlet, *Interactions between Estuaries, Coastal seas and Shelf seas*, T. Yanagi, ed., Terra Scientific Publishing Company, 139–159, 2000.

Buoyancy Driven Current during Cooling Periods in Ise Bay, Japan

TATEKI FUJIWARA

(Graduate School of Agriculture, Kyoto University, Kyoto, Japan, fujiwara@kais.kyoto-u.ac.jp)

1. Introduction

The process of convection in rotating fluids has been intensively studied over the last decade. It has been revealed that the convection phenomenon is sensitive to spatial inhomogeneities in the cooling intensity and to the preexisting stratification. As a result, lateral gradients in density and mixed-layer depth are formed. These lateral density gradients drive a thermal-wind circulation. The shear of the thermal-wind modifies upright convection to slantwise convection; the overturning fluid moves systematically in slanting paths and maintains a nonvanishing stratification [*Haine and Marshall,* 1998; Review by *Marshall and Schot,* 1999].

Spatial inhomogeneities in buoyancy flux and stratification are typical aspects of water in regions of freshwater influence (ROFI). Buoyancy is supplied laterally from the river mouth as freshwater discharge and lost upward through the sea surface as heat. In general, the stratification is stronger near the river mouth than in the offshore area due to salinity stratification. Therefore, it is expected that cooling exerts an influence on both freshwater spreading and basin-wide estuarine circulation in ROFIs.

In this work, we have studied a buoyancy driven current and resultant basin-wide estuarine circulation in Ise Bay, Japan during a cooling period. We have made use of the following working hypothesis: that surface cooling causes convection and mixed-layer deepening in the bay whereas the mixed-layer remains shallow in the region where river plume caps the surface; this difference in the mixed-layer depth creates a horizontal density gradient, which drives rotation of the deep mixed-water mass in thermal-wind balance. To verify this hypothesis, we conducted a series of longitudinal hydrographic observations from the bay head (river mouth) to off the bay mouth at roughly 10-day intervals over a period of 1.2 years. Prior to these observations, we simultaneously measured flow structures and density fields by using ADCP and CTD techniques during a cooling period in 1994 [*Fujiwara et al*., 1997]. Flow fields were calculated from the measured density field by using a diagnostic numerical model and compared with the flow fields measured with the ADCPs. This data set was also used to specify the flow structure in the cooling period. In this paper, hydrographic properties and flow structures during cooling period are described and above working hypothesis is verified.

2. Results and discussion

Longitudinal distributions of salinity and temperature measured on 27 October 2000, 26 January 2001 and 13 February 2001 are presented in Figure 1. These dates fall in the early, central, and late stages of the cooling period, respectively. Density distributions (not shown) are similar to the salinity distributions for all dates. Towards the end of October (Figure 1a), hydrographic conditions in the Bay have changed from a strongly stratified to a weakly stratified regime. A well-defined halocline ($31 < S < 32$) separates the upper water from the lower water. The river plume, which is characterized by low salinity ($S < 30$), covers the bay head area from the river mouth to station 3, while well-mixed water, which has salinity 30 ~ 31, occupies the upper 20 m between stations 3 and 5. Hereinafter, we refer to the former and latter areas as the river plume region and the convection region, respectively.

The halocline is shallow in the river plume region (depth ~ 10 m) and deep in the convection region (depth ~ 20 m). The mixed-water mass exhibits a reversed-dome shape in the convection region. We refer to this water mass as a mixed-water lens. Considering the rotational effect, we can expect that this mixed-water lens is rotating anti-cyclonically.

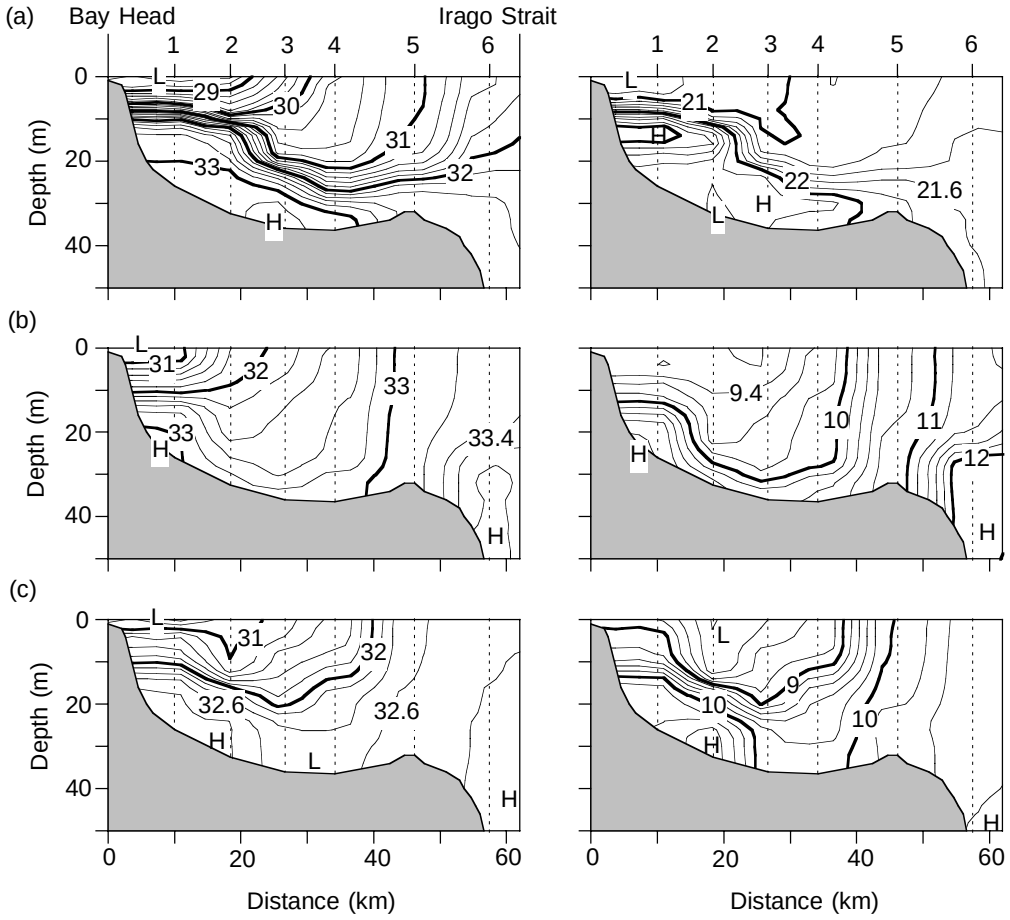

Figure 1 Longitudinal distributions of salinity (left) and temperature (right) observed on 27 October 2000 (a), 26 January 2001 (b), and 13 February 2001 (c). The abscissa is distance from the bay head measured along the thalweg.

The features described above are common to hydrographic conditions measured on other dates. However, the mixed-water mass expands and almost reaches the bottom on 26 January (Figure 1b). The river plume region shrinks in a narrow range near the river mouth, due to the decrease in river discharge. In this region the water is still strongly stratified.

Horizontal distributions of salinity at the surface and at 15 m depth in the late October are represented in Figures 2a and 2b, respectively. The river plume water covers the northern half of the bay (Figure 2a), while homogeneous mixed water ($31 < S < 32$) extends to the southwest of the river plume front ($S = 31$). In contrast to the surface salinity distribution, the salinity at 15 m depth is lower in the south than in the north (Figure 2b). This somewhat peculiar phenomenon is caused by the fact that the halocline is shallower than 15 m in the north and deeper than 15 m in the south. The shaded area, where $S < 32$, represents the area of the convection region. This region is surrounded by a band of crowded isohalines along its northeastern periphery.

Horizontal distributions of the residual flows at the surface calculated by the diagnostic model are depicted in Figures 2c, together with the trajectories of water particles tracked for 6 days (Figure 2d). The surface flow pattern is highly correlated with the salinity distribution at deeper level (Figure 2b). The water in the convection region rotates anti-cyclonically. The water strongly flows along a course traced by the band of crowded isohalines at 15 m depth, which surround the convection region.

An anti-cyclonic circulation occupies the convection region. Due to this circulation, strong southward flow (jet) arises along the east coast. On the other hand, western water in the bay slowly flows to the bay head along the southwestern coast. This direction opposes the direction of the basin-wide estuarine circulation in the upper layer. Because strong flows concentrate in relatively narrow belts, water particles released off the river mouth are conveyed along the meandering pathways on their journey to the sea (Figure 2d).

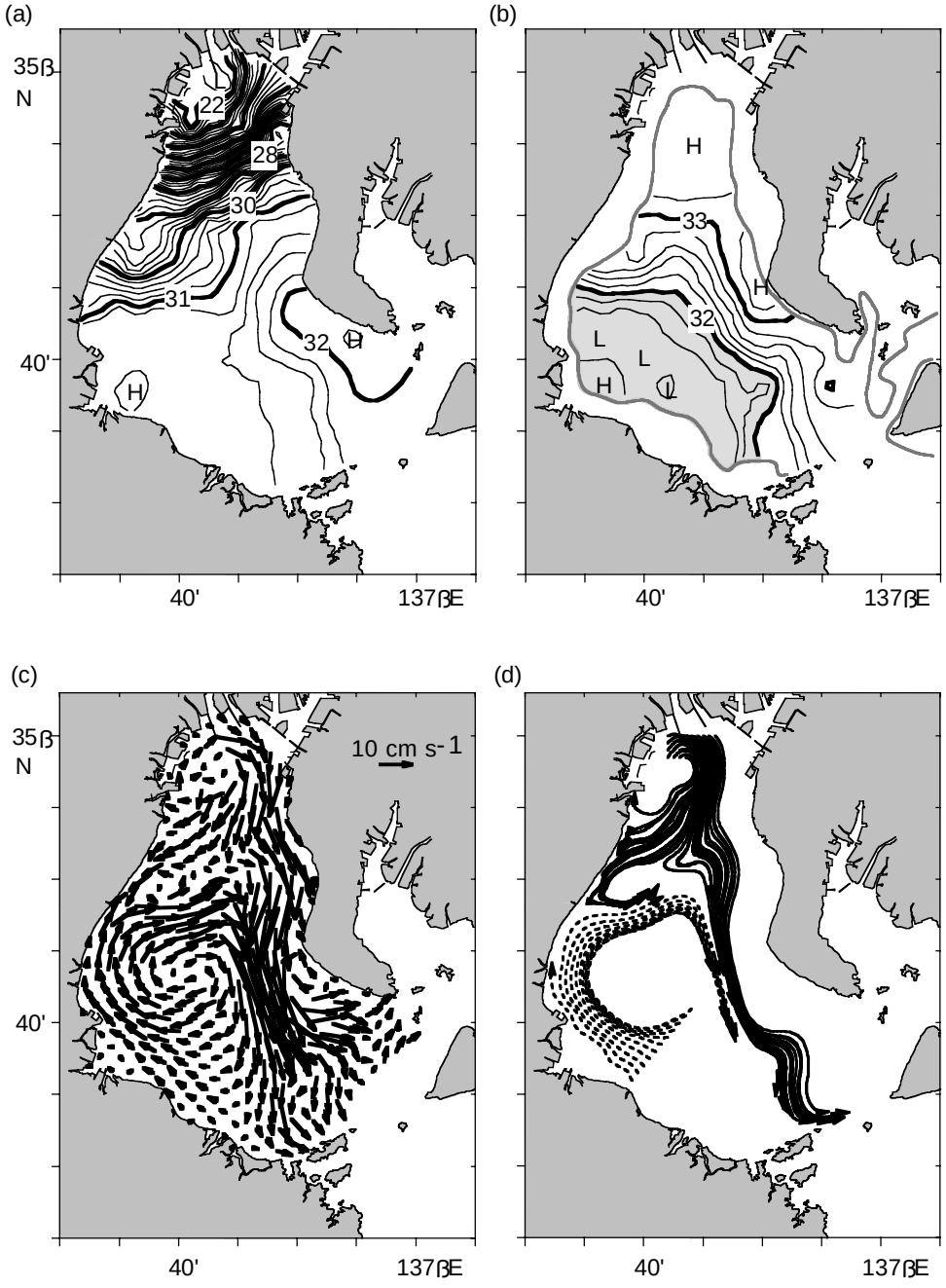

Figure 2 (a) Salinity distribution at the surface, (b) that at 15 m depth measured on 29 and 30 October 1994, (c) flow field at the surface calculated by the diagnostic model, and (d) trajectories of water particles tracked for 6 days.

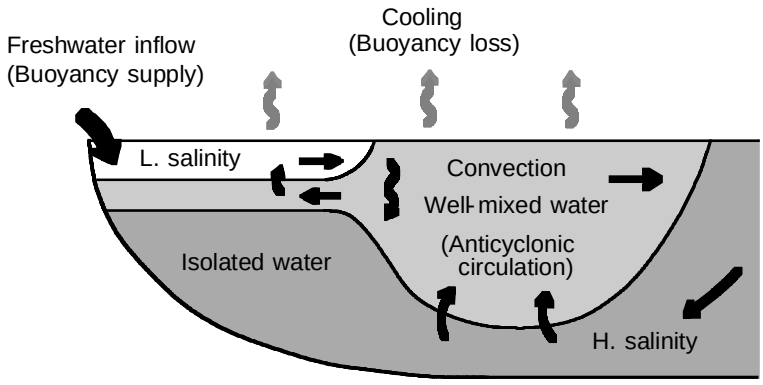

Figure 3 Schematic illustration of hydrodynamic condition and buoyancy driven currents during cooling periods.

The results obtained in this study are schematically illustrated in Figure 3. In the river plume region, strong salinity stratification stabilizes the water column and suppresses convective mixing. Here the pycnocline is shallow, whereas it is deep in the convection region. In the central bay, the deepening of the mixed water generates a light-water lens, which rotates anti-cyclonically under the geostrophic balance. The location of the lens varies depending on the river discharge. In addition, the accompanying anti-cyclonic circulation also changes its location. When the river discharge decreases, the lens approaches the river mouth. The location and size of the circulation exert large influences on the basin-wide flow fields.

Acknowledgments. The auther thanks Y. Sugiyama of Chyubu Electric Power Co., Inc., who conducted the observations in 1994, and also T. Kimura and the crew of R/V *Iseshio* of the Japan Coast Guard, who accomplished the longitudinal observations in 2000 ~ 2001 with A. Kasai of Kyoto University. The auther also thanks Dr. J. P. Matthews for improving this manuscript and appreciates the help of M. Fujihara of Ehime University and S. Kakehi of Kyoto University in the numerical model analysis.

References:

Fujiwara, T., Sanford, L.P., Nakatsuji, K., and Sugiyama, Y., Anti-cyclonic circulation driven by the estuarine circulation in a gulf type ROFI, *J. Marine Systems*, 12, 83 - 99, 1997.

Haine, T. W. N. and J. Marshall, Gravitational, symmetric, and baroclinic instability of the ocean mixed layer, *J. Physical Oceanography*, 28, 634 - 658, 1998.

Marshall, J. and F. Schott, Open-ocean convection: observations, theory, and models, *Reviews of Geophysics*, 37, 1 - 64, 1999.

Role of straits in transport processes in the Seto Inland Seas, Japan

XINYU GUO

(Center for Marine Environmental Studies, Ehime University, 3 Bunkyo, Matsuyama 790-8577, Japan, guoxinyu@dpc.ehime-u.ac.jp)

AKIRA FUTAMURA

(Graduate School of Science and Engineering, Ehime University, 3 Bunkyo, Matsuyama 790-8577, Japan, futamura@ship.yuge.ac.jp)

HIDETAKA TAKEOKA

(Center for Marine Environmental Studies, Ehime University, 3 Bunkyo, Matsuyama 790-8577, Japan, takeoka@dpc.ehime-u.ac.jp)

1. Introduction

As one of the most important coastal water, the material transport processes in the Seto Inland Sea are always an important issue in the Japanese coastal oceanography community (see *Takeoka*[2002] for a review). With the community to attach more and more importance to the role of the nutrient from the open ocean, the processes to distribute the nutrient in the sea must also be paid attention.

One important feature of the Seto Inland Sea is that there are as many as about 1000 islands in the sea. No matter of the size of islands, they form many straits and relatively extensive sea regions (*Nada* in Japanese). Forced by the tide wave from the Pacific, the ability of tide mixing is therefore completely different between the strait and Nada. As expected, tidal front is formed in many places in the Sea (*Yanagi*[1990]). Although the geostrophic component prevents the cross front material transport, the ageostrophic component is suggested to promote the exchange of nutrient between the upper and bottom layer in the stratified region with a path through the mixing region (*Takeoka*[2002]).

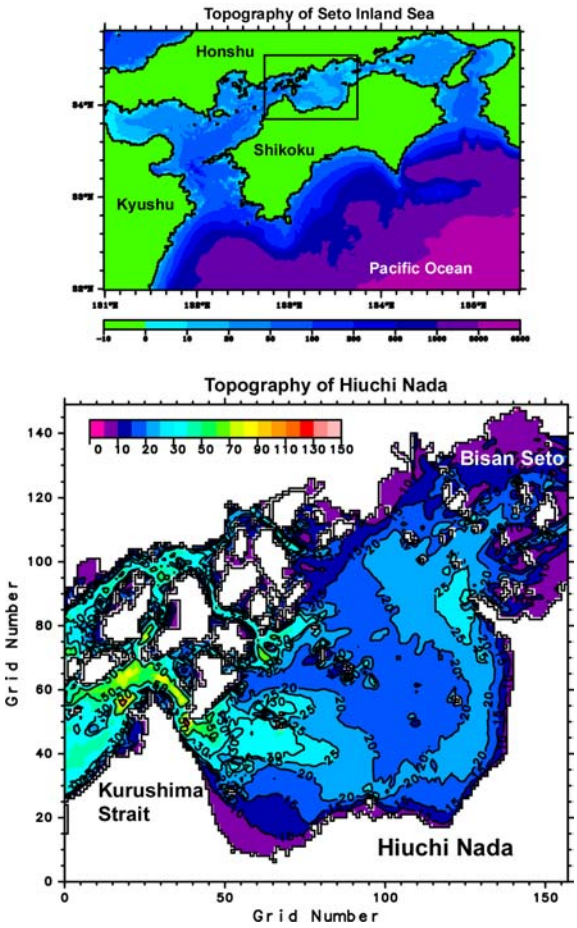

Figure1: Map of Seto Inland Sea (upper panel) and Hiuchi Nada (lower panel)

In this study, we choose Hiuchi Nada (Fig.1) as a representation of such strait-Nada system. Hiuchi Nada is located in the central part of the Seto Inland Sea. Its size is approximately 50km_30km and its average depth is 20m. Except for the Bisan Seto, the river discharge into this Nada is small. Its western and eastern boundaries are the Kurushima Strait and Bisan Seto, respectively (Seto means region of strong current in Japanese). The tide in the Hiuchi Nada is characterised as a standing wave and the M_2 tidal amplitude is about 1m. Along with the sea level change in the Nada, the tidal currents at the Kurushima Strait and Bisan Seto are naturally very strong

and the water there is well mixed throughout a year. On the other hand, as a result of the weak tidal current, the heating in summer usually induces a strong stratification in the eastern part of the Nada where the oxygen-deficient water mass is usually found in the bottom layer.

Up to now, because of the social impact of the oxygen-deficient water mass, the studies in the Hiuchi Nada were almost concentrated on its eastern region. Here we treat the Hiuchi Nada, Kurushima Strait and Bisan Seto as a whole system. With repeated CTD observations over the whole Nada and the use of a numerical model, we want to clarify the distribution of water masses, their formation processes and the related residual current field.

2. Observations and results

Seven times of ordinary CTD observations were carried out in the summers of 2000 and 2001. Figure 2 shows the distribution of CTD stations and Table 1 the dates of each observation and observed stations. The measurements were always finished in one day.

Figure 3 shows the distribution of water temperature at three layers. In the upper layer (2m depth), an obvious warm core exists in eastern region while the western region is low temperature; in the middle layer (10m depth), the central part shows a high temperature while the western and eastern sides shows a little of low temperature; in the lower layer (20m depth), a clear cold core is found in the eastern area. In the northern area, partially mixed warm water exists, which might come from the shallow Bisan Seto.

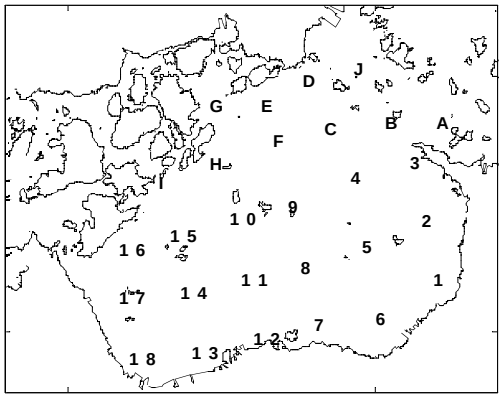

Figure2: Distribution of CTD stations

In general, the vertical difference of temperature increases from Kurushima Strait to the eastern part of Hiuchi Nada. And, the horizontal temperature gradient is relatively weak in the middle layer but strong in the upper and lower layers.

Date	Station
2000 Aug. 1-2	1,2,3,4,5,6,7,8,9,10,11,12,13,14,15,16,17,A,B,C,D,E,F,G,H,I
2000 Aug. 28	1,2,3,4,5,6,7,8,9,10,11,12,B,C,F,G,H
2001 May. 27	4,5,6,8,11,14,17,C,D,E,G,J
2001 Jul. 1	2,3,4,5,8,9,10,11,14,15,16,17,B,C,D,E,F,G,J
2001 Jul. 25	4,5,8,9,10,11,14,15,16,17,C,E,F,G,H,I
2001 Aug. 8	1,2,3,4,5,6,7,8,9,10,11,12,13,14,15,16,17,18,A,B,C,D,E,F,G,H,I,J
2001 Sep. 25	1,2,3,4,5,6,7,8,9,10,11,12,13,14,15,A,B,C,D,E,F,G,H,I,J

Table1: Stations and dates of observations.

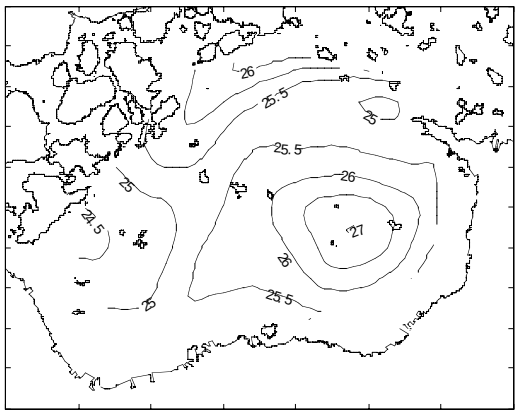

(a). Depth=2m

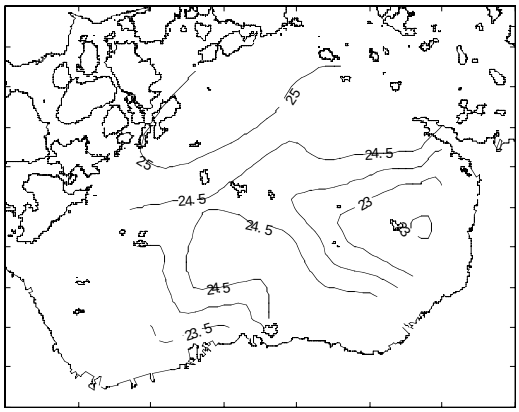

(b). Depth=10m

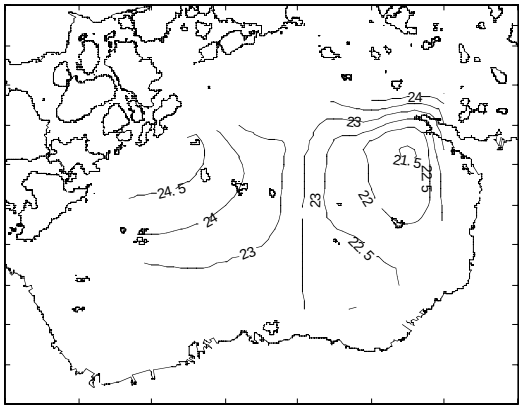

(c). Depth=20m

Figure 3: Horizontal distribution of water temperature at the depth of (a)2m, (b)10m, (c)20m in Hiuchi Nada on Aug.1 2000

3. Numerical model and results

Based on Princeton Ocean Model (POM), a numerical model for the Hiuchi Nada, Kurushima Strait and Bisan Seto is configured. The horizontal resolution is about 500m and there are 20 layers in the vertical. The model are driven by the tidal current, heat fluxes, river discharge, wind stresses and the flow-in or flow-out residual current along its western and eastern boundaries. The necessary harmonic constants of tidal current along the western and eastern boundaries are calculated by a tide model for the whole Seto Inland Sea.

The model results are saved every hour and a digital filter (*Hanawa and Mitsutera*[1985]) is used to remove the tidal signal. In addition to the ordinary diagnostic and prognostic calculation for residual current, several tracer experiments are also carried out in order to clarify the fate of passive material initially set in the Straits and Nada.

Here we only show the variation of sea level and M_2 tidal current during 12 hours (Fig.4) that demonstrates a clear standing wave characteristic. As the sea level reaches its positive or negative maximum value at 1 or 7 h, the tidal current in the Kurushima Strait is weakest; as the sea level becomes almost flat at 4 or 10 hour, the tidal current in the Kurushima Strait is strongest. Moreover, the strength of tidal current varies largely horizontally, that is, in the eastern part of Hiuchi Nada the tidal current is always as weak as 10~20cm/s while those in the Kurushima Strait and Bisan Seto could be over 1~2 m/s.

Taking this tidal field as the background, we carried out some numerical experiments to clarify the influence of heating, river discharge, wind and forcing at lateral boundaries on the residual current field and the formation of stratification. The results as well as those of tracer experiments will be presented in the presentation.

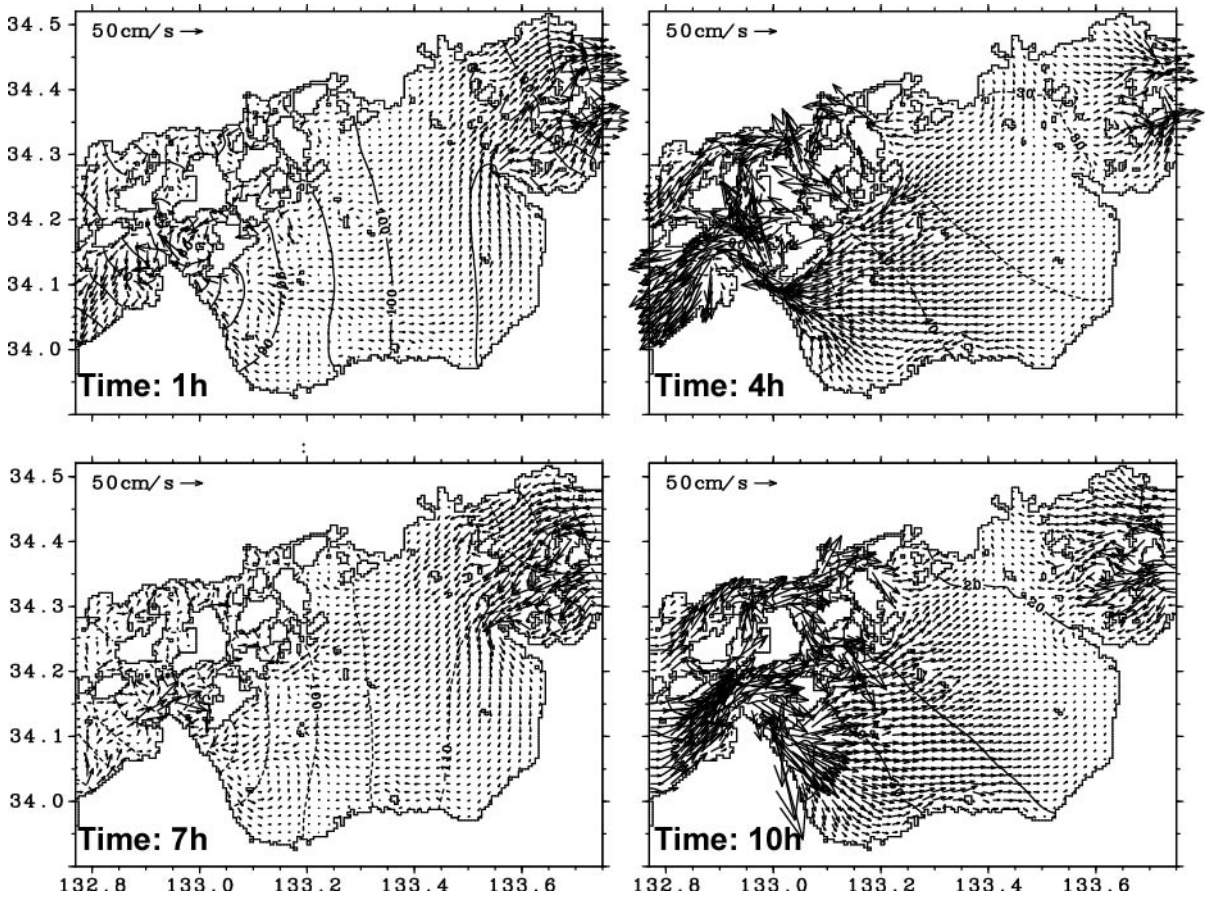

Figure 4: Variations of sea level and M_2 tidal current in the Hiuchi Nada during 12 hours.

Acknowledgments: This research is supported by Grant-in-Aid for Scientific Research (A) from Japan Society for Promotion of Science (No. 12308027).

References:

Takeoka, H., Progress in Seto Inland Sea Research, *Journal of Oceanography, 58*, 93-107, 2002.

Yanagi, T., Temporal and spatial variations of coastal fronts in the Seto Inland Sea, Japan, in *Physics of Shallow Seas*, ed. Wang, H-T., et al., China Ocean Press, Beijing, 279-290, 1990.

Effects of steep topography on the flow and stratification near Palmyra Atoll

ILSE M. HAMANN

(Institute of Oceanography, University of Hamburg, Troplowitzstrasse 7, 22529 Hamburg, Germany, hamann@ifm.uni-hamburg.de)

GEORGE W. BOEHLERT

(Oregon State University, Hatfield Marine Science Center, 2030 SE Marine Science Dr., Newport, OR 97365-5296, USA, george.boehlert@hmsc.orst.edu)

CHRISTOPHER D. WILSON

(NMFS Alaska Fisheries Science Center, RACE Division, 7600 Sand Point Way NE, Building 4, Seattle, WA 98115-0070, USA, Chris.Wilson@noaa.gov)

1. Introduction

Two interdisciplinary cruises aimed at relating the ecology of marine fish populations to oceanographic conditions were fielded during the late summer and late winter seasons (1990 and 1992) near Palmyra Atoll (5.9 ºN, 162.1 ºW) in the Line Islands in tropical Central Pacific.

2. Background circulation and flow around Palmyra Island

During the first cruise (August/September 1990) satellite-tracked surface drifters and acoustic Doppler current profiler (ADCP) measurements showed a strong eastward setting North Equatorial Counter Current (NECC), with maximum speeds exceeding 1 m sec -1 at about 80 m depth (Fig. 1). This current turned southeastward on closer approach to Palmyra.

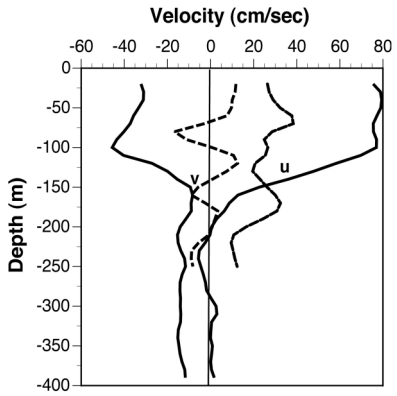

Figure 1: Vertical profile of eastward and northward ADCP current components in the core of the North Equatorial Countercurrent at 163 °W longitude. Data are averaged over 10 m depth intervals. Data from TC90-07 (solid lines) is at 6°N latitude; TC92-01 (dashed lines) is at 5.6°N latitude.

The drifter paths exhibited excursions with zonal wavelength of about 250 km, meridional amplitude of 25 km, and period of about 5 days. These undulations can be explained as expressions of inertial waves in the presence of a northward pressure gradient, and are excited by windbursts or sudden weakening of the steady northeast trades. A detail of the path of one drifter during one inertial period after a total slackening of the winds is shown in Fig. 2.

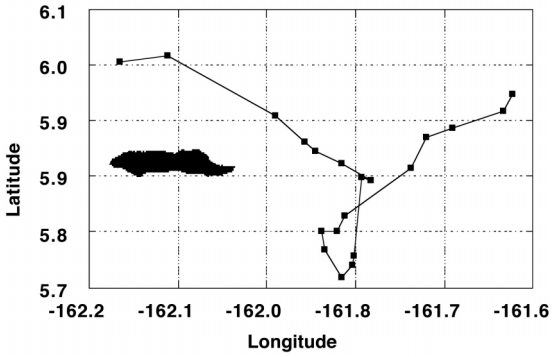

Figure 2: Path of drifter 15087 (TC90-07) near Palmyra demonstrating inertial oscillation.

During the second cruise (February/March 1992), the ADCP-derived speeds of the NECC were weaker (maxima about 33 cm sec -1) while the relative geostrophic flow component was of similar magnitude to that in 1990 and the signal of zonal geostrophic currents reached much deeper to about 650 m depth as compared to 150 m in 1990.

In the relatively thick upper mixed layer (75 to 100 m) the eastward flow decelerated on approach of the island in 1990 between 163 ºW and 162.2 ºW, but increased again off Palmyra's north and south flanks (Fig. 3). Close to Palmyra's north and south shores there was a zone of retardation of the alongshore currents and weak offshore components. In fact, this area of reduced flow extends out to the eastern downstream waters in the lee of the island, where an area of flow reversal occurs ($u < 0$ cm s^{-1}). In this vicinity the contours of the corresponding meridional current component v exhibit a rich structure as well, indicative of some island wake pattern, for example an attached and one or two detached eddies off Palmyra's southeast corner.

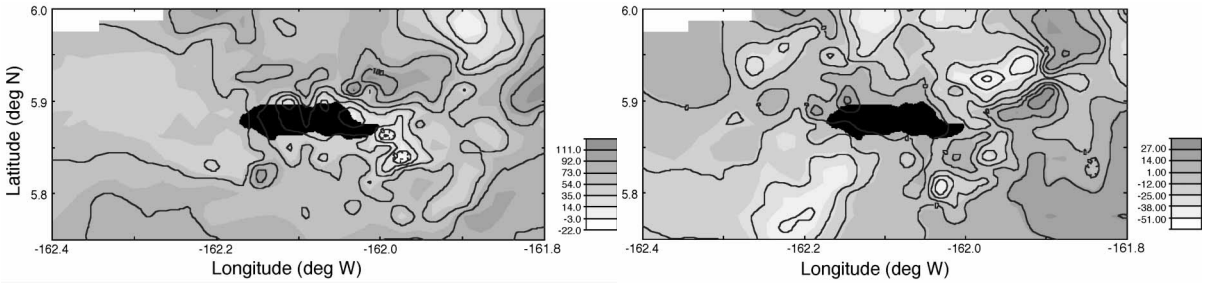

Figure 3: Contours of layer-averaged ADCP eastward (u) and northward (v) current velocity components around Palmyra Atoll, core of the NECC (55-111 m, TC90-07).

The observed convoluted flow structure off Palmyra led us to investigate criteria for flow separation that were derived theoretically and/or from laboratory experiments. We estimated parameters of turbulent 2-dimensional wake theory, e.g. Rossby, Ekman and Reynolds numbers from the topographic dimensions, flow speeds, Coriolis acceleration, and a range of values for the turbulent eddy viscosity. While the resulting numbers are suggestive of formation of eddies in the lee of the island, we did not, however, detect any circular motions with the sampling and instrumentation applied during either expedition.

3. Thermohaline structure at Palmyra Atoll

Doming isopycnals beneath the surface mixed layer as well as thick (20-40 m) internal mixed layers were found near Palmyra during both cruises, with slightly different position relative to the island

(Fig. 4). The discontinuous vertical temperature profiles may have been a result of strong boundary mixing due to breaking internal waves on Palmyra's steep slopes (Fig. 5).

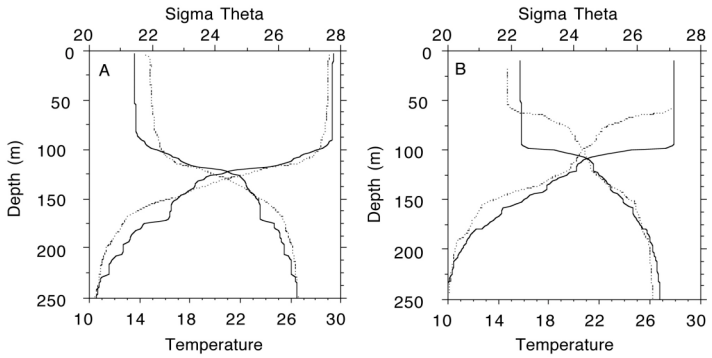

Figure 4: Depth profiles of temperature and density at two CTD stations
a) during TC90-07: CTD Stn. 6, dotted line; CTD Stn. 35, solid line.
b) during TC92-01: CTD Stn. 6, dotted line; CTD Stn. 58, solid line.

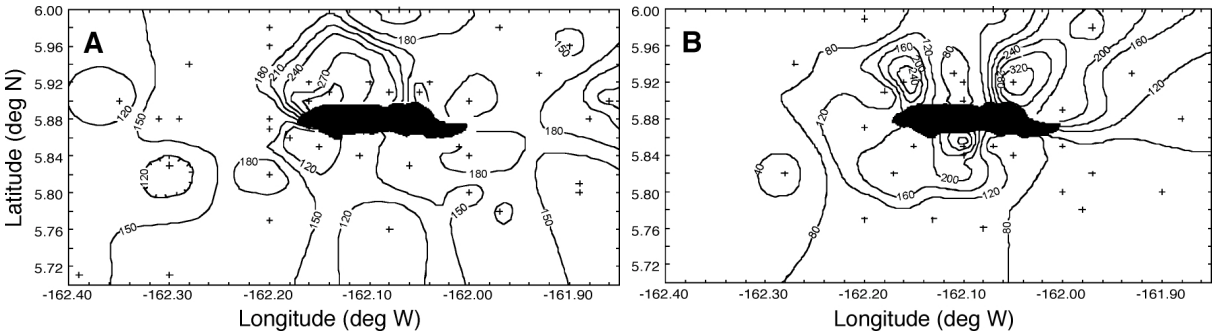

Figure 5: Spatial distribution of the intensity of vertical mixing between 100 and 300 m. Contours are the variance of the vertical temperature gradient dT/dz (x 10^4) taken over 2 m vertical distances between the 100 and 300 m depth horizons. a) TC90-07; b) TC92-01.

In the immediate vicinity of the island variations in flow speed, stratification and 'mixing' both in the alongshore and cross-isobath directions were observed.

4. Conclusions

Ocean current and hydrographic measurements made in two different seasons and two years apart near an island located in the eastward setting North Equatorial Counter Current revealed interaction of the flow with the steep topography on large, intermediate and small spatial scales.

Overall, the current speeds were reduced during the second cruise in February/March 1992, the peak time of the 1991-1993 warm event in the tropical Pacific.

Paths of drifters drogued in the surface layer during the first cruise in August/September 1990 suggest that a combination of atmospheric and topographic forcing may have been responsible for the observed veering of the drifters east of the island.

The location with its observed high energy motions appears to be suitable for another experiment with state-of-the-art turbulence instrumentation and derivation of more accurate estimates of the turbulent eddy viscosity, turbulent energy dissipation rates and mixing, all of which are crucial quantitives for an accurate description of near-island marine ecosystems.

Resuspension process of muddy sediments in Tokyo Bay, Japan

YASUYUKI NAKAGAWA

(Port and Airport Research Institute, Nagase 3-1-1, Yokosuka 239-0826, Japan, y_nakagawa@ipc.pari.go.jp)

1. Introduction

Since fine sediment particles such as silt and clay are easily stuck with contaminants, it is important subject to study fine sediment transport processes in estuarine and coastal area for restoration and maintenance of their environment. The transportation and deposition rate of fine sediments depends on different external force conditions and supply processes of sediment etc. In case of less tidally dominated and shallow estuary, wind waves have a key role of sediment transport processes (Sanford 1994). In order to examine the mobility of muddy bottom sediment by waves, a field observation was carried out at inner Tokyo Bay (Fig.1), where tidal energy is not so strong and wave is considered to be a key factor for sediment transport process.

2. Field Observations

The resuspension studies were carried out over 15 days during February in 2001 at the site in Tokyo Bay as shown in Fig.1. The site is 3km off the north east coast of the bay with average depth of about 10m. In order to see time variation of suspended sediment concentration near the bottom, optical backscatter sensor was set so that the measuring point is 10cm above the bottom. Out put of the OBS were subsequently converted to total suspended particulate concentration in mg/l by applying a calibration result with Kaolin clay. For measurement of particle size of suspended sediment, an in-situ type particle size analyser, LISST100 (Agrawal and Pottsmith, 2000), was also set next to the OBS. Turbidity and particle size distribution were recorded at 5 min and 30 min intervals respectively. For current measurement, an electro magnetical current meter was set to measure current velocity 50cm above the bed. Pulse-coherent type acoustic Doppler velocity profiler was also used to get the vertical profile of near bottom current with high resolution record in space and time, 5cm pitch vertically and 2Hz for 2min burst every 30min. Ultrasonic type wave meter was set to measure the wave condition. Sediment traps were deployed 3 times during the survey period and cylinders (caliber: 15cm) were set with trap level of 1m and 2.7m above the bed. Trapped matters are applied for analysis of wet and dry weight, particle size, and organic matter concentration.

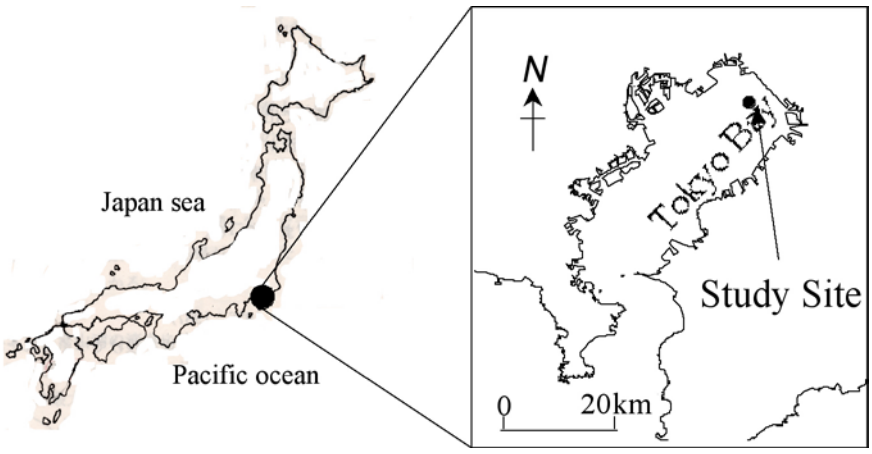

Figure 1: Tokyo Bay and location of study site.

3. Results

(1)Relationship between SS concentration and external forces

Time series data of wind, near bottom current (averaged in 10 min.), and wave during the period with relatively higher wind condition is shown in Fig.2. The bottom shear stress induced by waves is also indicated in the figure, which was estimated as maximum bottom shear stress due to waves with the following equation (e.g. Grant and Madsen 1986).

$$\tau_b = 1/2\, f_W \rho U_b^2 \qquad (1)$$

where ρ is the density of the water. U_b , the maximum orbital velocity near the bottom, was obtained as the value of monoclomatic wave with significant wave hight and period through the linear wave thory. The wave friction factor, f_w, was set as 0.03 considering a typical wave period and sediment grain size in the area.

The bottom current due to wind exceeds 10cm/s in the afternoon on February 16, 2001, which is the highest record during the deployment, but apparent resuspension of the sediment does not occur under the current. On the other hand, the suspended sediment concentration above the bed was extremely increased under the effect of the wave induced bed shear stress in the before noon on February 16, 2001, and the result implicates that waves play a key role for sediment transport process in the bay. Although the wave height was still high in the afternoon of the day, waves less disturbed the bottom sediment because wave period became relatively short due to the change in the wind direction.

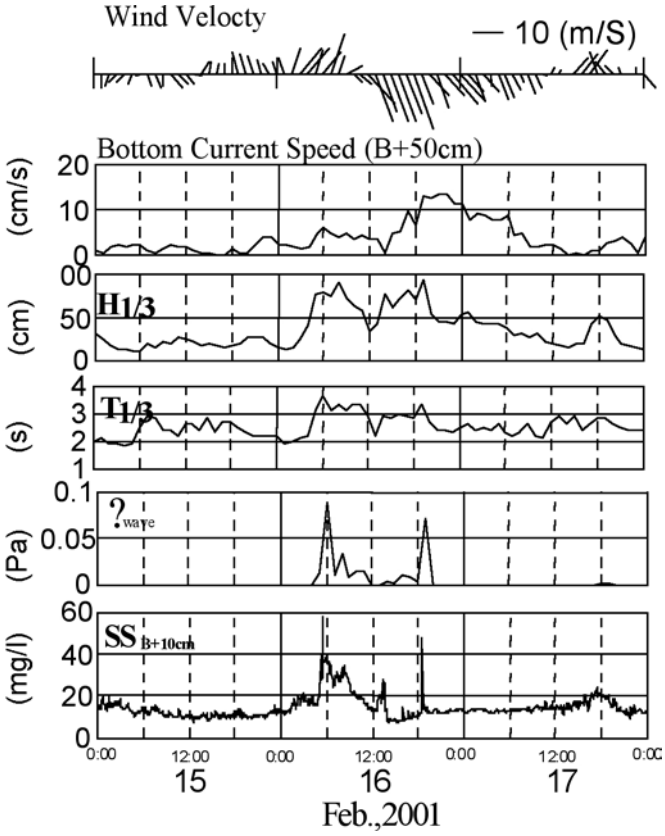

Figure 2: Temporal evolution from wind velocity vectors, bottom current speed, significant wave height, significant wave period, bed shear stress due to wave and suspended sediment concentration above the bed during the observation.The events of resuspension of sediment due to wave occur twice during the observation.

In order to examine the critical shear stress for these resusupension or erosion of the bed by the effect of waves, suspended sediment concentrations are compared with the bed shear stress due to wind waves in Fig.3. The suspended sediment concentrations drastically increase between the shear stress of 0.001-0.01 Pa and it may correspond to the range of critical shear stress for erosion.

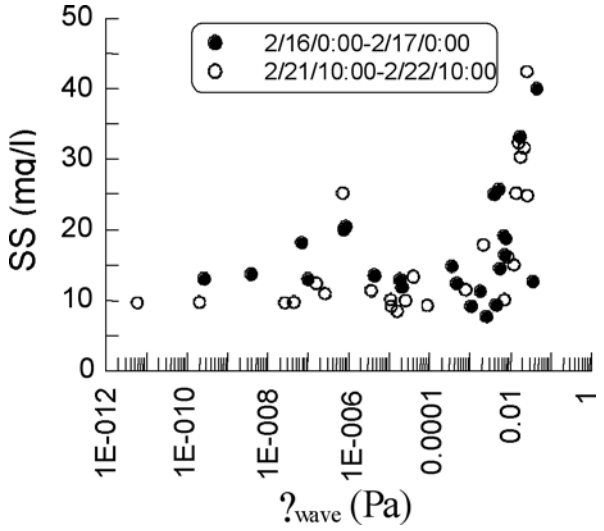

Figure 3: Relationship between suspended sediment concentration and bed shear stress due to waves.

(2)Particle size distribution characteristic of suspended sediment

Figure 4 shows the size distributions of suspended sediment in the volume concentration measured with LISST-100, comparing the data during high wave event and calm conditions before and after the events on February 16 (Left fig.) and 22 (Right fig.), 2001. Both particle size distributions during the resuspension events measured at 6:00 on February 16, and at 1:30 on February 22 have a peak around 200 μm with a second peak around 20-30 μm. The similarity of the particle size distributions between these suspended sediment and bottom sediment shown in the Fig.5 indicates that the suspended sediment during wave events are dominated by the bottom sediment at the study site rather than advected from surrounding area.

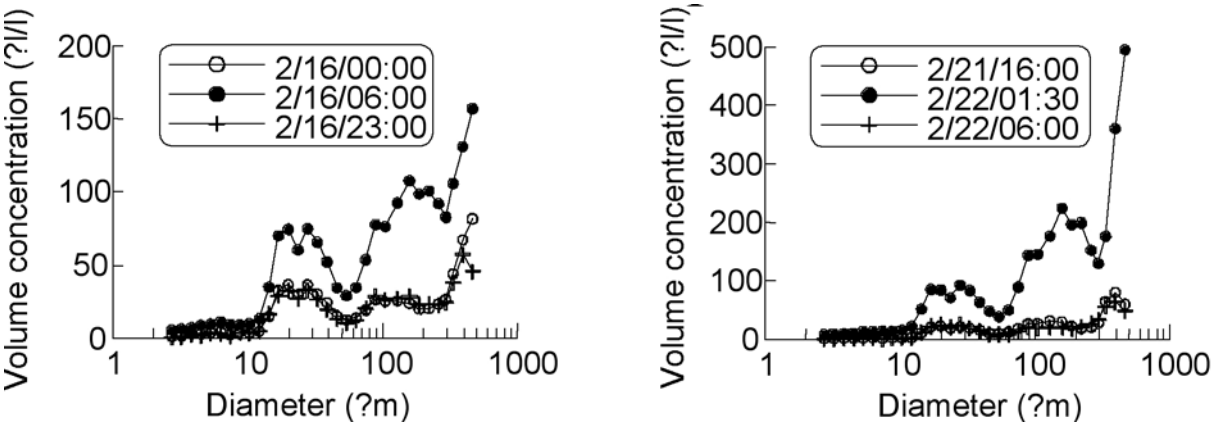

Figure 4: Particle size distribution of suspended sediment during resuspension events.

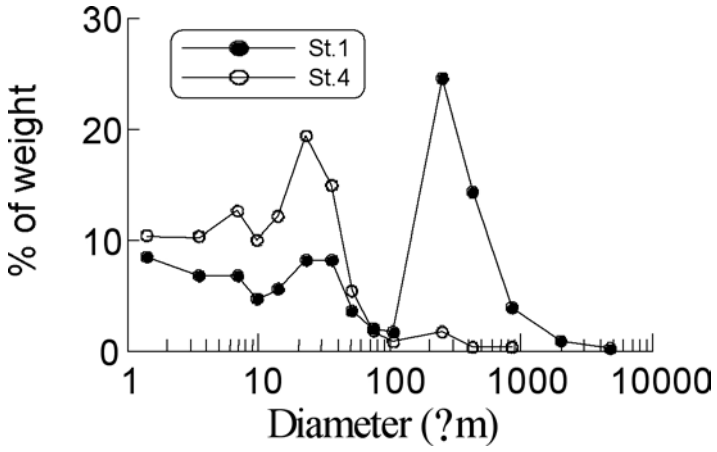

Figure 5: Grain size distribution at the study site (St.1).

4. Conclusions

Field observation of turbidity, current and waves during the winter of 2001 in Tokyo Bay has revealed the following aspects. (1) Wind waves are more dominant than tidal current for resuspension of the sediment at the study site. (2) Critical bottom shear stress induced by wind waves is estimated between 0.001-0.01Pa, and (3) Particle diameter distribution of suspended particles near the bed during the period of wave forced resuspension event is close to the grain size distribution of the bottom sediment.

References:

Agrawal,Y.C., and H.C.Pottsmith (2000):Instruments for Particle Size and Settling Velocity Observations in Sediment Transport, Marine Geology,Vol.168,pp.89-114.

Sanford, L.P. (1994): Wave-Forced resuspension of upper Chesapeake Bay Muds, Estuaries, 17, No.1B, 148-165.

Grant, W. D., and O. S. Madsen (1986): The Continental-Shelf Bottom Boundary Layer, Ann. Rev. Fluid Mech. 18,pp.265-305.

Numerical modelling of suspended matter transport

ANDREI PLESKATCHEVSKI

(GKSS Research Centre Max-Planck-Str.1, D-21502 Geesthacht, Germany, andrei@gkss.de)

GERHARD GAYER

(GKSS Research Centre Max-Planck-Str.1, D-21502 Geesthacht, Germany, Gerd.Gayer@gkss.de)

WOLFGANG ROSENTHAL

(GKSS Research Centre Max-Planck-Str.1, D-21502 Geesthacht, Germany, Wolfgang.Rosenthal@gkss.de)

1. Introduction

In many satellite borne ocean colour images of the North Sea a plume is visible, which is caused by the scattering of suspended particulate matter (SPM) in the upper ocean layer *[Doerfer and Fischer 1994]* (cf. Fig.1*)*. This structure can be seen in most ocean-colour images with different intensity and it is particularly visible after strong storm events. The origin of the plume is located near to the cliffs of Suffolk, Great Britain, and it extends along the coast of the Netherlands and Germany towards Denmark. The intensity and length of the plume varies and depends strongly on the local current and wave field. The objective of this study is to investigate the cause of the development of the plume and to set-up a numerical model. SPM concentration is governing the light attenuation, which is important for primary production.

A Suspended Particulate Matter Transport model (SPMT), which can be operated in a quasi 3-D and a fully 3-D mode, was developed for the North Sea. The fully 3-D model is presently implemented as a SPM module into the operational transport model of the Bundesanstalt für Seeschifffahrt und Hydrographie (BSH). The module contains the following processes: settling of SPM, vertical exchange due to currents and waves in the water column, sedimentation, re-suspension and erosion in the bottom layer, and processes of bioturbation and diffusion in the upper 20 cm of the bottom layer. The main new aspect of the model is the derivation of the vertical exchange considering the local current speed and wave height. Calibration was done with satellite data of surface SPM concentration.

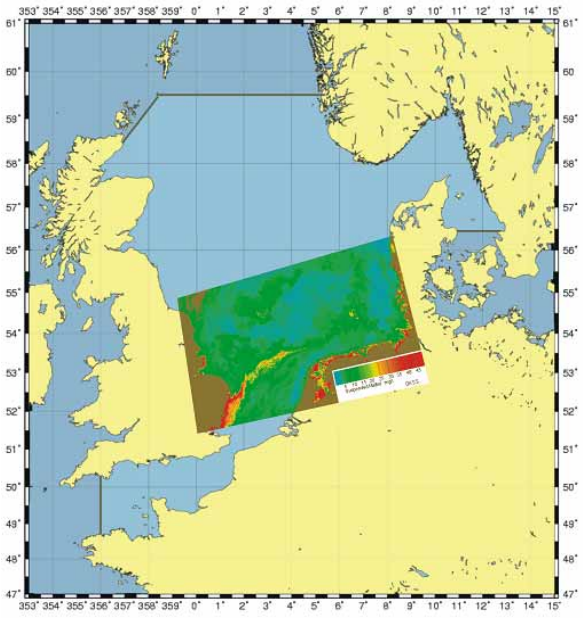

Figure 1: Model area and SPM retrieved from the Satellite Borne Coastal Zone Colour Scanner (SCZC)

2. Set-up of SPM models

The BSH transport model calculates the transport on nested grids with a horizontal resolution of 6 nm for North and Baltic Sea and 1 nm for the German Bight with up to 9 vertical layers. The forcing of erosion und sedimentation processes results from the local shear stress velocity derived in time and space under consideration of currents and waves according to Soulsby *[Soulsby 1997]*. In the model the sources of SPM are rivers, concentration at the open boundary, bottom sediment and erosion at three English cliffs Suffolk, Norfolk and Holderness. 3 SPM fractions with different settling velocities are considered.

The vertical exchange coefficient A_v is assumed to be the sum of the vertical exchange due to currents A_v^{cur} and due to waves A_v^{wav}:

$$A_v(z) = A_v^{cur}(z) + A_v^{wav}(z) \,, \tag{1}$$

$$A_v^{wav}(z) = K_{wav}^2 \cdot U(z)_{wav}^2 T \,, \tag{2}$$

$$A_v^{cur}(z) = K_P^2 \frac{du}{dz} \,, \tag{3}$$

Where z is the vertical coordinate, U_{wav} is the orbital velocity of the significant wave, T is the wave period and u is the current velocity. The coefficients K_{wav} - a function of significant wave height - and K_P - the Prandtl mixing length (m) - are unknowns, which have to be determined in synergy with ocean colour satellite data.

The computation of the SPM bottom processes considers bioturbation by benthos (crabs and worms) and diffusion in the upper 20 cm of the bottom layer.

The main new aspects of the model are dependency of cliff erosion on significant wave height and derivation of vertical exchange on consideration of local current speed and wave height using ocean colour data from MOS and SCZC satellites for calibration and validation.

From the yearly mean erosion rates *[Puls et al 1997]* of the Suffolk, Norfolk and Holderness cliffs and the statistics of significant wave height H_s in the years 1993-1995 constant factors have been estimated for storms (H_s >2m) and calm weather (H_s <2m) to distribute the yearly erosion over significant wave height.

3. Vertical exchange coefficient

It is assumed that the SPM plume structure at the surface results from the vertical SPM distribution mainly caused by vertical mixing processes due to currents and waves. This distribution can be described with a profile function determined by SPM settling velocities and vertical mixing processes. The surface SPM concentration, known from satellite ocean colour images, is the upper boundary condition of this profile. In synergy with the results of the two dimensional transport model, determining the mean concentration in the water column, the vertical exchange coefficient A_v is adjusted.

In the quasi 3-D model the vertical distribution of SPM is given by:

$$C(z) = C_{sur} e^{\frac{w_s z}{\overline{A_v}}} \tag{4}$$

Where C_{sur} is the surface SPM concentration, w_s the settling velocity of SPM, A_v the vertical exchange coefficient, and z the vertical coordinate.

The vertical mean SPM concentration is defined as:

$$\overline{C} = \frac{1}{h}\int_0^h C(z)dz \tag{5}$$

Replacing $C(z)$ in (5) by (4) and solving the integral results in:

$$\overline{C} = \frac{C_{sur}}{h} \cdot \frac{\overline{A}_v}{w_s}\left(e^{\frac{w_s h}{\overline{A}_v}} - 1\right) \tag{6}$$

The surface SPM concentration from CZCS and MOS images acquired during calm weather and the mean SPM concentration retrieved from the SPM transport model the current component $\overline{A}_v^{cur}$ of the vertical exchange coefficient can be calculated. The storm periods *[Hetscher et al. 1998]* are used to derive the wave component $\overline{A}_v^{wav}$.

In a second step the parameters K_p and K_{wav} for $A_v^{cur}(z)$and $A_v^{wav}(z)$ of the fully 3-D model are fitted.

4. Erosion depth parameter and SPM bottom deposits

For most areas the SPM bottom deposition is unknown. It can be calculated with the help of ocean colour images and the SPM model.

Step 1: fitting of the model parameter "erosion depth" with measured bottom SPM depositions.

After a storm the surface SPM concentration is known from MOS data. Assuming a mixed water column the mass of SPM can be estimated. Otherwise the eroded SPM mass M_{ero} can be estimated from the measured bottom deposition

$$M_{ero} = \rho_{spm}\mu_{20}z_{ero}, \tag{7}$$

Where μ_{20} is the bottom deposition of SPM (%), ρ_{spm} is the SPM density (kg/m^3), z_{ero} is the eroded bottom layer thickness (m). Now the erosion depth z_{ero} during the storm can be calculated iteratively with known wave data and bottom deposition SPM μ_{20}.

Step 2: update of SPM bottom deposits with the fitted parameter "erosion depth" for other sites where measurements are not available.

5. Primary results

The storm 25.01.2000-04.02.2000 was simulated. The significant wave heights in the Northern part of the German Bight were over 8 m. The model (Fig.2) reproduced the surface SPM plume structure visible in the satellite colour image from MOS. The vertical mixing due to waves was the dominant process to erode the SPM bottom deposits and to bring the material to the sea surface.

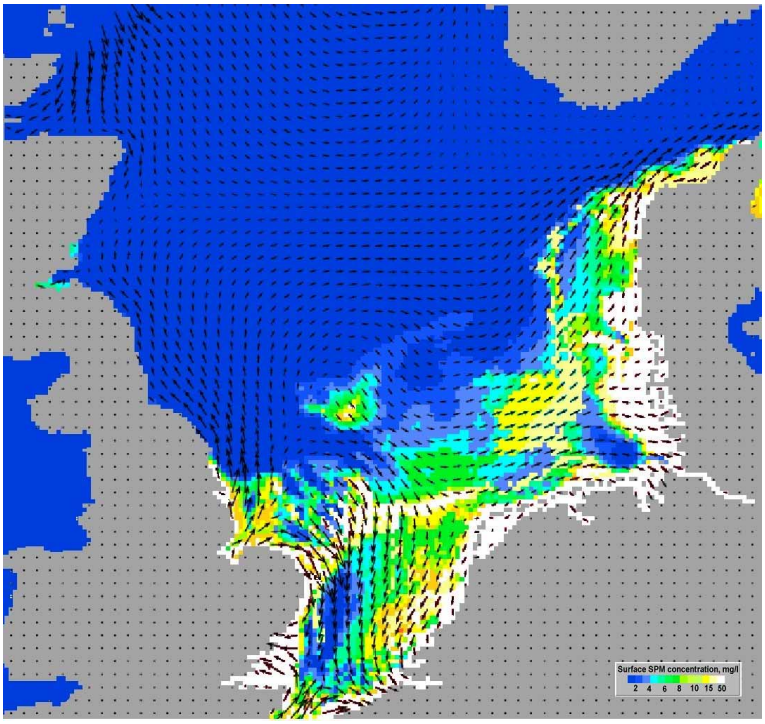

Figure 2: Model simulation of the SPM plume structure during a storm

6. Conclusions and Outlook

The SPM plume visible in ocean colour images was well represented by the SPM-model. The importance of the waves for the vertical mixing of SPM was clearly demonstrated.

Further steps will be additional validation of the SPM-model using ocean colour images and in-situ data. Assimilation of satellite data (ASAR, MERIS etc.) and extension of the model for primary production in cooperation with the Bundesanstalt für Seeschifffahrt und Hydrographie (BSH) are planned. Charts of SPM bottom deposits updated in synergy with model results and satellite data are a further challenge.

References:

Doerffer, R., Fischer, J. *Concentrations of chlorophyll, suspended matter and gelbstoff in case II waters derived from satellite coastal zone colour scanner data with inverse modelling methods*. Journal Geophysical Research 1994, 99: 745-7466.

Soulsby, R. *Dynamics of marine sands*. *A manual for practical application*. Thomas Telford Services Ltd, London, 1997.

Hetcher, M, H.Krawczyk, A.Neumann, T. Walzel and Zimmermann, *Capabilities for the retrieval of coastal water constituents (case II) using multispectral satellite data*, Int. Symp. on Rem. Sens., Barcelona, Spain, in Proc. of SPIE Vol.3496, 1998.

Puls, W., T. Pohlmann and J. Sündermann, *Suspended particulate matter in the southern North Sea: application of a numerical model to extend NERC North Sea project data interpretation*, Dt. Hydr. Z., 49(2/3), 307-327, 1997.

Deep and shallow estuarine circulation controlling the development of hypoxic water mass in Ise Bay

TETSUYA TAKAHASHI

(Department of Agriculture, University of Kyoto, Sakyo-ku, Kyoto, Japan, tetsuya@kais. kyoto-u.ac.jp)

TATEKI FUJIWARA

(Department of Agriculture, University of Kyoto, Sakyo-ku, Kyoto, Japan, fujiwara@kais. kyoto-u.ac.jp)

1. Introduction

The hypoxic water mass formed below the pycnocline causes the mortality of benthos in temperate coastal seas (e.g. *Diaz and Rosenberg, 1995*). Many factors such as physical and bio-chemical processes influence the concentrations of dissolved oxygen (DO). Physical processes involve vertical mixing and horizontal advection of oxygenated water. Bio-chemical processes contain pelagic metabolism, microbial decomposition and benthic respiration. Physical processes play a role in supplying oxygen to the lower layer, whereas bio-chemical processes cause oxygen demands. Many previous works on the hypoxic water have been focused on vertical oxygen flux and oxygen consumption rate (e.g. *Officer et al., 1984, Jørgensen*, *1990, Kelly and Doering, 1999*), but the horizontal flux by the advection has been somewhat ignored.

In Ise Bay, severe hypoxia and anoxia occur every year. *Fujiwara et al.* (*2002*) showed that DO distributions are not determined by the oxygen consumption rate but by the residence time of water, which is determined by the physical processes during the stratified period in Ise Bay. The strait-water is well-mixed and oxygenerated by strong tidal stirring, while the bay-water is strongly stratified and stagnant. The oxygenerated strait-water intrudes into the bay along the eastern coast, receiving the Coriolis force. In constrast, the water mass in the west is isolated from the water exchange and becomes hypoxic. The inflow depth of the strait-water varies throughout the year and effect of this variation on the hypoxia has not been well known. In this study, the effect of the inflow of the oceanic water on the hypoxia was studied in Ise Bay. Closely spaced measurement of temperature, salinity, and DO were conducted in Ise Bay during the stratified season in 1997. In addition, longer time scale variations in DO were also analysed based on the historical data set, which is made by Mie Prefecture. The mechanism which governs DO distribution and variation were demonstrated by using a numerical model.

2. Data and Analysis

From June to October in 1997, hydrographic and water quality observations along a longitudinal and lateral transects were conducted at monthly intervals. Temperature and salinity are measured at each 0.5 m depth. DO and nutrients are measured at each 2-5 m depth. The station locations on the longitudinal transect are shown in Figure 1 by mark (+). A CTD attached with DO meter was cast at every station. Temperature, salinity, dissolved oxygen, and nutrients have been collected monthly from 1989 to 1992 at 20 stations throughout Ise Bay by the Fisheries Research Institute of Mie. These data were also anlysised. These observations have been conducted at the beginning of each month. The measurement depths are 0, 2, 5, 10, 20, 30 m, and 1 m above the bottom (B-1m). Inflow depth is defined as the depth where the density of the bay water (station 11) equals to the density of the strait-water (station 11).

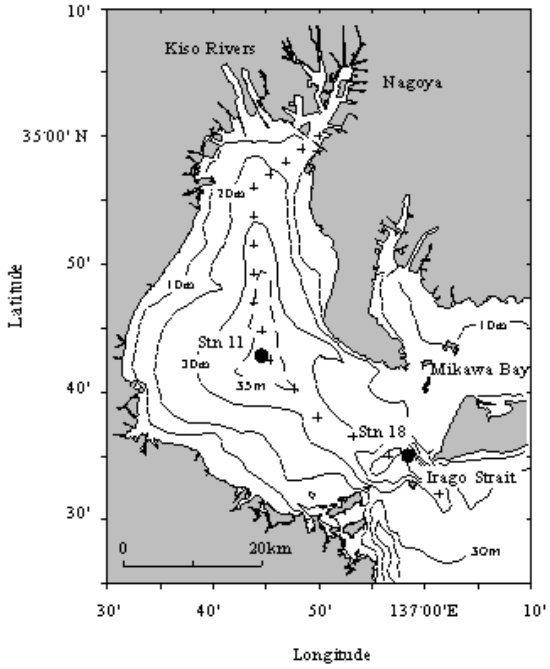

Figure 1: Map of Ise Bay and station locations.

3. Model

We constructed a filling box-model to predict temperature and DO change below the pycnocline at station 11 during 4 years (1989 - 1992). The water column below the pycnocline in the bay was divided into 26 boxes (1x1x1m) and temperature and DO in each box was calculated by a one-dimensional advection–diffusion equation. The pycnocline depth was set to be 7 m from the density profiles observed at station 11. The oceanic water intrudes at the inflow depth, upwells, and outflows from the uppermost box, which corresponds to the pycnocline (Figure 2). The inflow depths of the mixed-water are given from the measured values. The governing equation is

$$\frac{\partial C}{\partial t} = K_z \frac{\partial^2 C}{\partial z^2} - \frac{\partial wC}{\partial z} - R_w(-R_b)$$

where C is DO concentration, w is upwelling velocity, K_z is vertical diffusive coefficient; R_w (0.06 $gm^{-3}day^{-1}$) and R_b (1.0 $gm^{-2}day^{-1}$) are respirations in the water column and sediments, respectively. Respiration in sediments was set only in the lowest box. The water column and sediment respirations were justified to minimize the error between the observed and calculated DO. The vertical profile of DO observed at Station 11 on 6 January 1989, was chosen as the initial value: DO of surface and bottom were 8.2 and 8.4 mgl^{-1}, respectively. DO of the uppermost layer and of the intruding water are given from the measured values. The time step is 0.5 h.

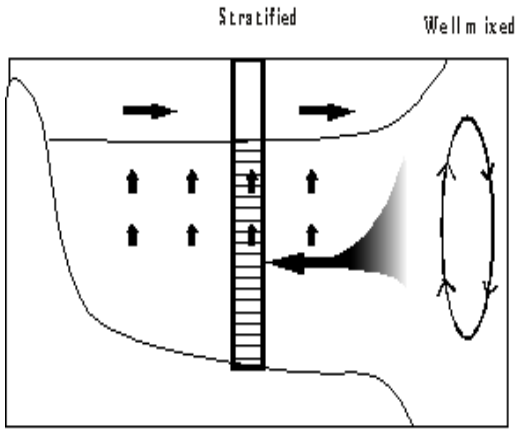

Figure 2: Schematic view of the model.

4. Results and Discussion

Variations in DO and inflow depths at stn.11 during 1989-1992 are shown in Figure 3. The strait water flows into the intermediate and bottom layers. There is a tendency that the strait water flows in the intermediate layer during the heating periods and on the bottom during the cooling periods. There is a high correlation between the inflow depth and DO.

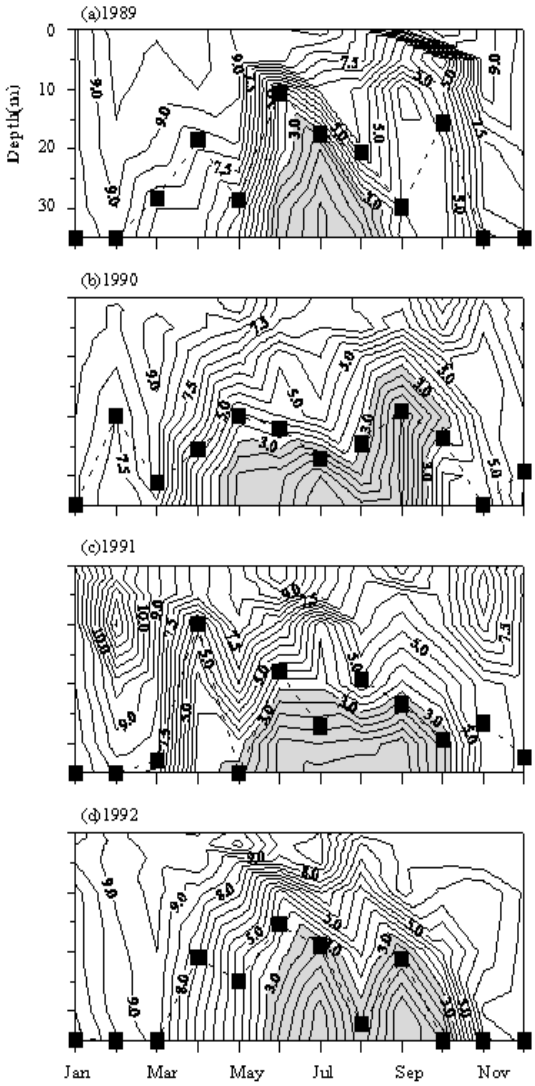

Figure 3: Variations in observed DO during 1989-1992 at stn.11. Black squares indicate the intrusion depth of strait-water.

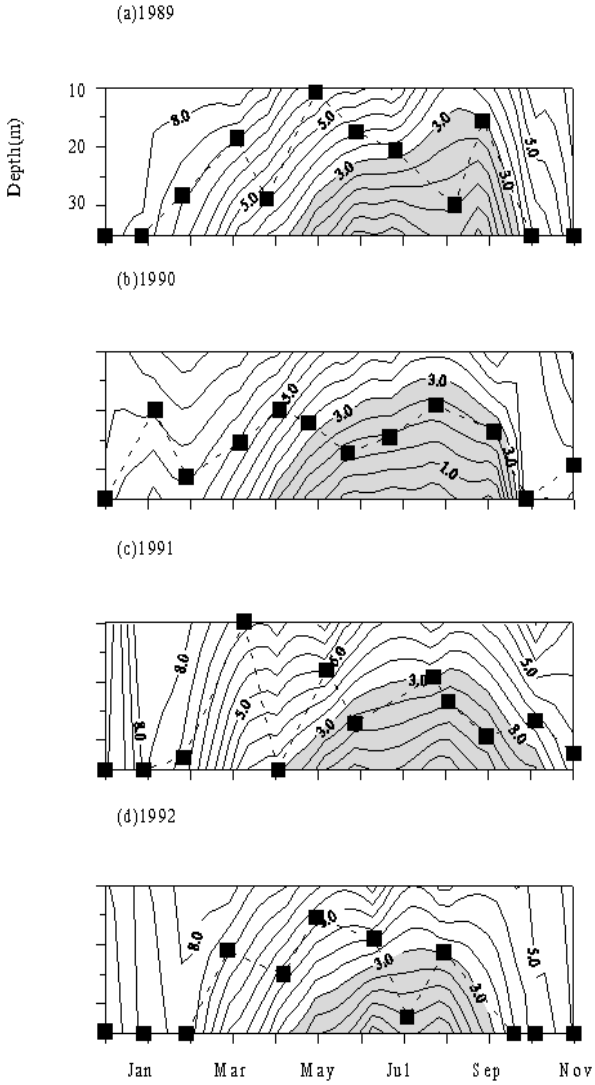

Figure 4: Variations in calculated DO during 1989-1992 at stn.11. Black squares indicate the intrusion depth of strait-water.

The model well reproduced the variations in the observed DO (r^2=0.8) though oxygen consumpion rate and vertical mixing are set to be constant. The model predicted that the hypoxia occurs during periods when the strait-water intrudes in the middle layer (Figure 4). This indicates that DO variations are mainly determined by the inflow depth.

5. Conclusion

The estuarine circulation has two patterns in Ise Bay. One is the shallow estuarine circulation with the intermediate inflow of the strait-water; this circulation tends to occur during the heating period. The other is the deep estuarine circulation with the bottom inflow, which tends to occur during the cooling period. Changes of the circulation pattern control the hypoxia in Ise Bay.

Acknowledgments: The authors are grateful to Dr.Akihide Kasai who discussed about this paper.

References:

Diaz, R., J. and Rosenberg, R., Marine benthic hypoxia: A review of its ecological effects and the behavioural resoponces of benthic macrofauna. *Oceanography and Marine Biology*, 33, 24-303, 1995.

Fujiwara, T., Takahashi, T., Kasai, A., Sugiyama, Y., and Kuno, M.: The role of circulation in the development of hypoxia in Ise Bay, Japan. *Estuarine, Coastal and Shelf Science*, 54, 19-31, 2002.

Jørgensen, B., B.: Mineralization of organic matters in the sea bed: The role of sulfate reduction. *Nature*, 643-645, 1982

Kelly, J. R. and Doering, P. H.: Seasonal deepening of the pycnocline in a shallow shelf ecosystem and its influence on near-bottom dissolved oxygen. *Marine Ecology Progress Series* 178, 151-168, 1999.

Officer, C. B., Biggs, R. B., Taft, J. L., Cronin, L. E., Tyler, M. A. and Boynton, W. R.: Chesapeake Bay anoxia:origin, development, and significance. *Science*, 223, 22-27, 1984.

Inflow of nutrient rich shelf water into a coastal embayment: Kii Channel, Japan

TOSHINORI TAKASHI AND TATEKI FUJIWARA

(Graduate school of Agriculture, Kyoto University, Kyoto, 606-8502, Japan, takashi1@kais.kyoto-u.ac.jp, FUJIWARA@KAIS.KYOTO-U.AC.JP)

TOSHIAKI SUMITOMO

(Fisheries Reserch Institute, Tokushima Agriculture, Forestry and Fisheries Technology Centre, Hiwasa-cho, Tokushima, 779-2304, Japan)

YOSHIHISA KANEDA AND YUKIO UETA

(Fisheries Division, Tokushima Prefectural Government, Bandai-cho, Tokushima, 770-0941, Japan)

JUNICHI TAKEUCHI

(Fisheries Experimental Station, Wakayama Research Center of Agriculture, Forestry and Fisheries, Kushimoto, Nishimuro-gun, Wakayama, 649-3503, Japan)

1. Introduction

A large amount of anthropogenic nutrient flows into Osaka Bay (Fig. 1) and causes red tide and hypoxia. It has been believed that the anthropogenic nitrogen and phosphorus discharged into Osaka Bay flows out through the Kii Channel to the Pacific Ocean by water exchange. However, Fujiwara *et al*. (1997) directly measured nutrient flux passing through a cross-section at the southern end of the Kii Channel in summer 1995, and obtained the result that nutrient flows into the Kii Channel from the outer ocean.

The Kuroshio Current flows eastward off the Kii Channel. Variation in the Kuroshio-path influences physical and chemical conditions in the Kii Channel. When the distance of the Kuroshio-axis from Cape Shionomisaki (hereinafter we refer to as Kuroshio-distance) is smaller than 20 n-miles (= 37 km) and the path of the Kuroshio is stable, warm Kuroshio-upper-water frequently intrudes into the Kii Channel in summer. On the other hand, when the Kuroshio-distance is larger than 30 n-miles (= 55.5 km), cooler Kuroshio-subsurface-water intrudes into the lower layer of the Kii Channel (Takeuchi *et al*., 1997). Therefore, it can be expected that the variation in the Kuroshio-distance exerts influence on the nutrient flux into the Kii Channel.

In this study, we have conducted nutrient-flux-measurements in the Kii Channel at monthly intervals for three years to reveal seasonal and yearly variations in the nutrient flux and to clarify the relationship between the Kuroshio-distance and the nutrient flux in the Kii Channel.

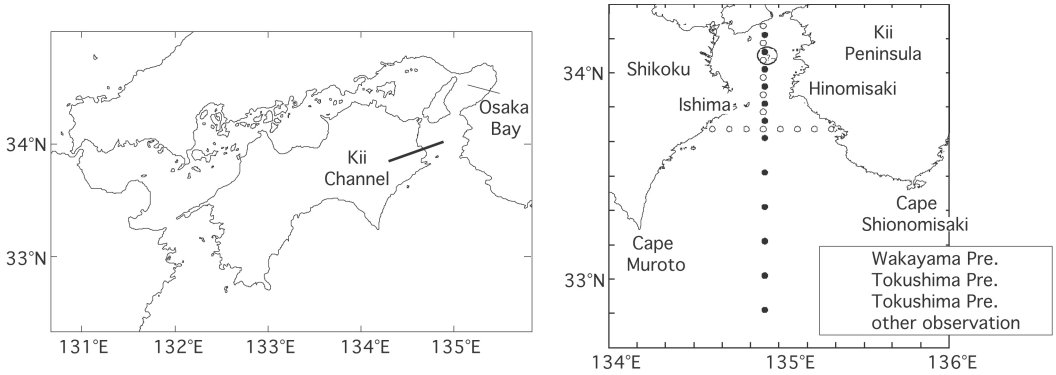

Figure.1 (left) Map of Seto Inland Sea. (right) Map of the Kii channel and station locations.

2. Observation and analysis

The Tokushima Prefectural Fisheries Research institute has been measuring water temperature, salinity and nutrient concentrations (NO3-N, NO2-N, NH4-N, PO4-P) at the stations on longitudinal and lateral transects at monthly intervals. The Wakayama Prefectural Fisheries Research institute has also been measuring water temperature and salinity on a longitudinal transect from the head of the Kii Channel to the outer ocean. The nutrient flux through the lateral cross-section was obtained by integrating the product of the nutrient concentration and the geostrophic velocity.

3. Conclusion and discussion

Fig. 2 represents temporal variation in the temperature from 1999 to 2001 at a point indicated by a circle in Fig. 1. The entire water column is cooled and becomes well-mixed from October to the next March. The temperature indicates different variation patterns year by year from April to September. Water warmer than 25 degree-C appears in the upper layer from July to August 1999. The bottom temperature suddenly decreases to T < 23 degree-C in September in 1999 and to T < 20 degree-C in 2000 and 2001. Water warmer than 24 degree-C occupies from the surface to the bottom in September 2001.

Fig. 3 shows temporal variations in DIN and phosphate during a period from 1999 to 2001. In winter (from October to the next March),

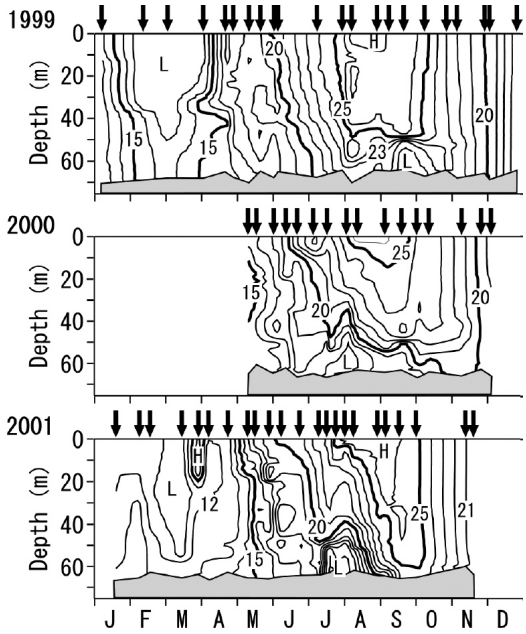

Fig.2 Temporal variation in the temperature in 1999,2000,2001. The arrow marks the times of the observation.

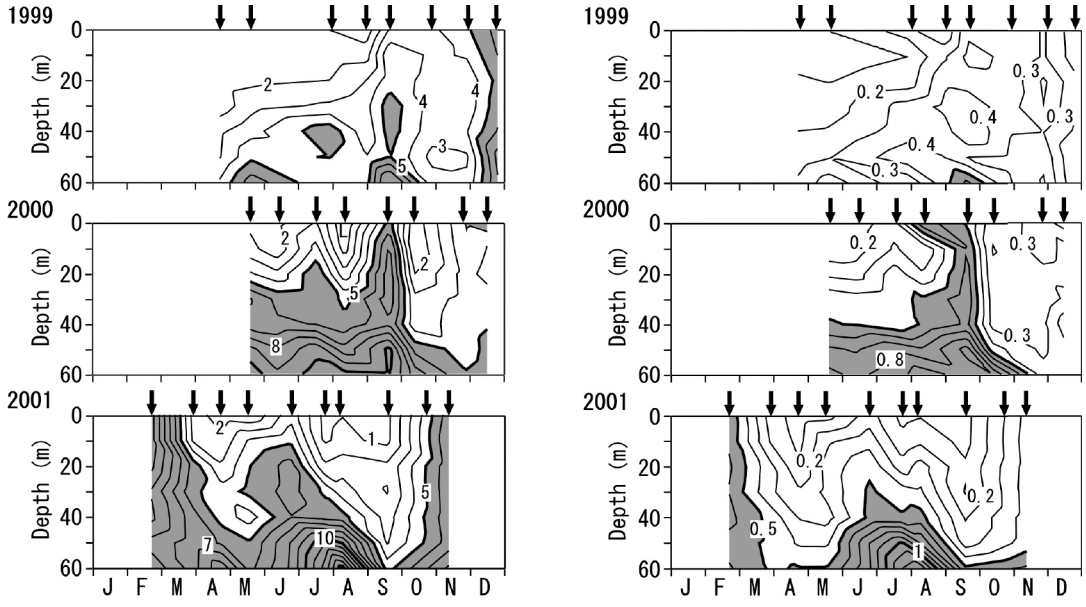

Fig.3 Temporal variation in the concentration of a)DIN and b)Phosphate. Shadow area represents more than 5μM(DIN) and 0.5μM(Phosphate) .

concentrations of DIN and phosphate are relatively high (DIN > 5 micro mol/L, phosphate > 0.5 micro mol/L), and their vertical distributions are nearly homogeneous. The concentrations of DIN and phosphate are low in the upper layer from April to September because nutrients in the euphotic upper layer are used by phytoplankton and depleted. The concentrations of nutrients in the lower layer are low in 1999, whereas they are high (DIN > 5 micro mol/L, Phosphate > 0.5 micro mol/L) in 2000 and 2001. However, the concentrations of these nutrients suddenly decrease in September 2001. In summer, DIN and phosphate concentrations well correlate with temperature. This suggests that the cold and nutrient rich water originates from the subsurface-water in the Kuroshio region.

Fig. 4 shows time series of the Kuroshio-distance. The Kuroshio-distance corresponds to the intrusion of the cold subsurface-water in summer (from July to September). When the Kuroshio-distance is larger than 20n-miles, the subsurface-water intrudes into the Kii Channel. On the contrary, no intrusion occurs when the Kuroshio-distance is smaller than 20n-miles. We cannot find significant relationship between Kuroshio-distance and temperature in other seasons.

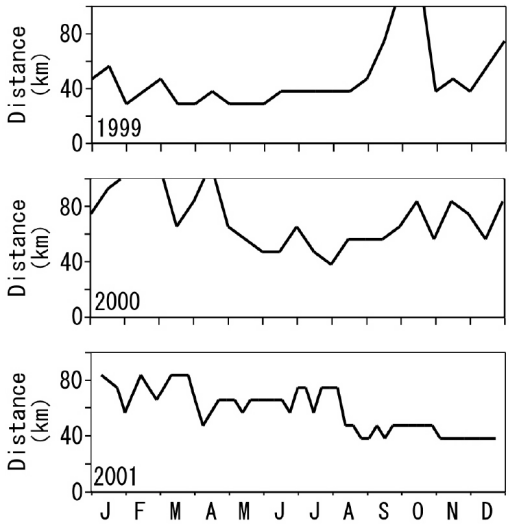

Fig.4 Time series of the distance of the Kuroshio axis from cape Shionomisaki.

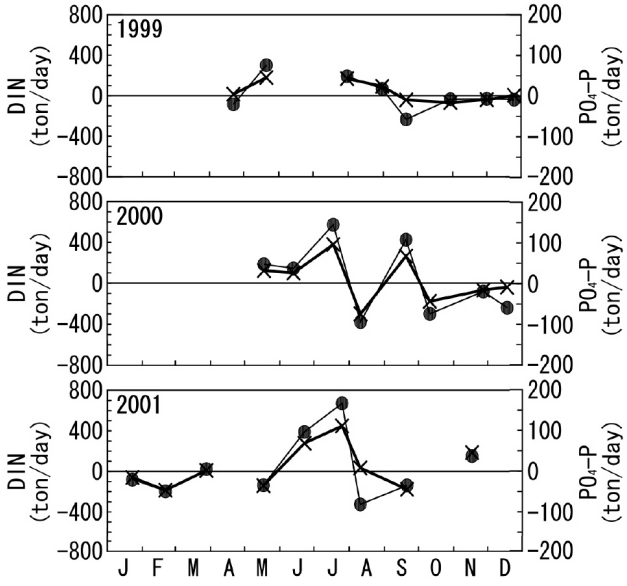

Fig.5 Temporal variation in flux of DIN (thin line), PO4-P (thick line).

Fig. 5 shows temporal variations in fluxes of DIN and phosphate through the lateral transect; inflow is positive. The nutrient fluxes fluctuate throughout the year. The nutrient fluxes indicate a tendency to flow out the Kii Channel in winter, when thermohaline front appears near the mouth of the Kii Channel. The nutrient rich coastal-water and the nutrient poor Kuroshio-water may exchange across the front and transport nutrients outward. Nutrients fluxes indicate large positive values in summer. Especially, when the Kuroshio-distance increases, the nutrient fluxes are large.

Flow in the Kii Channel consists of intrusion/retreat of the Kuroshio-subsurface-water and estuarine-circulation-like flow. The former is governed by the Kuroshio-distance and the latter, which is relatively steady and weak, is driven by the horizontal salinity gradient. We classify the observation period into four regimes depending on the Kuroshio-distance.

When the Kuroshio-distance is stably smaller than 20n-miles, the nutrient concentrations are a little higher in the lower layer than in the upper layer. Thus, a little amount of nutrients are transported into the Kii Channel by the estuarine-circulation-like flow. During periods when the Kuroshio-distance keeps a value larger than 20n-miles (e.g. in July 2000), large difference in the nutrient concentration

appears between the lower layer and the upper layer. Thus, a medium amount of nutrients are transported into the Kii Channel by the estuarine-circulation-like flow.

When the Kuroshio-distance increases and exceeds 20n-miles, the nutrient rich Kuroshio-subsurface-water intrudes into the Kii Channel and causes a large nutrient inflow. Conversely, decrease of the Kuroshio-distance induces a large nutrient outflow (e.g. August 2000 and August 2001).

References:

Fujiwara, T., N. Uno, M. Tada, K. Nakatsuji, A. Kasai, W. Sakamoto, Nutrient flux and residual current in Kii Channel, Umi-to-Sora, 73, 63-72, 1998. (In Japanese)

Takeuchi, J., Y. Nakaji, T. Kokubo, Intrusion of surface warm water and bottom cold water into the Kii Channel, Umi-to-Sora, 73, 81-92, 1998. (In Japanese).